united nations
educational, scientific
and cultural
organization

international atomic
energy agency

the
abdus salam
international centre for theoretical physics

SMR/1270-31

SCHOOL ON SYNCHROTRON RADIATION

6 November - 8 December 2000

Miramare - Trieste, Italy

Supported in part by the Italian Ministry of Foreign Affairs in connection with the SESEME project

Co-sponsors: Sincrotrone Trieste, Società Italiana di Luce di Sincrotrone (SILS) and the Arab Fund for Economic and Social Development

Photoemission II

Chuck Fadley
Lawrence Berkeley Laboratory
Berkeley, United States of America

strada costiera 11 - 34014 trieste italy - tel. +39 040224011 fax +39 040224163 - sci_info@ictp.trieste.it - www.ictp.trieste.it

9

The Study of Surface Structures by Photoelectron Diffraction and Auger Electron Diffraction

Charles S. Fadley

ABBREVIATIONS AND ACRONYMS

AED	Auger electron diffraction
APD	azimuthal photoelectron diffraction
ARPEFS	angle-resolved photoemission fine structure (acronym for scanned-energy photoelectron diffraction)
CMA	cylindrical mirror analyzer
DL	double-layer model
EELS	electron energy loss spectroscopy
ESDIAD	electron stimulated desorption ion angular distributions
EXAFS	extended X-ray absorption fine structure
FT	Fourier transform
FWHM	full width at half maximum intensity
GIXS	grazing incidence X-ray scattering
HT	high temperature limit (in SPPD experiment)
LEED	low energy electron diffraction
LT	lower temperature of measurement (in SPPD experiment)
ML	monolayer
MEIS	medium-energy ion scattering
MQNE	magnetic quantum number expansion
MS	multiple scattering
MSC	multiple scattering cluster
MTL	missing-top-layer model
NEXAFS	near edge X-ray absorption fine structure = XANES

Charles S. Fadley • Department of Chemistry, University of Hawaii, Honolulu, Hawaii 96822. *Present address:* Department of Physics, University of California–Davis, Davis, California 95616, *and* Materials Science Division, Lawrence Berkeley Laboratory, Berkeley, California 94720.

Synchrotron Radiation Research: Advances in Surface and Interface Science, Volume 1: Techniques, edited by Robert Z. Bachrach, Plenum Press, New York, 1992.

NPD	scanned-energy photoelectron diffraction with normal emission
ODAC	one-dimensional alkali-chain model
OPD	scanned-energy photoelectron diffraction with off-normal emission
PD, PhD	photoelectron diffraction
PLD	path-length difference
PPD	polar photoelectron diffraction
PW	plane-wave scattering
RBS	Rutherford back scattering
SEXAFS	surface extended X-ray absorption fine structure
SMSI	strong metal support interaction
SPAED	spin polarized Auger electron diffraction
SPPD	spin polarized photoelectron diffraction
SRMO	short-range magnetic order
SS	single scattering
SSC	single scattering cluster
STM	scanning tunneling microscopy
SW	spherical-wave scattering
XANES	X-ray absorption near-edge structure = NEXAFS
XPD	X-ray photoelectron diffraction, typically at energies of 500–1400 eV
XPS	X-ray photoelectron spectroscopy

1. INTRODUCTION

A knowledge of the atomic identities, positions, and bonding mechanisms within the first 3–5 layers of a surface is essential to any quantitative microscopic understanding of surface phenomena. This implies knowing bond directions, bond distances, site symmetries, coordination numbers, and the degree of both short-range and long-range order present in this selvedge region. A number of surface-structure probes have thus been developed in recent years in an attempt to provide this information.[1] Each of these methods has certain unique advantages and disadvantages, and they are often complementary to one another.

We will here concentrate on the basic experimental and theoretical aspects of photoelectron diffraction (PD or PhD) and its close relative, Auger electron diffraction (AED). Although the first observations of strong diffraction effects in X-ray photoelectron emission from single-crystal substrates by Siegbahn *et al.*[2] and by Fadley and Bergstrom[3] took place almost 20 years ago, and the use of such effects at lower energies to determine surface structures was proposed by Liebsch[4] 15 years ago, it was not until about 10 years ago that quantitative experimental surface-structure studies were initiated by Kono *et al.*,[5] Woodruff *et al.*,[6] and Kevan *et al.*[7] By now both photoelectron diffraction and Auger electron diffraction are becoming more widely used to study surface atomic geometries.[8–13] We will thus consider here both the present status and future prospects of these methods, and then return at the conclusion of this chapter to make a critical comparison of them with several other surface-structure probes such as LEED, grazing incidence X-ray scattering (GIXS), and scanning tunneling microscopy (STM).

The basic experiment in PD or AED involves exciting a core photoelectron or a relatively simple core-like Auger transition from an atom in a single-crystal environment and then observing modulations in the resulting peak intensities that are due to final-state scattering from atoms neighboring the emitter. For a general Auger peak of the type XYZ, it is thus important that the upper levels Y and Z involved are not so strongly influenced by chemical bonding as to induce an anisotropy in emission that is more associated with initial-state electronic structure. The directly emitted photoelectron- or Auger electron–wave exhibits interference with various scattered waves, and this interference pattern is analyzed to derive structural information. Peak intensities can be monitored as a function either of the emission direction or, in the case of photoelectron diffraction, of the exciting photon energy. In AED, excitation can also derive from anything producing core holes: an electron beam, VUV/soft-X-ray radiation, or even an ion beam.

The three basic types of measurement possible are as shown in Fig. 1: an azimuthal or ϕ scan, a polar or θ scan, and, for photoelectron diffraction, a scan of energy in a normal or off-normal geometry. Several abbreviations and acronyms have arisen in connection with such measurements. With soft X-ray excitation at about 1.2–1.5 keV at the typical X-ray photoelectron spectroscopy (XPS) limit, scanned-angle measurements have been termed X-ray photoelectron diffraction (XPD).[5,9] Scanned-energy photoelectron measurements spanning the VUV-to-soft-X-ray regime have also been called normal photoelectron diffraction (NPD),[7,8,14] off-normal photoelectron diffraction (OPD),[15] or angle-resolved photoemission fine structure (ARPEFS)[8] to emphasize their similarity to the more familiar surface extended X-ray absorption fine structure (SEXAFS).[16] Both standard X-ray sources and synchrotron radiation can be used for excitation, with photon energies being as low as 60 eV[6,17,18] and as high as a few keV.[7,8,19] Synchrotron radiation adds the capability of varying the photon energy continuously and of studying the dependence of the diffraction on polarization.

The degree of modulation of intensity observed in PD or AED experiments can be very large, with overall values of anisotropy as high as $(I_{max}-I_{min})/I_{max} = \Delta I/I_{max} = 0.5$–$0.7$. Thus, it is not uncommon to observe 30–50% changes in the peak intensity as a function of direction or energy, and such effects are relatively easy to measure. This is by contrast with the related surface-structure technique

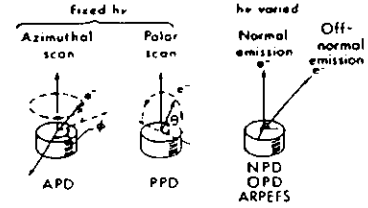

FIGURE 1. The three basic types of photoelectron or Auger electron diffraction measurement: an azimuthal (ϕ) scan at constant polar angle, sometimes referred to as azimuthal photoelectron diffraction or APD; a polar (θ) scan at constant azimuthal angle, referred to as polar photoelectron diffraction or PPD; and a scan of $h\nu$ in fixed geometry that can be done only in photoelectron diffraction and for emission either normal or off-normal to the surface (denoted NPD or OPD, respectively). The scanned-energy type has also been referred to as angle-resolved photoemission fine structure or ARPEFS. Note that θ is measured with respect to the surface.

of SEXAFS,[16] in which typical modulations are about one tenth as large. This difference arises from the fact that SEXAFS effectively measures an angle-integrated photo electron diffraction pattern as a function of energy, and it is not surprising that this integration averages over various phases and leads to considerably lower relative effects.

We shall consider both scanned-angle photoelectron and Auger results and scanned-energy photoelectron results here. To date, scanned-angle studies are much more numerous; this is due to their greater simplicity, since scanned-energy work has several requirements in addition: the sweeping of photon energy with a synchrotron radiation source, the correct normalization of photon fluxes and electron-analyzer transmissions as a function of energy, and the possibility of allowing for interference between Auger peaks and photoelectron peaks in certain kinetic-energy ranges. Finally, it requires more-complex theoretical calculations in that scattering phase shifts and other nonstructural parameters have to be generated for all of the energies in a scan.[8,19–22] However, an advantage in scanned-energy work is that Fourier transform (FT) methods can be used to estimate the path-length differences for various strong scatterers.[8,20–22]

A key element in either photoelectron or Auger electron diffraction is the energy dependence of the relevant elastic-scattering factors. Figure 2 illustrates this for the case of atomic Ni with curves of the plane-wave scattering amplitude $|f_{Ni}|$ as a function of both the scattering angle θ_{Ni} and the electron energy. For low energies of 50–200 eV, it is clear that there is a high amplitude for scattering into all angles. For the intermediate range of about 200–500 eV, it is a reasonable approximation to think of only forward scattering ($\theta_{Ni} = 0°$) and backscattering ($\theta_{Ni} = 180°$) as being important. However, at energies above 500 eV, we see that the scattering amplitude is significant only in the forward direction, in which it is strongly peaked. The degree of forward peaking increases as the energy is increased. The utility of such forward scattering at higher energies in surface-structural studies was noted in very early XPD investigations,[5,23] and it has more recently been termed a "searchlight effect"[11] or "forward focusing"[24] in connection with XPD analyses of epitaxial overlayers. This effect turns out to be one of the most useful and simply interpretable aspects of higher-energy photoelectron or Auger electron diffraction, and we will make reference to it in several of the examples considered in following sections. These qualitative observations concerning the energy dependence of the scattering factor will later also assist in explaining which multiple scattering effects may be the most significant. A special aspect of such scattering factors is that they may exhibit zeroes for certain angles and energies; this has been termed a generalized Ramsauer–Townsend effect, and its influence on the analysis of ARPEFS data is considered elsewhere.[21,25]

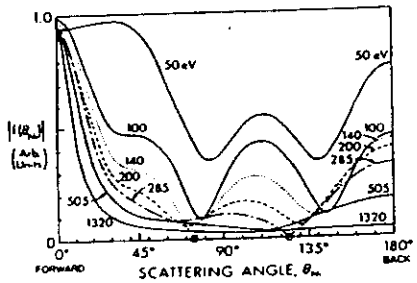

FIGURE 2. Nickel plane-wave scattering factor amplitudes $|f_{Ni}|$ as a function of both the scattering angle θ_{Ni} and the photoelectron kinetic energy. Note the zeroes occurring for both 140 eV and 285 eV, which have been termed a generalized Ramsauer–Townsend effect. (From Ref. 21.)

A final important aspect of either photoelectron or Auger electron diffraction is that both are *atom-specific* probes of *short-range order*. Thus, each type of atom in a sample can in principle be studied, and each will have a unique diffraction signature associated with the neighbors around it. Previous work shows that the principal features of diffraction curves are due to the geometry of the first 3–5 spheres of scatterers around a given emitter, although data may exhibit useful fine structure that is associated with scatterers as far as 20 Å away.[20,26] This short-range sensitivity is thus shared with SEXAFS. We will later point out the potential uses of PD and AED in studying the degree of order present in the near neighbors of the emitter.

The remainder of this chapter begins by briefly reviewing the experimental requirements of these methods and considering both the simplest single-scattering model and other more accurate models that have been used to analyze both PD and AED data. The bulk of the text discusses several illustrative cases to which these techniques have been applied. This is not intended to be an exhaustive listing of all such studies to date, but the examples have been chosen to demonstrate certain basic phenomena, to illustrate the range of structural information that can be obtained, and to provide some idea of the different classes of systems that can be fruitfully studied. In certain cases, the limitations of the analysis or the need for future improvements are pointed out. Finally, some particularly interesting new directions for the future are discussed, and comparisons to other currently used structural probes are also made.

The studies discussed represent a mixture of work utilizing both standard X-ray or electron excitation sources and synchrotron radiation, with the number of investigations using standard sources certainly being greater to date. Thus, the methods discussed here are not limited to synchrotron radiation, by contrast with several others discussed in this volume.[27,28] However, both PD and AED will benefit greatly by the use of the higher-intensity facilities in the vacuum ultraviolet/soft X-ray range that are now becoming more available, and we return to this point toward the end of the chapter.

2. EXPERIMENTAL CONSIDERATIONS

The basic experimental requirements for carrying out photoelectron or Auger electron diffraction measurements are relatively simple. A minimal experiment can consist of the excitation source, a specimen holder with only one axis of angular motion (usually the polar angle as defined in Fig. 1), and an electron energy analyzer with an angular resolution of at least approximately ±5°. Thus, most of the commercially available hemispherical analyzers are suitable, and even a cylindrical mirror analyzer (CMA) with some sort of baffle at its entry slit can be used. Peak intensities can be measured very simply as the difference in

height between some point at the maximum and a point in the high-energy background. Measurements at this level are thus quite easy to take, and interesting surface-structural information has been obtained from them.[11]

Going beyond this minimal experiment to be able to tap all of the information available in the diffraction pattern involves several possible elaborations:

- The specimen holder should have both polar and azimuthal axes of rotation (cf. Fig. 1) so that the electron emission direction can be oriented arbitrarily with respect to the surface. The optimal scanning capabilities in this case are to be able to vary θ from grazing excitation incidence to grazing electron exit and to vary ϕ over a full 360° or more. The latter is very useful for establishing the symmetry of the surface and for verifying the reproducibility of features from one symmetry-equivalent azimuthal direction to another. Scanning ϕ over its full range is the most difficult to achieve in practice if there are electrical or mechanical connections to the sample for heating, cooling, or measuring temperature, but designs of this type have been in use for some time.[9] The reproducibility and accuracy of both of these motions should be at least ±0.5°, with even smaller values on the order of ±0.1° being required for very high angular resolution work.
- Automated scanning of spectra, determining of peak intensities by more accurate area-integration and/or peak-fitting procedures, and stepping of angles under computer control are also essential for efficiently obtaining the most reliable data. Systems for doing this are discussed elsewhere.[9,29]
- It also may be desirable to rotate both the specimen and the analyzer (or excitation source) on two axes so as to be able to orient the excitation source at various positions with respect to the electron emission direction. In photoelectron diffraction, this permits making use of the radiation polarization to preferentially excite the direct wave toward different scatterers while at the same time observing the electron intensity along a special direction.[8,19] This is particularly important in studies utilizing synchrotron radiation. In Auger electron diffraction, it can also be useful for assessing the degree to which the penetration of the exciting flux along different incidence directions influences the outgoing diffraction pattern, even though results to date indicate that such effects are minor.[30] (Similar anisotropic penetration might also be expected with X-rays due to Bragg reflections,[2,3] but such effects have so far not been found to be significant in photoelectron diffraction patterns.)
- Improving the angular resolution of the analyzer to the order of ±1.0° has also been found to yield data at higher energies with considerably more fine structure.[10,26] Achieving this may involve specially designed entrance optics,[31,32] or more simply the use of movable tube-array baffles at the entry to a more standard analyzer.[33] High-resolution results of this kind will be discussed in more detail in sections 4.2.1, 4.2.2, and 5.1.
- Improving the energy resolution of the system to on the order of 0.1 eV is also desirable, because it permits resolving small chemical shifts or surface shifts of core levels and studying the diffraction patterns of these species separately.[18]
- Scanning angle or energy obviously involves an added cost in time for any study, and so it is desirable to have the highest overall count rates. This can be achieved by using a more-intense excitation source (as, for example, from insertion-device-generated synchrotron radiation) and/or the most efficient and highest-speed electron analyzer and detection system. Making the latter as effective as possible is important, since there are always potentially deleterious effects of radiation damage as the excitation intensity is increased. Analyzer improvements include the use of multichannel energy-detection systems involving several single-channel electron multipliers or a microchannel plate[32,34] and the use of special spectrometer geometries in which spectra at several angles can be recorded at the same time.[35–37] However, a potential disadvantage of systems recording several angles at once is that the angular resolution may be limited, particularly if it is desired to scan kinetic energies to several hundred eV. A final method for increasing data acquisition rates with a pulsed synchrotron radiation source is to use a time-of-flight analysis system;[38] a logistical problem with such systems however, is that they may require running the storage ring in a less frequently used "timing" mode with fewer electron bunches. Leckey[39] has recently reviewed many of the more novel proposals for analyzers with high energy resolution, high angular resolution, and/or high data acquisition rates.
- Finally, if scanned-energy photoelectron diffraction is to be performed, it is essential to use a reasonably stable synchrotron radiation source and to have an analyzer system whose transmission properties as a function of energy are well understood. This is because photon energies must be scanned in small steps over a total period on the order of hours in present experiments, and the influences of both the decay of photon flux with time and the change of the analyzer's sensitivity with kinetic energy must be corrected out of the final intensity data so as to yield something that is truly proportional to the energy-dependent photoelectric cross section in a given emission direction. Methods for making these corrections are discussed elsewhere.[8,20]

3. THEORETICAL MODELING

3.1. Single-Scattering Theory

3.1.1. Overview of Model

Since the first theoretical paper on low-energy photoelectron diffraction by Liebsch,[4] several detailed discussions of the modeling of photoelectron and Auger electron diffraction have appeared in the literature.[9,15,21,24,25,40–45] Thus, we will begin here by presenting only the essential ingredients of the simplest approach, the single-scattering cluster (SSC) model, and then comment toward the end of this section on several improvements that can be made to it, as well as on some effects expected due to multiple scattering (MS) events.

The basic elements of this single-scattering cluster model are shown schematically in Fig. 3(a). The fundamental assumptions are essentially identical to those used in describing extended X-ray absorption fine structure (EXAFS),[41] and a similar model has also been applied some time ago to angle-resolved Auger emission at very low energies of ≤100 eV.[40] We consider photoelectron emission first and then discuss the modifications required to describe Auger emission.

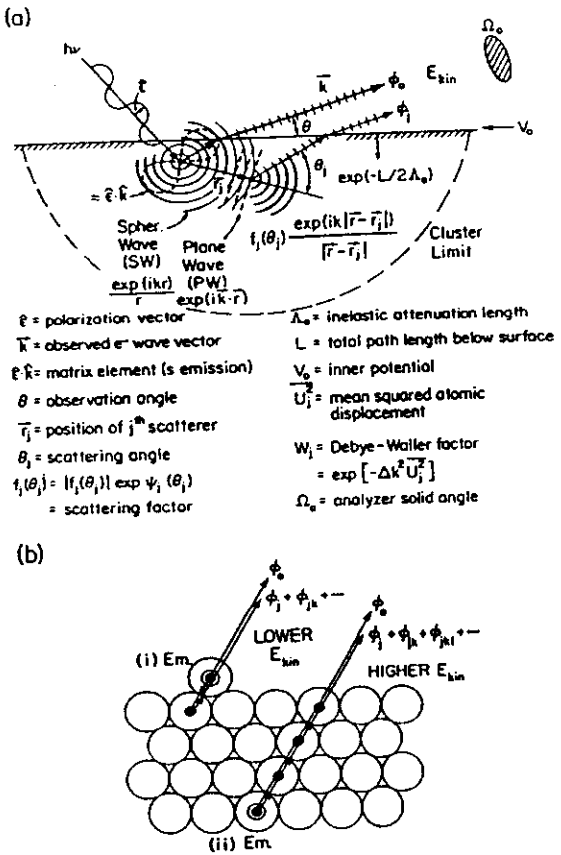

FIGURE 3. (a) Illustration of the assumptions used in the single-scattering cluster (SSC) model, with various important quantities indicated. (b) Two types of multiple-scattering corrections to the SSC model that may be significant for certain energies and geometries: (i) at lower energies of <200 eV, backscattering from a nearest-neighbor atom behind the emitter and then forward scattering by the emitter (from Ref. 25); (ii) multiple forward scattering along lines of closely spaced atoms that leads to a reduction of the expected intensity enhancement, particularly at higher energies of >500 eV (from Refs. 24 and 73).

Radiation with polarization $\hat{\mathbf{e}}$ is incident on some atom in a cluster, from which it ejects a core-level photoelectron. (In Fig. 3a, the emitting atom is shown near the surface, but it could as well be any atom in the substrate.) If the initial core-electron wave function is denoted by $\psi_c(\mathbf{r})$ and the final photoelectron wave function corresponding to emission with wave vector $\mathbf{k}$ by $\psi(\mathbf{r}, \mathbf{k})$, then the

observed intensity will be given in the dipole approximation by

$$I(\mathbf{k}) \propto |\langle \psi(\mathbf{r}, \mathbf{k}) | \hat{\mathbf{e}} \cdot \mathbf{r} | \psi_c(\mathbf{r}) \rangle|^2. \quad (1)$$

The final-state wave function in single scattering is further described as being the superposition of a direct wave $\phi_0(\mathbf{r}, \mathbf{k})$ and all singly scattered waves $\phi_j(\mathbf{r}, \mathbf{r}_j \rightarrow \mathbf{k})$ that result from initial ϕ_0 emission toward a scatterer j at $\mathbf{r}_j$ and then subsequent scattering so as to emerge from the surface in the direction of $\mathbf{k}$. Thus, the overall wave function can be written as[21,41]

$$\psi(\mathbf{r}, \mathbf{k}) = \phi_0(\mathbf{r}, \mathbf{k}) + \sum_j \phi_j(\mathbf{r}, \mathbf{r}_j \rightarrow \mathbf{k}). \quad (2)$$

Because the detector is situated at essentially infinity along $\mathbf{k}$, all of the waves in Eq. (2) can finally be taken to have the limiting spherical forms $\phi_0 \propto \exp(ikr)/r$ or $\phi_j \propto \exp(ik|\mathbf{r} - \mathbf{r}_j|)/|\mathbf{r} - \mathbf{r}_j|$, although the effective amplitudes and phases of each type in a given direction will be modulated by the photoexcitation matrix element and, for each ϕ_j, also $\exp(ikr_j)/r_j$ and the scattering factor. Flux conservation also dictates that the portion of ϕ_0 which passes to the scatterer j to produce ϕ_j decays in amplitude as a spherical wave, or as $1/r_j$. This decay is a principal reason why PD and AED are short-range probes, although the effects of inelastic scattering contribute additionally to this. If the scattering angle is θ_j, the overall path length difference (PLD) between ϕ_0 and any ϕ_j is $r_j(1 - \cos\theta_j)$, and it is these PLDs that provide most of the bond-length information in photoelectron or Auger electron diffraction.

3.1.2. Matrix Elements and Final-State Interference

When this model has been applied to photoelectron emission, the dipole matrix element has usually been treated as involving a p-wave final state (that is, the case that is appropriate for emission from an s subshell). This yields a matrix-element modulation of the form $\hat{\mathbf{e}} \cdot \hat{\mathbf{k}}$ for an arbitrary direction of emission $\hat{\mathbf{k}}$.[21,41] For emission from other subshells with l not equal to zero, more complex expressions including both of the interfering $l + 1$ and $l - 1$ channels are involved,[43,45–47] and we return below to consider how important these effects can be. However, at higher energies, the assumption of a p-wave final state has been found to be reasonably adequate in several prior studies of non-s emission.[9,10,48–50]

Since the differential photoelectric cross section $d\sigma_n/(\hat{\mathbf{e}}, \mathbf{k})/d\Omega$ is proportional to intensity rather than amplitude, another possible approximation might be to use a ϕ_0 modulation of $[d\sigma_n/(\hat{\mathbf{e}}, \mathbf{k})/d\Omega]^{1/2}$.[51] Although this is not strictly correct and it also does not account for possible sign changes in the matrix element with direction due to the photoelectron parity,[15,52] it may be a reasonably adequate approximation for higher-energy XPD in which the forward-dominated electron-scattering process selects out $\mathbf{r}_j$ choices very nearly parallel to $\mathbf{k}$. That is, for the range of $\mathbf{r}_j$ directions near the $\mathbf{k}$ direction that produce significant scattering, the matrix element varies little, so that a very precise description of it is not required. In fact, predicted XPD patterns have not been found to be very sensitive to the

exact way in which the matrix-element modulation is included. At lower energies, such simplifications are not generally possible, however, and Treglia[53] has, for example, recently shown that not using the correct final-state angular momenta can have a strong effect on predicted azimuthal diffraction patterns at energies of about 30 eV.

Such final-state momentum and interference effects have been studied in more detail recently by Friedman and Fadley,[47] who have made use of a newly developed Green's function matrix approach due to Rehr and Albers.[54] Representative results as a function of electron kinetic energy are presented in Fig. 4. Here, a Cu emitter is 3.5 Å away from a single Cu scatterer, and three different electron kinetic energies of 100, 300, and 1000 eV are considered. Scattering is in all cases full spherical wave. The intensity fluctuations as a function of scattering angle are normalized to the unscattered intensity I_0 as $\chi = [I - I_0]/I_0$. In order to illustrate in these calculations only the effects of changing the final-state angular momenta that are involved, emission from a Cu $2p$ orbital was taken as a reference. For this p-emission case, the correct final-state interference involves s

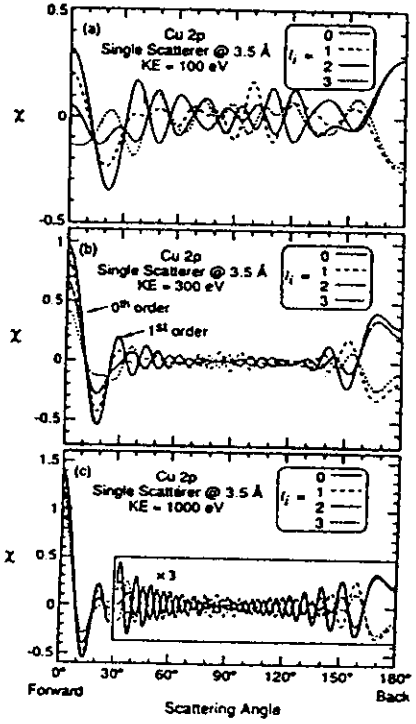

FIGURE 4. Theoretical calculations of electron scattering from a single Cu atom at a distance of 3.5 Å from the emitter and for energies of (a) 100 eV, (b) 300 eV, and (c) 1000 eV. Intensity is shown as the normalized function $\chi = (I - I_0)/I_0$. Full spherical-wave (SW) scattering is used, and different final-state assumptions are compared: l_f = 0 (s to a single p channel), l_f = 1 (p to interfering $s + d$ channels), l_f = 2 (d to $p + f$), and l_f = 3 (f to $d + g$). The radiation is taken to be unpolarized, with the plane of polarization lying in the plane of r_{Cu} and k. Note the sign reversals due to photoelectron parity in the backscattering direction. (From Ref. 47.)

and d waves, and includes the radial matrix elements R_s and R_d and the phase shifts δ_s and δ_d. These have been calculated using an atomic cross-section program due to Manson.[55] The ratio R_d/R_s changes relatively little, from 4.62 to 3.91, as we go from 100 eV to 1000 eV. The curves shown for $l_i = 0$ are the simple limit, discussed previously, of an s initial state and single p final state with no interference. The results for $l_i = 1$ are the correct description of Cu $2p$ emission. For the other two cases of $l_i = 2$ and $l_i = 3$ shown, emission into final waves at $l_f = 1$ and 3 and $l_f = 2$ and 4, respectively, is allowed, and the same radial matrix elements R_s and R_d and phase shifts δ_s and δ_d were used for the $l_f = l_i + 1$ and $l_f = l_i - 1$ channels in both cases. These sets of four curves thus permit systematically observing only the effect of the different final-state character and interference associated with the dipole matrix element.

Several general conclusions can be drawn from the curves of Fig. 4:

- Increasing the angular momenta in the final state from 1 to 0 + 2 to 1 + 3 to 2 + 4 is found to decrease systematically the amplitude of forward scattering, thus constituting a reason for which calculations using the p final state may overpredict the degree of anisotropy for emission from subshells with $l_i \geq 1$.
- In the backscattering direction, the parity of the photoelectron waves is evident, since the odd waves from $l_i = 0$ and 2 exhibit the same sign of χ, and the opposite sign is seen for the even waves from $l_i = 1$ and 3. The previously discussed approximation of using the square root of the differential cross section neglects these sign differences. It implicitly assumes photoelectron waves of even character unless an *ad hoc* sign change is introduced as appropriate for emission angles greater than 90° with respect to the polarization vector.[15]
- The smallest differences between different final-state angular momenta are for the highest energy, where, in the dominant forward direction, the main effect is a reduction of amplitudes in the forward scattering direction, but little change occurs in the shapes of the '0th-order' peak at a scattering angle of 0° and, for $l_i < 3$, also in the 1st-order peak at about 22°. However, as energy is decreased to 100 eV, the differences between the curves become increasingly more significant, and they begin also to involve phase changes in the regions of both of these peaks nearest forward scattering.
- At the highest energy typical of the XPS limit, one thus expects the general shape of the 0th order or forward scattering peak to be the same regardless of final-state angular momenta, and to see a general suppression of the relative importance of the higher-order features.

Overall, these results indicate that the use of the correct final-state angular momenta with interference will probably be important for energies below about 500 eV. For higher energies of 1000 eV or move, forward scattering should be reasonably well treated by the simple p final state (as has been verified in prior XPD studies), although both overall anisotropies and the relative intensities of higher-order features may be overestimated. Similar conclusions concerning the suppression of higher-order diffraction features have been reached by both Parry[46] and Sagurton[56] using more approximate calculations based upon plane-wave scattering and/or plane-wave final states.

Keeping in mind the discussion of the last paragraphs, we shall for simplicity and heuristic reasons in what follows still use the p final state and its factor $\hat{\epsilon} \cdot \hat{k}$ in describing photoelectron emission.

3.1.3. Electron–Atom Scattering

The electron–atom scattering that produces ϕ_j is most simply described by a complex plane-wave (PW) scattering factor

$$f_j(\theta_j) = |f_j(\theta_j)| \exp [i\psi_j(\theta_j)]. \tag{3}$$

where $\psi_j(\theta_j)$ is the phase shift associated with the scattering. The scattering factor is in turn calculated from partial-wave phase shifts δ_l according to the usual expression:

$$f(\theta) = (2ik)^{-1} \sum_{l=0}^{\infty} (2l + 1)[\exp (2i\delta_l) - 1]P_l(\cos \theta), \tag{3'}$$

where the P_l are Legendre polynomials. For large r, the scattered wave ϕ_j is thus proportional to $f_j(\theta_j) \exp (ik|\mathbf{r} - \mathbf{r}_j|)/|\mathbf{r} - \mathbf{r}_j|$, with an overall phase shift relative to ϕ_0 of $kr_j(1 - \cos \theta_j) + \psi_j(\theta_j)$ that is due to both path-length difference and scattering. The use of this form for ϕ_j implicitly assumes that the portion of ϕ_0 incident on the jth scatter has sufficiently low curvature compared to the scattering potential dimensions to be treated as a plane wave. This is the so-called small-atom approximation,[57] and its limitations in comparison to the more accurate spherical-wave (SW) scattering[21,25,58,59] of Fig. 4 are discussed below.

The PW scattering factor $f_j(\theta_j)$ is thus determined by applying the partial-wave method to a suitable spherically symmetric scattering potential for each atomic type in the cluster. The number of partial-wave phase shifts needed for convergence goes up with energy, and for a typical scattering potential of effective radius 1.5 Å would be ≥8 for $E_{kin} = 500$ eV and ≥24 for 1500 eV. Tabulations of free-atom scattering factors at energies going up to the XPS regime also exist.[60] Alternatively, scattering potentials more appropriate to a cluster of atoms with overlapping charge densities and potentials can be constructed via the muffin-tin model employed, for example, in LEED theory.[61] The free-atom f_j is generally larger in magnitude in the forward direction than its muffin-tin counterparts due to the neglect of charge and potential overlap.[42] Both types of f_j have been employed in higher-energy PD and AED calculations, and they usually do not yield markedly different $I(\mathbf{k})$ curves, although the use of the free-atom f_j is expected to predict slightly higher peak intensities due to its larger amplitudes in the forward direction. The PW scattering factor amplitudes in Fig. 2 were calculated using the more accurate muffin-tin procedure. Whatever procedure is used to calculate these scattering factors, there are two useful generalizations concerning their behavior as atomic number is varied:

- The forward scattering amplitude $|f_j|$ at higher energy is found to be primarily sensitive to the radius of the atom (or muffin tin) involved. It is for this reason that free-atom forward scattering amplitudes are always larger than those for a muffin tin in which the potential is effectively truncated at the tin radius. This behavior can be rationalized by a classsical argument in which it is noted that forward scattering trajectories graze the outer reaches of the scattering potential and so are only deflected slightly; these trajectories are thus primarily sensitive to the outer regions of the potential.
- The backscattering amplitude at higher energy is by contrast found to increase monotonically with atomic number. This also is expected from a classical argument in which backscattering involves strongly deflected trajectories that pass close to the nucleus.

3.1.4. Inelastic Scattering

The effects of *inelastic* scattering on wave amplitudes during propagation below the surface must also be included. If intensity falls off as $\exp(-L/\Lambda_e)$, where L is an arbitrary path length below the surface and Λ_e is the inelastic attenuation length, then *amplitude* is expected phenomenologically to fall off as the square root of this or $\exp(-L/2\Lambda_e) \equiv \exp(-\gamma L)$. Each wave ϕ_0 or ϕ_j is multiplied by such an exponential factor involving an L value which includes the total path length below some surface cutoff point (cf. Fig. 3*a*). This surface cutoff is often chosen to be the substrate surface as defined by hard-sphere atoms,[42] although this choice should not influence the diffraction patterns unless some atoms are positioned above the cutoff. Thus, the attenuation coefficient $\gamma = 1/2\Lambda_e$, although γ values up to 1.3–2 times this have been suggested in prior EXAFS,[41,62] AED,[12] and PD[42,48,63] analyses. That is, the effective inelastic attenuation length Λ_e in these diffraction experiments is suggested to be about 0.50–0.75 times literature values based upon intensity-attenuation measurements or theoretical calculations.[64] In fact, some inelastic attenuation lengths derived from EXAFS measurements do not appear to take account of the difference between amplitude and intensity mentioned above.[62]

These reduced values of Λ_e are not surprising in view of several factors: Uncertainties of at least ±20% are common in measurements of attenuation lengths,[64,65] and some recent measurements in fact yield values that are significantly lower than others in the literature.[65] The effects of elastic scattering and diffraction on intensities can introduce additional uncertainties of this order,[66,67] and it is, for example, now well recognized that the actual mean free path between inelastic scattering events is about 1.4 times the attenuation length discussed above. Finally, the effective attenuation length in a diffraction measurement should be shorter than in a simple intensity-attenuation experiment, because quasielastic scattering events of small energy (e.g., from phonons) that leave the electron kinetic energy within the peak being measured[68] can still introduce direction changes and phase shifts that effectively remove such electrons from the coherent intensity for diffraction. In addition, multiple elastic-scattering events similarly cause a reduction of the effective coherent intensity in a single-scattering theory. Thus, one overall expects effective attenuation lengths related as Λ_e(intensity) > Λ_e(multiple-scattering diffraction) > Λ_e(single-scattering diffraction).

Fortunately, electron diffraction features for most cases are not strongly affected by varying Λ_e over its plausible range, and so its choice is in general not crucial to final structural conclusions. Nonetheless, it is desirable to verify this insensitivity by varying Λ_e in model calculations.[42,48,63]

3.1.5. Vibrational Effects

Vibrational attenuation of interference effects is furthermore potentially important and can be included in the simplest way by multiplying each ϕ_j by its associated temperature-dependent Debye–Waller factor:

$$W_j(T) = \exp[-\Delta k_j^2 \overline{U_j^2}(T)] = \exp[-2k^2(1 - \cos\theta_j)\overline{U_j^2}(T)], \quad (4)$$

where Δk_j is the magnitude of the change in wave vector produced by the scattering, and $\overline{U_j^2}(T)$ is the temperature-dependent one-dimensional mean-squared vibrational displacement of atom j. At this level of approximation, $\overline{U_j^2}$ is assumed to be isotropic in space, and any correlations in the movements of near-neighbor atoms are neglected. (The importance of *correlated* vibrational motion in certain types of lower-energy diffraction experiments is considered below.) Suitable bulk and surface $\overline{U_j^2}$ values or Debye temperatures can be obtained from the literature. At high energy, the electron scattering is significant only when θ_j is rather close to zero, and this acts through the $(1 - \cos\theta_j)$ factor in the argument of Eq. (4) to yield W_j very close to unity for all important scattered waves. So vibrational effects are to first order not very significant in forward-scattering-dominated XPD or AED, although they can be very important in LEED, EXAFS, and lower-energy PD and AED, where backscattering is the dominant diffraction mode and thus $1 - \cos\theta_j$ is a maximum.

An alternate method for allowing for vibrational effects is to assume some probability distribution of atomic positions due to vibration (as, for example, a harmonic-oscillator envelope) and then to numerically sum separate weighted diffraction intensities for all possible combinations of atomic positions. This is cumbersome, but it has been used to quantitatively look at the effects of specific types of wagging molecular vibrations at surface.[23,69]

3.1.6. Single-Scattering Cluster Model

With these assumptions, the simplest SSC–PW expression for photoelectron intensity $I(\mathbf{k})$ can now be written down from Eqs. (1–3) as

$$I(\mathbf{k}) \propto \int \left| \hat{\boldsymbol{\varepsilon}} \cdot \hat{\mathbf{k}} e^{-\gamma L} + \sum_j \frac{\hat{\boldsymbol{\varepsilon}} \cdot \hat{\mathbf{r}}_j}{r_j} |f_j(\theta_j)| W_j e^{-\gamma L_j} \{\exp i[kr_j(1 - \cos\theta_j) + \psi_j(\theta_j)]\} \right|^2 d\hat{\boldsymbol{\varepsilon}}$$
$$+ \sum_j \int (\hat{\boldsymbol{\varepsilon}} \cdot \hat{\mathbf{r}}_j)^2 \frac{|f_j(\theta_j)|^2}{r_j^2} (1 - W_j^2) e^{-2\gamma L_j} d\hat{\boldsymbol{\varepsilon}}. \quad (5)$$

Here, $\hat{\boldsymbol{\varepsilon}} \cdot \hat{\mathbf{k}}$ and $\hat{\boldsymbol{\varepsilon}} \cdot \hat{\mathbf{r}}_j$ represent p-wave photoemission matrix-element modulations along the unit vectors $\hat{\mathbf{k}}$ and $\hat{\mathbf{r}}_j$, respectively, and $\exp(-\gamma L)$ and $\exp(-\gamma L_j)$ are

appropriate inelastic attenuation factors. Thus, $(\hat{\boldsymbol{\varepsilon}} \cdot \hat{\mathbf{k}}) \exp(-\gamma L)$ is the amplitude of the direct wave $\phi_0(\mathbf{r}, \mathbf{k})$ and $(\hat{\boldsymbol{\varepsilon}} \cdot \hat{\mathbf{r}}_j)|f_j(\theta_j)| W_j \exp(-\gamma L_j)/r_j$ is the effective amplitude of $\phi_j(\mathbf{r}, \mathbf{r}_j \rightarrow \mathbf{k})$ after allowance for both inelastic scattering and vibrational attenuation of interference. The complex exponential allows for the total final phase difference between ϕ_0 and each ϕ_j.

The integrals on $\hat{\boldsymbol{\varepsilon}}$ simply sum over the different polarizations perpendicular to the radiation progagation direction, as appropriate to the particular case at hand. Closed-form expressions for a totally unpolarized source that are applicable to high-energy work are given elsewhere;[42] however, the simplest way to carry out this integration for a general case is just to sum the intensities for two perpendicular polarizations of convenient orientation.

The second $\sum_j$ corrects the first absolute value squared for the incorrect inclusion of Debye–Waller attenuations in terms involving a product of a scattered wave with itself. That is, in expanding the absolute value squared, only products involving unlike waves like $\phi_0\phi_j^*$ or $\phi_j\phi_l (j \neq l)$ should include Debye–Waller products of W_j or W_jW_l, respectively. The $(1 - W_j^2)$ factor in the second summation is thus necessary to yield overall correct products of the form $\phi_j\phi_j^*$ without any W_j^2 factor. The second sum has been called thermal diffuse scattering,[40] and it is often quite small with respect to the overall modulations. Equation (5) is thus the basic starting point of the single-scattering cluster model.

In modifying this model to describe Auger emission, the usual assumption is that the much freer mixing of angular momenta in the final state overall leads to an outgoing wave with s character.[12,40,70–73] Although selection rules do limit the allowed final angular momentum states in Auger emission,[72] for certain cases, the $l = 0$ channel is dominant. Also, if filled subshells are involved in both the initial and final levels of the transition, the implicit sums over all initial and final m_l values would be expected to produce an overall distribution of emitted primary intensity that could be approximated as an s wave. Although it is possible for higher-l components to be present in the final state that could affect the scattering,[72,73] these are often found at higher energies to be minor effects.[12,70,71] For Auger emission into such an assumed s final state, we thus simply remove all factors involving $\hat{\boldsymbol{\varepsilon}} \cdot \hat{\mathbf{k}}$ and $\hat{\boldsymbol{\varepsilon}} \cdot \hat{\mathbf{r}}_j$ in Eq. (5). Non-s character in Auger final states deserves further study however.

It is also worth noting here that the cluster sum on j in Eq. (5) makes no explicit use of the 2- or 3-dimensional translational periodicities that may be present, even though the atomic coordinates $\mathbf{r}_j$ used as inputs may incorporate such periodicities. Thus, neither surface- nor bulk-reciprocal lattice vectors $\mathbf{g}$ are explicitly involved, and it is not appropriate at this level of description to speak of diffraction "beams" associated with certain $\mathbf{g}$ vectors as in LEED. However, in section 5.1 we will consider the relationship of this model to an alternative Kikuchi-band picture that does involve $\mathbf{g}$ vectors and the idea of Bragg reflections from sets of planes.

The last parameter of importance in actually using Eq. (5) is the range of j or the choice of a suitable cluster of atoms. This is done empirically so as to include all significant scatterers by verifying that the predicted diffraction patterns do not change in any significant way with the addition of further atoms at the periphery of the cluster. Clusters can range from a few atoms for near-normal high-energy emission from a vertically oriented diatomic molecule on a surface[23] to as many as

several hundred atoms for substrate emission in which both the emission and the scattering must be summed over several layers into the bulk.[42] In the latter case, each structurally unique type of atom emits incoherently with respect to the other, so that intensities from each must be added layer by layer. However, even for the largest clusters so far considered, the inherent simplicity of Eq. (5) still yields calculations which do not consume excessive amounts of computer time, especially by comparison with those necessary for such procedures as multiple-scattering LEED simulations.

A further physical effect of importance in making comparisons to experiment is the possibility of electron refraction at the surface in crossing the surface barrier or inner potential of height V_0. Even at the relatively high energies of XPS, for emission angles near grazing, refraction effects of a few degrees can be produced (cf. Fig. 14 in Ref. 9). Thus, for lower takeoff angles relative to the surface and/or lower kinetic energies, a proper allowance for refraction is necessary. This is accomplished most simply by using a suitable inner potential V_0 derived from experiment and/or theory to predict the internal angle of emission θ' for a given external propagation direction θ.[9] The resulting expression for an electron energy of $E'_{kin} = E_{kin} + V_0$ inside the surface is

$$\theta' = \cos^{-1}\left\{\left[\frac{E_{kin}}{E_{kin} + V_0}\right]^{1/2} \cos\theta\right\}, \tag{6}$$

where, as before, θ and θ' are measured with respect to the surface. In the presence of an adsorbate, the exact form of the surface potential barrier thus becomes important, as it may not then be possible to assume an abrupt rise to the vacuum level at the substrate surface. Also, the presence of adsorbate atoms may alter V_0 through changes in the work function, and these atoms also may occupy positions above the surface in which only a fraction of V_0 is appropriate. In some photoelectron diffraction studies, V_0 has also been treated as an adjustable parameter.[20,25,63] Although prior studies indicate that structural conclusions are not particularly sensitive to the choice of V_0,[25,42] it is important to realize that not allowing for it properly may shift theoretical diffraction patterns by as much as a few degrees with respect to the actual θ values at which they will be observed. The precise method of allowing for inner potential and related image–force effects has also been considered in more detail theoretically.[25]

We stress also at this point that any uncertainties in final structures associated with the choices of nonstructural parameters such as the scattering phase shifts, the attenuation length for inelastic scattering, vibrational attenuation, and the inner potential are equally well shared with the techniques of LEED, EXAFS, and SEXAFS, although in EXAFS/SEXAFS, empirical phase shifts from known structures can sometimes be used.

A final step in any realistic calculation based upon this model is to integrate the direction of emission $\mathbf{k}$ over the solid angle Ω_0 accepted into the electron analyzer. For most of the calculations reported here, this has been over a cone of ±3.0–3.5° half angle, although for certain high-resolution cases a smaller cone of ±1.0–1.5° has been used.

3.1.7. Improvements to the Model

We now consider some possible improvements to this simple SSC–PW model:

- A first possible correction is to choose a *more correct form for the primary wave as it leaves the emitter*. The SSC–PW result of Eq. (5) assumes a simple outgoing plane wave from the emitter which then scatters to produce an outgoing spherical wave from each scatterer. In fact, the correct primary wave should be of the type used in free-atom photoelectric cross sections and should consist of an ingoing spherical wave plus the outgoing plane wave.[21,41,45,74] Such a primary wave experiences the emitter potential and represents the correct solution to the Schrödinger equation inside of a muffin-tin-like region centered on the emitter. If this form of the primary wave is used, the equivalent of Eq. (5) with neglect of effects due to vibrations is:[21,41]

$$I(\mathbf{k}) \propto \int \left|\hat{\boldsymbol{\epsilon}}\cdot\hat{\mathbf{k}}e^{-r_0/L} + \sum_j \frac{\hat{\boldsymbol{\epsilon}}\cdot\hat{\mathbf{r}}_j}{r_j}|f_j(\theta_j)|\,e^{-r_j/L}\{\exp i[kr_j(1-\cos\theta_j) + \psi_j(\theta_j)]\} + \sum_j \frac{\hat{\boldsymbol{\epsilon}}\cdot\hat{\mathbf{r}}_j}{r_j^2} f_j(\pi) f_{em}(\pi-\theta_j) e^{-r_j/L+2r_j)}\{\exp i[2kr_j]\}\right|^2 d\hat{\boldsymbol{\epsilon}}. \tag{7}$$

This result, although still single scattering in assumption, now contains, through the scattering of the incoming wave, a second sum of terms that are the classic double scattering events of the type emitter → scatterer → emitter → detector discussed in EXAFS theory.[41] Because these added terms are in effect double scattering and also exhibit stronger attenuation due to both $1/r_j^2$ and $e_j^{-2r_j}$, this sum is expected for many cases to be a small correction to Eq. (5). This should be especially true for higher energies where backscattering is negligible. In fact, the inclusion of this sum can be shown to lead to the central-atom (emitter) phase shift that is always present in EXAFS theory, and we comment further on this later in this section.

- A next important correction is the use of *spherical-wave (SW) scattering* instead of the asymptotic and much simpler plane-wave (PW) scattering. The nature of such SW corrections in reducing forward scattering amplitudes in XPD was first pointed out some time ago,[23] but more recent studies have presented detailed comparisons of PW and SW results for different systems.[58,59] For example, Fig. 5 compares PW and SW scattering at energies from 50 eV to 950 eV,[58] with the results being displayed in a format identical to that of Fig. 4. Emission from an s level ($l_i = 0$, $l_f = 1$) to a single Ni scatterer 2.49 Å away is considered. For larger scattering angles (≳40°) and higher energies (≳200 eV), the PW and SW results are essentially identical. However, for lower energies and in the forward scattering direction, there are significant differences. In particular, for energies ≳100 eV, the forward scattering peak is significantly reduced in amplitude by a factor that can be as low as 0.5. As expected, the differences between PW and SW curves also decrease as the scatterer is moved away from the emitter,[58] because in the limit of a scatterer at infinity, the incident wave is

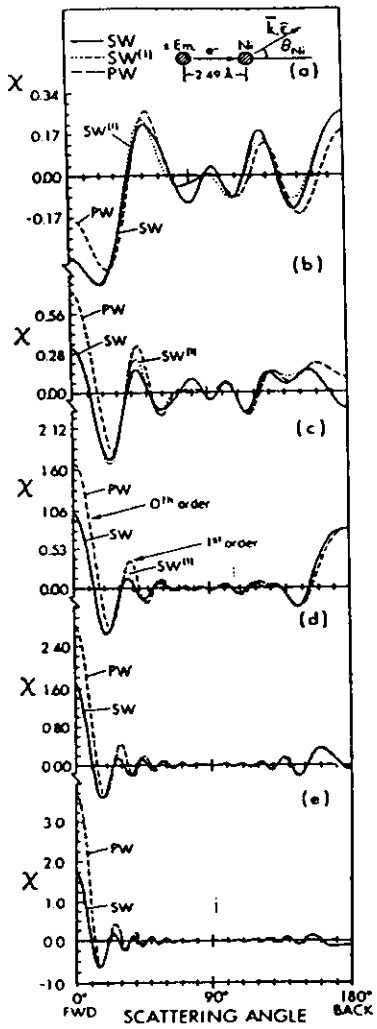

FIGURE 5. As in Fig. 4, but comparing plane-wave (PW) and spherical-wave (SW) scattering from a single Ni scatterer at a distance of 2.5 Å from the emitter with energies of (a) 50 eV, (b) 100 eV, (c) 200 eV, (d) 500 eV, and (e) 950 eV. Here, PW results are compared to SW results for the case of $\ell = 0$ (s emission to a single p channel). Polarization is parallel to the emission direction. The curves labelled $SW^{(1)}$ represent a first-order approximation to the full SW scattering. (From Refs. 21 and 58.)

planar. One general conclusion from these results is thus that, at higher energies, the primary effect of including curvature in ϕ_0 is to reduce the amplitudes of the forward-scattering peaks in $I(\mathbf{k})$ for near-neighbor atoms as compared to those predicted from Eq. (3).

Fortunately, such SW corrections can now be very simply and accurately

incorporated into the SSC framework via effective SW scattering factors developed by Barton and Shirley using a Taylor-series magnetic quantum number expansion (MQNE)[25] and by Rehr *et al.* using separable Green's function approaches.[45,54] For example, Rehr *et al.*[45] derive an equation identical to Eq. (7) in form, but in which the plane-wave scattering factors $f_j(\theta)$ are replaced by three effective spherical-wave scattering factors $f^{(1)}_{j,\text{eff}}(\theta, r_j)$, $f^{(2)}_{j,\text{eff}}(\pi, r_j)$, and $f^{(3)}_{\text{em,eff}}(\pi - \theta, r_j)$ that are used to describe the three types of scattering events present. These effective scattering factors depend on r_j, as they must converge to the PW result as r_j goes to infinity. They are also very simply calculable, involving expressions closely related to that in Eq. (3').

However, particularly at higher energies, the much simpler PW approximation is still found to yield results very similar in form to those with SW scattering, and it has been found possible to draw useful structural conclusions with it. Sometimes, PW scattering at high energy has been used together with an empirical reduction factor of forward scattering amplitudes by a factor of 0.4–0.5[42] that can be largely justified as being due to SW effects (cf. Fig. 5).

• An additional important correction for some cases is the use of *correlated vibrational motion* in which atoms that are near neighbors of the emitter have lower vibrational amplitudes relative to the emitter, and thus Debye–Waller factors for diffraction that are nearer unity. This correction is more important in special geometries and at lower energies for which large-angle or, particularly, backscattering events become more important, as first pointed out in connection with the interpretation of scanned-energy data by Sagurton *et al.*[21] and also discussed by Barton and Shirley.[25] This more correct form for vibrational attenuation involves a factor W_j^{corr} of the form:[21]

$$W_j^{\text{corr}}(T) = \exp\left[\frac{-\Delta k_j^2 \sigma_j^2(T)}{2}\right] = \exp\left[-k^2(1 - \cos\theta_j)\sigma_j^2(T)\right], \tag{8}$$

where $\sigma_j^2(T) = \langle(\Delta\hat{\mathbf{k}}_j \cdot \mathbf{u}_j)^2\rangle$ is a thermal average of the projection of the atomic displacement $\mathbf{u}_j$ as measured with respect to the emitter onto the direction of the change in wave vector produced by the scattering $\Delta\hat{\mathbf{k}}_j$. Thus, each scatterer in a photoelectron diffraction experiment is sensitive to a different type of vibrational displacement, varying from no effects for forward scattering, to small effects for small-angle scattering associated with components of $\mathbf{u}_j$ perpendicular to the emitter–scatterer axis, to maximum effects for backscattering associated with components of $\mathbf{u}_j$ along this axis. By contrast, in SEXAFS, it is only the along-axis components that contribute. Correlation effects are also expected to be largest for atoms that are backscatterers, because along-axis vibrations will be reduced more than those perpendicular to this axis. Ultimately, this might make it possible to measure anisotropies in vibration in a more precise way with temperature-dependent photoelectron diffraction, for example, by looking at the variation of different peaks in Fourier transforms of scanned-energy data. A first attempt at this has recently been made by Wang *et al.*[75] Also, even forward scattering features at high energy contain vibrational information because of peak broadening by motion perpendicular to a bond,[23,69] and this has permitted

Wesner *et al.*[76] to determine the vibrational amplitude anisotropy for an adsorbed molecule, as discussed further in section 4.1.3.

• A final aspect of the model which might be improved but which has only been discussed in a limited way to date is *more accurate allowance for both surface refraction and attenuation due to inelastic scattering*. Refraction has been treated differently from the phenomenological approach indicated here both by Lee[41] and by Tong and Poon,[77] who have considered the proper matching of the attenuated photoelectron wave inside the surface to the free electron wave outside the surface. However, the latter have found that, if refraction is allowed for in the way described here in calculating the path length for inelastic scattering in approaching the surface, the net result is very little different from the correct treatment of the wave matching. Another more complex problem is choosing the proper value for the inelastic attenuation length: As we have noted above, these lengths in electron-diffraction problems appear empirically to be only about 0.5–0.75 times the typical literature values based upon intensity attenuation. It would be desirable to understand these attenuation lengths more quantitatively, including both elastic and inelastic effects, for example, within the framework of more accurate methods of measuring peak intensities developed by Tougaard.[78] Finally, it might be useful to consider the possibility of *nonuniform or anisotropic inelastic scattering*. Such effects have been considered in both LEED[79a] and EXAFS,[79b] where the use of complex scattering phase shifts is proposed; but the influence of such effects on predicted diffraction patterns in PD or AED has not been assessed. More recently, Treglia *et al.*[80a] have used SSC–SW calculations to describe very low energy photoelectron diffraction at about 30 eV from different surfaces of *W*. They see evidence for a significantly different inelastic attenuation length in emission from W (001) and W (110). This could well be possible, but at this low energy, it would also be useful to carry out full MS calculations to eliminate such effects as another cause of effective anisotropic attenuation. In another recent paper, Frank *et al.*[80b] have discussed Auger electron diffraction data from Pt(111) with various adsorbates and for energies varying from about 65 eV to 420 eV. They have analyzed these results in terms of a classical model of anisotropic inelastic attenuation which totally neglects all wave inteferences and diffraction phenomena. Unfortunately, there is no basis in prior experiment or theory for this extreme model, even though it seems to fortuitously fit some of the features in the experimental data. Thus, this classical analysis by Frank *et al.* provides neither a useful method for analyzing AED data, nor any new information concerning the possibility of anisotropic inelastic attenuation. Such attenuation is in any case expected to produce only small corrections to the strong anisotropies associated with diffraction effects.

3.1.8. Relationship to EXAFS/SEXAFS Theory

As a further aspect of the SSC model, we note that it can be directly reduced to an expression very close to that used in EXAFS/SEXAFS analyses if it is assumed that all scattered waves ϕ_j are small in magnitude in comparison to ϕ_0.[15] Then, if we begin at Eq. (5) (for simplicity neglecting any averaging over $\hat{\epsilon}$), we see that all terms such as $\phi_j\phi_j^*$ and $\phi_j\phi_j^*$ can be neglected in expanding the absolute value squared. The thermal diffuse scattering term can also be neglected. After some

simple algebra, it can then be shown that

$$I(\mathbf{k}) \propto (\hat{\epsilon}\cdot\hat{\mathbf{k}})^2 e^{-2\gamma L} + 2(\hat{\epsilon}\cdot\hat{\mathbf{k}})e^{-\gamma L}\sum_j \frac{\hat{\epsilon}\cdot\hat{\mathbf{r}}_j}{r_j}|f_j(\theta_j)|\,W_j e^{-\gamma L_j} \times \cos[kr_j(1-\cos\theta_j)+\psi_j(\theta_j)]. \quad (9)$$

and that this can be converted to a normalized function $\chi(\mathbf{k})$ if we take the unscattered intensity to be $I_0 = (\hat{\epsilon}\cdot\hat{\mathbf{k}})^2 e^{-2\gamma L}$ and finally write

$$\chi(\mathbf{k}) \equiv \frac{I(\mathbf{k})-I_0}{I_0} \propto \frac{2}{(\hat{\epsilon}\cdot\hat{\mathbf{k}})e^{-\gamma L}}\sum_j \frac{\hat{\epsilon}\cdot\hat{\mathbf{r}}_j}{r_j}|f_j(\theta_j)|\,W_j e^{-\gamma L_j} \times \cos[kr_j(1-\cos\theta_j)+\psi_j(\theta_j)]. \quad (10)$$

This last equation thus has a form very close to the standard kinematical expression for EXAFS/SEXAFS, with the only differences being that double scattering events of the type emitter → scatterer → emitter → detector in Eq. (7) are included in the integration over direction in EXAFS to better describe the primary wave,[41] with these producing the central-atom phase shift; and the integration over direction changes the cosine function here finally to a sine function for EXAFS/SEXAFS. Equations (9) and (10) were first used in connection with the interpretation of ARPEFS data by Orders and Fadley,[15] and they have later been refined in this context by Sagurton *et al.*[21] Their form also suggests the possibility of using Fourier transform methods in scanned-energy PD to derive information concerning the set of path-length differences associated with a given structure, as discussed first by Hussain *et al.*[14] and now in active use by Shirley and co-workers[20,25] as a preliminary step of ARPEFS analysis.

As a final comment concerning this level of the diffraction theory, we consider the conservation of photoelectron flux. In the small-atom (or large r_j) limit, where PW scattering is adequate, the usual optical theorem assures that flux will be conserved if it is integrated over 4π.[81] Thus, even if high-energy scattering produces forward-scattering peaks, there will be, somewhere else, sufficient phase space with reduced intensity to exactly cancel them. However, in using the SSC–PW model for cases in which some scatterer distances require SW corrections, it is doubtful that flux will be conserved properly.[40] Nonetheless, with SW scattering correctly included, Rehr *et al.*[45] have shown that their SW equivalent of Eq. (7) does conserve flux and lead to a generalized optical theorem on each *l* channel involved.

In subsequent sections, we will consider several applications of this SSC model to the interpretation of experimental data, including especially several substrate and adsorbate systems of known geometry to test the degree of its validity.

3.2 *Effects beyond Single Scattering*

Finally, the possible importance of multiple scattering (MS), particularly along rows of atoms in a multilayer substrate, has been discussed qualitatively for some time,[9,42] and more recent papers have presented quantitative estimates of such effects and suggested improved methods for including MS corrections if they

are needed.[24,25,54,82–84] In general, the MS analogue of Eq. (2) can be written as

$$\psi(\mathbf{r},\mathbf{k}) = \phi_0(\mathbf{r},\mathbf{k}) + \sum_j \phi_j(\mathbf{r},\mathbf{r}_j \rightarrow \mathbf{k}) + \sum_j \sum_k \phi_{jk}(\mathbf{r},\mathbf{r}_j \rightarrow \mathbf{r}_k \rightarrow \mathbf{k}) + \sum_j \sum_k \sum_l \phi_{jkl}(\mathbf{r},\mathbf{r}_j \rightarrow \mathbf{r}_k \rightarrow \mathbf{r}_l \rightarrow \mathbf{k}) + \sum_j \sum_k \sum_l \sum_m \phi_{jklm}(\mathbf{r},\mathbf{r}_j \rightarrow \mathbf{r}_k \rightarrow \mathbf{r}_l \rightarrow \mathbf{r}_m \rightarrow \mathbf{k}) + \text{higher orders}, \quad (11)$$

where events up to fourth order are shown here and, in the multiple scattering sums, the combinations of j, k, l, and m are limited only in that they do not involve consecutive scattering by the same scatterer. Such MS calculations have been done in two basic ways: first by Tong and co-workers using LEED-type methods that require full translational symmetry along the surface,[24] and more

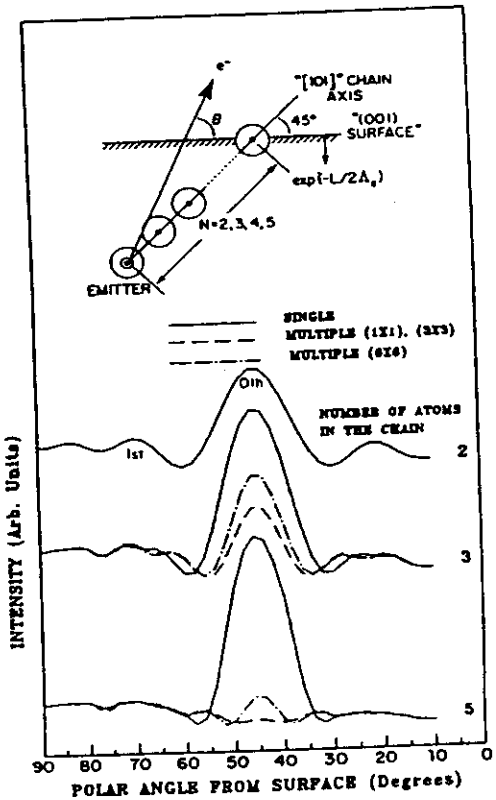

FIGURE 6. Calculated Auger electron diffraction patterns at 917 eV from linear chains of Cu atoms in single and multiple scattering. The geometry of the calculation with the emitter at the base of the chain is shown at the top. The primary outgoing Auger wave is treated as having s character. The multiple scattering results are shown at three levels of the matrix used to describe the scattering: (1 × 1), (3 × 3), and the most accurate, (6 × 6). The (1 × 1) and (3 × 3) cases are found to be superimposable for this case. (From Ref. 84, with similar results also appearing in Refs. 73 and 83(b).)

recently by Barton and co-workers using a cluster approach with SW scattering and the Taylor series MQNE method to simplify the calculations.[25,82,83] The cluster method is really more appropriate to the physics of such a short-range order probe, and we will term it MSC–SW. More recently, Rehr and Albers[54] have proposed a Green's-function matrix method for such MSC–SW calculations that shows promise as an alternate approach in extensive applications by Kaduwela *et al.*[84]

One effect of MS first discussed by Poon and Tong[24] is a defocusing of intensity occurring in multiple forward scattering at higher energies along a dense row of atoms, such that an SSC–PW or SSC–SW calculation along such a row may overestimate the intensity by a factor of two or more. This is illustrated schematically in Fig. 3b(ii). For an embedded species at some distance from the surface but again emitting along such a row, it has more recently been shown that these defocusing effects may be even more dramatic.[73,82,83]

Such defocusing effects have been very nicely illustrated in recent MSC–SW calculations by Barton, Xu, and van Hove[73,82,83] and by Kaduwela *et al.*[84] for emission from chains of Cu atoms of variable length. Some recent results of this type are shown in Figs. 6 and 7. In both figures, chains of 2, 3, or 5 atoms with the emitter at their base are tilted at 45° with respect to the surface of a medium of uniform density that simply serves to attenuate the emitted waves inelastically (see inset in Fig. 6). This geometry thus simulates the intensity distribution expected for emission from the 2nd, 3rd, and 5th layers along a low-index [110]

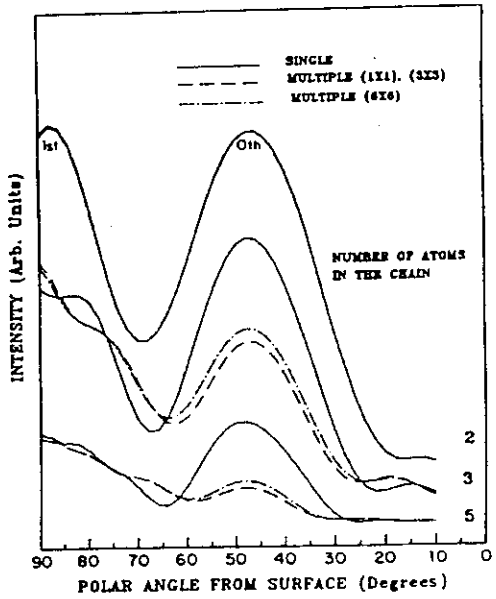

FIGURE 7. As in Fig. 6 (bottom), but for an energy of 100 eV.

row of Cu with (001) orientation, but without any diffraction effects due to scatterers adjacent to the row. Emission into a simple *s*-wave final state approximating Auger emission is treated. Both single-scattering and fully converged (6 × 6) multiple-scattering calculations are shown for each case.

In Fig. 6, for an emission energy of 917 eV, it is clear that the single- and multiple-scattering curves are identical for the two-atom case (as appropriate to a diatomic adsorbate, for example), but they diverge more and more as additional scatterers are added between the emitter and the detector. For the five-atom chain, the forward scattering peak is suppressed to only about 10–15% of its value for single scattering. There is also a systematic narrowing of the width of this peak as more defocussing due to multiple scattering comes into play. For scattering angles more than about ±15° from the chain axis, the differences between single and multiple scattering are much more subtle, as is to be expected since strong multiple forward scattering is no longer possible directly in the emission direction. At the much lower energy of 100 eV in Fig. 7, one expects less strongly peaked forward scattering, as shown by the wider peaks along a polar angle of 45°. Here again, the single-scattering and multiple-scattering results are identical for a two-atom chain, but one sees a suppression and narrowing of the forward scattering peak with increasing chain length that is qualitatively similar to, but less severe than, that observed at the higher energy.

Overall, these and other recently published results by Xu and van Hove[73] indicate that, for emitters in the first one or two layers of a surface and/or for which the emission direction does not involve near parallelism with a dense row of scatterers, a single scattering model should be quite accurate. For atoms further below the surface and/or for emission directions along such high-density rows, certain forward scattering features are expected to be suppressed by multiple scattering, but single-scattering calculations should nonetheless predict their positions with good accuracy.

An additional important multiple scattering effect pointed out by Barton *et al.*[25] is due to strong nearest-neighbor backscattering at lower energies. This they find in certain scanned-energy cases to significantly increase intensity due to events of the type emitter → neighbor → emitter → detector, as illustrated in Fig. 3b(i).

A further important point in connection with such multiple-scattering calculations is that events up to at least the fifth order have to be included to assure reasonable convergence.[25,84] In fact, it is found that including only second-order events can often lead to curves which are in much poorer agreement with experiment than the corresponding first-order calculation![84] This is similar to the experience in EXAFS theory, in which including only lower-order multiple-scattering corrections can yield worse results than those of single scattering.[57,85] A more reasonable procedure is to include events up to, say, the fifth order if the total path length $r_j + r_{jk} + r_{kl} + \cdots$ is less than some cutoff value of 10–20 Å,[20,25,57,85] although an inproved cutoff criterion has been suggested by Kaduwela *et al.*[84]

As noted previously, there is by now a considerable body of data which indicates that useful structural information can be derived at the SSC–SW or even SSC–PW level, and we will show illustrations of this in subsequent sections. Nonetheless, MS effects such as those described above can cause discrepancies

between experiment and theory for certain classes of system, and full MS treatments of both photoelectron and Auger electron diffraction are beginning to be more often used. Several advances in the simplification of these methods, as well as rapid improvements in computer technology, should lead to a greater reliance on MS approaches in future work. In the examples which follow, a variety of theoretical models have been used, and the specific approach followed will be indicated with each set of results to permit the reader to draw his or her own conclusions.

4. ILLUSTRATIVE STUDIES OF DIFFERENT TYPES

4.1. Small-Molecule Adsorption and Orientation

We here consider primarily the case of small-molecule adsorption as studied by higher-energy XPD. The cases treated are thus of considerable interest in studies of surface chemistry and catalysis, and they provide the first simple illustrations of the utility of the forward-scattering peaks discussed in the preceding section. Auger peaks at similar energies of about 1000 eV could also in principle be used for such studies, but all of the cases to date involve photoelectron diffraction.

4.1.1. CO/Ni (001)

We begin with the first system of this type studied by Petersson *et al.*[23] and Orders *et al.*:[69] $c(2 \times 2)$ CO on Ni (001). Figure 8 compares experimental C 1*s*

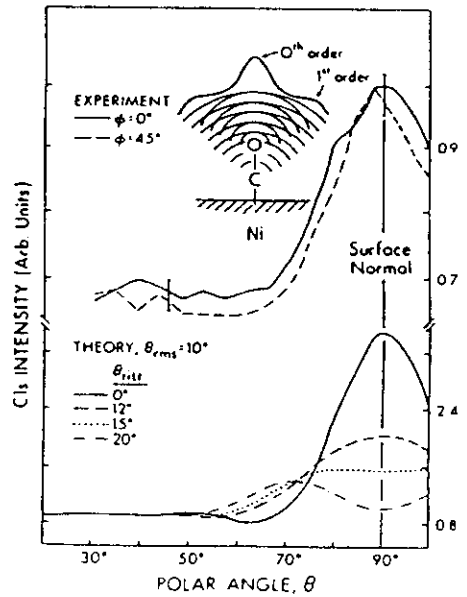

FIGURE 8. Comparison of polar-scan C 1*s* XPD data from $c(2 \times 2)$ CO on Ni (001) at a kinetic energy of 1202 eV with SSC-PW theory. The inset indicates the type of intramolecular forward scattering and interference involved. Note definitions of zeroth-order and first-order effects, as shown also in Figs. 4 and 5. (From Ref. 69.)

polar scans in two high-symmetry azimuths (normalized by dividing by the O 1*s* intensity to eliminate the θ-dependent instrument-response function) to SSC–PW calculations for varying degrees of CO tilt relative to the surface normal.[69] The theoretical model also includes a wagging or "frustrated-rotation" molecular vibration with an rms displacement of 10 Å. The experimental curves are essentially identical along both azimuths and show a strong peak along the surface normal that represents about a 35% anisotropy. Comparing experiment and theory furthermore permits concluding very conservatively that CO is within 10° of normal for this overlayer and that it has no preferential azimuthal orientation.

The inset in this figure also indicates that, in addition to the forward scattering or zeroth-order diffraction peak, one expects higher-order features such as the first-order peak indicated. (These also appear in the single-scatterer calculations of Figs. 4 and 5, where higher orders also are shown.) The first-order peak corresponds to a 2π phase difference between the direct wave and the scattered wave, or a path length difference of approximately one deBroglie wavelength. We will further consider such higher-order features in the next case and subsequent examples.

4.1.2. CO/Fe (001)

A more recent and more complex case of CO adsorption is that on Fe (001). In Figs. 9a and 9b, we show both polar and azimuthal C 1*s* data obtained by Saiki *et al.*[86] from CO adsorbed at room temperature on Fe (001) so as to form predominantly the so-called α_3 state. This rather unusual species has been the subject of prior studies by several techniques, including EELS, ESDIAD, and NEXAFS.[87] Its structure is of considerable interest because it is thought to be bound in a highly tilted geometry with a significantly weakened C–O bond and thus to be a possible intermediate state for the dissociation of the molecule. However, the best that the tilt angle could be determined from NEXAFS data was 45 ± 10°, and no information was obtained on the most likely azimuthal orientation(s) of the molecules. It is thus of interest to see what more can be learned about such a species from XPD.

The strong peak in the normalized C 1*s* polar-scan results for the [100] azimuth shown in Fig. 9a immediately permits a direct estimate of the tilt angle with respect to the surface normal as $\theta_{tilt} = 55 \pm 2°$ (that is, with the molecule oriented 35° from the surface). Also, the fact that this forward scattering peak is not seen in polar scans along the [1$\bar{1}$0] azimuth indicates that the preferred tilt is along ⟨100⟩ directions, or into the open sides of the fourfold-hollow sites that are the sterically most reasonable choices for the bonding location. Complementary evidence confirming this structure comes from the azimuthal data at a polar angle with respect to the surface of $\theta = 35°$ in Fig. 9b. These results again show the preferred tilt in the ⟨100⟩ azimuths via strong peaks along $\phi = 0°$ and 90°. It is thus concluded that the CO molecules are tilted along the four ⟨100⟩ axes, perhaps in separate but equally populated domains, as illustrated schematically for one fourfold-hollow site in Fig. 9c.

As a self-consistency check of these data, it is also of interest that the overall effects seen in both parts a and b of Fig. 9 are of very nearly the same magnitude.

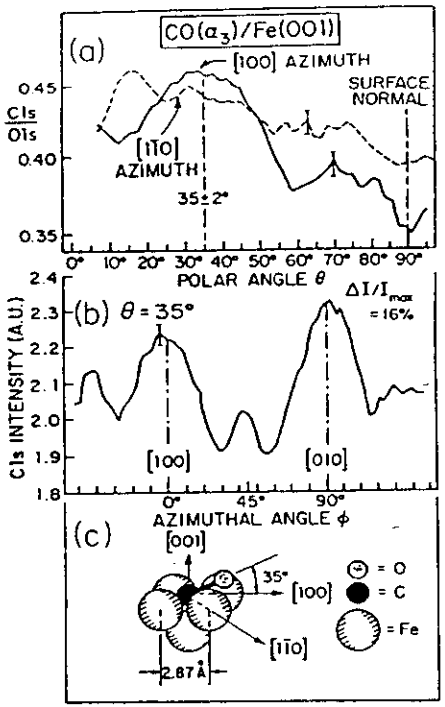

FIGURE 9. (a) Experimental polar scans of the C 1*s*/O 1*s* intensity ratio for the α_3 state of CO on Fe (100). The C 1*s* kinetic energy is 1202 eV. Curves are shown for two azimuths: [100] (solid curve) and [1, $\bar{1}$, 0] (dashed curve). (b) Experimental azimuthal scan of C 1*s* intensity for the α_3 state of CO at a polar angle of 35° chosen to coincide with the peak in the [100] data of part (a). (c) The bonding geometry as deduced from these data. (From Ref. 86.)

That is, if the overall anisotropy as mentioned previously is measured as a percentage by $\Delta I/I_{max}$, we find about a 14% effect in Fig. 9a and a 16% effect in Fig. 9b. Thus, it is possible to reliably measure rather small diffraction effects with XPD, particularly in the azimuthal data, which do not need to be corrected for any systematic instrumental changes in intensity. By contrast, polar scans will always be influenced by a θ-dependent instrument-response function[9] and must somehow be corrected for this. Since the O 1*s* intensity is not expected to be very much affected by final-state scattering and diffraction, using the C 1*s*/O 1*s* ratio in Fig. 9a acts to normalize out any such instrumental effects.

Another useful observation from Figs. 9a and b is that the main peaks exhibit very similar full widths at half-maximum intensity (FWHM) of 30–35°. Thus, the resolutions for determining both the polar and the azimuthal senses of the tilt are about the same.

The results in Fig. 9b also exhibit much smaller but quite reproducible peaks along the ⟨110⟩ azimuths (that is, at $\phi = 45°$) that could be due to scattering from Fe atoms in the ⟨110⟩ corners of the hollow. A more detailed theoretical analysis of these azimuthal results using the SSC–SW model in fact shows that these peaks are due to constructive addition of first-order scattering from oxygen

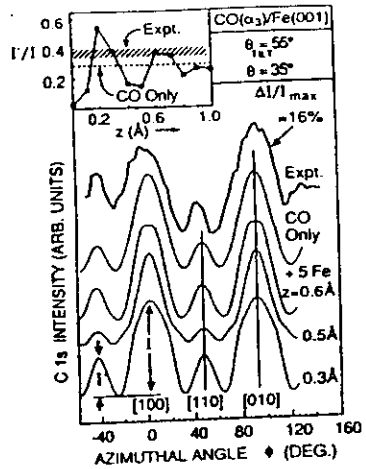

FIGURE 10. Experimental results of Fig. 9(b) are compared with theoretical SSC-SW calculations of C 1s azimuthal scans for CO on Fe (001) tilted at 35° with respect to the surface along the ⟨100⟩ directions and assumed to be in four equally populated domains. In the top theoretical curve, no Fe scatterers are included. In the lower theoretical curves, five Fe scatterers are added, as in Fig. 9(c). The C atom is centered in the fourfold hollow, and the distance z with respect to the Fe surface plane is varied. The inset shows the ratio of the two main peak intensities I'/I as a function of z. (From Ref. 86.)

(see inset in Fig. 8) and second- or third-order scattering from the corner Fe atoms, depending upon the distance z of the tilted CO from the Fe surface. Some results of these calculations of the azimuthal scan of Fig. 9b are compared to experiment in Fig. 10. The top theoretical curve is from a calculation in which only CO molecules are present; these are assumed to be present in four equally populated domains tilted at $\theta = 35°$. This very simple calculation correctly predicts the positions and approximate widths of the strong forward scattering peaks along ⟨100⟩ azimuths, as well as the additional weaker first-order features seen along ⟨110⟩ at $\theta = 45°$. However, if the five Fe nearest neighbors are also included as scatterers (as shown in Fig. 9c) and the C atom is further assumed to be centered in the fourfold hollow but with variable vertical distance z relative to the first Fe layer, we arrive at what should be a more realistic set of curves. These are striking in that the small peaks along ⟨110⟩ are predicted to oscillate in intensity, as shown in the figure inset. Comparing experiment and theory for the ratio I'/I as indicated yields z values of both about 0.22 ± 0.10 Å and 0.63 ± 0.10 Å that agree best; these z values also correspond to very reasonable C–Fe distances of 1.6–2.0 Å. Multiple-scattering calculations for this system by Kaduwela *et al.*[84] also quantitatively confirm the single-scattering results shown here; this is as expected in view of the high energy and high takeoff angles relative to the surface.

Figure 11 shows a further aspect of this analysis in which the experimental polar scans of Fig. 9a are compared to SSC–SW theory for the two azimuths involved and for several z distances. Polar scans are also seen to be sensitive to both azimuth and vertical distance, with in particular the results for the [110] azimuth favoring a z value nearer 0.3 Å. This study thus indicates the significant advantage of having both polar and azimuthal XPD data for such systems.

The theoretical anisotropies $\Delta I/I_{max}$ in Figs. 8, 10, and 11 are found to be about 2–3 times larger than those of experiment. This kind of discrepancy has

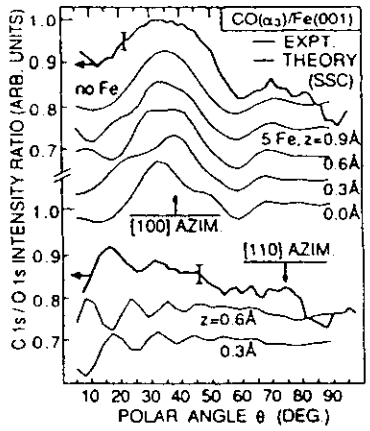

FIGURE 11. Comparison of experimental C 1s polar scans for α_3 CO on Fe (001) to SSC-SW theory for two azimuths and different vertical distances z. (From Ref. 86.)

been found in most previous XPD studies of adsorbates[9,10,23,69] and can be explained by the combined effects of the following:

- Molecular vibration. This has not been included in the calculations for CO/Fe (001) shown here, but is considered in prior work for CO/Ni (001).[23,69]
- The presence of more than one type of emitter on the surface. For the present case, this could be due either to the method of formation of the α_3 state or to adsorption at defects. There could also be additional C-containing impurities beyond those associated with CO and its dissociation products on the surface. All of these act to diminish diffraction features relative to background and thus to reduce the experimental anisotropy. Such effects will tend to be present in any adsorbate system to some degree.

4.1.3. CO/Ni (110)

A final example of a molecular adsorbate system is that of CO on Ni (110), as studied with polar-scan measurements by Wesner, Coenen, and Bonzel.[76,88] For this case, Fig. 12 shows a comparison of normalized C 1s polar scans from CO adsorbed to saturation on Ni (110) at two different temperatures of 300 K and 120 K. The polar scans are markedly different, with the high-temperature results being very similar to those of CO on Ni (001) (cf. Fig. 8), and thus suggestive of a simple vertical adsorption of the CO, and the low-temperature results being widely split into a doublet along the [001] azimuth, but retaining a weaker peak along the normal for the [1$\bar{1}$0] azimuth. The low-tempeature, higher-coverage results have been explained by a structure in which the CO molecules are tilted by ±21° along the [001] azimuth, as shown in Fig. 12d.[89] This structure is nicely confirmed in Fig. 12c, where SSC–PW calculations with an rms vibrational amplitude of 8° are found to yield excellent agreement with experiment.

Wesner *et al.*[88] have also considered the effect of adsorbing CO on a Ni (110)

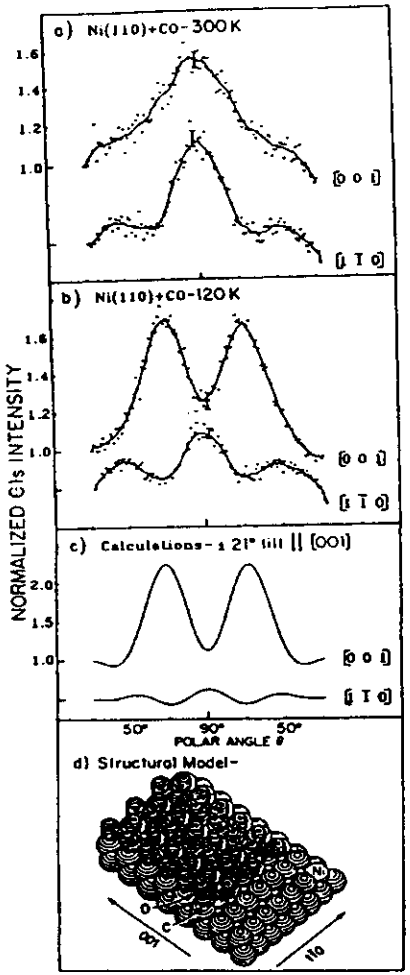

FIGURE 12. (a) Experimental polar scans in two azimuths of the C 1*s* intensity from CO adsorbed on Ni (110) at 300 K. The kinetic energy is 970 eV. (b) As in (a), but for adsorption at 120 K. (c) SSC-PW calculations modeling the data in (b), with an assumed tilt of ±21° along [001] and an rms vibrational amplitude of 8°. (d) The geometric model assumed for the calculations of (c). [(a)–(c) from Ref. 88. (d) from Ref. 89.]

surface pretreated with K, which is known to act as a promoter in many catalytic reactions. This system is found to have both vertical and more highly tilted CO species present. Finally, the same group has made use of the temperature dependence of the widths of peaks such as those in Fig. 12 for CO on Ni (011) to study the anisotropy of wagging vibrational amplitudes in different azimuths.[76]

4.1.4. Other Systems and Other Techniques

These simple examples thus show that XPD (or in principle also higher-energy AED) is a very powerful tool for studying the orientations and bonding of small molecules on surfaces, and that it is well suited to even very highly tilted species that may exhibit enhanced reactivity and thus be important in such phenomena as catalysis. Each of the cases discussed here is also significant in that other surface structural probes have been applied to the same problem without being capable of a clean resolution of the structure. Similar XPD measurements and theoretical analyses have also recently been applied to several other systems: CO and CH_3O on Cu (110) by Prince *et al.*[90] and CO on Pt (111) treated with K as a promoter by Wesner *et al.*[91]

Similar forward-scattering effects have also been seen by Thompson and Fadley[92] in emission from an atomic adsorbate on stepped surfaces: oxygen on Cu (410) and Cu (211). For this case, scattering by near-neighbor atoms up the step face from the emitter is found to be particularly strong. Stepped surfaces in fact represent a particularly attractive kind of system for study by this technique, since any atomic or molecular adsorbate that bonds preferentially at the base of the step has atoms on the step face as nearest-neighbor forward scatterers in the upstep direction.

The use of intramolecular forward scattering also appears to have several advantages for determining molecular or fragment orientations on surfaces in comparison to other techniques such as high-resolution electron energy loss spectroscopy (EELS),[93] electron stimulated desorption-ion angular distributions (ESDIAD),[94] and NEXAFS[95] or SEXAFS.[16] In EELS, the presence of a titled species can be detected by which vibrational modes are excited, but estimating the magnitude of the tilt is difficult.[87a,93] In ESDIAD, the ion angular distributions for bond tilts away from normal can be significantly distorted by image forces and ion-neutralization effects,[87b,94] and tilts further away from normal than 25–30° therefore cannot in practice be measured accurately, if at all. In NEXAFS[95] and SEXAFS,[16] the experimental intensities of different features vary only relatively slowly with polarization, as $\sin^2\alpha$ or $\cos^2\alpha$, if α is the angle between the radiation polarization and the appropriate molecular symmetry axis. In forward-scattering XPD or AED, by contrast, it is the much narrower peak in the scattering amplitude $|f|$ near 0° (cf. Fig. 2 and Fig. 8) that controls the precision of orientation determinations, leading to FMWHs of 25–35° for all molecules studied to date. Comparing these values to the effective widths of $\sin^2\alpha$ or $\cos^2\alpha$ thus leads to the conclusion that forward scattering in XPD or AED should be about 3–4 times more precise in determining bond directions. An additional problem in NEXAFS is that a correct assignment of the peak(s) to be studied is necessary.

We close this section by noting that scanned-energy photoelectron diffraction or ARPEFS also has been applied recently to the study of small-molecule fragments such as formate (HCOO) and methoxy (CH_3O) adsorbed on Cu (100). The lower energies involved in this work imply that information on bond distances to backscattering neighbors below the adsorbate are also derivable. Such studies are described in more detail in the chapter by Haase and Bradshaw in Volume 2 of this set.

...d the Oxidation of Metals

...1. Oxygen/Ni (001)

Saiki and co-workers[26] have carried out an XPD/LEED investigation of the interaction of oxygen with Ni (001) over the broad exposure range from $c(2 \times 2)$ O at 30 Langmuirs (L) to saturated oxide at 1200 L. Scanned-angle measurements were performed with Al $K\alpha$ radiation at 1486.6 eV for excitation. Although this system has been extensively studied in the past by various structural and spectroscopic probes,[96-98] several questions remain as to the exact structures formed. The combined use of XPD and LEED proves capable of answering several of these, as well as pointing out some new features of XPD that should be generally useful in surface-structure studies.

For example, in Fig. 13a, we show azimuthal scans of O 1*s* intensity at a relatively high polar angle θ of 46° with respect to the surface for four oxygen exposures from the onset of sharp $c(2 \times 2)$ LEED spots (30 L) to full oxide saturation (1200 L). The experimental curves are compared to SSC–SW calculations for a $c(2 \times 2)$ overlayer in simple fourfold sites with a vertical oxygen distance of $z = 0.85$ Å above the first Ni layer (the by now generally accepted structure), for two monolayers (ML) of NiO (001) with ideal long-range order, and for two monolayers of NiO (111) with long-range order. The dominant peaks at $\phi = 0°$ and 90° for the highest two exposures of 150 L and 1200 L are correctly predicted by theory and are due to simple forward scattering of photoelectrons emitted from oxygen atoms below the surface by oxygen atoms situated in the upper layers of the oxide, as indicated by the arrows in Fig. 13b. These peaks furthermore persist as the strongest features down to 30 L, indicating very clearly the existence of buried oxygen emitters, probably in small nuclei of NiO (001), over the full region of observation of the $c(2 \times 2)$ overlayer. The presence of such oxide nuclei in varying degrees on Ni (001) surfaces prepared in different laboratories is thus a likely cause of some of the previous controversy surrounding the vertical positions of both $c(2 \times 2)$ and $p(2 \times 2)$ oxygen on this surface,[96,97] but XPD provides a sensitive probe of the presence of any sort of buried species via such forward-scattering effects.

Comparing the 1200-L experimental curve and the theoretical curve for 2 ML of ideal Ni (001) in Fig. 13a for the region near $\phi = 45°$ shows qualitative agreement as to the existence of a region of enhanced intensity for $30° < \phi < 60°$, but disagreement as to exact fine structure, with theory showing a doublet where experiment shows a single broad peak. However, annealing this saturated oxide to approximately 250 °C for ≈10 minutes to increase its degree of long-range order parallel to the surface (as well as perhaps its thickness)[97] is found to yield a significantly altered XPD curve, with a doublet centered at $\phi = 45°$ that is in very good agreement with theory for NiO (001), as shown in the higher-resolution results of Fig. 14. It is also striking that the annealed oxide overlayer shows much more fine structure and generally narrower features, even though the dominant peaks in both the unannealed and annealed data are still those for simple forward scattering along (101) directions (i.e., at $\phi = 0°$ and 90°). The theoretical curves for 2 ML or 3 ML of ideal NiO (001) in Fig. 14 are

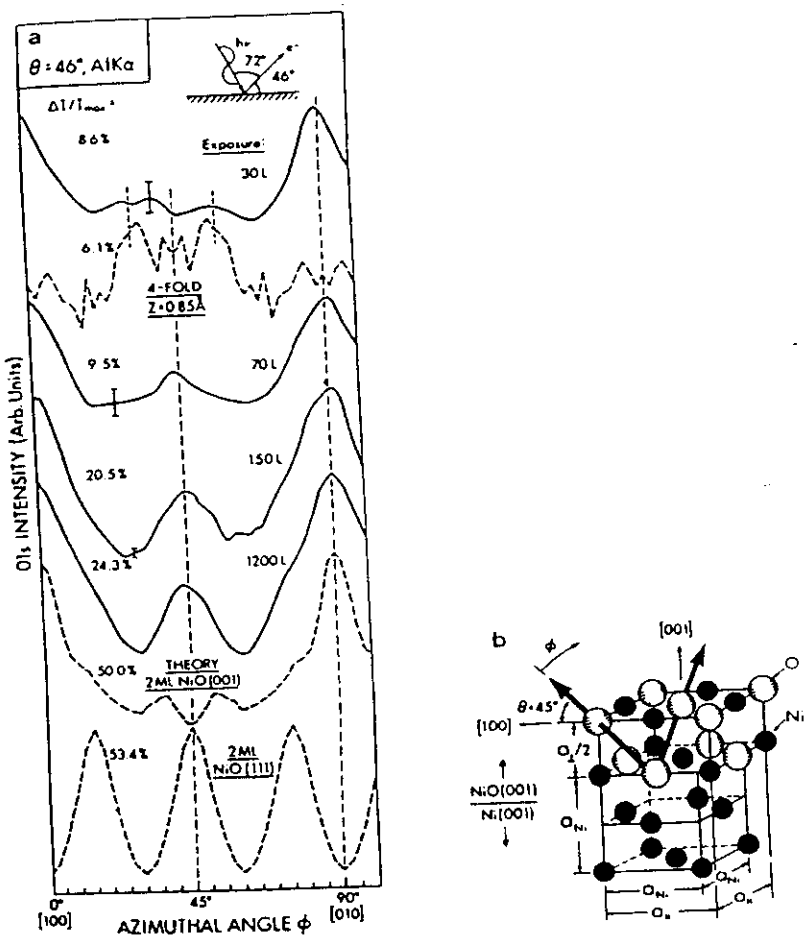

FIGURE 13. (a) O 1*s* azimuthal XPD data from oxygen on Ni (001) at four exposures from the $c(2 \times 2)$ regime (30 L) to saturated oxide (1200 L). The kinetic energy is 945 eV. The polar angle of 46° involves scanning very close to the ⟨110⟩ directions at $\theta = 45°$ and $\phi = 0°$ and 90°. Also shown are SSC-SW calculations for fourfold $c(2 \times 2)$ oxygen at $z = 0.85$ Å and fully ordered 2 ML overlayers of NiO with both (001) and (111) orientations. (b) An approximate representation of the structure of the dominant Ni (001) formed at high exposures, indicating the oxide lattice expansion and strain involved. Also shown as arrows are the directions of the strong forward-scattering peaks observed at $\phi = 0°$, 90° in (a). (From Ref. 26.)

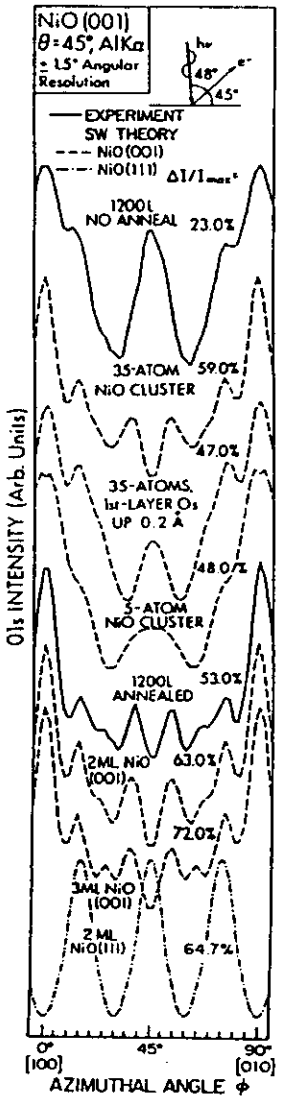

FIGURE 14. O 1*s* azimuthal XPD data from the saturated oxide formed at 1200 L exposure on Ni (001) obtained at a high angular resolution of ±1.5° with an emission angle of 45° with respect to the surface. Experimental curves are shown for both the ambient-temperature oxide and the same overlayer after a brief low-temperature anneal. SSC-SW calculations are also shown for several cases: smaller five-atom and 35-atom clusters to simulate loss of long-range order and strain and large fully converged clusters to simulate ideal NiO growing in either the (001) orientation (with 2 ML or 3 ML thickness) or the (111) orientation (with 2 ML thickness). (From Ref. 26.)

also in remarkably go
annealing has produced a ve
unannealed oxide exhibits diffra

The data shown in Fig. 14 are
point in being obtained at a very high an
angular resolution has in this case been obt
arrays of the proper length-to-diameter ratio, as
al.[33] Note the additional fine structure in the unanne
as compared to that of Fig. 13a.

The bottom theoretical curves in Figs. 13a and 14 are for
an orientation of oxide growth which is also thought from LEED
NiO (001) on this surface.[97] The total lack of agreement of the NiO
with experiment makes it clear that this is only a minority species affect
more than 5% of the NiO present.

In order to better understand the unannealed oxide data in Figs. 13a and 14, we also show in Fig. 14 theoretical curves for smaller 35-atom and 5-atom clusters of NiO (001). The previous calculations discussed involved much larger clusters with about 100 atoms per layer to insure full convergence. The 35-atom cluster includes atoms in about the first $1\frac{1}{2}$ unit cells around a given oxygen emitter; the 5-atom cluster is minimal and represents only nearest-neighbor and next-nearest-neighbor scatterers. The results for the full 2-ML cluster and the 35-atom cluster are found to be very close except for somewhat more fine structure in the full-cluster curve. This is consistent with prior XPD studies which have concluded that near-neighbor scatterers dominate in producing the observed patterns. However, much better agreement with the unannealed oxide results is seen if either the first-layer oxygen atoms (but not the nickel atoms) in the 35-atom cluster are relaxed upward by 0.2 Å or the effective cluster size is reduced to five atoms. Both of these models are consistent with a highly strained unannealed oxide overlayer of (001) orientation in which the long-range order is severely disturbed. The LEED spots for NiO (001) in fact indicate a lattice expanded by very nearly $\frac{1}{8}$ relative to the underlying Ni (001) surface, as indicated schematically in Fig. 13b. Although these results do not permit choosing between these two possibilities for stress relief in such a disordered system, they are significant in that both the experimental and theoretical XPD curves are quite sensitive to these more subtle deviations from an ideal NiO (001) overlayer with long-range order. This suggests a broad range of applications of XPD or higher-energy AED to studies of epitaxy and overlayer growth.

It is also significant in the comparisons of experimental data for annealed oxide with theory for 2–3 ML of NiO (001) in Fig. 14 that the agreement extends even to the overall degree of anisotropy, as judged again by $\Delta I/I_{max}$. The theoretical anisotropies are only about 1.2–1.3 times those of experiment. As noted previously, theory is in general expected to overestimate these anisotropies, in some previous cases by as much as factors of 2–3. One important reason for this kind of discrepancy is the lack of allowance in the calculations for atoms bound at various defect or impurity sites along or below the surface, as these are expected to produce a rather diffuse background of intensity, thus lowering the overall anisotropy. However, for the present case, the very good

agreement suggests that the annealed oxide overlayer consists of oxygen atoms that are almost completely bound in a highly ordered NiO (001) structure.

At lower exposures, XPD has also been used to determine the $c(2 \times 2)$ *oxygen structure on Ni* (001).[26] The high θ values of Figs. 13 and 14 minimize the effects of any forward-scattering events in emission from oxygen in the $c(2 \times 2)$ overlayer (cf. Fig. 2), so that the 30-L curves here are dominated by the

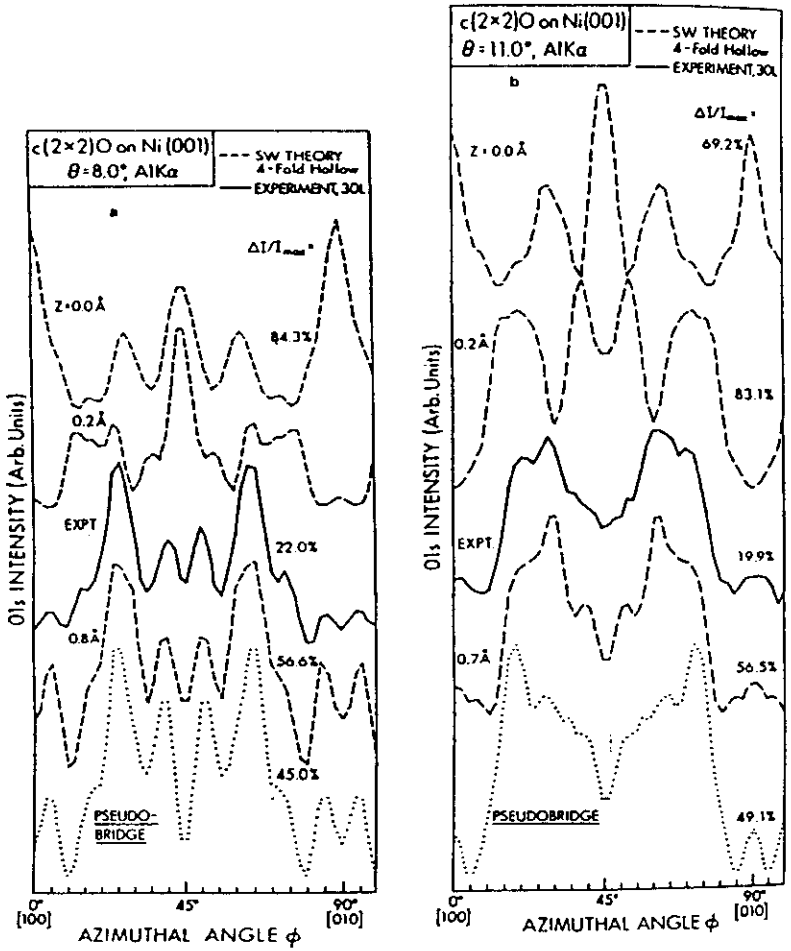

FIGURE 15. (a) Grazing-emission O 1s azimuthal data from $c(2 \times 2)$ O on Ni (001) at $\theta = 8°$. The experimental data are compared to SSC-SW curves for four possible fourfold-hollow $c(2 \times 2)$ structures, including the pseudobridge geometry of Ref. 98. (b) As in (a), but for $\theta = 11°$. (From Ref. 26.)

presence of a certain fraction of buried oxygen, probably in oxide nuclei. However, at very low takeoff angles with respect to the surface of approximately 8°–15°, forward elastic scattering from adsorbed oxygen becomes much stronger, and the signal from buried oxygen is also suppressed by enhanced inelastic scattering.[9] Thus, the diffraction patterns at such low θ values are expected to be more strongly associated with overlayer effects.

Figure 15 shows such experimental and theoretical results for two representative θ values, 8° and 11,° of the four angles studied (data were also obtained for 14° and 17°). Experiment is here compared with SSC–SW theoretical curves for four possible $c(2 \times 2)$ structures: in-plane fourfold bonding ($z = 0.0$ Å); slightly-above-plane fourfold bonding ($z = 0.2$ Å); the vertical distance in fourfold bonding yielding the empirical best fit to experiment at that θ value as judged both visually and by R factors;[26d] and the so-called pseudobridge geometry suggested by Demuth *et al.* on the basis of a LEED analysis.[98] For this last geometry, $z = 0.8$ Å and the oxygen atoms are offset horizontally by 0.3 Å in the fourfold hollow toward any of the four symmetry-equivalent (110) directions.

In Fig. 15a for $\theta = 8°$, it is very clear that $c(2 \times 2)$ oxygen does not occupy a position in the 0.0-to-0.2-Å range, although certain prior studies have suggested this as the most likely bonding position.[96,97] Simple fourfold bonding at $z = 0.80$ Å, by contrast, yields excellent agreement with experiment, with all observed features being present in the theoretical curve. The only points of disagreement are the relative intensity of the weak doublets centered at $\phi = 0°$ and 90°, which is too strong in theory; and the degree of anisotropy $\Delta I/I_{max}$, which is predicted to be too high by approximately a factor of 2.6. The latter discrepancy could be due to a significant fraction of oxygen atoms occupying defect or buried sites, e.g., in the oxide nuclei mentioned previously. Also, for such a low takeoff angle that begins to be within the forward scattering cone at this kinetic energy (≈954 eV), there may be some defocusing and reduction of peak heights due to multiple scattering effects; in fact, $\phi = 0°$ and 90° are the directions of nearest-neighbor oxygen scatterers in the $c(2 \times 2)$ structure, as shown in Fig. 16a. The pseudobridge geometry does not fit experiment as well, since the relative intensity of the doublet centered at $\phi = 45°$ is too high.

In Fig. 15b, for $\theta = 11°$, the two geometries close to being in plane again do not agree at all with experiment, which is very well described by simple fourfold bonding at an optimum z of 0.70 Å. The pseudobridge geometry in this case also differs considerably from experiment as to the shape of the two main peaks. When these results are combined with those at the other two θ values studied,[26] it can overall be concluded that $c(2 \times 2)$ oxygen does not bond in either simple fourfold positions at $0.0 < z < 0.3$ Å or in the pseudobridge geometry, but does occupy simple fourfold positions at $z = 0.80 \pm 0.10$ Å. This choice of structure is also confirmed by an R-factor comparison of experiment and various theoretical curves. The z distance found here also agrees very well with several more recent structural studies of this system.[96,97]

A final point in connection with the results of Fig. 15 is that, in order for theory to adequately reflect all of the fine structure seen in experiment, the cluster used in the calculations must include all O and Ni atoms within the first few layers of the surface (adsorbate plus two layers of Ni) and out to a relatively

large radius of about 20 Å from the emitter. The rate of convergence with cluster size is illustrated in Fig. 16. Due to the rotational symmetry of the surface, calculations need be performed only over the 45° wedge indicated in Fig. 16a, but it is important to include sufficient atoms at the edge of this wedge. It is clear from the diffraction curves in Fig. 16b that going out to only 10 Å in radius does not yield the correct diffraction fine structure. This indicates sensitivity in forward scattering at grazing emission to well beyond the first 3–5 spheres of neighbors. The effective *diameter* of the cluster is thus about 40 Å.

Thus, these results for a prototypical surface oxidation over a broad exposure range, from ordered overlayers at partial monolayer coverage to saturated oxide, indicate several very useful types of structural information that can be derived from XPD (or by implication also by high-energy AED) in conjunction with SSC calculations.

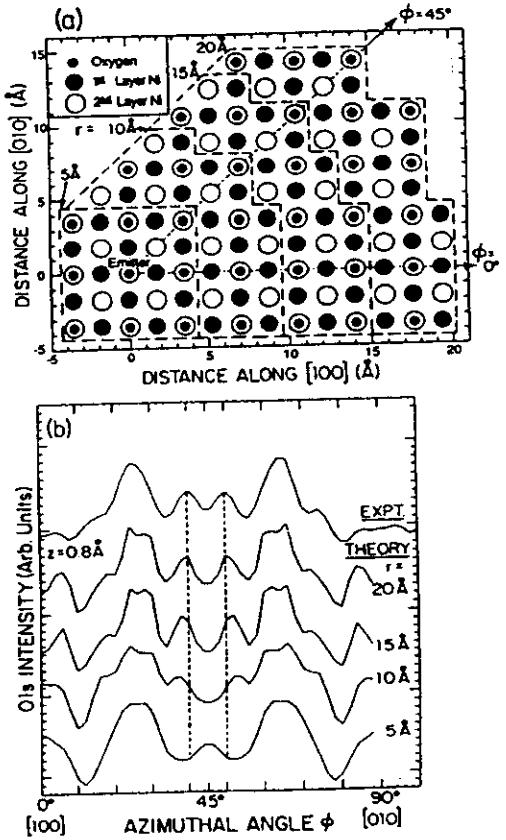

FIGURE 16. (a) Choices of cluster. Different-sized clusters used in testing the convergence of the SSC-SW curves for $\theta = 8°$ in Fig. 15(a), labelled with the approximate radii outward from the emitter that they represent. (b) Convergence with cluster size. Calculated curves for the clusters of (a) with $z = 0.8$ Å are compared to experiment. Note that a radius of at least 20 Å is required to yield optimum agreement. (From Ref. 26.)

4.2.2. Sulfur/Ni (001)

The sulfur/Ni (001) system has been much used as a test case for surface-structure techniques because it represents a rather unique example of a system for which there is a general consensus on a structure: the $c(2 \times 2)$ sulfur overlayer is bound with atomic S in fourfold sites at a distance z of 1.3–1.4 Å above the first Ni plane.[99] Several photoelectron diffraction studies have been made of this system,[14,15,19,21,25,99] including both scanned-angle and scanned-energy measurements, and we will consider a few of these.

Higher-energy scanned-angle XPD measurements have been made for this system by Connelly *et al.* (Fig. 44 in Ref. 9), and experimental azimuthal scans of S 2*p* emission at grazing takeoff angles are found to be in good agreement with SSC–PW calculations for the known structure. However, for a structure with this high a distance above the Ni surface, the effects of forward scattering become weaker, since the scattering angle from any near-neighbor Ni atom becomes larger. For example, for the Ni nearest neighbors in the fourfold hollow, a very low emission angle of 5° with respect to the surface still corresponds to a minimum scattering angle of approximately 43° that is well outside of the forward scattering cone at high energy (cf. Fig. 2). Thus, the strongest contribution to azimuthal anisotropy is scattering from the other (coplanar) S adsorbate atoms, for which the scattering angle is simply the emission angle with respect to the surface. The sensitivity of such XPD measurements to the vertical S–Ni distance is thus expected to be lower than for more nearly in-plane or below-plane adsorption, and it has been questioned as to whether such measurements will be sensitive enough to determine structures for any adsorbate sitting well above the surface.[9] Several possibilities appear to exist for improving the positional sensitivity for such cases: working at higher angular resolutions and taking advantage of additional diffraction fine structure, using lower energies for which large-angle and backscattering are stronger, and/or using special polarization geometries to enhance certain substrate scatterers. Some of these possibilities thus involve synchrotron radiation, and we consider now their application to the S/Ni case in both the scanned-angle and scanned-energy modes.

We first look at the influence of higher angular resolution. S 2*p* azimuthal XPD data at a polar angle of 13° obtained by Saiki *et al.*[100] with a high angular resolution of about ±1.0° are shown in Fig. 17. The data were obtained in scans over 100° in ϕ and then mirror-averaged across [110] to improve statistical accuracy, but all of the features shown were reproduced in the full scan. These results exhibit considerably more fine structure than similar data obtained with a ±3.0° resolution, and the anisotropy is found to go up from 31% to a very high 40% with increased resolution. Also, when these data are compared with the SSC–SW curves shown in this figure for different z positions of S above the fourfold hollow, they exhibit a high sensitivity to position. A more quantitative analysis of these high-resolution results by Saiki *et al.*[100] using R factors for comparing experiment and theory[26d] in fact yields a z value of 1.39 Å for this structure that is in excellent agreement with prior work. This analysis furthermore permits estimating the first nickel–nickel interplanar distance (d_{12}), which is found to be expanded to about 1.86 Å from the bulk value of 1.76 Å. Thus, there

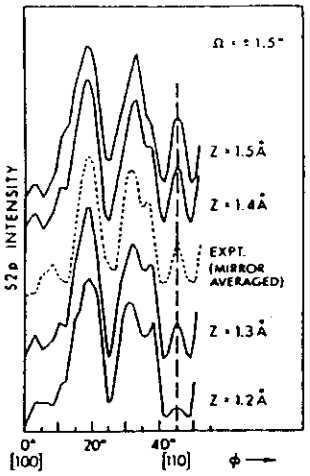

FIGURE 17. Azimuthal XPD data for S 2*p* emission from $c(2 \times 2)$ S on Ni (001) at a kinetic energy of 1085 eV obtained with a high angular resolution of approximately ±1.5°. The polar angle is 13° with respect to the surface. The anisotropy $\Delta I/I_{max}$ is a high 40% for these results, compared to only 31% for the same measurement with a ±3.0° angular resolution; the fine structure is also considerably enhanced with higher resolution. SSC-SW calculations are shown for various distances *z* of the S above the Ni surface. (From Ref. 100.)

is considerable potential in using high-energy measurements with high angular resolution, even for adsorption at large *z* distances above approximately 1.0Å.

Going to lower energies with synchrotron radiation in such azimuthal measurements also has potential for such studies. We show in Fig. 18 results for S 1*s* emission from the $c(2 \times 2)$S overlayer on Ni (001) obtained by Orders *et al.*[19b] Here, the experimental geometry was chosen so that the polarization vector

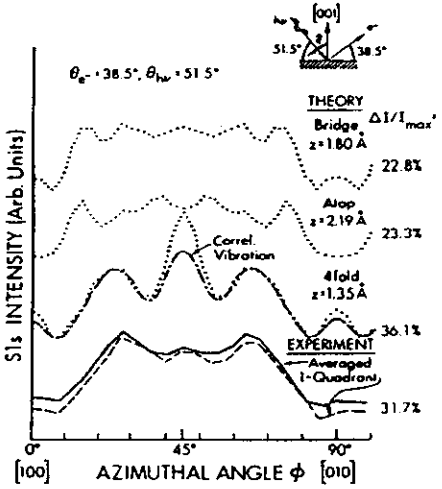

FIGURE 18. Synchrotron radiation excited S 1*s* intensity from $c(2 \times 2)$ S on Ni (001) at a kinetic energy of 282 eV. The geometry chosen emphasized nearest-neighbor backscattering because the polarization vector was oriented directly toward the relevant Ni nearest neighbor, as shown in the inset at upper right. SSC-PW calculations for three possible adsorption sites of bridge, atop, and fourfold are shown as dotted curves. The dashed-dotted fourfold curve involves a more correct inclusion of correlated vibrational effects. (From Refs. 19(b) and 101.)

was directed rather precisely toward nearest-neighbor Ni atoms for certain azimuthal positions in a φ scan. Backscattering from this type of Ni atom should also be rather strong at the photoelectron energy of 282 eV chosen (cf. Fig. 2). This energy is nonetheless high enough that a single-scattering model should still be reasonably quantitative. The experimental data is here compared with SSC–PW calculations for three different bonding sites (bridge, atop, and fourfold) with reasonable S–Ni bond distances, and the correct fourfold site is clearly in better agreement with experiment. The agreement is also significantly improved if a more accurate allowance for correlated vibrations is included in the SSC calculations, as shown by the dashed–dotted curve.[101]

However, a note of caution is in order concerning the use of different polarization orientations, since experimental and theoretical work on S/Ni by Sinkovic *et al.*[19a] indicates that a geometry in which the polarization is nearly perpendicular to the electron emission direction (instead of parallel, as in Fig. 18) increases the importance of multiple-scattering events and causes more significant deviations from a simple theoretical model. This is thought to occur through a weakening of that portion of the photoelectron wave emitted directly in the detection direction in comparison to the various scattered waves that can interfere with it. The intensity distribution is thus produced by the interference of direct and scattered waves that are all of the same magnitude, a situation rather like that in LEED where all contributions to intensity are those due to relatively weak backscattering; thus, MS effects might be expected to be more important. In most photoelectron and Auger experiments, the direct-wave amplitudes are stronger than those of the scattered waves, and it can be argued that this is a fundamental reason for the higher degree of applicability of a single-scattering approach.

Finally, we consider scanned-energy or ARPEFS measurements on S/Ni (001) of the type pioneered by Shirley and co-workers.[8,25] In this type of experiment, an adsorbate core intensity is measured as a function of $h\nu$ in a fixed θ, φ geometry, and the resulting EXAFS-like oscillations are analyzed in order to derive the adsorbate position. The data are usually analyzed as a normalized $\chi(E)$ or $\chi(k)$ function. Figure 19 shows typical experimental data of this type in a normal-emission geometry, for S 1*s* emission from $c(2 \times 2)$ S/Ni (001).[8] Allowance has been made here for the interference between the S Auger peak at 155–160 eV and the S 1*s* photoelectron peak. These results are compared to both MSC–SW calculations by Barton and Shirley[25] in Fig. 19a and SSC–SW calculations by Sagurton *et al.*[21] in Fig. 19b. The agreement is very good for both sets of theoretical curves, provided that the first nickel–nickel interlayer distance (d_{12}) is relaxed outward from the bulk value of 1.76 Å to 1.84 Å (*cf.* the two theory curves in Fig. 19b). This interlayer relaxation, as first pointed out by Barton and Shirley, thus illustrates the high sensitivity of photoelectron diffraction to subtle structural changes on the order of 0.10 Å or less.

It is also clear from this figure and other work on the S/Ni system[21,22] that both the single-scattering and multiple-scattering approaches describe the experimental results well and that they also lead to very similar structural conclusions, with only the perpendicular distance for S being different by 0.05 Å between the two analyses. Thus, although the MSC–SW approach is certainly in principle more accurate and does lead to $\chi(k)$ amplitudes in better agreement

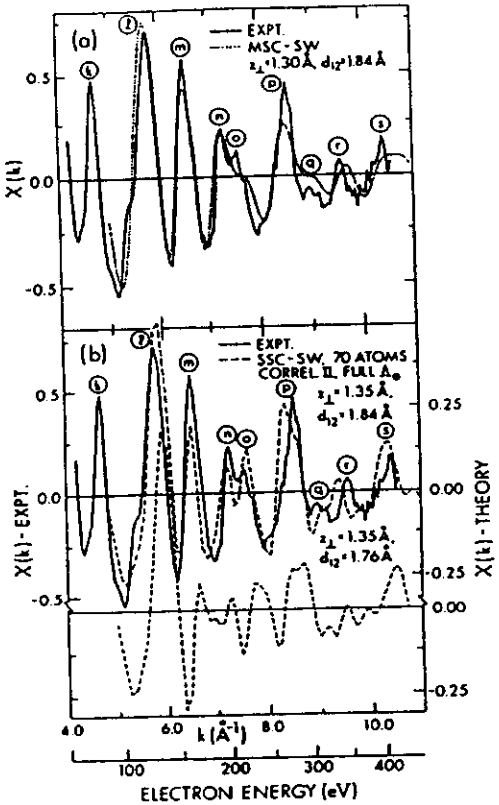

FIGURE 19. Comparison of scanned-energy S 1s data for $c(2 \times 2)$ S on Ni (001), θ_{in} = 70°, θ_{e-} = 0° (From Ref. 8) with: (a) a multiple-scattering cluster spherical-wave (MSC-SW) calculation due to Barton and Shirley (From Ref. 25), and (b) single-scattering cluster spherical wave (SSC-SW) calculations due to Sagurton *et al.* (From Ref. 21). Both the sulfur vertical distance z and the first Ni–Ni interplanar distance d_{12} are specified. (Fig. from Ref. 21.)

with experiment, the SSC–SW method appears capable of a usefully quantitative description of the observed oscillations and fine structure.

Another aspect of this analysis noted by Barton and Shirley[25] is that nearest-neighbor backscattering followed by emitter forward scattering (cf. Fig. 3b–i) can be an important factor in producing the full amplitude of the ARPEFS oscillations at low energies. This may be the reason why the single-scattering curves in Fig. 19b have lower amplitudes, although a different allowance for vibrational effects also could play a role.[21]

An additional useful aspect of such ARPEFS data is in being able to Fourier transform $\chi(k)$ curves to yield peaks which are for some (but not necessarily all) of the strongest scatterers rather directly related to interatomic distances via the path-length difference and the scattering angle [cf. Eq. (10)]. The degree to which Fourier transforms can be used in this way is discussed in detail elsewhere.[21,25] However, ARPEFS Fourier transforms (FTs) need not be as simply associated with certain spheres of neighbors as are those of EXAFS and SEXAFS; the reason for this

is the potentially large number of scattering events and various possible scattering angles that can be associated with a given region in the transform.[21] Nonetheless, such FTs have been used to rule out certain structures as part of a more detailed structure determination; we consider such an example in the next section.

4.2.3. Sulfur/Cr (001)

We now turn to a recent study of $c(2 \times 2)$ S/Cr (001) by Terminello *et al.*[20] that serves to represent a state-of-the-art analysis of scanned-energy or ARPEFS data. In this work, S 1*s* intensities were scanned as a function of energy up to about 475 eV above threshold; two different emission directions were studied; [001] and [011], with polarizations oriented in general along the emission direction (35° off normal toward [011] for [001] emission and along [011] for [011] emission). Special care was taken to avoid spurious energy-dependent effects in the measuring of intensities, with normalization being needed for both the incident photon flux and the transmission function of the electron-energy analyzer. As for S/Ni (001), the interference between the S Auger peak at 155–160 eV and the S 1*s* photoelectron peak was allowed for by carefully subtracting out the former. Fourier transforms of the data were made, with the inner potential being treated as an adjustable parameter and the $\chi(k)$ data being multiplied by a Gaussian window function to reduce ringing effects in the final FTs. The strongest peaks in these transforms were then taken to be semiquantitatively indicative of certain near-neighbor path-length differences; this analysis thus implicitly assumes that the single-scattering Eq. (10) represents a good first-order description of the diffraction and that there are no significant interferences between the effects of different near-neighbor scatterers. The approximate geometric information from the FT peak positions was found to point to the fourfold-hollow site as the adsorption position.

The final quantitative determination of the site type and the structure was made by directly comparing the experimental $\chi(k)$ curves (Fourier filtered to remove effects due to path-length differences beyond about 20 Å) with multiple-scattering cluster calculations using spherical-wave scattering. As one example of these results, Fig. 20*a* compares experimental curves along the two directions with curves calculated for S adsorbed on three types of sites. It is very clear here that the fit is best for the fourfold site (cf. similar comparison for the scanned-angle S/Ni results in Fig. 18).

Pursuing the fourfold site further by means of an R-factor comparison of experiment and MSC–SW theory, the authors derive a geometry that includes a determination of S–Cr distances down to the fifth layer of the substrate. Some of the results of this R-factor analysis are shown in Fig. 21. It is interesting here that the two sets of data for emission along [001] and [011] azimuths and with polarization nearly parallel to each emission direction are complementary in their sensitivities to different structural parameters. The [001] results are much more sensitive to the Cr_2-atop position because strong single and multiple backscattering can be involved (cf. Fig. 3b–i). By contrast, the [011] data is much more sensitive to the Cr_2-open position for the same reason. The polarization orientations enhance these effects by preferentially directing the initial photoelectron wave toward these scatterers (cf. Fig. 3a). The final results of this

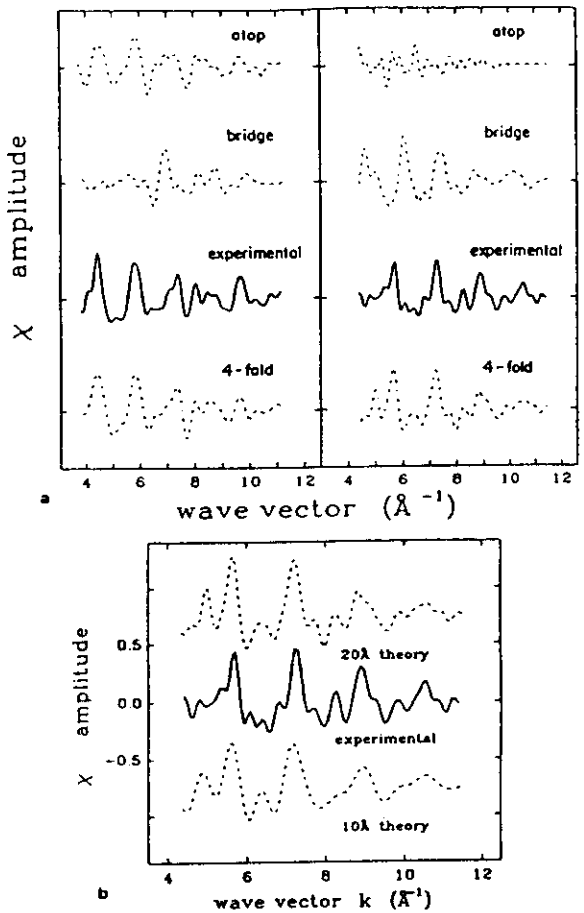

FIGURE 20. (a) Comparison of scanned-energy S 1*s* experimental data for emission from *c*(2 × 2) S on Cr (001) along the [001] direction (left panel) and [110] direction (right panel) with MSC-SW calculations for different adsorption sites of atop, bridge, and fourfold. (b) As in (a), but comparing the data obtained in the [011] azimuth to MSC-SW theory for the final optimized fourfold-hollow structure with different path-length cutoffs of 20 Å and 10 Å. (From Ref. 20.)

R-factor analysis show an 8% reduction of the mean separation of the first and second Cr layers (compare the 3% expansion in similar S/Ni results in Fig. 19) and further suggest a slight corrugation of the second layer and a slight expansion of the separation of the second and third layers, although the latter are not fully conclusive within the error limits of 0.02–0.03 Å estimated by the authors.

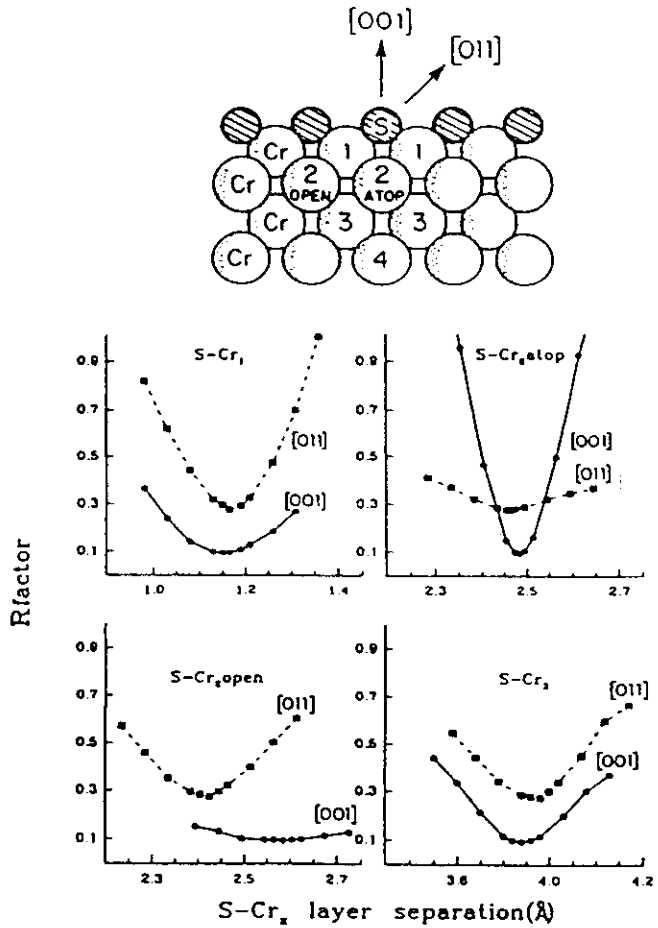

FIGURE 21. *R*-factor analysis of the scanned-energy results of Fig. 20, showing the geometry involved and the variation of the *R* factor with various S–Cr layer separations. (From Ref. 20.)

A further important point made in this work is that the $\chi(k)$ curves exhibit fine structure associated with path-length differences out to about 20 Å. Such fine structure in ARPEFS data and the need to use rather large clusters of up 50–100 atoms to adequately model S/Ni data have also been discussed previously (see Fig. 19 and Ref. 21). The work by Terminello *et al.* shows this explicitly by comparing experimental $\chi(k)$ curves for S/Cr with MSC–SW curves that have

been cut off at both 10 Å and 20 Å total scattering lengths; these results are presented in Fig. 20b, where it is clear that the fine structure in experiment is better modeled by the 20-Å curve, especially for wave vectors above about 7 $Å^{-1}$. This sensitivity permitted a final determination of Cr layer spacings down to that between the fourth and fifth layers, although the accuracy decreases from an estimated ±0.02–0.03 Å for the first three spacings to ±0.07 Å for the fourth spacing measured. It is, finally, worth noting that the approximately 20 Å limit noted here is in the same range as that found in the higher-energy scanned-angle O/Ni results presented in Fig. 16. Thus, both methods seem to have similar sensitivity to more-distant neighbors.

This work demonstrates the full power of the scanned-energy approach, provided that the initial intensities are measured carefully and that the final results are analyzed by means of a quantitative comparison of experimental $\chi(k)$ curves with calculations for a range of choices of geometrical parameters. A very similar analysis has been carried out for the system $c(2 \times 2)$ S/Fe (001) by Zhang *et al.*[102] Although much more time-consuming multiple-scattering calculations were used for all of the geometries tried in these cases, it should be possible in general to do a much more rapid search for promising geometries in single scattering, with only fine tuning of the parameters then being required in multiple scattering.

4.3. Epitaxial Oxide, Metal, and Semiconductor Overlayers

4.3.1. NiO/Ni (001)

Although the case of NiO grown on Ni (001) considered in the previous section does not represent perfect epitaxy, the degree of agreement between experiment at 1200 L and theory in Figs. 13a and 14 clearly shows that the predominant form of NiO present is of (001) orientation. Certain structural conclusions concerning the form of this oxide and its degree of long-range order before and after annealing have also been made (section 4.2.1 and Refs. 26b,c). An analysis of the LEED spot patterns (including a splitting of the NiO (001) spots and corresponding XPD data in fact suggests a two-dimensional superlattice growth of NiO (001) with a lattice constant expanded by exactly $\frac{1}{4}$ with respect to the underlying Ni substrate (cf. Fig. 13b). Although LEED patterns for the unannealed oxide also exhibit a 12-spot ring throught to be due to NiO (111),[97] the XPD results of Figs. 13a and 14 indicate that it is at most a minority species of the total NiO present, since NiO (111) would produce 12-fold symmetric XPD patterns (bottom theory curves in Figs. 13a and 14) that are not seen experimentally. This example thus indicates a very useful sensitivity of high-energy XPD to the orientation of an epitaxial overlayer and its degree of short-range order under various conditions of annealing and deposition.

4.3.2. Cu/Ni (001) and Fe/Cu (001)

We now consider two very different limits of metal-on-metal epitaxial growth taken from some of the first experimental studies in this field, those by Egelhoff

and co-workers and Chambers and co-workers: pseudomorphic epitaxial growth of Cu on Ni[11,103] and island formation by Fe on Cu (001).[104]

Figure 22 illustrates high-energy AED for the first case of Cu on Ni (001). The different near-neighbor forward scattering events allowed as each new Cu layer is added are illustrated by the arrows in Fig. 22a. In Fig. 22b, experimental data from Egelhoff[11] are compared to theoretical SSC–PW curves from Bullock and Fadley.[71] In Fig. 22c, some of the same experimental data are compared to very recent multiple-scattering calculations by Xu and van Hove.[73]

In Fig. 22b, the relatively abrupt appearance at certain overlayer thicknesses of forward-scattering features such as those at $\theta = 45°$ and 90° (normal emission) can be used as a direct measure of the number of overlayers in the range of about 0–3 ML. Comparison with Fig. 22a also shows that the appearance of each of these two peaks corresponds to the onset of forward scattering by the two nearest neighbors encountered in this polar scan from [100] to [001]. The simple origin of these two peaks has also been directly verified by comparing SSC calculations with and without these important scatterers present.[71]

Thus, simple forward scattering peaks from nearest and next-nearest neighbors are very useful in studies of epitaxy, as we have also discussed for the oxide case in the last section. However, the interpretation of weaker features such as those at $\phi \approx 20°$ and 70° in Fig. 22b need not be so simple. Calculations with various atoms removed from the cluster show that these have more complex origins which require at least a full SSC calculation for their explanation.[71] For example, the peak near 70° is a superposition of simple forward scattering by atoms along [103] and [102] and, more importantly, first-order effects (cf. the inset of Fig. 8) from the atoms along [001] and [101]. Thus, for atoms that are further away than the first three or four spheres of neighbors, a mixed origin in forward scattering and higher-order interference effects is generally to be expected. This conclusion has also been confirmed in a recent analysis by Osterwalder *et al.*[48] of an extensive set of high-resolution Ni $2p_{3/2}$ data from bulk Ni (001) that we discuss further in section 5.1.

Figure 22a also makes it clear that, in pseudomorphic growth with the lateral lattice constants locked to those of Ni, the vertical spacing of the Cu layers will determine the θ position of the peak near 45°. A ±1° change in this peak position from 45° would correspond to a ±0.12-Å change in the vertical lattice parameter or a ±0.06-Å change in the interplanar spacing. This sensitivity has in fact recently been used by Chambers *et al.*[12a,b] to measure the degree of outward vertical relaxation in thin Cu overlayers on Ni (001). It should thus be possible to measure interlayer spacings with accuracies of better than 0.1 Å in this way[24,71,73] although doing some sort of theoretical modeling at least at the SSC–PW or SSC–SW level (as Chambers *et al.* have done[12]) is advisable to verify peak origins, shapes, and predicted shifts with relaxation. Using higher angular resolution also should be beneficial for such studies by making it possible to determine forward-scattering peak positions more precisely.

The main point of discrepancy between experiment and SSC–PW theory in Fig. 22b is that the peak for forward scattering along the nearest-neighbor [101] direction has a relative intensity too high for thicker overlayers by about a factor of about 2. As expected from the prior discussion of Fig. 5, using spherical-wave

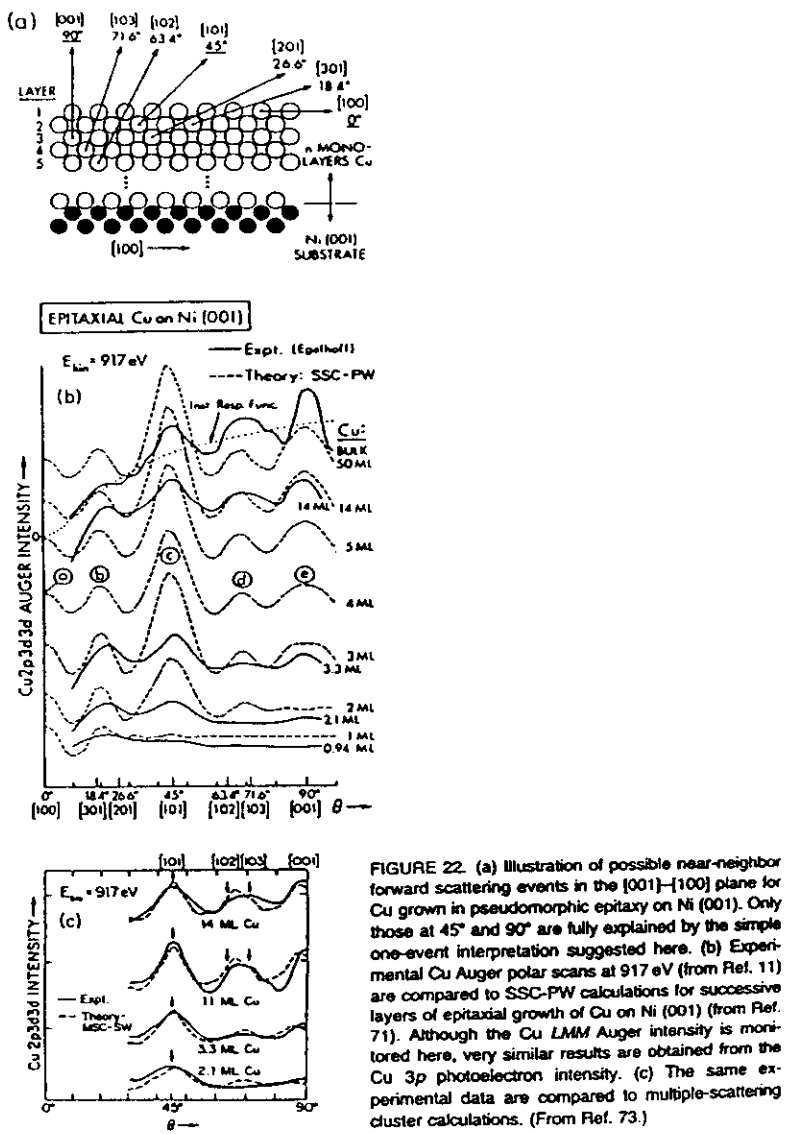

FIGURE 22. (a) Illustration of possible near-neighbor forward scattering events in the [001]–[100] plane for Cu grown in pseudomorphic epitaxy on Ni (001). Only those at 45° and 90° are fully explained by the simple one-event interpretation suggested here. (b) Experimental Cu Auger polar scans at 917 eV (from Ref. 11) are compared to SSC-PW calculations for successive layers of epitaxial growth of Cu on Ni (001) (from Ref. 71). Although the Cu *LMM* Auger intensity is monitored here, very similar results are obtained from the Cu 3*p* photoelectron intensity. (c) The same experimental data are compared to multiple-scattering cluster calculations. (From Ref. 73.)

scattering in the SSC model is found to significantly improve agreement for this relative intensity by reducing it to about $\frac{2}{3}$ of the magnitudes seen in Fig. 22b for thicknesses >3.0 ML[50b]; it is nonetheless still too high by 1.3–1.5 times in comparison with experiment. The remaining discrepancy is due to multiple scattering effects, and the calculations of Fig. 22c include the additional defocusing of intensity along the [101] direction. Much more quantitative agreement with experiment is obtained here. However, even though certain forward-scattering peaks may have their relative intensities decreased by multiple scattering, it should nonetheless still be possible to use the peaks along [001] and [101] in the simple way described in the preceding paragraphs to monitor overlayer thicknesses and determine interlayer relaxations.[71,73]

A more recent paper by Egelhoff[103] has also looked experimentally at a single pseudomorphic Cu (001) layer on Ni (001) buried under various numbers of Ni (001) overlayers. In this work, the attenuation and broadening of certain features with increasing layer thickness is interpreted as evidence of stronger multiple-scattering effects in emission from greater depths. Although the defocusing effects seen in the MS results of Fig. 6 make this a plausible conclusion, Herman *et al.*[105] have made SSC–SW predictions for the cases studied, and these are found to show very similar attenuation to the experimental data. As one example of this comparison of experiment and SSC–SW theory, Fig. 23 shows results for the 917 Auger peak; the experimental data have been corrected for the θ-dependent instrument response by dividing by the curve for a single Cu

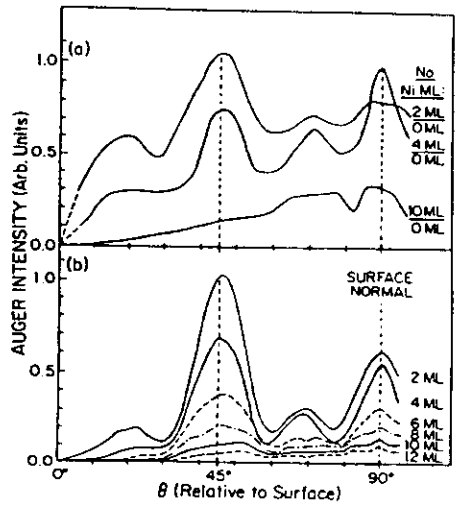

FIGURE 23. (a) Experimental data for Auger emission from a single pseudomorphic Cu (001) layer on top of Ni (001) buried underneath different numbers of layers of epitaxial Ni, also in (001) orientation. (From Ref. 103) (b) Theoretical calculations within the SSC-SW approximation of the results in (a), including curves for other overlayer thicknesses. (From Ref. 105.)

monolayer with no overlying Ni (shown as "0 ML"). Although the relative intensity of the peak at 45° compared to that at 90° is again predicted in theory to be too high, the trends in experiment as the Ni overlayer is increased in thickness are surprisingly well reproduced by the SSC calculations. In particular, the change in the absolute intensity of the peak at 45° with thickness is well reproduced by the calculations, and its final broadening out and diminution of importance in comparison to the peak at 90° is also correctly predicted. Discrepancies noted are that the broad, flat feature seen in experiment at about 70° is not fully developed in the single scattering theory and that an initial narrowing of the peak along 45° that may be due to multiple-scattering effects (cf. the discussion of Fig. 6 and Fig. 22c) is not seen. Experimental errors of as much as ±10–20% in measuring the number of monolayers (cf. calculated curves at other thicknesses), as well as the possible presence of defects in the growing Ni layer,[12a,b] could also affect the agreement between experiment and theory. More recent multiple-scattering calculations for this buried-monolayer system by Xu and van Hove[73] and by Kaduwela *et al.*[84] yield a more quantitative description of the decrease in intensity of the peak at $\theta = 45°$, although the experimental overlayer thicknesses have to be decreased by from 0.6 to 1.5 ML in the calculations to yield optimum agreement. However, on going to thicker overlayers on the order of ten layers, there is still a stronger peak in MS theory than in experiment near $\theta = 70°$.

Thus, although such a deeply imbedded emitter layer clearly represents an extreme case of the type shown in Fig. 3b–ii, for which multiple-scattering effects ought to be maximized, the case for these data definitely exhibiting such effects is not as strong as might be expected, and the SSC approach still yields at least a semiquantitative description of the data.

A final note of caution in connection with this study[103] concerns the idea that classical trajectories can be used to predict when and how multiple scattering will be important in AED or XPD. Although classical arguments can be didactically useful once the correct answer is known, taking them further seems to be very risky, particularly when the quite simple and wave-mechanical SSC model is already available for comparisons to experiment and to more-accurate calculations including higher-order multiple scattering.

We now turn to the second system: Fe/Cu (001) as studied by Chambers, Wagener, and Weaver[104a] and by Steigerwald and Egelhoff.[104b] Figure 24 shows a similar set of AED data from the latter study for the case of Fe deposited on Cu (001) at ambient temperature and compares it to results like those in Fig. 22b. It is striking here that coverages of one monolayer or less (even down to 0.1 ML) already exhibit the strong forward-scattering peak at 45° characteristic of *fcc* Fe in islands or clusters at least two layers thick, as well as the beginning of the peak along the surface normal associated with three-layer structures. In fact, the 1-ML Fe curve looks very similar to that for 3.3 ML of pseudomorphic Cu in Fig. 22b. These results[104b] and a more detailed set of polar and azimuthal data discussed by Chambers *et al.*[104a] thus show that at least the first one or two layers of Fe grown under these conditions have a strong tendency to agglomerate on Cu (001), a conclusion that has important implications for the magnetic properties of such overlayers.[104] This work nicely demonstrates the general usefulness of such

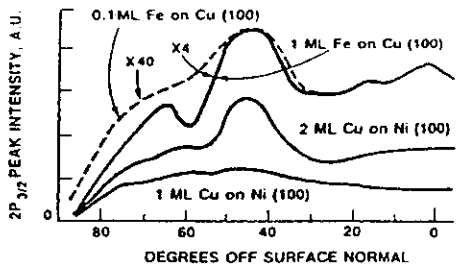

FIGURE 24. Experimental polar scan data for Fe $2p_{3/2}$ emission at 780 eV from Fe deposited at ambient temperature on Cu (001). Data for both 0.1 ML and 1 ML total coverages are compared to similar results for Auger emission from Cu deposited up to 1 ML and 2 ML on Ni (001); cf. Fig. 22(b). Note the presence of strong forward scattering peaks at 45° in both Fe curves and the beginning of a peak along normal for the 1-ML Fe data. [From Ref. 104(b), with more detailed polar and azimuthal data appearing in Ref. 104(a).]

scanned-angle measurements for detecting the presence of island or cluster formation, as discussed further in section 4.5.

4.3.3. Fe/GaAs (001)

We now consider another example from the work of Chambers *et al.*[12a,b] in which Auger electron diffraction has been applied to the growth of epitaxial layers of Fe on GaAs (001). This system has been studied extensively because of its interesting magnetic anisotropies in the surface plane, as first discussed by Krebs, Jonker, and Prinz.[106] It is complicated by the fact that outward diffusion of As is thought to occur, even though at the same time the Fe atoms appear in LEED to be growing in (001) epitaxy. A polar scan in the [100] azimuth of the $L_3M_{4,5}M_{4,5}$ Fe Auger peak at approximately 710 eV kinetic energy provides further information on how this might be occurring, as illustrated in Fig. 25. Here, the experimental AED curve of Chambers *et al.* for a 10-ML Fe overlayer on GaAs is compared to an analogous experimental Fe $2p_{3/2}$ XPD curve for a clean *bcc* Fe (001) surface due to Herman *et al.*[107]; the XPD peak furthermore has a kinetic energy of about 780 eV, very close to that of the Auger peak, so that the two diffraction patterns would be expected to be very similar for a given crystal structure. In fact, the two experimental curves are very different, with the *bcc* Fe (001) showing a much lower intensity for the peak along [101] and different fine structure at polar angles of about 15–30° and 60–75°.

Also shown in Fig. 25 are SSC–PW theoretical curves for three overlayer crystal structures: *bcc* Fe with $a = 2.82$ Å [the bulk-lattice constant which also gives a very good match to the GaAs (001)], primitive cubic (*pc*) Fe with $a = 2.82$ Å, and *fcc* Fe with $a = 2.82$ Å. It is clear that the *fcc* calculation gives the best agreement with the Fe/GaAs experimental data as to both the relative intensity of the [101] peak and the fine structure. The calculations for the other two structures seriously underestimate the intensity of the peak along the [101] direction. The *bcc* calculation also agrees best with the XPD curve from clean Fe (001), particularly as to the relative intensities of the weaker features from $\theta = 15°$ to 75°, even if all of the fine structure is not correctly predicted. All

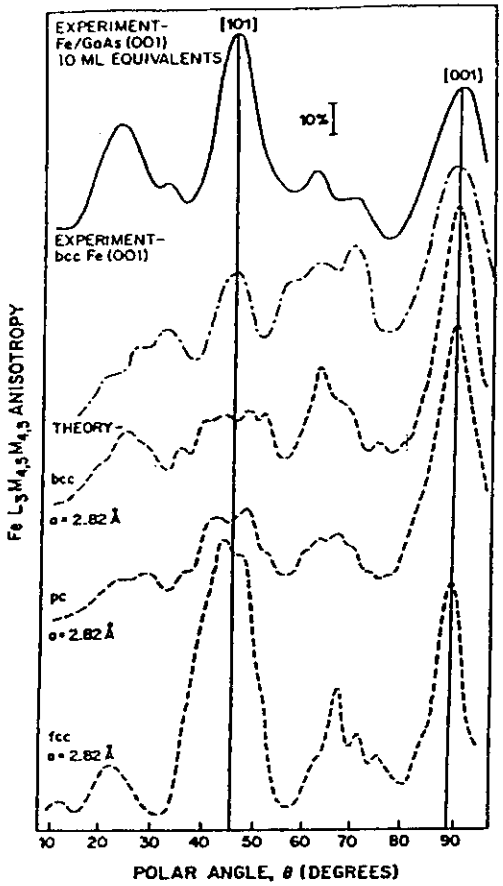

FIGURE 25. Experimental polar scan of the Fe *LMM* Auger intensity at 703 eV from 10 ML of Fe deposited on GaAs (001) (solid curve) is compared to theoretical calculations for various Fe lattices (dashed curves). (From Ref. 12(b).) The scans are in the [100] azimuth (ϕ = 0°), with the directions [101] and [001] indicated. The calculations are at the SSC-PW level, and they are shown for Fe in three crystal structures: *bcc*, *pc* (primitive cubic), and *fcc* (which is proposed to be *bcc* Fe with As atoms outwardly diffused into the *fcc* interstitial sites). Also shown for comparison is an experimental polar scan for bulk Fe (001) in the same azimuth (dot-dash curve) from a separate study. (From *ref.* 107.)

calculations predict a strong peak along the normal or [001] direction; this is due to forward scattering from atoms with a closest spacing of 1.000a for all three structures. Along the [101] direction, by contrast, the *fcc* structure has nearest-neighbor scatterers at a distance of $a/\sqrt{2} = 0.707a$ (cf. Fig. 22a) whereas, in the *bcc* and *pc* structures, the nearest scatterers are twice that distance away at $\sqrt{2}a = 1.414a$. This explains the stronger forward-scattering peak along [101] in the *fcc* theory.

The combined experimental and theoretical results in Fig. 25 thus suggest that the local structure in Fe/GaAs has scatterers that are at the *fcc* positions. These results have been explained by the interesting proposal[12a,b] that the outward-diffusing As atoms occupy the face-centered positions in a *bcc* Fe lattice so as to yield an overall AED pattern that is essentially *fcc* in nature. Although Fe and As are slightly separated in atomic number (26 and 33, respectively) so that the all-Fe calculations of Fig. 25 are not in that case strictly correct, the forward-scattering strength that is dominant at these energies is not a strong function of atomic number (but rather of atomic size, as noted in section 3.1.3), and thus these theoretical simulations should be reasonably accurate for the hypothesized structure as well.

This work thus illustrates another aspect of higher-energy AED and XPD that should be generally useful in studying the detailed structures of complex epitaxial overlayers that may have impurities present, such as atoms diffusing outward from the substrate or inward from the surface. An obvious complementary and useful type of data that could be derived for such a system would be to look at the AED or the XPD of the impurity. For the example of Fe/GaAs, if the hypothesized structure is correct, As also should show an *fcc* type of diffraction pattern, although perhaps weaker or with less fine structure if it is preferentially segregated to the surface of the Fe overlayer. Another recent example of this type is a combined AED/XPD study of dopant P and Sb atoms in Ge epitaxial layers on GaAs (001) by Chambers and Irwin;[12c] here P was found to occupy lattice sites, whereas Sb was segregated to the surface.

4.3.4. $Hg_{1-x}Cd_xTe$ (111)

As a final example of an epitaxial system, we consider a recent scanned-angle XPD study by Granozzi, Herman *et al.*[108] of $Hg_{1-x}Cd_xTe$ (111) grown by liquid-phase epitaxy. This sample underwent transport at atmospheric pressure before being studied and was minimally ion-bombarded so as to remove a thin oxide layer from the surface. It was not subjected to bakeout or annealing after ion bombardment, to avoid depleting Hg from the surface region. At the time of measurement, the value of x was approximately 0.4. In spite of the less-than-ideal surface expected to remain after such a treatment, XPD modulations of $\Delta I/I_{max} \approx 15$–25% were seen in all of the major photoelectron peaks observable (Hg $4f_{7/2}$ at a kinetic energy of 1383 eV, Cd $d_{5/2}$ at 1078 eV, and Te $3d_{5/2}$ at 910 eV). Qualitatively comparing Hg, Cd, and Te diffractions curves immediately indicated that the Hg and Cd atoms were occupying similar lattice sites, as expected.

As another more subtle structural problem resolvable from this data, the question of the nature of the termination of the surface also was addressed. That is, was the surface terminated preferentially with double layers having cationic Cd (or Hg) on top and anionic Te on the bottom (termed Model *A*) or with the reverse (termed Model *B*)? Comparing the azimuthal XPD patterns for Cd and Te obtained at several polar angles with SSC–SW calculations for both Models *A* and *B* permits determining the dominant type of termination, even for a surface that probably has a reasonable amount of damage on it. Some of this data is shown in Fig. 26, where Cd emission at $\theta = 19°$ and 35° (both chosen to pass through near-neighbor scattering directions) is considered. It is clear that, for both angles of emission, the agreement between experiment and theory as to both visual fit and *R* factor[26d] is much better for a Model *A* termination; peak relative intensities, positions, and fine structure are much better predicted. Similar conclusions can be drawn from analogous Te azimuthal scans.

As one further aspect of this study, we consider the forward scattering origin of the various major peaks observed in Fig. 26 with the aid of Fig. 27, which indicates the several near-neighbor forward-scattering events possible in a surface terminated as in Model *A*. For the data at $\theta = 19°$, the effects of the event labelled as $\theta = 19°$, $\phi = 0°$ are clear in both experiment and theory. For the data at $\theta = 35°$, the principal peaks are due to events of the types labelled $\theta = 35°$, $\phi = 60°$ and $\theta = 30°$, $\phi = 30°$, 90°.

The analogous Te curves at these polar angles are very different from those of Cd in both experiment and theory, with peak shifts and relative intensity

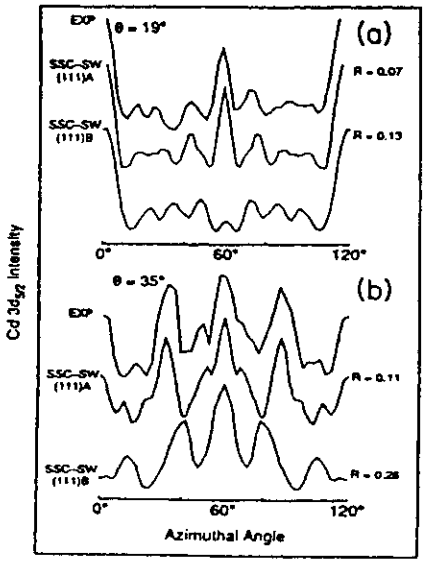

FIGURE 26. Al *Kα*-excited azimuthal scans of Cd $3d_{5/2}$ intensities from $Hg_{1-x}Cd_xTe$(111) ($x = 0.4$) at polar angles of (a) 19° and (b) 35° passing through or very close to forward-scattering low-index directions shown in Fig. 27 as $\theta = 19°$, $\phi = 0°$, $\theta = 35°$, $\phi = 60°$, and $\theta = 30°$, $\phi = 30°$, 90°. Also shown are SSC–SW curves for the two possible surface terminations (Model A = Cd or Hg on top, Model B = Te on top), together with *R* factors comparing experiment and theory. (From Ref. 108.)

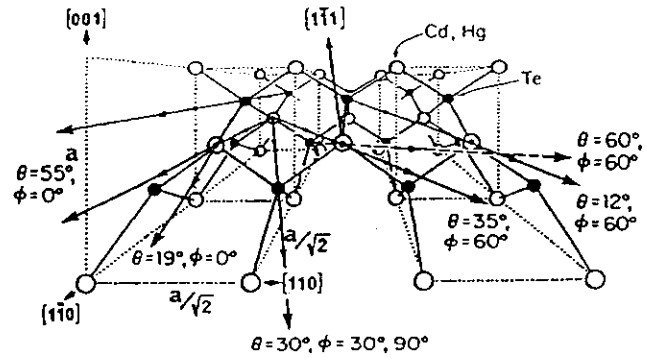

FIGURE 27. Perspective view of the unreconstructed (111) surface of $Hg_{1-x}Cd_xTe$(111) in the Model *A* surface termination of Fig. 26, with the θ, ϕ coordinates of various near-neighbor/low-index directions along which forward scattering might be expected to be strong. These directions would be the same for the unreconstructed (111) surfaces of any material with the zincblende or diamond structure, as will be used later in discussing Fig. 36.

changes. In particular, the peaks at $\theta = 35°$, $\phi = 30,°$ and 90° for Cd disappear in Te and are replaced by two weaker features at $\theta = 35°$, $\phi = 38°$ and 80°. This is easily explained, since Fig. 27 shows that, in an *A*-type termination, the peaks that disappear are only strong forward-scattering events in the first double layer for Cd emission; thus, they are not expected to be seen for Te.

Inspection of other azimuthal data of this type shows that most of the strong features can be assigned an origin in the various simple near-neighbor forward-scattering effects illustrated in Fig. 27, although it is again important to realize that higher-order interference effects can significantly influence the intensities due to forward scattering by atoms further from the emitter (cf. the discussion of Fig. 22 and, below, Figs. 37 and 38).

This study thus illustrates the further use of higher-energy XPD for epitaxial systems, for which bonding sites of substitutional atoms and the type of surface termination of a compound semiconductor can be determined.

4.3.5. Diffraction Effects in Quantitative Analysis and Photoelectron-detected EXAFS

We conclude this discussion of epitaxial systems with two notes of caution concerning the strong diffraction effects that are expected in either photoelectron or Auger emission from well-ordered lattices.

Diffraction Effects Must Be Carefully Allowed for in Any Attempt to Do Quantitative Analyses of Surface Composition. Methods of correcting for such effects have been considered by both Connelly *et al.*, for simple adsorption on a metal,[109] and more recently for semiconductor surfaces by Alnot *et al.*[110] Not adequately allowing for such effects can lead to errors of as high as ±50% in

measured stoichiometries! Some of the methods for such corrections are averaging over diffraction curves obtained in more than one polar or azimuthal scan, taking advantage of the crystal-structure symmetry to find scans in which different constituents will have nearly identical diffraction patterns (e.g., this is possible in the zincblende structure[110]), or using theoretical calculations to try to determine directions in which diffraction effects can be neglected.

By contrast, a potentially useful aspect of diffraction effects for surface analysis is in monitoring intensities along different directions as a function of coverage during epitaxial growth, as suggested by Idzerda *et al.*[67] Model calculations of such curves in the SSC–PW model suggest that it should be possible to resolve the completion of the first few layers of growth.

The Use of Photoelectron Intensities to Monitor EXAFS-like Oscillations Requires Sufficient Angular Averaging. The idea of using photoelectron intensities to measure EXAFS oscillations for near-surface species has recently been proposed by Rothberg *et al.*[111] and applied to semiconductor systems by Choudhary *et al.*[112] It is clear from the strong oscillations of up to 70% seen in scanned-energy photoelectron diffraction and their dramatic dependence on emission direction (cf. Fig. 20) that an adequate averaging over direction must be undertaken to yield something related to the 4π-averaged EXAFS signal. Although this is automatic for disordered or polycrystalline systems,[111] it is problematic in single-crystal studies. Lee[41] has in fact questioned on theoretical grounds whether even the maximum 2π averaging possible in photoemission for such cases is sufficient to yield the EXAFS limit. Nonetheless, preliminary experimental results of this type[112] using the modest type of averaging inherent in the conical solid angle of a cylindrical mirror analyzer (CMA) appear to yield EXAFS-like data. However, it is the author's opinion that a single-geometry CMA measurement does not represent sufficient angular averaging to reliably yield the EXAFS limit and that the close similarity of these result to EXAFS data may have a fortuitous component. Perhaps measuring intensities for several different orientations of the specimen with respect to the analyzer would improve the reliability of this approach, but it is not clear that this has been done to date. The solid-angle averaging of a particular analyzer could also be checked by carrying out SSC calculations over the directions involved and summing these intensities, as was done recently by Idzerda *et al.* in another context.[67]

Overall, both XPD and AED thus have considerable potential for the study of the morphology of the first 1–5 layers of an epitaxial system. The strongest peaks are expected to be directly connected with simple forward scattering from the first few spheres of neighbors around a given emitter. Weaker features may involve a superposition of several types of scattering events. Thus, a quantitative analysis of the full intensity profile will require calculations at least at the SSC level. Predicting peak relative intensities correctly if emission along a dense row of atoms is involved may also require the inclusion of multiple scattering. However, much useful information about the surface structure, layer thickness, morphology, impurity-site type, and surface termination should be derivable from a consideration of the possible strong forward-scattering peaks due to the nearest

neighbors (cf. Figs. 22 and 27) combined with theoretical modeling at the single scattering level.

4.4. Metal–Semiconductor Interface Formation

We now consider two recent examples of the application of higher-energy XPD to the study of metal–semiconductor interface formation. This kind of XPD study was pioneered by Kono and co-workers, and more detailed discussions appear elsewhere, including work on other metal–semiconductor combinations.[49,113,114] The examples chosen here both involve the initial stage of metal reaction with Si surfaces and represent structures over which controversy still exists. The examples differ in the final structure proposed. The first case, K/Si (001), is a metal overlayer relatively far above the Si surface. The second case, Ag/Si (111), is a metal layer nearly coplanar with the first Si layer. This strongly affects the degree and manner in which forward scattering by Si or metal atoms influences the observed diffraction patterns.

4.4.1. K/Si (001)

In this study by Abukawa and Kono,[114] azimuthal K 2*p* XPD data have been obtained for the structure formed by depositing K to saturation onto the Si (001) (2 × 1) reconstructed surface. The substrate surface is thought from a number of previous studies to consist of rows of dimers, as shown by the small open circles in Fig. 28. The most-often-discussed model for the potassium structure on this surface is the so-called one-dimensional-alkali-chain (ODAC) model illustrated in Fig. 28a; it corresponds to a $\frac{1}{2}$ ML coverage, and leaves open grooves adjacent to each high-lying row. However, there is still considerable controversy surrounding the structure of K adsorbed on Si (001), and this geometry has not been directly determined.[115] There is also disagreement as to what constitutes the saturation coverage of K on the surface.[114,115b]

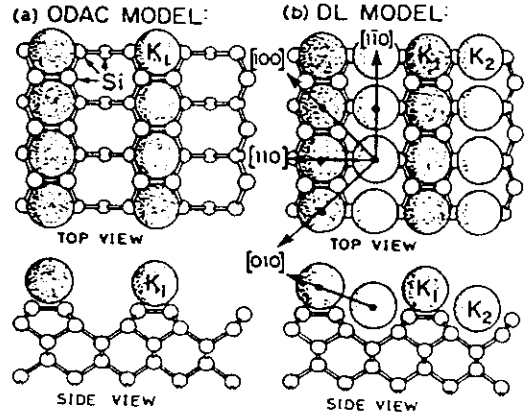

FIGURE 28. Schematic illustration of two structural models for the Si (001) (2 × 1) surface saturated with K: (a) one-dimensional-alkali-chain (ODAC) model, (b) double-layer (DL) model proposed from an analysis of azimuthal XPD data (see Fig. 29). Silicon dimers appear along the [1, −1, 0] rows in both models. Each model can exist in two domains rotated by 90° with respect to one another. Some strong forward-scattering directions in the DL model are shown by arrows. (From Ref. 114.)

Even before considering the actual XPD data, we note that, if only atoms of type K_1 in the ODAC structure are present, the diffraction patterns would be dominated by forward scattering from other K_1 atoms, and this would furthermore be strong only for very low θ and along the $\langle 1,-1,0\rangle$ rows for which the interatomic distances are shortest. The Si atoms should play only a minor role, perhaps producing fine structure in the azimuthal curves for very low takeoff angles.

A set of azimuthal experimental data for this system with emission angles relative to the surface of 14°–22° is shown as the points in Fig. 29. The strongest peak is seen along $\langle 100\rangle$ for a relatively high value of $\theta = 14°$, an observation which already seems at odds with the ODAC model. Considering also the experimental anisotropy $\Delta I/I_{max}$ (scale along left of figure), we see that it can be as high as about 30%, a value which is significantly above those expected in general for such higher-θ scattering from neighbor atoms that are either all in-plane or all below-plane relative to the emitter (cf. Fig. 15 for $c(2\times 2)$ O/Ni (001) as a typical example).

These results suggest trying in addition to the ODAC model another structure in which there are scatterers well above some K emitters. One such model is the obvious one of putting rows of atoms of type K_2 in all of the grooves to yield a 1-ML coverage, as illustrated in Fig. 28b. For this double-layer (DL) model, strong forward scattering can occur for higher takeoff angles, as indicated by the arrows along both $\langle 110\rangle$ and $\langle 100\rangle$ directions. For very low takeoff angles approaching zero, either model is expected to show strong forward scattering for emission along the K rows parallel to $\langle 1,-1,0\rangle$. The presence of two equivalent domains of either structure rotated by 90° with respect to one another also implies

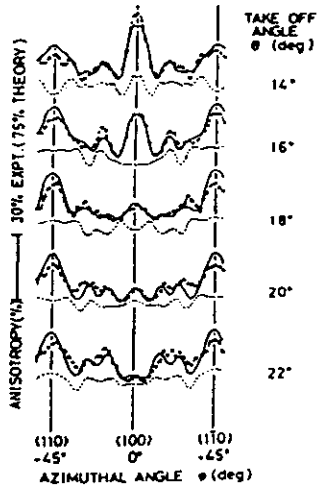

FIGURE 29. Azimuthal data for Al $K\alpha$-excited K 2p emission from the Si(001) (2 × 1) surface saturated with K at polar angles from 14° to 22° above the surface. Experiment is compared with SSC-PW calculations for the two models shown in Fig. 28: ODAC = dashed curves and DL model best fitting data = solid curves. Very similar curves were also obtained with SSC-SW calculations. (From Ref. 114.)

summing two diffraction patterns in the analysis and overall C_{4v} symmetry in both the observed and calculated patterns.

Comparing these experimental data to SSC–PW (or very similar SSC–SW) calculations for the two models[114] is now found to yield clearly superior agreement for the DL model (solid curves in Fig. 29). The strong peak at $\phi = 0°$ which grows in for θ approaching 14° can be explained as being due to emission from K_2 atoms and scattering by their second-nearest K_1 neighbors along $\langle 100\rangle$. The peaks along $\langle 110\rangle$ and $\langle 1,-1,0\rangle$ are due to K_2 emission again, but now involve scattering from nearest-neighbor K_1 atoms (and a sum over domains 90° apart). Additional azimuthal data for θ as low as 4°[114] show strong peaks for $\phi = \pm 45°$ that can be ascribed to the expected forward scattering along $\langle 1,-1,0\rangle$ directions within either K_1 or K_2 rows. Not surprisingly, these latter peaks are also present for very low θ in the theoretical curves for both models, and they are the most significant features in calculations for the ODAC model. Comparing experiment and theory for these lower-θ data also is found to support the DL model. By testing various vertical placements of the two K row types, the authors were able to determine a 1.1 Å vertical separation between the two K rows, and less accurately to determine that the bottom K row was not lower than about 0.5 Å above the first Si layer. For such a 1.1-Å separation, the K_1–K_2 distance is 3.99 Å and slightly larger than the K–K distance of 3.84 Å along either the K_1 or K_2 rows. It is also interesting that, for this structure, the $K_2 \rightarrow K_1$ forward scattering peaks should occur at $\theta \approx 16°$ along [110] and $\theta = 11°$ along [100]; this explains the strong peaks seen in the data over this range of polar angles. The registry of the DL along $\langle 1,-1,0\rangle$ with respect to the underlying Si surface was not determined, but the six-coordinate site shown in Fig. 28b for atoms of type K_1 is that predicted by theory to be the lowest energy.[115a,d]

In a more recent theoretical study of this system by Ramirez,[115d] it is found that adsorption in groove sites (including type K_2 in Fig. 28b) is significantly lower in energy than the six-coordinate site shown for K_1 atoms. Thus, adsorption in the grooves is supported by theory as well. However, the 1-ML structure proposed in this study is different from Fig. 28b in that the atoms of type K_2 are shifted along the $\langle 1,-1,0\rangle$ direction so as to be directly opposite the Si dimers. The K_2 atoms in this model are also predicted to be approximately in-plane with respect to the Si dimers. However, it is doubtful that this structure would yield the strong forward scattering peak seen in XPD along $\phi = 0°$ for relatively high theta values of 12–16°. Thus, even though these calculations[115d] indicate that a double layer with such shifted K_2 atoms is lower in energy than the structure shown in Fig. 28b, the latter structure still represents a better choice based upon the XPD data.

Overall, these XPD results thus provide important new insights into the bonding of K on Si (001) and illustrate several aspects of the use of this technique for metal–semiconductor studies.

4.4.2. Ag/Si (111)

The Ag/Si (111) system has been studied by almost every modern surface-science technique and is known to exhibit, among other things, a well-ordered

$(\sqrt{3} \times \sqrt{3})$ Ag structure and the formation of *fcc* Ag clusters or islands with (111) orientation for exposures that go above the 0.7–1.0 ML needed just to form the $(\sqrt{3} \times \sqrt{3})$ structure.[49,50,116,117] In the following section, we consider the use of XPD in studying such clusters; here, we concentrate on a recent XPD study by Bullock *et al.* of the $(\sqrt{3} \times \sqrt{3})$ structure.[50a,b]

In this study, polar and azimuthal Ag $3d_{5/2}$ XPD data were obtained for a well-ordered and very stable $(\sqrt{3} \times \sqrt{3})$Ag structure, and these experimental results are summarized in Figs. 30a and 31. The smooth and structureless nature of the polar scans in Fig. 30a indicates an absence of strong forward scattering effects, except perhaps at very low takeoff angles of $\theta \approx 4$–$8°$ where a four-peak structure is seen in Fig. 31. A simple geometric calculation then permits the conclusion that the Ag cannot be more than approximately 0.5 Å below the surface Si layer. This is also consistent with the lower anisotropy values of no more than 21% that are found for the azimuthal scans of Fig. 31. It can thus be concluded that there are no strong forward scatterers above the Ag. The azimuthal data are also fully consistent with an earlier XPD study of this system by Kono *et al.*,[49] but they are more detailed in involving full 360° ϕ scans and more θ values.

It is beyond the scope of this review to discuss the many models that have been and are being proposed for this structure, but all known structures have been tested against this azimuthal data by Bullock *et al.*, using *R* factors[26d] as the final quantitative measure of goodness of fit. The calculations were carried out at the SSC–SW level, and in final optimizations also with the full final-state interference of 3*d* emission into *p* and *f* channels. (This latter correction was not found to alter the structural conclusions, a result which is expected to be true in general for higher-energy XPD, but certainly not for work at less than a few hundred eV, as discussed in section 3.1.2).

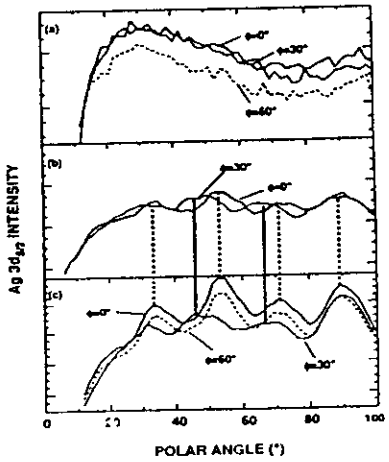

FIGURE 30. Polar XPD scans of Ag $3d_{5/2}$ intensity at 1120 eV from: (a) the $(\sqrt{3} \times \sqrt{3})$ Ag structure on Si (111) formed after annealing an ~1.3-ML Ag overlayer to 550°C; (b) a Ag overlayer of approximately 2 ML average thickness at 450°C; and (c) a thick Ag overlayer of approximately 6 ML thickness at ambient temperature. (From Ref. 50.)

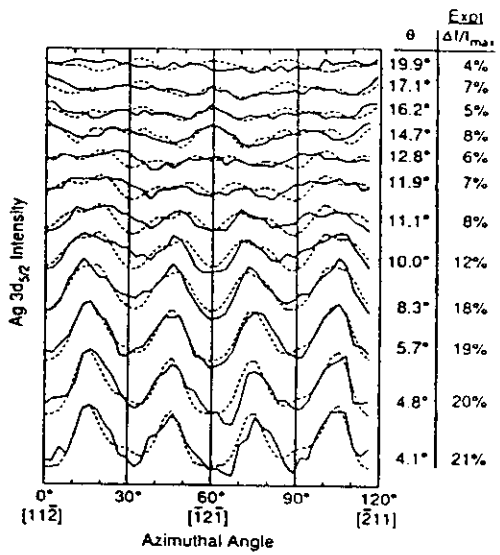

FIGURE 31. Azimuthal XPD scans of Ag $3d_{5/2}$ intensity from $(\sqrt{3} \times \sqrt{3})$ Ag/Si (111) at polar angles from 4° to 20° (solid lines) are compared to SSC-SW calculations for the optimized two-domain model of Fig. 32 (broken lines), for which $s_1 = s_2 = 0.86$ Å; $z_1 = -0.10$ Å, $z_2 = -0.30$ Å, and a 50:50 mixture of the two domains. Full final-state interference in the *d*- to $-p + f$ emission process has been included. This comparison yields an *R* factor of 0.14 (cf. values in Figs. 21 and 26). (From Ref. 50.)

The final model proposed on the basis of this work is for two nearly equivalent domains of Ag in a honeycomb array on a Si surface that has had the top layer of the first Si double layer removed. This two-domain missing-top-layer (MTL) model is illustrated in top view in Fig. 32. The optimized structural parameters are a contraction of the Si trimers toward one another in both domains of $s_1 = s_2 = 0.86$ Å, vertical distances of the Ag relative to the Si layer of $z_1 = -0.1$ Å for Domain 1 and $z_2 = -0.3$ Å for Domain 2 (that is, the Ag is very nearly coplanar with the Si in both domains, but just slightly below it), and a mixture of the two domain types that is between 50:50 and 40:60, with Domain 2 perhaps being slightly more predominant. The fits between experiment and theory for this fully optimized structure are shown in Fig. 31. All other models that have been tried yield significantly worse agreement as judged both visually and by *R* factors. This two-domain model is also closely related to one derived in a prior XPD study by Kono *et al.*: a single-domain MTL Ag honeycomb structure of type 1 with $s = 0.66$ Å and a vertical distance of -0.15 Å. The presence of Domain 2 is suggested to explain the four-peak structure at low θ values in Fig. 31, as illustrated by the nearest-neighbor forward-scattering peaks for the two domains shown at the bottom of Fig. 32. For

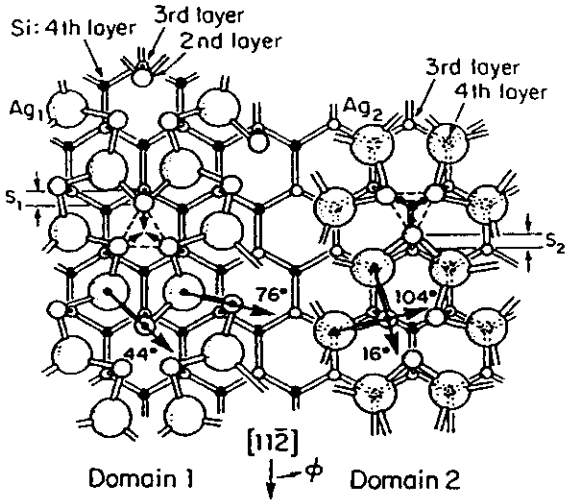

FIGURE 32. The two-domain missing-top-layer (MTL) honeycomb model proposed for ($\sqrt{3} \times \sqrt{3}$) Ag/Si (111). The parameters characterizing it are: vertical positions $z_1 = -0.1$ Å and $z_2 = -0.3$ Å, Si trimer contractions of $s_1 = s_2 = 0.86$ Å, and a 50:50 mixture of Domains 1 and 2. The lower half of the figure shows the two sets of nearest-neighbor Si forward-scattering peaks that produce the four-peak structure seen at low θ values in Fig. 31. (From Ref. 50.)

the lowest θ values near 4°, an additional correction of possible importance is the reduction of nearest-neighbor Si forward-scattering strengths due to multiple scattering effects along the nearly linear rows of atoms that can be labelled Ag emitter → Si first-neighbor scatterer → Si second-neighbor scatterer (cf. Figs. 32, 3b, and 6); very recent MS calculations by Herman *et al.*[50c] show that this reduces the absolute peak intensities for $\theta = 4°$ and $\phi = 16°$, 44°, 76°, and 104° by about 30%, thus improving the agreement of theoretical and experimental anisotropies.

A further interesting point in connection with this structure is that a recent LEED study of the clean Si (111) surface by Fan *et al.*[117] concludes that a little-studied ($\sqrt{3} \times \sqrt{3}$) Si reconstruction has very nearly the same geometry as Domain 1 in Fig. 32 if Ag adatoms are replaced by Si adatoms. Although these authors do not consider the possibility of a second domain of type 2 for ($\sqrt{3} \times \sqrt{3}$) Si, it might be expected to have approximately the same energy (due to weak fourth-layer interactions) and thus also to exist on the clean surface. This work thus lends support to the two-domain model for ($\sqrt{3} \times \sqrt{3}$) Ag, since one can imagine its growth simply by replacing the Si adatoms with Ag atoms.

This structure is still very controversial, and these results thus cannot be called conclusive, but they further illustrate the way XPD can be used for such metal–semiconductor studies. This study is also state-of-the-art for XPD in that it

involves a large azimuthal data set, SSC–SW calculations with correct final-state interference, and the use of R factors[26d] to judge goodness of fit. As one qualitative figure of merit in connection with this study, the minimum R factors of 0.14 found are about $\frac{1}{2}$ of those found in recent LEED studies of the same system.[117,118]

4.5. *Supported Clusters*

In this section, we briefly consider two examples of how higher-energy XPD has been used to study the formation of three-dimensional clusters on surfaces. (A third example has already been considered in the data for Fe deposited on Cu (001) shown in Fig. 24, where agglomeration effects are visible even for very low coverages.)

4.5.1. Ag/Si (111)

We have noted in the last section that Ag readily forms islands and three-dimensional clusters on the Si (111) surface if the coverage exceeds the 0.7–1.0 ML needed for the ($\sqrt{3} \times \sqrt{3}$) Ag structure. If these clusters are more than one atomic layer in thickness, then strong forward-scattering effects are expected for emitters in the lower layer(s) of the cluster. Such effects are illustrated in Fig. 30b,c, where polar scans of Ag $3d_{5/2}$ intensity have been measured first in Fig. 30c for a thick Ag reference layer of approximately 6 ML thickness, and then after heating to 450 °C so as to desorb all but an average coverage of about 2 ML. In Fig. 30c, a LEED pattern characteristic of the epitaxial Ag (111) that is known to grow on Si (111) is seen, and strong diffraction peaks due to buried-atom emission from this thick overlayer are found. In Fig. 30b, the Ag (111) LEED pattern is weakly present and there are still clear remnants of the photoelectron-diffraction features seen in the thick overlayer. Thus, such XPD patterns are very sensitive to the presence of three-dimensional islands.

The previous discussion of Figs. 22 and 23 also suggests that it might be possible to estimate the average thickness of such clusters up to about 5 ML, where the XPD features begin to converge to the bulk pattern. An additional type of information that could be very useful for some systems is the orientation of the cluster crystal axes with respect to the surface normal. In fact, even if clusters grow in a textured way (that is, without preferred azimuthal orientation), polar scans of the type shown here should permit determining whether there is any preferred vertical axis. Bullock and Fadley[50b,119] have also recently pointed out that, even for two-dimensional islands, it should be possible to use low-θ azimuthal scans to determine the island orientation and, for smaller islands, the average number of atoms present.

4.5.2. Pt/TiO_2

As a second example of cluster studies using XPD, Tamura *et al.*[120] have considered the interaction of Pt with three low-index faces of TiO_2, a system of interest in catalysis and for which the so-called strong metal-support interaction

(SMSI) can occur. In this study, Pt was deposited at room temperature to a mean thickness of about 10 ML onto the (110), (100), and (001) surfaces of TiO_2, and azimuthal XPD measurements were made at different polar angles for the Ti 2*p* and O 1*s* photoelectron peaks before deposition and for the Pt 4*f* peaks after deposition. Similar Pt 4*f* measurements were made after annealing the samples up to 800 K.

Some of these results are shown in Fig. 33a for the (110) surface at $\theta = 40°$ and Fig. 33b for (100) at $\theta = 45°$. Considering first Fig. 33a, we see that curves (i) and (ii) show weak diffraction features for both Ti 2*p* (clean) and Pt 4*f* (just after the deposition). The nonconstant background under these curves, particularly for (ii), is thought to be due to a nonuniform deposition over the region of the sample seen by the electron analyzer; thus, with changes in ϕ, a slightly different area and average Pt thickness might be seen. After the high-temperature anneal, the Pt 4*f* features in (iii) are strongly enhanced, with a concomitant increase in the anisotropy $\Delta I/I_{max}$ from 16% to 29%. This is consistent with the growth of thicker or larger clusters upon annealing, although (ii) indicates that some sort of ordering must be present even without annealing. Finally, (iv) shows a theoretical calculation based upon PW-cluster calculations with the effects of double scattering included. (The possible risk of including only double-scattering events has been mentioned already in section 3.2). The Pt clusters assumed had (111) orientation and contained 13 atoms in three planes; two symmetry-equivalent orientations with respect to the substrate 180° apart were considered. The resulting curve in (iv) is found to agree rather well with the annealed Pt 4*f* experimental results, suggesting that the clusters are growing with preferred (111) orientation.

A similar set of data for the (100) surface are shown in Fig. 33b. Here, (i) and (ii) exhibit strong diffraction from the O 1*s* and Ti 2*p* peaks of the substrate. Curve (iii) shows the strong diffraction of Pt 4*f* after the anneal. (A more uniform deposition of Pt has here made the background levels very flat.) Finally, curve (iv) is calculated for the same type of two-domain, three-layer Pt cluster [but with different assumed registry with the (100) surface], and it again shows good agreement with experiment, suggesting (111) orientation for the clusters on this surface as well.

For the third (001) surface studied, it is interesting that the Pt 4*f* oscillations were weak both before and after annealing, indicating a different kind of overlayer growth and/or a lower degree of cluster formation.

Together the three studies related to clusters that have been considered up to this point illustrate the utility of both polar and azimuthal XPD or AED data for studying the amount of cluster formation present and the average orientation and morphology of the aggregates formed. Two possible limitations of this kind of study are that XPD and AED average over all of the clusters present and so cannot easily be used to estimate the cluster-size distribution. In certain cases, it might even be difficult to detect the difference between, for example, a full 4-ML epitaxial overlayer and a collection of independent clusters with an average thickness of 4 ML, even if the crystallographic orientation could be easily determined. Although with careful measurements of both substrate and deposited-atom intensities before and after deposition and/or heat treatment, the

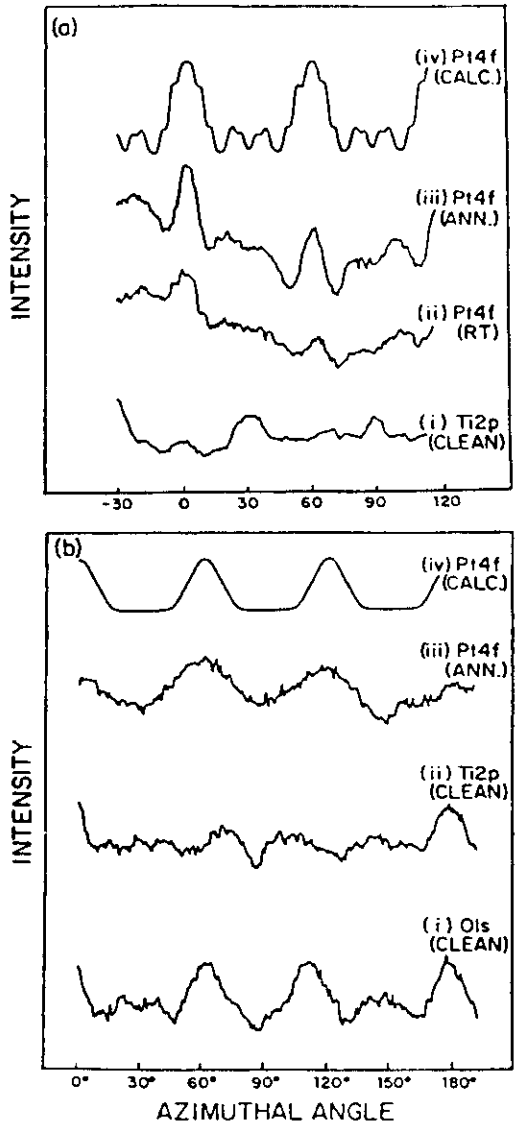

FIGURE 33. (a) Azimuthal XPD data for Pt 4*f* and Ti 2*p* emission from Pt on TiO_2 (110) at $\theta = 40°$ are compared to PW cluster calculations including double scattering for Pt emission from a (111)-oriented metal cluster of about 15 Å diameter. Al *Kα* radiation was used for excitation. (b) As in (a) but for Pt 4*f*, Ti 2*p*, and O 1*s* emission from Pt on TiO_2 (100) at $\theta = 45°$. (From Ref. 120.)

implicit effects of "patching" in cluster growth should be evident in deposited-atom–substrate relative intensities. Simple formulas for analyzing such patched-overlayer relative intensities appear elsewhere.[9] It is also clear that combining XPD or higher-energy AED with scanning tunneling microscopy (STM) would yield a particularly powerful set of data for cluster and epitaxial growth studies. This is because STM can be used to measure directly both the cluster size distribution and the step and defect densities that are averaged over in XPD/AED. But it may be difficult or impossible with STM to see into a cluster or overlayer so as to determine its crystallographic orientation or thickness. This is because STM cannot probe below the surface density of states and also is not atom-specific.

4.6. Core Level Surface Shifts and Chemical Shifts

A further type of problem that has been studied by low-energy photoelectron diffraction using synchrotron radiation for excitation is metal core level surface shifts.[18,53,80,121,122] In particular, Sebilleau, Treglia *et al.*[18,53,80] have tuned the photoelectron energy to low values to achieve high surface sensitivity and have looked with high energy resolution at photoelectron diffraction from such surface-shifted core levels.

Some of their results for tungsten 4*f* emission from W (100) are illustrated in Fig. 34, where both the surface and bulk peaks are shown, together with their individual azimuthal diffraction patterns and corresponding SSC–PW theoretical curves. The two types of peaks clearly exhibit very different diffraction patterns, and both of these are rather well predicted by the SSC model, even at this quite low photoelectron energy of approximately 30 eV. It is remarkable that a single-scattering approach is so quantitative at such a low energy, and this may to some degree be fortuitous. However, later work by Treglia *et al.*[18c,53,80] has reached similar conclusions, with the only qualification being that it is necessary at such energies to use the correct final-state angular momenta, as expected from the discussion of Fig. 4 in section 3.1.2. For the low energy of this case, the $4f$-to-εd channel is assumed to be dominant.

This work thus illustrates the added ability of photoelectron diffraction to carry out independent structure determinations of physically or chemically different species of the same atom through core level shifts. These shifts are not limited to the clean-surface type considered above, but may also involve the well-known chemical shifts commonly seen when different chemical bonding or oxidation states are present. Such state-specific structure studies should be a very powerful probe of surface reactions, overlayer growth, and interface formation. They will, however, require very high energy resolutions of 0.3 eV or better to be fully effective in resolving small shifts.

As an obvious example for future work, it should also be possible to do state-specific diffraction studies on semiconductor surfaces, since both clean surfaces[123a,b] and chemically reacted surfaces[123c] exhibit shifted core levels characteristic of the different bonding sites and/or oxidation states.

One technologically important example of a semiconductor system for which more structural information concerning different chemical species would be useful

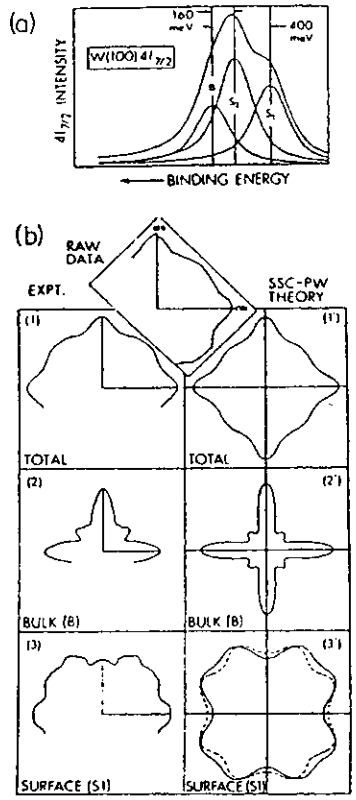

FIGURE 34. (a) A W $4f_{7/2}$ spectrum from W (001) at a kinetic energy of ≈30 eV, showing two surface-shifted core levels (S_1 and S_2) as well as a bulk peak (B). (b) The azimuthal dependences of these intensities at a polar angle of 60° above the surface: (1) represents the total $4f_{7/2}$ intensity, (2) the bulk intensity (B), and (3) the surface intensity (S_1). SSC-PW calculations of these intensities are shown in (1'), (2'), and (3'), respectively. The inset represents raw data for the total intensity. (From Ref. 18(a).)

is the formation of the interface between SiO_2 and Si. Figure 35 shows high-resolution Si $2p_{3/2}$ core spectra obtained by Himpsel *et al.*[123c] from Si (100) and Si (111) surfaces that were thermally oxidized in UHV conditions (2.5 Torr O_2, 750° C, 20 sec) so as to produce a very thin 5-Å oxide film. The overall resolution here was 0.3 eV, and it is striking that all of the oxidation states of Si are clearly seen, from the elemental substrate to the 4+ dioxide. The different nature of the oxidizing surface for Si (111) is further found to lead to a suppression of the Si^{2+} state. These intermediate oxidation states are thought to be associated with the interface, and, from quantitative estimates of the different depth distributions of these states, it is concluded that an extended rather than abrupt interface is involved. Models of such an extended interface have been proposed by Himpsel *et al.*, but these cannot be tested in detail without additional data. It seems clear that separately measuring the scanned-angle photoelectron diffraction patterns of the different oxidation states would provide some very useful information in this

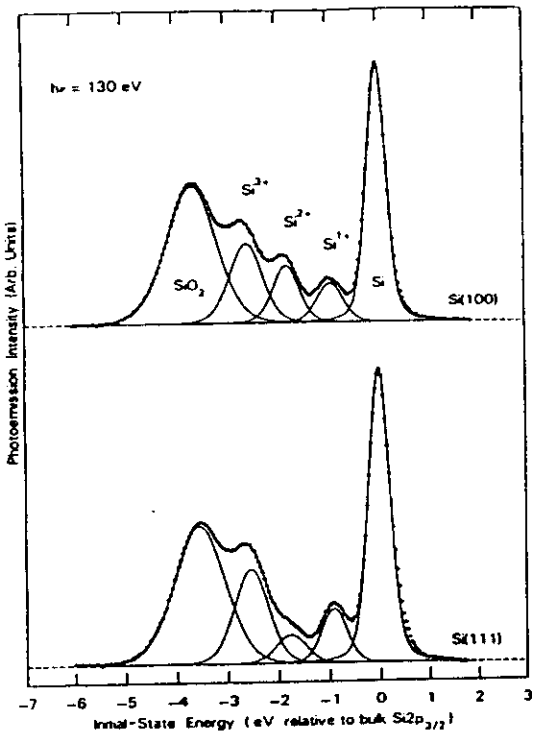

FIGURE 35. The Si $2p_{3/2}$ components of Si 2p spectra from thin oxide films of approximately 5 Å thickness thermally grown on Si (100) and Si (111) surfaces. Note the reduced intensity of Si^{2+} for Si (111), assumed to be due to structural differences in the interface. [From Ref. 123(c).]

direction, since each state is hypothesized to occupy one or at most a few distinct site types relative to the substrate lattice.

Although these are difficult experiments at present, the detailed state-by-state information derivable should help in unraveling the microscopic structures of many surface and interface systems. Being able to tune photon energy so as to vary surface sensitivity or to move on or off of resonant photoemission conditions would also be an advantage, as noted in prior studies.[123] Going to higher photon energy not only permits looking deeper into the material and assessing the relative depth distributions of the different species, but should also lead to more simply interpretable forward-scattering peaks for emission from interface-associated atoms. A disadvantage of higher energies is that the substrate signal tends to dominate the spectrum, but with high enough resolution and suitable reference spectra for subtracting the substrate signal, such high-energy measurements should be possible. Synchrotron radiation will thus be necessary to fully exploit this potential for studying interface growth by state-specific photoelectron diffraction.

4.7. Surface Phase Transitions

We conclude this discussion of applications of photoelectron diffraction and Auger electron diffraction by considering briefly their possible use in studying various types of surface phase transitions such as surface premelting, roughening, or disordering at a temperature below the bulk melting temperature,[124] as well as surface reconstructions that are temperature-dependent.[123a,b] The short-range order and directional sensitivity of both PD and AED suggest that they should be useful probes of such surface phase transitions, which may involve changes in near-neighbor atom positions and/or the introduction of considerably more disorder in these positions. The number of such studies is still very small, but the most recent are quite promising.

An unsuccessful attempt at observing surface premelting for Cu (001) in grazing-emission XPD was made some time ago by Trehan and Fadley.[63a] For this surface, roughening and possibly faceting was observed before any evidence was seen in the XPD anisotropies of the extra disorder associated with surface melting. However, much more recently, evidence for surface phase transitions involving surface disordering and perhaps premelting has been seen in XPD from two separate systems: Pb (110) by Breuer, Knauff, and Bonzel[125] and Ge (111) by Friedman, Tran, and Fadley.[126]

For the case of Ge (111), prior LEED studies and theoretical modeling by McRae and co-workers[127] indicate that there is a reversible surface order–disorder transition at a temperature of 1060 K that is 0.88 times the bulk melting temperature. Is this transition visible in XPD? In Fig. 36, we show such XPD data in which the Ge 3*d* azimuthal anisotropy was monitored as a function of temperature. The polar angle of 19° chosen here causes the emission direction to sweep through nearest-neighbor forward-scattering directions in the unreconstructed surface, as shown in Fig. 27. This relatively low θ value also leads to higher surface sensitivity.

Figure 36a shows four azimuthal scans taken at temperatures from ambient to about 50 K above the transition. (Note the expected similarity of the azimuthal scan at ambient temperature to that for $Hg_{1-x}Cd_xTe$ (111) in Fig. 26a.) As the temperature is increased, the azimuthal curves gradually lose much of their fine structure, and upon passing above the transition point, only two main peaks remain in the azimuths $[1, 1, -2]$ ($\phi = 0°$) and $[-1, 2, -1]$ ($\phi = 60°$). In Fig. 36b, the intensity of the $[1, 1, -2]$ peak corresponding to nearest-neighbor scattering is plotted against temperature, and it is clear that an abrupt drop occurs over the interval 850–1050 K. This drop furthermore cannot be explained by simple Debye–Waller modeling.

McRae *et al.*[127a] have measured the intensities of several LEED beams for the same system as a function of temperature, and their data is similar to Fig. 36b in that the intensities drop sharply toward 1060 K and level off thereafter. Some of the LEED intensities drop more rapidly than the curve of Fig. 36b near 1060 K;

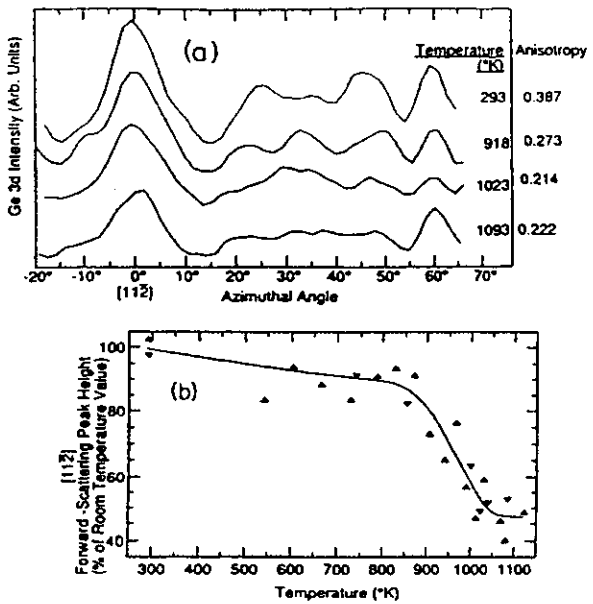

FIGURE 36. Temperature-dependent azimuthal XPD data for Ge 3*d* emission at 1458 eV from Ge(111) at low takeoff angle of $\theta = 19°$. This θ value corresponds to scanning through nearest-neighbor scattering directions for $\phi = 0°$, as shown in Fig. 27. (a) Four azimuthal scans at temperatures from ambient to above the order-disorder transition. (b) The detailed temperature dependence of the height of the peak along $\phi = 0°$. 1060 K is where a prior LEED study (Ref. 127(a)) has seen evidence for a surface-disordering transition. Upright triangles represent increasing temperature; inverted triangles, decreasing temperature. (From Ref. 126.)

some have a form very similar to this curve. Thus, it can be concluded that the same transition is observed in both sets of data, even though the LEED measurement is expected to be sensitive to longer-range order on a scale of approximately 100 Å, whereas XPD should probe distances on the order of 10–20 Å.

Although these XPD results have not as yet been analyzed in detail so as to derive additional structural information, it is clear that obtaining both polar and azimuthal data at temperatures below and above the transition temperature and comparing the diffraction structures seen with calculations for different types of disorder models should yield a better understanding of this and other surface phase transitions.

Similar abrupt changes in polar-scan diffraction anisotropies have also been seen by Breuer *et al.*[125] for the surface disordering of Pb(110), which has been observed previously with Rutherford backscattering and low-energy electron diffraction.[128]

As one interesting future direction for such work, the study of surface phase transitions should also benefit greatly from doing separate diffraction measurements on the various core peaks observed. For example, the Ge(111) surface exhibits one bulk peak and two surface peaks[123a,b] that could all be studied separately. However, the small shifts of only about 0.3–0.7 eV involved here would require very-high-resolution data and the use of curve-deconvolution procedures.

5. FUTURE DIRECTIONS

5.1. Measurements with High Angular Resolution and Bragg-like Reflections

As noted previously, most prior PD and AED measurements have been carried out with resolutions of at best a few degrees in half angle. In many systems, the acceptance solid angle is also not a simple cone, but may have different dimensions along two perpendicular axes.[29] For future work, the question thus arises as to what additional information might be gained by going to much better conic resolutions of, for example, ±1.0°.

As discussed in section 2, various methods exist for limiting angular spreads upon entry into the analyzer, but one which has the advantages of being very certain in its limits and operationally very convenient is the insertion of externally selectable angle-defining tube or channel arrays between sample and analyzer entry. The use of such channel arrays has been discussed by White *et al.*,[33] and they have been used to precisely limit angles to ±1.5° or better (that is, $<\frac{1}{4}$ of typical prior solid angles).

We have already discussed two examples of this kind of data: for NiO grown on Ni (001) in Fig. 14 and for $c(2 \times 2)$ S on Ni(001) in Fig. 17. For these cases, we have pointed out the greater sensitivity to the degree of short-range order and the adsorbate position, respectively.

As a final example of the dramatic effects seen in going to high angular resolution, we compare in Figs. 37a and b low- and high-resolution XPD data obtained by Osterwalder, Stewart *et al.*[48] for Ni $2p_{3/2}$ emission from a clean Ni(001) surface at $\theta = 47°$. A great deal more fine structure is seen in the data with ±1.5° resolution, and the form of the fine structure for $\phi \approx 25°$–$65°$ is in fact completely changed due to a lower degree of angular averaging over such structures. Very narrow features of only a few degrees at FWHM are also seen in the results at high resolution.

Figure 37c summarizes a more complete set of such high-resolution azimuthal data for Ni $2p_{3/2}$ that represents the most detailed investigation of XPD fine structure to date. Here, the polar angle of emission was varied in 1° steps from $\theta = 40°$ to 50°, passing through the high-symmetry value of $\theta = 45°$ which contains the ⟨110⟩ directions of nearest-neighbor scattering in its ϕ scan. Full 360° scans were used to generate each curve, and fourfold averages of this data into one quadrant shown elsewhere[10,48] agree excellently with the single-quadrant results presented here. This three-dimensional plot makes it clear that high-energy electron diffraction features can change extremely rapidly with either θ or

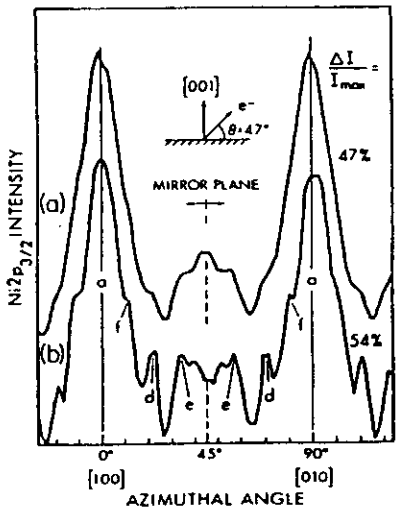

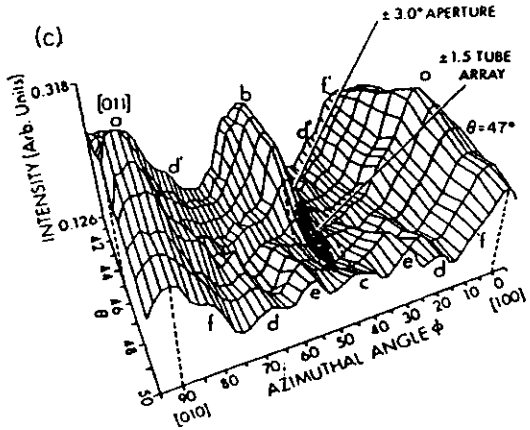

FIGURE 37. Effect of increasing angular resolution on Ni $2p_{3/2}$ azimuthal XPD data from a clean Ni (001) surface at 632 eV. (a) and (b) show single scans at $\theta = 47°$ with resolutions defined by a single aperture of nominal ±3.0° acceptance and a tube array yielding ±1.5° or less, respectively. (c) a three-dimensional summary of a series of single-quadrant high-resolution Ni $2p_{3/2}$ scans with a ϕ step of only 1°. The regions averaged over with the two different angle-defining devices in (a) and (b) are shown as shaded. (From Ref. 48.)

ϕ. These results also qualitatively explain how the approximately ±3.0° averaging in Fig. 37a yields features for $\phi \approx 25°$–$65°$ that are so different from those for the high-angular-resolution curve in Fig. 37b. That is, Fig. 37a represents an average over all of the curves in Fig. 37c from $\theta = 44°$ to $\theta = 50°$, as bounded by the lighter-shaded elliptical area, and the steeply rising ridge toward $\theta = 44°$ thus accounts for the peak seen at $\phi = 45°$ with lower resolution. The results in Fig. 37b, by contrast, represent an average over only the darker-shaded area in Fig. 37c, and so retain a minimum at $\phi = 45°$.

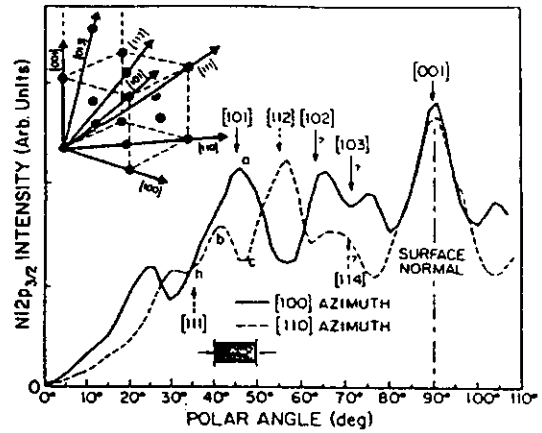

FIGURE 38. High-resolution Al Kα polar scans of Ni $2p_{3/2}$ intensity above Ni (001) in two different azimuths, with certain low-index directions and special points noted [cf. lower-case letter labeling in Fig. 37(c)]. The region covered by Fig. 37(c) is shaded. The inset shows the near-neighbor/low-index directions within an *fcc* unit cell. (From Ref. 48.)

Figure 38 shows two high-resolution polar scans from the same study of Ni (001). The unit cell of the metal and various near-neighbor scatterers along low-index directions is also indicated to permit judging how well various strong features correlate with them (cf. also Fig. 22a). These polar scans also show considerable extra fine structure, for example, as compared to the same sort of [100] polar scan for higher-energy Auger emission from bulk Cu (001) shown in Fig. 22b. These high-resolution data are found to exhibit peaks for emission along some, but not all, of the near-neighbor directions shown. Peaks are found at positions corresponding closely to the nearest neighbors (and fourth-nearest neighbors) along [101], the second neighbors along [001], and the third neighbors along [112]. However, minima and/or significant peak shifts are seen for the fifth neighbors along [103] and the sixth neighbors along [111]. Neighbors even further away along [102] and [114] are also found to show significant shifts compared with the observed peaks. In particular, the [111] direction corresponds to a local minimum (indicated as point *h*), with enhanced intensity on either side of the minimum; a ϕ scan through [111] at $\theta = 35°$ shows the same sort of profile. As noted previously in the discussion of Fig. 22, this is due to the influence of higher orders of interference[71] and perhaps multiple scattering effects.[73] Thus, we conclude that the first 3–4 spheres of neighbors in any lattice will probably produce strong and simply interpretable forward scattering peaks. Beyond these spheres, more-complex origins will require modelling at least at the SSC–PW level for interpretation.

Three-dimensional data of the type shown in Fig. 37c have also been obtained at lower angular resolution by Baird, Fadley and Wagner for XPD from

Au (001)[129] and by Li and Tonner for high-energy AED from Cu (001).[29] These two data sets span a high fraction of the 2π solid angle above these two surfaces, and they exhibit very similar intensity contours, as expected since they both represent high-energy emission from the same *fcc* crystal structure. The more recent data of Li and Tonner serves as a more accurate reference for the overall features of such *fcc* XPD/AED patterns at lower angular resolution. These studies also agree with the preceding paragraph and the discussion of section 4.3.2 in seeing simple correlations of peaks with near-neighbor forward-scattering directions out only to the fourth shell, with directions such as [111], [114], [102], and [103] showing more complex behavior.

The Ni data discussed here and the other high-resolution results discussed previously thus make it clear that, at least in higher-energy XPD and AED, using resolutions that are much worse than ±1.0° will blur out some features and lead to a loss of structural information. Such sharp features are generally the result of superpositions of several scattering events, since the relevant scattering factor by itself exhibits nothing narrower than the forward scattering peak of some 20–25° FWHM. These features also tend to involve scatterers further away from the emitter and thus to be associated with the degree of short-range order around the emitter. (This is nicely illustrated by the NiO/Ni (001) results of Fig. 14.) Thus, there is little doubt that XPD or AED with high resolution will contain more fine details of the structure under study.

At lower energies, by contrast, one expects generally wider features due to the broader, more diffuse scattering factors involved (cf. Fig. 2) and the larger de Broglie wavelengths that spread out different orders of interference (cf. the curves in Figs. 4 and 5). However, even for such energies, it is possible for superpositions of multiple events to produce rather narrow features, and high resolution might also be a benefit in this case.

The most obvious disadvantage of working at high angular resolution is the longer data-acquisition times, which may be 10–30 times those of typical low-resolution operation.[33] A second disadvantage is that it is likely that the effects of multiple scattering will tend to be averaged out somewhat in lower-resolution data because of cancellations of phases in the many events involved.[21] Conversely, in high-resolution data, such MS effects may be more important, even though the information content is inherently greater.

A further aspect of the relationship of such high-resolution data to more complex interference effects and more distant neighbors is the influence of Bragg-like diffraction effects from planes in multilayer substrate emission. In the presence of the strong inelastic damping characteristic of both PD and AED, such Bragg-like events lead to what has been termed a Kikuchi-band model of these phenomena.[2,3,63b,129,130] Although a fully quantitative Kikuchi-band theory of higher-energy PD or AED based upon the superposition of many Bragg-like scattered waves is lacking, simple model calculations have been carried out by Baird *et al.*,[129] by Goldberg *et al.*,[130] and more recently also by Trehan *et al.*,[63b] and they are found to semiquantitatively reproduce the results of XPD measurements on both Au (001) and Cu (001). In particular, the superposition of several Kikuchi bands along low-index directions yields the forward-scattering peaks seen in both experiment and SSC calculations.

More interestingly, there are features in experimental data at high angular resolution that appear to be associated with specific Bragg events from low-index planes (such as features *d* and *f* in Fig. 37b here and as discussed in connection with Fig. 31 of Ref. 9). This suggestion has been given more quantitative support in a recent high-resolution study of Ni (001) by Osterwalder *et al.*[48a] Furthermore, calculations with the SSC model exhibit these same Bragg-like features if the cluster size is permitted to be large enough and/or the inelastic damping is sufficiently reduced,[48a,63b] thus verifying that a cluster-based theory can be used for problems varying from short-range order to long-range order.

This formal equivalence of the SSC model and the Kikuchi-band picture for describing bulk-like multilayer emission was first pointed out some time ago,[9,42,130] but additional clarification seems appropriate in view of misleading statements concerning the role of the Kikuchi model in the interpretation of XPD and AED that have nonetheless appeared in the more recent literature.[11] From an experimental point of view, the essentially identical intensity profiles for LMM Auger electron diffraction and backscattered LEED "Kikuchi patterns" from Ni (001) at 850 eV observed by Hilferink *et al.*[70a] provide a particularly clear verification of this equivalence. From a theoretical point of view, the relationship of the two approaches, if both are carried to comparable quantitative accuracy, is analogous to the equivalence of the so-called short-range-order and long-range-order theories of EXAFS, as discussed elsewhere.[63b,131] It is clear, however, that the SSC and MSC approaches are of greater generality in that they can be applied to both surface- and bulk- emission and to problems of differing degrees of order. The Kikuchi-band picture is, by contrast, formulated on a basis of inelastically attenuated Bloch states that reflect long-range translational order. Thus, the cluster-based theories are inherently more rapidly convergent and are more appropriate ways to look at near-surface diffraction from adsorbates and thin overlayers, as noted previously.[42,130] But it is absolutely incorrect to say that the ability of the cluster approach to explain forward-scattering features makes the Kikuchi-band model invalid for describing substrate emission.[11]

In summary, the use of high angular resolutions on the order of ±1.0° should permit even more precise structural conclusions to be derivable from both photoelectron diffraction and Auger electron diffraction, especially at energies of >500 eV. Such data should contain information on neighbors further away from the emitter, including features related to Bragg-like scattering events. It is also clear that the use of resolutions of ±3.0° or worse may conceal a great deal of fine structure inherent in the experimental curves.

5.2. Spin-Polarized Photoelectron and Auger Electron Diffraction

Beyond increasing both the energy resolution and the angular resolution in PD and AED as means of deriving more detailed structural information, we can also ask what is to be gained if the last property of the electron, its spin, is also somehow resolved in the experiment. This prospect has so far been considered quantitatively and observed experimentally only in the case of photoelectron diffraction, but we return at the end of this section to comment on how it might also be possible in Auger electron diffraction.

In the first attempts at what has been termed spin-polarized photoelectron diffraction (SPPD), the fundamental idea has been to use core-level multiplet splittings to produce internally referenced spin-polarized sources of photoelectrons that can subsequently scatter from arrays of ordered magnetic moments in magnetic materials. Figure 39a illustrates how such a splitting can give rise to spin-polarized photoelectrons for 3*s* emission from high-spin Mn^{2+}. The splitting is intra-atomic in origin and arises from the simple *LS* terms of ^5S and ^7S in the final ionic state of Mn^{+3} with a 3*s* hole.[132] The net effect is to cause the peaks in the doublet to be very highly spin-polarized, with ^5S predicted to be 100% spin-up and ^7S to be 71% spin-down relative to the net 3*d* spin of the emitting atom.[133,134] The relatively large exchange interaction between the highly overlapping 3*s* and 3*d* electrons is responsible for the easily resolvable splitting of 6.7 eV between the ^5S and ^7S final states of the photoemission process.

The basic experiment in SPPD thus involves looking for spin-dependent scattering effects that make two such peaks behave slightly differently in the presence of a magnetically ordered set of scatterers. Such effects were first discussed theoretically by Sinkovic and Fadley,[134a] and they have several special properties:[135,136]

- There is no need for any kind of external spin detector beyond an electron spectrometer capable of resolving the two peaks in energy.

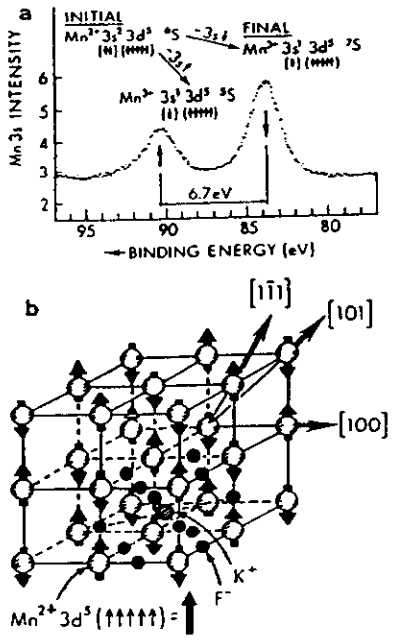

FIGURE 39. (a) The Al $K\alpha$-excited Mn 3*s* spectrum of $KMnF_3$, with the initial and final states leading to the multiplet splitting indicated, together with the predominant photoelectron spin expected in each peak. (b) The crystal structure of $KMnF_3$, with the antiferromagnetic ordering of the Mn^{2+} spins also indicated. [From Ref. 134(a).]

- The fact that the photoelectron spins are referenced to that of the emitting atom or ion means that SPPD should be capable of sensing magnetically ordered scatterers even when the specimen has no net magnetization. Thus, studies of both ferromagnetic and antiferromagnetic materials should be possible, and meaningful measurements should also be feasible above the relevant macroscopic transition temperatures (Curie or Neel temperatures, respectively). For the latter case, the photoelectrons in each peak would be unpolarized with respect to any external axis of measurement but still polarized relative to the emitting atom.
- The photoelectron emission process is also very fast, with a time scale of only about 10^{-16} to 10^{-17} seconds; thus, such measurements should provide an instantaneous picture of the spin configuration around each emitter, with no averaging due to spin–flip processes, which are much slower at roughly 10^{-12} seconds.
- Finally, the previously discussed strong sensitivity of any form of photoelectron diffraction to the first few spheres of neighboring atoms means that SPPD should be a probe of short-range magnetic order (SRMO) in the first 10–20 Å around a given emitter. Thus, provided that a sufficiently well-characterized and resolved multiplet exists for a given material, this technique has considerable potential as a rather unique probe of SRMO for a broad variety of materials and temperatures.

Before discussing the first observations of such spin-dependent scattering and diffraction effects, it is appropriate to ask to what degree final-state effects such as core-hole screening may alter or obscure these multiplets. We note first that the cases of principal interest in SPPD are outer core holes, which are more diffuse spatially than inner core holes and for which the interaction with the surrounding valence electrons is thus not as strongly polarizing as for inner core holes (which can often be very well described in the equivalent-core approximation). Nonetheless, it has been suggested by Veal and Paulikas[137] that both screened and unscreened multiplets corresponding to $3d^{n+1}$ and $3d^n$ configurations, respectively, are present in the 3*s* spectra of even highly ionic compounds such as MnF_2.

As such effects would make the carrying out of SPPD measurements more difficult (although still certainly not impossible) due to the potential overlap of peaks of different spin polarization, Hermsmeier *et al.*[138] have explored this problem in a study of Mn 3*s* and 3*p* multiplets for which the experimental spectra from several reasonably ionic solid compounds have been directly compared to the analogous spectra from gaseous Mn, a simple free-atom system in which no extra-atomic screening can occur. In Fig. 40, we show their compilation of 3*s* spectra for the diluted magnetic semiconductor $Cd_{0.3}Mn_{0.7}Te$ (a), single-crystal MnO with (001) orientation (b), polycrystalline MnF_2 as obtained some time ago by Kowalczyk *et al.*[139] (c), gaseous atomic Mn (d), and a free-ion theoretical calculation of these multiplets by Bagus *et al.* including configuration interaction, but totally neglecting extra-atomic screening (e).[140] From a consideration of the experimental data only, it is striking that for both 3*s* multiplets and 3*p* multiplets (not shown here, but discussed in Ref. 138) the solid-state spectra are very similar to the gas-phase spectra, with the only differences being some extra broadening in the solid state and some small changes in peak positions that are not at all surprising. Thus, even without resorting to theory, it seems clear that these

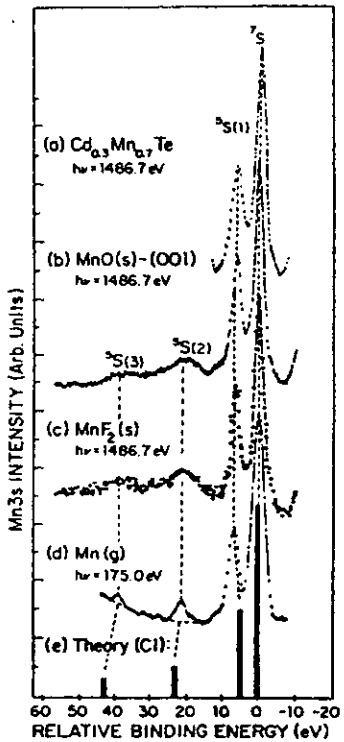

FIGURE 40. Experimental Mn 3*s* spectra for (a) the diluted magnetic semiconductor $Cd_{0.3}Mn_{0.7}Te$, (b) MnO (001), (c) polycrystalline MnF_2 (Ref. 139), and (d) gaseous atomic Mn are compared to (e) theoretical calculations for emission from a free Mn^{2+} ion including final-state configuration interaction (Ref. 140). (From Ref. 138.)

spectra are very free-atom–free-ion like, and that a simple multiplet interpretation such as that in Fig: 39a should rather accurately describe the spin polarizations of the photoelectrons involved.

If we consider now the best available free-ion theoretical prediction for the 3*s* spectra, this conclusion becomes even more convincing. In Fig. 40e, the results of a calculation by Bagus, Freeman, and Sasaki[140] for Mn^{3+} with a 3*s* hole and limited configuration interaction (CI) are shown. There is excellent agreement with experiment not only for the two dominant members of the multiplet that would be most useful in SPPD, but also for the two much weaker satellites that directly result from including CI. Similar conclusions are reached in a comparison of experiment and theory for analogous 3*p* spectra.[138] We thus conclude that extra-atomic screening does not cause a major perturbation of these multiplet splittings and thus also that outer core holes such as 3*s* and 3*p* should exhibit relatively free-atom–free-ion like multiplets for a variety of high-spin systems. Such multiplets in turn should be useful as spin-resolved sources in SPPD.

Direct experimental evidence of spin polarization in core spectra also exists. A recent measurement with an external spin detector of the spin polarization over the 3*p* peak from ferromagnetic Fe by Kisker and Carbone[141] yields significant spin-up polarization at lower kinetic energy and spin-down polarization at higher kinetic energy that are in the same sense as those expected for a simple 3*p* multiplet.[138] These results thus suggest that SPPD should be possible with ferromagnetic metals as well, particularly on the simpler and more widely split 3*s* peaks.

Returning now to a consideration of the SPPD experiments carried out to date, we have shown in Fig. 39b the crystal structure of the first material for which such effects were observed: a (110)-oriented sample of the simple antiferromagnet $KMnF_3$. It is clear from this that the relative spins of the emitter and the first scatterer encountered can be different for different directions of emission, as for example, between [100] and [101]. Spin-dependent scattering effects were first observed for this system by Sinkovic, Hermsmeier, and Fadley[142] as small changes of up to about 15% in the ratios of the $^5S(1)$ (spin-up) and ^7S (spin-down) peaks in the dominant doublet shown in Fig. 39a. For this study, a lower energy of excitation of 192.6 eV (Mo Mζ radiation) was used in order to yield lower-energy photoelectrons at approximately 100 eV, which are expected to exhibit significant spin-dependent effects in scattering.[134a] This requirement of low kinetic energies thus makes SPPD inherently well suited to synchrotron radiation with its tunable energy.

The $^5S(1):^7S = I(\uparrow)/I(\downarrow)$ intensity ratio was found to be sensitive to both direction of emission (as qualitatively expected from Fig. 39a) and temperature. Its variation with temperature is furthermore found to exhibit a surprisingly sharp transition at a point considerably above the Neel temperature (T_N), as shown in Fig. 41a. Here, we plot a normalized intensity ratio or "spin asymmetry" S_{expt} that is measured relative to the value of $I(\uparrow)/I(\downarrow)$ at a limiting high-temperature (HT) paramagnetic limit. This asymmetry is defined in the inset of Fig. 41a; it goes to zero at high temperature.

The abrupt high-temperature change observed in S_{expt} has been suggested to be due to the final destruction of the short-range magnetic order that is expected to dominate in producing such spin-polarized photoelectron diffraction effects. Note also that the short-range-order transition temperature T_{SR} at which this occurs is approximately $2.7T_N$.

In an important confirmation and extension of this earlier work, very similar SPPD effects have also more recently been observed by Hermsmeier *et al.* for (100)-oriented MnO,[143] and two of their curves for the temperature dependence of the spin asymmetry are shown in Fig. 41b. As for $KMnF_3$, there is a relatively sharp change in the $^5S(1):^7S$ ratio at a temperature that is again well above the long-range-order transition temperature at $T_{SR} = 4.5T_N$. For both $KMnF_3$ and MnO, it is also interesting that the form of the short-range order transition is very sensitive to emission direction, being steepest for the nearest-neighbor scattering direction in Fig. 41a and changing sign with only a 15° shift of emission direction in Fig. 41b. This sensitivity to direction is qualitatively consistent with single-scattering calculations of the spin-dependent exchange-scattering processes that may be involved.[134,143,144]

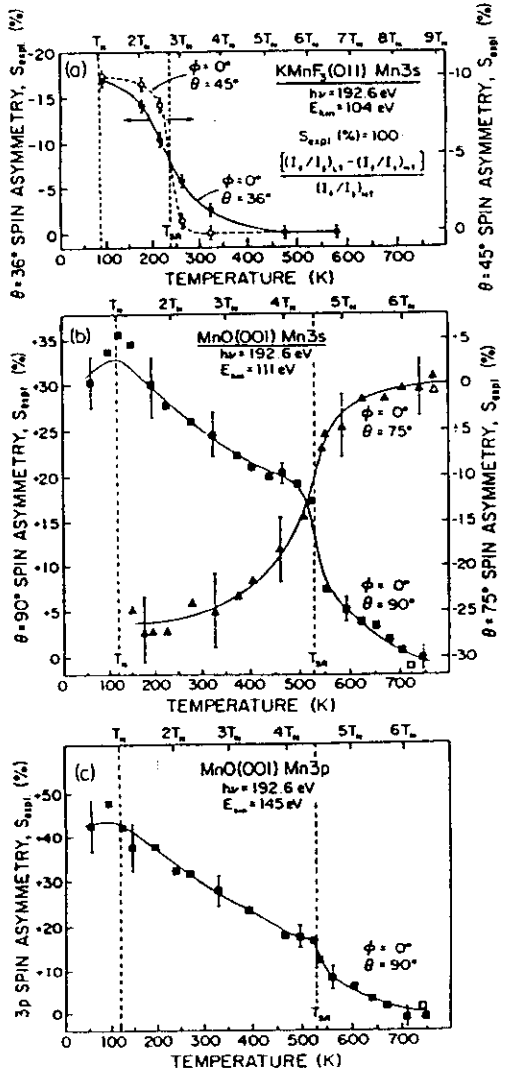

FIGURE 41. Spin-polarized photoelectron diffraction data indicating the presence of a high-temperature transition in antiferromagnetic short-range order. (a) Experimental spin asymmetries for the Mn 3*s* doublet from $KMnF_3$ with (110) orientation, as a function of temperature. Mo $M\zeta$ radiation at 192.6 eV was used for excitation to photoelectron energies of approximately 100 eV. The spin asymmetry is defined in the inset, where $I(\uparrow)/I(\downarrow)$ is the ratio of spin-up (^5S) to spin-down (^7S) intensities, HT refers to the highest temperature of measurement. Data are shown for two emission directions, one of which is along the [100] nearest-neighbor direction and the other 9° away from this. (From Ref. 142.) (b) As in (a), but for Mn 3*s* emission from MnO with (001) orientation. Note the different signs of the spin asymmetries for this case. (From Ref. 143.) (c) As in (b), but for Mn 3*p* emission from MnO with (001) orientation and treating the spin-up (^5P) and spin-down (^7P) peaks. (From Ref. 143.)

Although we have discussed only 3*s* emission thus far, the more complex 3*p* multiplets also should be spin polarized.[138,143] And in fact, a very similar transition has also been seen for MnO in the more widely split $^5P(1):^7P = I(\uparrow)/I(\downarrow)$ doublet at the same temperature T_{SR},[143] as shown in Fig. 41c. The fact that the same sort of transition is seen for these two peaks in spite of the fact that they are different from $^5S(1):^7S$ in both energy separation and mean kinetic energy provides strong support for the conclusion that this is a new type of magnetic transition.

It is also interesting that the T_{SR} values are, for both cases, approximately equal to the Curie–Weiss temperatures of the two materials, a connection which may be associated with the fact that this constant is proportional in mean-field theory to the sum of the short-range magnetic interactions.[145]

A final observation concerning this data is that the results for MnO in Figs. 41b and c show a possible indication of sensitivity to the long-range-order transition at T_N, as both curves possess a weak peak at T_N which is just outside of the estimated-error bar of the ratio measurement. If this is true, it is perhaps not surprising in view of the longer-range sensitivity of PD to neighbors that may be 20 Å from the emitter, as discussed in connection with both Figs. 16 and 20b.

A number of questions are thus raised by these results concerning the nature of short-range order above the long-range-order transition temperature and the way in which such effects can be incorporated in a spin-polarized variant of photoelectron diffraction theory. Although a quantitative theory of all aspects of the short-range-order transition and its inclusion in a spin-dependent modeling of the diffraction process does not yet exist, results in qualitative or semiquantitative agreement with experiment have been obtained in a few previous studies.[134,136,143,144]

The observation that Auger spectra from ferromagnetic materials exhibit strong spin polarization from one part of the manifold of features to another by Landolt and co-workers[146] also suggests that spin-polarized Auger electron diffraction (SPAED) should be possible. The more complex nature of Auger spectra in general will make the *a priori* prediction of the type of spin polarization more difficult, but for ferromagnets with net magnetization, an external spin detector could be used to first calibrate the spectrum for polarization.[146] Then, measurements of spin-up–spin-down ratios as functions of direction and/or temperature could be taken in the same way as for the spin-split core multiplets in SPPD. Even in antiferromagnetic systems with equal numbers of up and down 3*d* moments so that external calibration is impossible, any transition involving the polarized 3*d* valence electrons might be expected to show a net polarization that would again be internally referenced to the emitter.

A final aspect of such spin-polarized studies is to make use of left or right circularly polarized radiation, in conjunction with spin–orbit interaction in the energy levels involved, to preferentially excite one or the other spin polarization, as discussed recently by both Schuetz and co-workers[147] and Schoenhense and co-workers.[148] The use of such radiation already has produced very interesting spin-polarized NEXAFS and EXAFS structure from ferromagnets and ferrimagnets[147] and circular dichroism angular distributions (CDAD) from nonmagnetic surfaces and adsorbates.[148] In CDAD for light elements with negligible spin–orbit effects,

no net spin polarization of the photoelectron flux is involved, but such measurements provide the interesting possibility of measuring the contributions of individual m_l components to photoemission and photoelectron diffraction.[148] The CDAD studies require lifting the degeneracy of the m_l sublevels, and so have been carried out on valence levels; however, with very high energy resolution, it might be possible to do similar measurements on outer core levels with, for example, small crystal-field and/or spin–orbit splittings present.

With the availability of higher-intensity sources of circularly polarized radiation from next-generation insertion devices, it should be possible to greatly expand both of these kinds of study so as to look in more detail at both the angle and the energy dependence of the photoelectron intensities. For example, spin-polarized EXAFS requires measuring very accurately the differences in absorption for right and left polarizations, because the overall effects may be as small as a few times 10^{-4} in K-shell absorption.[147] However, studying L_2- and L_3 absorption for heavier elements with $Z \geq 60$ leads to considerably larger effects that can be on the order of 10^{-3}–10^{-2}. Extending this to do SPPD would thus imply measuring similarly accurate ratios or differences of photoelectron intensities. In this case, the magnitudes of the photoelectron spin polarizations are only on the order of 1% for K-shell emission, but for heavier elements, they can be up to 40–50% in L_2 emission and 20–25% in L_3 emission.[147] The latter two cases are thus about $\frac{1}{3}$–$\frac{1}{2}$ as highly polarized sources as a high-spin multiplet such as that in Fig. 39a. One advantage of such an approach would be to expand such studies to cases for which a suitable high-spin multiplet is not available. A disadvantage is that an external axis of polarization is involved, so that only ferro- or ferrimagnetic specimens could be studied. However, in CDAD experiments, this last restriction is not present.[148]

SPPD is thus a very new area of photoelectron diffraction, but it has considerable potential for providing information on the short-range spin order and spin–spin correlation functions around a given type of emitter site in the near-surface region of magnetic materials. Other antiferromagnetic and also ferromagnetic materials are currently being studied in order to better establish the systematics of the short-range-order transition and the range of utility of this method. Spin-polarized Auger electron diffraction and other measurements making use of circularly polarized radiation for excitation also should be possible.

5.3. Synchrotron Radiation–Based Experiments

Looking ahead to the much more intense and/or much brighter synchrotron radiation sources in the VUV/soft X-ray region that are currently either coming into operation or being conceived as next-generation devices based upon undulators or wigglers, one can see much-expanded possibilities for all of the types of photoelectron diffraction measurements discussed up to this point.

Measurements with both high-energy resolution (to distinguish different surface layers or chemical states as shown in Figs. 34 and 35, respectively) and high angular resolution (to enhance fine structure and thus structural sensitivity) should be possible. For some types of experiments (e.g., with maximum surface sensitivity and/or with spin-polarized diffraction in mind), lower photoelectron

energies of approximately 50–100 eV may be necessary, but for much structural work, energies of 1000 eV or even higher will be beneficial in yielding strongly peaked forward scattering and more nearly single-scattering phenomena. Being able to go to much higher photoelectron energies of up to 5000–10,000 eV may also be of interest in yielding even narrower forward-scattering peaks (as considered from a theoretical viewpoint by Thompson and Fadley[149]), more true bulk sensitivity via the longer electron attenuation lengths, and simpler theoretical interpretation. Being able to tune energy is also essential for the scanned-energy or ARPEFS experiments; it should be possible to carry these out much more rapidly and over a broader energy range above threshold. The polarization vector can also be oriented in either scanned-angle or scanned-energy measurements so as to enhance the contributions of various important scatterers (cf. Figs. 3a and 18). And we have already considered in the last section the possibility of using circularly polarized radiation. Finally, photoelectron *microscopy* with resolutions on the order of 500 Å or less is currently being developed,[150] and the additional dimension of using simultaneous photoelectron diffraction to probe the local atomic structure in such a small spot is quite exciting.

Auger electron diffraction may not benefit as much from synchrotron radiation, because excitation can be achieved with either photons or electrons and because the spectral form is not dependent on the excitation utilized if the initial hole is formed well above threshold. However, even for this case, synchrotron radiation could provide a more intense and less destructive excitation source than, for example, an electron beam or a standard X-ray tube. Also, it would be interesting to look at the diffraction process as the excitation energy is swept through threshold, so as to yield a purer one-hole initial state.

5.4. Combined Methods and Novel Data-Analysis Procedures: Photoelectron Holography?

It is clear from the foregoing examples that both scanned-angle and scanned-energy photoelectron diffraction measurements can provide useful information concerning surface structures, but that scanned-angle measurements are simpler in general to perform. Going to higher energies leads to easily interpretable forward-scattering features for many systems, but at the same time provides little information on the atoms that are below or behind the emitting atom as viewed from the detection direction. Thus, there are clear advantages to using lower energies as well, even if these lead to a potentially greater influence of multiple scattering. In the scanned-energy ARPEFS work discussed in sections 4.2.2 and 4.2.3, a major reason why interlayer spacings down into the bulk were derivable is that these lower energies exhibit the strongest backscattering effects and provide the largest oscillations in the $\chi(k)$ curves (cf. Fig. 20).

It is thus easy to suggest that the ideal photoelectron diffraction experiment based upon present methodology would consist of carrying out both high-energy measurements at kinetic energies greater than approximately 500 eV and low-energy measurements at approximately 50–100 eV. Being able to scan $h\nu$ would also be desirable, but not essential. A typical structure could then be analyzed by first making scanned-angle measurements at high energy and using the real-space

aspects of any forward-scattering effects to narrow down the range of possible structures (cf., for example the discussion of Figs. 29 and 30). Combining scanned-angle measurements at high and low energies then should permit determining structures in detail, including atomic positions both below and above the emitter in the sense mentioned above. Or scanned-energy measurements could be performed as a second step as well, leading to the utility of Fourier transform methods for narrowing down the number of structures. Using an electron spectrometer that can simultaneously analyze and detect electrons over a range of emission directions[35-38] would also clearly speed up such studies, with the only likely drawback being that angular resolution is often lower in such systems, particularly when working at higher energies. In all of these methods, the final precise structural determination would require comparison of experimental diffraction curves or χ functions with calculated curves for a number of geometries, with the most quantitative method of comparison being via some sort of R factor.[20,26d] This is thus exactly the same methodology employed in LEED, except that in photoelectron diffraction, a single scattering approach should already provide useful information for many cases and there is additional readily available structural information concerning the type of local bonding site that can assist in ruling out structures.

As a final new direction in the analysis of scanned-angle data, we consider the recent interesting proposal by Barton,[151] based on an earlier suggestion by Szoeke,[152] that it should be possible to directly determine atomic positions via photoelectron holography. According to this idea, the photoelectron leaving the emitter is treated in first approximation as a spherical outgoing wave that, by virtue of the scattering and diffraction from its neighbors, produces an intensity modulation outside of the surface that can be considered a hologram. This hologram is then simply the intensity distribution of a given peak over a two-dimensional range in θ, ϕ (or, equivalently, some two-dimensional range in k_x, k_y). This intensity distribution can then be described by a formula of exactly the same type as Eq. (10), but with some important generalizations. These generalizations are that the scattering amplitude $|f_j|$ and phase shift ψ_j, together with the factors for the excitation matrix element and attenuation due to spherical wave, inelastic, and vibrational effects, must be replaced by an overall wave amplitude $|F_j|$ and phase ψ_j for each scatterer that sums over all single- and multiple-scattering events which terminate in atom j as the last scatterer before the detector. It can then be shown[151] that inverting this two-dimensional hologram mathematically to produce a real image is equivalent to a double Fourier integral in k_x and k_y, in which the desired z plane of the image is a variable paremeter within the integral. Thus, two dimensional x–y cross sections at different z positions are in principle possible with this method.

Barton has carried out a theoretical simulation of this new method using MSC–SW intensity distributions in θ, ϕ for the $c(2 \times 2)$ S/Ni (001) system at a kinetic energy of 548 eV and with a width of angular detection in both the k_x and k_y directions of ±40°. The inversion of this hologram is found to have maxima that can be directly related to different near-neighbor Ni atoms, with an estimated resolution in x and y of 0.5 Å and in z of a much higher 2.3 Å. The x and y resolutions are ultimately limited by the Rayleigh criterion for a lens

(hologram) of a given opening angle. For the maximum reasonable detection-angle ranges in a spectrometer of ±40° to ±60°, this in turn yields resolution limits Δx and Δy that are very close to the de Broglie wavelength of the electron (i.e., 0.52 Å at 548 eV). This is a likely reason why a rather high kinetic energy in the typical XPS range was used for this simulation.

As noted by Barton, some limitations and/or problems that need to be addressed in the further development of this technique are the relatively low position-resolution obtainable, particularly in z; the presence of twin images at $\pm z$ for each atom (a universal effect in holography), which could cause serious overlap problems for bonding geometries involving atoms that are below-plane; the fact that multiple scattering effects on the F_j may cause deviations of the image positions from the actual sites, thus requiring an iterative correction via theoretical calculations of these generalized scattering amplitudes for an assumed geometry; the fact that several images at different energies, or even an additional Fourier transform of energy-dependent data at each θ, ϕ, may be necessary to effect this correction; and the added experimental difficulty in requiring some sort of high-speed multichannel electron analyzer that can obtain such large data sets in a reasonable amount of time.[35]

Another limitation not mentioned in connection with this theoretical simulation is that the high energy used implies relatively weak backscattering effects of only 15% or so compared to forward scattering (cf. Fig. 2); thus, the actual degree of modulation in intensity observed may be quite small, making the measurements rather difficult. Going to higher energies to improve resolution via shorter de Broglie wavelengths will make this problem worse due to even weaker backscattering. Thus, for an adsorbate or surface atom that has not significantly penetrated a surface, there will always be a tradeoff between resolution and ease of measurement in photoelectron holography. Of course, if the emitter is found below the surface, then strong forward scattering of the type discussed previously here can take place, and the resulting hologram should then show larger intensity modulations; however, forward scattering effects by themselves contain bond direction information, but not bond length information, so that the weaker modulations due to higher-order features would still need to be accurately measured in order for the inversion of the hologram to yield the full structure.

As a potentially more convenient experimental alternative for holography, a suitable Auger peak involving three filled levels might be useful as a source of a more nearly spherical wave as assumed in the image reconstruction, although the poorly understood mixing in of other l components could complicate a precise theoretical analysis of the effective amplitudes $|F_j|$ and phases ψ_j. Also, using Auger peaks that are too broad in energy would reduce the degree of monochromaticity (i.e., coherence) required in the source.[21b]

No matter how these problems are dealt with, even low-resolution three-dimensional images from such holography could be useful in ruling out certain bonding geometries in a semiquantitative way, much as Fourier transforms in ARPEFS can be useful through the approximate path-length differences they provide. It will be interesting to see what the first inversion of an experimental photoelectron hologram brings. (Please see the added note on holographic methods at the end of this chapter.)

6. COMPARISONS TO OTHER TECHNIQUES AND CONCLUDING REMARKS

We begin this concluding section by comparing photoelectron and Auger electron diffraction to several other current probes of surface structure in order to assess their relative strengths and weaknesses. As a first overall comment, it is clear from any perusal of the current literature (e.g., Ref. 1) that no one surface-structure probe directly and unambiguously provides all of the desired information on atomic identities, relative numbers, chemical states, positions, bond distances and bond directions in the first 3–5 layers of the surface. The very small number of surface structures for which there is a general consensus in spite of several decades of careful study of some of them testifies to the need for using complementary information from several methods.

To provide some idea of this complementarity of approaches, we show in Table 1 several techniques assessed according to a number of characteristics: photoelectron diffraction (PD) in both scanned-angle and scanned-energy forms, Auger electron diffraction (AED), surface extended X-ray absorption fine structure (SEXAFS),[16] near-edge X-ray absorption fine structure NEXAFS,[95,153,154] low-energy electron diffraction (LEED),[61] surface-sensitive grazing incidence X-ray scattering (GIXS),[27] scanning tunneling microscopy (STM),[155] and Rutherford backscattering (RBS) or medium-energy ion scattering (MEIS).[156] This is not intended to be a complete list of modern structure probes, but it roughly represents the group most used at present.

These techniques are rated, first, according to whether they directly provide information on atomic identity (a positive feature of all techniques except for LEED, GIXS, and STM) and chemical state (possible only with PD, AED, and NEXAFS). Atom identification is possible in GIXS only if use is made of anomalous dispersion near a certain absorption edge. State-specific information is not derivable in typical SEXAFS measurements because of the overlap of different oscillatory absorption structures above a given edge.

Also, we assess whether other subsidiary types of structural and bonding information can be obtained in a straightforward manner. Of course, once a structure has been determined and optimized to fit the data of any one of these methods, it has implicit in it bond directions, bond distances, site symmetries, and coordination numbers, but the table entries have been chosen to reflect the directness with which these can be extracted from the raw data with a minimum of data analysis. The types of information considered are valence electronic levels or excitations (directly accessible only in NEXAFS and STM), bond directions (particularly easy to determine in high-energy PD/AED with forward scattering—as discussed in comparison to other techniques in section 4.1.4—and RBS/MEIS with shadowing and blocking), bond distances (very direct in SEXAFS Fourier transforms), local bonding-site symmetries (easiest to determine with PD, AED, SEXAFS, and RBS/MEIS), and coordination numbers (derivable directly from high-energy PD and AED and less directly from the amplitudes of SEXAFS oscillations). STM can also directly image surface atoms and thus provide coordination numbers, but it is limited to looking at only the outermost surface density of states, and so does not probe the bonding below this level in a direct

way. Distinguishing between structures that are related to atomic positions and protrusions in the density of states can also be a problem in STM. It has been suggested that NEXAFS resonance energies can be used to measure bond distances,[153] but this approach may be limited to well-calibrated series of homologous molecules, and has been called into question.[154]

The estimated accuracies of finally determining atomic positions with the current state of these techniques is also indicated. Numbers smaller or larger than these will be found for some cases in the literature, but it is the author's opinion that the numbers in the table are a better representation of the true absolute accuracies if all of the various uncertainties in both experimental parameters and the modelling or treatment of the data are taken into account. Surface X-ray diffraction is the most accurate, but its principal sensitivity is to horizontal positions, with vertical positions being derivable only via the more difficult method of measuring rod profiles normal to the surface. PD in any of its forms and AED should be inherently as accurate as SEXAFS, if not more so, particularly if the latter has been analyzed only with transform and back-transform methods without any final theoretical modeling. PD should also ultimately be as accurate as LEED,[73] particularly for a given amount of input to the theoretical analysis.

The degree to which these techniques probe short-range order in the first 10–20 Å around a given site versus longer-range order over 100 Å or more is also considered. Except for LEED and X-ray diffraction, all of the techniques are primarily sensitive to short-range order, although we have also pointed out that PD and AED actually have sensitivity extending over a region of diameter as large as 40 Å. Although inherently larger-scale probes, LEED and X-ray diffraction can with spot profile analysis be used to study the breakdown of long-range order in such phenomena as surface phase transitions.

Next, several characteristics relating to the ease of obtaining data and analyzing it theoretically are indicated: the overall percentage change in intensity as one measure of the ease of determining the signal (which is particularly large for PD, AED, and LEED); the possibility of using a simple, usually kinematical, theory to analyze the results; and the feasibility of using Fourier transform methods to more directly derive structural parameters. The overall figures for percentage effect should be assessed carefully, however, since the inelastic background under some photoelectron and Auger spectra can be high, thus making even a 50% modulation of the peak intensity difficult to measure. By contrast, for some applications of SEXAFS, background effects can be much reduced by using X-ray fluorescence detection,[157] although surface specificity is then lost. Problematic background effects can also arise in SEXAFS scans such as Auger-photoelectron interferences if either type of peak is being used to monitor the absorption and sharp spikes or glitches of intensity due to Bragg reflection of X-rays from very well-ordered crystals such as semiconductors. Auger-photoelectron interferences can also make the use of scanned-energy photoelectron diffraction more difficult if there are any Auger peaks from the sample that lie in the kinetic-energy range from about 100 eV to 400 eV. Standard Auger tabulations show that this could yield difficult background subtraction problems for the atomic number ranges 4–7, 14–22, and 37 upward. As examples of this, sulfur at 16 involves such an interference, as noted previously in sections 4.2.2 and 4.2.3,

TABLE 1. Comparison of Several Surface-Structure Techniques by Different Criteria ("yes" and "no" responses based on deriving a given type of information with minimal data analysis)

	Scanned-angle PD	Scanned-energy PD	AED	SEXAFS	NEXAFS	LEED	GIXS	STM	RBS/MEIS
Atom specific?	Yes	Yes	Yes	Yes	Yes	No	No[a]	No	Yes
Chemical-state specific?	Yes[b]	Yes[b]	Yes[b]?	No	Yes	No	No	No	No
Bond directions?	Yes[c]	Yes	Yes[c]	Yes[c]	Yes[c]	No	No	Yes[d]	Yes[e]
Bond distances?	Yes	Yes[f]	Yes	Yes[f]	No[g]	No	No	Yes[d]	Yes[e]
Adsorption site symmetries?	Yes[h]	Yes?	Yes[h]	Yes?	No	No	No	Yes[d]	Yes
Coordination numbers?	Yes[c]	Yes	Yes[c]	Yes	No	No	No	Yes[d]	Yes
Position accuracies?	~0.02–0.05 Å	~0.02–0.05 Å	≤0.05 Å	~0.02–0.05 Å	?[i]	~0.01–0.05 Å	~0.001 Å (Horizontal) ?[j] (Vertical)	~0.3 Å (Horizontal) ~0.05 Å (Vertical)	~0.01 Å
Valence-electron states?	No	No	No	No	Yes	No	No	Yes	No
Short-range order (~10–20 Å)?	Yes	Yes	Yes	Yes	Yes	No	No	Yes[d]	Yes
Long-range order (>100 Å)?	No	No	No	No	No	Yes	Yes	Yes[d]	No
Overall % effects?	20–70%	20–70%	20–70%	~5%	Variable	70–90% in I–V	Weaker surface peaks	Large	~10%[k]
Kinematical theory?	Yes[l]	Yes[l]	Yes[l]	Yes[l]	No	No	Yes	No	Yes
Fourier transform analysis?	No[k]	Yes[f]	No	Yes[f]	No	No	Yes	Yes[l]	No
Requires synchrotron radiation?	No	Yes	No	Yes	Yes	No	Yes	No	No

[a] GIXS only atom-specific if anomalous dispersion used
[b] If core shifts/fine structure can be resolved in PD/AED, but more difficult in Auger spectra
[c] Forward scattering in high-energy PD and AED yields ~3 times better resolution for bond directions than in polarization-dependent NEXAFS and SEXAFS. Also directly gives coordination numbers for neighbors between emitter and detector.
[d] STM senses only *surface* density of state contours, so that structural parameters are for outermost atoms only.
[e] Via shadowing and blocking in RBS/MEIS.
[f] Fourier transforms to yield path-length differences in scanned energy PD may be complicated by overlap of close-lying differences; SEXAFS Fourier transforms are simpler in this respect.
[g] Only via correlation of bond length with NEXAFS resonance energies that may be limited in application (see Refs. 153 and 154).
[h] May be very direct from azimuthal PD or AED data.
[i] Vertical position information in GIXS less accurate and available only by measuring vertical rod profiles.
[j] Some multiple scattering effects may have to be considered in all of PD, AED, and SEXAFS (see Refs. 57 and 85), and dynamical effects also may have to be included in the analysis of GIXS data for some scattering geometries (see Ref. 27).
[k] Only if holographic imaging is possible.
[l] Fourier transforms of STM images are useful for detecting lateral symmetries present.

and the Ag/Si system considered in section 4.4.2 was found in a recent scanned-energy experiment[50(c)] to exhibit extensive interferences over the full 90–350 eV range due to the various peaks in both the Si *KLL* and the Ag *MNN* spectra.

As a last and important criterion for the present volume, we indicate whether a given technique requires synchrotron radiation, as about half of them do.

The ideal structural probe would have "yes" for all of the nonquantitative characteristics in this table except the last one, which for reasons of broadest utility would be "no." It is clear that each method has positive features, but none constitutes this ideal probe. Thus, complementary information from several methods is in general desirable for fully resolving any structure. PD and AED are positive on sufficient points to be attractive additions to this list. AED is easier to excite (e.g., with photons or electrons), but the more complex nature of Auger spectra will prevent doing state-specific diffraction measurements for many cases, and an accurate theory, especially for lower energies, will be more difficult. Not being able to use radiation polarization to selectively excite towards a given scatterer is also a disadvantage of AED. As one disadvantage of scanned-angle PD and AED, we note the present lack of being able to use Fourier transform methods to determine structure directly (although photoelectron holography is a proposal to do this); thus it may be necessary to carry out a number of calculations for various structures, a procedure analogous to that used in LEED. However, some aspects of the data (e.g., forward scattering peaks at high energy) provide structural information very directly, and a good deal of any analysis should be possible within the framework of a simple single scattering picture. And in any case, the final test of any structural model derived in PD, AED, or SEXAFS should be to compare experiment to a diffraction calculation on a cluster of atoms of sufficient size to adequately include all significant scatterers.

Thus, although photoelectron diffraction and its close relative Auger electron diffraction are relatively new additions to the array of tools for studying surface structures, they have already proven to be useful for a broad variety of systems. Even at the present stage of development of both techniques with, for example, standard X-ray tubes or electron guns as excitation sources, and theory at the single-scattering-cluster–spherical-wave level, structurally useful and unique information can be derived for a range of problems including adsorption, molecular orientation, oxidation, epitaxial growth, metal–semiconductor interface formation, cluster growth, surface phase transitions, and short-range magnetic order. The use of higher angular resolutions promises to provide more precise structural information, particularly concerning longer-range order. The wider availability of synchrotron radiation, especially from the next generation of high-brightness insertion devices, will enormously increase the speed of both scanned-angle and scanned-energy measurements, thus permitting more studies of surface dynamics. The accurate-intensity ratio measurements at low kinetic energy required in spin-polarized photoelectron diffraction will also become easier. Some degree of lateral-resolution photoelectron microscopy-plus-diffraction should also become possible. And with focused electron beams, Auger electron microscopy-plus-diffraction is also feasible. Also, high-brightness radiation sources should permit increased energy resolutions of the order of 0.3 eV even at the higher photon

energies of 1.0–2.0 keV that are optimum for taking advantage of forward scattering and a single-scattering approach. Separate diffraction patterns will be obtainable for the various peaks in a given spectral region that are produced by chemical shifts, multiplet splittings, or more complex final-state effects. Using both linearly and circularly polarized radiation will also permit the selection of specific scatterers and spin-polarized final states, respectively. State-specific structural parameters should thus be derivable in a way that is not possible with other methods.

NOTE ON HOLOGRAPHIC METHODS

Since the original writing of this review, the use of holographically motivated Fourier-transform inversion methods for deriving surface structural information from both photoelectron- and Auger electron-diffraction data (cf. discussion in section 5.4) has advanced considerably. Some of these developments are discussed below.

The first experimental data have successfully been inverted to yield direct images of atomic positions near Cu surfaces by Tonner *et al.*[158] More recently, the same types of images have been observed for the semiconductors Si and Ge by Herman *et al.*[159] and for the simple adsorbate system $c(2 \times 2)$ S/Ni (001) by Saiki *et al.*[100] In general, these images are accurate to within about ±0.2–0.3 Å in planes parallel to the surface and more or less perpendicular to strong forward scattering directions, but only to within about ±0.5–1.0 Å in planes perpendicular to the surface or containing forward scattering directions.

Methods have been proposed for eliminating the observed distortions in atomic images due to both the anisotropic nature of the electron–atom scattering and the phase shift associated with the scattering by Saldin *et al.*,[160] Tong *et al.*,[161] and Thevuthasan *et al.*[162] Preliminary tests of these methods are encouraging, but more applications to experimental data are needed to assess them fully. Further image distortions due to anisotropies in the electron emission process have been discussed,[160,161] and corrections for these also appear to be useful. Additional spurious features that may arise in images due to the strength of the electron–atom scattering and resultant self-interference effects have been pointed out by Thevuthasan *et al.*[162] By contrast, the multiple scattering defocusing illustrated in Figs. 3b–ii and 6 has been shown to reduce the image distortions for the special case of buried emitters that are separated by several atoms from the detector.[162]

Finally, Barton[163] has shown in theoretical simulations that the simultaneous analysis of photoelectron holographic data obtained at several different photon energies, involving in effect an additional Fourier sum on energy, should act to reduce the influence of both twin images and multiple scattering on atomic images.

Thus, the holographic analysis of both photoelectron and Auger electron data is in an intense period of evaluation, with several indications already that it may ultimately provide reasonably good starting-point structures which can then be refined by the more classic trial-and-error methods discussed previously in this review, but in much reduced time.

ACKNOWLEDGMENTS

Some of the work reported here has been supported by the Office of Naval Research under Contract N00014-87-K-0512, the National Science Foundation under Grant CHE83-20200, and the New Energy Development Organization (NEDO) of Japan. Some of the studies discussed here have also benefitted by grants of Cray XMP/48 time at the San Diego Supercomputer Center. The author is also very grateful to his various former and present co-workers at the University of Hawaii for their significant contributions to the development of these techniques. J. J. Rehr has also provided various ideas concerning efficient methods of treating both spherical-wave effects and multiple scattering. Special thanks also go to D. J. Friedman for critically reading this chapter, and to S. A. Chambers and G. Schoenhense for providing helpful comments concerning it. The fine work of M. Prins on many of the figures is also gratefully acknowledged. I also thank J. Hanatani for assistance with preparing this manuscript.

REFERENCES

1. Excellent summaries of the current status of most of these techniques can be found in the proceedings of three International Conferences on the Structure of Surfaces: (a) *The Structure of Surfaces* (M. A. Van Hove and S. Y. Tong, eds.), Springer Verlag, Berlin (1985); (b) *The Structure of Surfaces II* (J. F. van der Veen and M. A. van Hove, eds.), Springer-Verlag, Berlin (1988); (c) *The Structure of Surfaces III* (S. Y. Tong, M. A. Van Hove, K. Takayanagi, and X. D. Xie, eds.), Springer-Verlag, Berlin (1991).
2. K. Siegbahn, U. Gelius, H. Siegbahn, and E. Olsen, *Phys. Lett.* **32A**, 221 (1970).
3. C. S. Fadley and S. A. L. Bergstrom, *Phys. Lett.* **35A**, 375 (1971).
4. A. Liebsch, *Phys. Rev. Lett.* **32**, 1203 (1974); *Phys. Rev.* **B13**, 544 (1976).
5. S. Kono, C. S. Fadley, N. F. T. Hall, and Z. Hussain, *Phys. Rev. Lett.* **41**, 117 (1978); S. Kono, S. M. Goldberg, N. F. T. Hall, and C. S. Fadley, *Phys. Rev. Lett.* **41**, 1831 (1978).
6. D. P. Woodruff, D. Norman, B. W. Holland, N. V. Smith, H. H. Farrell, and M. M. Traum, *Phys. Rev. Lett.* **41**, 1130 (1978).
7. S. D. Kevan, D. H. Rosenblatt, D. Denley, B.-C. Lu, and D. A. Shirley, *Phys. Rev. Lett.* **41**, 1565 (1978).
8. J. J. Barton, C. C. Bahr, Z. Hussain, S. W. Robey, J. G. Tobin, L. E. Klebanoff, and D. A. Shirley, *Phys. Rev. Lett.* **51**, 272 (1983); J. J. Barton, C. C. Bahr, Z. Hussain, S. W. Robey, L. E. Klebanoff, and D. A. Shirley, *J. Vac. Sci. Technol.* **A2**, 847 (1984); J. J. Barton, S. W. Robey, C. C. Bahr, and D. A. Shirley in *The Structure of Surfaces* (M. A. van Hove and S. Y. Tong, eds.), Springer Verlag, Berlin (1985) p. 191.
9. C. S. Fadley, *Prog. in Surf. Sci.* **16**, 275 (1984).
10. C. S. Fadley, Phys. Scr. **T17**, 39 (1987) and earlier references therein.
11. (a) W. F. Egelhoff, *Phys. Rev.* **B30**, 1052 (1984); (b) R. A. Armstrong and W. F. Egelhoff, *Surf. Sci.* **154**, L225 (1985); (c) W. F. Egelhoff, *Phys. Rev. Lett.* **59**, 559 (1987).
12. (a) S. A. Chambers, H. W. Chen, I. M. Vitomirov, S. B. Anderson, and J. H. Weaver, *Phys. Rev.* **B33**, 8810 (1986); (b) S. A. Chambers, I. M. Vitomirov, S. B. Anderson, H. W. Chen, T. J. Wagener, and J. H. Weaver, *Superlattices and Microstructures* **3**, 563 (1987); (c) S. A. Chambers and T. J. Irwin, *Phys. Rev.* **B38**, 7858 (1988); and earlier references therein.
13. C. S. Fadley, in *Core-Level Spectroscopy in Condensed Systems* (J. Kanamori and A. Kotani, eds.), Springer Verlag, Berlin (1988), p. 236.
14. Z. Hussain, D. A. Shirley, C. H. Li, and S. Y. Tong, *Proc. Natl. Acad. Sci. USA.* **78**, 5293 (1981). The use of Fourier transforms was here first thought to yield interlayer distances but later shown to provide path-length difference information, as discussed in Refs. 15 and 21.

15. P. J. Orders and C. S. Fadley, *Phys. Rev.* **B27**, 781 (1983).
16. (a) P. Citrin, in *Springer Series on Surface Science*, Vol. II, Springer Verlag, Berlin (1985), p. 49; (b) D. Norman, *J. Phys.* **C19**, 3273 (1986); (c) J. Stohr, in *X-Ray Absorption: Principles, Applications, Techniques of EXAFS, SEXAFS, and XANES* (R. Prins and D. Konigsberger, eds.), Wiley, New York (1987).
17. N. V. Smith, H. H. Farrell, M. M. Traum, D. P. Woodruff, D. Norman, M. S. Woolfson, and B. W. Holland, *Phys. Rev.* **B21**, 3119 (1980); H. H. Farrell, M. M. Traum, N. V. Smith, W. A. Royer, D. P. Woodruff, and P. D. Johnson, *Surf. Sci.* **102**, 527 (1981).
18. (a) D. Sebilleau, M. C. Desjonqueres, D. Chauveau, C. Guillot, J. Lecante, G. Treglia, and D. Spanjaard, *Surf. Sci. Lett.* **185**, L527 (1987); (b) M. C. Desjonqueres, D. Sebilleau, G. Treglia, D. Spanjaard, C. Guillot, D. Chauveau, and J. Lecante, *Scanning Electron Microsc.* **1** 1557 (1987); (c) D. Sebilleau, G. Treglia, M. C. Desjonqueres, D. Spanjaard, C. Guillot, D. Chauveau, and J. Lecante, *J. Phys. (Paris)* **49**, 227 (1988).
19. (a) B. Sinkovic, P. J. Orders, C. S. Fadley, R. Trehan, Z. Hussain, and J. Lecante, *Phys. Rev.* **B30**, 1833 (1984); (b) P. J. Orders, B. Sinkovic, C. S. Fadley, Z. Hussain, and J. Lecante, *Phys. Rev.* **B30**, 1838 (1984).
20. L. J. Terminello, X. S. Zhang, Z. Q. Huang, S. Kim, A. E. Schach von Wittenau, K. T. Leung, and D. A. Shirley, *Phys. Rev.* **B38**, 3879 (1988).
21. (a) M. Sagurton, E. L. Bullock, and C. S. Fadley, *Phys. Rev.* **B30**, 7332 (1984); and (b) *Surf. Sci.* **182**, 287 (1987).
22. D. P. Woodruff, *Surf. Sci.* **166**, 377 (1986).
23. L. G. Petersson, S. Kono, N. F. T. Hall, C. S. Fadley, and J. B. Pendry, *Phys. Rev. Lett.* **42**, 1545 (1979).
24. H. C. Poon and S. Y. Tong, *Phys. Rev.* **B30**, 6211 (1984); S. Y. Tong, H. C. Poon, and D. R. Snider, *Phys. Rev.* **B32**, 2096 (1985).
25. J. J. Barton and D. A. Shirley, (a) *Phys. Rev.* **B32**, 1892 (1985) and (b) *Phys. Rev.* **B32**, 1906 (1985); (c) J. J. Barton, Ph.D. Thesis, U. Cal., Berkeley (1985); J. J. Barton, S. W. Robey, and D. A. Shirley, *Phys. Rev.* **B34**, 778 (1986).
26. (a) R. S. Saiki, A. P. Kaduwela, J. Osterwalder, M. Sagurton, C. S. Fadley, and C. R. Brundle, *J. Vac. Sci. Technol* **A5**, 932 (1987); (b) R. S. Saiki, A. P. Kaduwela, J. Osterwalder, C. S. Fadley, and C. R. Brundle, *Phys. Rev.* **B40**, 1586 (1989); (c) R. S. Saiki, A. P. Kaduwela, J. Osterwalder, C. S. Fadley, and C. R. Brundle, to be published; (d) The R factors used in this study are generally the $R1$ defined in M. A. van Hove, S. Y. Tong, and M. H. Elconin, *Surf. Sci.* **64**, 85 (1977), although final checks have also been made with the other possibilities $R2$–$R5$ discussed there.
27. Chapter 8 in this volume by P. H. Fuoss, K. S. Liang, and P. Eisenberger.
28. Chapter 3 of Vol. 2 of this set by J. Haase and A. M. Bradshaw.
29. H. Li and B. P. Tonner, *Phys. Rev.* **B37**, 3959 (1988).
30. S. A. Chambers, H. W. Chen, S. B. Anderson, and J. H. Weaver, *Phys. Rev.* **B34**, 3055 (1986).
31. S. D. Kevan, *Rev. Sci. Instrum.* **54**, 1441 (1983).
32. S. D. Kevan, Ph.D. thesis, U. Cal., Berkeley (1980).
33. R. C. White, C. S. Fadley, and R. Trehan, *J. Electron Spectros. Relat. Phenom.* **41**, 95 (1986).
34. J. Osterwalder, M. Sagurton, P. J. Orders, C. S. Fadley, B. D. Hermsmeier, and D. J. Friedman, *J. Electron. Spectros. Relat. Phenom.* **48**, 55 (1989).
35. D. E. Eastman, J. J. Donelon, N. C. Hien, and F. J. Himpsel, *Nucl. Instrum Methods* **172**, 327 (1980).
36. R. C. G. Leckey and J. D. Riley, *Appl. Surf. Sci.* **22/23**, 196 (1985).
37. H. A. Engelhardt, W. Back, and D. Menzel, *Rev. Sci. Instrum.* **52**, 835 (1981); H. A. Engelhardt, A. Zartner, and D. Menzel, *Rev. Sci. Instrum.* **52**, 1161 (1981).
38. M. G. White, R. A. Rosenberg, G. Gabor, E. D. Poliakoff, G. Thornton, S. H. Southworth, and D. A. Shirley, *Rev. Sci. Instrum.* **50**, 1268 (1979); Z. Hussain and D. A. Shirley, private communication.
39. R. C. G. Leckey, *J. Electron Spectros. Relat. Phenom.* **43**, 183 (1987).
40. L. McDonnell, D. P. Woodruff, and B. W. Holland, *Surf. Sci.* **51**, 249 (1975).
41. P. A. Lee, *Phys. Rev.* **B13**, 5261 (1976).
42. S. Kono, S. M. Goldberg, N. F. T. Hall, and C. S. Fadley, *Phys. Rev. Lett.* **41**, 1831 (1978); *Phys. Rev.* **B22**, 6085 (1980).

43. T. Fujikawa, *J. Phys. Soc. Jpn.* **50**, 1321 (1981); **51**, 251 (1982); **54**, 2747 (1985); *J. Electron. Spectros. Relat. Phenom.* **26**, 79 (1982).
44. H. Daimon, H. Ito, S. Shin, and Y. Murata, *J. Phys. Soc. Jpn.* **54**, 3488 (1984).
45. J. J. Rehr, R. Albers, C. Natoli, and E. A. Stern, *Phys. Rev.* **B34**, 4350 (1986); J. J. Rehr, J. Mustre de Leon, C. R. Natoli, and C. S. Fadley, *J. Phys.* (*Paris*) **C8**, Suppl. 12, 213 (1986); J. J. Rehr, J. Mustre de Leon, C. R. Natoli, C. S. Fadley, and J. Osterwalder, *Phys. Rev.* **B39**, 5632 (1989).
46. D. E. Parry, *J. Electron. Spectros. Relat. Phenom.* **49**, 23 (1989).
47. D. J. Friedman and C. S. Fadley, *J. Electron Spectrosc.* **51**, 689 (1990).
48. (a) J. Osterwalder, E. A. Stewart, D. Cyr, C. S. Fadley, J. Mustre de Leon, and J. J. Rehr, *Phys. Rev.* **B35**, 9859 (1987); (b) J. Osterwalder, A. Stuck, D. J. Friedman, A. P. Kaduwela, C. S. Fadley, J. Mustre de Leon, and J. J. Rehr, *Phys. Scr.* **41**, 990 (1990); (c) J. Osterwalder, E. A. Stewart, D. J. Friedman, A. P. Kaduwela, C. S. Fadley, J. Mustre de Leon, and J. J. Rehr, unpublished results.
49. S. Kono, K. Higashiyama, and T. Sagawa, *Surf. Sci.* **165**, 21 (1986) and references to prior structure studies therein.
50. (a) E. L. Bullock, G. S. Herman, M. Yamada, D. J. Friedman, and C. S. Fadley, *Phys. Rev.* **B**, **41**, 1703 (1990); (b) E. L. Bullock, Ph.D. thesis, U. Hawaii (1988); (c) A. P. Kaduwela, D. J. Friedman, M. Yamada, E. L. Bullock, C. S. Fadley, Th. Lindner, D. Ricker, A. W. Robinson, and A. M. Bradshaw in *Structure of Surfaces III* (S. Y. Tong, M. A. Van Hove, K. Takayanagi, and X. D. Xie, eds.), Springer-Verlag, Berlin (1991), p. 600; and to be published.
51. M. Owari, M. Kudo, Y. Nihei, and H. Kamada, *J. Electron. Spectros. Relat. Phenom.* **21**, 131 (1981).
52. D. H. Rosenblatt, S. D. Kevan, J. G. Tobin, R. F. Davis, M. G. Mason, D. A. Shirley, J. C. Tang, and S. Y. Tong, *Phys. Rev.* **B26**, 3181 (1982).
53. G. Treglia, in *Core-Level Spectroscopy in Condensed Systems* (J. Kanamori and A. Kotani, eds.), Springer Verlag, Berlin (1988), p. 281.
54. J. J. Rehr and E. A. Albers, *Phys. Rev.* **B41**, 8139 (1990).
55. S. T. Manson, *Adv. Electron. Electron. Phys.* **41**, 73 (1976).
56. M. Sagurton, private communication.
57. P. A. Lee and J. B. Pendry, *Phys. Rev.* **B11**, 2795 (1975).
58. M. Sagurton, E. L. Bullock, R. Saiki, A. P. Kaduwela, C. R. Brundle, C. S. Fadley, and J. J. Rehr, *Phys. Rev.* **B33**, 2207 (1986).
59. H. C. Poon, D. Snider, and S. Y. Tong, *Phys. Rev.* **B33**, 2198 (1986).
60. M. Fink and A. C. Yates, *At. Data Nucl. Data Tables* **1**, 385 (1970); M. Fink and J. Ingram, *At. Data Nucl. Data Tables* **4**, 129 (1972); D. Gregory and M. Fink, *At. Data Nucl. Data Tables* **14**, 39 (1974).
61. J. B. Pendry, *Low Energy Electron Diffraction*, Academic Press, London (1974); M. A. van Hove and S. Y. Tong, *Surface Crystallography by LEED*, Springer-Verlag, New York (1979).
62. E. A. Stern, B. A. Bunker, and S. M. Heald, *Phys. Rev.* **B21**, 5521 (1980).
63. (a) R. Trehan and C. S. Fadley, *Phys. Rev.* **B34**, 6784 (1986); (b) R. Trehan, J. Osterwalder, and C. S. Fadley, *J. Electron. Spectros. Relat. Phenom.* **42**, 187 (1987).
64. M. P. Seah and W. A. Dench, *SIA, Surf. Interface Anal.* **1**, 2 (1979); C. J. Powell, *Scanning Electron Micros.* **4**, 1649 (1984); S. Tanuma, C. J. Powell, and D. R. Penn, *SIA Surf. Interface Anal.* **11**, 577 (1988).
65. P. M. Cadman and G. M. Gossedge, *J. Electron. Spectros. Relat. Phenom.* **18**, 161 (1980); C. M. Schneider, J. J. de Miguel, P. Bressler, J. Garbe, S. Ferrer, R. Miranda, and J. Kirscher, *J. Phys.* (*Paris*) *C*, Suppl. 12, **49**, 1657 (1988).
66. O. A. Baschenko and V. I. Nefedov, *J. Electron. Spectros. Relat. Phenom.* **21**, 153 (1980) and **27**, 109 (1982) and earlier references therein.
67. Y. U. Idzerda, D. M. Lind, and G. A. Prinz, *J. Vac. Sci. Technol.* **A7**, 1341 (1989).
68. N. E. Erickson and C. J. Powell, *Phys. Rev.* **B40**, 7284 (1989).
69. P. J. Orders, S. Kono, C. S. Fadley, R. Trehan, and J. T. Lloyd, *Surf. Sci.* **119**, 371 (1981).
70. (a) H. Helferink, E. Lang, and K. Heinz, *Surf. Sci.* **93**, 398 (1980); (b) P. J. Orders, R. E. Connelly, N. F. T. Hall, and C. S. Fadley, *Phys. Rev.* **B24**, 6161 (1981).
71. E. L. Bullock and C. S. Fadley, *Phys. Rev.* **B31**, 1212 (1985).

72. R. G. Weissman and K. Muller, *Surf. Sci. Rep.* **1**, 251 (1981).
73. M. L. Xu and M. A. van Hove, *Surf. Sci.* **207**, 215 (1989).
74. G. Breit and H. Bethe, *Phys. Rev.* **94**, 888 (1954).
75. L.-Q. Wang, A. E. Schach von Wittenau, Z. G. Ji, L. S. Wang, Z. Q. Huang, and D. A. Shirley, *Phys. Rev.* **B44**, 1292 (1991); and unpublished results.
76. D. A. Wesner, F. P. Coenen, and H. P. Bonzel, *Surf. Sci.* **199**, L419 (1988).
77. S. Y. Tong and H. C. Poon, *Phys. Rev.* **B37**, 2884 (1988).
78. S. Tougaard, *SIA, Surf. Interface Anal.* **11**, 453 (1988) and earlier references therein.
79. (a) J. B. Pendry and B. S. Ing, *J. Phys.* **C8**, 1087 (1975); (b) B. K. Teo and P. Lee, *J. Am. Chem. Soc.* **1979**, 101 (1979).
80. (a) G. Treglia, M. C. Desjonqueres, D. Spanjaard, D. Sebilleau, C. Guillot, D. Chauveau, and J. Lecante, *J. Phys.* (*Paris*) **1**, 1879 (1989); (b) D. G. Frank, N. Batina, T. Golden, F. Lu, and A. T. Hubbard, *Science* **247**, 182 (1990) and references therein.
81. L. I. Schiff, *Quantum Mechanics*, 3rd ed., McGraw-Hill, New York (1968), p. 136.
82. J. J. Barton, M.-L. Xu, and M. A. van Hove, *Phys. Rev.* **B37**, 10475 (1988).
83. (a) M.-L. Xu, J. J. Barton, and M. A. van Hove, *J. Vac. Sci. Technol* **A6**, 2093 (1988) and (b) *Phys. Rev.* **B39**, 8275 (1989).
84. A. P. Kaduwela, G. S. Herman, D. J. Friedman, C. S. Fadley, and J. J. Rehr, *Phys. Scr.* **41**, 948 (1990); A. P. Kaduwela, G. S. Herman, D. J. Friedman, and C. S. Fadley, *J. Electron Spectrosc. Relat. Phenom.* **57**, 223 (1991).
85. (a) R. C. Albers and J. J. Rehr, to be published; (b) K. Baberschke, in *The Structure of Surfaces II* (J. F. van der Veen and M. A. van Hove, eds.), Springer-Verlag, Berlin (1988), p. 174; (c) P. Rennert and N. V. Hung, *Phys. Status Solid* **148**, 49 (1988).
86. R. S. Saiki, G. S. Herman, M. Yamada, J. Osterwalder, and C. S. Fadley, *Phys. Rev. Lett.* **63**, 283 (1989).
87. (a) D. W. Moon, S. L. Bernasek, D. J. Dwyer, and J. L. Gland, *J. Am. Chem. Soc.* **107**, 4363 (1985); (b) C. Benndorf, B. Kruger, and F. Thieme, *Surf. Sci.* **163**, L675 (1985); (c) D. W. Moon, S. Cameron, F. Zaera, W. Eberhardt, R. Carr, S. L. Bernasek, J. L. Gland, and D. J. Dwyer, *Surf. Sci.* **180**, L123 (1987).
88. (a) D. A. Wesner, F. P. Coenen, and H. P. Bonzel, *Phys. Rev. Lett.* **60**, 1045 (1988); (b) *Phys. Rev.* **B39**, 10770 (1989).
89. H. Kuhlenbeck, M. Neumann, and H.-J. Freund, *Surf. Sci.* **173**, 194 (1986).
90. K. C. Prince, E. Holub-Krappe, K. Horn, and D. P. Woodruff, *Phys. Rev.* **B32**, 4249 (1985); E. Holub-Krabbe, K. C. Prince, K. Horn, and D. P. Woodruff, *Surf. Sci.* **173**, 176 (1986).
91. D. R. Wesner, F. P. Coenen, and H. P. Bonzel, *Phys. Rev.* **B33**, 8837 (1986).
92. K. A. Thompson and C. S. Fadley, *Surf. Sci.* **146**, 281 (1984).
93. H. Ibach and D. L. Mills, *Electron Energy Loss Spectroscopy*, Academic Press, New York (1982).
94. T. E. Madey, David E. Ramaker, and R. Stockbauer, *Ann. Rev. Phys. Chem.* **35**, 215 (1984).
95. J. Stohr and R. Jaeger, *Phys. Rev.* **B26**, 4111 (1982); A. L. Johnson, E. I. Muetterties, J. Stohr, and F. Sette, *J. Phys. Chem.* **89**, 4071 (1985); J. Stohr and D. A. Outka, *Phys. Rev.* **B36**, 7891 (1987).
96. See discussion and references in I. P. Batra and J. A. Barker, *Phys. Rev.* **B29**, 5286 (1984) and R. L. Strong and J. L. Erskine, *Phys. Rev.* **B31**, 6305 (1985).
97. An excellent review of the O/Ni (001) system is by C. R. Brundle and J. Q. Broughton in *The Chemical Physics of Solid Surfaces and Heterogeneous Catalysis* (D. A. King and D. P. Woodruff, eds.), Elsevier, Amsterdam (1991), Vol. 3a.
98. J. E. Demuth, N. J. DiNardo, and C. S. Cargill, *Phys. Rev. Lett.* **50**, 1373 (1983).
99. J. J. Barton, C. C. Bahr, Z. Hussain, S. W. Robey, J. G. Tobin, L. E. Klebanoff, and D. A. Shirley, *Phys. Rev. Lett.* **51**, 272 (1983) and earlier references therein.
100. R. S. Saiki, A. P. Kaduwela, Y. J. Kim, D. J. Friedman, J. Osterwalder, S. Thevuthasan, E. Tober, R. Ynzunza and C. S. Fadley, to be published.
101. M. Sagurton, B. Sinkovic, and C. S. Fadley, unpublished results.
102. X. S. Zhang, L. J. Terminello, S. Kim, Z. Q. Huang, A. E. Schach von Wittenau, and D. A. Shirley, *J. Chem. Phys.* **89**, 6583 (1988).
103. W. F. Egelhoff, *Phys. Rev. Lett.* **59**, 559 (1987).

104. (a) S. A. Chambers, T. J. Wagener, and J. H. Weaver, *Phys. Rev.* **B36**, 8992 (1987); (b) D. A. Steigerwald and W. F. Egelhoff, *Phys. Rev. Lett.* **60**, 2558 (1988).
105. G. Herman, J. Osterwalder, and C. S. Fadley, unpublished results.
106. J. J. Krebs, B. T. Jonker, and G. A. Prinz, *J. Appl. Phys.* **61**, 2596 (1987).
107. G. S. Herman, T. Lindner, R. S. Saiki, and C. S. Fadley, unpublished results.
108. G. Granozzi, A. Rizzi, G. S. Herman, D. J. Friedman, C. S. Fadley, J. Osterwalder, and S. Bernardi, *Phys. Scr.*, **41**, 913 (1990); G. S. Herman, D. J. Friedman, C. S. Fadley, G. Granozzi, G. A. Rizzi, J. Osterwalder, and S. Bernardi, *J. Vac. Sci. Technol.* **B9**, 1870 (1991).
109. R. E. Connelly, C. S. Fadley, and P. J. Orders, *J. Vac. Sci. Technol.* **A2**, 1333 (1984).
110. P. Alnot, J. Olivier, F. Wyczisk, and C. S. Fadley, *J. Electron. Spectros. Relat. Phenom.* **43**, 263 (1987); P. Alnot, J. Olivier, and C. S. Fadley, *J. Electron. Spectros. Relat. Phenom.* **49**, 159 (1989).
111. G. M. Rothberg, K. M. Choudhary, M. L. denBoer, G. P. Williams, M. H. Hecht, and I. Lindau, *Phys. Rev. Lett.* **53**, 1183 (1984).
112. K. M. Choudhary, P. S. Mangat, A. E. Miller, D. Kilday, A. Filipponi, and G. Margaritondo, *Phys. Rev.* **B38**, 1566 (1988).
113. S. Kono in *Core-Level Spectroscopy in Condensed Systems* (J. Kanamori and A. Kotani, eds.), Springer-Verlag, Berlin (1988), p. 253.
114. T. Abukawa and S. Kono, *Phys. Rev.* **B37**, 9097 (1988).
115. (a) S. Ciraci and I. P. Batra, *Phys. Rev. Lett.* **56**, 877 (1986); (b) E. M. Oellig and R. Miranda, *Surf. Sci.* **177**, L947 (1986); (c) T. Kendelewicz, P. Soukassian, R. S. List, J. C. Woicik, P. Pianetta, I. Lindau, and W. E. Spicer, *Phys. Rev.* **B37**, 7115 (1988); (d) R. Ramirez, *Phys. Rev.* **B40**, 3962 (1989).
116. E. J. van Loenen, J. E. Demuth, R. M. Tromp, and R. J. Hamers, *Phys. Rev. Lett.* **58**, 373 (1987); R. J. Wilson and S. Chiang, *Phys. Rev. Lett.* **59**, 2329 (1987) and *J. Vac. Sci. Technol* **A6**, 800 (1988); T. L. Porter, C. S. Chang, and I. S. T. Tsong, *Phys. Rev. Lett.* **60**, 1739 (1988); and earlier references therein.
117. W. C. Fan, A. Ignatiev, H. Huang, and S. Y. Tong, *Phys. Rev. Lett.* **62**, 1516 (1989).
118. S. Y. Tong, H. Huang, C. M. Wei, W. E. Packard, F. K. Men, G. Glander, and M. B. Webb, *J. Vac. Sci. Technol* **A6**, 615 (1988).
119. E. L. Bullock and C. S. Fadley, unpublished results.
120. K. Tamura, U. Bardi, M. Owari, and Y. Nihei, in *The Structure of Surfaces II* (J. F. van der Veen and M. A. van Hove, eds.), Springer-Verlag, Berlin (1988), p. 404.
121. D. Spanjaard, C. Guillot, M. C. Desjonqueres, G. Treglia, and J. Lecante, *Surf. Sci. Rep.* **5**, 1 (1985).
122. Y. Jugnet, N. S. Prakash, L. Porte, T. M. Duc, T. T. A. Nyugen, R. Cinti, H. C. Poon, and G. Grenet, *Phys. Rev.* **B37**, 8066 (1988).
123. (a) T. Miller, T. C. Hsieh, and T.-C. Chiang, *Phys. Rev.* **B33**, 6983 (1986); (b) J. Aarts, A.-J. Hoeven, and P. K. Larsen, *Phys. Rev.* **B38**, 3925 (1988); (c) F. J. Himpsel, F. R. McFeely, A. Taleb-Ibrahimim, J. A. Yarmoff, and G. Hollinger, *Phys. Rev.* **B38**, 6084 (1988).
124. E. Tosatti, in *The Structure of Surfaces II* (J. F. van der Veen and M. A. van Hove, eds.), Springer-Verlag, Berlin (1988), p. 535.
125. U. Breuer, O. Knauff, and H. P. Bonzel, *J. Vac. Sci. Tech.*, **A8**, 2489 (1990).
126. T. Tran, D. J. Friedman, Y. J. Kim, G. A. Rizzi, and C. S. Fadley, *Structure of Surfaces III* (S. Y. Tong, M. A. Van Hove, K. Takayanagi, and X. D. Xie, eds.) Springer-Verlag (1991), p. 522; T. Tran, S. Thevuthasan, Y. J. Kim, G. S. Herman, D. J. Friedman and C. S. Fadley, to be published.
127. (a) E. G. McRae and R. A. Malic, *Phys. Rev. Lett.* **58**, 1437 (1987) and *Phys. Rev.* **B38**, 13183 (1988); (b) E. G. McRae, J. M. Landwehr, J. E. McRae, G. H. Gilmer, and M. H. Grabow, *Phys. Rev.* **B38**, 13178 (1988).
128. J. W. M. Frenken, J. P. Toennies, Ch. Woell, B. Pluis, A. W. Denier van der Gon, and J. F. van der Veen, in *The Structure of Surfaces II* (J. F. van der Veen and M. A. van Hove, eds.), Springer-Verlag, Berlin (1988), p. 547.
129. R. J. Baird, C. S. Fadley, and L. F. Wagner, *Phys. Rev.* **B15**, 666 (1977).
130. S. M. Goldberg, R. J. Baird, S. Kono, N. F. T. Hall, and C. S. Fadley, *J. Electron. Spectros. Relat. Phenom.* **21**, 1 (1980).

131. W. Schaich, *Phys. Rev.* **B8**, 4078 (1973); E. A. Stern, *Phys. Rev.* **B10**, 3027 (1974).
132. See, for example, discussion of multiplets by C. S. Fadley in *Electron Spectroscopy: Theory, Techniques, and Applications* (C. R. Brundle and A. D. Baker, eds.), Vol. 2, Academic Press, London (1978), Ch. 1.
133. G. M. Rothberg, *J. Magn. Magn. Mater.* **15–18**, 323 (1980).
134. (a) B. Sinkovic and C. S. Fadley, *Phys. Rev.* **B31**, 4665 (1985); (b) B. Sinkovic, Ph.D. thesis, U. Hawaii (1988); (c) B. Sinkovic, D. J. Friedman, and C. S. Fadley, *J. Magn. Magn. Mater.* **92**, 301 (1991).
135. B. Hermsmeier, B. Sinkovic, J. Osterwalder, and C. S. Fadley, *J. Vac. Sci. Technol* **A5**, 1082 (1987).
136. C. S. Fadley in (*Magnetic Properties of Low-Dimensional Systems II: New Developments* (L. R. Falicov, F. Mejia-Lira, and J.-L. Moran-Lopez, eds.), Springer-Verlag, Berlin (1990), p. 36; See especially calculations by J. M. Sanchez and J.-L. Moran-Lopez for a frustrated antiferromagnetic system discussed therein.
137. B. W. Veal and A. P. Paulikas, *Phys. Rev. Lett.* **51**, 1995 (1983).
138. B. Hermsmeier, C. S. Fadley, B. Sinkovic, M. O. Krause, J. Jiminez-Mier, P. Gerard, and S. T. Manson, *Phys. Rev. Lett.* **61**, 2592 (1988).
139. S. P. Kowalczyk, L. Ley, R. A. Pollak, F. R. McFeely, and D. A. Shirley, *Phys. Rev.* **B7**, 4009 (1973).
140. P. S. Bagus, A. J. Freeman, and F. Sasaki, *Phys. Rev. Lett.* **30**, 850 (1973).
141. E. Kisker and C. Carbone, *Solid State Commun.* **65**, 1107 (1988).
142. B. Sinkovic, B. Hermsmeier, and C. S. Fadley, *Phys. Rev. Lett.* **55**, 1227 (1985).
143. B. Hermsmeier, J. Osterwalder, D. J. Friedman, and C. S. Fadley, *Phys. Rev. Lett.* **62**, 478 (1989); B. D. Hermsmeier, Ph.D. thesis, U. Hawaii (1989); B. Hermsmeier, J. Osterwalder, D. J. Friedman, B. Sinkovic, T. Tran, and C. S. Fadley, *Phys. Rev.* **B42**, 11895 (1990).
144. D. J. Friedman, B. Sinkovic, C. S. Fadley, *Phys. Scr.* **41**, 909 (1990).
145. J. E. Smart, *Effective Field Theories of Magnetism*, Saunders, New York (1966), Ch. 4.
146. M. Landolt and D. Mauri, *Phys. Rev. Lett.* **49**, 1783 (1982); D. Mauri, R. Allenspach, and M. Landolt, *Phys. Rev. Lett.* **52**, 152 (1984); M. Taborelli, R. Allenspach, and M. Landolt, *Phys. Rev.* **B34**, 6112 (1996); R. Allenspach, D. Mauri, M. Taborelli, and M. Landolt, *Phys. Rev.* **B35**, 4801 (1987).
147. G. Schuetz, W. Wagner, W. Wilhelm, P. Keinle, R. Zeller, R. Frahm, and G. Materlik, *Phys. Rev. Lett.* **58**, 737 (1987); G. Schuetz, R. Frahm, P. Mautner, R. Wienke, W. Wagner, W. Wilhelm, and P. Kienle, *Phys. Rev. Lett.* **62**, 2620 (1989); G. Schuetz, *Phys. Scr.* **T29**, 172 (1989); G. Schuetz and R. Wienke, *Hyperfine Interactions* **50**, 457 (1989).
148. G. Schoenhense, *Appl. Phys.* **A41**, 39 (1986); C. Westphal, J. Bansmann, M. Getzlaff, and G. Schoenhense, *Phys. Rev. Lett.* **63**, 151 (1989); G. Schoenhense, *Phys. Scr.*, **T31**, 255 (1990).
149. K. A. Thompson and C. S. Fadley, *J. Electron, Spectros. Relat. Phenom.* **33**, 29 (1984).
150. P. L. King, A. Borg, P. Pianetta, I. Lindau, G. Knapp, and M. Keenlyside, *Phys. Scr.* **41**, 413 (1990); B. P. Tonner, *Phys. Scr.* **T31**, (1990); W. Ng, A. K. Ray-Chaudhuri, R. K. Cole, S. Crossley, D. Crossley, C. Gong, M. Green, J. Guo, R. W. C. Hansen, F. Cerrina, G. Margaritondo, J. H. Underwood, J. Kortright, and R. C. C. Perera, *Phys. Scr.* **41**, (1990); H. Ade, J. Kirz, S. L. Hulbert, E. D. Johnson, E. Anderson, and D. Kern, *Appl. Phys. Lett.* **56**, 1841 (1990).
151. J. J. Barton, *Phys. Rev. Lett.* **61**, 1356 (1988) and private communication.
152. A. Szoeke, in *Short Wavelength Coherent Radiation: Generation and Applications* (D. T. Attwood and J. Bokor, eds.), AIP Conf. Proc. No. 147, American Institute of Physics, New York (1986).
153. J. Stohr, J. L. Gland, W. Eberhardt, D. A. Outka, R. J. Madix, F. Sette, R. J. Koestner, and U. Doebler, *Phys. Rev. Lett.* **51**, 2414 (1983); J. Stohr, F. Sette, and A. L. Johnson, *Phys. Rev. Lett.* **53**, 1684 (1984); A. P. Hitchcock and J. Stohr, *J. Chem. Phys.* **87**, 3253 (1986).
154. M. N. Piancastelli, D. W. Lindle, T. A. Ferrett, and D. A. Shirley, *J. Chem. Phys.* **86**, 2765 (1987) and **87**, 3255 (1987).
155. P. K. Hansma and J. Tersoff, *J. Appl. Phys.* **61**, R1 (1987). J. Tersoff, in *The Structure of Surfaces II* (J. F. van der Veen and M. A. van Hove, eds.) Springer-Verlag, Berlin (1988), p. 4; and references therein.

156. T. Gustafsson, M. Copel, and P. Fenter, in *The Structure of Surfaces II* (J. F. van der Veen and M. A. van Hove, eds.) Springer-Verlag, Berlin (1988), p. 110; and references therein.
157. F. Sette, S. J. Pearton, J. M. Poate, J. E. Rowe, and J. Stohr, *Phys. Rev. Lett.* 56, 2637 (1986).
158. G. R. Harp, D. K. Saldin, and B. P. Tonner, *Phys. Rev. Lett.* 65, 1012 (1990), and *Phys. Rev.* **B42,** 9199 (1990).
159. G. S. Herman, S. Thevuthasan, T. T. Tran, Y. J. Kim, and C. S. Fadley, *Phys. Rev. Lett.* 3 Feb., 1991.
160. D. K. Saldin, G. R. Harp, B. L. Chen, and B. P. Tonner, *Phys. Rev.* **B44,** 2480 (1991) and earlier references therein.
161. S. Y. Tong, C. M. Wei, T. C. Zhao, H. Huang, and H. Li, *Phys. Rev. Lett.* **66,** 60 (1991); S. Y. Tong, H. Li, and H. Huang, *Phys. Rev. Lett.* **67,** 3102 (1991).
162. S. Thevuthasan, G. S. Herman, A. P. Kaduwela, R. S. Saiki, Y. J. Kim, W. Niemczura, M. Burger, and C. S. Fadley, *Phys. Rev. Lett.* **67,** 469 (1991).
163. J. J. Barton, *Phys. Rev. Lett.* **67,** 3406 (1991).

ELSEVIER

Journal of Electron Spectroscopy and Related Phenomena 75 (1995) 273–297

JOURNAL OF ELECTRON SPECTROSCOPY and Related Phenomena

Photoelectron diffraction: new dimensions in space, time, and spin

C.S. Fadley[a,b,*], M.A. Van Hove[b], Z. Hussain[c], A.P. Kaduwela[a,b]

[a] *Department of Physics, University of California–Davis, Davis, CA 95616, USA*
[b] *Materials Science Division, Lawrence Berkeley National Laboratory, Berkeley, CA 94720, USA*
[c] *Advanced Light Source, Lawrence Berkeley National Laboratory, Berkeley, CA 94720, USA*

Received 13 October 1995; accepted 1 November 1995

Abstract

The current status of photoelectron diffraction studies of surface structures is briefly reviewed, and several recent developments and proposals for future areas of application are then discussed. The application of full-solid-angle diffraction data, together with simultaneous characterization by low energy electron diffraction and scanning tunneling microscopy, to epitaxial growth is first considered. New instrumentation for carrying out such studies with third-generation synchrotron radiation is then presented and several types of results obtained with it are discussed. These results include photoelectron diffraction from surface and interface atoms, the possibility of time-resolved measurements, and circular dichroism in photoelectron angular distributions. The addition of spin to the photoelectron diffraction measurement is also considered, and can be achieved either through core-level multiplet splittings or by circular-polarized excitation of spin–orbit-split levels. This last development makes it possible to study short-range magnetic order, perhaps even in a holographic fashion.

Keywords: Holography; Photoelectron diffraction; Photoelectron spectroscopy; Surface structure; Synchrotron radiation

1. Introduction

In photoelectron diffraction (PD), a photon excites an electron from a core level, and the outgoing photoelectron wave is scattered from the atoms neighboring the emitter, producing an interference pattern. Strong modulations in intensity of as much as ±40% are observed as a function of either the direction of electron emission or the energy of excitation, leading to what have been termed scanned-angle or scanned-energy measurements, respectively. The first set of papers on PD began appearing 25 years ago [1], and the Shirley group was a pioneer in scanned-energy PD, publishing the initial paper in 1978 [1f]. The aim of these measurements is to deduce information about the atomic structure around the emitter, or perhaps also the type of magnetic order surrounding it. There are by now a number of groups in the world engaged in such experiments, using both laboratory X-ray sources and synchrotron radiation (SR), and a variety of systems have been studied to date with this technique, including systems exhibiting surface core-level shifts, adsorbed atoms and molecules, epitaxial overlayers, and atoms at buried interfaces. Several reviews of this field have appeared in recent years [2–7], and it will thus not be our aim to survey it in detail. Rather, we will

* Corresponding author.

SSDI 0368-2048(95)02545-6

begin by briefly describing those basic characteristics that make PD an attractive structural probe, consider some of its limitations and difficulties, and then go on to concentrate on several more recent developments involving both laboratory and next-generation SR sources that promise to make it an even more widely used tool for surface, interface, and nanostructure studies in the future.

We begin with the positive aspects of PD, several of which will be illustrated with more specific examples in the following sections.

(i) Atom specificity. PD is an atom-specific probe by virtue of the fact that a certain core level is probed. Thus, the structure around each type of atom in the sample can be probed separately.

(ii) Chemical-state or site specificity. With sufficient resolution, core binding energy shifts with chemical state (e.g. the different oxidation states of a given atom) or binding site (e.g. between the bulk and surface of a metal or semiconductor) can be used to study the atomic structure around each type of atom separately [8].

(iii) Spin-specificity. Although not nearly as much explored, the diffraction patterns of photoelectrons of different spins can also be studied separately, yielding the promise of determining the local magnetic order around both magnetic atoms and non-magnetic atoms surrounded by magnetic atoms. Such spin sensitivity can be achieved by using the multiplet splitting inherent in the core spectra of various transition metals or rare-earth elements, by exciting spin–orbit-split core levels with circularly polarized radiation, or by some combination of these two effects. This leads to what has been termed spin polarized photoelectron diffraction (SPPD) [9].

(iv) Polarization dependence. Beyond using circular polarization to produce spin polarization, varying polarization from linear to left or right circular to unpolarized further permits selectively directing the outgoing photoelectron probe wave into different regions of the atomic structure surrounding the emitter, so that complementary structural information can be obtained for different relative orientations of light and sample [2,4].

(v) Energy dependence. PD makes use of energy dependence in three basic ways. At higher energies of more than 500 eV, the electron–atom scattering factor is highly peaked in the forward direction, producing pronounced peaks in diffraction patterns along, for example, bond directions in adsorbed molecules and low-index directions in epitaxial layers [2,3,5]. For lower energies below 300 eV, the scattering factor is more uniform over all directions, and usually has a strong peak in the backward direction; thus, the locations of atoms behind the emitter as viewed from the detector can be studied [4,6], although their bond directions cannot be as directly determined as in forward scattering. Being able to vary energy between these two limits using synchrotron radiation thus permits the full structural environment of a given emitter to be studied. Going to lower energies in the 50–100 eV range further leads to increased sensitivity to the surface (via the reduced inelastic attenuation length) and to magnetic scattering effects, (via the enhanced exchange interaction); such energies are thus those of relevance in SPPD measurements [9]. Finally, the energy dependence of the photoelectron de Broglie wavelength is also what leads to the modulations measured in scanned-energy photoelectron diffraction.

(vi) Simple first-order theoretical interpretation. In a number of studies to date, it has proven possible to derive useful surface structural information by comparing experimental data with the results of rather straightforward single-scattering (SS or kinematical) theoretical calculations [2,3a]. However, it is also by now clear that a fully quantitative treatment of all of the features in both low-energy and high-energy diffraction patterns will require more sophisticated calculations at a fully converged multiple scattering (MS) level [10] that have many similarities to those used in low energy electron diffraction (LEED) analyses. We shall illustrate below both types of theoretical analysis.

(vii) Direct derivation of structural parameters. A final advantage is that there are several ways in which it is possible to directly derive structural parameters from PD data. We have already noted that forward scattering peaks directly give bond or low-index directions [2,3,5]. Beyond this, a Fourier transform of scanned-energy PD data yields path-length differences for different scatterers that can often be used to rule out some adsorbate geometries in a search for the true structure [2,4,6b,11].

Finally, taking a larger data set that involves varying both energy and angle over some volume in the momentum space of the photoelectron can be used with several recently suggested transform algorithms to holographically derive atomic positions in three dimensions [12–19], a topic to which we shall return in connection with spin-resolved studies.

By contrast, some difficulties with PD are as follows.

(i) More complex equipment. Relative to a standard laboratory photoelectron spectroscopy system, a more precise, computer-driven sample manipulator is required. For the most versatile and powerful experiments with variable energy and/or variable polarization, access to a synchrotron radiation beamline is also necessary.

(ii) Long measuring times. Measuring hundreds or perhaps even a few thousand separate core spectra to produce a single angle or energy scan or a more complex scan over both angle and energy that can be used in a holographic sense [12–19] can be very time consuming, and take between hours and days with most present systems. However, next-generation synchrotron radiation beamlines, coupled to appropriately high-throughput spectrometers and detectors, promise to reduce these times to the minutes-to-hours range. This should also permit a broader range of dynamical studies on surfaces.

(iii) Macroscopic domain averaging. At present, PD data are taken from the full area illuminated by the radiation, which is typically of the order of 1 mm^2 to 10 mm^2. Thus, many domains are averaged over, and structural conclusions can be confused by the resulting overlap of diffraction patterns from different site types. Various kinds of photoelectron microscopy are currently being tested at different synchrotron radiation sources around the world, as discussed in the article in this issue by Tonner et al. [20]. These developments may ultimately permit PD to be carried out on areas as small as a few hundred angstroms in radius, thus focussing on a single domain or nanostructure on the surface. This last prospect is to be sure a tour de force experiment for third-generation (or even fourth-generation) synchrotron radiation sources, but realizing it would be exciting indeed, because a further space dimension could then be accessed.

(iv) Complex multiple-scattering theoretical interpretation. We have already noted above that data can often be analyzed to a useful point within a single-scattering framework, but future studies will no doubt make more use of the more quantitative multiple-scattering model. However, a number of groups by now have multiple scattering programs operating [10], and these will no doubt become faster, more accurate, and more user friendly; as they have in LEED analysis.

We will now turn to a few recent examples of PD data and its theoretical interpretation, and to the development of next-generation instrumentation for such measurements. These examples are chosen primarily from the work of our groups, but we hope that they are illustrative of both some current forefronts of PD studies and some of the more exciting future directions in this field.

2. Full-solid-angle diffraction data

Although the first full-solid-angle PD pattern was measured some time ago [21a], it is only in recent years that these time-consuming experiments have been performed on a more routine basis, beginning particularly in the Osterwalder group [7,21b–e]. We here illustrate the utility of this kind of data for a recent study of the growth of iron oxides on Pt(111) [22]. In this work, another noteworthy element was added in that X-ray photoelectron diffraction (XPD) measurements in a laboratory-based system were combined with in situ characterization by both LEED and scanning tunneling microscopy (STM), such that the complementary nature of these surface structure probes could be exploited.

Some of the data from this study for a 1 monolayer (ML) overlayer of FeO on Pt(111) are shown in Fig. 1, where a LEED pattern, STM image, and full-solid-angle XPD patterns for all three atoms present (Pt, Fe, and O) are compared for the same surface preparation. The LEED pattern shows the basic Pt(111) spots, but with a rosette of superstructure spots around each one indicative of some longer range order. This longer range

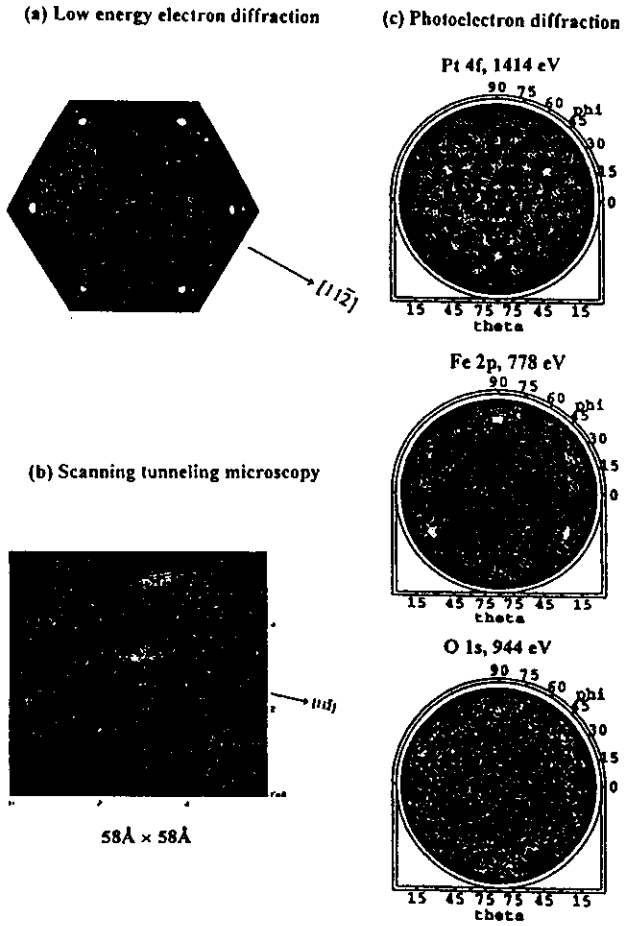

Fig. 1. LEED, STM, and XPD data for 1 ML of FeO on Pt(111). The full-solid-angle XPD patterns for Pt4f, Fe2p, and O1s emission are shown. (From Ref. [22].)

order is directly imaged by STM, with a hexagonal unit cell of approximately 26 Å × 26 Å superimposed on the atomic-resolution hexagonal oxide unit cell of 3.1 Å × 3.1 Å. Such combined LEED and STM data led Galloway et al. [23] to propose a particular superstructure or lateral Moiré pattern consisting of a hexagonal-symmetry bilayer of FeO(111) composed of a layer of Fe atoms on

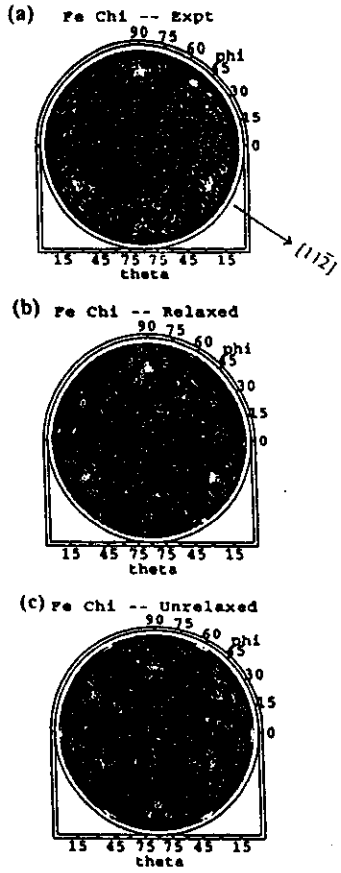

Fig. 2. The full-solid-angle Fe2p XPD pattern for 1 ML of FeO on Pt(111): (a) experimental data; (b) single scattering theory with an Fe–O interplanar distance of 0.65 Å; (c) single-scattering theory with an Fe–O interplanar distance of 1.25 Å as in bulk FeO. (From Ref. [22].)

top of, or below, a layer of O atoms. However, this model left several questions about this overlayer unanswered. Among these questions were: Which atomic layer is outermost, Fe or O? What is the interplanar distance between Fe and O? Is there a preferred relative orientation of the FeO bilayer in its growth with respect to the underlying Pt?

The XPD results in Fig. 1 serve to answer all three of these questions. The Pt4f diffraction pattern is dominated by scattering in the substrate crystal, and so does not contain any easily-derivable information concerning the structure of the overlayer. It does, however, provide a direct internal reference in the data for the orientation of the overlayer. The Fe2p diffraction pattern contains three strong peaks with some fine structure around them, immediately suggesting that there are forward scattering atoms between Fe and the detector. Thus, O appears to be the outermost layer. Finally, the O1s pattern is devoid of any significant diffraction features, further confirming that it is the outermost layer. The second question regarding interlayer spacing is also easily answered by measuring the polar angle at which the Fe–O forward scattering peaks occur, and combining this with the lateral unit cell dimensions of the FeO overlayer from LEED and/or STM. Simple trigonometry then yields an interplanar distance of only 0.65 Å that is much contracted from the 1.25 Å between (111) planes in bulk FeO. This distance can be further checked by carrying out single-scattering diffraction calculations for this overlayer, with single-scattering being a very good approximation for this situation in which there are no chains of forward scattering atoms [2]. Theoretical calculations for both 0.65 Å and 1.25 Å interplanar spacings are compared to experiment in Fig. 2. The agreement between experiment and the calculation for 0.65 Å is excellent, including even the weak diffraction features around the forward scattering peaks. For a 1.25 Å spacing, agreement is poor, both for the polar angle position of the forward scattering peaks and the weaker features. Finally, the fact that there are only three forward scattering peaks in the Fe diffraction pattern immediately implies that only one orientation of the hexagonal O overlayer with respect to the underlying Pt surface exists, even though two O overlayer orientations rotated by 180° with respect to one another are equally likely as far as the Fe layer is concerned. Thus, there is an O–Pt interaction through the Fe layer that is strong enough to select only one orientation of

the O overlayer, a subtle aspect of the growth process that would be difficult to determine with any other method.

This is thus an illustrative example of both how useful full-solid-angle diffraction patterns can be (see also Refs. [7] and [21] for other examples) and how important it is to have additional complementary structural probes in the same experimental chamber, with LEED and STM being two particularly useful ones.

3. A next-generation photoelectron spectrometer/diffractometer

In Fig. 3, we show a schematic view of a photoelectron spectrometer that has been configured for high-resolution, high-intensity spectroscopy and diffraction measurements, and initially installed on bending magnet beamline 9.3.2 at the Advanced Light Source in Berkeley. Fig. 4 shows a photograph of the system, with major components labelled. The electron energy analyzer is a tuneable-resolution large-diameter hemispherical electrostatic system (Scienta ES200) that has been incorporated into a chamber which can rotate over 60° in the plane of the electron storage ring. This rotation is made possible by a large-diameter bellows linking the chamber to the beamline, as shown in these figures. Such in-plane analyzer rotation, although common for much smaller analyzers mounted inside the vacuum system, has not been attempted before in such an ex situ mounting, and it permits selectively varying of the fundamental excitation cross section, keeping the photon-sample geometry fixed while measuring intensities over a large fraction of the 2π solid angle above the surface, and scanning the analyzer with the sample polar-angle motion to keep the photoelectron escape process constant. The analyzer is presently equipped with a single multichannel detector capable of an integrated count rate of about 100 kHz, but will in the near future be modified to include a much higher speed multichannel detector operating up to the gigahertz range, together with an alternative spin detector of the so-called microMott type that will be interchangeable in situ. The spherical grating monochromator and analyzer together should be capable of operating at energy resolutions of $1:10^4$. The analyzer is also equipped with a demountable collimator at its entry to limit the solid angle of acceptance to ±1.5° for high angular resolution studies. The beamline optics also permit radiation to be taken both above and below the plane of the electron orbit, thus obtaining a high degree of left or right circular polarization, and linear polarization with in-plane operation. This beamline and end station has been constructed as a collaborative project with the Shirley group. We now briefly consider some first results obtained with this instrumentation.

3.1. Full-solid-angle photoelectron diffraction from surface and bulk atoms of a clean surface

In Fig. 5(a), we show the geometry for an experiment in which the surface and bulk W4f peaks from a clean W(110) surface have been measured with this system. It is well known that the clean (110) surface exhibits a surface component shifted to lower binding energy by 320 meV [8a,24a], and this is cleanly resolved in the spectrum of Fig. 5(b). The 120 meV full width at half maximum (FWHM) for the bulk peak is slightly narrower than anything measured before [24a], and is essentially limited by the various sources of natural linewidth for this level. PD has been measured before for this case [8a,24b,c], but has only involved a few scans in azimuthal angle or in energy. The high rate of data acquisition possible with this new system (a spectrum like that in Fig. 5(b) can be obtained in 20 s or less) has now permitted measuring essentially the full solid angle of data for both the bulk and surface peaks, as shown in Figs. 5(c) and 5(d), respectively [25]. The photoelectron energies here are in the very surface sensitive 39–40 eV range. Thus, it is obvious that it will be possible in the future to obtain much more complete photoelectron diffraction information than in prior studies.

One immediate benefit of such data sets is the possibility of making more rigorous tests of the multiple scattering theory that is now being used by several groups to analyze PD data. In particular, we have carried out multiple-scattering and single-scattering calculations to simulate the surface-atom

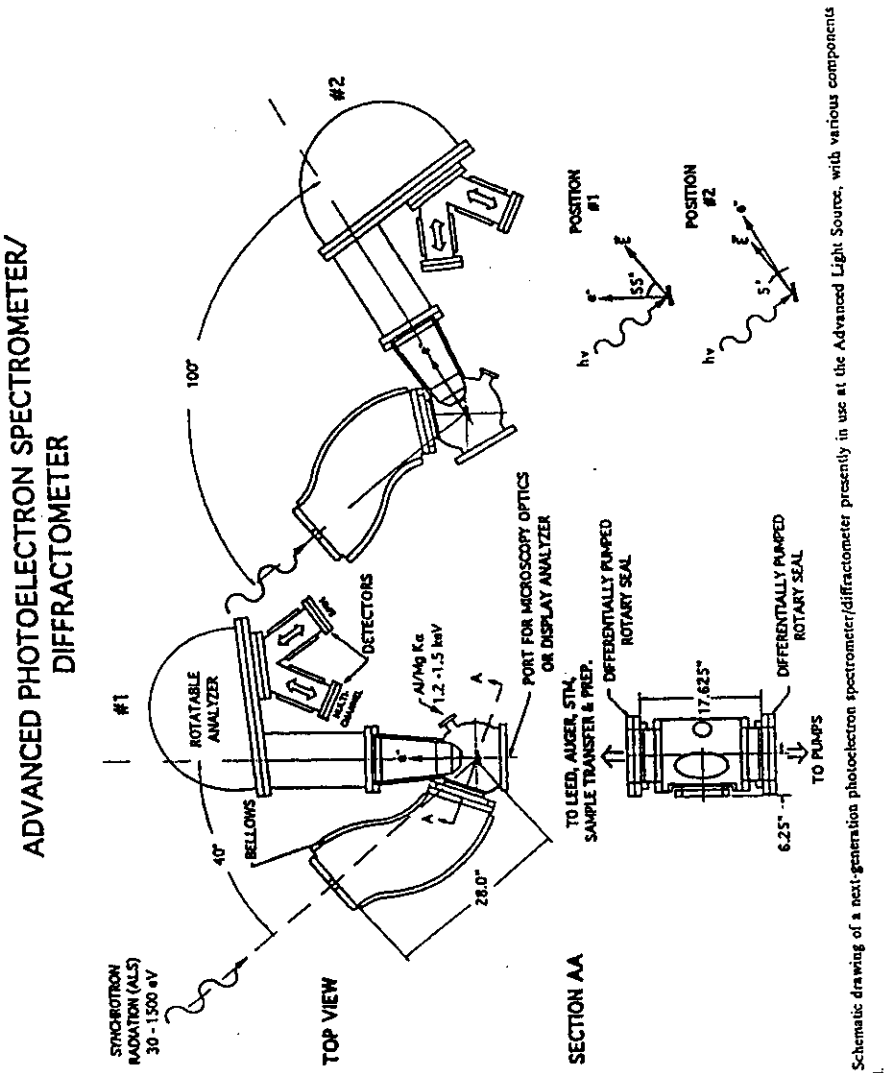

Fig. 3. Schematic drawing of a next-generation photoelectron spectrometer/diffractometer presently in use at the Advanced Light Source, with various components labelled.

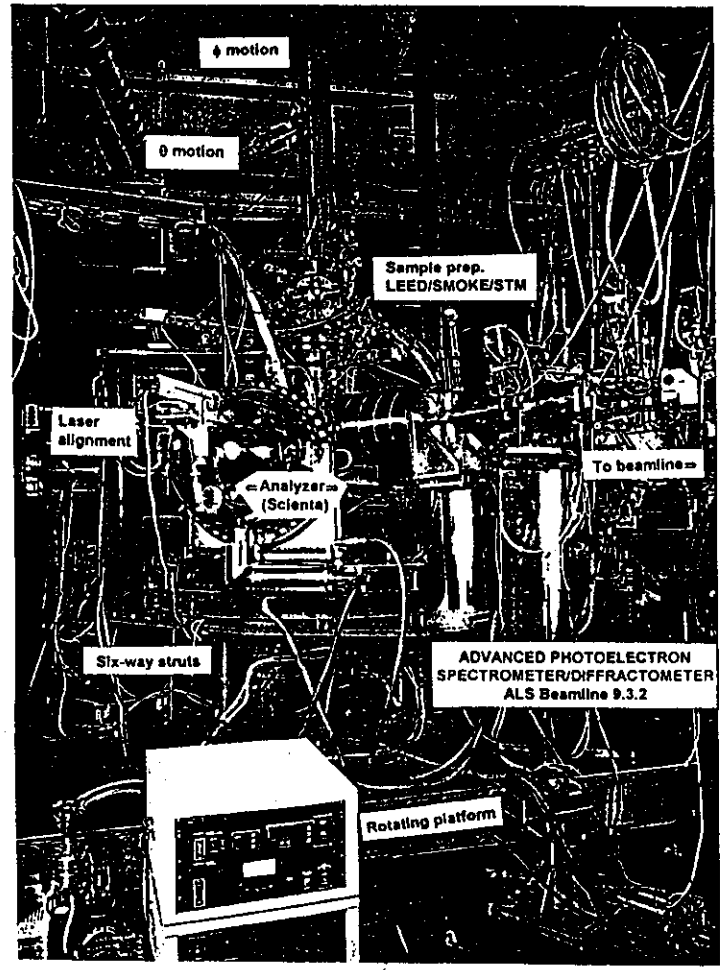

Fig. 4. Photograph of the photoelectron spectrometer/diffractometer of Fig. 3.

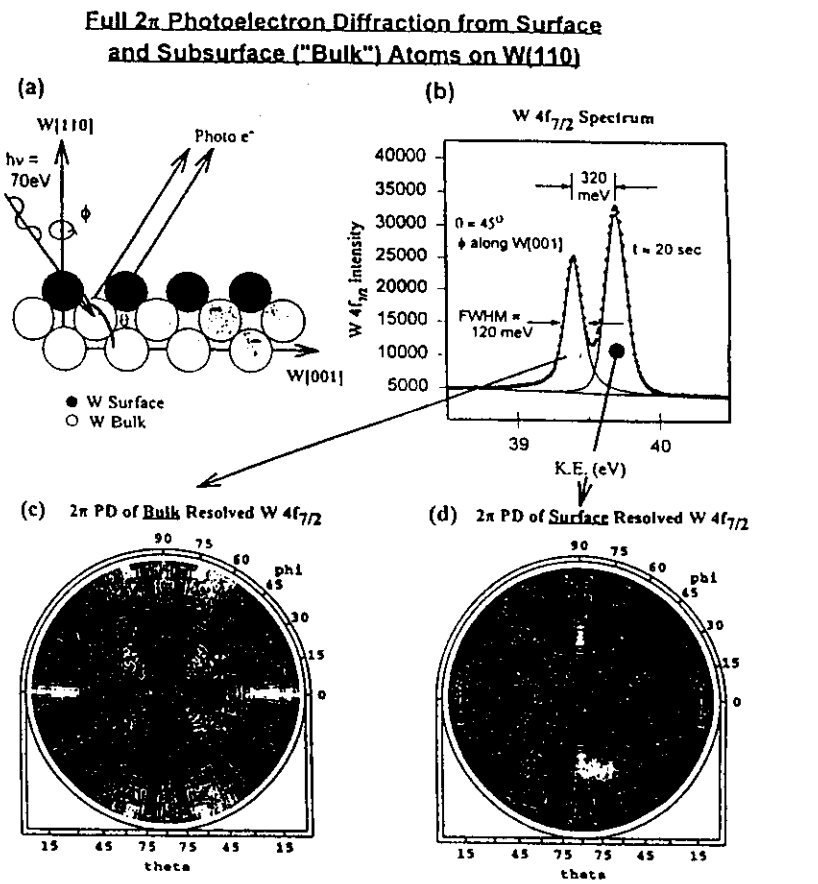

Fig. 5. Full-solid-angle photoelectron diffraction from clean W(110): (a) the experimental geometry; (b) a high-resolution W4f$_{7/2}$ spectrum, resolved into surface and bulk components; (c) the full diffraction pattern for the bulk component; (d) the full diffraction pattern for the surface component. (From Ref. [25].)

diffraction pattern in Fig. 5(d), using a program developed by Kaduwela et al. [10e] and based on the convenient Rehr–Albers approximation for treating multiple scattering [10d]. The experimental data for surface emission are shown again in Fig. 6(a), where they are compared to both multiple scattering and single-scattering results. The "non-structural" parameters for the calculations of inner potential V_0 and inelastic attenuation length Λ_e were determined from the PD data by optimizing the fit of the MS calculations to experiment and analyzing azimuthally-averaged surface-to-bulk ratios as a function of photoelectron takeoff angle relative to the surface; the values of

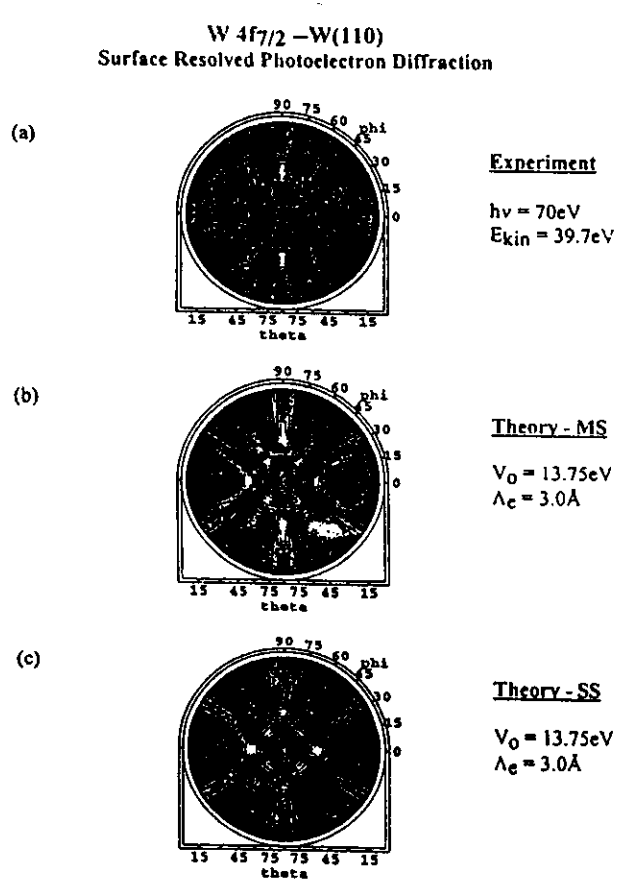

Fig. 6. Full-solid-angle diffraction from the surface atoms of W(110): (a) experimental data; (b) multiple scattering theory; (c) single scattering theory. (From Ref. [25].)

13.75 eV and 3.0–4.0 Å so derived are in excellent agreement with independent determinations from band structure and other theoretical calculations. Moreover, the MS calculations are in excellent agreement with experiment for all the major diffraction features, thus showing that existing PD theory is capable of an accurate description of such data even at such low kinetic energies. The SS calculations based on the same input parameters show similar diffraction features, but clearly do not describe the data as well as the MS results; thus MS effects will definitely need to be included for a quantitative description of such low-energy data.

3.2. Photoelectron diffraction from interface atoms

The detailed structure of interfaces, e.g. between an epitaxial overlayer and the substrate on which it is grown, is clearly one of the most important current surface-structure problems. It is also a difficult problem to solve, because most surface structure probes either cannot uniquely resolve interface atoms from their neighbors or cannot probe very deeply below the surface. PD with high energy resolution has been shown to be capable of studying interface atoms that are at least a few atomic layers below the surface [8d], and future experimental capabilities promise to expand this application dramatically.

As one illustration of what is possible, we show in Fig. 7 results obtained with the system in Figs. 1 and 2 for the case of 1.2 ML of Gd deposited on W(110) [26]. It has been shown by Tober et al. [27] in a combined STM and LEED study that this first monolayer forms a lateral superstructure or Moiré pattern with (7 × 14) periodicity in which a hexagonal Gd(0001) layer is formed on the surface with relatively little lattice constant change compared to bulk Gd. However, this layer is only weakly bound to the underlying W, and many types of Gd–W bonding sites are involved over the (7 × 14) unit cell. Fig. 7(b) shows that it is nonetheless possible to clearly resolve the interface W atoms via the 4f spectrum, and that these interface atoms exhibit a binding energy that is even lower than that for the clean W surface. A likely reason for this lowering of binding energy is the additional core-hole screening possible in the Gd monolayer, which has only a very weak bonding interaction with the substrate. It has also been possible to measure the separate PD patterns for the bulk and interface W peaks in this system, and they are compared in Fig. 7(c), (d) with the corresponding patterns for the clean surface. Because there are many scattering geometries between either an interface W atom or a bulk W atom and the overlying Gd atoms, it is not surprising that the interface diffraction curve is very much like the surface diffraction curve, and that the two bulk curves are also very similar. Overall the Gd scattering here acts to simply produce a nearly uniform background of intensity underneath the dominant pattern associated with W-atom scattering. However, for other kinds of metal–metal epitaxy such as pseudomorphic growth in registry with the substrate, the overlayer would be expected to produce more dramatic changes in the diffraction. Future applications of high-resolution interface PD to metal–metal, metal–semiconductor, and oxide semiconductor overlayer growth are thus very promising.

3.3. Time-dependent measurements

As one illustration of how rapidly it should be possible to take PD data in the future, we show in Fig. 8(a), (b) two lower-resolution spectra from W(110) that were the beginning and end points of a rapid accumulation of over 180 spectra taken in a 70 min time interval. Each spectrum was obtained in only about 4 s. The initially nearly clean surface was exposed to about 6×10^{-10} Torr of O_2 above a 2×10^{-10} Torr base pressure over this time, and the surface peak thus slowly decreased in intensity and shifted toward the bulk peak in energy (an effect that has been seen before [24a]), while a weak oxide peak grew in at about 0.35 eV higher binding energy than the bulk peak. The curves in Fig. 8(c) illustrate the time dependence of the surface and oxide intensities and the surface peak position (which becomes more uncertain as its intensity dies away). These data thus clearly indicate the potential for kinetics studies in which intensities are measured at several key energies or directions as a function of time, thus yielding time-resolved PD. With further optimization of the beamline and end station on which these data were obtained, and/or carrying out the same type of measurement on a more intense third-generation undulator beamline, we estimate that it should be possible to improve these data acquisition speeds by at least one order of magnitude, if not two.

4. Circular dichroism in photoelectron angular distributions

Circular dichroism in photoelectron angular distribution (often termed CDAD) was first

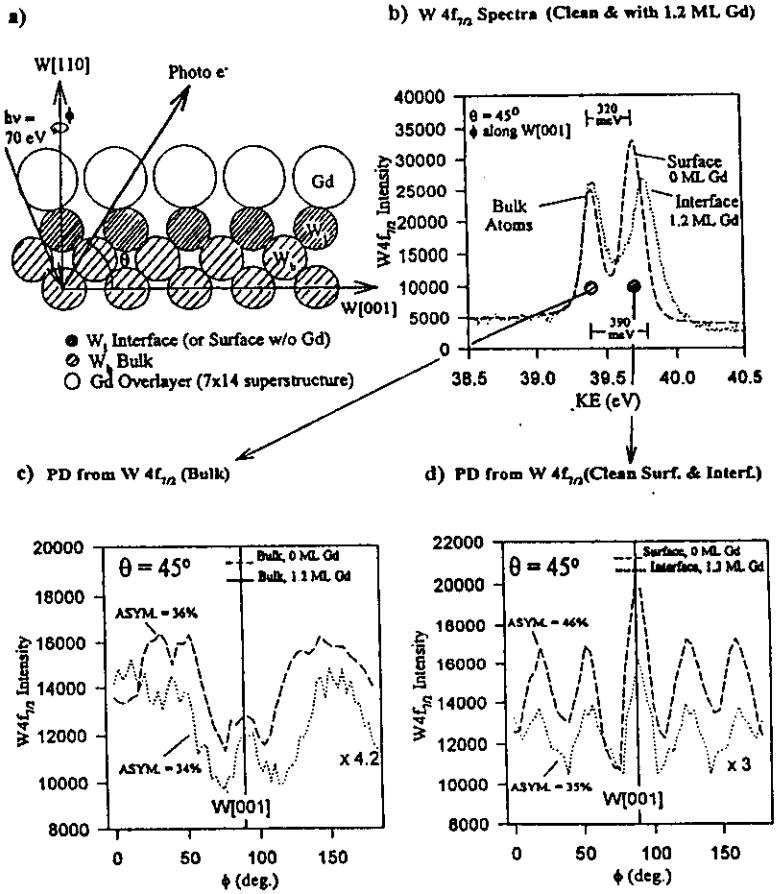

Fig. 7. Photoelectron diffraction from interface W atoms below one monolayer of Gd on W(110): (a) the experimental geometry; (b) comparison of W4f$_{7/2}$ spectra for clean W(110) and 1.2 ML of Gd on W(110) at a takeoff angle of 45° with respect to the surface; (c), (d) azimuthal photoelectron diffraction data at a takeoff angle of 45° for both the clean W(110) and 1 ML Gd/W(110). In (c), the bulk diffraction is compared for the two cases, and in (d) the surface-atom and interface-atom diffraction is compared for the two cases. (From Ref. [26].)

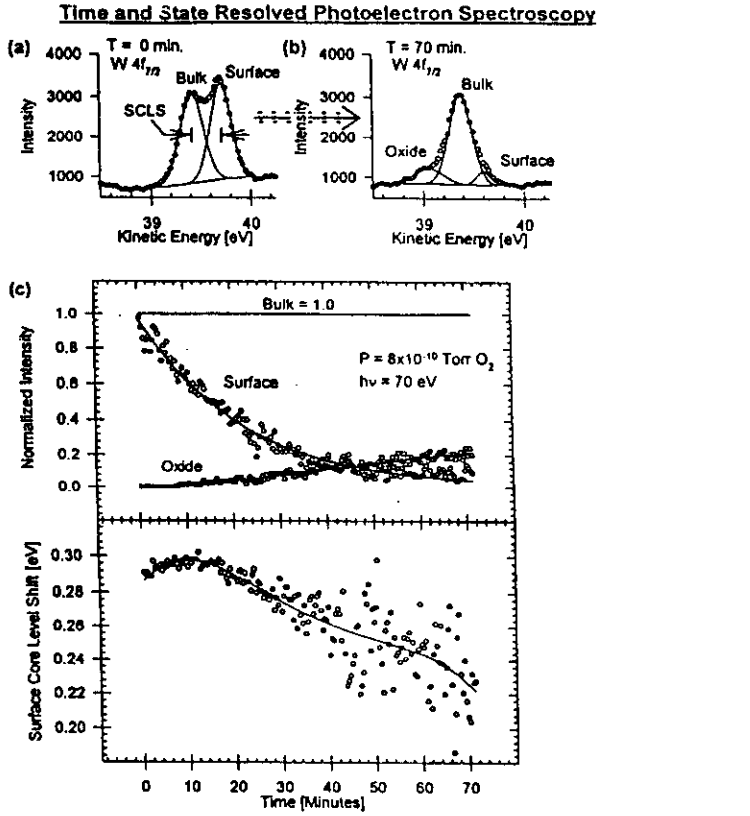

Fig. 8. Time and state resolved photoelectron spectra for a clean W(110) surface exposed to oxygen: (a) clean surface W4f$_{7/2}$ spectrum at start of scans ($T = 0$); (b) surface after 70 min, with depleted surface peak and "oxide" peak associated with adsorbed oxygen, (c) time dependence of surface and "oxide" intensities, together with surface core level shift. (From Ref. [25].)

observed for emission from a core level for the case of an adsorbed molecule on a surface (C1s emission from CO/Pd(111)) by Schönhense and co-workers [28]. This dichroism, or difference between the intensities with left and right circularly polarized light (I^{RCP} and I^{LCP}, respectively), is most conveniently measured via a normalized asymmetry that is defined as

$$A_{CDAD} = \frac{[I^{RCP}(\hat{k}) - I^{LCP}(\hat{k})]}{[I^{RCP}(\hat{k}) + I^{LCP}(\hat{k})]} \quad (1)$$

where $\hat{k}$ is the direction of electron emission. Changes in this asymmetry with direction by as much as ±75% were observed for CO/Pd. These measurements thus made it clear that even a non-chiral molecule can exhibit circular dichroism when

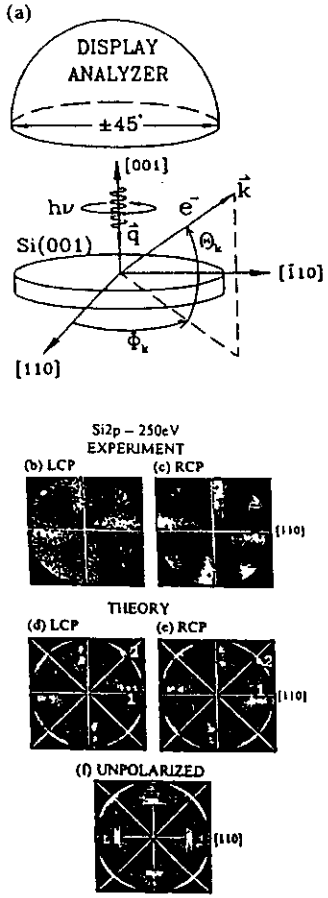

Fig. 9. Circular dichroism in the angular distributions of photoelectrons from Si(001): (a) the experimental geometry, with radiation incident normal to the surface and a display analyzer being used to simultaneously detect electrons over a ±45° cone; (b), (c) experimental Si2p intensity distributions at a kinetic energy of 250 eV and with left-circularly polarized (LCP) and right-circularly polarized (RCP) excitation, respectively; (d), (e) as (b), (c), but multiple scattering photoelectron diffraction theory; (f) analogous multiple scattering theory for excitation with unpolarized radiation. (From Refs. [30] and [31].)

it is fixed to a surface, provided that a certain geometrical condition is satisfied between the molecular axis $\hat{n}$, the light incidence direction $\hat{q}$, and $\hat{k}$: in particular A_{CDAD} can be non-zero whenever these three vectors are not co-planar. Such data were first interpreted using quantum-chemical theoretical methods for the isolated adsorbate molecule [29a]. However, the chirality must be associated with the final-state photoelectron wave function, because the initial core state is spherically symmetrical. This suggests using a PD point of view to interpret such results, as has been done more recently [29b]. In this picture, all information on the chirality is carried in the geometry of the light incidence, the locations of all scatterers around the emitter, and the direction of electron emission. This approach thus permits easy inclusion of contributions to the dichroism from atoms in the substrate. PD calculations were in fact also found to correctly predict the effects seen for CO/Pd(111) [29b].

More generally, it has now been realized that the emission from *any* core level in a single crystal specimen can exhibit non-zero CDAD effects, provided that the plane containing $\hat{q}$ and $\hat{k}$ does not also coincide with a plane of mirror symmetry perpendicular to the surface [30,31]. In particular, intensity distribution measurements for Si2s and Si2p emission from a Si(001) surface in a geometry with the light incident along the normal (see geometry in Fig. 9(a)) have shown that there are not only very strong CDAD effects of as high as about ±20%, but that the observed diffraction patterns exhibit what can in a first approximation be described as peak "rotations" across mirror planes. Some of these experimental data are shown in Fig. 9(b), (c), where all the main diffraction peaks clearly appear to move counterclockwise with LCP excitation, and clockwise with RCP excitation. Also shown in Fig. 9(d), (e) are corresponding diffraction patterns calculated from MS PD theory, and the agreement with the observed effects is excellent for both peaks of types "1" and "2" that can be seen in both experiment and theory. For reference, the theoretical pattern with unpolarized excitation (for which I^{UNP} can rigorously be shown to equal simply $I^{RCP} + I^{LCP}$ [31]) is shown in Fig. 9(f). Exciting with circularly polarized

radiation thus yields one or the other of the two components present in the unpolarized diffraction pattern, with unpolarized radiation producing broader features that are the sum of the two.

Considerable physical insight into the origin of the peak rotations seen in Fig. 9 can also be gained via an approximate model first introduced by Daimon et al. [30]. This notes that, for emission from a given $n_i l_i m_i$ state, the dipole selection rules for circularly-polarized radiation $\Delta m^{RCP} = m_f - m_i = -1$, and $\Delta m^{LCP} = m_f - m_i = +1$, coupled with the angular and radial integrations involved in calculating the photoelectric cross section, lead to a dominance in the final-state photoelectron wave of the spherical harmonics $l_f = l_i + 1$, $m_f = m_{f,min/max} = \mp(l_i + 1)$, respectively. These spherical harmonics then have an azimuthal dependence of $\exp(im_f\phi)$ which yields spiral, rather than cylindrical, constant-phase surfaces. Because photoelectron current will propagate perpendicular to such constant-phase planes, these two dominant components, which have spirals of opposite sense, will "rotate" any diffraction feature (for example, a forward scattering peak) in opposite directions. For circularly-polarized radiation incident perpendicular to a surface, a simple formula even results for these azimuthal rotations $\Delta\phi_{m_f}$

$$\Delta\phi_{m_f} = \frac{m_f}{R_\parallel k_\parallel} \qquad (2)$$

where $R_\parallel$ is the component of the nearest-neighbor distance along some forward scattering direction along the surface, and $k_\parallel$ is the component of the photoelectron wave vector along the surface. This simple formula is in fact very successful in predicting the peak rotations seen in Fig. 9(b), (c), as indicated by the black crosses. It is not however, expected to be fully quantitative for emission directions too far from the surface plane, nor for cases where there is significant mixing of different l_f, m_f components in the final state.

More recent data obtained with the system of Figs. 1 and 2 confirm the generality of such peak rotations, but also more quantitatively show the additional peak distortions that can occur in changing from LCP to RCP [32]. The case studied was a (1 × 1) oxide overlayer on W(110), prepared in a manner described previously [33]. The experimental geometry was very similar to that of the Si(001) experiment, as shown in Fig. 10(a). The W4f spectra for this surface shown in Fig. 10(b) are clearly split into oxide and bulk components, with a separation between them of about 0.70 eV. In Fig. 10(c), we show single azimuthal scans of the bulk and oxide peaks for a takeoff angle θ with respect to the surface of 26.5°, with excitation by linearly-polarized light (LP), and LCP and RCP light. The correct mirror symmetry across the [001] azimuth at 90° is seen in both bulk and oxide for LP excitation, but peak rotations and considerable distortions, are seen with LCP and RCP excitation. The overall diffraction patterns furthermore obey the symmetry expected from the normal-incidence experimental geometry, because the mirror image of the LCP intensities for both oxide and bulk are essentially identical to the RCP intensities. These symmetries and rotations are even more clearly seen in the oxide/bulk ratios of Fig. 10(d), in which various sources of absolute experimental intensity drift with time (and thus angle) are eliminated: in particular, a ±6° rotation is seen here between LCP and RCP. MS PD calculations furthermore well predict both the overall rotations of features and the peak distortions seen here [32].

Thus, such circular dichroism in photoelectron angular distributions is expected to be a very general phenomenon for any non-magnetic (or by implication also magnetic) system, and it can also be quantitatively described by PD theory. One reason for being interested in this effect is that circular dichroism in magnetic systems (magnetic circular dichroism or MCD) is usually a much more subtle difference in intensities that may be only a few percent in magnitude [34]. MCD effects in photoelectron angular distributions are due to a combination of the spin–orbit and multiplet splittings inherent in core spectra [34a] and possible spin-dependent exchange scattering from magnetic atoms during photoelectron escape from the surface. By contrast, the CDAD effects discussed in this section are due to the strong coulomb-plus-exchange scattering from every atom in the speci-

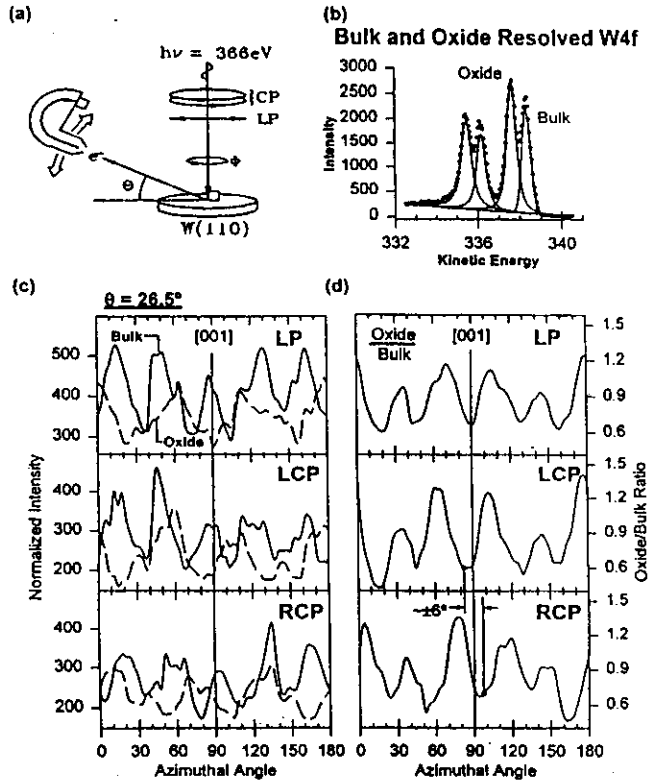

Fig. 10. Circular dichroism in the angular distributions of photoelectrons from (1 × 1) O/W(110) with a (1 × 12) oxide superstructure: (a) the experimental geometry, with radiation incident normal to the surface and the rotating analyzer of Figs. 3 and 4 being used to measure at various takeoff angles θ; (b) a W4f spectrum with oxide and bulk peaks resolved; (c) azimuthal scans at a takeoff angle of 26.5° for both bulk and oxide W4f components for linearly-polarized (LP) light, LCP light, and RCP light; (d) the oxide/bulk ratio over the same azimuthal scan, again for LP, LCP, and RCP excitation. (From Ref. [32].)

men. Thus, properly allowing for the latter will be essential to accurately measuring the former [29].

We also note that the interplay between strong non-magnetic scattering and diffraction effects and weaker magnetic dichroism effects will no doubt also exist in the more recently discovered magnetic linear dichroism (MLD) [35a, b] and magnetic unpolarized dichrosim (MUD) [35c–e], both of which effects manifest themselves in core-photoelectron angular distributions.

We now address the more subtle spin-dependent scattering effects in more detail.

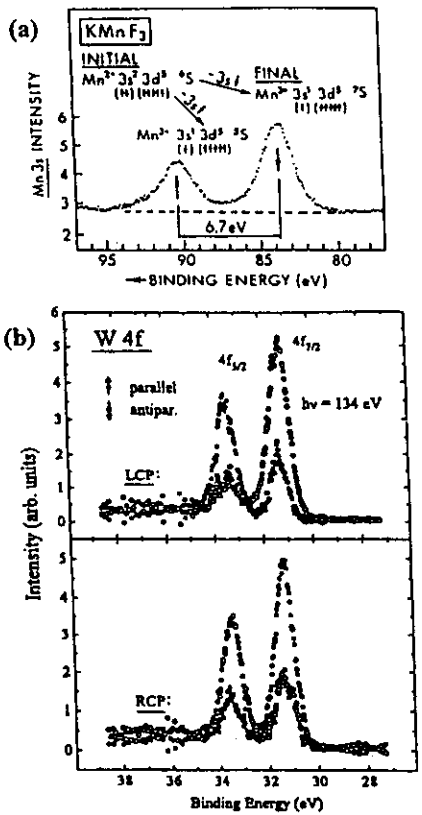

Fig. 11. Spin-polarized core photoelectron spectra: (a) a Mn3s spectrum from $KMnF_3$, with the electronic states and spin polarizations relative to the emitting Mn^{2+} ion indicated (from Ref. [9e]; (b) a W4f spectrum from W(110), excited by LCP light (top panel) and by RCP light (bottom panel). In (b), the spin-resolved intensities as measured parallel or antiparallel to the light incidence direction q are indicated. (From Ref. [39].)

5. Spin-polarized photoelectron diffraction and holography

5.1. Multiplet splittings and spin-polarized photoelectron diffraction

We have already noted that being able to separately measure intensity distributions for spin-up and spin-down photoelectrons should in principle make it possible to determine the short-range magnetic order around a given type of emitter via what can be called spin-polarized photoelectron diffraction (SPPD). The use of multiplet splittings for this purpose is by now well-established for both simple antiferromagnets [9] and ferromagnetic metals [36], and we show in Fig. 11(a) an exchange-split 3s spectrum from antiferromagnetic $KMnF_3$ (100) that is one of the few cases studied to date by SPPD. The predominant spin polarizations of the two components are indicated in this figure, together with the overall electron configurations and L–S multiplets associated with each peak: the ^5S peak at lower kinetic energy is expected to be 100% up-spin and the ^7S peak 71% down-spin; spin polarizations are here measured with respect to the emitting Mn^{2+} ion. In Fig. 12, some experimental [9c, d] and theoretical [37] results related to SPPD from the similar antiferromagnetic system MnO(001) are presented. Plotted in Fig. 12(a) is the temperature dependence of the spin asymmetry S, a normalized spin-up/spin-down intensity ratio that is defined to go to zero at the high-temperature (HT) "paramagnetic" limit of the experimental data via $S(T) = 100[R_T - R_{HT}]$ (in %) [9b–e]. Here $R = I_\uparrow/I_\downarrow$, and the subscripts indicate the temperature at which the ratio was measured. For a low average kinetic energy of 111 eV, this asymmetry shows dramatic changes at about 4.5 times the bulk Néel temperature, with the sense of this change being opposite for two different directions of observation. For a high kinetic energy of 1405 eV for which exchange scattering effects are expected to be negligibly small, no such effect is observed. These experimental results are in qualitative agreement with PD calculations assuming that there is an abrupt loss of short-range antiferromagnetic order at this high temperature, even

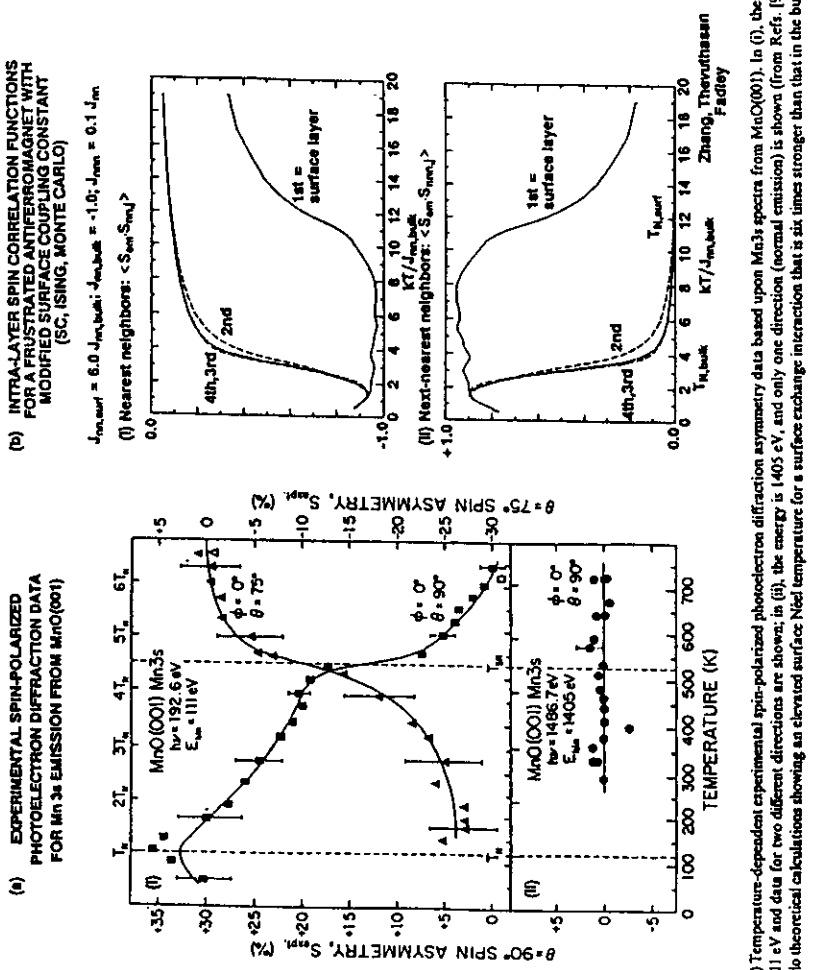

Fig. 12. (a) Temperature-dependent experimental spin-polarized photoelectron diffraction asymmetry data based upon Mn3s spectra from MnO(001). In (i), the electron energy is 111 eV and data for two different directions are shown; in (ii), the energy is 1405 eV, and only one direction (normal emission) is shown (from Refs. [9c,d]. (b) Monte Carlo theoretical calculations showing an elevated surface Néel temperature for a surface exchange interaction that is six times stronger than that in the bulk (from Ref. [37]).

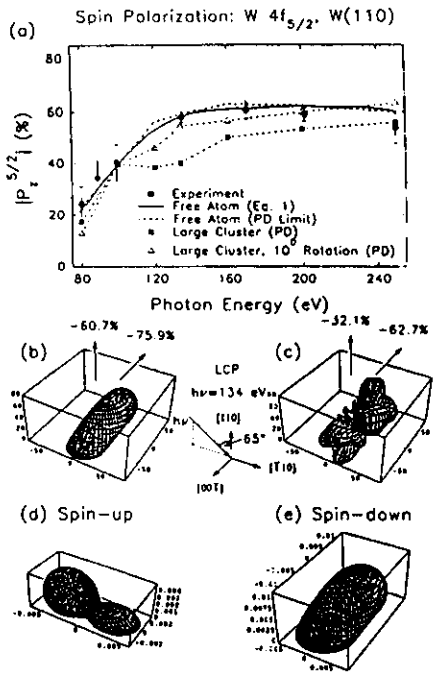

Fig. 13. Spin-polarization in W4f spectra excited by circularly-polarized light from W(110): (a) the absolute value of the $4f_{5/2}$ polarization as a function of photon energy, with experiment compared to both free-atom and MS cluster PD calculations; (b) the three-dimensional spin polarization for a free atom in the geometry shown in the inset and with an excitation energy of 134 eV; (c) as 9b), but for a MS cluster PD calculation in a five-atom cluster (an emitter below four surface scatterers); (d), (e) the separate spin-up and spin-down intensities excited in a free-atom. (From Ref. [39].)

though the bulk long-range order is lost at the much lower Néel temperature [9d]. One possible explanation for this effect is that there are local domains of short-range order that persist up to this higher temperature and then abruptly disappear. Another recently discussed possibility is that the surface Néel temperature could be significantly higher than that in the bulk [37]. Fig. 12(b) shows the results of Monte Carlo calculations for a simple-cubic Ising antiferromagnet of Mn^{2+} ions in which the surface exchange coupling between Mn^{2+} spins has been set to be 6.0 times that in the bulk. For this simple model, it is seen that the spin–spin correlation functions for both nearest neighbor Mn^{2+} ions and next neighbor Mn^{2+} ions show a relatively sharp transition in the surface layer (here indicated as the first layer) at a temperature that is a few times the transition temperature for the rest of the layers (i.e. the bulk in this model). Thus, it is also possible that these SPPD experiments have detected a highly elevated surface Néel temperature for this system. Although further experiments and theory will be necessary to fully clarify the nature of these observations, this work and other prior studies [9] indicates the potential of SPPD for studying short-range magnetic order. Exploiting this potential should be assisted enormously by the use of next-generation synchrotron radiation facilities.

5.2. Spin polarization from circular-polarized excitation

Spin-polarized photoelectrons can also be produced by exciting a spin–orbit-split core level, making use of the well known Fano effect from atomic physics [38]. We illustrate this with some very recent data obtained by Starke et al. for the non-magnetic system W(110) [39]. Fig. 11(b) shows spin-resolved W4f spectra in which the spin polarizations are here measured externally along the direction of light incidence, and the light has been changed from RCP to LCP. The experimental geometry is indicated in the inset of Fig. 13(b). There is a clear and strong spin polarization in both the 5/2 and 7/2 components, with the expected change of sign as the polarization of the light is changed. In Fig. 13(a), we show the absolute value of the spin polarization of the $W4f_{5/2}$ peak excited with circularly-polarized radiation, as a function of photon energy. Over the range from about 130 eV to 250 eV, the experimental polarization is very large and about 50–60%. The 7/2 peak is found to have the opposite sign of polarization to the 5/2 peak for RCP or LCP excitation, and a magnitude only 3/4 as large (the inverse ratio of subshell occupation numbers), as expected from

simple atomic considerations [39]. These polarizations are thus comparable to the 70–100% expected for simple 3s multiplets of the type discussed previously, and immediately suggest using such spectra as internal sources of spin-polarized photoelectrons for SPPD studies. Such SPPD studies based on circularly-polarized excitation have in fact been attempted for the first time recently [40]. Theoretical curves for the energy dependence of the 5/2 spin polarization are also shown in Fig. 13(a). Simple free-atom calculations based on the work of Cherepkov [41] agree very well with experiment, but with some deviations at lower and higher energies. PD calculations with only one emitter and no scatterers present (i.e. the free-atom limit of the algorithm) agree with the analytical free-atom results, an important self-consistency check. MS PD calculations from a large W(110) cluster in the nominal geometry of the experiment show the same general trend of polarization variation with energy as experiment, but have a significant dip at about 125 eV that is not seen in experiment. However, a small azimuthal rotation of the cluster by 10° that is within the experimental uncertainty of alignment suppresses this dip, and also yields excellent agreement with experiment. The change in the PD polarizations with cluster orientation, however, suggests that photoelectron scattering, even in a non-magnetic lattice, can significantly alter the degree of spin polarization in a core spectrum. To explore this effect further, we show in Fig. 13(b), (c) the full three-dimensional contours of the absolute value of the $W4f_{5/2}$ spin polarization, as plotted relative to the origin of the coordinate system. In Fig. 13(b) is shown the contour for a free atom, tilted toward the upper right due to the light incidence direction, as shown in the inset geometry. This is a smooth curve, with basically a donut shape and overall negative polarization. Fig. 13(c) shows the same kind of contour for a W emitter beneath four W scatterers: a five-atom cluster in the W(110) geometry. It is here obvious that scattering and diffraction effects cause a strong modulation of the spin polarization with direction, with one manifestation of this being the dip seen at 125 eV in Fig. 13(a). The origin of these dramatic changes is that the separate spin-up and spin-down intensity distributions excited from the 5/2 level have very different shapes, as shown in the plots of Fig. 13(d), (e), and they thus sample differently the non-magnetic scatterers around the emitting atom. Such effects should be very general, very strong, and occur in both non-magnetic and magnetic surroundings.

5.3. Spin-polarized photoelectron holography

Finally, we turn to another intriguing prospect for the future of spin-resolved photoelectron diffraction studies: the possibility of directly imaging the spins around a given emitter via holographic inversion methods. So-called "direct methods" for deriving three-dimensional atomic structures have been discussed in two other papers in this volume by Schaff et al. [6b] and by Terminello et al. [16e], and we thus introduce them here only briefly, to be able to discuss adding a spin-dependent aspect. All direct methods involve carrying out some kind of mathematical operation that is closely akin to a Fourier transform on a large set of data involving perhaps 1500–4000 distinct intensity measurements. In general, the photoelectron intensity $I(k)$ for a certain wave vector k is converted to a normalized χ function in a standard way via

$$\chi(k) = \frac{I(k) - I_0(k)}{I_0(k)} \quad \text{or} \quad \frac{I(k) - I_0(k)}{I_0(k)^{1/2}} \qquad (3)$$

where $I_0(k)$ is the intensity in the absence of any scatterers. Measurements of $\chi(k)$ are made at several directions of emission (several $\hat{k}$), and also perhaps at several energies of excitation (several $|k|$). The most common way to holographically invert such a $\chi(k)$ data set is to carry out the following transform over the relevant volume in k-space [12d,14a,b]

$$U(r) = \left| \int_{|k|} \exp(-i|k||r|) \iint_{\hat{k}} \times \exp(ik \cdot r)\chi(k)|k|^2 \, d|k| \sin\theta_k \, d\theta_k \, d\phi_k \right| \qquad (4)$$

where θ_k and ϕ_k are the angles defining the direction $\hat{k}$. Several prior studies have obtained successful three-dimensional images of near-neighbor atoms using this approach or close relatives of it [12–19], and it seems clear that, at least for back scattering atoms around a given emitter, very useful structural conclusions can be drawn. These images include some obtained with only one energy (e.g. Refs. [13,15a,b,d,16]) and others in which the transform of Eq. (4) is modified to allow for non-ideal scattering effects and/or to somehow focus on the region of image space that is most nearly ideal (e.g. Refs. [13,14,15,17b,18,19]).

We have already noted that two core photoelectron peaks can often be found at relatively closelying energies that are strongly spin-polarized in an opposite sense. This might be due to a core multiplet splitting or a spin–orbit doublet excited with circular polarization, or some mixture of these two effects. Thus, it is in principle possible to separately measure $\chi_\uparrow$ and $\chi_\downarrow$ for the two different spin orientations, and this could lead via spin-dependent scattering effects to the holographic imaging of the local magnetic order around a given type of emitter [42]. There are two obvious spin-sensitive imaging algorithms based on Eq. (4) and $\chi_\uparrow$ and $\chi_\downarrow$ [42b]

$$\Delta(r) = U_\uparrow(r) - U_\downarrow(r) \qquad (5)$$

with obvious notation, and

$$\Delta'(r) = \left| \int_{|k|} \exp(-i|k||r|) \iint_{\hat{k}} \exp(ik \cdot r)[\chi_\uparrow(k) - \chi_\downarrow(k)]|k|^2 \, d|k| \sin\theta_k \, d\theta_k \, d\phi_k \right| \qquad (6)$$

which is simply the image $U(r)$ calculated only on the difference of the spin-up and spin-down χ values. Additional vector-based spin-sensitive holographic imaging functions have also been proposed [42a].

As a brief indication of the potential of this kind of photoelectron holography, we show in Fig. 14 holographic inversions of multiple scattering calculations for emission of spin-up and spin-down electrons from Mn^{2+} ions in a small planar cluster representing a portion of the MnO(001) surface [42c]. The cluster is shown in Fig. 14(a). Spin-up Mn^{2+} scatterers in this cluster have been distinguished from spin-down scatterers by having an additional exchange potential due to five unpaired 3d electrons that interacts only with spin-up photoelectrons. Spin-down scatterers have the same 3d exchange potential, but it interacts only with spin-down photoelectrons. Thus, the potential is slightly more attractive when the photoelectron spin is parallel to that of the scatterer. Spin-up and spin-down holograms were calculated in a fully-converged MS way for 10 energies between 127 eV and 278 eV, and holographic images then derived via Eqs. (4)–(6). The normal images U in the plane of the cluster for spin-up and spin-down electrons are shown in Fig. 14(b), (c) together with the corresponding spin-sensitive images $\Delta(r)$ nd $\Delta'(r)$ in Fig. 14(d), (e). The normal images show features for all of the atoms in the cluster, including the four non-magnetic O atoms. These spin-up and spin-down images are also very similar, as expected because the 3d exchange scattering is only 5–15% of the total effective scattering potential at these energies. By contrast, neither $\Delta(r)$ nor $\Delta'(r)$ contains any image intensity for the O atoms, verifying that either of these choices of imaging algorithm is predominantly sensitive to only the magnetic scatterers. The peaks and valleys in the spin-sensitive images are in general about 7–9% as strong in transform amplitude as the normal images, suggesting the experimental possibility of carrying out such imaging, albeit a non-trivial exercise. $\Delta(r)$ and $\Delta'(r)$ are also inherently different in that $\Delta(r)$ images both orientations of scatterers in the same way, due the absolute value in Eq. (6), while $\Delta'(r)$ changes sign when the scatterer is flipped, and thus also is sensitive to the orientation of a given scatterer. $\Delta'(r)$ also involves the phase of the scattering factor, and thus can show sign changes over the region of a magnetic scatterer; however, it is clear from this and other calculations that the sign changes are exactly reversed if the orientation of the scatterer spin is flipped from up to down.

Thus, spin-polarized photoelectron holography represents an intriguing and challenging experimental possibility for the future, but one well matched to the new synchrotron radiation sources that are now becoming available.

6. Concluding remarks

Photoelectron diffraction is thus in some respects

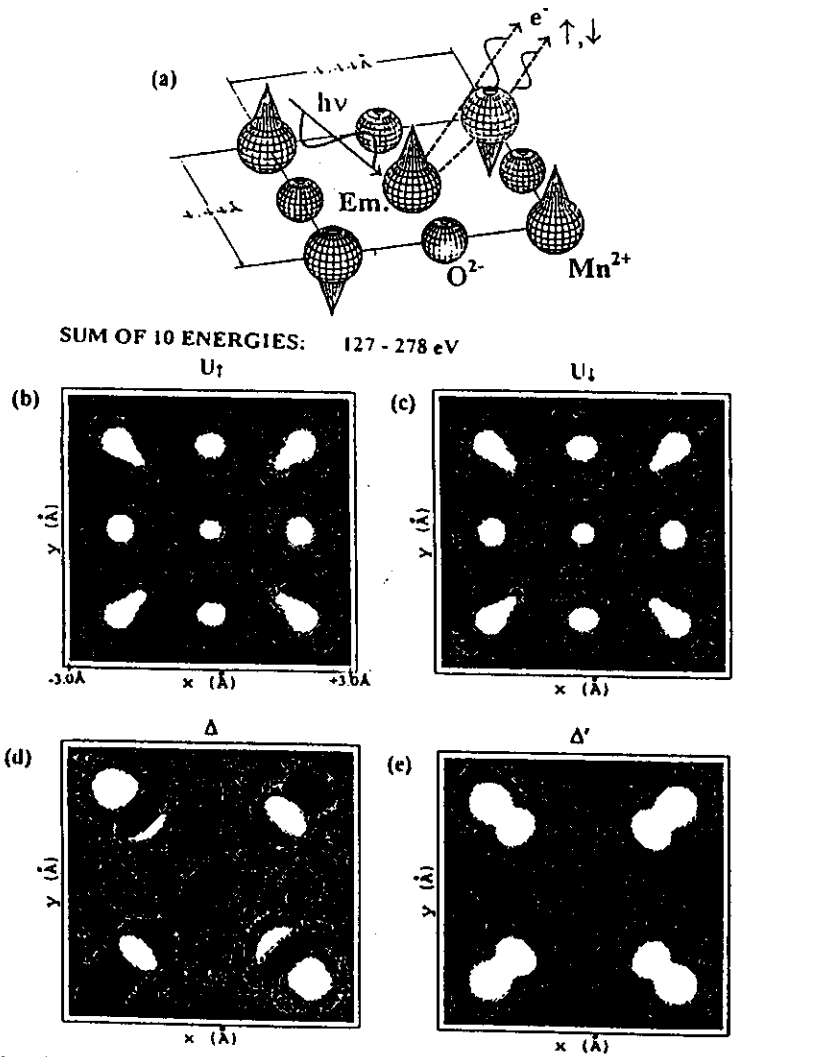

Fig. 14. A theoretical simulation of spin-polarized photoelectron holography: (a) a nine-atom cluster representing the (001) surface of MnO, with an emitter in its center; (b), (c) normal holographic images $U(r)$ generated by using Eq. (4) for ten energies between 127 and 278 eV; (d) the spin-sensitive holographic image $\Delta(r)$ generated by using Eq. (5); (e) the spin-sensitive holographic image $\Delta'(r)$ generated by using Eq. (6). (From Ref. [42b].)

a mature field, but at the same time one in which several exciting new possibilities for surface and magnetic structure studies are found. The simple extension to taking full-solid-angle data often permits much clearer conclusions regarding structures, especially when high energies with forward scattering are present, and complementary structure probes such as LEED and STM are used in situ with it. Next-generation instrumentation, particularly at third-generation synchrotron radiation sources, will much expand the use of state-resolved photoelectron diffraction, including the resolution of surface atoms and atoms at buried interfaces, time-dependent structural studies, and different types of dichroism in both non-magnetic and magnetic systems. The use of circularly-polarized radiation for excitation shows up new phenomena in diffraction peak rotations and distortions, and makes it possible to excite spin-polarized photoelectrons from any spin–orbit split level. Spin-polarized photoelectron diffraction and its more difficult cousin spin-polarized photoelectron holography also promise to provide information on local magnetic order in an element-specific, and also a site-specific, way.

Acknowledgments

We are grateful to R.X. Ynzunza and E.D. Tober for assistance with preparing some of the figures in this paper. We also thank our various co-workers who have contributed greatly to the equipment fabrication and the several specific studies presented here: R. Couch, C. Cummings, H. Daimon, K. Higashiyama, W.R.A. Huff, P.D. Johnson, S.A. Kellar, Y.J. Kim, T. Lauritzen, P. Len, G. Miner, E.J. Moler, J. Palomares, S. Ryce, S. Ruebush, W. Schattke, D.A. Shirley, K. Starke, S. Thevuthasan, E.D. Tober, Z. Wang, C. Westphal, R. Wright, H. Xiao, R.X. Ynzunza, and F. Zhang. This work has been supported by the Director, U.S. Department of Energy, Office of Basic Energy Sciences, Division of Materials Sciences under Contract DOE-AC03-76SF00098 and the U.S. Office of Naval Research under Contract No. N00014-94-0162.

References

[1] (a) K. Siegbahn, U. Gelius, H. Siegbahn and E. Olsen, Phys. Lett. A, 32 (1970) 221.
(b) C.S. Fadley and S.A.L. Bergstrom, Phys. Lett. A, 35 (1971) 375.
(c) A. Liebsch, Phys. Rev. Lett., 32 (1974) 1203; Phys. Rev. B, 13 (1976) 544.
(d) S. Kono, C.S. Fadley, N.F.T. Hall and Z. Hussain, Phys. Rev. Lett., 41 (1978) 117.
(e) D.P. Woodruff, D. Norman, B.W. Holland, N.V. Smith, H.H. Farrell and M.M. Traum, Phys. Rev. Lett., 41 (1978) 1130.
(f) S.D. Kevan, D.H. Rosenblatt, D. Denley, B.-C. Lu and D.A. Shirley, Phys. Rev. Lett., 41 (1978) 1565.
(g) S. Kono, S.M. Goldberg, N.F.T. Hall and C.S. Fadley, Phys. Rev. Lett., 41 (1978) 1831.
[2] (a) C.S. Fadley, Phys. Scr. T, 17 (1987) 39.
(b) C.S. Fadley, in R.Z. Bachrach (Ed.), Synchrotron Radiation Research: Advances in Surface Science, Plenum Press, New York, 1993.
(c) C.S. Fadley, Surf. Sci. Rep., 19 (1993) 231.
(d) C.S. Fadley, S. Thevuthasan, A.P. Kaduwela, C. Westphal, Y.J. Kim, R. Ynzunza, P. Len, E. Tober, F. Zhang, Z. Wang, S. Ruebush, A. Budge and M.A. Van Hove, J. Electron Spectrosc. Relat. Phenom., 68 (1994) 19.
(e) C.S. Fadley, in X. Xide, S.Y. Tong and M.A. Van Hove (Eds.), The Structure of Surfaces IV, World Scientific, Singapore, 1994b, pp. 1–28.
[3] (a) S.A. Chambers, Adv. Phys., 40 (1990) 357; Surf. Sci. Rep., 16 (1992) 261.
(b) W.F. Egelhoff, Jr., Crit. Rev. Solid State Mater. Sci., 16 (1990) 213.
[4] (a) L.J. Terminello, X.S. Zhang, Z.Q. Huang, S. Kim, A.E. Schach von Wittenau, K.T. Leung and D.A. Shirley, Phys. Rev. B, 38 (1988) 3879.
(b) L.-Q. Wang, Z. Hussain, Z.Q. Huang, A.E. Sachach von Wittenau, D.A. Shirley and D.W. Lindle, Phys. Rev. B, 44 (1991) 13771.
(c) D.A. Shirley, Y. Zhang, B.L. Petersen, Z. Hussain, W.A. Huff, J.J. Barton and L.J. Terminello, J. Electron Spectrosc. Relat. Phenom., 68 (1994) 49.
[5] H.P. Bonzel, Prog. Surf. Sci., 42 (1993) 219.
[6] (a) A.M. Bradshaw and D.P. Woodruff, in W. Eberhardt (Ed.), Applications of Synchrotron Radiation: High-Resolution Studies of Molecules and Molecular Adsorbates on Surfaces, Springer-Verlag, Berlin, 1993.
(b) O. Schaff, G. Hess, V. Fernandez, K.-M. Schindler, A. Theobald, Ph. Hofmann, A.M. Bradshaw, V. Fritzsche, R. Davis and D.P. Woodruff, J. Electron Spectrosc. Relat. Phenom., 75 (1995) 117.
[7] J. Osterwalder, P. Aebi, R. Fasel, D. Naumovic, P. Schwaller, T. Treutz, L. Schlapbach, T. Abukawa and S. Kono, Surf. Sci., 331–333 (1995) 1002.
[8] (a) D. Sebilleau, M.C. Desjonqueres, D. Chaveau, C. Guillot, J. Lecante, G. Treglia and D. Spanjaard, Surf. Sci. Lett., 185 (1987) L527.

(b) A. Nilsson, H. Tillborg and N. Mårtensson, Phys. Rev. Lett., 67 (1991) 1015.
(c). K.U. Weiss, R. Doppel, K.M. Schindler, P. Gardner, V. Fritsche, A.M. Bradshaw, A.L.D. Kilcoyne and D.P. Woodruff, Phys. Rev. Lett., 69 (1992) 3196.
(d) J.D. Denlinger, E. Rotenberg, U. Hessinger, M. Leskovar and M.A. Olmstead, Appl. Phys. Lett., 62 (1993) 2057; E. Rotenberg, J.D. Denlinger, U. Hessinger, M. Leskovar and M.A. Olmstead, J. Vac. Sci. Technol. B, 11 (1993) 1444.
[9] (a) B. Sinkovic and C.S. Fadley, Phys. Rev. B, 31 (1985) 4665.
(b) B. Sinkovic, B.D. Hermsmeier and C.S. Fadley, Phys. Rev. Lett., 55 (1985) 1227.
(c) B.D. Hermsmeier, J. Osterwalder, D.J. Friedman and C.S. Fadley, Phys. Rev. Lett., 62 (1989) 478.
(d) B.D. Hermsmeier, J. Osterwalder, D.J. Friedman, B. Sinkovic, T.T. Tran and C.S. Fadley, Phys. Rev. B, 42 (1990) 11895.
(e) B. Sinkovic, D.J. Friedman and C.S. Fadley, J. Magn. Magn. Mater., 92 (1991) 301.
[10] (a) C.H. Li and S.Y. Tong, Phys. Rev. Lett., 42 (1979) 901.
(b) J.J. Barton and D.A. Shirley, Phys. Rev. B, 32 (1985) 1892, 1906.
(c) A.P. Kaduwela, G.S. Herman, D.J. Friedman and C.S. Fadley, Phys. Scr., 41 (1990) 948.
(d) J.J. Rehr and R.C. Albers, Phys. Rev. B, 41 (1990) 81139.
(e) A.P. Kaduwela, D.J. Friedman and C.S. Fadley, J. Electron Spectrosc. Relat. Phenom., 57 (1991) 223.
[11] (a) P.J. Orders and C.S. Fadley, Phys. Rev. B, 27 (1983) 781.
(b) M. Sagurton, E.L. Bullock and C.S. Fadley, Phys. Rev. B, 30 (1984) 7332; Surf. Sci., 182 (1987) 287.
(c) V. Fritzsche and D.P. Woodruff, Phys. Rev. B, 46 (1992) 16128.
(d) P. Hofmann and K.M. Schindler, Phys. Rev. B, 47 (1993) 13942.
[12] (a) A. Szöke, in D.T. Attwood and J. Bokor (Eds.), Short Wavelength Coherent Radiation: Generation and Applications, AIP Conference Proceedings No. 147, AIP, New York, 1986.
(b) J.J. Barton, Phys. Rev. Lett., 61 (1988) 1356.
(c) J.J. Barton, J. Electron Spectrosc. Relat. Phenom., 51 (1990) 37.
(d) J.J. Barton, Phys. Rev. Lett., 67 (1991) 3106.
[13] (a) G.R. Harp, D.K. Saldin and B.P. Tonner, Phys. Rev. Lett., 65 (1990) 1012; Phys. Rev. B, 42 (1990) 9199.
(b) B.P. Tonner, Z.-L. Han, G.R. Harp and D.K. Saldin, Phys. Rev. B, 43 (1991) 14423.
(c) G.R. Harp, D.K. Saldin, X. Chen, Z.L. Han and B.P. Tonner, J. Electron Spectrosc. Relat. Phenom., 57 (1991) 331.
(d) D.K. Saldin, G.R. Harp, B.L. Chen and B.P. Tonner, Phys. Rev. B, 44 (1992) 2480.
(e) D.K. Saldin, G.R. Harp and B.P. Tonner, Phys. Rev. B, 45 (1992) 9629.
[14] (a) S.Y. Tong, C.M. Wei, T.C. Zhao, H. Huang and H. Li, Phys. Rev. Lett., 66 (1991) 60.
(b) S.Y. Tong, H. Li and H. Huang, Phys. Rev. Lett., 67 (1992) 3102.
(c) S.Y. Tong, H. Huang and C.M. Wei, Phys. Rev. B, 46 (1992) 2452.
(d) J.G. Tobin, G.D. Waddill, H. Li and S.Y. Tong, Phys. Rev. Lett., 70 (1993) 4150.
[15] (a) S. Thevuthasan, G.S. Herman, A.P. Kaduwela, R.S. Saiki, Y.J. Kim, W. Niemczura, M. Burger and C.S. Fadley, Phys. Rev. Lett., 67 (1991) 469.
(b) G.S. Herman, S. Thevuthasan, T.T. Tran, Y.J. Kim and C.S. Fadley, Phys. Rev. Lett., 68 (1992) 650.
(c) S. Thevuthasan, G.S. Herman, A.P. Kaduwela, T.T. Tran, Y.J. Kim, R.S. Saiki and C.S. Fadley, J. Vac. Sci. Technol. A, 10 (1992) 2261.
(d) S. Thevuthasan, R.X. Ynzunza, E.D. Tober, C.S. Fadley, A.P. Kaduwela and M.A. van Hove, Phys. Rev. Lett., 70 (1993) 595.
(e) P.M. Len, S. Thevuthasan, A.P. Kaduwela, M.A. van Hove and C.S. Fadley, Surf. Sci., in press.
(f) P.M. Len, F. Zhang, S. Thevuthasan, A.P. Kaduwela, M.A. van Hove and C.S. Fadley, J. Electron Spectrosc., Relat. Phenom., 76 (1995) 351.
[16] (a) L.J. Terminello, J.J. Barton and D.A. Lapiano-Smith, J. Vac. Sci. Technol. B, 10 (1992) 2088; Phys. Rev. Lett., 70 (1993) 599.
(b) B.L. Petersen, L.J. Terminello and D.A. Shirley, Mat. Res. Soc. Symp. Proc., 307 (1993) 285.
(c) B.L. Petersen, L.J. Terminello, J.J. Barton and D.A. Shirley, Chem. Phys. Lett., 220 (1994) 46.
(d) B.L. Petersen, Ph.D. Thesis, University of California-Berkeley, 1995.
(e) L.J. Terminello, B.L. Petersen and J.J. Barton, J. Electron Spectrosc. Relat. Phenom., 75 (1995) 299.
(f) Y. Zhou, X. Chen, J.C. Campuzano, G. Jennings, H. Ding and D.K. Saldin, Mat. Res. Soc. Symp. Proc., 307 (1993) 279.
[17] (a) H. Wu, G.J. Lapeyre, H. Huang and S.Y. Tong, Phys. Rev. Lett., 71 (1993) 251.
(b) H. Wu and G.J. Lapeyre, Phys. Rev. B, 51 (1995) 14549.
[18] S.Y. Tong, H. Li and H. Huang, Phys. Rev. B, 51 (1995) 1850.
[19] M.T. Sieger, J.M. Roesler, D.-S. Lin, T. Miller and T.-C. Chiang, Phys. Rev. Lett., 73 (1994) 311.
[20] B.P. Tonner, D. Dunham, T. Droubay, J. Kikuma, J. Denlinger and E. Rotenberg, J. Electron Spectrosc. Relat. Phenom., 75 (1995) 309.
[21] (a) R.J. Baird, C.S. Fadley and L.F. Wagner, Phys. Rev. B, 15 (1977) 666.
(b) J. Osterwalder, T. Greber, S. Hüfner and L. Schlapbach, Phys. Rev. B, 41 (1990) 12495.
(c) S. Hüfner, J. Osterwalder, T. Greber and L. Schlapbach, Phys. Rev. B, 42 (1990) 7350.
(d) G.S. Herman and C.S. Fadley, Phys. Rev. B, 43 (1991) 6792.
(e) T. Greber, J. Osterwalder, S. Hüfner and L. Schlapbach, Phys. Rev. B, 44 (1991) 8958.

[22] (a) Y.J. Kim, C. Westphal, R.X. Ynzunza, H. Xiao, Z. Wang, H.C. Galloway, M. Salmeron, M.A. Van Hove and C.S. Fadley, paper presented at the 1995 Natl. Symp. Am. Vac. Soc., to be published.
(b) Y.J. Kim, Ph.D. Thesis, University of Hawaii-Manoa, 1995.
[23] H.C. Galloway, J.J. Benitez and M. Salmeron, Surf. Sci., 198 (1993) 127; J. Vac. Sci. Technol. A, 12 (1994) 2302.
[24] (a) D.M. Riffe, G.K. Wertheim and P.H. Citrin, Phys. Rev. Lett., 53 (1989) 1976.
(b) D. Spanjaard, C. Guillot, M.-C. Desjonquères, G. Teglia and J. Lecante, Surf. Sci. Rep., 5 (1985) 1.
(c) B. Kim, J. Chen, J.L. Erskine, W.N. Mei and C.M. Wei, Phys. Rev. B, 48 (1993) 4735.
[25] R.X. Ynzunza, E.D. Tober, J. Palomares, Z. Wang, Z. Hussain, A.P. Kaduwela and C.S. Fadley, to be published.
[26] E.D. Tober, R.X. Ynzunza, Z. Wang, J. Palomares, Z. Hussain, A.P. Kaduwela and C.S. Fadley, to be published.
[27] E.D. Tober, R.X. Ynzunza, C. Westphal and C.S. Fadley, Phys. Rev. B, May 1996.
[28] (a) G. Schönhense, Phys. Scr. T, 31 (1990) 255.
(b) J. Bansmann, Ch. Ostertag, G. Schönhense, F. Fegel, C. Westphal, M. Getzlaff, F. Schafers and H. Petersen, Phys. Rev. B, 46 (1992) 13496.
[29] (a) V. McKoy and J.A. Stephens, personal communication, 1994.
(b) C. Westphal, A.P. Kaduwela, M.A. Van Hove and C.S. Fadley, Phys. Rev. B, 50 (1994) 6203.
[30] (a) H. Daimon, T. Nakatani, S. Imada, S. Suga, Y. Kagoshima and T. Miyahara, Jpn. J. Appl. Phys., 32 (1993) L1480.
(b) H. Daimon, personal communication, 1994.
[31] A.P. Kaduwela, H. Xiao, S. Thevuthasan, M.A. Van Hove and C.S. Fadley, Phys. Rev. B, 52 (1995) 14927.
[32] H. Daimon, R. Ynzunza, J. Palomares, Z. Wang, Z. Hussain, A.P. Kaduwela and C.S. Fadley, to be published.
[33] K.E. Johnson, R.J. Wilson and S. Chiang, Phys. Rev. Lett., 71 (1993) 1055.
[34] (a) L. Baumgarten, C.M. Schneider, H. Petersen, F. Schafers and J. Kirschner, Phys. Rev. Lett., 65 (1990) 492.
(b) H. Ebert, L. Baumgarten, C.M. Schneider and J. Kirschner, Phys. Rev. B, 44 (1991) 4406.
(c) G.D. Waddill, J. Tobin and D.R. Pappas, Phys. Rev. B, 46 (1992) 552.
[35] (a) Ch. Roth, F.U. Hillebrecht, H.B. Rose and E. Kisker, Phys. Rev. Lett., 70 (1993) 3479.
(b) F. Sirotti and G. Rossi, Phys. Rev. B, 49 (1994) 15682.
(c) M. Getzlaff, Ch. Ostertag, G.H. Fecher, N.A. Cherepkov and G. Schönhense, Phys. Rev. Lett., 73 (1994) 3030.
(d) N.A. Cherepkov, Phys. Rev. B, 50 (1994) 13813.
(e) E. Kisker, paper presented at VUV 11, Tokyo, Japan, August 1995. To be published in J. Electron Spectrosc. Relat. Phenom.
[36] F.U. Hillebrecht, R. Jungblut and E. Kisker, Phys. Rev. Lett., 65 (1990) 2450.
(b) R. Jungblut, Ch. Roth, F.U. Hillebrecht and E. Kisker, J. Appl. Phys., 70 (1991) 5923.
(c) R. Jungblut, Ch. Roth, F.U. Hillebrecht and E. Kisker, Surf. Sci., 269/270 (1992) 615.
(d) T. Kachel, C. Carbone and W. Gudat, Phys. Rev. B, 47 (1993) 15391.
(e) D.G. van Campen, R.J. Pouliot and L.E. Klebanoff, Phys. Rev. B, 48 (1993) 17533.
(f) P.D. Johnson, Y. Liu, Z. Xu and D.J. Huang, J. Electron Spectrosc. Relat. Phenom., 75 (1995) 245.
[37] F. Zhang, S. Thevuthasan, R.T. Schalettar, R.R.P. Singh and C.S. Fadley, Phys. Rev. B, 51 (1995) 12468.
[38] (a) U. Fano, Phys. Rev., 178 (1969) 131.
(b) U. Heinzmann, J. Kessler and J. Lorenz, Phys. Rev. Lett., 25 (1970) 1325.
[39] K. Starke, A.P. Kaduwela, Y. Liu, P.D. Johnson, M.A. Van Hove, C.S. Fadley, V. Chakarian, E.E. Chaban, G. Meigs and C.T. Chen, to be published.
[40] J.G. Tobin, C.D. Waddill, D.P. Pappas, E. Tamura and P. Sterne, J. Vac. Sci. Technol. A, 14 (1995) 1574.
[41] N.A. Cherepkov, Phys. Lett. A, 40 (1972) 119; Adv. At. Mol. Phys., 19 (1983) 395.
[42] (a) E.M.E. Timmermans, G.T. Trammell and J.P. Hannon, Appl. Phys., 73 (1993) 6183; Phys. Rev. Lett., 72 (1994) 832.
(b) A.P. Kaduwela, Z. Wang, M.A. Van Hove and C.S. Fadley, Phys. Rev. B, 50 (1994) 9656; to be published.
(c) Z. Wang and A.P. Kaduwela, to be published.

(5)

Pergamon

Progress in Surface Science, Vol. 54, No. 3/4, pp. 341–386, 1997

0079-6816/97 $32.00

PII: S0079-6816(97)00013-0

DIFFRACTION AND HOLOGRAPHY WITH PHOTOELECTRONS AND FLUORESCENT X-RAYS

C. S. FADLEY[#*]

With:

Y. Chen[*], R.E. Couch[#], H. Daimon[‡], R. Denecke[#*], J.D. Denlinger[/], H. Galloway[*@], Z. Hussain[†], A.P. Kaduwela[#*], Y.J. Kim[*&], P.M. Len[#*], J. Liesegang[£], J. Menchero[@*], J. Morais[#], J. Palomares[#*], S.D. Ruebush[#*], E. Rotenberg[+], M. B. Salmeron[*], R. Scalettar[#], W. Schattke[§], R. Singh[#], S. Thevuthasan[#], E.D. Tober[#*], M.A. Van Hove[*], Z. Wang[#*], and R.X. Ynzunza[#*]

[#]Department of Physics, University of California-Davis, Davis, CA 95616

[*]Materials Sciences Division, Lawrence Berkeley National Laboratory, Berkeley, CA 94720

[†]Advanced Light Source, Lawrence Berkeley National Laboratory, Berkeley CA 94720

[@]Department of Physics, University of California-Berkeley, Berkeley, CA 94720

[&]Department of Chemistry, University of Hawaii, Honolulu, Hawaii 96822

[‡]Dept. of Materials Physics, Osaka University, Toyonaka, Osaka 560, Japan

[/]University of Wisconsin-Milwaukee, Milwaukee, WI 53201

[+]University of Oregon, Eugene, OR 97403

[§]Institut für Theoretische Physik, Universität Kiel, D-24118 Kiel, Germany

[£]Dept. of Physics, Latrobe University, Bundoora 3083, Victoria, Australia

Abstract

We consider studies of the atomic and magnetic structure near surfaces by photoelectron diffraction and by the holographic inversion of both photoelectron diffraction data and diffraction data involving the emission of fluorescent x-rays. The current status of photoelectron diffraction studies of surfaces, interfaces, and other nanostructures is first briefly reviewed, and then several recent developments and proposals for future areas of application are discussed. The application of full-solid-angle diffraction data, together with simultaneous characterization by low energy electron diffraction and scanning tunneling microscopy, to the epitaxial growth of oxides and metals is considered. Several new avenues that are being opened up by third-generation synchrotron radiation sources are also discussed. These include site-resolved photoelectron diffraction from surface and interface atoms, the possibility of time-resolved measurements of surface reactions with chemical-state resolution, and circular dichroism in photoelectron angular distributions from both non-magnetic and magnetic systems. The addition of spin to the photoelectron diffraction measurement is also considered as a method for studying short-range magnetic order, including the measurement of surface magnetic phase transitions. This spin sensitivity can be achieved through either core-level

multiplet splittings or circular-polarized excitation of spin-orbit-split levels. The direct imaging of short-range atomic structure by both photoelectron holography and two distinct types of x-ray holography involving fluorescent emission is also discussed. Both photoelectron and x-ray holography have demonstrated the ability to directly determine at least approximate atomic structures in three dimensions. Photoelectron holography with spin resolution may make it possible also to study short-range magnetic order in a holographic fashion. Although much more recent in its first experimental demonstrations, x-ray fluorescence holography should permit deriving more accurate atomic images for a variety of materials, including both surface and bulk regions.

Acronyms

ALS	Advanced Light Source
CDAD	Circular dichroism in photoelectron angular distributions
FWHM	Full width at half-maximum intensity
LCP	Left circularly-polarized radiation
LEED	Low energy electron diffraction
LP	Linearly-polarized radiation
MCD	Magnetic circular dichroism
MCDAD	Magnetic circular dichroism in photoelectron angular distributions
MEXH	Multi-energy x-ray holography
ML	Monolayer
MLD	Magnetic linear dichroism
MS	Multiple scattering
MSC	Multiple scattering cluster
MUD	Magnetic unpolarized dichroism
PD	Photoelectron diffraction
PH	Photoelectron holography
RCP	Right circularly-polarized radiation
SR	Synchrotron radiation
SPPD	Spin-polarized photoelectron diffraction
SS	Single scattering
SSC	Single scattering cluster
STM	Scanning tunneling microscopy
UP	Unpolarized radiation
XFH	X-ray fluorescence holography
XH	X-ray holography using fluorescence emission (2 types)
XPD	X-ray photoelectron diffraction
XPS	X-ray photoelectron spectroscopy
XRD	X-ray diffraction

1. Introduction

A. Photoelectron Diffraction and Holography

The basic process involved in photoelectron diffraction (PD) is illustrated in Fig. 1. A photon excites an electron from a core level that is necessarily well localized in space, and the outgoing approximately-spherical photoelectron wave is scattered from the atoms neighboring the emitter, producing an interference pattern. It is the interference of the unscattered component ϕ_0 with the scattered components ϕ_j, (where j = 1, 2, 3, ...and is summed over an atomic cluster of sufficiently large size to be convergent) that produces the final diffraction pattern. Some of the key physical parameters controlling this process are indicated in the figure. These parameters are: $\vec{\epsilon}$ = the light polarization which influences the initial photoelectron excitation matrix element, $\vec{q}$ = the photon wave vector, $\vec{k}$ = the electron wave vector directly related to the momentum $\vec{p} = \hbar\vec{k}$ and the electron de Broglie wavelength $\lambda_e = 2\pi/|\vec{k}|$, $f_j(\theta_j)$ = the electron-atom scattering factor for a given scattering angle θ_j (describable in first order via plane-wave scattering but more accurately via spherical-wave scattering), Λ_e = the attenuation length controlling the exponential damping of the elastic photoelectron signal due to inelastic scattering, $\overline{U_j^2}$ = the mean-squared atomic vibrational amplitude involved in the damping of the diffraction pattern due to vibrational effects (as included most simply in a Debye-Waller factor), V_0 = the inner potential which produces refraction of the photoelectron in crossing this surface potential barrier, and Ω_0 = the effective analyzer acceptance solid over which the diffraction pattern is averaged in the actual experiment. All of these aspects will be included in the theoretical calculations presented here.

Beginning with the first experiments of this type [1], strong modulations in intensity of as much as ±50% have been observed as a function of either the direction of electron emission or the energy of excitation, leading to what have been termed *scanned-angle* or *scanned-energy* measurements, respectively. The aim of these measurements is to deduce information about the atomic structure around a given type of emitter, or perhaps also the type of magnetic order surrounding such an emitter. There are by now a number of groups in the world engaged in such experiments, using both laboratory x-ray sources and synchrotron radiation (SR), and a variety of systems have been studied to date with this technique, including adsorbed atoms and molecules, systems exhibiting surface and interface core-level shifts, epitaxial overlayers, surface structural and magnetic phase transitions, and atoms at buried interfaces. Several reviews of this field have appeared in recent years [2-7], and it will thus not be our aim to survey it in detail. Rather, we will begin by briefly describing those basic characteristics that make PD an attractive structural probe, consider some of its limitations and difficulties, and then go on to concentrate on several more recent developments involving both laboratory x-ray sources and next-generation SR sources that promise to make it an even more widely used tool for surface, interface, and nanostructure studies in the future.

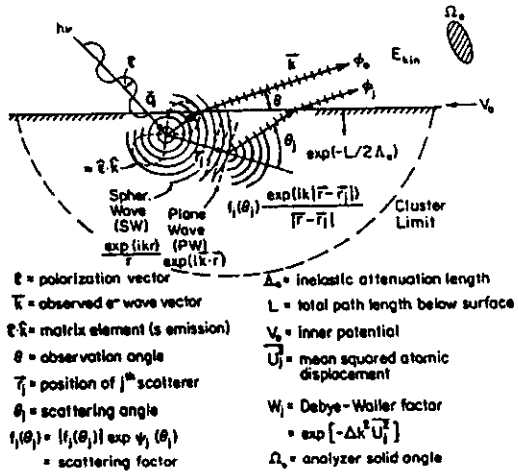

Fig. 1. Illustration of the basic photoelectron diffraction process, with various key physical quantities necessary for theoretically modeling such phenomena labelled and defined.

We begin with the positive aspects of PD, several of which will be illustrated with more specific examples in the following sections:

- *Atom specificity*: PD is an atom-specific probe by virtue of the fact that a certain core level is excited. Thus, the structure around each type of atom in the sample can be probed separately.
- *Chemical-state or site specificity*: With sufficient resolution, core binding energy shifts with chemical state (e.g., the different oxidation states of a given atom) or binding site (e.g, between the bulk and surface of a metal or semiconductor) can be used to study the atomic structure around each type of atom separately [8].
- *Spin-specificity:* Although not nearly as much explored, the diffraction patterns of photoelectrons of different spins can also be studied separately, yielding the promise of determining the local magnetic order around both magnetic atoms and non-magnetic atoms surrounded by magnetic atoms. Such spin sensitivity can be achieved by using the multiplet splitting inherent in the core spectra of various transition metals or rare-earth elements, by exciting spin-orbit-split core levels with circular-polarized radiation, or by some unavoidable combination of these two effects. This leads to what has been termed spin polarized photoelectron diffraction (SPPD). [9].

• *Variation of light polarization:* Beyond using circular polarization to produce spin polarization, varying polarization from linear (LP) to left or right circular (LCP or RCP, respectively) to unpolarized (UP) further permits selectively directing the outgoing photoelectron probe wave into different regions of the atomic structure surrounding the emitter, so that complementary structural information can be obtained for different relative orientations of light and sample [2,4].

• *Variation of excitation energy:* PD makes use of the ability to vary the excitation energy (and thus also the photoelectron kinetic energy) in several ways. At higher kinetic energies of ≥500 eV, the magnitude of the electron-atom scattering factor $|f_j(\theta_j)|$ is highly peaked in the forward direction, producing pronounced peaks in diffraction patterns along e.g. bond directions in adsorbed molecules and low-index directions in epitaxial layers [2,3,5]. For lower energies of ≤300 eV, the scattering factor for lower-Z atoms is more uniform over all directions, and often has a strong peak in the backward direction; thus, the locations of atoms behind the emitter as viewed from the detector can be fruitfully studied [2,4,6], although their bond directions cannot be as directly determined as in forward scattering. Being able to vary energy between these two limits using synchrotron radiation thus permits studying the full structural environment of a given emitter. Going to lower energies in the 50-100 eV range further leads to increased sensitivity to the surface, as this is where most materials possess a minimum in the inelastic attenuation length Λ_e for electrons.. Also, the 50-100 eV range is one in which magnetic scattering effects, particularly due to the exchange interaction are strongest; thus, such energies are those of relevance in SPPD measurements [9]. Being able to tune the photoelectron energy to maxima, minima, and/or resonances in the various photoelectric cross sections is a useful possibility in SR studies. And finally, the dependence of the photoelectron de Broglie wavelength on kinetic energy E_{kin}, which is given by $\lambda_e(\text{Å}) \approx \sqrt{150/E_{kin}(eV)}$, is of course also what leads to the modulations measured in scanned-energy photoelectron diffraction.

• *Simple first-order theoretical interpretation:* In a number of studies to date, it has proven possible to derive useful surface structural information by comparing experimental data to the results of rather straightforward single-scattering (SS or kinematical) theoretical calculations [2,3(a)]. However, it is also by now clear that a fully quantitative treatment of all of the features in both low-energy and high-energy diffraction patterns will require more sophisticated calculations at a fully-converged multiple scattering (MS) level [10]. These calculations have many similarities to those used in low energy electron diffraction (LEED) analyses . We will below illustrate both types of theoretical analysis.

• *Short-range order sensitivity:* The nature of the photoelectron emission process (into an outgoing spherical wave which decays as 1/r) and the inelastic scattering process (with very short attenuation lengths Λ_e in the ~5-20Å range) can be shown to make PD a probe of short-range atomic or magnetic structure, with primary sensitivity to the first 5 or so spheres of neighbors around a given emitting site, or within a sphere of maximum radius ~20 Å [2,4]. This can be of advantage in studying any sort of nanostructure which does not exhibit long-range order over a surface. LEED by comparison is generally used to probe longer-range order over perhaps 50-100 Å, although spot profile analysis is now being used to derive shorter-range information.

• *Direct derivation of structural parameters and photoelectron holography:* A final advantage is that there are at least three distinct ways in which it is possible to directly derive structural parameters from PD data with a minimum recourse to theoretical modeling. We have already noted that *forward scattering peaks* directly give bond or low-index directions [2,3,5]. Beyond this, *Fourier transforms of scanned-energy PD data* yield path-length differences for different scatterers that can often be used to rule out some adsorbate geometries in a search for the true structure [2,4,6(b),11]. Finally, *holographic transforms of larger data sets* that involve varying both energy and angle over some volume in the momentum space or $\vec{k}$-space of the photoelectron can be used to directly derive atomic positions in three dimensions [12-21]. This was first suggested by Szöke [12(a)]. The process is illustrated in Fig. 2(b), in which the unscattered component ϕ_0 is now identified with the holographic reference wave and the scattered components $\phi_1, \phi_2, \phi_3, \ldots$ with the object or subject waves. Various attempts have been made to derive atomic structures by photoelectron holography (PH), including several methodologies for generating atomic images [12-21]. Comparisons of these methods and general criteria for optimizing the taking of such holographic data so as to minimize measuring times also have been presented recently [15(e)-(g)].

By contrast, some difficulties and limitations of PD are:

• *More complex instrumentation:* Relative to a standard laboratory x-ray photoelectron spectroscopy (XPS) system, a more precise, computer-driven sample manipulator is required. However, adequate manipulators are now available from various commercial sources. For the most versatile and powerful experiments with variable energy and/or variable polarization, access to a synchrotron radiation beamline is also necessary, although much can still be done with a standard laboratory XPS system.

• *Longer measuring times:* Measuring hundreds or perhaps even a few thousand separate core spectra to produce a single angle or energy scan or a more complex scan over both angle and energy that can be used in a holographic sense [12-21] can be very time consuming, and may take between hours and days with most present systems. However, state-of-the-art laboratory XPS systems and next-generation synchrotron radiation beamlines, coupled with appropriately high-throughput spectrometers and detectors, promise to reduce these times to the minutes to hours range. Such instrumentation should also permit a broader range of dynamical studies on surfaces. We discuss below one such experimental system at the Advanced Light Source in Berkeley, and some time-resolved surface kinetics measurements that have been performed with it.

• *Macroscopic domain averaging:* As presently carried out, PD data is taken from the full area illuminated by the radiation, which is typically of the order of 1 mm^2 to 10 mm^2. Thus, many atomic domains are averaged over, and structural conclusions can be confused by the resulting overlap of diffraction patterns from different site types. Various kinds of photoelectron *microscopy* are currently being tested at different synchrotron radiation sources around the world, as reviewed recently elsewhere by Tonner et al. [22]. These developments may ultimately permit doing PD on

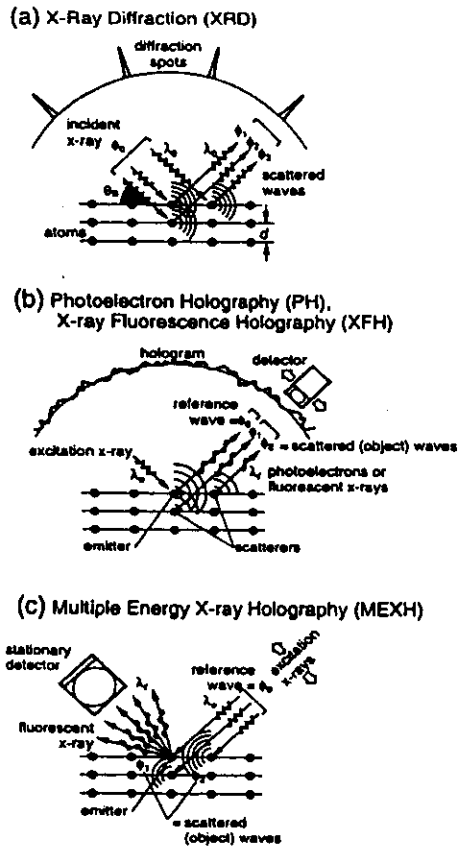

Fig. 2. Schematic illustration of some methods for determining atomic structure. (a) Conventional x-ray diffraction from a crystal, in which the incident wavefront ϕ_0 does not usually contribute to the diffracted intensity spots . (b) Localized-source holography in which a certain atom emits either a core photoelectron, yielding photoelectron holography (PH) or a core-derived fluorescent x-ray, yielding x-ray fluorescence holography (XFH). (c) A second type of x-ray holography in which the incident x-ray scatters from near-nrighbor atoms to create an interference at a certain emitter of fluorescent x-rays. This is the time-reversed version of XFH in (b).

areas as small as a few hundred Å in radius, thus focussing on a single domain or nanostructure on the surface. This last prospect is to be sure a *tour de force* experiment for third-generation (or even fourth-generation) synchrotron radiation sources, but realizing it would be exciting indeed, as two further spatial dimensions could then be accessed in the experiment.

• *More complex multiple-scattering theoretical interpretation:* We have already noted above that data can often be analyzed in a useful way within a single-scattering framework, but future studies will no doubt make more use of the more quantitative multiple-scattering model. However, a number of groups by now have multiple scattering programs operating [10], and these will no doubt become faster, more accurate, and more user friendly, as they have in the LEED community. We illustrate the need for this more accurate modeling in specific cases discussed below.

In what follows, we will present a few recent examples of PD data and its theoretical interpretation, and also consider the development of next-generation instrumentation for such measurements These examples are chosen primarily from the work of our group, but we believe that they are illustrative of both some current forefronts of PD studies and some of the more exciting future directions in this field.

B. X-Ray Fluorescence Holography

We will also consider a much more newly developed technique for directly determining short-range atomic structures, but one which is a very close relative of photoelectron holography (PH): x-ray holography (XH) [23,24]. In PH, the photoelectric effect creates an outgoing photoelectron wave from a given atomic center. As noted previously, the unscattered component of this wave is treated as a reference wave which interferes with the scattered components, with the latter being treated as the object or subject waves in a standard holographic exposure (cf. Fig. 2(b)). In the first method of doing XH, the deexcitation of a core hole in a given atom creates an outgoing fluorescent x-ray, with the unscattered and scattered components of this wave again serving as reference and subject in a holographic exposure. This also is shown in Fig. 2(b), and it has been termed x-ray flourescence holography (XFH). A second XH method called multi-energy x-ray holography (MEXH) and illustrated in Fig. 2(c) is in a sense the time-reversed version of XFH and will be introduced in more detail later.

Because x-rays scatter much more ideally from atoms than electrons (i.e., much more weakly and isotropically, and with negligible scattering phase shifts ψ_j), one expects either way of doing XH to yield more accurate holographic images than those from PH. However, the intensity modulations in an x-ray hologram are also expected to be much weaker (by a factor of $\sim 10^{-3}$-10^{-4}), so that such experiments will be inherently more difficult to perform. The much greater penetration depths of x-rays in matter also means that XH can be used to probe nanostructures quite far below a surface, with surface or interface specific studies being possible only if a certain atomic type is present only in the near-surface region to be studied. XH thus shares some of the advantages of PD/PH : atom specificity, variation of exciting light polarization, an even simpler kinematical theoretical interpretation, short-range order sensitivity, and direct derivation of three-dimensional atomic

structures. And it also shares some of the disadvantages: complex instrumentation, even longer measuring times, and macroscopic domain averaging. Nonetheless, the exciting promise of XH as a complement to the well-developed x-ray diffraction (XRD) methods for studies of atomic structure (cf. Fig. 2(a)) has led to a few pioneering measurements of this type [24] that we will briefly overview below.

2. Full-Solid-Angle XPD in Combination with LEED and STM

Although the first full-solid-angle photoelectron diffraction pattern was measured some time ago [25(a)], it is only in recent years that these time-consuming experiments have been performed on a more routine basis, beginning particularly in the Osterwalder group [7, 25(b),(c)]. We here illustrate the utility of this kind of data in two recent studies of epitaxial growth: iron oxide on Pt(111) [26] and Cu on Ru(0001) [27]. In the iron oxide work, another noteworthy element was added in that x-ray photoelectron diffraction (XPD) measurements in a laboratory-based system were combined with in situ characterization by both LEED and scanning tunneling microscopy (STM), such that the complementary nature of these surface structure probes could be exploited [26(b)].

Some data for a 1 monolayer (ML) overlayer of FeO on Pt(111) obtained by Kim et al. [26(b)] are shown in Fig. 3, where a LEED pattern, STM image, and full-solid-angle XPD patterns from all three atoms present (Pt, Fe, and O), as excited by Al Kα radiation at 1,487 eV, are compared for the same surface preparation. The LEED pattern in Fig. 3(a) shows the basic Pt(111) spots, but with a rosette of superstructure spots around each one indicative of some longer range order. This longer range order can in turn be directly imaged by STM [26(a)] as shown in Fig. 3(b), and it consists of a hexagonal unit cell of approximately 26 Å x26 Å superimposed on the atomic-resolution hexagonal oxide unit cell of 3.1 Å x 3.1 Å. Such combined LEED and STM data led Galloway et al. [26(a)] to first propose a particular superstructure or lateral Moiré pattern consisting of a hexagonal-symmetry bilayer of FeO(111) type and composed of a layer of Fe atoms on top of (or perhaps below) a layer of O atoms. But this model left several questions about this overlayer unanswered. Among these questions were: Which atomic layer is outermost, Fe or O? What is the interplanar distance between Fe and O? Is there a preferred relative orientation of the FeO bilayer in its growth with respect to the underlying Pt?

The XPD results in Fig. 3(c) serve to answer all three of these questions. The Pt 4f diffraction pattern is dominated by scattering in the substrate crystal, and so does not contain any easily-derivable information concerning the structure of the overlayer. It does however provide a direct internal reference in the data for the orientation of the overlayer, with the [11$\bar{2}$] direction lying in the Pt(111) surface indicated on the figure. The Fe 2p XPD pattern contains three strong peaks with some fine structure around them, immediately indicating that there are forward scattering atoms between Fe and the detector. Thus, O is immediately suggested to be in the outermost layer and responsible for this forward scattering. Finally, the O 1s pattern is devoid of any significant

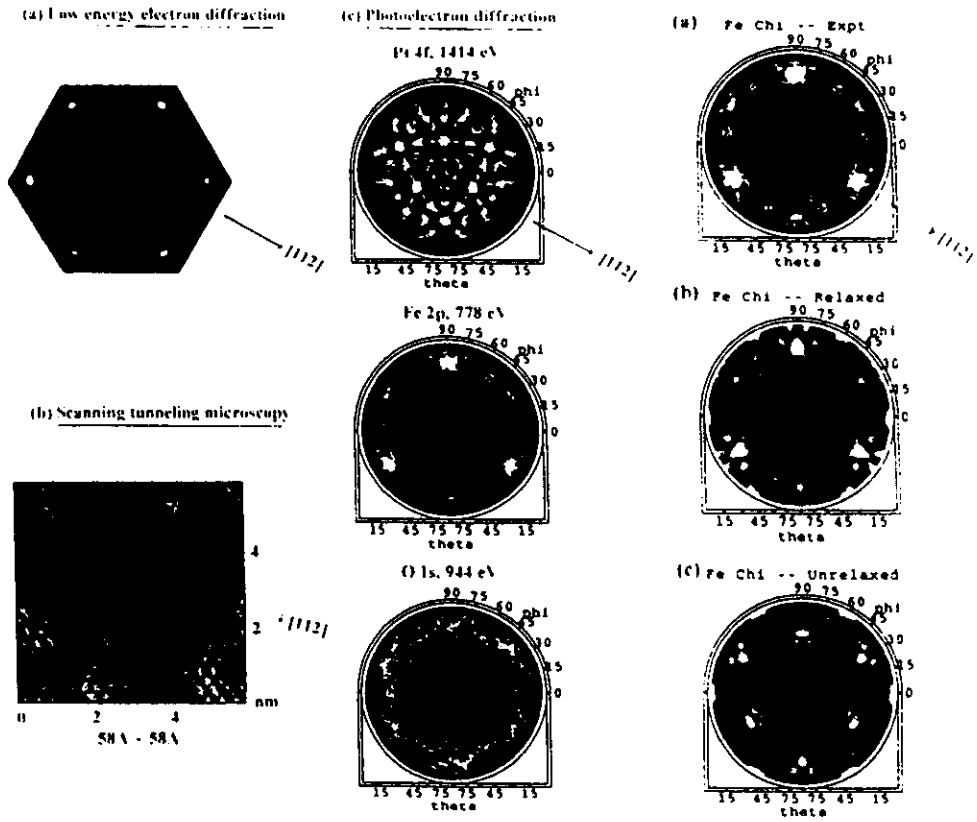

Fig. 3. (Upper left) (a) LEED, (b) STM, and (c) full-solid-angle XPD data for 1 monolayer (ML) of FeO on Pt(111). The XPD patterns for Pt 4f, Fe 2p, and O 1s emission are shown in stereographic projection. [From ref. 26(b).]

Fig. 4. (Upper right) Full-solid-angle Fe 2p XPD pattern for 1 ML of FeO on Pt(111): (a) experimental data, (b) single scattering theory with a best-fit Fe-O interplanar distance of 0.68 Å, (c) single-scattering theory with an Fe-O interplanar distance of 1.25 Å as in bulk FeO. [From ref. 26(b).]

diffraction features, further confirming that it is the outermost layer. The second question as to interlayer spacing is also easily answered by measuring the polar angle of 20° (measured with respect to the surface) at which the Fe-O forward scattering peaks occur, and combining this with the lateral unit-cell dimensions of the FeO overlayer as derived from LEED and/or STM. Simple trigonometry then yields an interplanar distance of only 0.65 Å that is much contracted from the 1.25 Å between (111) planes in bulk FeO. This distance can be further checked by carrying out single-scattering diffraction calculations for this overlayer, with single-scattering being an excellent approximation for this situation in which there are no chains of forward scattering atoms [2]. Comparing such calculations with experiment via R-factors developed specifically for the analysis of PD data [26(c)] [(as done also in quantitative LEED structural analyses) finally yields the most accurate interplanar distance of 0.68 Å that is very close to the simple estimate based on the forward scattering direction. Theoretical calculations for both 0.68 Å and 1.25 Å interplanar spacings are compared to experiment in Fig. 4. The agreement between experiment and the calculation for 0.68 Å is excellent, including even the weak diffraction features around the forward scattering peaks. For a 1.25 Å spacing, agreement is poor, both as to the polar angle position of the forward scattering peaks and the weaker features. Finally, the fact that there are only three forward scattering peaks in the Fe diffraction pattern immediately implies that only one orientation of the hexagonal O overlayer with respect to the underlying Pt surface exists, even though two O overlayer orientations rotated by 180° with respect to one another are equally likely as far as the Fe layer is concerned. Thus, there is an O-Pt interaction through the Fe layer that is strong enough to select only one orientation of the O overlayer; in fact, this interaction must involve second-layer Pt atoms. Thus, XPD can be used to determine a final subtle aspect of the growth process that would be difficult to arrive at with other methods.

Thus, this is an illustrative example of both how useful full-solid-angle diffraction patterns can be (see also refs. 7 and 25 for other examples, including a very recent application to C_{60} in ref. 25(c)) and how important it is to have additional complementary structural probes in the same experimental chamber, with LEED and STM being two particularly useful ones.

A second example of epitaxy recently studied using data from these combined techniques is Cu/Ru(0001), a system that at one level exhibits classic Stranski-Krastanov growth, but which on closer examination with STM by Günther et al. [27(a)] shows four stages of growth from a pseudomorphic first layer through various types of lateral contraction until finally reaching Cu(111)-like islands with essentially the bulk Cu structure. Subsequent theoretical analysis of these results by Hamilton and Foiles have successfully predicted these stages of growth as well [27(b)]. Ruebush, Couch et al. [27(c)] have now measured full-solid-angle XPD from both Cu and Ru for this system, and analyzed these results together with the STM results obtained by Günther et al. [27(a)]. Some of their experimental data for 1, 2, 3 and 4 ML Cu coverages are shown in Fig. 5 together with theoretical calculations based upon both multiple-scattering cluster (MSC) [10(e)] and single-scattering cluster (SSC) [10(c)] methods. In general, MSC theory better describes these data, for example, as to the sharpness of the two sets of sixfold rings seen for 1 ML, and the relative

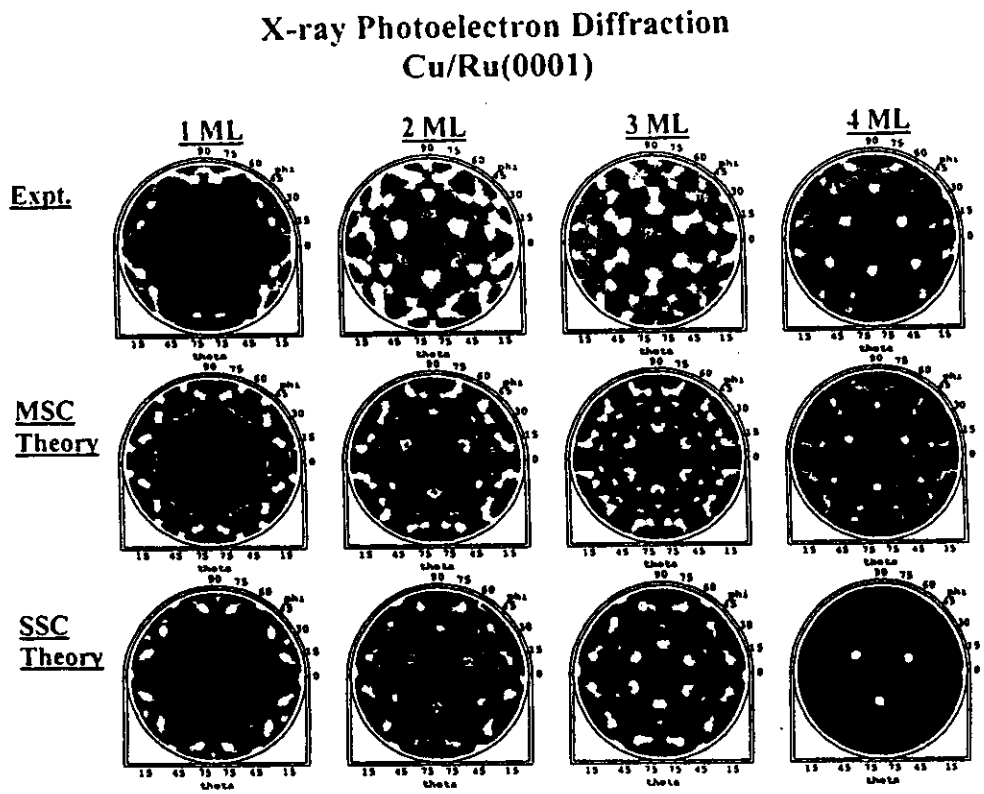

Fig. 5. X-ray photoelectron diffraction from the Cu $2p_{3/2}$ level of Cu on Ru(0001), for coverages of Cu from 1 to 4 ML. The kinetic energy is 556 eV. Also shown are the results of multiple scattering cluster (MSC) and single scattering cluster (SSC) calculations in which the interplanar spacings have first been varied to achieve best agreement with experiment. [From ref. 27(c).]

intensities of the most intense forward scattering peaks for 4 ML (which are too strong along these low-index directions in SSC). However, as noted before [2], SSC theory nonetheless predicts most of the major features away from such low-index directions. Comparing these XPD data with theory via PD-specific R-factors [26(c)] has furthermore permitted determining the average interlayer spacing of the Cu overlayers as a function of overlayer thickness, with the interesting result that significant contraction is found to persist even up to 5-8 ML coverages. A simple theoretical picture based on the Frenkel-Kontorova model [27(c)] on the other hand predicts a much quicker convergence to the bulk interlayer spacing than is seen in experiment. Accurately knowing such interlayer spacings is clearly important for an understanding of both the chemical reactivity and magnetic properties of such epitaxial metal overlayers, and full-solid-angle XPD can play a very useful role in such studies.

3. Photoelectron Diffraction Studies with Third Generation Synchrotron Radiation

There are at present several "third-generation" synchrotron radiation facilities either already operating or under construction, and these sources of very bright vacuum ultraviolet and soft x-ray radiation in roughly the 30-2000 eV range will permit a number of exciting new directions to be explored in both photoelectron diffraction and photoelectron holography. We illustrate some of these possibilities with data obtained at the Advanced Light Source (ALS) in Berkeley, using a new high-resolution spectrometer/diffractometer that has recently been built for use there.

A. Next-Generation Photoelectron Spectrometer/Diffractometer

In Fig. 6, we show a schematic view of a photoelectron spectrometer that has been configured for high-resolution, high-intensity photoelectron spectroscopy, diffraction, and holography measurements, and initially installed on bending magnet beamline 9.3.2 at the Advanced Light Source in Berkeley [2(f)]. Figure 7 shows a photograph of the system, with major components labelled. The electron energy analyzer is a tuneable-resolution large-diameter hemispherical electrostatic system (Scienta ES200) that has been incorporated into a chamber which can rotate over 60° in the plane of the electron storage ring. This rotation is made possible by a large-diameter bellows linking the chamber to the beamline, as shown in these figures. Such in-plane analyzer rotation, although common for much smaller analyzers mounted inside the vacuum system, has not been attempted before in such an *ex situ* mounting, and it permits probing the angular dependence of the fundamental photoelectron excitation cross section, keeping the photon-sample geometry fixed while measuring intensities over a large fraction of the 2π solid angle above the surface, and keeping the photoelectron-sample geometry fixed by scanning the analyzer synchronously with the sample polar-angle motion while measuring intensities as a function of light incidence direction. This analyzer is presently equipped with a single multichannel detector capable of an integrated count rate of about 500 kHz, but it will in the near future be modified so as to

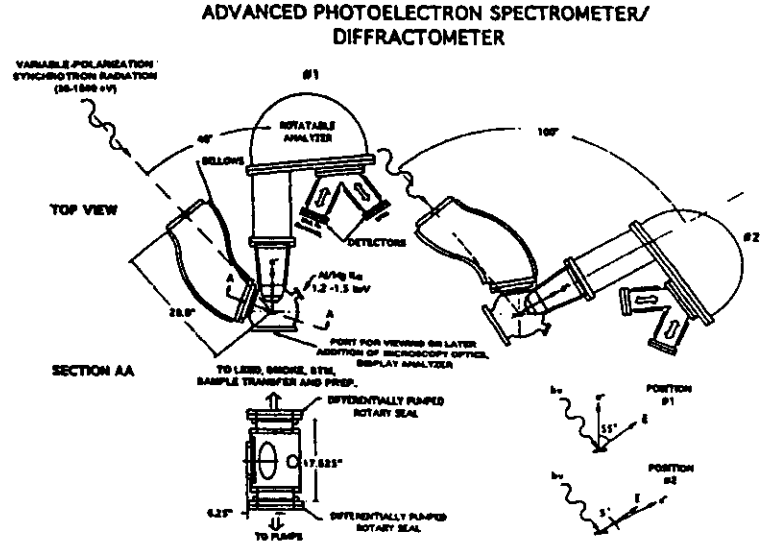

Fig. 6. Schematic drawing of the advanced photoelectron spectrometer/diffractometer (APSD) presently situated on beamline 9.3.2 of the Advanced Light Source. The rotation of the main chamber, including electron analyzer, and the range of photon-electron geometries possible are also indicated.

include a much higher speed multichannel detector operating up to the GHz range, as well as an alternative spin detector of the so-called microMott type that will be interchangeable *in situ*. The spherical grating monochromator in this beamline, together with the Scienta analyzer , are capable of operating at overall kinetic energy resolutions of $\Delta E/E_{kin} \approx 1:10^4$. The analyzer is also equipped with a demountable collimator at its entry to limit both the solid angle of acceptance to ~±1.5° for high angular resolution studies and the area of the sample surface seen by the analyzer. The 9.3.2 beamline optics also permit taking radiation both above and below the plane of the electron orbit, thus obtaining a high degree of left or right circular polarization, as well as linear polarization with in-plane operation. We discuss below the use of this capability in measuring circular dichroism effects in photoelectron angular distributions (CDAD). We now briefly consider some first results obtained with this instrumentation.

B. Full-Solid-Angle Photoelectron Diffraction from Clean-Surface and Bulk Atoms

In Fig. 8(a), we show the geometry for an experiment in which the surface and bulk W 4f peaks from a clean W(110) surface have been measured with this system. It is well-known that the clean (110) surface exhibits a surface component shifted to lower binding energy by 320 meV

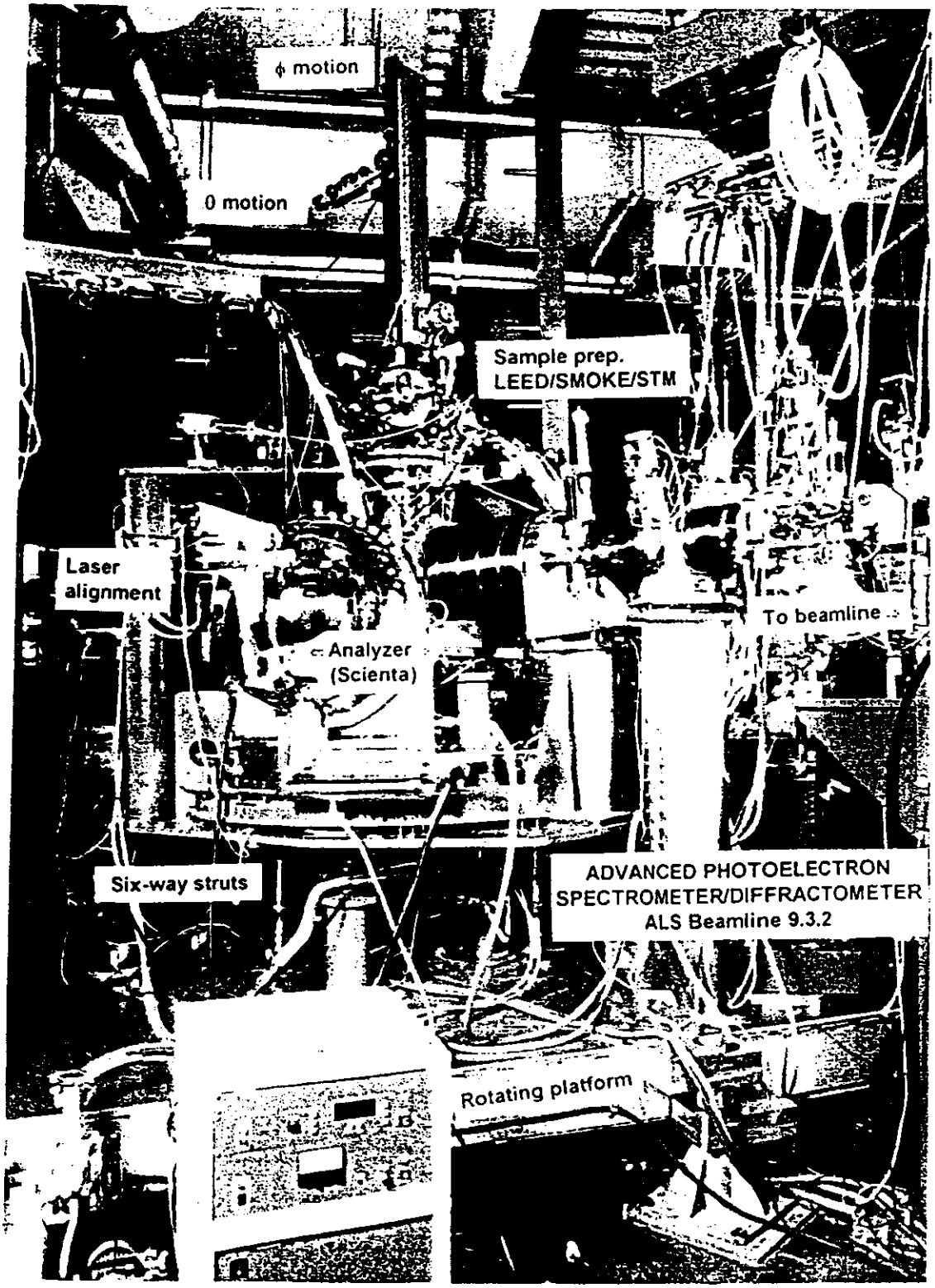

Fig. 7. Photograph of the APSD system in Fig. 6.

[8(a),28], and this is cleanly resolved in the spectrum of Fig. 8(b). The 120 meV full width at half maximum (FWHM) for the bulk peak is slightly narrower than anything measured before [28(a)], and is essentially limited by the various sources of natural linewidth for this level. PD has been measured before for this case [28(b)], but these studies involved only a few scans in azimuthal angle or in energy. The high rate of data acquisition possible with this new system (a spectrum like that in Fig. 8(b) can be obtained in 20 sec or less) has now permitted measuring essentially the full solid angle of data for both the bulk and surface peaks, as shown in Figs. 9(a) and 9(b), respectively [29]. The photoelectron energies here are also in the very surface sensitive 39-40 eV range. Thus, it will be possible in the future to obtain much more complete site-specific photoelectron diffraction information, and we discuss the application of this to holography below.

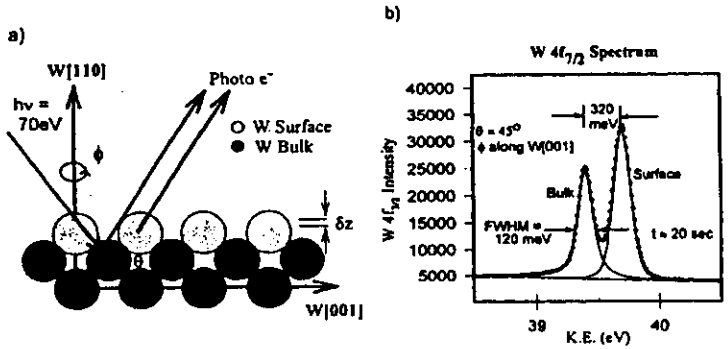

Fig. 8. (a) Experimental geometry used to study clean W(110), showing the two types of W atom sites resolved. (b) High-resolution W $4f_{7/2}$ spectrum from W(110), showing surface and bulk components. [From ref. 29.]

One immediate benefit of such data sets is the possibility of making more rigorous tests of the multiple scattering theory that is now being used by several groups to analyze PD data [10]. In particular, multiple-scattering and single-scattering calculations have been carried out to simulate these diffraction patterns [29], using programs developed by Kaduwela et al. [10(e)] and by Chen et al. [10(g)] and based on the convenient Rehr-Albers approximation for treating multiple scattering [10(d)]. These calculations have been carried out for a range of interlayer spacings z between the surface W layer and the second layer below, with PD-specific R-factors [26(c)] once more being used to determine the best estimate of the structure. Experiment and theory for the optimized

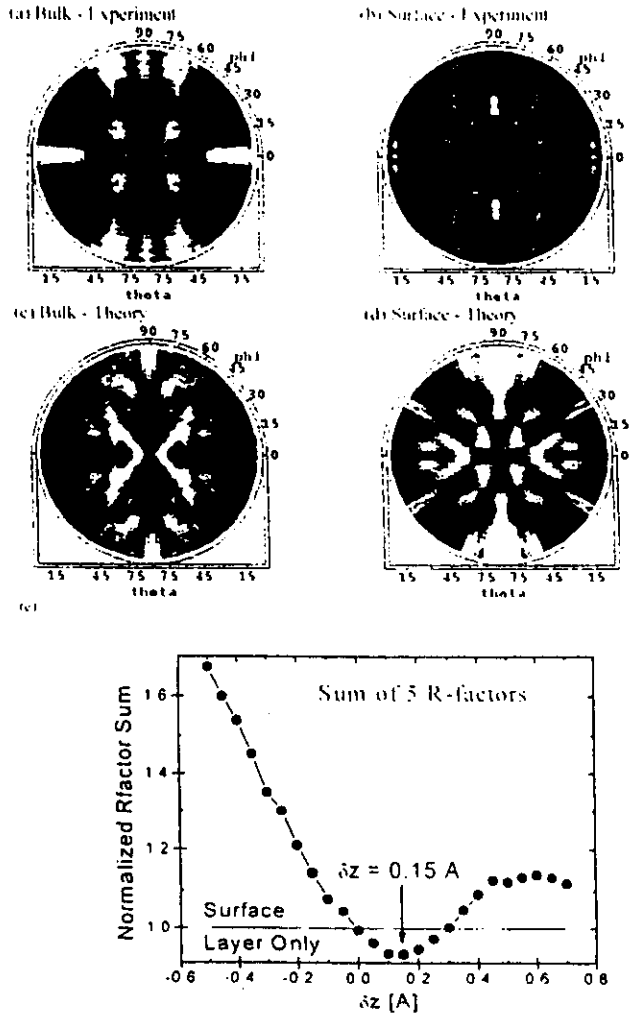

Fig. 9. Full-solid-angle W $4f_{7/2}$ photoelectron diffraction patterns (a) bulk-resolved experiment, (b) surface-resolved experiment, (c) bulk theory for the optimum interlayer distance, (d) surface theory for the optimum interlayer distance; and (e) R-factor comparison between experiment and multiple-scattering theory for the surface-atom W $4f_{7/2}$ photoelectron diffraction pattern of Fig. 9(b). The curve represents a normalized sum of five R-factors. The horizontal line corresponds to an R-factor for calculations in which no bulk scatterers were present [From ref. 29.]

distance are compared in Figs. 9(a)-(d), and the resultant R-factor curve from the more sensitive analysis of the surface-atom data is shown in Fig. 9(e). There is excellent agreement between experiment and theory for most of the features in the surface-atom diffraction pattern and very good agreement for the more complex bulk case, which involves emitters in various layers below the surface. The overall conclusion based on the surface diffraction pattern is that the surface W layer relaxes outward from the bulk position by 0.10-0.15±0.05 Å, corresponding to a very small change of 4.4-6.7% of the bulk interlayer spacing. These results furthermore agree in general with prior studies of this surface by PD and LEED [28(b) and refs. therein]. Corresponding SSC calculations based on the same input parameters show similar diffraction features, but are not found to describe the data as well as the MSC results shown in Fig. 9. Thus, MS effects will definitely need to be included for a quantitative description of such low-energy data.

C. Photoelectron Diffraction from Interface Atoms

The detailed structure of interfaces, e.g. between an epitaxial overlayer and the substrate on which it is grown, is clearly one of the most important current surface-structure problems. It is also a difficult problem to solve, because most surface structure probes either cannot uniquely resolve interface atoms from their neighbors or cannot probe very deeply below the surface. PD with high energy resolution has been shown capable of studying interface atoms that are at least a few atomic layers below the surface in studies by Olmstead and co-workers of insulator growth on a semiconductor [8(d)], and future experimental capabilities promise to expand this application dramatically.

As one illustration of what is now possible, we show in Fig. 10 photoelectron spectra obtained with the same experimental system at the ALS for the case of ~1 ML of Fe and ~1 ML of Gd deposited on W(110) [30]. The first monolayer of Fe is known to grow in a (1x1) structure on W(110), with presumably a single unique bonding site for every Fe atom [31]. On the other hand, it has been shown by Tober et al [32] in a combined STM and LEED study that the first monolayer of Gd forms a lateral superstructure or Moiré pattern with (7x14) periodicity in which a hexagonal Gd(0001) layer is formed on the surface with relatively little lattice constant change relative to bulk Gd. However, this layer appears to be only weakly bound to the underlying W, and many types of Gd/W bonding sites are involved over the (7x14) unit cell. Fig. 10 compares W $4f_{7/2}$ photoelectron spectra from the clean surface in (a) with those from Fe/W in (b) and Gd/W in (c). The W atoms at the Fe/W and Gd/W interfaces are clearly resolved from those in the bulk. For Fe/W, the second-layer W atoms are even displaced from the bulk due to their strong interaction with the Fe, as noted previously by Shinn et al. [31]. Thus, it has been possible to measure separate PD patterns for the bulk and interface W atoms in these systems, and for Fe/W also for the second-layer W atoms, and to use these data to directly probe the metal-metal interface structure [30]. Some of these results for Fe/W are shown in Fig. 11. Because there are many scattering geometries between either an interface W atom or a bulk W atom and the overlying Gd atoms, we find that the interface Gd/W diffraction patterns are very much like the clean-surface diffraction patterns, and that the two bulk

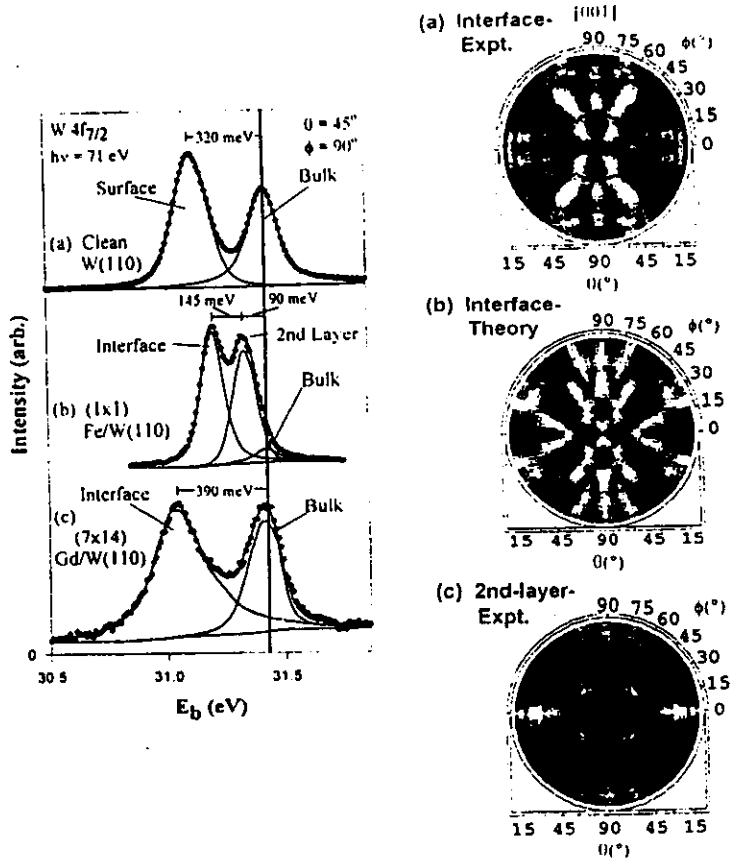

Fig. 10. (Upper left) W $4f_{7/2}$ photoelectron spectra taken with a photon energy of 71 eV from (a) the clean W(110) surface, (b) 1 ML of Fe in a (1x1) overlayer on W(110), and (c) 1 ML of Gd in a (7x14) Moiré superstructure on W(110). [From ref. 30.]

Fig. 11. (Upper right) Full-solid-angle W $4f_{7/2}$ photoelectron diffraction patterns for the (1x1) Fe/W(110) system taken from (a) experimental data for the -235 meV-shifted W interface peak, (b) theoretical multiple scattering calculations for the (1x1) Fe/W(110) interface with an optimized two-fold bridge adsorption site for Fe, and (c) experimental data for the -90 meV-shifted W 2nd-layer peak. The photoelectron kinetic energy outside the surface was E_{kin} = ~40 eV in all cases. The data shown span takeoff angles relative to the surface from 12° to 90°(normal emission), and the W(100) azimuth is toward the top of the page in each of these stereographic projections. [From ref. 30.]

patterns are also very similar [30] Thus, The Gd scattering here overall acts to simply produce a nearly uniform background of intensity underneath the dominant pattern associated with W-atom scattering. But for the Fe/Gd case, the interface-atom diffraction is much different from the clean surface diffraction (compare Fig. 11(a) with Fig. 9(b)) . Therefore, for this case, comparisons of experiment with theory for different Fe bonding geometries via R-factors [26(c)] has permitted determining the bonding site (a twofold bridge site which corresponds to continuing the W crystal) and the Fe-W interlayer distance (2.17 Å) for the first time. Future applications of high-resolution interface PD to metal-metal, metal-semiconductor, and oxide semiconductor overlayer growth are therefore very promising.

D. Time-Dependent Measurements

We now consider the possibility of time-resolved measurements of surface reaction kinetics and atomic structure. To illustrate this, Ynzunza et al. [29] studied an initially clean W(110) surface which was exposed to a constant O_2 pressure of 3×10^{-9} torr (riding on a base pressure in the system of 2×10^{-10} torr). The reaction of this surface with oxygen was monitored over 70 min. by taking many photoelectron spectra in rapid succession. We show in Figs. 12(a)-(c) three W $4f_{7/2}$ spectra that were taken at the beginning, middle, and end of this rapid accumulation of over 180 spectra. Each spectrum was obtained in 20 sec, and this provides some idea as to how rapidly it should be possible to accumulate PD data in parallel to such time-resolved spectra in the future. Four distinct states of W are seen in these spectra (as described below). The quantitative time evolution of these states is shown in Fig. 12(d), where intensities have been derived by fitting appropriate peak shapes to each spectrum of the series. The clean-surface peak decays to zero intensity over about the first 20 min. and comcomitant with this, the bulk peak actually grows in intensity over about the first 10 min. Simultaneously, a peak due to W atoms in interaction with chemisorbed oxygen begins to grow in at about 0.35 eV higher binding energy than the bulk peak, reaching its maximum intensity (corresponding to about 0.5 ML coverage) after about 30 min. Finally, a peak due to W atoms more strongly bound to oxygen in an incipient-oxide like state begins to grow in just as the chemisorbed species reaches its maximum intensity. This state can grow finally to a 1.0 ML coverage before saturating, although this is not reached during the time of our measurements. These data thus clearly indicate a strong interrelationship of these states via the kinetic mechanisms that are operative for this oxidation reaction, and further analysis of these results in this context is now underway. However, these data already illustrate the considerable potential for future studies of nanostructure growth kinetics in which intensities are measured at several key energies or directions as a function of time, thus yielding also time-resolved PD. With further optimization of the bend-magnet beamline and end station on which these data were obtained, and/or making the same type of measurement on a more intense third-generation undulator beamline, we estimate that it should be possible to improve these data acquisition speeds by at least one order of magnitude, and probably two, so that individual spectra could ultimately be obtained in ~0.1-1.0 seconds.

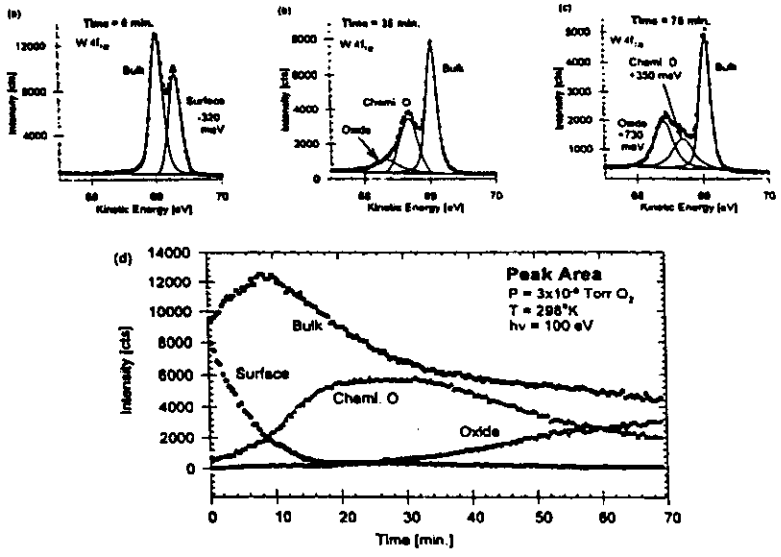

Fig. 12. Time- and state- resolved W $4f_{7/2}$ photoelectron spectra for a clean W(110) surface exposed to oxygen at 3×10^{-9} torr for 70 min.: (a) t = 0 min.--initial clean surface showing the surface core level shifted peak at -320 meV with respect to bulk; (b) t = 35 min--surface after 35 min., showing the two oxygen-induced peaks at -350 meV and -730 meV; (c) t = 70 min.--final spectrum of the series after 70 min, showing the increase of the oxide peak at the expense of the chemisorbed oxygen peak; (d) time dependence of the intensities of the four peaks observed in these spectra. [From ref. 29.]

E. Circular Dichroism in Photoelectron Diffraction

(i) Non-magnetic systems. Circular dichroism represents another aspect of photoelectron diffraction that can be explored with synchrotron radiation, and we here briefly discuss its essentials, with more detailed accounts appearing elsewhere [33-37]. Circular dichroism in photoelectron angular distributions (often termed CDAD) was first observed for emission from a core-level for the case of an adsorbed molecule on a surface (C 1s emission from CO/Pd(111)) by Schönhense and co-workers [33(b)]. Such dichroism is defined via the difference between the intensities with left and right circular-polarized light (I^{RCP} and I^{LCP}, respectively), and is most conveniently measured using

a normalized asymmetry : $A_{CDAD} = \left[I^{RCP}(\hat{k}) - I^{LCP}(\hat{k})\right] / \left[I^{RCP}(\hat{k}) + I^{LCP}(\hat{k})\right]$, where $\hat{k}$ is the direction of electron emission. Changes in this asymmetry with direction by as much as ±75% were observed for CO/Pd. These measurements thus made it clear that even a non-chiral molecule can exhibit circular dichroism when it is fixed to a surface, provided that a certain geometrical condition is satisfied between the molecular axis $\hat{n}$, the light incidence direction $\hat{q}$, and $\hat{k}$: in particular A_{CDAD} can be non-zero whenever these three vectors are not co-planar. Such data were first interpreted using quantum-chemical theoretical methods for the isolated adsorbate molecule [33(b),34(a)]. However, the chirality must be associated with the final-state photoelectron wave function, since the initial core state is spherically symmetric. This suggests using a photoelectron diffraction point of view to interpret such results, as has been done more recently [34(b)]. In this picture, all information on the chirality is carried in the geometry of the light incidence, the locations of all scatterers around the emitter, and the direction of electron emission. This approach thus permits easily including contributions to the dichroism from atoms in the substrate. PD calculations were in fact found to correctly predict the effects seen for CO/Pd(111) [34(b)].

More generally, it has now been realized that the emission from *any* core level in a single crystal specimen can exhibit non-zero CDAD effects, provided that the plane containing $\hat{q}$ and $\hat{k}$ does not also coincide with a plane of mirror symmetry perpendicular to the surface [35,36]. In particular, intensity distribution measurements for Si 2s and 2p emission from a Si(001) surface in a geometry with the light incident along the normal by Daimon et al. [35] have shown that there are not only very strong CDAD effects of as high as ~±20%, but that the observed diffraction patterns exhibit what can in first approximation be described as peak "rotations" across mirror planes perpendicular to the surface. Daimon et al. [35] have also discussed a simple physical model for understanding why individual features should appear to rotate one way in azimuth with one polarization and the other way with the other polarization. This model considers the transfer of the z-component of angular momentum from the radiation to the outgoing photoelectron wave, and its influence on forward scattering diffraction peaks. In addition, more quantitative multiple scattering PD calculations have been shown to well predict these alterations in diffraction patterns with a change in polarization [36].

More recent data obtained at the ALS by Daimon, Ynzunza et al. [37] confirm the generality of such peak rotations, but also more quantitatively show that additional peak distortions beyond a simple rotation can occur in changing from LCP to RCP. The case studied was a 1 ML coverage of oxygen on W(110) in the incipient oxide overlayer associated with the +730 meV peak in Fig. 12(c), and prepared in a manner described previously [38]. The experimental geometry was very similar to that of the Si(001) experiment [35], and is shown in Fig. 13(a). The W 4f spectra for this surface shown in Fig. 13(b) are clearly split into oxide and bulk components, with a separation between them of 0.73 eV. In the solid curves of Figs. 13(c),(d), we show single azimuthal scans of the oxide and bulk peaks for a takeoff angle θ with respect to the surface of 26.5°, and with excitation by linear-polarized (LP) light, as well as circular-polarized LCP and RCP light. With LP excitation, the

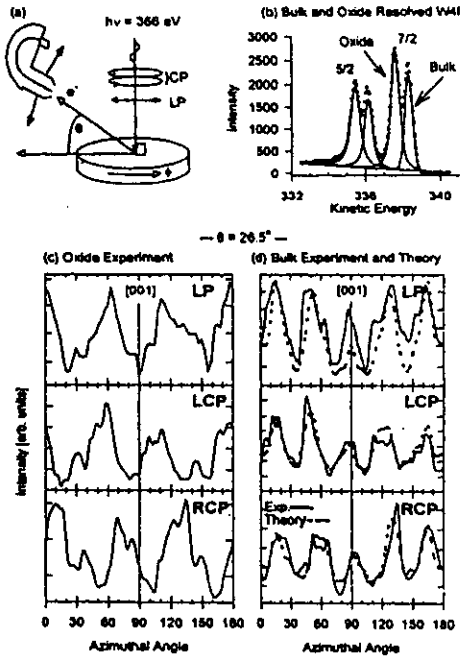

Fig. 13. Circular dichroism in the angular distributions of photoelectrons from (1x1)O/W(110) with a (1x12) incipient-oxide superstructure: (a) the experimental geometry, with radiation incident normal to the surface and the rotating analyzer of Figs. 6 and 7 being used to measure at various takeoff angles θ with respect to the surface; (b) a W 4f spectrum with oxide and bulk peaks resolved; (c),(d) azimuthal scans at a takeoff angle of 26.5° for both oxide and bulk W 4f components for linear-polarized (LP) light, left-circular-polarized (LCP) light, and right-circular-polarized (RCP) light (solid curves). In (d) is also a comparison of the experimental curve for bulk emission with theoretical photoelectron diffraction calculations (dashed curve). [From ref. 37.]

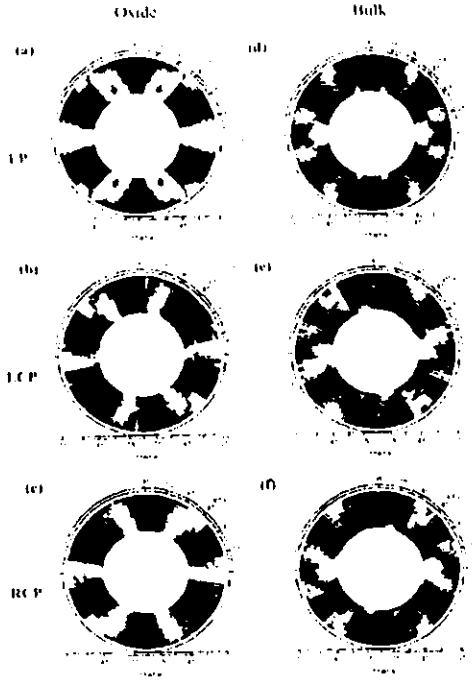

Fig. 14. Large-solid-angle photoelectron diffraction patterns for oxide [(a),(b),(c)] and bulk [(d),(e),(f)] W 4f emission from a (1x1)-(1x12) oxygen overlayer on W(110). Panels (a) and (d) are for LP excitation, (b) and (e) are for LCP excitation, and (c) and (f) are for RCP excitation. Note the apparent rotation of certain major features in the patterns between LCP and RCP, particularly for the oxide patterns. [From ref. 37.]

correct mirror symmetry across the [001] azimuth at ϕ = 90°is seen to within statistical uncertainty in both oxide and bulk. But with LCP and RCP excitation, differences which can be interpreted as peak "rotations", as well as other relative intensity changes and distortions, are found. The rotations appear as a general leftward movement of peaks and valleys with LCP, and a general rightward movement with RCP. The overall diffraction patterns furthermore obey the symmetry expected from the normal-incidence experimental geometry, as the mirror image of the LCP intensities across [001] for both oxide and bulk are within statistics identical to the RCP intensities. These symmetries and rotations are even more clearly seen in the large-solid-angle data sets in Fig. 14. In particular, an approximately ±5-6° rotation of the most prominent peaks is very clear in the oxide data between LCP and RCP. MSC PD calculations furthermore well predict both the overall rotations of features and the peak distortions seen here [37], and the dashed curves in Fig. 13(d) present some preliminary theoretical results.

Thus, such circular dichroism in photoelectron angular distributions is expected to be a very general phenomenon for any non-magnetic system (or by implication, also any magnetic system), and such effects can also be quantitatively described by PD theory. One reason for being interested in this phenomenon is that circular dichroism in magnetic systems (*magnetic* circular dichroism or MCD) is usually a much more subtle difference in intensities that may be only a few % in magnitude [39]. MCD effects in photoelectron angular distributions are due to a combination of the spin-orbit and multiplet splittings inherent in core spectra [39(a)], as well as possible spin-dependent exchange scattering from magnetic atoms during photoelectron escape from the surface [9]. By contrast, the CDAD effects discussed in this section are due to the strong Coulomb-plus-exchange scattering from every atom in the specimen. Thus, properly allowing for the latter will be essential to accurately measuring the former [34(b),35,36]. The same kind of allowance will be necessary in the more recently discovered magnetic linear dichroism (MLD) [40(a)] and magnetic unpolarized dichroism (MUD) [40(b)] effects in core photoelectron angular distributions.

(ii) Magnetic systems. As a recent example of the kinds of magnetic circular dichroism effects seen in ferromagnetic systems, we show in Fig. 15(a) some Gd 4d spectra from Gd(0001) obtained by Morais, Denecke et al. [41]. Both of these spectra are split into various final-state multiplets, with the five-component fine structure clearly resolved for the higher energy peak. The Gd has been magnetized in a mirror plane of the crystal, along $\vec{M}$ as shown in the inset, and the two spectra correspond to having $\vec{M}$ parallel or anti-parallel to the plane containing $\hat{q}$, the surface normal $\hat{n}$, and $\hat{k}$ (i.e., the angle ϕ_M = 0° or 180°, respectively). There is a dramatic difference between these spectra, and it results in the MCD signal shown in Fig. 15(b), which is as large as ±30%. Figure 15(c) now shows a free-atom theoretical calculation of such effects by Van der Laan et al. [42], and the agreement with experiment is excellent, including a state-by-state prediction of the degree of MCD.

Figure 16 now shows the azimuthal angular dependence of this Gd MCD, with the sample being rotated about its normal so as to vary ϕ_M and the MCD always being measured as a difference

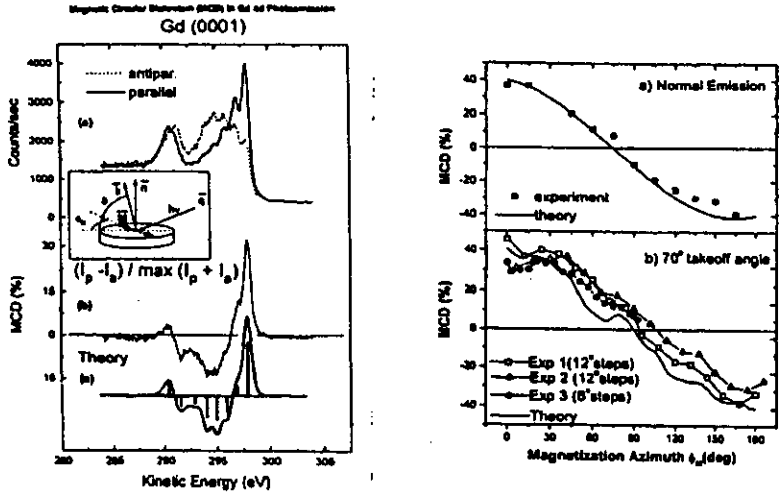

Fig. 15. (Upper left) (a) Gd 4d photoemission spectra taken at a photon energy of 450 eV using left circular polarized light. The solid-curve spectrum was taken with the sample magnetization $\bar{M}$ parallel to the azimuth of the light incidence direction (Φ_M=0°), and the dotted-curve spectrum an antiparallel arrangement (Φ_M = 180°). (b) The normalized difference of the spectra in (a) or MCD asymmetry. (c) A free-atom theoretical calculation of the MCD asymmetry, taken from ref. 42. The inset shows the experimental geometry. [From ref. 41.]

Fig. 16. (Upper right) Angle dependence of the overall MCD effect for Gd 4d core-level emission. (a) Normal emission, (b) Electron takeoff angle = 70° (20° from normal). In both cases the solid lines show theoretical curves calculated for the respective cases. In (a) the calculation is for a free atom, in (b) it is for emission from an atomic cluster three layers thick in order to account for photoelectron diffraction effects. [From ref. 41.]

of spectra for ϕ_M and ϕ_M + 180°. There is a strong ~±35% variation of this signal with ϕ_M, including an overall cosine-like behavior that is characteristic of the free atom and dominant in Fig. 16(a) for normal emission. But additional reproducible fine structure in the ~±5% range is also present in Fig. 16(b) for emission 20° off normal. Such magnetic circular dichroism effects in photoelectron angular distributions (MCDAD) thus will be useful in studying magnetic order and local structure in an element-specific way, but it is clear that a fully quantitative understanding and use of them will require considering final state photoelectron scattering and diffraction.

4. Spin Polarization in Photoelectron Diffraction

A. Multiplet Splittings and Spin-Polarized Photoelectron Diffraction

Being able to separately measure intensity distributions for spin-up and spin-down photoelectrons should in principle make it possible to determine the short-range magnetic order around a given type of emitter via what has been termed spin-polarized photoelectron diffraction (SPPD) by Sinkovic et al. [9(a),(b)]. This is because the scattering of spin-up and spin-down photoelectrons is slightly different in the presence of magnetic order, primarily due to the exchange interaction between the photoelectron and the unfilled d or f valence shells responsible for the magnetic order. The use of multiplet splittings for deriving such spin-resolved spectra is by now well-established for both simple antiferromagnets [9] and ferromagnetic metals [43], and we show in Fig. 17(a) a multiplet-split 3s spectrum from antiferromagnetic $KMnF_3$(100) that is one of the few cases studied to date by SPPD. The predominant spin polarizations of the two components are indicated in this figure, together with the overall electron configurations and L-S multiplets associated with each peak: the $3s^1...3d^5\ ^5S$ peak at lower kinetic energy is expected to be 100% up-spin and the $3s^1...3d^5\ ^7S$ peak to be 71% down-spin. *Spin polarizations are in the case of such multiplets measured with respect to the emitting atom or ion.* The spin-up/spin-down intensity ratio $I_\uparrow / I_\downarrow$ in such multiplets has been measured previously for both $KMnF_3$(110) and MnO(001) as a function of both temperature and direction [9(b)-(d)], and these results indicate some sort of high-temperature magnetic phase transition which occurs at 3-5 times the bulk transition temperature or Neél temperature of these materials. Some of these results due to Hermsmeier et al. [9(c),(d)] are shown in Fig. 18(a). Plotted in this figure is the temperature dependence of the spin asymmetry S(T), a normalized spin-up/spin-down intensity ratio that is defined so as to go to zero at the high-temperature (HT) "paramagnetic" limit of the experimental data via $S(T) = 100[R_T - R_{HT}]$ (in %) [9(b)-(e)]. Here, $R = I_\uparrow / I_\downarrow$, with the subscripts indicating the temperature at which the ratio was measured. For a low average kinetic energy of 111 eV, this asymmetry shows dramatic changes at about 540 K or 4.5 times the bulk Néel temperature, with the sense of this change being opposite for two different directions of observation. Thus, the effect shows a strong dependence on emission direction. For a high kinetic energy of 1405 eV for which exchange scattering effects are expected to be negligibly small, no such effects are observed. These experimental results are in qualitative agreement with PD calculations assuming that there is an

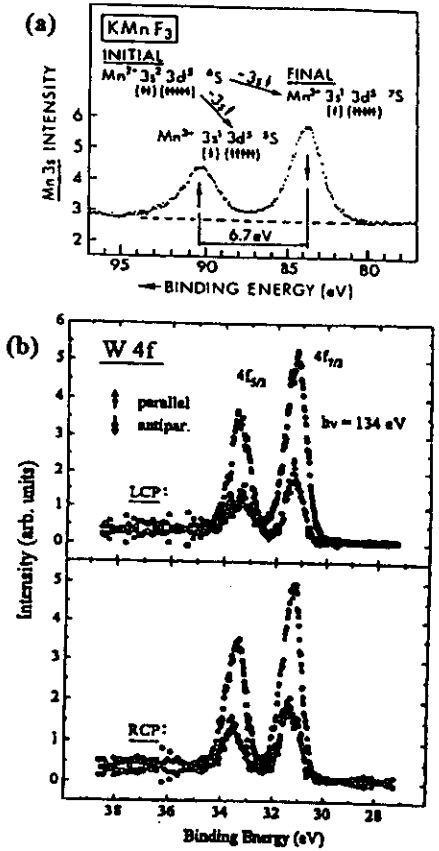

Fig. 17. Spin-polarized core photoelectron spectra: (a) a Mn 3s spectrum from $KMnF_3$, with the electronic states and spin polarizations relative to the emitting Mn^{2+} ion indicated [From ref. 9(e).]; (b) a spin-resolved W 4f spectrum from W(110), excited by LCP light (top panel) and by RCP light (bottom panel). [From ref. 46.] In (b), the spin-resolved intensities as measured parallel or antiparallel to the light incidence direction $\hat{q}$ are indicated.

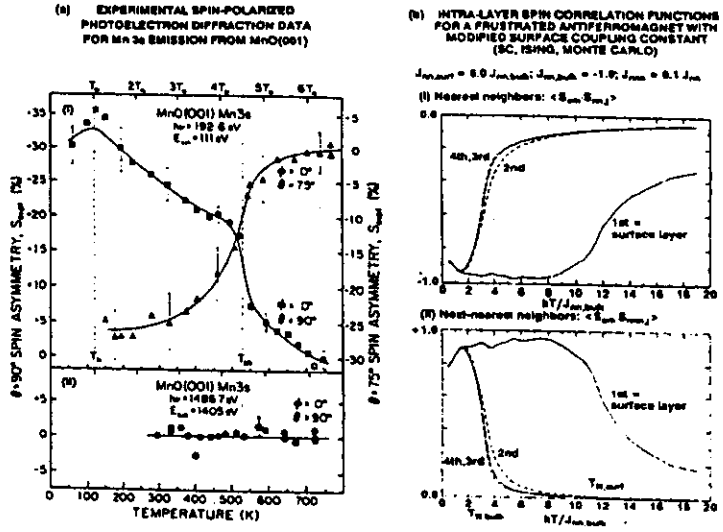

Fig. 18. (a) Temperature-dependent experimental spin-polarized photoelectron diffraction asymmetry data based upon Mn 3s spectra from MnO(001): In the top panel (i), the electron energy is 111 eV and data for two different directions are shown; in the lower panel (ii), the energy is 1405 eV, and only one direction (normal emission) is shown. [From refs. 9(c),(d).] (b) Monte Carlo theoretical calculations showing an elevated surface Néel temperature for a surface exchange interaction that is six times stronger than that in the bulk. [From ref. 44.]

abrupt loss of short-range antiferromagnetic order at this high temperature, even though the bulk long-range order is lost at the much lower Néel temperature [9(d)]. One possible explanation for this effect is that there are local domains of short-range order that persist up to this higher temperature and then abruptly disappear. Another possibility recently discussed by Zhang et al. [44] is that the surface Néel temperature could be significantly higher than that in the bulk. Figure 18(b) shows the results of Monte Carlo calculations for a simple-cubic Ising antiferromagnet of Mn^{2+} ions in which the surface exchange coupling between Mn^{2+} spins has been set to be 6.0 times that in the bulk. For this simple model, it is seen that the spin-spin correlation functions for both nearest neighbor Mn^{2+} ions and next nearest neighbor Mn^{2+} ions show a relatively sharp transition in the surface layer (here indicated as the first layer) at a temperature that is a few times the transition temperature for the rest of the layers (i.e., the bulk in this model). Thus, it is also possible that these SPPD experiments have detected a highly elevated surface Néel temperature for this system, although it remains to be seen whether the surface exchange coupling is really enough higher than that in the bulk to produce such an effect.

In a more recent study, Tober et al. [45] have used the analogous Gd 4s and 5s multiplets to carry out SPPD measurements on Gd(0001), an interesting system because it is thought to have a surface Curie temperature that is 20-60 K above that of the bulk [46]. For this case, the relevant multiplets are $ns^1...4f^7$ ^7S and ^9S in symmetry, and they again yield the predominantly spin-up and spin-down intensities, respectively. The temperature dependence of the spin asymmetry S for this case is shown in Fig. 19 for four different cases, three directions with 5s emission and one direction with 4s emission. There is strong angular dependence in the 5s results, with broad peaks spanning ~ 275-375 K for the first two cases in Figs. 19(a) and (b), and no visible effect of temperature beyond a monotonic decrease for the third case in (c). This angular dependence is found to be consistent with diffraction theory [45]. The presence of two distinct transitions is particularly dramatic in the Gd 4s results of Fig. 19(d). Overall, these results thus confirm that there are two different magnetic transitions about 60-80 K apart, with the bulk Curie temperature being at 293 K and the surface Curie temperature at about 360-380 K.

Although further experiments and theory will be necessary to fully clarify the nature of the magnetic transitions observed in SPPD experiments to date [9,45], these studies indicate the considerable potential of this technique for studying short-range magnetic order in both antiferromagnetic and ferromagnetic systems. Exploiting this potential should be assisted enormously by the use of next-generation synchrotron radiation facilities.

B. Spin Polarization from Circular-Polarized Excitation

Spin-polarized photoelectrons can also be produced by exciting a spin-orbit-split core level with circular-polarized radiation, making use of the well-known Fano effect from atomic physics [47]. We illustrate this with some very recent data obtained by Starke et al. [48] for the non-magnetic system W(110), in the experimental geometry shown in the inset between Figs. 20(b) and (c). Figure 17(b) shows spin-resolved W 4f spectra for the two different circular polarizations of the

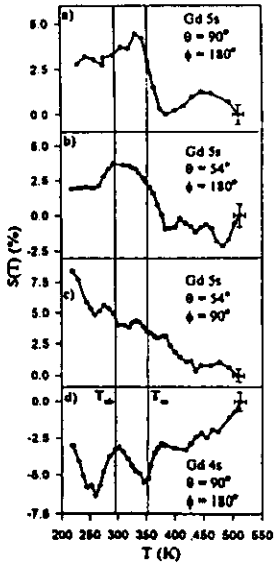

Fig. 19. Experimental spin asymmetry S(T) derived from Gd 5s and 4s multiplet intensity ratios $R = I_\uparrow / I_\downarrow$ as a function of temperature T for (a) Gd 5s emission along the normal ($\theta = 90°$, $\phi = 180°$ along the "c" axis), (b) Gd 5s emission ($\theta = 54°$, $\phi = 180°$ along the "-b" axis), (c) Gd 5s emission ($\theta = 54°$, $\phi = 90°$ along the "a" axis), and (d) Gd 4s emission ($\theta = 90°$, $\phi = 180°$ along the "c" axis). Note the strong angle and level dependence of these results, with broad peaks in (a) and (b) for 5s, no visible effect in (c) for 5s, and two distinct features in (d) for 4s.

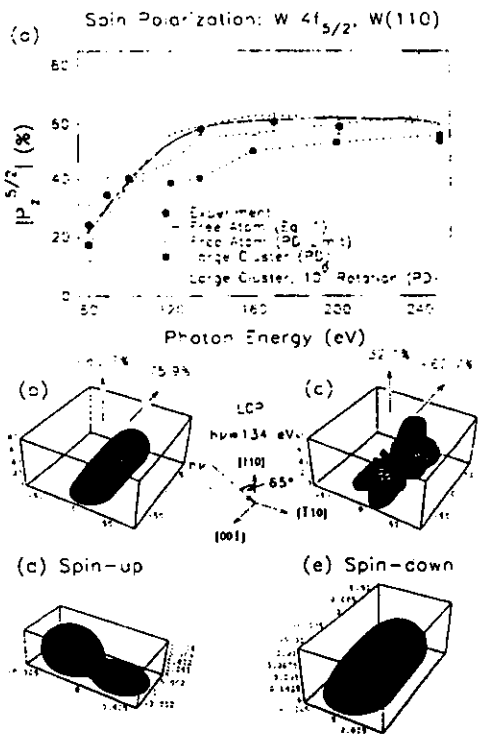

Fig. 20. Spin-polarization in W 4f spectra excited by circular-polarized light from W(110): (a) the absolute value of the $4f_{5/2}$ polarization as a function of photon energy, with experiment compared to both free-atom and MS cluster PD calculations; (b) the three-dimensional spin polarization for a free atom in the experimental geometry shown in the inset and with an excitation energy of 134 eV; (c) as (b), but for a MS cluster PD calculation in a 5-atom cluster (an emitter below 4 surface scatterers); (d),(e) the separate spin-up and spin-down intensities excited in a free-atom. [From ref. 48.]

incident radiation, with the photoelectron spin being measured either parallel or antiparallel to the resulting direction of the light helicity, which is in turn parallel or antiparallel to the light incidence direction. That is, for this case, the *spin polarizations are referenced externally to the direction of light incidence*. There is a clear and strong spin polarization in both the 5/2 and 7/2 components, with the expected change of sign as the polarization of the light is changed. These spin polarizations are also found to increase markedly with photon energy from 80 eV to about 130 eV, and to remain large at about 50-60% over the range from 130 eV to 240 eV, as shown in Fig. 20(a). These polarizations are thus comparable to the 70-100% expected for simple ns multiplets in high-spin atoms of the type discussed previously for Mn [9] and Gd [45], and immediately suggest using such spectra also as internal sources of spin-polarized photoelectrons for SPPD studies. Such SPPD studies based on circular-polarized excitation have in fact been attempted for the first time recently [49]. Theoretical calculations of such effects have also been carried out. For example, for the W $4f_{5/2}$ results in Fig. 20(a), the simple free-atom calculations [50] shown as the solid curve agree very well with the energy dependence seen in experiment. MSC PD calculations from a large W(110) cluster in the nominal geometry of the experiment show the same general trend of polarization variation with energy as experiment, but have a significant dip at about 125 eV that is not observed experimentally. However, a small azimuthal rotation of the cluster by 10° that is within the experimental uncertainty of alignment suppresses this dip, and yields very good agreement with experiment as well. This predicted change in the PD polarizations with cluster orientation however suggests that photoelectron scattering, *even in a non-magnetic lattice*, can significantly alter the degree of spin polarization in a core spectrum [48]. The origin of these changes is that the separate spin-up and spin-down intensity distributions excited from the 5/2 or 7/2 levels have very different shapes, and that they thus sample differently the non-magnetic scatterers around the emitting atom. These effects are illustrated in the theoretical calculations in Figs. 20(b)-(e): the three-dimensional distribution of polarization for the free-atom in (b) is significantly altered when emission from a 5-atom cluster is considered in (b). This alteration can furthermore be qualitatively understood from the dramatic differences in the separate spin-up and spin-down intensity distributions for the free-atom in (d) and (e). Such effects should be very general, very strong, and occur in both non-magnetic and magnetic surroundings.

Finally, we note that the separate measurement of spin-up and spin-down intensities over a range of directions and/or energies can in principle lead to spin-polarized photoelectron *holography* [51], a prospect that we discuss briefly below.

5. Photoelectron Holography

We now turn to the potential for directly determining short-range atomic structures by holographically inverting data sets that may span both photoelectron direction and energy. All of these so-called "direct" methods involve carrying out some kind of mathematical operation that is closely akin to a Fourier transform on a large set of data involving ≥1000 distinct intensity

measurements. In general, the photoelectron intensity $I(\vec{k})$ for a certain wave vector $\vec{k}$ is converted to a normalized χ function in a standard way via:

$$\chi(\vec{k}) = \frac{I(\vec{k}) - I_0(\vec{k})}{I_0(\vec{k})} \quad \text{or} \quad \frac{I(\vec{k}) - I_0(\vec{k})}{I_0(\vec{k})^{1/2}}, \tag{1}$$

where $I_0(\vec{k}) \propto |\phi_0|^2$ is the intensity in the absence of any scatterers. Measurements of $\chi(\vec{k})$ are made at several directions of emission (several $\hat{k}$), and also perhaps at several energies of excitation (several $|\vec{k}|$). The most common way to holographically invert such a $\chi(\vec{k})$ data set is to carry out the following transform over the relevant volume in k-space, as first suggested by Szöke for single-energy data [12(a)], and amplified upon by Barton et al. [12(d)], and by Tong et al. [14(a)] for multi-energy data:

$$U(\vec{r}) = \left| \int_{|\vec{k}|} \exp(-i|\vec{k}||\vec{r}|) \iint_{\hat{k}} \exp(i\vec{k}\cdot\vec{r})\chi(\vec{k})|\vec{k}|^2 \, d|\vec{k}| \sin\theta_k d\theta_k d\phi_k \right|. \tag{2}$$

Here θ_k and ϕ_k are the angles defining the direction $\hat{k}$. Several prior experimental and theoretical studies have obtained successful three-dimensional images of near-neighbor atoms using this approach or close relatives of it [12-21], and it seems clear that, at least for back scattering atoms around a given emitter, useful structural conclusions can be drawn. These images include some obtained with only one energy [e.g., 15(a),(b),(d); 17], and others in which the transform of Eq. (2) is modified to allow for non-ideal scattering effects and/or to somehow focus on the region of image space that is most nearly ideal [e.g., 13,14,15,18(b),(c),20].

We will illustrate this method as applied to a first-of-a-kind extended data set obtained by Denlinger, Rotenberg et al. on beamline 7.0 at the Advanced Light Source, and analyzed recently by Len et al. [52]. The clean W(110) surface discussed previously has been used as a test case, with the intensities of the bulk and surface peaks in spectra such as that in Fig. 8(b) being measured over essentially the full hemisphere above the surface and for kinetic energies between 41 eV (about like that in Figs. 8(b) and 9) and 302 eV. A total of about 20,000 unique intensities was thus measured. Figure 21 shows the separate data sets thus derived for both bulk and surface emission, in a cutaway volume representation. Fig. 22(a) now shows a holographic atomic image reconstructed via Eq. (2) (here referred to as Method A from among several considered elsewhere [15(g),52]) from the surface-atom intensity data, as first normalized to produce $\chi(\vec{k})$ via Eq. (1). This image is in the vertical $(\bar{1}\,1\bar{2})$ plane, the emitter position is indicated by a dashed square, and the ideal positions of the neighboring atoms are indicated by circles. We see that the back scattering atom just below the emitter (denoted $[\bar{1}\,\bar{1}\,0]$) is very well imaged, with a sharp peak that is centered very close to the true atomic position (within ~0.2 Å). The side scattering atoms surface atoms just next to the emitter (denoted $[\frac{1}{2}\,\frac{\bar{1}}{2}\,\frac{\bar{1}}{2}]$ and $[\frac{\bar{1}}{2}\,\frac{1}{2}\,\frac{1}{2}]$) are also clearly imaged, but with some smearing in the vertical

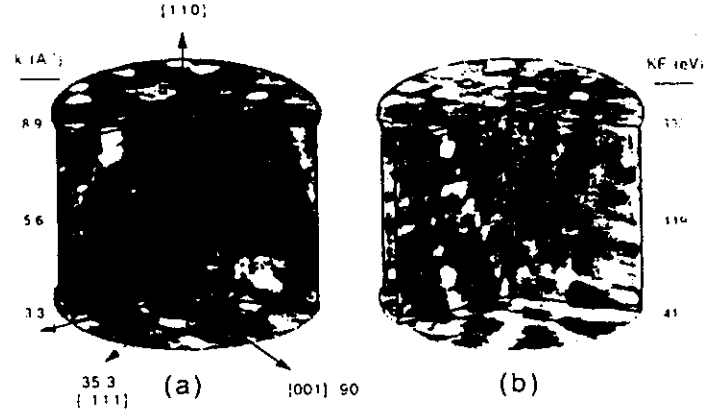

Fig. 21. Cutaway views of volume representations of the normalized intensities $\chi(k)$ for W $4f_{7/2}$ emission from clean W(110), with (a) from the bulk peak and (b) from the surface peak (as shown in Fig. 8(b)). The vertical scales are kinetic energy (KE) and wavevector, and each plane represents a stereographic projection of a nearly full-hemisphere data set taken over directions from the surface normal to within 10° of the surface. [From ref. 50.]

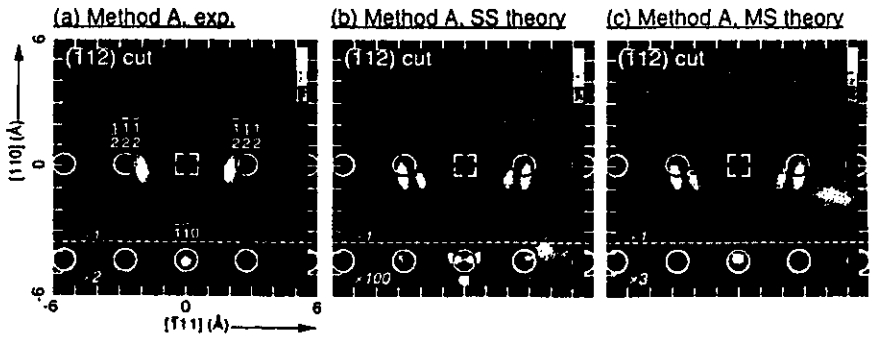

Fig. 22. W(110) holographic atomic images in the vertical $(\bar{1}\,1\bar{2})$ plane, as reconstructed using Eq. (2) from (a) the experimental surface-resolved W $4f_{7/2}$ data set of Fig. 21(b), (b) corresponding single scattering calculations, and (c) corresponding multiple scattering calculations. The surface-atom emitter is indicated by a dashed square, and the near-neighbor scatterers by circles. Image intensities for vertical coordinates ≤-3.5 Å have been rescaled, with the scale factors indicated on the figures. [From ref. 50.]

direction, and positions that are further from the true positions, being shifted inward toward the emitter by about 0.7 Å and downward from the surface plane by about 0.2 Å. Nonetheless, this experimental image could be used to provide a good first-order estimate of the local geometry around these W surface atoms if it were not already known (e.g. via the PD analysis in Fig. 9 and other prior studies discussed in ref. 28).

In Figs. 22(b) and (c) are now shown corresponding images derived from both single scattering and multiple scattering calculations. Single scattering is found not to agree as well with experiment, for example for the form and relative intensity of the image of the back scattering atom. The image of this atom is found to be split and much weaker in intensity than is found in experiment. Multiple scattering is found to much better predict the image of this back scattering atom in both form and intensity. Both theoretical images are found to show a doubling of the side scattering atomic images that is not as evident in experiment, but they agree in predicting inward and downward shifts in the center of gravity of these images, as seen in experiment. Thus, experiment and multiple scattering theory are in very good agreement, but with the experimental images being even cleaner representations of these nearest-neighbor atomic images than found in theory.

Similar results for a bulk emitter are not as encouraging, with the forward scattering atoms above a typical emitter showing elongated and shifted images that would make it difficult to use them for a precise structural prediction [52]. Various other imaging algorithms (denoted Methods A', B-D) have also been applied to these surface and bulk holographic data to assess the degree to which they improve the atomic images [52]. Overall, it is concluded that backscattering atoms below and side-scattering atoms beside a given emitter that is in turn at or near the surface can be imaged successfully, with forward scattering atoms above an emitter that is below the surface not being imaged as accurately. Large data sets of the type considered here should permit exploiting holographic imaging to a maximum degree in the future, although it should not be necessary for most cases to obtain more that 3,000-5,000 intensities to accurately image the near-neighbor region [15(e),(f)].

6. Spin-Polarized Photoelectron Holography

We turn now to another intriguing prospect for the future of spin-resolved photoelectron diffraction studies: the possibility of directly imaging the scatterer spins around a given emitter via holographic inversion methods. We have already noted that two core photoelectron peaks can often be found at relatively close-lying energies that are strongly spin-polarized in an opposite sense. This might be due to a core multiplet splitting or a spin-orbit doublet excited with circular polarization, or some mixture of these two effects. Thus, it is in principle possible to separately measure $\chi_\uparrow(\bar{k})$ and $\chi_\downarrow(\bar{k})$ for the two different spin orientations, and this could lead via spin-dependent scattering effects to the holographic imaging of the local magnetic order around a given type of emitter [51]. There are two obvious spin-sensitive imaging algorithms based on Eq. (2) and separate measurements of $\chi_\uparrow(\bar{k})$ and $\chi_\downarrow(\bar{k})$ [51(b),(c)]:

$$\Delta(\bar{r}) = U_\uparrow(\bar{r}) - U_\downarrow(\bar{r}) , \qquad (3)$$

with obvious notation, and

$$\Delta'(\bar{r}) = \left| \int_{|\bar{k}|} \exp(-i|\bar{k}||\bar{r}|) \iint_{\bar{k}} \exp(i\bar{k}\cdot\bar{r}) \left[\chi_\uparrow(\bar{k}) - \chi_\downarrow(\bar{k}) \right] |\bar{k}|^2 \, d|\bar{k}| \sin\theta_k d\theta_k d\phi_k \right| , \qquad (4)$$

which is simply an image like $U(\bar{r})$ but calculated only on the difference of the spin-up and spin-down χ's. Additional vector-based spin-sensitive holographic imaging functions have also been proposed by Timmermans et al. [51(a)].

As a brief indication of the potential of this kind of photoelectron holography, we show in Fig. 23 holographic inversions of multiple scattering calculations for emission of spin-up and spin-down electrons from Mn^{2+} ions in a small planar cluster representing a portion of the MnO(001) surface [51(c)]. The cluster is shown in Fig. 23(a). Spin-up Mn^{2+} scatterers in this cluster have been distinguished from spin-down scatterers by having an additional exchange potential due to five unpaired 3d electrons that interacts only with spin-up photoelectrons. Spin-down scatterers have the same 3d exchange potential, but it interacts only with spin-down photoelectrons. Thus, the potential is slightly more attractive when the photoelectron spin is parallel to that of the scatterer. Spin-up and spin-down holograms were calculated in a fully-converged MSC way for 10 energies between 127 eV and 278 eV, and holographic images then derived via Eqs. (1)-(4). The normal images $U_\uparrow$ and $U_\downarrow$ in the plane of the cluster for spin-up and spin-down electrons are shown in Figs. 23(b),(c), together with the corresponding spin-sensitive images $\Delta(\bar{r})$ and $\Delta'(\bar{r})$ in Figs. 23(d),(e). The normal images show features for all of the atoms in the cluster, including the four non-magnetic O atoms. These spin-up and spin-down images are also very similar, as expected since the 3d exchange scattering is only 5-15% of the total effective scattering potential at these energies. By contrast, neither $\Delta(\bar{r})$ nor $\Delta'(\bar{r})$ contains any image intensity for the O atoms, verifying that either of these choices of imaging algorithm are predominantly sensitive to only the magnetic scatterers. The peaks and valleys in the spin-sensitive images are in general about 7-9% as strong in transform amplitude as the normal images, suggesting the experimental possibility of carrying out such imaging, albeit a non-trivial exercise. $\Delta(\bar{r})$ and $\Delta'(\bar{r})$ are also inherently different in that $\Delta'(\bar{r})$ images both orientations of scatterers in the same way, due the absolute value in Eq. (4), while $\Delta(\bar{r})$ changes sign when the scatterer is flipped, and thus also is sensitive to the orientation of a given scatterer. $\Delta(\bar{r})$ also involves the phase of the scattering factor, and thus can show sign changes over the region of a magnetic scatterer; however, it is clear from this and other calculations that the sign changes are exactly reversed if the orientation of the scatterer spin is flipped from up to down.

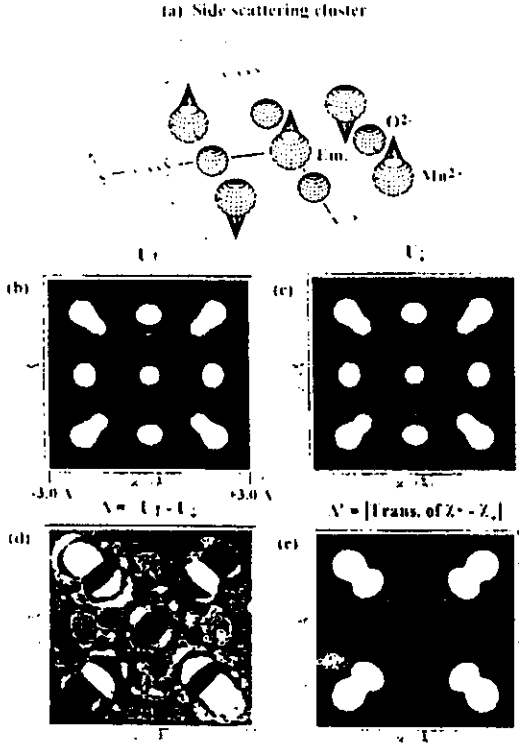

Fig. 23. A theoretical simulation of spin-polarized photoelectron holography: (a) a nine-atom cluster representing the (001) surface of MnO, with an emitter in its center; (b),(c) normal holographic images $U(\vec{r})$ $U(\vec{r})$ generated for the two different photoelectron spins by using Eq. (2) and holograms at 10 energies between 127 and 278 eV; (d) the spin-sensitive holographic image Δ generated by using Eq. (3), (e) the spin-sensitive holographic image $\Delta'(r)$ generated by using Eq (4) [From refs. 49(c),(d)]

Thus, spin-polarized photoelectron holography represents an intriguing and challenging experimental possibility for the future, but one well matched to the new synchrotron radiation sources that are now becoming available.

7. X-Ray Holography Using Fluorescence Emission

A. X-Ray Fluorescence Holography

We now consider an alternative type of holography involving the scattering of x-rays by the near neighbors to a given atom that is emitting fluorescent x-rays. This method has been discussed previously from a theoretical point of view [23], but the the much weaker diffraction modulations involved have prevented the first experimental explorations of it until very recently [24(a),(c),(d)]. The first method for doing such x-ray holography, which has been termed x-ray fluorescence holography (XFH), is illustrated in Fig. 2(b). As indicated, it is identical in philosophy to photoelectron holography, except that it is now a fluorescent x-ray which scatters instead of a photoelectron. This makes the scattering much weaker, by 10^{-3} or 10^{-4}, but much more ideal and optical in character. The former means that such measurements will be more difficult to measure, but the latter means that they should be more accurate, and thus worth assessing. Comparing Fig. 2(a) with Fig. 2(b) also points out the fundamental difference between a classic x-ray diffraction (XRD) measurement and XFH. In XRD, scattered waves ϕ_1, ϕ_2, ϕ_3,...from the various atomic planes in a sample *with long-range order* constructively interfere to yield various Bragg reflections, and the reference wave ϕ_0 is lost into the crystal. Thus, a direct holographic inversion of such data is not possible, although there are by now several well-established approaches for solving the resulting "phase problem" so as to determine unique atomic structures [53], and more recently, the use of x-ray standing waves has also been discussed for this purpose [54(a)]. In XFH by contrast, the reference wave is involved in producing the diffraction pattern, which is created by the scattering from the near neighbor atoms involved in the *short-range order* around a given emitter. Thus, a true hologram is generated, and inversion of it using Eqs. (1) and (2) becomes feasible. Scattering of fluorescent x-rays from the *long-range order* in the crystal also can occur, and this produces features known as *Kossel lines* which have also been suggested as an alternate way of doing x-ray holography [54(b)]. In fact, photoelectrons exhibit such features as well, which are called *Kikuchi bands* [55]. But we will focus here on the short-range-order effects in XFH that are completely analogous to the dominant effects in a normal photoelectron diffraction pattern.

The first XFH measurements were performed recently by Tegze and Faigel [24(a)]. They measured the hologram by monitoring the single-energy Sr Kα emission (E = 14.10 keV, k = 7.145 Å) from a single crystal of $SrTiO_3$. Approximately 2,400 intensities were measured over a cone of 60° half angle above the surface. The final hologram was found to have anisotropies in intensity of $\Delta I/I_0 \approx 0.3\%$. These small effects mean that much more demanding detector counting statistics are required in x-ray holography measurements than with comparable photoelectron holography measurements in which $\Delta I/I_0$ can be 50%. The reconstruction of this hologram via the algorithm of

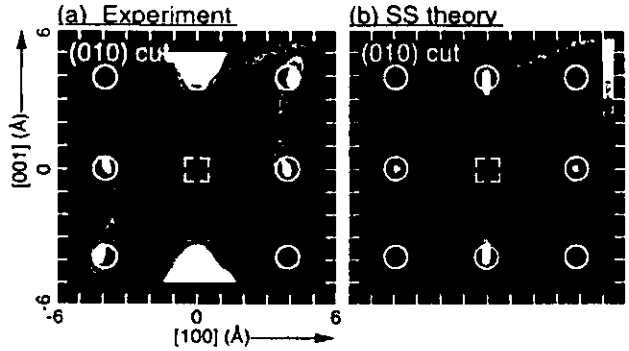

Fig. 24. Single-energy x-ray fluorescence holography (XFH) atomic images of $SrTiO_3$ in the vertical (010) plane, obtained from (a) experimental [24(a)] and (b) theoretical [24(b)] Sr Kα $\chi(k)$ data sets, via Eq. (2). The Sr emitter site is indicated by the dashed square, and nearest-neighbor and next-nearest-neighbor Sr scatterers are indicated by circles.

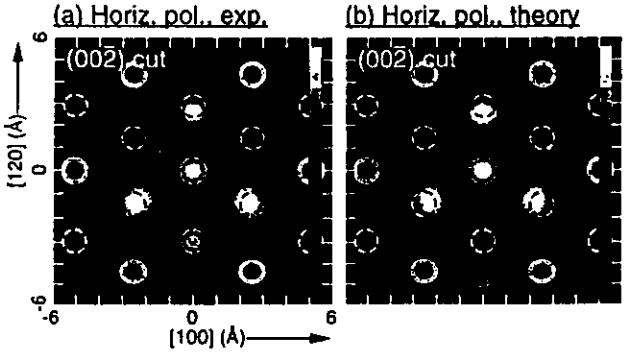

Fig. 25. Multiple energy x-ray holography (MEXH) atomic images of α-Fe_2O_3(001) in the horizontal (00$\bar{2}$) plane situated 6.89Å below each of the two types of Fe emitters, obtained from (a) experimental and (b) theoretical Fe Kα $\chi(k)$ data sets, via Eq. (2) [24(c)]. Fe scatterers in the bi-layer just above or below this plane are indicated by dashed circles, and Fe scatterers in relative positions common to both inequivalent Fe emitters are indicated by bold circles.

Eq. (2) (as now reduced to a single integral over direction) yields images of the Sr atoms only, as the much weaker scattering strength of the Ti and O atoms renders their images invisible compared to those of the Sr atoms. Fig. 24(a) shows the experimental image reconstructed in the vertical (010) plane [24(a)], and it is compared in Fig. 24(b) to an image reconstructed from a theoretical $\chi(\vec{k})$ for Sr Kα emission from a simple-cubic Sr cluster of 27 atoms (24(b)). Based on previously discussed criteria [13(d)], the expected atomic image resolutions at this hologram energy and angular range are $\delta x \approx 0.3$Å in the horizontal [100] direction, and $\delta z \approx 0.9$Å in the vertical [001] direction, and these numbers are in general agreement with the atomic images of Figs. 24(a),(b).

Reconstructing three-dimensional atomic images from a single-wavenumber hologram is known to yield twin images [12-15, 23]. That is, each $U(\vec{r})$ has associated with it a $U(-\vec{r})$ of equal magnitude. In any structure without inversion symmetry, these twins can overlap with real atomic images so as to confuse structural interpretation. In addition, the real and twin atomic images for a particular wavenumber and system can overlap completely out of phase, leading to an artificial suppression of atomic image intensities [23]. As in photoelectron holography [12(c),12(d),23(c)], it is thus advantageous to reconstruct direct atomic images from multiple-wavenumber $\chi(\vec{k})$ data sets so as to avoid such real-twin image overlaps. However, such XFH holograms cannot be measured at arbitrary wavenumbers, with the latter being limited by the intensity and number of fluorescence lines of the photoemitting species.

B. Multi-Energy Time-Reversed X-Ray Holography

To overcome this single-energy, or at most few-energy, limitation in XFH, another method for obtaining x-ray holographic information at conveniently chosen multiple energies has also very recently been proposed and demonstrated experimentally for the first time by Gog et al. [24(c)]. This method has been termed multiple energy x-ray holography (MEXH), and its basic principle is illustrated in Fig. 2(c). MEXH is essentially the time-reversed version of the conventional geometry of XFH (Fig. 2(b)), in that the wave motions are reversed, and the emitter and detector positions are interchanged. The exciting external x-ray beam now produces the reference and object waves, and the fluorescing atom acts only to detect the interference between the direct and scattered wavefronts. That is, the strength of the angle-integrated fluorescence signal is used to monitor the x-ray field strength at the emitting atom. The emitted x-rays are now collected by a distant detector with a large acceptance solid angle, in principle yielding much higher effective counting rates. The excitation x-ray source can also now be set to any energy above the fluorescence edge of the emitting species, thus permitting holograms at multiple wavenumbers and yielding in principle atomic images with no real-twin image overlaps [12(c),12(d),14(a),24(c)]. Specifically, multiple-wavenumber x-ray holograms have been measured to date for hematite (α-Fe_2O_3(001))[24(c)], and for Ge(001) [24(d)].

We illustrate the results of applying the inversion algorithm of Eq. (2) to both experimental MEXH data for (α-Fe_2O_3(001)) measured by Gog and co-workers on Beamline X-14A of the National Synchrotron Light Source at Brookhaven National Laboratory [24(c)] and to theoretical

simulations of this data. Fe Kα fluorescence was excited by horizontally polarized radiation at three energies in the range hν= 9.00keV to 10.30keV (k = 4.561Å^{-1} to 5.220Å^{-1}) that was incident on the sample surface over a polar range of 60° ≤ θ ≤ 90° = surface normal. These data points were measured at three wavenumbers with intervals of δk = 0.329Å^{-1} (δE = 650eV), and at angular intervals of (δθ,δφ) = (5°,5°), making a total of 435 unique measurements in a symmetry-reduced 1/3rd of the total solid-angle above the sample. The resulting modulation in $\chi(\vec{k})$ was ~0.5% and so similar to that found in the XFH results for $SrTiO_3$ [24(a)].

For comparison to the experimental results, a single-scattering model [23(c)] was used to calculate a theoretical $\chi(\vec{k})$ for an ideal α-Fe_2O_3(001) cluster containing 384 Fe atoms with two inequivalent Fe emitter sites, as appropriate to the hematite lattice. The O atoms were not included due to their much smaller scattering power. The orientation of the radiation polarization with respect to the crystal during the crystal rotation of the measurement was also taken into account.. In particular, because the incident radiation is linearly polarized, the x-ray scattering factor must be further multiplied by the Thomson scattering factor, which has the form $\sin^2\Theta_c^{\hat{q}'}$, where $\Theta_c^{\hat{q}'}$ is the angle between the polarization vector of the incident radiation $\vec{\epsilon}$, and the direction $\hat{q}'$ of the scattered radiation. Thus, there will be nodes in the incoming scattered object waves along the polarization direction, and emitter atoms near this direction will not be as strongly influenced by x-ray scattering.

Figures 25(a) and (b) show the resulting MEXH atomic images for experiment and theory, respectively, in the [00$\bar{2}$] plane situated at z = -6.89Å below the emitter. There is excellent agreement between experiment and theory, and the positions of the atoms are very close to those in the known lattice (~0.2 Å inward displacement toward the emitter in experiment, and ~0.4 Å inward displacement in theory. The expected image resolutions in the horizontal ([100] and [1$\bar{2}$0]) directions are δx = δy = 0.6Å [13(d)] The experimental and theoretical images are very similar in that three of the Fe atoms from the neighboring upper Fe bi-layer intrude into the [00$\bar{2}$] image plane. This intrusion is due to the limited wavenumber and angular range of the $\chi(\vec{k})$ data points in $\vec{k}$-space (as compared to the larger wavenumber and angular range for the electron $\chi(\vec{k})$'s in the previous section). This results in atomic images much less resolved in the vertical [001] direction and a resolution limit of δz ≈ 2.5 Å [13(d)]. Still, since these images are reconstructed from a multiple-wavenumber $\chi(\vec{k})$ data set, they should be freer of real-twin image overlaps [23(c)]. And they do indicate for the first time that such multi-energy data can be obtained and analyzed.

Thus, although x-ray holography using fluorescent x-rays is really just beginning to become a reality, it already shows considerable promise of becoming a complementary tool to x-ray diffraction and other surface and bulk structure probes. Its key advantages are that it is element-specific, that the theoretical interpretation is much simpler than for electrons, and that it can probe the short-range structure in systems for which long-range order may be lacking (as for example, in mosaic crystals). For certain kinds of surface, interface, and nanostructure work, both XFH and MEXH thus could be very useful, as discussed in more detail in recent comparative papers [24(e),24(f)]. Fully exploiting these new methods will also require the high brightness excitation sources of third-generation synchrotron radiation facilities

8. Concluding Remarks

Photoelectron diffraction is thus in some respects a mature technique, but at the same time it is one in which several exciting new possibilities for surface, interface, and nanostructure structure studies are found. The simple extension to taking full-solid-angle data often permits much clearer conclusions as to structures, especially when high energies with forward scattering are present, and complementary structure probes such as LEED and STM are used *in situ* with it. Next-generation instrumentation, particularly at third-generation synchrotron radiation sources, will much expand the use of chemical state- or site- resolved photoelectron diffraction, including the resolution of surface atoms and atoms at buried interfaces, time-dependent structural studies, and different types of dichroism in both non-magnetic and magnetic systems. The use of circular-polarized radiation for excitation shows up new phenomena in diffraction peak rotations and distortions, as well as making it possible to excite spin-polarized photoelectrons from any spin-orbit split level. Spin-polarized photoelectron diffraction and its more difficult cousin spin-polarized photoelectron holography also promise to provide information on local magnetic order in an element-specific, and also site-specific, way. Photoelectron holography also are beginning to provide direct three-dimensional images of short-range atomic structure, with useful accuracy for neighbors beside or below an emitter that is a surface of near-surface species. Finally, x-ray holography of either the x-ray fluorescence type or the multi-energy time-reversed type represents a new and closely related technique with considerable potential for imaging short-range atomic structure with higher accuracy.

Acknowledgments

We are very grateful to various co-workers and collaborators who have contributed greatly to the beamline installation and testing, equipment fabrication, and some of the specific studies presented here: T. Anderson, C. Cummings, P. Dyer, T. Gog, K. Higashiyama, B. Holbrook, W.R.A. Huff, P.D. Johnson, S.A. Kellar, J. Kortright, T. Lauritzen, G. Materlik, C.E. Miner, E.J. Moler, M. Rice, S. Ryce, D.A. Shirley, K. Starke, C. Westphal, R. Wright, H . Xiao, J.J. Zaninovich, and F. Zhang. This work has been supported by the Director, Office of Energy Research, Office of Basic Energy Sciences, Division of Division of Materials Sciences, of the U.S. Department of Energy, under Contract DOE-AC03-76SF00098 and the U.S. Office of Naval Research under Contract No. N00014-94-0162.

References

1. (a) K. Siegbahn, U. Gelius, H. Siegbahn and E. Olsen, Phys. Lett. 32A, 221 (1970); (b) C.S. Fadley and S.A.L. Bergstrom, Phys. Lett. 35A, 375 (1971); (c) A. Liebsch, Phys. Rev. Lett. 32, 1203 (1974); and Phys. Rev. B13, 544 (1976); (d) S. Kono, C.S. Fadley, N.F.T. Hall and Z. Hussain, Phys. Rev. Lett. 41, 117 (1978); (e) D.P. Woodruff, D. Norman, B.W. Holland, N.V. Smith, H.H. Farrell, and M.M. Traum, Phys. Rev. Lett. 41, 1130 (1978); (f) S.D. Kevan, D.H. Rosenblatt, D. Denley, B.-C. Lu, and D.A. Shirley, Phys. Rev. Lett. 41, 1565 (1978); (g) S. Kono, S.M. Goldberg, N.F.T. Hall, and C.S. Fadley, Phys. Rev. Lett. 41, 1831 (1978)
2. (a) C.S. Fadley, Phys. Scripta T17, 39 (1987); (b) C.S. Fadley in *Synchrotron Radiation Research: Advances in Surface Science*, R.Z. Bachrach (Ed.), (Plenum Press, New York, 1993); (c) C.S. Fadley, Surf. Sci. Repts. 19, 231 (1993); (d) C.S. Fadley et al., J. Electron Spectrosc. 68, 19 (1994); (e) C.S. Fadley, in *The Structure of Surfaces IV*, X. Xide, S.Y. Tong, and M.A. Van Hove (Eds.), (World Scientific, 1994); (f) C.S. Fadley, M.A. Van Hove, Z. Hussain, and A.P. Kaduwela, J. Electron Spectrosc. 75, 273 (1995).
3. (a) S.A. Chambers, Adv. in Phys. 40, 357 (1990); S.A. Chambers, Surf. Sci. Rep. 16, 261 (1992); (b) W.F. Egelhoff, Jr. in *Critical Reviews in Solid State and Materials Sciences*, 16, 213 (1990).
4. (a) L.J. Terminello, X.S. Zhang, Z.Q. Huang, S. Kim, A.E. Schach von Wittenau, K.T. Leung, and D.A. Shirley, Phys. Rev. B 38, 3879 (1988); (b) L.-Q. Wang, Z. Hussain, Z.Q. Huang, A.E. Schach von Wittenau, D.A. Shirley, and D.W. Lindle, Phys. Rev. B 44 , 13771 (1991); (c) D.A. Shirley et al., J. Electron Spectrosc. 68, 49 (1994).
5. H.P. Bonzel, Prog. in Surf. Sci. 42, 219 (1993) and references therein.
6. (a) A.M. Bradshaw and D.P. Woodruff, in *Applications of Synchrotron Radiation: High-Resolution Studies of Molecules and Molecular Adsorbates on Surfaces*, W. Eberhardt (Ed.), (Springer-Verlag, Berlin, 1993); (b) O. Schaff, G. Hess, V. Fernandez, K.-M. Schindler, A. Theobald, Ph. Hofmann, A.M. Bradshaw, V. Fritzsche, R. Davis. and D.P. Woodruff, J. Electron Spectrosc. 75, 117 (1995).
7. J. Osterwalder, P. Aebi, R. Fasel, D. Naumovic, P. Schwaller, T. Treutz, L. Schlapbach, T. Abukawa, and S. Kono, Surf. Sci. 331-333, 1002 (1995)
8. (a) D. Sebilleau, M.C. Desjonqueres, D. Chaveau, C. Guillot, J. Lecante, G. Treglia, and D. Spanjaard, Surf. Sci. Lett. 185, L527, (1987); (b) A. Nilsson, H. Tillborg, and N. Mårtensson, Phys. Rev. Lett. 67, 1015 (1991); (c) K.U. Weiss et al., Phys. Rev. Lett. 69, 3196 (1992); (d) J.D. Denlinger, E. Rotenberg, U. Hessinger, M. Leskovar, and M.A. Olmstead, Appl. Phys. Lett. 62, 2057 (1993), and E. Rotenberg, J.D. Denlinger, U. Hessinger, M. Leskovar, and M.A. Olmstead, J. Vac. Sci. Tech. B11, 1444 (1993).
9. (a) B. Sinkovic and C.S. Fadley, Phys. Rev. B31, 4665 (1985); (b) B. Sinkovic, B.D. Hermsmeier, and C.S. Fadley, Phys. Rev. Lett. 55, 1227 (1985); (c) B.D. Hermsmeier, J. Osterwalder, D.J. Friedman, and C.S. Fadley, Phys. Rev. Lett. 62, 478 (1989); (d) B.D. Hermsmeier, J. Osterwalder, D.J. Friedman, B. Sinkovic, T.T. Tran, and C.S. Fadley, Phys. Rev. B42, 11895 (1990); (e) B. Sinkovic, D.J. Friedman, and C.S. Fadley, J. Magn. Magn. Mater. 92, 301 (1991).
10. (a) C.H. Li and S.Y. Tong, Phys. Rev. Lett. 42, 901 (1979); (b) J.J. Barton and D.A. Shirley, Phys. Rev. B32, 1892 (1985); and Phys. Rev. B32, 1906 (1985); (c) A.P. Kaduwela, G.S. Herman, D.J. Friedman and C.S. Fadley, Phys. Scripta 41, 948 (1990), as based on a method described in (d); (d) J.J. Rehr and R.C. Albers, Phys. Rev. B41, 81139 (1990); (e) A.P. Kaduwela, D.J. Friedman, and C.S. Fadley, J. Electron Spectrosc. 57, 223 (1991); (f) D.K. Saldin, G.R. Harp, and X.Chen, Phys. Rev. B48, 8234 (1993); (g) Y. Chen, H. Wu, and D.A. Shirley, private communication.
11. (a) P.J. Orders and C.S. Fadley, Phys. Rev. B27, 781 (1983); (b) M. Sagurton, E.L. Bullock, and C.S. Fadley, Phys. Rev. B30, 7332 (1984) and (c) Surf. Sci. 182, 287 (1987); (d) V. Fritzsche and D.P. Woodruff, Phys. Rev. B46, 16128 (1992); and (e) P. Hofmann and K.M. Schindler, Phys. Rev. B47, 13942 (1993).
12. (a) A. Szöke, in *Short Wavelength Coherent Radiation: Generation and Applications*, D.T. Attwood and J. Bokor (Eds.), AIP Conference Proceedings No. 147 (AIP, New York, 1986); (b) J.J. Barton, Phys. Rev. Lett. 61, 1356 (1988); (c) J.J. Barton, J. Electron Spectrosc. 51, 37 (1990); (d) J.J.Barton,, and L.J. Terminello, paper presented at the Third International Conference on the Structure of Surfaces, Milwaukee, July 1990, and in *Structure of Surfaces III*, S. Y. Tong, M. A. Van Hove, X. Xide, and K. Takanayagi, eds., (Springer Verlag, Berlin, 1991) p. 107, and J.J. Barton, Phys. Rev. Lett. 67, 3106 (1991).
13. (a) G.R. Harp, D.K. Saldin, and B.P. Tonner, Phys. Rev. Lett. 65, 1012 (1990); (b) G.R. Harp, D.K. Saldin, and B.P. Tonner, Phys. Rev. B42, 9199 (1990); (c) B.P. Tonner, Z.-L. Han, G.R. Harp, and D.K. Saldin, Phys. Rev. B43, 14423 (1991); (d) G.R. Harp, D.K. Saldin, X. Chen, Z.L. Han, and B.P. Tonner, J. Electron Spectrosc. 57, 331 (1991); (e) D.K. Saldin, G.R. Harp, B.L. Chen and B.P. Tonner, Phys. Rev. B44, 2480 (1992); (f) D.K. Saldin, G.R. Harp, and B.P. Tonner, Phys. Rev. B45, 9629 (1992)
14. (a) S.Y. Tong, C.M. Wei, T.C. Zhao, H. Huang, and H. Li, Phys. Rev. Lett. 66, 60 (1991); (b) S.Y. Tong, H. Li, and H. Huang, Phys. Rev. Lett. 67, 3102 (1992); (c) S.Y. Tong, H. Huang, and C.M. Wei, Phys. Rev. B46, 2452 (1992); (d) J.G. Tobin, G.D. Waddill, H. Li, and S.Y. Tong, Phys. Rev. Lett. 70, 4150 (1993).
15. (a) S. Thevuthasan, G.S. Herman, A.P. Kaduwela, R.S. Saiki, Y.J. Kim, W. Niemczura, M. Burger and C.S. Fadley, Phys. Rev. Lett. 67, 469 (1991); (b) G.S. Herman, S. Thevuthasan, T.T. Tran, Y.J. Kim, and C.S. Fadley, Phys. Rev. Lett. 68, 650 (1992); (c) S. Thevuthasan, G.S. Herman, A.P. Kaduwela, T.T. Tran, Y.J. Kim, R.S. Saiki, and C.S. Fadley, J. Vac. Sci. Technol. A10, 2261 (1992); (d) S. Thevuthasan, R.X. Ynzunza, E.D. Tober, C.S. Fadley, A.P. Kaduwela, and M.A. van Hove, Phy. Rev. Lett. 70, 595 (1993); (e) P.M. Len, F.Zhang, S. Thevuthasan, A.P. Kaduwela, M.A. van Hove, and C.S. Fadley, J. Electron Spectrosc. 76, 351 (1995); (f) P.M Len, S. Thevuthasan, A.P. Kaduwela, M.A. van Hove, and C.S. Fadley, Surf. Sci. 365, 535 (1996); P.M. Len, S. Thevuthasan, A.P. Kaduwela, and C.S. Fadley, J. Electron Spectrosc., to appear.
16. (a) L.J. Terminello, J.J. Barton, and D.A. Lapiano-Smith, J. Vac. Sci. Technol. B10, 2088 (1992) and Phys. Rev. Lett. 70, 599 (1993); (b) B.L. Petersen, L.J. Terminello, and D.A. Shirley, Mat. Res. Soc. Symp. Proc. 307, 285 (1993); (c) B.L. Petersen, L.J. Terminello, J.J. Barton, and D.A. Shirley, Chem. Phys. Lett. 220, 46 (1994); (d) B.L. Petersen, Ph.D. Thesis, University of California-Berkeley, 1995; (e) L.J. Terminello, B.L. Petersen, and J.J. Barton, J. Electron Spectrosc. 75, 299 (1995).
17. Y. Zhou, X. Chen, J.C. Campuzano, G. Jennings, H. Ding, and D.K. Saldin, Mat. Res. Soc. Symp. Proc. 307, 279 (1993).
18. (a) H. Wu, G.J. Lapeyre, H. Huang, and S.Y. Tong, Phys. Rev. Lett. 71, 251 (1993); (b) H. Wu and G.J. Lapeyre, Phys. Rev. B51, 14549 (1995); (c) S.Y. Tong, H. Li, and H. Huang, Phys. Rev. B51, 1850 (1995)
19. M. Zharnikov, M. Weinelt, P. Zebisch, M. Stichler, H.-P. Steinrück, Surf. Sci. 334, 114-134 (1995), and references therein.
20. M.T. Sieger, J.M. Roesler, D.-S. Lin, T. Miller, and T.-C. Chiang, Phys. Rev Lett. 73, 311 (1994).
21. R. Denecke, R. Eckstein, L. Ley, A.E. Bocquet, J.D. Riley, and R.C.G. Leckey, Surface Science 331-333, 1085 (1995).
22. B.P. Tonner, D. Duhham, T. Droubay. J. Kikuma, J. Denlinger, and E. Rotenberg, J. Electron Spectrosc. 75, 309 (1995).

23. (a) M.Tegze and G. Faigel, Europhys. Lett. 16, 41 (1991); (b) C.S. Fadley. Mat. Res. Soc. Symp. Proc. 307, 261 (1993); (c) P.M. Len S. Thevuthasan, C.S. Fadley, A.P. Kaduwela, and M.A. Van Hove, Phys. Rev. B, Rap. Comm. 50, 11275 (1994).
24. (a) M. Tegze and G. Faigel, Nature 380, 49 (1996); (b) C.S. Fadley and P.M. Len, Nature 380, 27 (1996) and unpublished results; (c) T. Gog, P.M. Len, G. Materlik, G. Bahr, C. Sanchez-Hanke, and C.S. Fadley, Phys. Rev. Letters 76, 3132 (1996); (d) T. Gog, R.-H. Menk, F. Arfelli, P.M. Len, C.S. Fadley, and G. Materlik, Synchrotron Radiation News 9, 30 (1996); (e) P.M. Len, T. Gog, C.S. Fadley, and G. Materlik, Phys. Rev. B 55, February, 1997; (f) P.M. Len, C.S. Fadley, and G. Materlik, Proceedings of the X-96 Conference, Hamburg, September, 1996, AIP Proceedings, to appear., 1997.
25. (a) R.J. Baird, C.S. Fadley, and L.F. Wagner, Phys. Rev. B15, 666 (1977); (b) J. Osterwalder, T. Greber, S. Hüfner, and L. Schlapbach, Phys. Rev. B41, 12495 (1990); S. Hüfner, J. Osterwalder, T. Greber, and L. Schlapbach, Phys. Rev. B42, 7350 (1990); G.S. Herman and C.S. Fadley, Phys. Rev. B43, 6792 (1991); T. Greber, J. Osterwalder, S. Hüfner, and L. Schlapbach, Phys. Rev. B44, 8958 (1991); (c) R. Fasel, P. Aebi, R.G. Agostino, D. Naumovic, J. Osterwalder, A. Santaniello, and L. Schlapbach, Phys. Rev. Letters 76, 4733 (1996).
26. (a) H.C. Galloway, J.J. Benitez, and M. Salmeron, Surf. Sci. 198, 127 (1993) and J. Vac. Sci. Technol. A12, 2302 (1994); (b) ; Y.J. Kim, Ph. D. thesis, University of Hawaii-Manoa, 1995; Y.J. Kim, C. Westphal, R.X. Ynzunza, Z. Wang, H.C. Galloway, M. Salmeron, M.A. Van Hove, and C.S. Fadley, to be published; (c) R. Saiki, A. P. Kaduwela, J. Osterwalder, D.J. Friedman, C. S. Fadley, and C. R. Brundle, Surf. Sci. 282, 33 (1993).
27. (a) C. Günther, J. Vrijmoeth, R.Q. Hwang, and R.J. Behm, Phys. Rev. Lett. 74, 754 (1995); (b) J.C. Hamilton and S.M. Foiles, Phys. Rev. Lett. 75, 882 (1995); (c) S.D. Ruebush, R.E. Couch, S. Thevuthasan, Z. Wang, and C.S. Fadley, Surf. Sci. Lett., to appear.
28. (a) D.M. Riffe, G.K. Wertheim, and P.H. Citrin, Phys. Rev. Lett. 53, 1976 (1989); (b) D. Spanjaard, C. Guillot, M.-C. Desjonquères, G. Treglia, and J. Lecante, Surf. Sci. Repts. 5, 1 (1985); B. Kim, J. Chen, J.L. Erskine, W.N. Mei, and C.M. Wei, Phys. Rev. B48, 4735 (1993).
29. R.X. Ynzunza, F.J. Palomares, E.D. Tober, Z. Wang, H. Daimon, Y. Chen, Z. Hussain, J. Liesegang, M.A. VanHove, and C.S. Fadley. to be published.
30. E. D. Tober, R. X. Ynzunza, F. J. Palomares, Z. Wang, Z. Hussain, M. A. Van Hove, and C. S. Fadley, Phys. Rev. Lett, to appear.
31. N.D. Shinn, B. Kim, A.B. Andrews, J.L. Erskine, K.J. Kim, and T.-H. Kang, Mat. Res. Soc. Symp. Proc. 307, 167 (1993).
32. E.D. Tober, R.X. Ynzunza, C. Westphal, and C.S. Fadley, Phys. Rev. B53, 5444 (1996).
33. (a) G. Schönhense, Physica Scripta T31, 255 (1990); (b) J. Bansmann, Ch. Ostertag, G. Schönhense, F. Fegel, C. Westphal, M. Getzlaff, F. Schafers, and H. Petersen, Phys. Rev. B46, 13496 (1992); (c) G. Schönhense and J. Hormes, in *VUV and Soft X-Ray Photoionization*, U. Becker and D.A. Shirley (Eds.), (Plenum Press, New York, 1996).
34. (a) V. McKoy and J.A. Stephens, private communication; (b) C. Westphal, A.P. Kaduwela, M.A. Van Hove, and C.S. Fadley, Phys. Rev. B50, 6203 (1994).
35. H. Daimon, T. Nakatani, S. Imada, S. Suga, Y. Kagoshima, and T. Miyahara, Jpn. J. Appl. Phys. 32, L1480 (1993); and H. Daimon, private communication.
36. A.P. Kaduwela, H. Xiao, S. Thevuthasan, M.A. Van Hove, and C.S. Fadley, Phys. Rev. B 52, 14297 (1995).
37. H. Daimon, R.X. Ynzunza, F.J. Palomares, E.D. Tober, Z. Wang, Z. Hussain, M.A. Van Hove, and C.S. Fadley, to be published.
38. K.E. Johnson, R.J. Wilson, and S. Chiang, Phys. Rev. Lett. 71, 1055 (1993) and refs. therein.

39. (a) L. Baumgarten, C.M. Schneider, H. Petersen, F. Schafers, and J. Kirschner, Phys. Rev. Lett. 65, 492 (1990); (b) H. Ebert, L. Baumgarten, C.M. Schneider, and J. Kirschner, Phys. Rev. B44, 4406 (1991); (c) G.D. Waddill, J. Tobin, and D.R. Pappas, Phys. Rev. B46, 552 (1992).
40. (a) Ch. Roth, F.U. Hillebrecht, H.B. Rose, and E. Kisker, Phys. Rev. Lett. 70, 3479 (1993); F. Sirotti and G. Rossi, Phys. Rev. B49, 15682 (1994); (b) M. Getzlaff, Ch. Ostertag, G. H. Fecher, N.A. Cherepkov, and G. Schönhense, Phys. Rev. Lett. 73, 3030 (1994); N.A. Cherepkov, Phys. Rev. B50, 13813 (1994); A. Fanelsa, R. Schellenberg, F.U. Hillebrecht, E. Kisker, J.G. Menchero, A.P. Kaduwela, C.S. Fadley, and M.A. Van Hove, Phys. Rev. B54, 17962 (1996).
41. J. Morais, R. Denecke, R. X. Ynzunza, J.G. Menchero, J. Liesegang, J. Kortright, Z. Hussain, and C.S. Fadley, to be published.
42. G. van der Laan, E. Arenholz, E. Navas, A. Bauer, and G. Kaindl, Phys. Rev. B53, R5998 (1996).
43. F.U. Hillebrecht, R. Jungblut, and E. Kisker, Phys. Rev. Lett. 65, 2450 (1990); R. Jungblut, Ch. Roth, F.U. Hillebrecht, and E. Kisker, J. Appl. Phys. 70, 5923 (1991); R. Jungblut, Ch. Roth, F.U. Hillebrecht, and E. Kisker, Surf. Sci. 269/270, 615 (1992); T. Kachel, C. Carbone, and W. Gudat, Phys. Rev. B47, 15391 (1993); D.G. van Campen, R.J. Pouliot and L.E. Klebanoff, Phys. Rev. B48, 17533 (1993); P.D. Johnson, Y. Liu, Z. Xu, and D.J. Huang, J. Electron Spectrosc. 75, 245 (1995).
44. F. Zhang, S. Thevuthasan, R.T. Scalettar, R.R.P.Singh, and C.S. Fadley, Phys. Rev. B51, 12468 (1995).
45. E.D. Tober, F. J. Palomares, R.X. Ynzunza, Z. Wang, Z. Hussain, and C.S. Fadley, to be published.
46. D. Weller, S. F. Alvarado, W. Gudat, K. Scröder, and M. Campagna, Phys. Rev. Lett. 54, 1555 (1985); B. Kim, A. B. Andrews, J. L. Erskine, K. J. Kim, and B. N. Harmon, Phys. Rev. Lett. 68, 1931 (1992); H. Tang, D. Weller, T. G. Walker, J. C. Scott, C. Chapert et al., Phys. Rev. Lett. 71, 444 (1993); C. Rau and M. Robert, Phys. Rev. Lett. 58, 2714 (1987);C. Rau, J. Mag. and Mag. Mat. 31-34, 874 (1983);C. Rau and S. Eichner, Phys. Rev. B34, 6347 (1986) & in *Nuclear Methods in Materials Research*, K. Bethge, H. Burman, H. Jex, and F. Rauch (Eds.), (Viewig, Braunschweig, 1980), p. 354.
47. U. Fano, Phys. Rev. 178, 131 (1969); U. Heinzmann, J. Kessler, and J. Lorenz, Phys. Rev. Lett. 25, 1325 (1970).
48. K. Starke, A.P. Kaduwela, Y. Liu, P.D. Johnson, M.A. Van Hove, C.S. Fadley, V. Chakarian, E.E. Chaban, G. Meigs, and C.T. Chen, Phys. Rev. B53, R10544 (1996).
49. J.G. Tobin, C.D. Waddill, D.P. Pappas, E. Tamura, and P. Sterne, J. Vac. Sci. Tech. A13, 1574 (1995).
50. N.A. Cherepkov, Phys. Lett. A40, 119 (1972) and Adv. At. Mol. Phys. 19, 395 (1983).
51. (a) E.M.E. Timmermans, G.T. Trammell, and J.P. Hannon, Appl Phys. 73, 6183 (1993) and Phys. Rev. Lett. 72, 832 (1994); (b) C.S. Fadley, Mat. Res. Soc. Symp. Proc. 307, 261 (1993) and Surf. Sci. Rep. 19, 231 (1993); (c) A.P. Kaduwela, Z. Wang, M.A. Van Hove, and C.S. Fadley, Phys. Rev. B50, R9656 (1994); (c)Z.Wang, A.P. Kaduwela, S. Thevuthasan, M.A. Van Hove, and C.S. Fadley, to be published.
52. P.M. Len, E. Rotenberg, J.D. Denlinger, B.P. Tonner, S.D. Kevan, M.A. Van Hove, and C.S. Fadley,to be published.
53. W.N. Lipscomb, Acta Crystallographica 2, 193 (1949); J. Karla and H.A. Hauptmann, Acta Crystallographica 3, 18 (1950); K. Hümmer and H. Billy, Acta Crystallographica A38, 841 (1982); S. L. Chang, Phys. Rev. Letters 48, 163 (1982).
54. (a) M.J. Bedyzk and G. Materlik, Physical Review B32, 6456 (1985); (b) J.T. Hutton, G.T. Trammell, and J.P. Hannon, Phys. Rev. B31, 420 (1985), and Phy. Rev.B31, 743 (1985).

55. S. M. Goldberg, R. J. Baird, S. Kono, N. F. T. Hall, and C. S. Fadley, J. Electron Spectrosc. 21, 1 (1980); R. Trehan, C. S. Fadley and J. Osterwalder, J. Electron Spectrosc. 42, 187 (1987).

LBNL-39580

Invited paper appearing in
X-Ray and Inner-Shell Processes: 17th International Conference
R.L. Johnson, H. Schmidt-Boekering, and B.F. Sonntag, Eds.
AIP Conference Proceedings No. 389 (AIP, New York, 1997) pp. 295-319.

Atomic Holography with Electrons and X-rays

P. M. Len[1], C. S. Fadley[1,2], G. Materlik[3]

[1]*Department of Physics, University of California, Davis, CA 95616 USA*

[2]*Materials Sciences Division, Lawrence Berkeley National Laboratory, Berkeley, CA 94720 USA*

[3]*Hamburger Synchrotronstrahlungslabor (HASYLAB) am Deutsches Elektronen-Synchrotron (DESY), 22603 Hamburg, Germany*

Gabor first proposed holography in 1948 as a means to experimentally record the amplitude and phase of scattered wavefronts, relative to a direct unscattered wave, and to use such a "hologram" to directly image atomic structure. But imaging at atomic resolution has not yet been possible in the way he proposed. Much more recently, Szöke in 1986 noted that photoexcited atoms can emit photoelectron or fluorescent x-ray wavefronts that are scattered by neighboring atoms, thus yielding the direct and scattered wavefronts as detected in the far field that can then be interpreted as holographic in nature. By now, several algorithms for directly reconstructing three-dimensional atomic images from electron holograms have been proposed (*e.g.* by Barton) and successfully tested against experiment and theory. Very recently, Tegze and Faigel, and Gog *et al.* have recorded experimental x-ray fluorescence holograms, and these are found to yield atomic images that are more free of the kinds of aberrations caused by the non-ideal emission or scattering of electrons. The basic principles of these holographic atomic imaging methods are reviewed, including illustrative applications of the reconstruction algorithms to both theoretical and experimental electron and x-ray holograms. We also discuss the prospects and limitations of these newly emerging atomic structural probes.

INTRODUCTION

Historical Origin of Atomic Holography

Dennis Gabor first outlined in 1948 a direct experimental method of recording diffraction phases as well as intensities in an effort to surpass the then current resolution and lens aberration limits of electron microscopy and thus achieve atomic-scale image resolution (1). In Gabor's original scheme, an electron

wavefront (of wavenumber k_0 and wavelength λ_0) diverging from a point focus illuminates an object as well as a detector (or image plate) directly. The interference pattern at this detector involves the wavefronts scattered by the object, and explicitly records the phases of these wavefronts relative to the direct or reference wavefront (Fig. 1(a)). This interference "hologram" thus contains spatial information about the scattering object, which can be retrieved as an image in several ways. Gabor suggested that the developed image plate could simply be re-illuminated by a visible light reference wavefront (of wavenumber k *and wavelength* λ), as shown in Fig. 1(b). The wavefronts thus diffracted by the image plate would create a virtual image of the original object visible to the naked eye, and magnified by a factor of k_0/k. But the image reconstruction can also be performed numerically using a Fourier-transform-like integral, as first pointed out by Wolf (2). Holography is now of course widespread in science and technology, with lasers at usually optical wavelengths providing the reference waves. Note that, since the three-dimensional information of the r-space object field $u(\mathbf{r})$ (shown in Fig. 1 as an optical mask of the letter "F") is "encoded" holographically into a single-wavenumber two-dimensional k-space diffraction pattern $\chi(\hat{\mathbf{k}})$, both a real and twin image of the optical mask are retrieved. This is due to the loss of spatial information perpendicular to the plane of the image plate recording the diffraction pattern, and is by now overcome in optical holography by recording a volume of holographic intensities by means of a thick recording medium (3).

Until recently, Gabor's goal of imaging at atomic resolution had not been attained, due to the lack of a source of sufficiently coherent radiation at such short wavelengths. However, in 1986, Szöke observed that there is an atomic-scale analog of Gabor's holographic scheme: photoexcited atoms produce outgoing photoelectron or fluorescent-x-ray wavefronts, which then reach a far field detector either directly, or after scattering by neighboring atoms surrounding the emitter (5). With a sub-Ångström source size and wavelength, scattered wavefront amplitudes and phases from atoms surrounding the emitter can thus be referenced to the directly emitted wavefront, as shown for the case of fluorescence in Fig. 2(a). It was also pointed out a little later by Barton (4a,4b) and subsequently by Tong *et al.* (4c) that, by measuring diffraction patterns at different wavenumbers, three-dimensional spatial information could be completely encoded into a three-dimensional k-space volume of diffraction intensities $\chi(\mathbf{k})$, from which atomic images free of twin-image effects and other aberrations should be directly obtainable.

Two other approaches for obtaining structural information at the atomic scale should also be mentioned, as illustrated in Fig. 3. First, atomic order and electron density maps can be determined by so-called direct methods from the kinematical (single-scattering) diffraction technique, which exploits the translational symmetry (Bragg planes) of a crystal (6) (Fig. 3(a)). The second is the use of multiple, dynamical scattering from single crystals to solve the phase

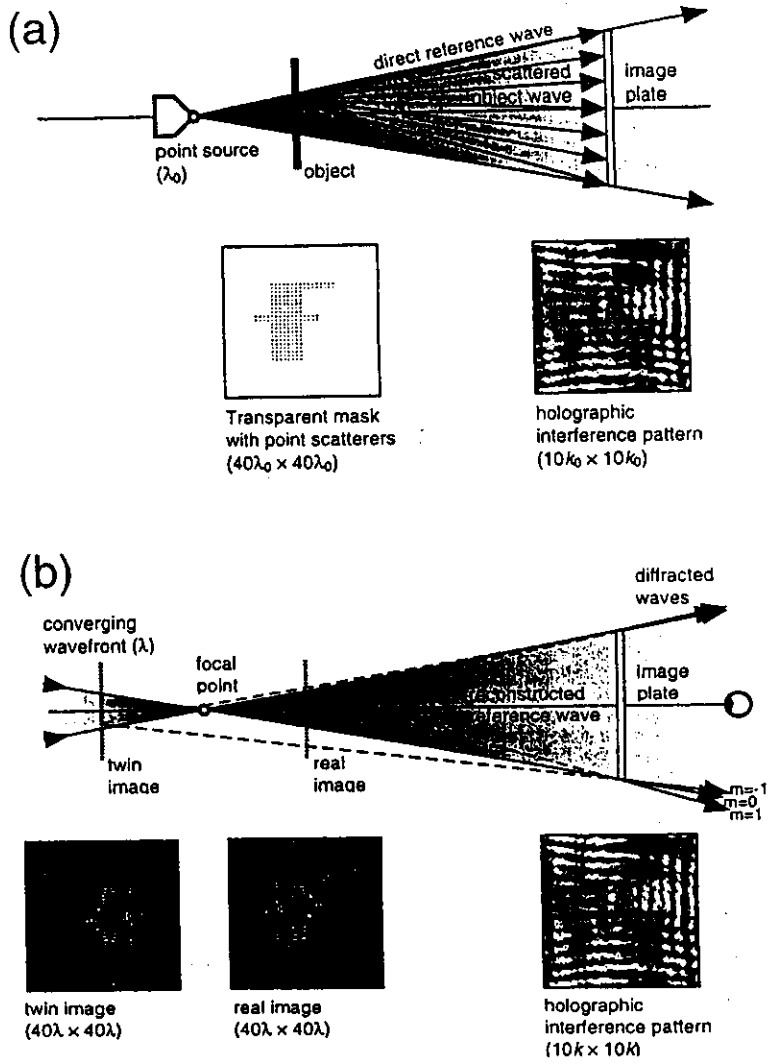

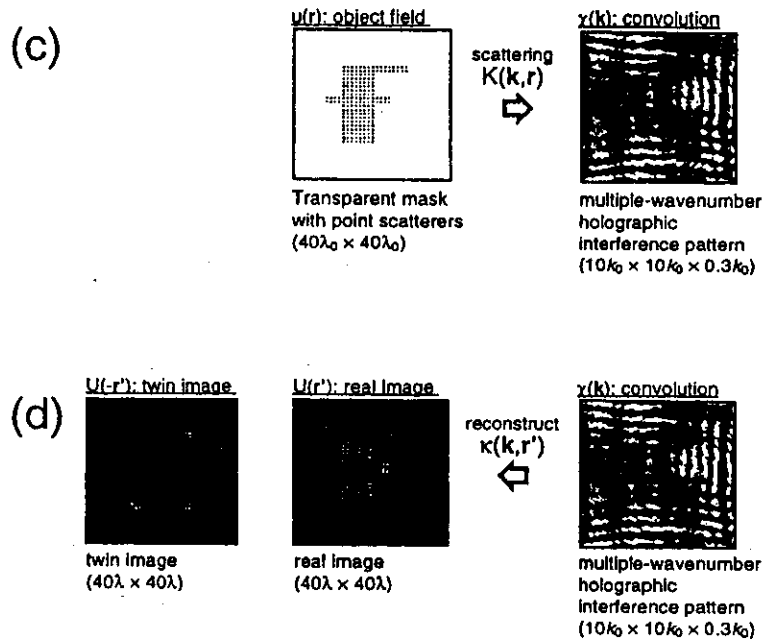

FIGURE 1. (a)-(b) An idealized numerical demonstration of the creation and inversion of single-wavenumber optical Gabor in-line holograms. (a) A point source of coherent radiation at the origin illuminates a transparent mask with point scatterers creating the letter "F" at r, as well as an image plate. This image plate is then exposed by a direct wavefront, as well as by the wavefronts scattered by the mask, which produces a holographic interference pattern. (b) The developed image plate is later re-illuminated by a reference wavefront. The wavefronts diffracted by the image plate produce a virtual (real) image of the mask at r, and a virtual conjugate twin image at the inverse position -r. (c)-(d) An analogous demonstration of the creation and inversion of optical multiple-wavenumber holograms. (c) A multiple-wavenumber normalized $\chi(k)$ hologram data set (of which one wavenumber is shown) is calculated from the object field $u(r)$ by means of an r-space convolution, using a kernel $K(k,r)$ that describes the emission and scattering physics involved (here, optical scattering in the far field regime). (d) The object field $u(r)$ is recovered as an image intensity $U(r')$ by a k-space deconvolution of $\chi(k)$, using a kernel $\kappa(k,r')$ that is sufficiently orthogonal to $K(k,r)$. Note that the conjugate twin image $U(r = -r')$ has been suppressed, due to the volume of k-space enclosed in the multiple-wavenumber $\chi(k)$ considered here.

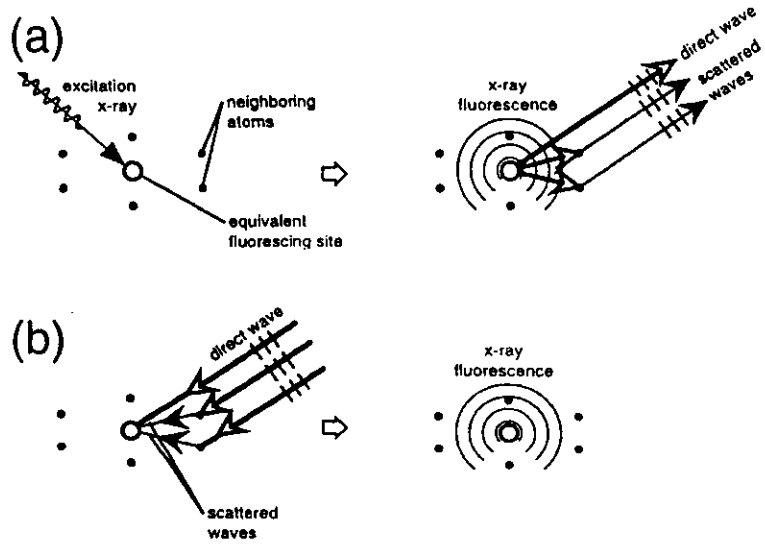

FIGURE 2. Atomic-scale analogs of Gabor holography. (a) The first scheme suggested by Szöke (5), in which an excitation x-ray first creates an inner-shell hole in one of many equivalent fluorescing atoms, and this atom then emits fluorescent x-ray (or electron) wavefronts that illuminate neighboring atoms, as well as a far field detector. This detector senses the interference between the direct wavefront and wavefronts scattered by the neighboring atoms. Moving the detector over a large solid-angle range builds up a holographic interference pattern. (b) The time-reversed case of (a) as suggested by Gog *et al.* (15), where a coherent far field excitation x-ray illuminates and photoexcites an emitter, and also illuminates and is scattered from atoms neighboring the emitter. The emitting atom senses the interference between the direct wavefront and wavefronts elastically scattered by the neighboring atoms. The net photoexcitation is then detected by a stationary, large solid-angle detector. Moving the far field source over a large solid-angle range builds up a holographic interference pattern. In both (a) and (b), atomic images can be reconstructed numerically.

problem of crystallography (7-9), either via Kossel lines (Fig. 3(b)) (10) or standing-wave methods (Fig. 3(c)) (11). The holographic approach is different from these two methods in that it uses the interference pattern which results from the direct unscattered wavefront emitted by a source atom, and the wavefronts which have been singly scattered from neighboring atoms. This does not require translational order (only rotational alignment) between the atomic neighborhoods to be imaged.

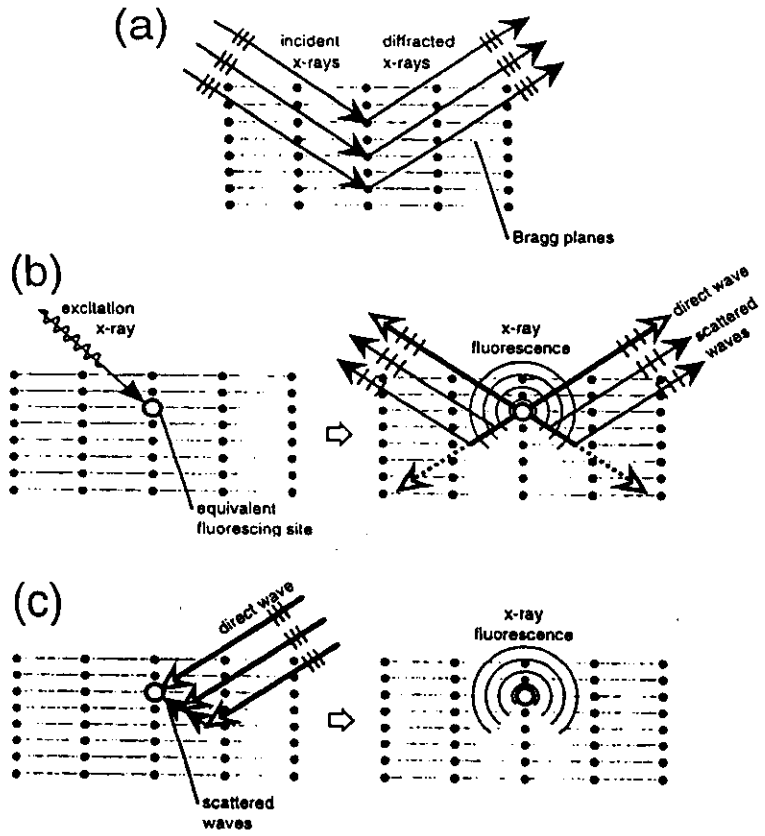

FIGURE 3. Diffraction probes of atomic structure related to atomic holography. (a) Conventional x-ray crystallography, where x-rays are diffracted by Bragg planes of atoms. Diffraction phases are determined by the simultaneous analysis of many Bragg intensities and other methods. (b) Kossel patterns (or Kikuchi bands, for the case of electrons). Fluorescent x-rays (or electrons) from a photoexcited emitter are diffracted by Bragg planes of atoms. Diffraction phases are thus here directly referenced to the unscattered portion of the fluorescence. (c) X-ray standing waves. This is the optical reciprocal of (b), where a coherent plane wave illuminates a fluorescing atom either directly, or after being scattered by Bragg planes of atoms. The interference between these wavefronts determines the amount of fluorescence by the emitter. Note that in all these above cases, the structure to be determined must have long-range atomic order, in contrast to the methods illustrated in Fig. 2.

Basic Principles of Atomic Holography

The process by which three-dimensional atomic image intensities are numerically reconstructed is to first measure the intensity $I(\mathbf{k})$ from a localized source over some range of directions $\hat{\mathbf{k}} = \mathbf{k}/k$ and perhaps also some range of wavenumbers k. Normalized holographic intensities $\chi(\mathbf{k})$ are then derived from either $[I(\mathbf{k})-I_0(\mathbf{k})]/\sqrt{I_0(\mathbf{k})}$ or $[I(\mathbf{k})-I_0(\mathbf{k})]/I_0(\mathbf{k})$, where $I(\mathbf{k})$ is the raw measured intensity, and $I_0(\mathbf{k})$ is the intensity that would be measured in the absence of atomic scattering; that is, $I_0(\mathbf{k})$ is the unperturbed intensity of the reference wave. The overall imaging process can be understood by first considering the hologram to be a convolution of the r-space object field $u(\mathbf{r})$:

$$\chi(\mathbf{k}) = \iiint_R d^3\mathbf{r}\cdot K(\mathbf{k},\mathbf{r})u(\mathbf{r}) + \iiint_R d^3\mathbf{r}\cdot K^*(\mathbf{k},\mathbf{r})u^*(\mathbf{r}), \tag{1}$$

where the convolution kernel $K(\mathbf{k},\mathbf{r})$ somehow describes the physics of the emission and atomic scattering of the photoexcited wavefronts, and R denotes the volume in real space over which the object exists. This produces a three-dimensional $\chi(\mathbf{k})$ volume in k-space, so as to completely encode three-dimensional spatial information of the object field $u(\mathbf{r})$. The reconstruction algorithm is then most simply a k-space deconvolution of $\chi(\mathbf{k})$ to obtain a real-space $U(\mathbf{r}')$ image intensity:

$$U(\mathbf{r}') = \iiint_K d^3\mathbf{k}\cdot\kappa^*(\mathbf{k},\mathbf{r}')\chi(\mathbf{k}), \tag{2}$$

where the reconstruction kernel $\kappa(\mathbf{k},\mathbf{r}')$ has been chosen to be orthogonal to the scattering kernel $K(\mathbf{k},\mathbf{r})$, as integrated over a sufficiently large k-space volume, that is, so that:

$$\begin{aligned} &\iiint_K d^3\mathbf{k}\cdot\kappa^*(\mathbf{k},\mathbf{r}')K(\mathbf{k},\mathbf{r}) \propto \delta(\mathbf{r}-\mathbf{r}'), \\ &\iiint_K d^3\mathbf{k}\cdot\kappa^*(\mathbf{k},\mathbf{r}')K^*(\mathbf{k},\mathbf{r}) \approx 0 \end{aligned} \tag{3}$$

If such a $\kappa(\mathbf{k},\mathbf{r}')$ can be found, then the object field $u(\mathbf{r})$ can thus be recovered as the image intensity $U(\mathbf{r}')$ from Eqs. (1)-(3):

$$\begin{aligned} U(\mathbf{r}') &= \iiint_R d^3\mathbf{r}\cdot\left[u(\mathbf{r})\iiint_K d^3\mathbf{k}\cdot\kappa^*(\mathbf{k},\mathbf{r}')K(\mathbf{k},\mathbf{r}) + u^*(\mathbf{r})\iiint_K d^3\mathbf{k}\cdot\kappa^*(\mathbf{k},\mathbf{r}')K^*(\mathbf{k},\mathbf{r})\right] \\ &= \iiint_R d^3\mathbf{r}'\,u(\mathbf{r})\delta(\mathbf{r}-\mathbf{r}') \\ &= u(\mathbf{r}'). \end{aligned} \tag{4}$$

So once the emission and scattering process that creates $\chi(\mathbf{k})$ can be sufficiently modeled by a $K(\mathbf{k},\mathbf{r})$ convolution kernel, then a deconvolution kernel $\kappa(\mathbf{k},\mathbf{r}')$ can in principle be formulated so as to directly reconstruct atomic images using Eq. (2).

Atomic Holography Reconstruction

The basic algorithms used in reconstructing atomic holographic images can be understood in the context of a single scattering (or kinematical) model of the scattering process. We consider e^{-ikr}/kr to represent the photoexcited electron or x-ray spherical wavefront that illuminates the (point-like) scattering atoms surrounding the emitter (with the emitted wave assumed to be isotropic for simplicity), $f(\Theta_r^k)$ to be the complex plane-wave atomic scattering factor ($\equiv |f(\Theta_r^k)|\exp[i\psi(\Theta_r^k)]$), where Θ_r^k is the scattering angle, and $\mathbf{k}\cdot\mathbf{r}$ is the phase of the scattered portion of this wavefront as it reaches the far field detector (Fig. 4). Thus the total geometrical path-length phase difference between the reference and scattered wavefronts is ($\mathbf{k}\cdot\mathbf{r}$ - kr). The convolution kernel for this scattering process can then be expressed as:

$$K(\mathbf{k},\mathbf{r}) = \frac{f(\Theta_r^k)}{kr} e^{i(\mathbf{k}\cdot\mathbf{r}-kr)}. \tag{5}$$

This choice for $K(\mathbf{k},\mathbf{r})$ does not include any allowance for anisotropy in magnitude or phase of the outgoing reference wave, which for the simple example of *s*-level photoemission, takes the form of an additional factor of $\boldsymbol{\varepsilon}\cdot\mathbf{k}$, where $\boldsymbol{\varepsilon}$ is the polarization vector of the radiation (12). Thus, in photoemission, reference wave anisotropy is almost always present. However, for the case of Kα x-ray fluorescence to be considered below, the outgoing reference wave should be isotropic *and* randomly polarized, and thus be well described by Eq. (5).

Another advantage of x-rays lies in the nature of $f(\Theta_r^k)$. Figure 5 shows the magnitudes and phases of Ni atomic scattering factors for both x-rays and electrons with wavelength $\lambda = 0.79$Å (or wavenumber $k = 8.0$Å^{-1}). Note that the x-ray scattering factors (Fig. 5(a)) are much weaker (by ~1/2000) and more nearly constant in magnitude than those for electrons (Fig. 5(b)), and that the scattering phase shifts for x-rays are also much smaller (by ~1/100) and more nearly constant than those for electrons. Thus, for x-rays $|f(\Theta_r^k)| \approx$ constant $= f_0$, and $\psi(\Theta_r^k) \approx \psi_0 \approx 0$, such that the simplest possible optical scattering kernel results: $K_O(\mathbf{k},\mathbf{r}) \propto e^{i(\mathbf{k}\cdot\mathbf{r}-kr)}$. The reconstruction kernel that is most simply orthogonal to this optical scattering kernel is thus $\kappa_O(\mathbf{k},\mathbf{r}') \equiv e^{i(\mathbf{k}\cdot\mathbf{r}'-kr')}$, as first suggested by Barton and Terminello (4b). Thus for the scattering of fluorescent x-rays, the

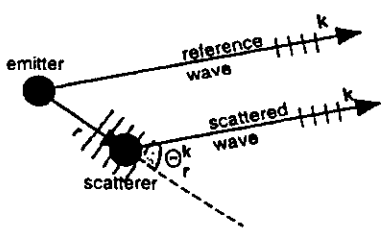

FIGURE 4. Scattering geometry between a photoemitter and a neighboring scattering atom. The photoemitter is placed at the origin, while the scatterer is located at the relative position r. The far field detector lies in the direction k. The portion of the direct wavefront that is scattered by the neighboring atom into the detector at r depends on the scattering angle Θ_r^k between r and k according to the complex phase factor $f(\Theta_r^k)$.

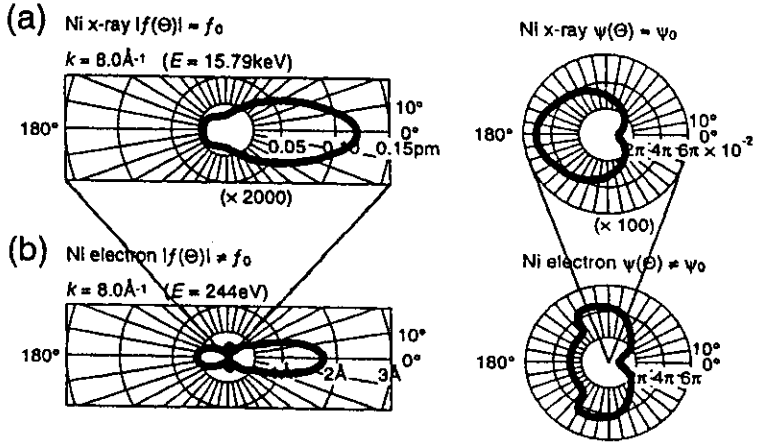

FIGURE 5. Ni scattering factor magnitudes ($|f(\Theta_r^k)|$) and phases ($\psi(\Theta_r^k)$), as a function of scattering angle Θ_r^k for (a) $k = 8.0$ Å^{-1} ($E = 15.79$keV) x-rays. (b) $k = 8.0$ Å^{-1} ($E = 244$eV) electrons. $\Theta_r^k = 0°$ is the forward scattering direction, $\Theta_r^k = 180°$ is the backscattering direction.

reconstruction algorithm of Eq. (2) becomes to a good approximation:

$$U(\mathbf{r}') = \iiint_K d^3\mathbf{k}\cdot e^{-i(\mathbf{k}\cdot\mathbf{r}-kr')}\chi(\mathbf{k}). \tag{6}$$

This simple optical reconstruction algorithm has been used recently to obtain direct atomic images from experimental single-wavenumber (13,14) and multiple-

wavenumber (15,16) x-ray holographic data sets, as discussed further below.

For example, Fig. 1(c) schematically shows the optical holographic $\chi(\mathbf{k})$ intensities that were numerically calculated from the transparent "F" mask using Eqs. (1) and (5), over a range of different directions ($\hat{\mathbf{k}}$) and wavenumbers (k). Figure 1(d) shows the numerically reconstructed real and twin images obtained from the volume $\chi(\mathbf{k})$ of Fig. 1(c). Due to the three-dimensional spatial information that was encoded in the k-space volume encompassed by $\chi(\mathbf{k})$, the reconstruction algorithm of Eq. (6) suppresses the spurious twin image, while increasing the fidelity of the desired real image (*cf.* Fig. 1(b)).

The optical reconstruction algorithm of Eq. (6) was in fact first used to reconstruct data from electron holographic data sets, *e.g.* from photoelectron diffraction (17-21). However, because of the generally anisotropic nature of the photoemitted source wave, and the strong, non-optical and often multiple nature of electron scattering, the single-scattering optical convolution kernel $K_o(\mathbf{k},\mathbf{r}') \propto e^{i(\mathbf{k}\cdot\mathbf{r}'-kr')}$ does not accurately describe the process by which electron holograms are produced, and consequently the optical reconstruction kernel $\kappa_o(\mathbf{k},\mathbf{r}') = e^{-i(\mathbf{k}\cdot\mathbf{r}'-kr')}$ will not in general satisfy the orthogonality condition (Eq. (3)) for electrons. Thus Eq. (6), when applied to electron holograms, often results in images which suffer from aberrations and position shifts (22-24). Nonetheless, useful atomic structure information has been derived from electron holography, with various modifications to the basic optical reconstruction kernel $\kappa_o(\mathbf{k},\mathbf{r}')$, and to the definition of the reconstruction integral (Eq. (2)) itself being proposed (25-29), and comparative reviews of different methods appearing elsewhere (30,31).

In summary, the atomic scattering of x-rays is much more nearly ideal than that of electrons, and this suggests that a simple optical reconstruction kernel as in Eq. (6) can be straightforwardly used to directly obtain atomic images from holographic x-ray intensities. However, more sophisticated reconstruction kernels and deconvolution integrals will probably be necessary to account for the non-ideal nature of the propagation and scattering of electrons, in order to successfully obtain the most accurate atomic images from holographic electron intensities, as discussed elsewhere (25-31).

ATOMIC ELECTRON HOLOGRAPHY

In this section, we discuss the results of applying the imaging algorithm of Eq. (6) to experimental and theoretical photoelectron diffraction results for W 4*f* emission from the surface atoms of clean W(110), with the experimental data being obtained by Denlinger, Rotenberg, and co-workers at Beamline 7.0 of the Advanced Light Source at the Lawrence Berkeley National Laboratory (31). The 4*f* photoelectron peak (which contains *d* and *g* components due to the dipole selection rule) can be resolved into bulk and surface core-level-shifted components, of which atomic images reconstructed from only surface photoemission will be considered here. Photoelectron spectra were measured for kinetic energies of E = 41eV to 197eV (wavenumbers k = 3.3Å^{-1} to 7.2Å^{-1}), and collected over a polar takeoff angle range of $14° \le \theta \le 90°$ ≡ normal emission. These data points were measured at wavenumber intervals corresponding to δk = 0.1Å^{-1}, and angular intervals of $(\delta\theta,\delta\phi) = (3°, 3°\cos\theta)$ corresponding roughly to equal solid angle elements, making a total of 12,280 unique measurements in a symmetry-reduced 1/4th of the total solid-angle above the sample. For each different wavenumber and direction, the W 4*f* peak was resolved into bulk and surface emission components by integrating the areas under the lower and higher flanks of the bulk and surface W 4*f* peaks, respectively, as shown in Fig. 6(a). Figures 6(b)-(c) show the bulk and surface $I(\mathbf{k})$ data sets in k-space, respectively, as viewed down along $[\bar{1}\,\bar{1}\,0]$. Data points in the lower right quadrant have been cut away to reveal the intensities $I(\mathbf{k})$ for the minimum k = 3.3Å^{-1}; the other quadrants show the intensities $I(\mathbf{k})$ for the maximum k = 7.2Å^{-1}. The dark bands at the perimeter indicate the locations in k-space on these iso-wavenumber surfaces where data was not collected. Due to the strong atomic scattering of electrons, the anisotropy of the raw $I(\mathbf{k})$ data, which we measure as $\Delta I / I_0 \equiv (I_{max} - I_{min}) / I_0$, is found to be ≈ 30%, and is easily discernible with this gray scale.

In order to determine the normalized $\chi(\mathbf{k})$ from the raw $I(\mathbf{k})$ intensities of Figs. 6(b)-(c), $I_0(\mathbf{k})$ was determined by fitting a low order polynomial in wavenumber k and polar angle θ to $I(\mathbf{k})$:

$$I_0(\mathbf{k}) = a_{00} + \sum_{m=1}^{3}\sum_{n=1}^{3} a_{mn} k^m \cos[(2n-1)\theta], \qquad (11)$$

where the coefficients a_{mn} are determined by a least-squares fit to $I(\mathbf{k})$. This is in contrast to previous more approximate methods for determining $I_0(\mathbf{k})$ where simple linear, low-order polynomial, or spline fits were separately made for each set of different wavenumbers along a given direction: $I_k(\hat{\mathbf{k}})$, or each set of different directions at a given wavenumber: $I_{\hat{\mathbf{k}}}(k)$. Such separate normalizations within each scanned-wavenumber or scanned-angle set of data points in $I(\mathbf{k})$ arose from the historical development of electron holography, in which data tended to be collected with k-space resolution that was either fine-in-direction/coarse-in-wavenumber or coarse-in-direction/fine-in-wavenumber (30,31). There has in fact been a recent proposal to consider these k-space sampling choices as distinct atomic structure probes (17(e)), but these choices simply represent extremes of a continuous range of k-space sampling, of which the optimal choice has been shown to be in the intermediate range of roughly equally resolved direction and wavenumber data steps (30). Thus, this distinction (17(e)) is artificial, and not

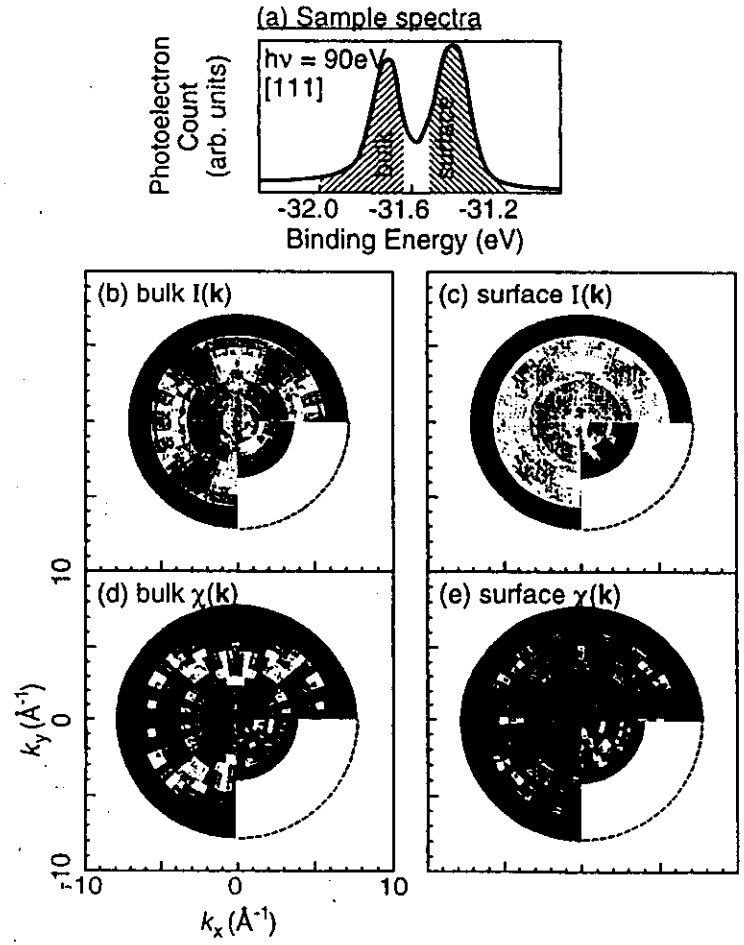

FIGURE 6. (a) Example W $4f_{7/2}$ photoelectron spectrum from clean W(110), with the bulk and surface emitter contributions used to generate the I(k) intensity data points of (b)-(c) shaded in. (b)-(c) Schematic k-space representations of the raw I(k) intensity data sets for bulk and surface W $4f_{7/2}$ emission, respectively. (d)-(e). Normalized bulk and surface emission χ(k) data sets, respectively, corrected for the unscattered intensity I_0 (as derived from Eq. (11)) and an inner potential of V_0 = 14V.

consistent with the optimal use of the holographic methodology. As a consequence, the normalization of I(k) intensities should ideally be made via the determination of a general wavenumber and direction dependent I_0(k) background, as done here, rather than determined separately for each wavenumber or direction in the I(k) data set.

Figures 6(d)-(e) show the normalized bulk and surface χ(k) functions obtained from the raw I(k) intensities of Figs. 7(b)-(c), using the wavenumber and angle fit I_0(k) of Eq. (11), and after correcting for an inner potential of V_0 = 14V (32) to yield electron wavenumbers and directions beneath the surface of the sample. These data points were then remapped to a δk = 0.1Å^{-1}, and $(\delta\theta,\delta\phi)$ = (5°,5°) grid over the range k = 3.85Å^{-1} to 7.45Å^{-1} (E = 56eV to 211eV), and 40° ≤ θ ≤ 90° range, for a final total of 6,697 unique intensities in the symmetry-reduced 1/4th of the solid angle above the sample.

For comparison, single-scattering and multiple-scattering models were used to calculate the surface emission I(k) from a theoretical W(110) cluster (33). These theoretical photoemission intensities were then also normalized using Eq. (11).

Figure 7 shows the reconstructed images in the vertical $(\bar{1}1\bar{2})$ plane obtained from applying the optical reconstruction kernel of Eq. (6) to: (a) the experimental surface emission χ(k) of Fig. 6(e); (b) the theoretical single-scattering χ(k); and (c) the theoretical multiple-scattering χ(k). The expected atomic image resolution for this wavenumber and angular range of χ(k) in the horizontal $[\bar{1}11]$ direction is given by $\delta x \approx \pi/\Delta k_x \equiv \pi/(2k_{max}sin(\theta_{max}-\theta_{min})) \approx 0.3$Å, and in the vertical [110] direction is given by $\delta z \approx \pi/\Delta k_z \equiv \pi/(k_{max}-k_{min}\cos(\theta_{max}-\theta_{min})) \approx 0.6$Å (34), and these numbers are comparable to the actual atomic image resolutions in Fig. 7. As noted above, Eq. (6) makes no special effort to suppress aberrations due to the non-optical nature of the electron scattering process. In all of these images, the $\bar{1}\bar{1}0$ backscattering atom and the $\frac{1\bar{1}\bar{1}}{2\,2\,2}$ and $\frac{\bar{1}1\,1}{2\,2\,2}$ side scattering atoms are well-resolved, with experiment and the more accurate multiple-scattering theory showing the sharpest features for the backscattering atoms. In the experimental image of Fig. 7(a), the $\frac{1\bar{1}\bar{1}}{2\,2\,2}$ and $\frac{\bar{1}1\,1}{2\,2\,2}$ atoms are shifted in toward the emitter (by ≈ 0.7Å), and downward from the z = 0Å surface (by ≈ 0.2Å), this is probably primarily due to anisotropies in the photoemitted source wave and the atomic scattering factor for such side-scattering directions. As expected, the backscattering $\bar{1}\bar{1}0$ atom is better resolved due to the more ideal nature of electron backscattering (*cf.* Fig. 5), with no significant position shift. The experimental backscattering image is also less intense (≈50%) than the side scattering atomic images; and image intensities above and below z = -3.5Å have been scaled accordingly. This difference in relative image intensity is qualitatively expected due to the longer inelastic attenuation path of the wavefront that illuminates, and is subsequently scattered by, the backscattering atom, as compared to the wavefront paths that involve the side scattering atoms. Despite these

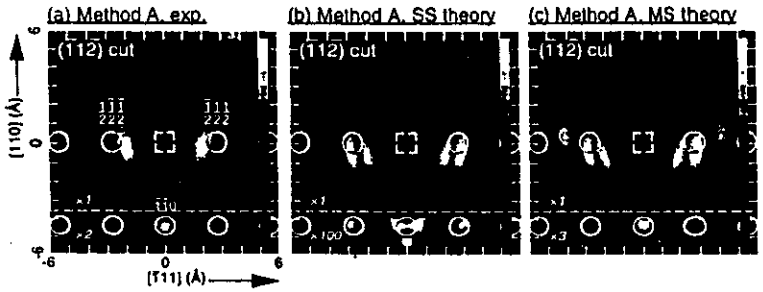

FIGURE 7. (a) W(110) atomic images obtained in the vertical $(\bar{1}1\bar{2})$ plane from experimental and theoretical W $4f_{7/2}$ surface emission $\chi(k)$ data sets, via (Eq. (6)). The surface emitter site is indicated by the dashed square, and the positions of the scatterers (assuming no surface relaxation) are indicated by circles. The nearest and next-nearest scattering positions have been labeled. Axes are marked off in 1Å units. Image intensities for $z \leq -3.5$Å have been rescaled, with the scale factors indicated on the figures. (a) Images reconstructed from the experimental $\chi(k)$ data set of Fig. 6(e). (b) Images reconstructed from a theoretical single scattering $\chi(k)$ data set. (c). Images reconstructed from a theoretical multiple scattering $\chi(k)$ data set.

position shifts and aberrations, this atomic image overall gives good *ab initio* estimates of the positions of the atoms surrounding the surface W(110) emitter, which could then be refined *e.g.*, using *R*-factor comparisons of experiment with model diffraction calculations for various structures.

The single and multiple scattering images of Figs. 7(b)-(c) are similar to experiment in that the $\frac{1}{2}\frac{1}{2}\frac{1}{2}$ and $\frac{\bar{1}}{2}\frac{1}{2}\frac{1}{2}$ side scatterers exhibit side lobes which are shifted in towards the emitter, and downward from the surface. However, the side scattering atomic images of Figs. 7(b)-(c) differ from those of Fig. 7(a) in that the theoretical image peaks are split. This splitting may be due to a number of reasons, among them the differences between the theoretical and actual wavenumber-dependent photoexcitation cross-sections, photoemitted source wave angular distributions, and atomic scattering factors. Still, these single- and multiple-scattering models produce other image features that rather closely match the experimental image of Fig. 7(a), even including the faint aberrations seen at $(x,z) \approx (\pm 4\text{Å}, 0\text{Å})$. The most marked difference between the experimental image of Fig. 7(a) and the single-scattering image of Fig. 7(b) is the triply-split backscattering $\bar{1}\,\bar{1}\,0$ atom in the latter, which is also very much weaker in intensity ($\approx$ 1%) relative to the $\frac{1}{2}\frac{1}{2}\frac{1}{2}$ and $\frac{\bar{1}}{2}\frac{1}{2}\frac{1}{2}$ image peaks. This is mainly due to the oversimplification of the single-scattering model, as seen by comparing Figs. 7(b) and (c). Note that in the multiple-scattering image of Fig. 7(c), the backscattering $\bar{1}\,\bar{1}\,0$ peak intensity relative to the side scattering $\frac{1}{2}\frac{1}{2}\frac{1}{2}$ and $\frac{\bar{1}}{2}\frac{1}{2}\frac{1}{2}$ image peaks ($\approx$ 33%) is more nearly that of Fig. 7(a) ($\approx$ 50%). This dramatic difference between single and multiple scattering can arise because each of the atoms in the multiple-scattering model becomes a secondary emitter, which can then illuminate the atoms surrounding them, especially the atom located at the $\bar{1}\,\bar{1}\,0$ relative position. In this way more scattering events contribute to the backscattering signal in the resulting holographic $\chi(k)$ intensities, and as such the reconstructed $\bar{1}\,\bar{1}\,0$ atomic intensity is much stronger for the image reconstructed from the multiple-scattering model than that from the single-scattering model. Thus, the closer match between Fig. 7(c) and the experimental image of Fig. 7(a) graphically illustrates that multiple-scattering more accurately describes the nature of the creation of the experimental holographic photoelectron intensities $I(k)$.

Atomic electron holography has been extensively tested on both bulk and surface structures, with some notable successes to date being the determination of structures of adsorbate overlayers (17c,19a,20a,27b-c,) and reconstructed surface structures (17e,19b). This technique is most useful in that initial atomic position estimates can be determined, which can then be refined using a more standard comparison of experiment and theory. Further improvements of image quality in atomic electron holography will lie primarily in the refinement of reconstruction kernels and algorithms that more accurately account for the non-ideal atomic scattering and propagation of electron wavefronts, as well as the wavenumber dependences and anisotropies in the source wave. Other holographic experiments that await implementation in the near future are the monitoring of temperature and coverage dependent structural phase changes; and spin-polarized photoelectron holography (SPPH) (35), where spin-specific photoemission (or detection) could be exploited to yield images of local atomic spin order.

ATOMIC X-RAY HOLOGRAPHY

In this section we review two experimental techniques for acquiring holographic x-ray data, and show the results of imaging experimental and theoretical x-ray holographic data sets involving both single and multiple wavenumbers.

The first atomic x-ray holographic images were recently obtained using what can be termed *x-ray fluorescence holography (XFH)*, as shown in Fig. 2(a). In this work, Tegze and Faigel (13) measured the hologram by monitoring the single-wavenumber Sr Kα emission ($k = 7.145\text{Å}^{-1}$, $E = 14.10$keV) from a single crystal of $SrTiO_3$. 2,402 intensities were measured over a full cone of 60° half angle above the surface. The final hologram was found to have anisotropies in intensity

of $\Delta I / I_0 \approx 0.3\%$. These much smaller effects mean that more demanding detector counting statistics are required in x-ray holographic measurements than with comparable atomic electron holography measurements. The reconstruction of this hologram via the optical kernel algorithm of Eq. (6) yields images of the Sr atoms only, as the much weaker scattering strength of the Ti and O atoms renders their images invisible compared to those of the Sr atoms. Figure 8(a) shows the experimental image reconstructed in the (010) plane (36), and it is compared in Fig. 8(b) to an image reconstructed from a theoretical $\chi(k)$ for Sr Kα emission from a simple-cubic Sr cluster of 27 atoms (14). The expected atomic image resolutions at this hologram wavenumber and angular range are $\delta x \approx 0.3$Å in the horizontal [100] direction, and $\delta z \approx 0.9$Å in the vertical [001] direction (34), and are roughly comparable to the atomic images of Figs. 8(a)-(b).

Reconstructing three-dimensional atomic images from a single-wavenumber hologram yields twin images. In any structure with inversion symmetry, these twins can overlap with real atomic images so as to confuse structural interpretation (37,38). In addition, the real and twin atomic images for a particular wavenumber and system can overlap completely out of phase, leading to an artificial suppression of atomic image intensities (37,38). It is thus advantageous to reconstruct direct atomic images from multiple-wavenumber $\chi(k)$ data sets so as to avoid such real-twin image overlaps (4a,4b,38). However, such XFH holograms cannot be measured at arbitrary wavenumbers, with the latter being limited by the intensity and number of fluorescence lines of the photoemitting species (38,39).

Another method for obtaining x-ray holographic information at conveniently chosen multiple wavenumbers has also very recently been demonstrated for the first time by Gog *et al.* (15,16), and its basic principle is illustrated in Fig. 2(b). This method has been termed *multiple energy x-ray holography* (MEXH). MEXH is the time-reversed version of the conventional geometry of XFH (Fig. 2(a)), in that the wave motions are reversed, and the emitter and detector positions are interchanged (Fig. 2(b)) (15,16,39,40). The exciting external x-ray beam now produces the reference and object waves, and the fluorescent atom acts only to detect the interference between the direct and scattered wavefronts in the near field. The emitted x-rays are now collected by a distant detector with a large acceptance solid angle, in principle yielding much higher effective counting rates. The far field source wave can be set to any wavenumber (energy) above the fluorescence edge of the emitting species. thus permitting holograms at multiple wavenumbers and yielding in principle atomic images with no real-twin image overlaps (15,16,39). Specifically, multiple-wavenumber x-ray holograms have been measured to date for hematite ($\alpha - Fe_2O_3(001)$) (15,40), and for Ge(001) (16).

We show the results of applying the optical kernel algorithm of Eq. (6) to experimental and theoretical MEXH data for $\alpha - Fe_2O_3(001)$ as measured by Gog and co-workers on Beamline X-14A of the National Synchrotron Light

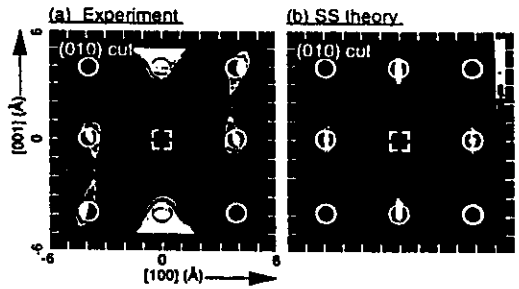

FIGURE 8. X-ray fluorescence holography atomic images of $SrTiO_3$ in the vertical (010) plane, obtained from (a) experimental (13) and (b) theoretical (14) Sr Kα $\chi(k)$ data sets, via Eq. (6). The Sr emitter site is indicated by the dashed square, and nearest-neighbor and next-nearest-neighbor Sr scatterers are indicated by circles. Axes are marked off in 1Å units.

Source at Brookhaven National Laboratory (15,40). Fe Kα fluorescence was excited by horizontally polarized radiation in the range $k = 4.561$Å^{-1} to 5.220Å^{-1} ($E = 9.00$keV to 10.30keV) that was incident on the $\alpha - Fe_2O_3(001)$ sample surface over a polar angle range of $60° \le \theta \le 90°$ = surface normal. These data points were measured at three wavenumbers with intervals of $\delta k = 0.329$Å^{-1} ($\delta E = 650$eV), and at angular intervals of $(\delta\theta, \delta\phi) = (5°, 5°)$, making a total of 435 unique measurements in a symmetry-reduced 1/3rd of the total solid-angle above the sample. Figure 9(a) illustrates the orientation of the sample with respect to the horizontal ($\hat{\epsilon}_1$) polarization vector, with the vertical ($\hat{\epsilon}_2$) polarization vector shown also to permit discussing other possible experimental geometries. Figure 9(b) shows the raw measured $I(k)$ data set in k-space, as viewed down along $[00\bar{1}]$, in the same format as Figs. 6(b)-(d). Data points in the fourth quadrant have been cut away to reveal the $k = 4.561$Å^{-1} $I(k)$ intensities, while the other quadrants show the $k = 5.220$Å^{-1} $I(k)$ intensities. Note that the much weaker atomic scattering of x-rays renders the anisotropy of the raw $I(k)$ data ($\Delta I / I_0 \approx 0.5\%$) barely discernible with this linear gray scale.

Due to the limited wavenumber range of this $I(k)$ data set, a separate $I_0(k)$ was determined for each of the three different wavenumber holograms via a low-pass filter (34), thereby including in $I_0(k)$ the reference wave, as well as corrections for the effects of x-ray absorption during both excitation and emission. Figure 9(c) shows the normalized $\chi(k)$ obtained by this method from the raw $I(k)$ intensities of Fig. 9(b).

For comparison to the experimental results, a single-scattering model (38,41)

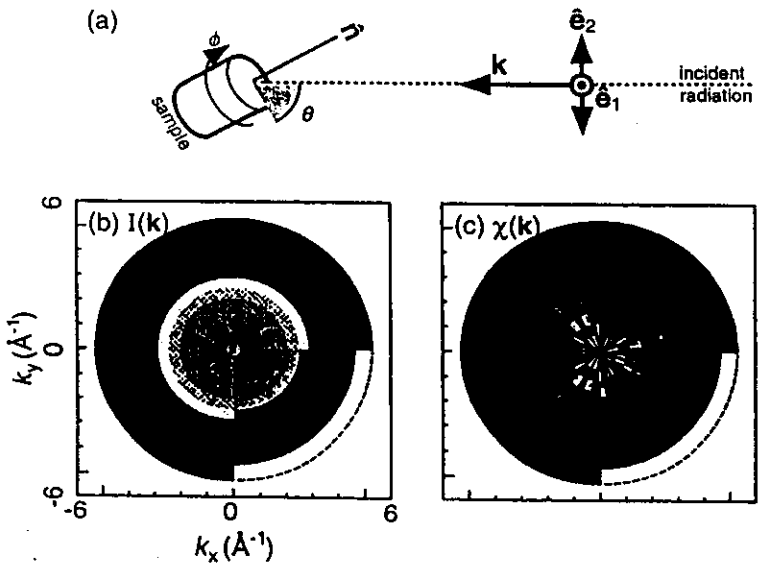

FIGURE 9. (a) Orientation of the sample (where $\hat{n}$ is the surface normal) with respect to the horizontal ($\hat{e}_1$) and vertical ($\hat{e}_2$) polarization vectors of the incident radiation k. (b) Schematic k-space representation of the raw measured $I(k)$ intensity data set for Fe Kα fluorescence from α-Fe_2O_3(001) excited by horizontally polarized radiation. (c) The normalized χ(k) data set. The format is the same as Figs. 6(b)-(d).

was used to calculate a theoretical χ(k) from an ideal $\alpha - Fe_2O_3(001)$ cluster containing 384 Fe atoms with two inequivalent Fe emitter sites as appropriate to the hematite lattice. The O atoms were not included due to their much smaller scattering power (15). The incident radiation in this model calculation is polarized horizontally with respect to the $\hat{\theta}$ and $\hat{\phi}$ rotation axes of the cluster (*cf.* Fig. 9(a)), as was the case in the measurement of the experimental $I(k)$ data set discussed above. Because the incident radiation is polarized, the x-ray scattering factor in Fig. 5(a) must be further multiplied by the Thomson scattering factor, which has the form $\sin^2 \Theta_\varepsilon^{k'}$, where $\Theta_\varepsilon^{k'}$ is the angle between the polarization vector of the incident radiation ε, and the direction k' of the scattered radiation. Thus, there will be nodes in the incoming scattered object waves along the polarization direction, and emitter atoms near this direction will not be strongly influenced by x-ray scattering. For the present case, the use of horizontal polarization is therefore a

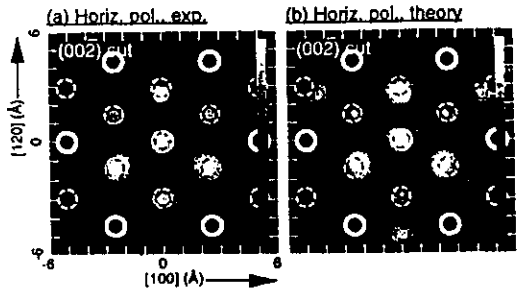

FIGURE 10. Multiple energy x-ray holography (MEXH) atomic images of α-Fe_2O_3(001) in the horizontal (00$\bar{2}$) plane situated 6.89Å below each of the two types of Fe emitters, obtained from (a) experimental and (b) theoretical Fe Kα χ(k) data sets, via Eq. (6). Fe scatterers in the bi-layer just above or below this plane are indicated by dashed circles, and Fe scatterers in relative positions common to both inequivalent Fe emitters are indicated by bold circles. Axes are marked off in 1Å units.

disadvantage in the imaging of horizontal planar structures such as those in $\alpha - Fe_2O_3(001)$, which is comprised of closely stacked horizontal Fe bi-layers with (001) orientation. The effect of such horizontally polarized incident radiation (via the Thomson cross section) is thus to strongly suppress atomic images in the basal (001) plane of the emitter, but to much less suppress images in horizontal planes farther above and below the emitter plane (40).

Figures 10(a) and (b) show the reconstructed atomic images in the (00$\bar{2}$) plane situated at z = -6.89Å below the emitter and obtained by applying Eq. (6) to the experimental and single-scattering theoretical χ(k) data sets, respectively. The expected image resolutions in the horizontal ([100] and [1$\bar{2}$0]) directions are $\delta x = \delta y \approx 0.6$Å (34). The experimental and theoretical images are very similar in that three of the Fe atoms from the neighboring upper bi-layer intrude into the (00$\bar{2}$) image plane. This intrusion is due to the limited wavenumber and angular range of the χ(k) data points in k-space (as compared to the larger wavenumber and angular range for the electron χ(k)'s in the previous section), which results in atomic images much less resolved in the vertical [001] direction: $\delta z \approx 2.5$Å (34). Still, since these images are reconstructed from a multiple-wavenumber χ(k) data set, they should be freer of real-twin image overlaps (4,15,16,38-40).

As a future prospect, using unpolarized incident radiation in MEXH, or perhaps rotating the entire sample-detector complex by 90° so as to measure holograms with both horizontal polarization and vertical polarization (with the polarization vector in the plane formed by the azimuthal rotation axis (the normal

of the sample surface) and the x-ray incidence direction, would allow atomic images to be reconstructed for atoms in all horizontal and vertical planes.

In fact, however, there also exist some classes of structures where it would be sufficient to utilize horizontally polarized incident radiation, and for which vertical structural information is more important than horizontal planar structure. These include some surface structure problems and buried epitaxial atomic layers. We specifically illustrate what might be learned for a buried atomic layer by considering theoretically a single Ge "δ-layer" buried in Si(001) (40). The Ge atoms in the δ-layer are assumed to lie in horizontal epitaxial sites with respect to the surrounding Si(001), such that structural information in the horizontal plane of a Ge emitter is relatively unimportant compared to the possibly strained vertical distances between the Ge δ-layer atoms and the Si neighbors above and below them (42). Thus using horizontally polarized incident radiation to record a MEXH Ge Kα $\chi(k)$ data set for this system may prove to be sufficient, and perhaps even advantageous.

As an example, Figs. 11(a)-(c) show the Thomson scattering factors for unpolarized, horizontally polarized, and vertically polarized incident radiation, respectively. Figs. 11(d)-(f) show the reconstructed atomic images in the vertical $(1\bar{1}0)$ plane obtained from applying Eq. (6) to a theoretical single-scattering $\chi(k)$ data set calculated for these polarization modes (unpolarized, horizontally polarized, and vertically polarized) for an ideal Ge δ-layer buried in a Si(001) cluster with no vertical strain. These MEXH $\chi(k)$ intensities were calculated at 7 wavenumbers (energies) for radiation of $k = 6.081\text{Å}^{-1}$ to 9.122Å^{-1} ($E = 12.00$keV to 18.00keV) that was incident over a polar takeoff angle range of $10° \le \theta \le 90°$, and with wavenumber (energy) steps of $\delta k = 0.507\text{Å}^{-1}$ ($\delta E = 1.00$keV) and angle steps of $(\delta\theta,\delta\phi) = (5°,5°)$, yielding a total of 1,897 unique data points in the symmetry-reduced 1/4th of the total solid-angle above the cluster. The higher wavenumber and larger wavenumber and angular ranges of these MEXH $\chi(k)$ data sets ensure better resolved atomic images ($\delta x = \delta y \approx 0.2\text{Å}$; $\delta z \approx 0.4\text{Å}$) than those of Fig. 10 (34). The Ge δ-layer atoms are well-defined in the image obtained with unpolarized radiation (Fig. 11(d)), and the Si atoms in the layer directly above the Ge δ-layer are fairly well resolved, but the Si atoms in the top center of the image along the [001] direction are poorly resolved, being farther away from the emitter. In contrast, in the image obtained with horizontally polarized radiation (Fig. 11(e)), the Si atoms above and below the Ge δ-layer, including those at top center and bottom center of the image along the [001] direction, are clearly imaged compared to those in the basal plane of the Ge δ-layer. Thus, it appears that the strained vertical interlayer distances could be determined in an MEXH experiment on this system using horizontally polarized incident radiation. Figure 11(f) shows the image obtained with vertically polarized incident radiation, where in contrast to Fig. 11(e), the Ge δ-layer atoms are strongly evident, compared to the suppressed images of the Si atoms above and below. Should both vertical *and* horizontal

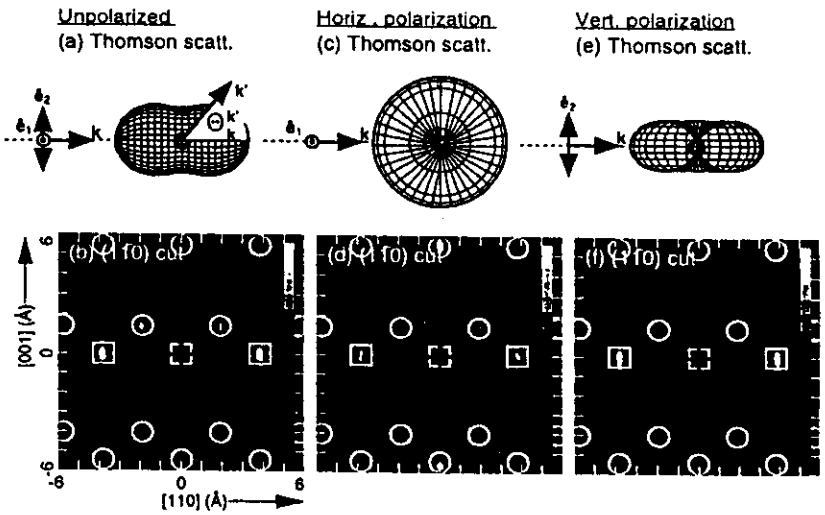

FIGURE 11. (a)-(c) Thomson scattering factors for unpolarized, horizontally polarized, and vertical polarized incident radiation, respectively. (d)-(f) Multiple energy x-ray holography images of a single Ge layer embedded in Si(001) (Si(001)/Ge-δ/Si(001)) in the vertical $(1\bar{1}0)$ plane obtained from theoretical Ge Kα $\chi(k)$ data sets via Eq. (6), for: unpolarized, horizontally polarized, and vertically polarized incident radiation, respectively. The Ge emitter site is indicated by the dashed square, and the Ge δ-layer scatterers are indicated by solid squares. The Si atoms directly above and below the Ge δ-layer are indicated by circles. Axes are marked off in 1Å units.

structural information be desired for a given system with only linearly polarized incident radiation for excitation, then $\chi(k)$ intensities measured using horizontally and vertically polarized radiation separately could simply be added to determine the MEXH $\chi(k)$ intensities for most of the solid angle above the sample that one would measure using unpolarized incident radiation (40). The use of circularly polarized incident radiation should also be advantageous in this respect (40). In order to determine the vertical strain in this system (an effect of a few percent), increased spatial resolution of atomic images could be obtained by measuring holographic $\chi(k)$ intensities at higher wavenumbers (34).

Thus atomic x-ray holography holds much promise for the imaging of local atomic structure surrounding a specific emitter species of interest. The more ideal atomic scattering nature of x-rays produces reconstructed images that are relatively free of the aberrations, artifacts, and position shifts that are usually found in comparable electron atomic holographic images. XFH and MEXH also share

the advantage of being element specific; thus the local structure around each atomic type in a sample can be determined. In addition, neither XFH or MEXH requires a sample with long range crystalline order; it need only be minimally ordered to within the potential imaging volume surrounding the emitter site that can be resolved with the k-space resolution of a given $\chi(k)$ data set (30,38). In contrast to the bulk structures considered in the initial implementation of this technique, atomic x-ray holography would be advantageously used to image structures with only short-range order which cannot be determined using conventional x-ray diffraction probes, such as surface and buried atomic layers; strained atomic lattice positions surrounding dopant sites (Fig. 12(a)); as well as

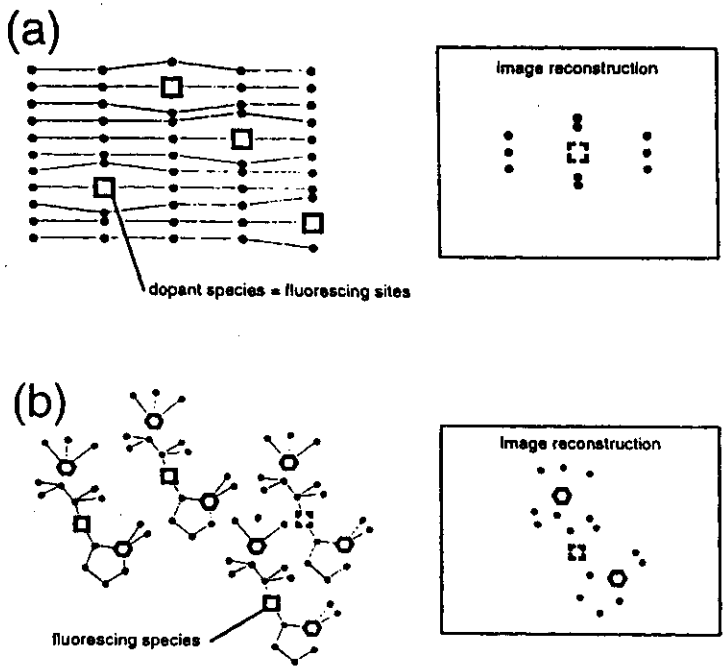

FIGURE 12. Schematic representation of two types of short-range-order atomic structures that could be fruitfully studied using atomic x-ray holography, together with their expected reconstructed images. (a) Strained lattice atoms surrounding dopant sites. (b) Rotationally aligned macromolecules with poor long-range translational symmetry.

the structure of macromolecules which do not exhibit perfect translational symmetry in crystal form (Fig. 12(b)). But one can also imagine using x-ray holography as a adjunct to conventional x-ray diffraction, with good estimates of local structures and phase relationships being derived to assist the diffraction analysis. Exploitation of linear and circularly polarized incident radiation in MEXH may also be utilized to emphasize horizontal and/or vertical structures of interest.

CONCLUDING REMARKS

In conclusion, holographic atomic imaging with localized single-atom sources of electrons or x-rays promises to become an important structural probe that will complement, or in some respects even surpass, conventional diffraction methods or other atomic structure probes. These holographic methods should be applicable to a wide variety of systems of practical and fundamental interest. X-ray holography of either the single-wavenumber fluorescence type or the multiple-wavenumber (inverse) type promises to yield more accurate images due to the more ideal scattering of x-rays, although the much weaker diffraction effects observed with x-rays also present challenges in measurement. However, with brighter sources of x-rays at next-generation synchrotron radiation facilities, and the development of faster detectors, these experimental problems should be surmountable. Thus, although much experimental and theoretical work lies ahead if we are to develop both the electron and x-ray techniques to their fullest potential, the final fulfillment of Gabor's dream for atomic-resolution holography seems well worth the effort.

ACKNOWLEDGEMENTS

Research at UC-Davis was supported in part by the Office of Naval Research (Contract Nos. N00014-90-5-1457 and N00014-94-1-0162), by the Director, Office of Energy Research, Office of Basic Energy Sciences, Materials Sciences Division of the U. S. Department of Energy (Contract No. DE-AC03-76SF00098), the National Energy Research Supercomputer Center, and by the International Centre for Diffraction Data. The authors would like to thank T. Gog, J. D. Denlinger, E. Rotenberg, F. Arfelli, R. A. Eisenhower, A. P. Kaduwela, R. H. Menk, D. Novikov, and S. Thevuthasan for their experimental and theoretical collaborative efforts, and M. A. Van Hove and R. L. Johnson for their useful comments during the preparation of this manuscript. Use of a preliminary version of a new multiple-scattering photoelectron diffraction program package was made possible by Y. Chen, H. Wu, and D. A. Shirley.

REFERENCES

1. Gabor, D. *Nature* (London) **161**, 777-778 (1948).
2. Wolf, E. *Optics Communications* **1**, 153-156 (1969), and *Optical Society of America* 60, 18-20 (1970).
3. Syms, R. R. A., *Practical Volume Holography*, Oxford: Clarendon Press, 1990, ch. 1, pp. 21-28.
4. (a) Barton, J. J., *Physical Review Letters* **61**, 1356-1359 (1988), and *Physical Review Letters* **67**, 3106-3109 (1991). (b) Barton, J. J., and Terminello, L. J., paper presented at the Third International Conference on the Structure of Surfaces, Milwaukee, July 1990, and in *Structure of Surfaces III*, S. Y. Tong, M. A. Van Hove, X. Xide, and K. Takanayagi, eds., (Springer Verlag, Berlin, 1991) p. 107. (c) Tong, S. Y., Huang, H., and Wei, C. M., *Physical Review B* **46**, 2452-2459 (1992), and references therein.
5. Szöke, A., *Short Wavelength Coherent Radiation: Generation and Applications*, T. Attwood, J. Boker (eds.), AIP Conference Proceedings No. 147, (AIP, New York, 1986) pp. 361-367.
6. Karla, J., and Hauptmann, H. A., *Acta Crystallographica* **3**, 18 (1950).
7. Lipscomb, W. N., *Acta Crystallographica* **2**, 193 (1949).
8. Hümmer, K., Billy, H., *Acta Crystallographica A* **38**, 841 (1982).
9. Chang., S., L., *Physical Review Letters* **48**, 163 (1982).
10. Hutton, J. T., Trammell, G. T., and Hannon, J. P., *Physical Review B* **31**, 743 (1985), and *Physical Review B* **31**, 6420 (1985).
11. Bedyzk, M. J., and Materlik, G., *Physical Review B* **32**, 6456 (1985).
12. Saldin, D. K., Harp, G. R., Tonner, B. P., *Physical Review B* **45**, 9629 (1992).
13. Tegze, M., and Faigel, G., *Nature* **380**, 49-51 (1996).
14. Fadley, C. S., and Len, P. M., *Nature* **380**, 27-28 (1996), and unpublished results.
15. Gog, T., Len, P. M., Materlik, G., Bahr, D., Sanchez-Hanke, C., and Fadley, C. S., *Physical Review Letters* **76**, 3132-3135 (1996).
16. Gog., T., Menk, R.-H., Arfelli, F., Len, P. M., Fadley, C. S., and Materlik, G., *Synchrotron Radiation News* **9**, 30-35 (1996).
17. (a) Terminello, L. J., Petersen, B. L., and Barton, J. J., *Journal of Electron Spectroscopy and Related Phenomena* **75**, 229-308 (1995), and references therein. (b) Wu, H., Lapeyre, G. J. Huang, H., and Tong, S. Y., *Physical Review Letters* **71**, 251-254 (1993) and references therein. (c) Zharnikov, M., Weinelt, M., Zebisch, P., Stichler, M., Steinrück, H.-P., *Surface Science* **334**, 114-134 (1995), and references therein. (d) Denecke, R., Eckstein, R., Ley, L., Bocquet, A. E., Riley, J. D., Leckey, R. C. G., *Surface Science* **331-333**, 1085-1092 (1995). (e) Tobin, J. G., Waddill, G. D., Li, H., Tong, S. Y., *Surface Science* **334**, 263-275 (1995), and references therein.
18. (a) Li, H., Tong, S. Y., Naumovic, D., Stuck, A., and Osterwalder, J., *Physical Review B* **47**, 10036-10039 (1993). (b) Saldin, D. K., Harp, G. R. and Chen, X., *Physical Review B* **48**, 8234-8245 (1993), and references therein.
19. (a) Han, Z.-L., Hardcastle, S., Harp, G. R., Li, H., Wang, ,X.-D. Zhang, J., and Tonner, B. P., *Surface Science* **258**, 313-327 (1991), and references therein. (b) Hong, I. H., Shyu, S. C., Chou, Y. C., and Wei, C. M., *Physical Review B* **52**, 16884-16891 (1995), and references therein.
20. (a) Mendez, M. A., Glück, C., Guerrero, J., Andres, P. L., Heinz, K., Saldin, D. K., and Pendry, J. B., *Physical Review B* **45**, 9402-9405 (1992), and references therein. (b) Wei, C. M., Tong, S. Y., Wedler, H., Mendez, M. A., and Heinz, K., *Physical Review Letters* **72**, 2434-2437 (1994), and references therein.
21. Tong, S. Y., Huang, H., and Guo, X. Q., *Physical Review Letters* **69**, 3654-3657 (1992).
22. Saldin, D. K., Harp, G. R., Chen, B. L., and Tonner, B. P., *Physical Review B* **44**, 2480-2494 (1991).
23. (a) Thevuthasan, S., Herman, G. S., Kaduwela, A. P., Tran, T. T., Kim, Y. J., Saiki, R. S., and Fadley, C. S., *Journal of Vacuum Science and Technology A* **10**, 2261-2270 (1992). (b) Herman, G. S., Thevuthasan, S., Tran, T. T., Kim, Y. J., and Fadley, C. S., *Physical Review Letters* **68**, 650-653 (1992). (c) Tran, T. T., Thevuthasan, S., Kim, Y. J., Friedman, D. J., Fadley, C. S., *Physical Review B* **45**, 12106-12109 (1992), and *Surface Science* **281**, 270-284 (1993). (d) Thevuthasan, S., Ynzunza, R. X., Tober, E. D., Fadley, C. S., Kaduwela, A. P., and Van Hove, M. A., *Physical Review Letters* **70**, 595-598 (1993).
24. Hu, P. and King, D. A., *Physical Review B* **46**, 13615-13618 (1992).
25. Tonner, B. P., Han, Z.-L., Harp, G. R., and Saldin, D. K., *Physical Review B* **43**, 14423-14433 (1991).
26. Thevuthasan, S., Ynzunza, R. X., Tober, E. D., Fadley, C. S., Kaduwela, A. P., and Van Hove, M. A., *Physical Review Letters* **70**, 595 (1993).
27. (a) Tong, S. Y., Li, H., and Huang, H., *Physical Review B* **51**, 1850-1854 (1995). (b) Wu, H., and Lapeyre, G. J. *Physical Review B* **51**, 14549-14553 (1995). (c) Roesler, J. M., Sieger, M. T., and Chiang, T.-C., *Surface Science* **329**, L588-592 (1995), and references therein.
28. Rous, P. J. and Rubin, M. H., *Surface Science* **316**, L1068-1074 (1994).
29. Hofmann, P., Schindler, K.-M., Fritzsche, V., Bao, S., Bradshaw, A. M., and Woodruff, D. P., *Journal of Vacuum Science and Technology A* **12**, 2045-2050 (1994), *Surface Science* **337**, 169-176 (1995), and references therein.
30. (a) Len, P. M., Thevuthasan, S., Kaduwela, A. P., Van Hove, M. A., and Fadley, C. S., *Surface Science* **365**, 535-546 (1996). (b) Len, P. M., Zhang, F., Thevuthasan, S., Kaduwela, A. P., Van Hove, M. A., and Fadley, C. S., *Journal of Electron Spectroscopy and Related Phenomena* **76**, 351-357 (1995). (c) Len, P. M., Zhang, F., Thevuthasan, S., Kaduwela, A. P., Fadley, C. S., and Van Hove, M. A., submitted to the *Journal of Electron Spectroscopy and Related Phenomena*.
31. Denlinger, J. D., Rotenberg, E., Len, P. M., Kevan, S. D., Tonner, B. P., and Fadley, C. S., in preparation.
32. Ynzunza, R. X., private communication.
33. SCAT photoelectron diffraction program package, Chen, Y., Wu, H., and Shirley, D. A., private communication.
34. Harp, G. R., Saldin, D. K., Chen, X., Han, Z.-L., and Tonner, B. P., *Journal of Electron Spectroscopy and Related Phenomena* **57**, 331-355 (1991).
35. (a) Timmermans, E. M. E., Trammell, G. T., and Hannon, J. P., *Physical Review Letters* **72**, 832-835 (1994). (b) Kaduwela, A. P., Wang, Z., Thevuthasan, S., Van Hove, M. A., and Fadley, C. S., *Physical Review B* **50**, 9656-9659 (1994).
36. Faigel, G., private communication.
37. Tegze, M., Faigel, G., *Europhysics Letters* **16**, 41-46 (1991).
38. Len, P. M., Thevuthasan, S., Fadley, C. S., Kaduwela, A. P., and Van Hove, M. A., *Physical Review B* **50**, 11275-11278 (1994).
39. Len, P. M., Gog, T., Fadley, C. S., and Materlik, G., submitted to *Physical Review B*.
40. Len, P. M., Gog, T., Novikov, D., Eisenhower, R. A., Materlik, G., and Fadley, C. S., submitted to *Physical Review B*.
41. *International Tables for X-ray Crystallography*, edited by K. Lonsdale (Reidel, Dordrecht, 1968), Vol. III.
42. Falta, J., Gog, T., Materlik, G., Muller, B. H., and Horn-von Hoegen, M., *Physical Review B* **51** 7598-7602 (1995), and references therein.

UNITED NATIONS EDUCATIONAL, SCIENTIFIC AND CULTURAL ORGANIZATION
INTERNATIONAL ATOMIC ENERGY AGENCY
INTERNATIONAL CENTRE FOR THEORETICAL PHYSICS
I.C.T.P., P.O. BOX 586, 34100 TRIESTE, ITALY, CABLE: CENTRATOM TRIESTE

H4.SMR/1013-7

SCHOOL ON THE USE OF SYNCHROTRON RADIATION
IN SCIENCE AND TECHNOLOGY:
"John Fuggle Memorial"

3 November - 5 December 1997

Miramare - Trieste, Italy

Theoretical Aspects of Electron Emission Holography [2)]

Luciano Fonda
ICTP - Trieste, Italy

Review Article

phys. stat. sol. (b) 188, 599 (1995)

Subject classification: 79.60; 61.14

Department of Theoretical Physics, University of Trieste, and International Center for Theoretical Physics, Trieste[1])

Theoretical Aspects of Electron Emission Holography[2])

By

L. FONDA

Contents

1. Introduction

Starting from a suggestion of Szöke [1] and Barton [2], a new surface structure determination approach, called either photoelectron or Auger electron holography depending on the process under consideration, to get three-dimensional images of the close vicinity of a given near-surface atom emitter, has recently been developed. The idea goes back to Gabor's discovery of holography [3]. He realized that, by recording on a photographic plate the interference pattern (hologram) of a known *reference* wave with an unknown *object* wave and then illuminating with an appropriate decoding wave the so obtained hologram, one can obtain the image of the object.

In the case of a photoelectron or of an Auger electron, the reference wave is assumed to be the direct wave emitted by the excited atom a. The object wave is then the superposition of the waves emitted coherently by the atoms surrounding a as a consequence of the process of single double ... multiple scattering experienced by the emitted electron. By taking the detector to be a spherical photographic film, the decoding wave referred to above is then chosen to be the spherical wave, converging on the film, obtained from the asymptotic reference wave via the operation of time reversal [1, 2]. This wave is transmitted through

[1]) POB 586, Strada Costiera 11, I-34100 Trieste, Italy.

[2]) Supported in part by the Istituto Nazionale Fisica Nucleare.

the film and in this process it collects the information contained in the hologram. The images of the atoms of the object are then obtained by means of computer reconstruction using a mathematical method similar to the one employed in optical holography.

In this way, one therefore realizes the inverse process of recovering the structure of the object from the knowledge of the hologram.

The advantage of this holographic method lies in the knowledge of the reference wave, a point which is not shared by structure determination approaches using an external beam of particles, such as e.g. X-ray and neutron diffractions, where the reference wave is lost and the experimentalist is therefore faced with the so-called "phase problem".

In Section 2, the theory of electron emission holography is expounded in full detail. In Sections 3 and 4, the weak points of the theory, such as the appearance of twin images, of "ghost atoms", and of some other artificial byproducts of the method, are discussed and ways to eliminate them are reviewed.

Applications of this holographic technique have appeared in the literature. For a complete list of references, the reader is referred to the review papers by Chambers [4] and Fadley [5].

2. Photoelectron and Auger Electron Holography

Let us first consider the way the hologram is obtained. We place a spherical photographic film around our object. The centre of the sphere is at the origin 0 of the reference frame placed at the centre of the atom emitter a. The radius of the sphere is R. Each point of the film is characterized by the polar angles defining the vector R.

The interference pattern is encoded on this photographic film. It is obtained by evaluating the component of the emitted electron vector probability current density in the direction perpendicular to the sphere surface (for simplicity, we neglect the refraction of the electron wave at the surface of the sample subject to measurement),

$$I(R) \equiv j(R) \cdot R/R \,. \tag{2.1}$$

If the detector is in the far field (R large with respect to the dimensions of the object), this probability is just proportional to the modulus square of the emitted electron wave function $\psi(R)$ evaluated at the position R,

$$I(R) \propto |\psi(R)|^2 \,. \tag{2.2}$$

On the sphere surface the wave function $\psi(R)$ can be expressed in terms of the scattering matrix

$$\psi(R)_{R\,\text{large}} \approx -\frac{m(2\pi)^{1/2}}{\hbar^2}\,\frac{e^{ikR}}{R}\,T_{f-i} \,. \tag{2.3}$$

T_{f-i} is the T-matrix for the process evaluated on the energy shell. In the standard single-particle approach, it is given by

$$T_{f-i} \equiv \langle \psi_f^{(-)}(k) \,|\, A_c \rangle \,, \tag{2.4}$$

where the PhotoElectron state vector $|A_c^{PhE}\rangle$ and the Auger $|A_{c12}^{Auger}\rangle$ are defined by (see [6], Sections 2 and 6)

$$|A_c^{PhE}\rangle = \langle 0|\, H_1 \,|1_i\rangle\, |\psi_c\rangle \,, \tag{2.5a}$$

$$\langle r_2 \,|\, A_{c12}^{Auger}\rangle = \int \mathrm{d}^3 r_1 \, \psi_c^*(r_1)\, \frac{e^2}{|r_2 - r_1|}\, [\psi_{i1}(r_1)\, \psi_{i2}(r_2) - \psi_{i2}(r_1)\, \psi_{i1}(r_2)] \,. \tag{2.5b}$$

In the case of photoemission, the initial state vector is the product of the incoming free photon state vector $|1_i\rangle$ (the subscript i symbolizes the initial photon momentum and the polarization) times the vector $|\psi_c\rangle$ which represents the initial single-electron normalized bound state relative to the *core* level c. The final state is given by the product of the normalized photon vacuum $|0\rangle$ times the single-electron scattering state $|\psi_f^{(-)}(k)\rangle$, satisfying an incoming wave boundary condition, describing the emitted electron, with asymptotic momentum $\hbar k \equiv \hbar kR/R$, in interaction with the ionized atom emitter a and with its neighbours in the condensed material. For simplicity, in this paper we shall forget about the spin of the emitted electron. To the first order in the radiation field, the interaction Hamiltonian is given by: $H_I = -(e/mc)\, A \cdot p$, where m and p are the electron mass and momentum operator, respectively, and $A(r)$ is the quantized photon field in the Coulomb gauge $\nabla \cdot A(r) = 0$.

In the case of Auger emission, the process is one in which an electron of the ionized atom a makes a transition from the core level 1 (core level 2) to the empty core level c, while an electron from the core level 2 (core level 1) is ejected from the atom a. This emitted Auger electron, represented in (2.4) by the usual scattering state $|\psi_f^{(-)}(k)\rangle$, propagates then in the material and suffers multiple scatterings from the atoms surrounding the doubly ionized atom a until, after having finally assumed the momentum $\hbar k$, it reaches the detector.

The expression of the T-matrix in terms of all multiple scatterings is known from the literature. We write here (3.37) of [6] (L is a combined orbital angular momentum index $L \equiv l, m$),

$$T_{f-i} = \sum_{L'} \mathscr{T}_{L'} \mathscr{M}_{cL'}\,, \tag{2.6a}$$

$$\mathscr{T}_{L'} = \sum_{L} (2\pi)^{-3/2} (-i)^{l} Y_{L}(k) \times \left\{ \delta_{LL'} + \sum_{\substack{p=a \\ q=a}} \sum_{L_p L_q} [\delta_{L'L_q} e^{ik\cdot R_{aq}} + t_{l'}^{a} g_{L'L_q}(R_{aq})]\, \tau^{qp}_{L_q L_p} g_{L_p L}(R_{pa}) \right\}. \tag{2.6b}$$

Apart from the consideration of inelasticities and thermal vibrations, to be introduced with proper attenuation factors [5], (2.6) is, within the single-particle framework, the correct T-matrix.

The matrix $\tau^{qp}_{L_q L_p}$ is the representative in angular momentum space of the scattering path operator [7]. The integral equation defining this operator is given by (3.38) of [6],

$$\tau^{qp}_{L_q L_p} = t^{p}_{l_p} \delta_{qp} \delta_{L_q L_p} + \sum_{m \neq q} \sum_{L_m} t^{q}_{l_q} [g_{L_q L_m}(R_{qm})]\, \tau^{mp}_{L_m L_p}\,, \tag{2.7}$$

$R_{qp} = R_q - R_p$ is the bond vector pointing from atom p to atom q, $t_l^p = -e^{i\delta_l^p} \sin \delta_l^p$ is the l-th wave T-matrix for scattering of the electron from the atom p, the form factor $\mathscr{M}_{cL}$ is given by

$$\mathscr{M}_{cL} = \int d^3r \, \frac{\psi_{sl}^{(+)}(k, r)}{kr} Y_L^*(r) \langle r | A_c \rangle\,, \tag{2.8}$$

where $\psi_{sl}^{(+)}(k, r)$ is the physical radial scattering wave function, satisfying an outgoing wave boundary condition, belonging to the angular momentum l, for the emitted electron in the field of the potential U_a of the atom emitter a.

The g-propagator (structure factor) is given by

$$g_{L_p L_q}(R_{pq}) = -i \sum_{L} 4\pi i^{l+l_p-l_q} \langle Y_{L_p} Y_L \,|\, Y_{L_q} \rangle\, Y_L(R_{pq})\, h_l^{(+)}(kR_{pq})\,. \tag{2.9}$$

Using (2.3), (2.6), and (2.7), we can easily split the wave function, at the sphere surface, into *reference* and *object* terms,

$$\psi(R) = \psi_{ref}(R) + \psi_{obj}(R) \equiv -\frac{m(2\pi)^{1/2}}{\hbar^2} \frac{e^{ikR}}{R} \sum_{L} [\mathscr{T}_L^{ref} + \mathscr{T}_L^{obj}]\, \mathscr{M}_{cL}\,, \tag{2.10a}$$

$$\mathscr{T}_L^{ref} = (2\pi)^{-3/2} (-i)^{l} Y_L(k)\,, \tag{2.10b}$$

$$\mathscr{T}_L^{obj} = (2\pi)^{-3/2} \sum_{p,q} \sum_{L_p L_q} (-i)^{l_q} Y_{L_q}(k)\, e^{ik\cdot R_{aq}}\, \tau^{qp}_{L_q L_p} (1 - \delta_{pa})\, g_{L_p L}(R_{pa})\,. \tag{2.10c}$$

Note that the object wave contains also all waves which, after having undergone multiple scattering, have atom a as the last scatterer (term $q = a$ of (2.10c)). These particular multiple-scattering contributions are unknown and therefore, even though consisting of waves eventually outgoing from the atom emitter, cannot be included in the reference wave. They are at least of second order with respect to the latter wave.

To decode the information contained in the interference pattern appearing on the spherical film, we imagine to illuminate the film with a converging spherical wave

$$\psi_{decoding}(r) = \frac{e^{-ikr}}{r}; \qquad r > R \tag{2.11}$$

obtained, apart from a constant, from the asymptotic expression of the reference wave via the operation of time reversal. This converging wave is transmitted through the film. We suppose that the interference pattern $I(R)$ is imprinted on a positive photographic film which, by proper development, has the contrast value $\gamma = 2$ [8]. As a consequence, the transmittance is linearly related to the intensity $I(R)$ measured on the film and the *transmitted wave* ψ_T on the internal side of the surface of the sphere is therefore given by:

$$\psi_T(R) = (1 + CI(R)) \frac{e^{-ikR}}{R}\,. \tag{2.12}$$

The transmitted wave satisfies the Helmholtz wave equation

$$(\Delta + k^2)\, \psi_T(r) = -4\pi C_0 \delta^3(r); \qquad r \leq R \tag{2.13}$$

subject to the (Dirichelet) boundary condition (2.12) on the surface of the sphere. $\psi_T(r)$ is singular in the origin $r = 0$ (position of the atom emitter a). This can be understood from the fact that, if there is no hologram ($I = 0$), ψ_T must coincide with the decoding wave (2.11) which satisfies (2.13) with $C_0 = 1$.

In order to find ψ_T in a given point P_0 (of coordinate vector r_0) inside the sphere, we consider the Green's function $K(r \,|\, r_0)$ satisfying the Helmholtz equation,

$$(\Delta + k^2)\, K(r \,|\, r_0) = -4\pi \delta^3(r - r_0) \tag{2.14}$$

with boundary condition to be specified in a moment.

We multiply (2.13) by $K(r \mid r_0)$ and (2.14) by $\psi_T(r)$ and subtract member by member one equation from the other. We integrate the so obtained expression on the whole volume of the sphere. Using then the Green's theorem, we get

$$\psi_T(r_0) - C_0 K(0 \mid r_0) = \frac{1}{4\pi} \int [K(r \mid r_0)\, \Delta\psi_T(r) - \psi_T(r)\, \Delta K(r \mid r_0)]\, dV$$

$$= \frac{1}{4\pi} \int \left[\psi_T(r) \frac{\partial K(r \mid r_0)}{\partial n} - K(r \mid r_0) \frac{\partial \psi_T(r)}{\partial n} \right]_{r=R} dS, \quad (2.15)$$

where ∂n is the normal to the surface directed into the interior of the sphere.

A natural choice for the Green's function would be [2, 9]: $K(r \mid r_0) = (\exp ik|r - r_0|)/|r - r_0|$. In that case, however, from (2.15) we see that knowledge of ψ_T and $\partial\psi_T/\partial n$ on the whole surface should be required to solve our problem. Apart from the fact that on the boundary we know only the values of ψ_T (from (2.12)), this might lead to the following mathematical contradiction: In practice the hologram can cover at most the 2π-hemisphere hanging over the sample subject to measurement; if symmetry arguments are not available in order to obtain mathematically the hologram on the "opaque" sides of the measuring apparatus, one usually assumes the vanishing of the surface integral (2.15) just on those opaque parts of the surface, which implies $\psi_T = \partial\psi_T/\partial n = 0$ there; but this implies, by a well-known theorem, that ψ_T vanishes identically in the whole space.

I shall require that the Green's function vanishes on the boundary surface.

$$K(R \mid r_0) = 0 \quad (2.16)$$

so that (2.15) can be rewritten as

$$\psi_T(r_0) = C_0 K(0 \mid r_0) + \frac{1}{4\pi} \int_S \psi_T(R) \frac{\partial K(r \mid r_0)}{\partial n}\bigg|_{r=R} dS. \quad (2.17)$$

We see that only the knowledge of ψ_T on the boundary is now required.

The integral on the right-hand side of (2.17) may extend now only on the portion S of the surface on which the hologram is actually measured. On the "opaque" parts of the surface we can safely place $\psi_T = 0$ without meeting contradictions of any sort.

We must now solve the Dirichlet boundary value problem posed by (2.14) and (2.16). The solution in the whole space can be found only by means of computer calculations. In fact, for the Helmholtz equation (2.14) an analytic solution satisfying (2.16) cannot be written down. Fortunately, however, we need only to know $\partial K/\partial n$ on the surface of the sphere. In order to find it there explicitly, I shall make a variation of the well-known method of images. This method has been invented for the case of a flat boundary [10]. Let us see which changes are needed for our curved boundary.

Suppose I want to find the value of $\partial K/\partial n$ in a given point $P_s \subset S$. I draw, through the point P_s, the plane T tangent to the surface S. I perform then the space reflection with respect to T and find the image of P_0 (see Fig. 1). Call this new point P_0^*, whose position vector is r_0^*. Consider now the auxiliary Green's function:

$$\bar{K}(r \mid r_0) = \frac{e^{ikr_1}}{r_1} - \frac{e^{ikr_2}}{r_2}, \quad (2.18)$$

where $r_1 = r - r_0$ and $r_2 = r - r_0^*$. In the interior of the sphere, $\bar{K}$ satisfies the Helmholtz equation (2.14) and it vanishes on the plane T (where $r_1 = r_2$), in particular in the point P_s.

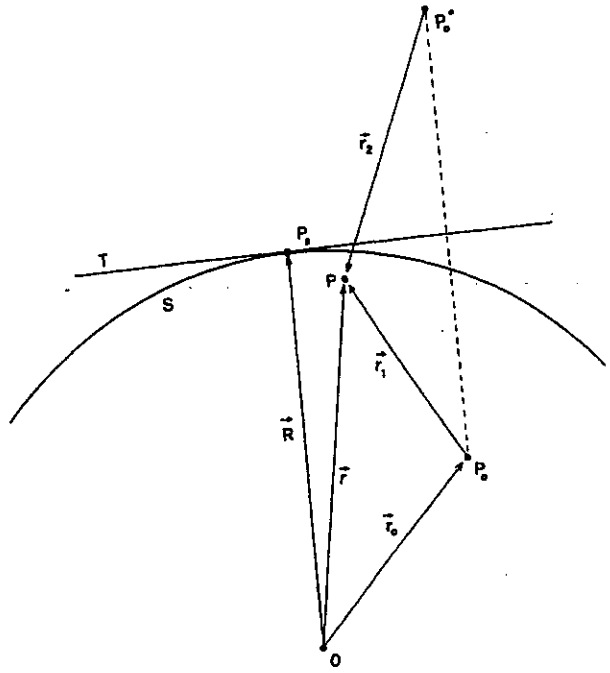

Fig. 1. Definition of points and vectors relative to the construction of the derivative of the Green's function with respect to the normal to the boundary surface

By construction, in any infinitesimal spherical neighbourhood of P_s, the Green's functions K and $\bar{K}$ differ by infinitesimal quantities and the same holds for their derivatives. We obtain then

$$\frac{\partial K(r \mid r_0)}{\partial n}\bigg|_{P=P_s} = \frac{\partial \bar{K}(r \mid r_0)}{\partial n}\bigg|_{P=P_s}$$

$$= \left[\left(ik - \frac{1}{r_1} \right) \frac{e^{ikr_1}}{r_1} \frac{\partial r_1}{\partial n} - \left(ik - \frac{1}{r_2} \right) \frac{e^{ikr_2}}{r_2} \frac{\partial r_2}{\partial n} \right]_{P=P_s}. \quad (2.19)$$

The evaluation of the derivatives $\partial r_1/\partial n$ and $\partial r_2/\partial n$ in the point P_s is straightforward under the consideration that r_0 is a typical vector spanning the object. Since holography is a short-range order probe ($r_0 < 1.5$ to 2.0 nm) we have that $r_0 \ll R$ and $r_0^* \approx 2R$. Indicating by R the position vector of P_s, we get

$$\frac{\partial r_1}{\partial n}\bigg|_{P=P_s} \equiv -\frac{\partial |R - r_0|}{\partial R} = -\frac{R - (r_0 \cdot R/R)}{|R - r_0|} \underset{r_0 \ll R}{=} -1, \quad (2.20a)$$

$$\frac{\partial r_2}{\partial n}\bigg|_{P=P_s} \equiv -\frac{\partial |R - r_0^*|}{\partial R} = -\frac{R - (r_0^* \cdot R/R)}{|R - r_0^*|} \underset{r_0^* \approx 2R}{=} +1. \quad (2.20b)$$

We therefore obtain

$$\left.\frac{\partial K(r\,|\,r_0)}{\partial n}\right|_{r=R} = -2\left(ik - \frac{1}{r_1}\right)\frac{e^{ikr_1}}{r_1}\bigg|_{R=R} \underset{kR\gg 1}{=} -2ik\frac{e^{ik|R-r_0|}}{|R-r_0|}; \quad r_0 \ll R, \tag{2.21}$$

where we have dropped a term of the order $(kR)^{-1}$ since $kR \gg 1$ (kR is 10^8 to 10^9 in our case).

Using again the smallness of r_0, on the right-hand side of (2.21) for $|R - r_0|$ we can substitute R in the denominator and $R - (R \cdot r_0/R)$ in the exponent. We finally get

$$\frac{\partial K(R\,|\,r_0)}{\partial n} = -2ik\frac{e^{ikR}}{R}e^{-ik\cdot r_0}; \quad r_0 \ll R, \tag{2.22}$$

where $k \equiv kR/R$. Using (2.12) and (2.22), and writing $dS \equiv R^2\,d\Omega_k$, (2.17) finally reads

$$\psi_T(r_0) = A_0 + A_1 \int_S d\Omega_k\, I(k)\, e^{-ik\cdot r_0}, \tag{2.23}$$

where $A_0 = C_0 K(0\,|\,r_0) - (ik/2\pi)\int_S d\Omega_k\, e^{-ik\cdot r_0}$, $A_1 = -ikC/2\pi$, and $I(k) \equiv I(R)$. A_0 constitutes an uninteresting background; as a function of r_0 it may peak only at the position $r_0 = 0$ of the atom emitter a. Therefore we shall drop it in what follows.

Since all quantities on the right-hand side of (2.23) are known, the wave function $\psi_T(r_0)$ is therefore determined. In the literature, (2.23) is referred to as the Helmholtz-Kirchhoff integral.

Now, also for ψ_T we define *reference* and *object* terms.

$$\psi_T = \psi_{T\,ref} + \psi_{T\,obj}. \tag{2.24}$$

Using (2.2), (2.10a), and (2.23) we get

$$\psi_{T\,ref}(r_0) = A\int_S d\Omega_k\, |\psi_{ref}(R)|^2\, e^{-ik\cdot r_0}, \tag{2.25a}$$

$$\psi_{T\,obj}(r_0) = A\int_S d\Omega_k [\psi^*_{obj}(R)\,\psi_{ref}(R) + \psi_{obj}(R)\,\psi^*_{ref}(R) + |\psi_{obj}(R)|^2]\, e^{-ik\cdot r_0}. \tag{2.25b}$$

The function appearing in the integral (2.25b):

$$\chi(k) \equiv |\psi(R)|^2 - |\psi_{ref}(R)|^2 = \psi^*_{obj}(R)\,\psi_{ref}(R) + \psi_{obj}(R)\,\psi^*_{ref}(R) + \psi^*_{obj}(R)\,\psi_{obj}(R) \tag{2.26}$$

is termed *anisotropy* in the literature. It must be obtained experimentally via subtraction of the reference wave flux. The reference flux is calculated theoretically. One must evaluate carefully the matrix elements $\mathcal{M}_{cL}$ given by (2.8). In the case of photoemission, the dipole excitation of an initial l-wave subshell leads to the interfering $l+1$ and $l-1$ final orbital angular momentum channels. The case of Auger emission is much more complex: in practical calculations it is often assumed that the initial state has an s-wave character [4, 5, 11].

Equation (2.25b) is the relevant integral to be evaluated in order to get the image of our object. It transforms the two-dimensional hologram into a three-dimensional image. The first two terms of the integral on the right-hand side of (2.25b) contain the usual hologram of optical holography, while the third term represents the self-interference or self-hologram.

From (2.10), the reference and object waves can be written as

$$\psi_{ref}(R) = \sum_L Y_L(k)\, A_L, \tag{2.27a}$$

$$\psi_{obj}(R) = \sum_q \sum_{L_q} Y_{L_q}(k)\, e^{ik\cdot R_{aq}}\, B^q_{L_q}. \tag{2.27b}$$

Using (2.25b) and (2.27), from a stationary-phase argument [2] we expect that $\psi_{T\,obj}(r_0)$ will yield peaks at

$$r_0 = \pm R_{aq}, \tag{2.28a}$$

$$r_0 = R_q - R_p. \tag{2.28b}$$

This is certainly correct for s-waves (as in the optical case, where s-wave scattering dominates), or in the case of s-wave emission combined with moderately angle dependent scatterings from the neighbours. The latter condition is better realized at low energies since electron scattering presents a high angular anisotropy and relevant phase shifts as the energy increases. As a consequence, artifacts, such as shifts of the position of the atoms and image asymmetry or broadening, appear in the Helmholtz-Kirchhoff integral (2.25b). In Section 4 we shall discuss possible ways to cure these unpleasant features.

In (2.28a), the minus sign is related to the peaks present in the first term of the Helmholtz-Kirchhoff integral (2.25b) and it corresponds to the real images of the atoms of the object; the plus sign corresponds to their twin images. For $q = a$ one gets the image (twin = real) of the atom emitter. The presence of both real and twin images is a problem shared with optical holography.

The uncertainty principle of course limits the ultimate resolution with which the positions of the atoms can be determined by this method [20, 4, 5]: $\Delta r \geqq 1/(k_{max} - k_{min})$, where the projections of $\hbar(k_{max} - k_{min})$ on the coordinate axes are the uncertainties on the measured electron momenta.

If one centres the relevant part of the hologram along the z-axis and calls θ the half opening angle of the corresponding cone, the Heisenberg principle yields $\Delta x = \Delta y = \pi/(k \sin\theta) = \lambda_e/(2\sin\theta)$ and $\Delta z = 2\pi/[k(1-\cos\theta)] = \lambda_e/(1-\cos\theta)$ showing that the resolution of the images of the atoms should improve for wider θ (with upper limit $\pi/2$) and using higher energy electrons.[3])

Equation (2.28b) corresponds to the third term of (2.25b) and yields peaks at the $\pm$ interdistances of all pairs of atoms, as an expression of the self-hologram; for $q = p$ one gets peaks at $r_0 = 0$, i.e. at the position of the atom emitter a, which after all is not too bad, but, more importantly, for $q \neq p$ peaks appear at positions where there are no atoms. These *ghost* images, which actually appear to be 10 to 20% in size of the real and twin

[3]) For $\theta = 60°$, at the electron energy of 100 eV one gets $\Delta x = \Delta y = 0.071$ nm, $\Delta z = 0.25$ nm. At 1000 eV: $\Delta x = \Delta y = 0.022$ nm, $\Delta z = 0.076$ nm.

images [12], would not be there if the holographic requirement $|\psi_{ref}| \gg |\psi_{obj}|$ were satisfied, as it happens in the simpler optical case. In the photoelectron or Auger electron holography this is not so since the electron–atom interaction is in general stronger, particularly for scattering in forward directions along a chain of atoms at high energies.

We shall see in Section 3 how one can eliminate the twin images and the noise due to the self-hologram in the case of photoelectrons.

We end this section by pointing out that the holographic method has the potential of getting information on near-surface atoms beyond nearest neighbours [4, 5], something which is not obtainable by the photoelectron or Auger electron diffraction approaches.

Methods of the type discussed in this section can also be applied to core level X-ray fluorescence [1, 13], to DLEED (diffuse low-energy electron diffraction) [14], and to Kikuchi patterns [15]. Spin-polarized photoelectron holography has been treated in [16, 17].

3. Elimination of Twin Images and Self-Hologram Effects in Photoelectron Holography

We shall treat in this section a method devised to cope with unphysical artifacts such as twin images and self-hologram effects in photoelectron holography.

The method suggested by Barton, Tong, and coworkers [18 to 23] introduces a Fourier transform operation in energy on $\psi_{Tobj}(r_0)$. In order to see this in detail, let us first apply the plane wave approximation (PWA) to our formulas. This approximation is able to render explicit the energy dependence of the propagators. It consists in fact in replacing, in the g-propagator, the Hankel function $h_l^{(+)}(kR)$ with its expression for large kR: $(-i)^{l+1} e^{ikR}/kR$.

For the g-propagator one then obtains

$$(g_{L_p L_q}(R_{pq}))_{PWA} = -\frac{4\pi}{k} i^{l_p - l_q} Y^*_{L_p}(R_{pq}) \frac{e^{ikR_{qp}}}{R_{pq}} Y_{L_q}(R_{pq}) . \tag{3.1}$$

We finally get the PWA expression of the object part of the wave function

$$\{\psi_{obj}(R)\}_{PWA} = -\frac{m}{2\pi\hbar^2} \frac{e^{ikR}}{R} \sum_L i^{l_{cL}} \sum_{\substack{p \neq a \\ q}} e^{ikR_{aq}} F^{PWA}_{qp}(k_{rq}; k_{pa}) \frac{e^{ikR_{pa}}}{R_{pa}} (-i)^l Y_L(R_{pa}) , \tag{3.2}$$

where the multiple scattering amplitude $F^{PWA}_{qp}(k_{xq}; k_{pa})$ is defined by (see [6], Section 4),

$$F^{PWA}_{qp}(k_{xq}; k_{pa}) = -\frac{4\pi}{k} \sum_{L_p L_q} i^{l_p - l_q} Y_{L_q}(k_{xq}) (\tau^{qp}_{L_q L_p})_{PWA} Y^*_{L_p}(k_{pa}) . \tag{3.3}$$

In terms of the scattering factor (scattering amplitude) f_p it satisfies the following multiple-scattering matrix equation:

$$F^{PWA}_{qp}(k_{xq}; k_{pa}) = \delta_{qp} f_p(k_{xp}; k_{pa}) + \sum_m f_q(k_{xq}; k_{qm}) \frac{e^{ikR_{qm}}}{R_{qm}} (1 - \delta_{qm}) F^{PWA}_{mp}(k_{qm}; k_{pa}) \tag{3.4}$$

with its perturbation expansion[4])

$$F^{PWA}_{qp}(k_{xq}; k_{pa}) = \delta_{qp} f_p(k_{xp}; k_{pa}) + f_q(k_{xq}; k_{qp}) \frac{e^{ikR_{qp}}}{R_{qp}} (1 - \delta_{qp}) f_p(k_{qp}; k_{pa}) + \sum_m f_q(k_{xq}; k_{qm}) \frac{e^{ikR_{qm}}}{R_{qm}} (1 - \delta_{qm}) f_m(k_{qm}; k_{mp}) \frac{e^{ikR_{mp}}}{R_{mp}} (1 - \delta_{mp}) \times f_p(k_{mp}; k_{pa}) + \dots . \tag{3.5}$$

Let us now discuss the general structure, as far as the energy dependence of the propagators is concerned, of the terms appearing under the sign of integration of the Helmholtz-Kirchhoff integral (2.25b). For the first term, using (3.2) and (3.5), we can write

$$\begin{aligned} &\int_S d\Omega_k \, e^{-ik\cdot r_0} \{\psi^*_{obj}(R) \, \psi_{ref}(R)\}_{PWA} \\ &= \int_S d\Omega_k \, e^{-ik\cdot r_0} \left\{ \sum_q M^*_q \, e^{-ik\cdot R_{aq}} \frac{e^{-ikR_{aq}}}{R_{qa}} (1 - \delta_{qa}) \right. \\ &+ \sum_{q,p} M^*_{qp} \, e^{-ik\cdot R_{aq}} \frac{e^{-ikR_{qp}}}{R_{qp}} (1 - \delta_{qp}) \frac{e^{-ikR_{pa}}}{R_{pa}} (1 - \delta_{pa}) \\ &\left. + \sum_{q,p,m} M^*_{qpm} \, e^{-ik\cdot R_{aq}} \frac{e^{-ikR_{qp}}}{R_{qp}} (1 - \delta_{qp}) \frac{e^{-ikR_{pm}}}{R_{pm}} (1 - \delta_{pm}) \frac{e^{-ikR_{ma}}}{R_{ma}} (1 - \delta_{ma}) + \dots \right\} . \end{aligned} \tag{3.6}$$

As suggested in [18 to 23], we now take the following energy Fourier transform on the Helmholtz-Kirchhoff integral (2.25b):

$$\psi'_{Tobj}(r_0) = \int_0^{+\infty} \{\psi_{Tobj}(r_0)\}_{PWA} \, e^{ikr_0} \, w(k) \, dk , \tag{3.7}$$

$w(k)$ is a proper weight function which can limit the integration interval. It could be a sum of Dirac δ-functions.

After application of the Fourier transform (3.7) to (3.6), we discover that, apart from particular cases which we shall discuss in a while, we are able to get the suppression of all but the first term on the right-hand side (which represents the single-scattering contributions from the neighbours of the atom a (note that $q \neq a$)): For this term in fact, the peaks which appear at the real positions of the atoms $r_0 = R_{qa} \equiv R_q - R_a$ after integrating over angles, get reinforced after the energy Fourier transform (3.7) is performed, as can be understood from the stationary phase argument applied to the phase factor $\exp[ik(r_0 - R_{qa})]$. On the

[4]) $f_q(k_{xq}; k_{qp}) \equiv f_q(\theta_{xqp})$ is the scattering factor describing the electron as being shot from the atom p, scattering from the atom q, and emerging in the direction x (θ_{xqp} is the corresponding polar angle of scattering). For the differential cross section one has: $d\sigma/d\Omega = |f(\theta)|^2$. The scattering factor is connected with the partial wave T-matrix as follows: $f_q(\theta) = -(4\pi/k) \sum_L Y^*_L(k) \, t^q_l Y_L(k')$. (Note that formulae like (3.5) must be read from right to left in order to follow the correct time arrow of the process.)

contrary, the other, multiple-scattering, terms of (3.6) are in general suppressed, since the peak resulting from the energy integration does not coincide with that obtained from the angular integration.

As mentioned above, there are, however, particular cases where multiple scatterings contribute.

Consider for example the second term of (3.6). The angular integral peaks again at $r_0 = R_{qa} \equiv R_q - R_a$. When its Fourier transform (3.7) is taken, the energy phase factor $\exp[ik(r_0 - R_{qp} - R_{pa})]$ will give a contribution if the atom p is aligned with q and atom a so that $R_{qp} + R_{pa} = R_{qa}$ (i.e. p lies in between a and q), since in this way the peaks resulting from angular and energy integrations coincide. The contribution of this a pq chain will then add up to the q-term of the first term of (3.6). Similar considerations hold for the other terms of (3.6) which contribute if chains a $jk \ldots pq$ of aligned atoms are realized so that $R_{qp} + \ldots + R_{kj} + R_{ja} = R_{qa}$.

However, the contribution of these multiple scatterings is not harmful since it enhances the single-scattering term corresponding to the end atom of the chain.

Another possibility, which we have already mentioned in Section 2, is the case $q = a$ which yields a peak at the position $r_0 = 0$. It represents the image (true = twin) of the atom emitter, and it appears at least as a second-order effect.

Let us now consider the second term of the Helmholtz-Kirchhoff integral (2.25b),

$$\int_S d\Omega_k\, e^{-ik\cdot r_0} \{\psi_{obj}(R)\, \psi^*_{ref}(R)\}_{PWA}$$

$$= \int_S d\Omega_k\, e^{-ik\cdot r_0} \left\{ \sum_q M_q\, e^{ik\cdot R_{aq}} \frac{e^{ikR_{aq}}}{R_{qa}} (1 - \delta_{qa}) \right.$$

$$\left. + \sum_{q,p} M_{qp}\, e^{ik\cdot R_{aq}} \frac{e^{ikR_{qp}}}{R_{qp}} (1 - \delta_{qp}) \frac{e^{ikR_{pa}}}{R_{pa}} (1 - \delta_{pa}) + \ldots \right\}. \tag{3.8}$$

The angular integration yields the twin images of the atoms of the object, at the positions $r_0 = -R_{qa} \equiv R_a - R_q$, space reflected of the positions of the true images. However, the Fourier transform (3.7) of expression (3.8) suppresses all the terms since the energy phase factors $\exp(ik(r_0 + R_{qa}))$ $(q \neq a)$ or $\exp(ik(r_0 + R_{qp} + \ldots + R_{ja}))$ are always highly oscillating whichever the positions of the atoms. At most, a little contribution to the "background" bump at the position $r_0 = 0$ of the emitter is obtained.

The purpose of eliminating the twin images has therefore been achieved.

We come now to the discussion of the third (self-hologram) term of (2.25b). Its energy Fourier transform is

$$\int_0^{+\infty} dk\, w(k)\, e^{ikr_0} \int_S d\Omega_k\, e^{-ik\cdot r_0} \{|\psi_{obj}(R)|^2\}_{PWA}$$

$$= \int_0^{+\infty} dk\, w(k)\, e^{ikr_0} \int_S d\Omega_k\, e^{-ik\cdot r_0} \left\{ \sum_{p,q} H_{qp}\, e^{ik\cdot(R_{ap} - R_{aq})} \frac{e^{ik(R_{pa} - R_{qa})}}{R_{pa} R_{qa}} (1 - \delta_{pa})(1 - \delta_{qa}) \right.$$

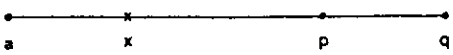

Fig. 2. After Fourier transform on the energy, in the self-hologram there still appear false atom (ghost) images along forward scattering chains of at least three atoms

$$+ \sum_{n,p,q} \left[H_{qpn}\, e^{ik\cdot(R_{ap} - R_{aq})} \frac{e^{ik(R_{pn} - R_{qn} - R_{na})}}{R_{pa} R_{qn} R_{na}} (1 - \delta_{pa})(1 - \delta_{qn})(1 - \delta_{na}) + \text{c.c.} \right]$$

$$+ \sum_{m,n,p,q} H_{qpnm}\, e^{ik\cdot(R_{ap} - R_{aq})} \frac{e^{ik(R_{pn} + R_{nm} - R_{qm} - R_{ma})}}{R_{pn} R_{na} R_{qm} R_{ma}}$$

$$\left. \times (1 - \delta_{pn})(1 - \delta_{na})(1 - \delta_{qm})(1 - \delta_{ma}) + \ldots \right\}. \tag{3.9}$$

Let us first consider the first, single-scattering, term on the right-hand side of (3.9). From the stationary phase argument, the integration over angles would peak at $r_0 = R_{ap} - R_{aq}$, while the integration over energies would peak at $r_0 = R_{qa} - R_{pa} > 0$. Only if these two maxima coincide we get a sizeable contribution to the integral, and this means $|R_{ap} - R_{aq}| = R_{qa} - R_{pa} > 0$ which is satisfied only if the vectors R_{ap} and R_{aq} are parallel: the atoms p and q are aligned with atom a (and the atom p lies in between a and q). Therefore, as shown in Fig. 2, we obtain a ghost image at the point x defined by $r_x = R_{ap} - R_{aq} \equiv R_q - R_p$ on the chain apq. If $q = p$ we of course get a contribution to the background at $r_0 = 0$.

Much the same can be said about the other, multiple-scattering, terms of (3.9). They all give contributions for forward scattering along chains of atoms and an enhancement of the background at $r_0 = 0$.

We see therefore that, by making a Fourier transform on the energy of the Helmholtz-Kirchhoff integral (2.25b), one is able to suppress the twin images and most of the self-hologram. As far as the latter is concerned, the only contribution left is the appearance of ghost images (i.e. false atoms) along forward scattering chains of at least three atoms.

A very good point of this procedure is that, having practically cancelled the multiple-scattering contributions, one is left only with the consideration of single scatterings (first term on the right-hand side of (3.6)).

4. Treatment of Angular Anisotropies

The angular anisotropies, arising both from the directly emitted (reference) wave and from the scattered (object) waves, lead to aberrations which include shifts of the atom positions and image distortions. As far as the scattered waves are concerned, while at low energy the atomic scattering factor is rather isotropic, as the energy increases it becomes increasingly anisotropic being very large in the forward direction.

In the literature, ways have been conceived to cope with this problem [19, 21, 24 to 28]. In these approaches the beauty of the holographic approach is a bit lost, as we shall see.

As a result of the considerations of Section 3, for the case of photoemission the image wave field is given by

$$\psi'_{\mathrm{Tobj}}(r_0) \equiv A \int_0^{+\infty} \mathrm{d}k\, w(k)\, \mathrm{e}^{\mathrm{i}kr_0} \int_S \mathrm{d}\Omega_k\, \chi(k)\, \mathrm{e}^{-\mathrm{i}k\cdot r_0}$$

$$\approx A \int_0^{+\infty} \mathrm{d}k\, w(k)\, \mathrm{e}^{\mathrm{i}kr_0} \int_S \mathrm{d}\Omega_k\, \psi^*_{\mathrm{obj}}(R)\, \psi_{\mathrm{ref}}(R)\, \mathrm{e}^{-\mathrm{i}k\cdot r_0} \tag{4.1}$$

and we can stick to single scatterings only.

The case of Auger emission will be treated here on the same basis, being understood that in the integral (4.1) one has $w(k) = \delta(k - k_f)$, where $\hbar k_f$ is the final momentum of the emitted Auger electron.

The single-scattering (SS) part of the wave function (2.10) reads

$$\psi^{\mathrm{SS}}(R) = \psi_{\mathrm{ref}}(R) + \psi^{\mathrm{SS}}_{\mathrm{obj}}(R)$$

$$= \bar{A}\frac{\mathrm{e}^{\mathrm{i}kR}}{R}\left\{\sum_L (-\mathrm{i})^l\, \mathrm{Y}_L(k)\, \mathscr{M}_{cL} + \sum_{p\neq a} \mathrm{e}^{\mathrm{i}k\cdot R_{ap}} \sum_L O^L_p(k; R_{ap})\, \mathscr{M}_{cL}\right\}, \tag{4.2}$$

where $\bar{A} = -m/(2\pi\hbar^2)$ and the object scattered-wave function O^L_p, and its plane wave approximation, is given by

$$O^L_p(k; R_{ap}) = \sum_{L_p} (-\mathrm{i})^{l_p}\, \mathrm{Y}_{L_p}(k)\, t^p_{l_p} g_{L_pL}(R_{pa}) \underset{\mathrm{PWA}}{\Rightarrow} f_p(\theta_{fpa})\frac{\mathrm{e}^{\mathrm{i}kR_{pa}}}{R_{pa}}(-\mathrm{i})^l\, \mathrm{Y}_L(R_{pa}), \tag{4.3}$$

where θ_{fpa} is the angle of scattering from the atom p defined by $\cos\theta_{fpa} = k \cdot R_{pa}/kR_{pa}$.

The presence of scattering phase shifts in (4.2) (see also (4.4) and (4.5) below) is responsible for the shift in the positions of the images of the atoms.

In the case of dipole photoemission from an s-subshell, (4.2) is very simply given in the PWA,

$$\{\psi^{\mathrm{SS}}_{\text{s-subshell}}(R)\}^{\text{dipole}}_{\mathrm{PWA}} = \hat{A}\mathscr{M}_{l=1}(k)\frac{\mathrm{e}^{\mathrm{i}kR}}{R}\left\{\frac{\varepsilon\cdot k}{k} + \sum_{p\neq a}\frac{\varepsilon\cdot R_{pa}}{R_{pa}}\frac{\mathrm{e}^{\mathrm{i}[kR_{pa}(1-\cos\theta_{fpa})+\varphi_p(\theta_{fpa})]}}{R_{pa}}|f_p(\theta_{fpa})|\right\}, \tag{4.4}$$

where $\hat{A} = em(\hbar\omega)^{1/2}/(2(2\pi)^3\hbar^2 k)$ is slowly energy dependent, ε and $\hbar\omega$ are the polarization unit vector and the energy of the incoming photon, and $\mathscr{M}_{l=1}(k) = \int_0^\infty r\,\mathrm{d}r\, \psi^{(+)}_{a,l=1}(k, r)\, R_{l=0}(r)$. We have written explicitly the amplitude $|f_p|$ and the phase φ_p of the scattering factor f_p.

In the case of Auger emission of an electron with final $L \equiv l, m$ angular momentum, in the PWA (4.2) reads

$$\{\psi^{\mathrm{SS}}_L(R)\}^{\mathrm{Auger}}_{\mathrm{PWA}}$$

$$= \hat{B}_L\frac{\mathrm{e}^{\mathrm{i}kR}}{R}\left\{\mathrm{Y}_L(k) + \sum_{p\neq a}\frac{\mathrm{e}^{\mathrm{i}[kR_{pa}(1-\cos\theta_{fpa})+\varphi_p(\theta_{fpa})]}}{R_{pa}}|f_p(\theta_{fpa})|\,\mathrm{Y}_L(R_{pa})\right\}, \tag{4.5}$$

where $\hat{B}_L = \hat{A}(-\mathrm{i})^l\mathscr{M}^{\mathrm{Auger}}_{cL}$.

From the structure of (4.2) we see that, if we divide the experimental photoemission anisotropy function $\chi(k)$ by the angular part of the reference wave,

$$\chi(k) \to \tilde{\chi}(k) = \frac{\chi(k)}{D_{\mathrm{ref}}(k)}, \tag{4.6a}$$

$$D_{\mathrm{ref}}(k) = \sum_L (-\mathrm{i})^l\, \mathrm{Y}_L(k)\, \mathscr{M}_{cL}, \tag{4.6b}$$

we eliminate altogether the distortions caused by this angular asymmetry. Note that for a dipole photoemission from an s-core level, (4.6) is tantamount to dividing by $\varepsilon \cdot k/k$, while for Auger s-wave emission the denominator $D_{\mathrm{ref}}(k)$ is of course a constant. The operation (4.6) can be considered as a redefinition of the boundary condition (2.12).

We need now to discuss how to cope with the anisotropies present in the object waves of the integrand of (4.1).

4.1 The SWEEP method

A first possible procedure is that proposed by Tong and collaborators [19, 21, 24]. To be consistent with our procedures, we shall rephrase it a bit.

We first evaluate (4.1) using the experimental $\chi(k)$ corrected as in (4.6) for the angular anisotropy of the reference wave. We then fix our attention on a particular bump p appearing at the distance R'_{ap} from the atom a and representing a neighbour of a. Pre-existing knowledge about the system in question, will avoid the risk that a self-hologram false atom of the type discussed at the end of Section 3 is taken for a good atom. We now perform the following operation on $\tilde{\chi}(k)$:

$$\tilde{\chi}(k) \to \chi_{\mathrm{SWEEP}}(k) = \frac{\tilde{\chi}(k)}{D_{\mathrm{obj}}(k; R'_{pa})}, \tag{4.7a}$$

$$D_{\mathrm{obj}}(k; R'_{pa}) = \mathrm{e}^{-\mathrm{i}kR'_{pa}} R'_{pa} \sum_L O^L_p(k; R'_{pa})\, \mathscr{M}_{cL} \underset{\mathrm{PWA}}{\approx} f_p(\theta_{fpa}) \sum_L (-\mathrm{i})^l\, \mathrm{Y}_L(R'_{pa})\, \mathscr{M}_{cL}, \tag{4.7b}$$

and carry out the integration (4.1). In the original papers, Tong et al. actually integrate only over the forward, or backward, peak on a small angular window of half angle $\approx 30^\circ$ centred along R'_{ap}. Their formalism is then known as the SWEEP method (for small-window energy extension process).

In (4.7), the outgoing scattered-wave function $O^L_p(k; R'_{ap})$, and the scattering factor $f_p(\theta_{fpa})$, are theoretical expressions evaluated for an atom p of a given chemical species. This second step should have yielded an improved position R''_{ap}. The procedure is repeated by dividing $\tilde{\chi}(k)$ as shown in (4.7), where now R'_{ap} is replaced by R''_{ap}. By iteration one should converge to a final value R_{ap} for the position vector of the atom p. One must repeat the same procedure also for the other bumps in order to complete the determination of the structure around the atom a.

4.2 The SWIFT method

A second procedure, proposed by Saldin and coworkers [25 to 28], is an original variation of the above approach. For coherence with the rest of our text, we discuss it within the framework of (4.1), i.e. by including also the energy Fourier transform.

After having corrected the experimental $\chi(k)$ as in (4.6) for the angular anisotropy of the reference wave, let us perform the following operation on $\tilde{\chi}(k)$ [25 to 28]:

$$\tilde{\chi}(k) \to \chi_{\text{SWIFT}}(k) = \frac{\tilde{\chi}(k)}{D_{\text{obj}}(k; r_0)}, \tag{4.8a}$$

$$D_{\text{obj}}(k; r_0) = e^{-ikr_0} r_0 \sum_L O_p^L(k; r_0)\, \mathcal{M}_{cL} \underset{\text{PWA}}{\approx} f(\theta_{r0_a}) \sum_L (-i)^l Y_L(r_0)\, \mathcal{M}_{cL}, \tag{4.8b}$$

and then carry out the integration (4.1).

Here the angle θ_{r0_a} is defined by: $\cos\theta_{r0_a} = k \cdot r_0/kr_0$ and the outgoing scattering-wave function $O_p^L(k; r_0)$ (or the scattering factor $f(\theta_{r0_a})$) is now a generalized scattering amplitude evaluated at the position of the image point r_0 as if a hypotetical atom would be sitting there. Since the transformation involves the scattering amplitude, the authors have named it SWIFT, for scattered-wave-included Fourier transform.

According to the calculations performed in [25 to 28], with this method an improvement of the atom positions and image distortions is actually realized at the stationary-phase points $r_0 = R_{a_p}$. As in the case of the SWEEP method, due care has to be applied to spot the existence of possible ghosts.

A good point of this procedure is that the entire interference pattern is inverted in only one step. No prior knowledge of the forward scattering directions locating the atoms is required. This method spoils, however, the simple structure of Fourier transform over the angles possessed by the Helmholtz-Kirchhoff algorithm (2.25b) (and also by (4.1)), as naturally obtained from the holographic approach.

Also operations (4.7) and (4.8), even within their artificiality, could be thought of as being redefinitions of the boundary condition (2.12).

5. Conclusions

In this article we have reviewed the theory of electron emission holography. Its formulation has been provided in Section 2 on a sound mathematical basis.

We have seen that, as in the optical case, one is faced with the presence of twin images. Besides, however, other artifacts appear in electron emission holography due to the fact that, at variance with the optical case, here the object wave is not small with respect to the reference wave and the scattering is in general not dominated by s-waves.

Sections 3 and 4 have been devoted to the discussion of these artifacts and to a review of the various correction procedures proposed in the literature for their elimination. In doing so, we have also seen that the proposal by Barton, Tong, and collaborators of performing an energy Fourier transform of the holography integral (2.23) is able to eliminate most of the multiple-scattering contributions to the hologram.

Apart from the complications mentioned above, the holographic method has the merit of being rather direct. One has to remember that in electron emission diffraction methods the structure information is obtained only after a lengthy trial-and-error procedure of comparing experimental spectra with those obtained by means of extensive multiple-scattering calculations. Holography requires, however, an increased amount of experimental data, and therefore of data acquisition times, with respect to the diffraction methods. But this is at hand now at the new high brightness synchrotron radiation sources.

We have seen in Section 2 that, with the use of the simple Helmholtz-Kirchoff holography integral (2.23), atoms can be located with an accuracy of a few hundredth nm at best. Taking

also into account the fact that, by performing an energy Fourier transform, one can improve this spatial resolution, we feel that, before the investigator involves himself with the more sophisticated trial-and-error method mentioned above, electron emission holography provides him with a quick tool to get within shooting range of a more accurate determination of the positions of atoms at or near a surface.

References

[1] A. Szöke, AIP Conf. Proc. 147, 361 (1986).
[2] J. J. Barton, Phys. Rev. Letters 61, 1356 (1988).
[3] D. Gabor, Proc. Roy. Soc. A 197, 454 (1949); Proc. Phys. Soc. B 64, 449 (1951).
[4] S. A. Chambers, Surface Sci. Rep. 16, 261 (1992).
[5] C. S. Fadley, Surface Sci. Rep., 19, 231 (1993).
[6] L. Fonda, phys. stat. sol. (b) 182, 9 (1994).
[7] B. L. Gyorffy and M. J. Stott, Solid State Commun. 9, 613 (1971).
[8] F. T. S. Yu, Optical Information Processing, J. Wiley & Sons, New York 1983.
[9] M. Born and E. Wolf, Principles of Optics, Pergamon Press, Oxford 1980 (p. 374).
[10] A. Sommerfeld, Optics, Academic Press, New York/London 1964 (p. 200).
[11] C. S. Fadley, in: Synchrotron Radiation Research: Advances in Surface and Interface Science, Vol. I, Techniques. Ed. R. Z. Bachrach, Plenum Press, New York 1992 (p. 421).
[12] S. Thevuthasan, G. S. Herman A. P. Kaduwela, R. S. Saiki, Y. J. Kim, W. Niemczura, M. Burger, and C. S. Fadley, Phys. Rev. Letters 67, 469 (1991).
[13] P. M. Len, S. Thevuthasan, C. S. Fadley, A. P. Kaduwela, and M. A. Van Hove, to be published.
[14] D. K. Saldin and P. L. de Andres, Phys. Rev. Letters 64, 1270 (1990).
[15] G. R. Harp, D. K. Saldin, and B. P. Tonner, Phys. Rev. Letters 65, 1012 (1990).
[16] A. P. Kaduwela, Z. Wang, M. A. Van Hove, and C. S. Fadley, to be published.
[17] E. M. E. Timmermans, G. T. Trammel, and J. P. Hannon, J. appl. Phys. 73, 6183 (1993).
[18] J. J. Barton and L. J. Terminello, in: Structure of Surfaces III, Ed. S. Y. Tong, M. A. Van Hove, X. Xide, and K. Takayanagi, Springer-Verlag, Berlin 1991 (p. 107).
[19] S. Y. Tong, Hua Li, and H. Huang, Phys. Rev. Letters 67, 3102 (1991).
[20] J. J. Barton, Phys. Rev. Letters 67, 3106 (1991).
[21] S. Y. Tong, H. Huang, and Hua Li, Mater. Res. Soc. Symp. Proc. 208, 13 (1991).
[22] H. Huang, Hua Li, and S. Y. Tong, Phys. Rev. B 44, 3240 (1991).
[23] L. J. Terminello, J. J. Barton, and D. A. Lapiano-Smith, J. Vacuum Sci. Technol. B 10, 2088 (1992), Phys. Rev. Letters 70, 599 (1993).
[24] S. Y. Tong, C. M. Wei, T. C. Zhao, H. Huang, and Hua Li, Phys. Rev. Letters 66, 60 (1991).
[25] S. Hardcastle, Z.-L. Han, G. R. Harp, J. Zhang, B. L. Chen, D. K. Saldin, and B. P. Tonner, Surface Sci. 245, L190 (1991).
[26] B. P. Tonner, Z.-L. Han, G. R. Harp, and D. K. Saldin, Phys. Rev. B 43, 14423 (1991).
[27] D. K. Saldin, G. R. Harp, B. L. Chen, and B. P. Tonner, Phys. Rev. B 44, 2480 (1991).
[28] D. K. Saldin, G. R. Harp, and B. P. Tonner, Phys. Rev. B 45, 9629 (1992).

(Received November 10, 1994)

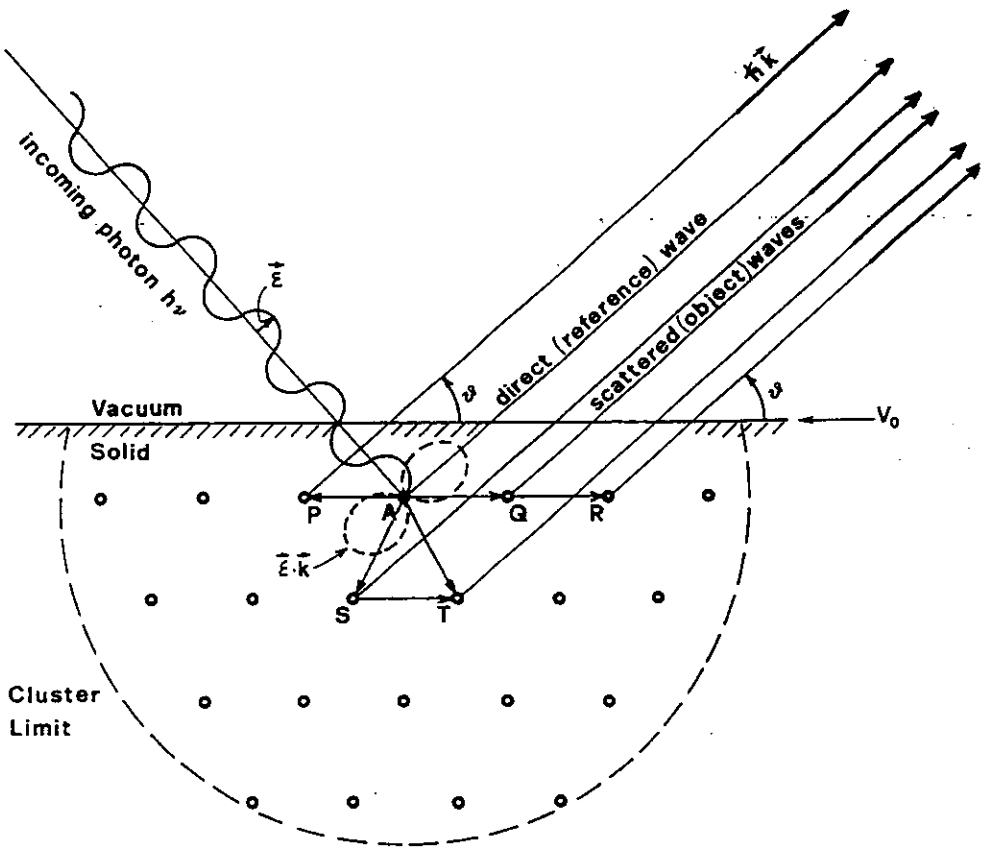
incoming photon hν
ε
ħk
direct (reference) wave
scattered (object) waves
ϑ
ϑ
Vacuum
Solid
V₀
P
A
Q
R
ε·k
S
T
Cluster
Limit

Fig. 1

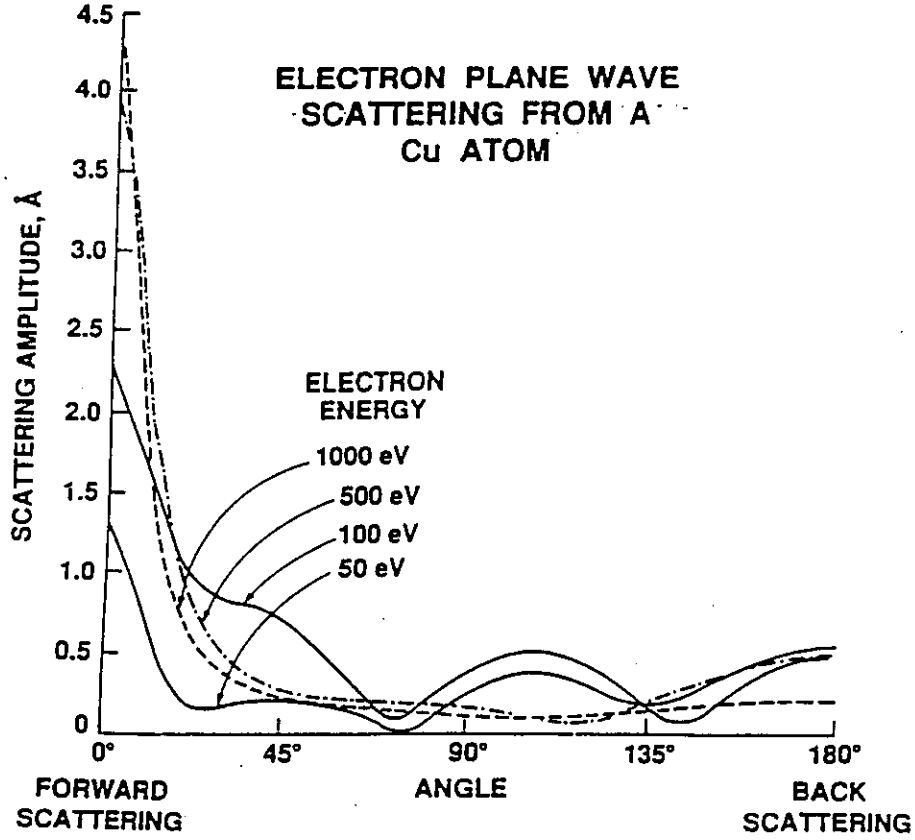
ELECTRON PLANE WAVE
SCATTERING FROM A
Cu ATOM
SCATTERING AMPLITUDE, Å
4.5
4.0
3.5
3.0
2.5
2.0
1.5
1.0
0.5
0
ELECTRON
ENERGY
1000 eV
500 eV
100 eV
50 eV
0°
45°
90°
135°
180°
FORWARD
SCATTERING
ANGLE
BACK
SCATTERING

Fig. 2

A.P. KADUWELA, D.K. SALDIN and B.P. TONNER

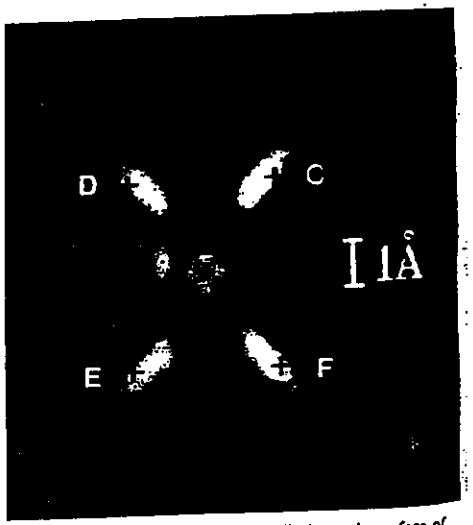

FIG. 4. A view in the plane perpendicular to the surface of the holographic reconstruction of the data from Fig. 1. The crosses mark positions of atoms in the ideal lattice. The elongated shape of the atom image is due to a reduction in resolution parallel to the electron emission direction.

Phys. Rev. Letters 65, 1012 (1990)

PETERSEN, TERMINELLO, BARTON and SHIRLEY

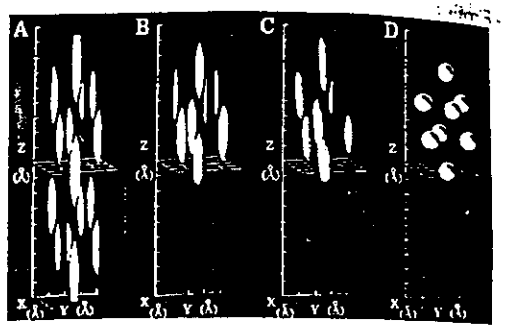

Fig. 10. Elimination of twin images as a result of the application of energy FT holography. Panel A shows a symmetry-averaged $\chi(k)$ at $k = 9.8$ Å^{-1} (366 eV). Twin images appear for $z < 0$. Panel B shows the result of phase-summing on eight values of k in the interval 8.8-10.2 Å^{-1}. Panel C shows the same pattern without symmetry averaging. Panel D represents a model showing the atoms in the positions as expected. (From Ref. 89.)

Chem. Phys. Lett. 213, 412(1993); 220, 46 (1994)

To appear in Physical Review B

Multi-Atom Resonant Photoemission Revisited

A.W. Kay[1,2], F.J. Garcia de Abajo[1,3], S.-H. Yang[1], E. Arenholz[4],
B.S. Mun[1,2], N. Mannella[1,2], Z. Hussain[4], M.A. Van Hove[1,2], and C.S. Fadley[1,2]

[1]Dept. of Physics, University of California-Davis, Davis, CA 95616
[2]Materials Sciences Division, Lawrence Berkeley National Laboratory, Berkeley, CA 94720
[3] Centro Mixto CSIC-UPV/EHU, San Sebastian, Spain
[4]Advanced Light Source, Lawrence Berkeley National Laboratory, Berkeley, CA 94720

PACS categories: 68.35.-p, 79.60.-i,78.20.Ci, 78.70.Dm, 78.70.En, 78.70.Ck

(July 18, 2000)

ABSTRACT

We present experimental and theoretical results related to multi-atom resonant photoemission (MARPE), in which the photoelectron intensity from a core level on one atom is influenced by a core-level absorption resonance on another. We point out that some prior experimental data has been strongly influenced by detector non-linearity and that the effects seen in new corrected data are smaller and of different form. Corrected data are found to be well described by an extension of resonant photoemission theory to the interatomic case, provided that interactions beyond the usual second-order Kramers-Heisenberg treatment are included. This microscopic theory is also found to simplify under certain conditions so as to yield results equivalent to a classical x-ray optical approach, with the latter providing an alternative, although less detailed and general, physical picture of these effects. The potential utility of these effects as near-neighbor probes, as well as their implications for x-ray emission and x-ray scattering experiments, are also discussed.

I. INTRODUCTION

In several recent papers by our group [1-5], it has been suggested that photoemission associated with a certain core electronic level of a given atom "A" can be significantly enhanced in intensity by tuning the photon energy through core-level absorption edges of a near-neighbor atom "B". The apparent enhancements seen in experimental data for several metal oxides (e.g. MnO, Fe_2O_3, and $La_{0.7}Sr_{0.3}MnO_3$ [1,2]), as well as in a series of Cr/Fe alloys and bilayers [3b] were very large, ranging

up to 40-100% of the non-resonant intensity, and they were furthermore observed to follow closely the x-ray absorption coefficient of atom B in shape [1-3]. The effects observed have been termed multi-atom resonant photoemission (MARPE) to distinguish them from the better-known intraatomic single-atom resonant photoemission (SARPE). Similar effects have also been reported in other transition metal compounds [6] and in adsorbates [7] by other groups. Analogous and presumed related enhancements also appeared to be present in the secondary decay processes of Auger electron and fluorescent x-ray emission, again tracking very closely the x-ray absorption coefficient in form [4]. A theoretical model based on an extension of normal SARPE theory has also been presented to describe these results, and first comparisons of calculations based on it yielded encouraging agreement with experiment [5]. The potential utility of such effects for studying near-neighbor atom identities and bonding have also been pointed out [1-4]. Independent of this work on core-core multi-atom resonant photoemission, other groups have reported the enhancement of valence photoemission intensities primarily associated with emission from a certain atom A upon tuning the photon energy through the core-level absorption edges of a nearby atom B, with this work including measurements near solid-solid interfaces [8,9] and on a free molecule [10]. No attempts have as yet been made to theoretically model this latter type of valence-core MARPE effect.

In this paper, we first point out that the measurement of the core-core multi-atom resonant photoemission effects mentioned above (or indeed any resonant--or non-resonant--photoemission effect) must be carried out with extreme care to avoid non-linearities in the electron detector response, and illustrate these effects by carrying out corrections on a few representative data sets for O 1s emission from MnO in resonance with the Mn 2p excitations. The corrected results are found to show significantly smaller MARPE effects on photoelectron intensities, with shapes now considerably different from the x-ray absorption coefficient. In addition, theoretical calculations based on the previously-discussed microscopic model [5], and on a simpler classical theory of x-ray optics [11] are presented and found to yield excellent agreement with the remaining experimental effects, thus clarifying the physics involved. We also comment on the implications of this work for other recent core-core and valence-core MARPE measurements [6-10,12,13], as well as for x-ray emission [4,14] and x-ray scattering experiments.

II. EXPERIMENTAL PROCEDURE AND DATA ANALYSIS

All photoelectrons were analyzed in energy and detected with a Scienta ES200 electron spectrometer system [15a], as situated either on a bend-magnet beamline (9.3.2) [15b] or an undulator beamline (4.0.2) at the Berkeley Advanced Light Source. The final multichannel detection system used is that provided as part of the standard equipment by the manufacturer: a microchannel plate multiplier followed by a phosphor screen at high voltage in vacuum, and a CCD video camera outside of vacuum to finally convert light pulses into counts. We have operated this detector in the "greyscale" or "analogue" mode in which integrated CCD charge is used for counting, rather than in the alternate "black-and-white" or "digital mode" in which individual pulses are counted. The detector has in addition been used as delivered and installed by the manufacturer; thus, the discriminator setting was left at its recommended value at setup. This spectrometer and detector system is furthermore the same as that used by some other groups attempting to measure multi-atom resonant photoemission effects [6,7]. We have in the present study calibrated our detector system in both analogue and black-and-white modes by using a standard x-ray tube with continuously-variable emission current at fixed high voltage, verifying initially that the total electron current from the sample tracked linearly with the emission current: thus, the emission current is directly proportional to the x-ray flux incident on the sample. The general methodology for this calibration and the final correction of spectra is discussed elsewhere [16,17], in one case together with previous data for a similar electron detection system [16].

III. RESULTS AND DISCUSSION

In Fig. 1(a) and its inset, we show the measured (dashed curve) vs. ideal or "true" (straight line) response of this detector as used in analogue mode over a countrate range spanning zero to 500 Hz in a typical x-y pixel of the approximately 70,000 pixels in the CCD camera used in normal operation. We have verified that all spatial regions of the detector behave in essentially the same manner [17], so the performance shown can be applied over the entire active region. The inset makes it clear that there is curvature in the response, with falloff and incipient saturation being seen as countrate increases. Although one might then expect linearity for the lowest countrates, the blowup of the 0-20 Hz region (the maximum used in all of our measurements to avoid falloff and saturation) shown in the main figure makes it clear that there is still significant non-linearity, including what is found to be a quadratic component as compared to an ideal detector with linear response that we define to be equal to that of the real detector in the limit of zero countrate (solid line of unit slope in figure and inset). For reference, the 20 Hz per pixel rate would correspond to a global countrate of 1.4 MHz (before a

"multiple counting" divisor introduced by the manufacturer's software is applied) for the entire useable portion of the detector phosphor and if the phosphor were evenly illuminated.

Thus, although measured and true rates can be conveniently defined to yield the same unit slope as countrates go to zero, the measured rates deviate significantly from linearity, showing quadratic overcounting over the full range of our earlier measurements. Almost identical quadratic effects were also found in the black-and-white mode, although this mode was not used in our measurements [17]. An additional effect of such quadratic overcounting is the narrowing or broadening of photoelectron peaks in energy as a high-intensity resonance is passed, depending on which portion of the non-linear response a given photon energy scan occupies, and we have in prior work [1-4] also used the additional criterion of constant peak width over an energy scan to try to minimize non-linearities. However, this criterion of constant peak width proves to be inadequate for avoiding spurious effects on peak intensity measurements. Using methods described in detail elsewhere [16,17], the detector response curve in Fig. 1(a) can be turned into an efficiency, and the inverse of this efficiency then used to correct individual spectra in a point-by-point fashion. Although it is possible that adjusting the discriminator setting on the detector could reduce these non-linearities, several other groups appear to have encountered the same type of non-linearity with the standard manufacturer's settings [6,7,18]. It has also been suggested that a change in CCD camera might improve this behavior [19], and this is another direction for future investigation.

Both uncorrected (as-measured) and corrected ("true") spectra are shown in Fig. 1(b) for O 1s emission from MnO, where the photon energies of 637.6 eV and 640.2 eV have been chosen to be just below the strong Mn $2p_{3/2}$ resonance and just on this resonance, respectively [1]. Because of the significantly increased background level associated with secondary decay processes and inelastically scattered electrons arising from the Mn $2p_{3/2}$ absorption, which in turn forces the detector countrate further up its non-linear response curve, the correction procedure acts to a greater degree on resonance. Thus, the intensity on resonance is artificially enhanced. In fact, in order to decrease these non-linear correction effects to negligibly low levels, we have found in data not shown here that the countrates had to be lowered by another order of magnitude from our prior typical operating points, or to about 2 Hz per pixel [17].

In Fig 1(c), we now show uncorrected and corrected O 1s intensities, measured as areas by fitting analytical peak shapes plus backgrounds to spectra such as those in Fig. 1(b), as a function of

photon energy, with curves such as these being discussed previously in terms of multi-atom resonant photoemission [1-4]. It is clear that the uncorrected MARPE scan follows very closely the previously published x-ray absorption curve for MnO in the Mn $2p_{3/2}$ region [1-3], which we also show in Fig. 1(c) as derived from the inelastic electron background under the O 1s spectra [1], with about a 32% enhancement of intensity of the O 1s intensity at the Mn $2p_{3/2}$ peak [1-4]. However, the corrected MARPE scan shows a much smaller effect of about 12% in overall excursion, and also of much different form, being negative just below the resonance and then going positive. In data obtained at other x-ray incidence angles over the range of 5°-30° [17], we have also found that these corrected effects are strongly dependent on angle, being largest for more grazing x-ray incidence angles, such as the analogous results for 10° shown in Fig. 1(d), which exhibit about 37% overall excursion, and quickly decaying in magnitude as this angle is increased. We estimate our overall systematic error in the corrected spectra as ±2%, with some channel-to-channel statistical scatter around this.

As a final point on this correction, it appears that, with constant UHV conditions of operation, the correction function does not change significantly over a period of months, with older data obtained via the same detector setup showing reasonable correctability. However, the correction function should in any case be checked frequently to avoid any drifts with time.

It is thus clear that detector non-linearity can have a dramatic effect on such measurements, with the solid curves in Figs. 1(b), 1(c), and 1(d) now representing much more accurately any effects beyond a simple one-electron picture of O 1s emission from MnO. Without such interatomic effects, one should observe a simple smooth curve of negative slope over this region in energy due to a combination of subshell cross section and electron inelastic attenuation length variation [11,20], as perhaps modulated by energy-dependent photoelectron diffraction (PD) [17,21]. The effects of scanned-energy photoelectron diffraction are in fact clearly shown in Fig. 1(e), which represents a broader energy scan for the same experimental conditions as in Fig. 1(c). Here, the long-wavelength oscillation with a maximum at ~634 eV has been verified via theoretical calculations to be due to PD effects [17].

We also note that, in addition to affecting photoemission results, prior measurements of secondary Auger and x-ray emission effects [4] also appear to have been strongly influenced by such detector non-linearities, for the former just as for the photoelectron case due to the identical

instrumentation, and for the latter via an x-ray absorption coefficient necessary for a self-absorption correction that was measured via secondary electrons in the same electron spectrometer.

Beyond the particular case of MARPE considered here, we also point out that such detector non-linearities need to be corrected for and/or minimized in any use of this detector system for quantitative peak intensity analysis, as any comparison of intensities obtained over a range of countrates, even in a single spectrum, can be significantly altered by these effects.

IV. THEORY AND DISCUSSION

A. Interatomic resonant photoemission model

We now consider several levels of theory in order to explain the remaining effects which link the O 1s intensity to the Mn 2p absorption process as seen in Figs. 1(c) and 1(d), first considering these effects via a prior microscopic many-body theoretical treatment of MARPE based on a resonant photoemission model [5], and then showing that this approach can be successively simplified for the case at hand to yield results essentially identical to those from classical x-ray optical theory. Focusing still on the case of O 1s photoemission from MnO(001) and the system initially prepared in its many-body ground state $|g\rangle$, the contribution of the direct or unscattered wave function to the photoelectron intensity can be written

$$I(\mathbf{k}) \propto \left|\phi_{\mathbf{k}}^{0}(\mathbf{r})\right|^{2} \propto \left|\sum_{l\mu} Y_{l\mu}(\hat{\mathbf{k}})\, i^{l} h_{l}^{(+)}(kr)\, M_{El\mu}\right|^{2}, \tag{1}$$

where $\mathbf{k}$ is the photoelectron wave vector, $\phi_{\mathbf{k}}^{0}(\mathbf{r})$ is the wave function at the detector, $Y_{l\mu}$ is a spherical harmonic, $h_{l}^{(+)}(kr)$ is a spherical Hankel function, and

$$M_{El\mu} = \langle El\mu, \underline{O1s}|\ T\ |g\rangle \tag{2}$$

is the matrix element describing the transition to the final state with a photoelectron $|El\mu\rangle$ of energy $E = \hbar^{2}k^{2}/2m$ and an O 1s hole. Final-state photoelectron diffraction effects can also be incorporated in this model by using $M_{El\mu}$ as input for self-consistent multiple-electron-scattering equations [22].

The transition matrix T can be conveniently expanded in a power series with respect to the perturbation of the radiation field V. One then has [23]

$$T = V + VG_0V + VG_0VG_0V + \cdots, \tag{3}$$

where G_0 is the Green function of the unperturbed solid. If we keep only terms up to second order in V, the part of Eq. (3) that makes a non-zero contribution to Eq. (2) reduces to the well-known Kramers-Heisenberg formula for resonant photoemission [24]

$$T = V^0_{\rm rad} + \sum_{j,m} V^j_{\rm AI} \frac{|m,j\rangle\langle m,j|}{\hbar\omega + E_g - E_m + i\Gamma_m/2} V^j_{\rm rad}, \tag{4}$$

where $V^0_{\rm rad}$ is the interaction of the radiation with the emitter, $V^j_{\rm rad}$ is the interaction with the resonating atom j, $V^j_{\rm AI}$ is the autoionizing Coulomb interaction between the emitter and atom j, E_g is the ground state energy, and the sums are over both Mn atoms j and their intermediate many-body states $|m,j\rangle$ of energy E_m and width Γ_m. We have here neglected exchange-type interactions via two-electron autoionization processes like $\langle El\mu;g|V^j_{\rm AI}|m,j;O1s\rangle$ that would lead to a greater overall similarity with the coulomb-plus-exchange matrix elements describing an interatomic Auger process, but such processes should be negligible for non-nearest neighbors and small for nearest-neighbors due to their strict dependence on non-zero orbital overlap. Such orbital overlap is not required for the coulombic term we have included here [1,5], which is associated with two-electron processes like $\langle El\mu;g|V^j_{\rm AI}|O1s;\ m,j\rangle$. A fully general theory of MARPE should include these exchange effects however. We also point out that the connection between MARPE and interatomic Auger electron emission is primarily formal, since the same sorts of matrix elements are embedded in the expressions describing both. However, the overall processes are fundamentally different.

We now note two special points that have been considered previously [5]:

--retardation effects must be considered in the interaction with the external radiation and in the autoionization interaction (see Eq. (4) in Ref. [5]), and

--the interatomic autoionization interaction must be generalized to the fully-relativistic Møller formula used previously in high-energy Auger theory [25,26] (see Eq. (5) in Ref. [5]).

At this level, the treatment should be capable of describing all many-electron interactions up to second order in the perturbation via Eq. (4), or up to arbitrary order via Eq. (3), including those for nearest-neighbors with the greatest overlap and thus enhanced many-electron interactions with the emitting atom.

If we now sacrifice some accuracy in describing nearest-neighbor behavior, the autoionization interaction can be conveniently expanded in multipoles that should be valid for resonator distances from the emitter $R_j >> r_1, r_2$, where r_1 and r_2 are electron-nuclear distances and are of the order of the relevant dimensions of the two core orbitals involved (here O 1s and Mn 2p). With these assumptions, and the further neglect of multipoles higher than dipoles, the effective interaction can be reduced to the following, in which several quantities are written out more explicitly than in prior work [5]:

$$V^j_{\rm AI} \approx e^2 r_1 r_2 \sum_{\mu_1\mu_2} F^{\mathbf{R}_j}_{\mu_1\mu_2} Y_{1\mu_1}(\hat{\mathbf{r}}_1) Y^*_{1\mu_2}(\hat{\mathbf{r}}_2), \tag{5}$$

where

$$F^{\mathbf{R}}_{\mu_1\mu_2} = \frac{-4\pi\ k^3}{3}\left[\frac{\delta_{\mu_1\mu_2}}{2\pi} h^{(+)}_0(kR) + h^{(+)}_2(kR)\ Y_{2,\mu_2-\mu_1}(\hat{\mathbf{R}})\ \langle Y_{1\mu_2}|Y_{2,\mu_2-\mu_1}Y_{1\mu_1}\rangle\right] \tag{6}$$

and the bracket represents a Gaunt integral with standard normalization [27]. Eqs. (5) and (6) can also be derived in a more rigorous way using non-relativistic quantum electrodynamics [22,28,29], where Eq. (6) is found to be simply proportional to the Green function of the photon field in the transverse gauge [28], and the remaining short-range longitudinal Coulomb coupling is neglected [29].

Combining results, we now find, in slightly different notation from, but equivalent meaning to, that in Ref. [5]

$$M_{El\mu} = A\ \langle E1|r|O1s\rangle\ \delta_{l,1} \sum_\lambda \varepsilon^{\rm eff}_\lambda\ \langle Y_{1\mu}|Y_{1\lambda}Y_{00}\rangle = A\ \langle E1|r|O1s\rangle\ \delta_{l,1}\ \varepsilon^{\rm eff}_\mu/\sqrt{4\pi}, \tag{7}$$

where A is a light-intensity normalization constant,

$$\varepsilon^{\rm eff}_\lambda = \varepsilon_\lambda - \sum_{\lambda'\mu_2} F_{\lambda\mu_2}\alpha_{\mu_2\lambda'}\varepsilon_{\lambda'} \tag{8}$$

is now the effective polarization vector that includes the effect of x-ray scattering at the Mn sites, and the magnitude of the resonance is controlled by a product of a structure-factor type of sum over Mn sites

$$F_{\lambda\mu_2} = \sum_j F^{\mathbf{R}_j}_{\lambda\mu_2} e^{i\mathbf{k}_{in}\cdot\mathbf{R}_j}, \tag{9}$$

and the Mn^{2+} polarizability tensor,

$$\alpha_{\mu_2\lambda'} = -\frac{4\pi e^2}{3}\sum_m \frac{\langle g|rY^*_{1\mu_2}|m\rangle\langle m|rY_{1\lambda'}|g\rangle}{\hbar\omega + E_g - E_m + i\Gamma_m/2}. \qquad (10)$$

The form for the polarizability given here makes it clear that it is directly related to the usual description of resonant photoemission in Eq. (4) and Ref. [24].

The polarizability has been calculated using a configuration interaction scheme for a central Mn^{2+} ion surrounded by six O^{2-} ions in an octahedral cluster [5,24], with interaction parameters derived previously from fits to both SARPE and x-ray absorption data, and an average over orientations of Mn magnetic moments, since the experiments have been performed above the MnO Néel temperature. In addition, $\alpha_{\mu_2\lambda'}$ can be well approximated by a quantity averaged over diagonal elements, as $\bar{\alpha}\delta_{\mu_2\lambda'}$, where $\bar{\alpha} = (\alpha_{-1-1} + \alpha_{00} + \alpha_{11})/3$ [5]. The above equations were used in Ref. [5] to calculate O 1s intensities. However, all resonant contributions to the O 1s intensities (i.e., the second term in Eq. (4)) were incorrectly multiplied by an extra factor of -4 in the computer calculations. Here, we present corrected theoretical results from this model, as well as results going beyond the earlier approximations used by considering higher order interactions in Eq. (3), and also compare these two sets of results to a theoretical approach based on more standard x-ray optical theory.

In Fig. 2(a) we compare experimental and theoretical results for the O 1s intensity as a function of photon energy and for light incident at an angle of 10° with respect to the surface. The connected points represent the corrected experimental results from Fig. 1(d) and the thin solid curve the theoretical results based on Eq. (3) above. The experimental data show a steeper negative slope than theory as energy is increased that we have verified by measurements and calculations to be due to a combination of decreasing photoelectric cross section and strong modulations due to photoelectron diffraction (cf. Fig. 1(e)) [17], both well understood effects [20,21]. If this difference in slope is , the agreement between experiment and theory is qualitatively good, although the amplitude of the intensity modulations is too small by a factor of 2-3 in theory,. Now going beyond this level of microscopic theory, we note that the remaining terms in the series expansion (3) describe processes in which an incoming photon is scattered by more than one Mn atom before it reaches the O emitter. In particular, they incorporate higher-order Mn-Mn interactions via the Møller formula [5,25,26]. This gives rise to extra terms in the effective polarizability of Eq. (7), which now becomes

$$\varepsilon_\lambda^{\text{eff}} = \varepsilon_\lambda - \bar{\alpha}\sum_{\lambda',j} \mathbf{F}^{\mathbf{R}_j}_{\lambda\lambda'} e^{i\mathbf{k}_{\lambda\lambda'}\cdot\mathbf{R}_j}\varepsilon_{\lambda'} + \bar{\alpha}^2 \sum_{\lambda'\lambda'',jj'} \mathbf{F}^{\mathbf{R}_{j'}}_{\lambda\lambda'} \mathbf{F}^{\mathbf{R}_j-\mathbf{R}_{j'}}_{\lambda'\lambda''} e^{i\mathbf{k}_{\lambda\lambda''}\cdot\mathbf{R}_{j'}}\varepsilon_{\lambda''} + \cdots, \qquad (11)$$

where the first two terms are the same as in Eq. (8) after approximating the polarizability by the average scalar $\bar{\alpha}$. This series can be summed up to an infinite order for a slab formed by a finite set of atomic planes [22], and a semi-infinite medium can be simulated by using a sufficiently-large number of layers. The result obtained in that case for the O 1s intensity is shown in Fig. 2(a) as a solid curve. The new terms in Eq. (11) bring the theoretical result much closer to the experimental one, making it evident that it is essential to include what is in effect multiple scattering of the incoming radiation in order to accurately describe such strong soft x-ray resonances. To our knowledge, this point has not been made before in discussing such resonances.

B. Relationship to an X-Ray Optical (Dielectric) Model

We now consider the relationship of this microscopic many-body theory to another related theoretical method for dealing with such effects: an x-ray optical approach based on Maxwell's and Fresnel's equations, as described in detail elsewhere [11,30]. Eq. (11) involves sums over Mn positions in the MnO crystal. However, the details of the atomic structure of the Mn sublattice should be irrelevant in the limit of long radiation wavelengths λ_x for which phase shifts along the scattered paths can be neglected. In this limit, Eq. (11) can be shown to reduce to the polarization vector derived from a macroscopic dielectric description based upon Maxwell's equations, in which the solid is represented by a local frequency-dependent dielectric function ε that is related to the atomic polarizability as $\varepsilon = 1 + 4\pi n_{Mn}\bar{\alpha}$, where n_{Mn} is the density of Mn atoms. This relationship between ε and $\bar{\alpha}$ can be derived from the Clausius-Mossotti relationship with the assumption that $\varepsilon \approx 1$, as is reasonable in the soft x-ray region. More specifically for the case of the Mn 2p resonance in MnO, the ratio of the wavelength to the Mn-Mn nearest-neighbor distance is ≈6.1. Therefore one would expect reasonable results to come out of the macroscopic description. We have here also implicitly assumed that the O atoms contribute only a small amount to the total polarizability in the vicinity of the Mn 2p resonances [5,22,30b,31].

Thus, an alternative, although more empirically-oriented, approach for calculating such effects is to derive the energy-dependent x-ray optical constants $\delta(h\nu)$ and $\beta(h\nu)$ in the index of refraction $n_r = \sqrt{\varepsilon} = 1 - \delta + i\beta$ [32] by measuring the absorption coefficient $\mu(h\nu) = 4\pi\beta(h\nu)/\lambda_x$ over the edges

in question (here Mn 2p), matching it in the non-resonant region to accurate theoretical and/or experimental data [30b, 31], and then using a Kramers-Kronig analysis to derive δ. These two parameters as derived experimentally in this study are shown as a function of photon energy in Fig. 2(b) (solid curves), where they are compared also to the same parameters as derived from the parameterized many-body model (dashed curves). The measured β has been fully corrected for the inelastic attenuation of the outgoing secondary electrons used to measure it via a set of measurements at varying takeoff angles [17,33]; taken together with the corrections for detector non-linearity, we thus believe that this curve, and the associated δ values are within ~1-2 % of the true values. However, such absorption coefficient measurements need to made with care, so that neither the measurement method (e.g. partial yield, total yield, fluorescence, collection angle) nor non-linearity in the detector distorts the final curves. The agreement between experiment and theory here is very good, with more fine structure in experiment, as expected. Note also that the variation in the experimental O 1s intensity in Fig. 2(a) about a mean value follows very closely the behavior of δ, a point to which we return below. Proceeding now via the Fresnel Equations to calculate the photoemission intensity as a function of photon energy, it can be shown that, for p-polarized radiation incident on a planar surface from vacuum with n = 1, and for a conducting or non-conducting, but non-magnetic, reflective medium, the ratio of the complex electric field magnitude just below the surface ($E(z = 0+)$) to the incident complex field magnitude just above the surface in vacuum ($E_{vac}^{inc}(z = 0-)$) is given by

$$t \equiv \frac{E(0+)}{E_{vac}^{inc}(0-)} = \frac{2\sin\theta_{h\nu}}{\sin\theta_{h\nu}' + n_r \sin\theta_{h\nu}} \quad , \tag{12}$$

where z is the coordinate perpendicular to the surface and $\theta_{h\nu}'$ is the complex angle of propagation below the surface, again measured relative to the surface. $\theta_{h\nu}'$ is further related to $\theta_{h\nu}$ via Snell's Law: $\cos\theta_{h\nu} = n_r \cos\theta_{h\nu}'$, with $\theta_{h\nu}$ real. The complex character of n_r also implies that E attenuates with z only according to $exp[-Im(k'z\sin\theta_{h\nu}')]$, where k' is the complex propagation wave vector inside the medium and equal to $2\pi n_r/\lambda_x$, and λ_x is the wavelength of the radiation. Normalizing the electric field inside the medium to the incident field just above the surface then gives for the electric field strength at depth z relevant for photoemission

$$|E(z)|^2 = |t|^2 \exp(-Im\{4\pi n_r z \sin\theta_{h\nu}' / \lambda_x\}). \tag{13}$$

The photoemission intensity $I(h\nu)$ can now be obtained by introducing the energy-dependent differential photoelectron cross section $d\sigma/d\Omega$ appropriate to the experimental geometry (which may in general also include the effects of photoelectron diffraction), the energy-dependent inelastic attenuation length for electrons Λ_e, and integrating over z as

$$I(h\nu) \propto \frac{d\sigma}{d\Omega} \int_0^\infty |E(z)|^2 \exp(-\frac{z}{\Lambda_e \sin\theta}) dz \, , \tag{14}$$

where we have not included factors of atomic density and solid angle acceptance of the analyzer that will be constant over an energy scan. Substituting Eq. (13) into Eq. (14) and integrating then yields finally

$$I(h\nu) \propto \frac{d\sigma}{d\Omega}(h\nu) \frac{|t(h\nu)|^2}{\frac{Im\{4\pi n_r(h\nu)\sin\theta_{h\nu}'(h\nu)\}}{\lambda_x(h\nu)} + \frac{1}{\Lambda_e(h\nu)\sin\theta}} \quad , \tag{15}$$

which is a completely general formula for photoemission intensity from a conducting or non-conduction, non-magnetic, semi-infinite substrate, with all dependences on energy explicitly indicated. Making use of Eq. 15 and the experimental values for δ and β in Fig. 2(b), we arrive at the dashed curve in Fig. 2(a), which is in excellent agreement with experiment, including all aspects of the fine structure. A similar degree of agreement is also found for other incidence angles $\theta_{h\nu}$.

This x-ray optical approach furthermore exhibits only small differences in fine structure with respect to the microscopic description based upon Eq. (11). These differences are due to differences in δ and β between theory and measurement (cf. Fig. 2(b)) and perhaps also to the fact that only the Mn polarizability has been considered in the microscopic theory, thus neglecting the small contributions from non-resonant O scattering over this energy range [30b,31]. In addition, we find that, if the infinite-order microscopic Eq. (11) is used together with the experimental x-ray optical constants to derive the polarizability, the calculated curve is essentially indistinguishable from that of Eq. (15), thus verifying the accuracy of the microscopic approach and its exact reduction to the x-ray optical model, provided that multiple scattering effects are included and certain conditions mentioned above are met.

In Fig. 2(c), we finally show normalized curves of the multi-atom effect on the O 1s intensity as a function of x-ray incidence angle, as calculated using the x-ray optical approach of Eq. (15). These curves make it clear that the effects are strongly sensitive to x-ray incidence angle, being much

smaller for angles greater than about 30 degrees, although very similar in shape for all angles. The calculated normalized +/- excursion of the effect as a function of incidence angle is further shown in the inset of Fig. 2(c), where it is compared to experimental results at four incidence angles. There is excellent agreement between experiment and theory, and theory furthermore predicts an asymptotic value of about 4.5% for the excursion at normal incidence. These results thus further confirm the accuracy of the x-ray optical analysis as compared to experiment, and also imply that such effects should be observable on crossing strong core-level resonances for <u>all</u> angles of x-ray incidence, although with greater difficulty of observation as $\theta_{h\nu}$ goes above about 20°-30°.

We also note that recent measurements have found similar MARPE effects in O 1s emission from CuO with Cu $2p_{3/2}$ resonance, and these show a overall excursion of ~20% that is similar to the magnitudes observed here for MnO [13]. Here, the effects have been termed "anti-resonances" to distinguish them from the all-positive effects reported in previous uncorrected data (cf. Fig. 1(c)), but the present work makes it clear that they are manifestations of the same interatomic resonant phenomenon. Although it was not possible in this work to see similar effects in O 1s emission from NiO [13], we believe that this could be due to the relatively high x-ray incidence angle of 35° used in this work, combined with the ~±2% statistical error in the data as compared to the few % effect that might be expected at this incidence angle (cf. inset of Fig. 2(c)).

It is now useful to compare these theoretical results with those from prior work by Henke on calculating photoelectron intensities via x-ray optics [30a]. We first note that he was interested in scanning the incidence angle $\theta_{h\nu}$ only, in which case δ, β, λ_x, and Λ_e all remain constant, and he was thus able to make certain approximations that we cannot due to the strong variation of both δ and β over a scan in photon energy. Nonetheless, if $|\delta|$, $\beta << 1$ over the energy scan, which Fig. 2(b) makes clear is an excellent assumption, our Eq. (15) can be simplified to

$$I(h\nu) \approx \frac{d\sigma}{d\Omega}(h\nu)\frac{|t(h\nu)|^2}{\frac{4\pi\beta(h\nu)\sin\theta_{h\nu}(h\nu)}{\lambda_x(h\nu)}+\frac{1}{\Lambda_e(h\nu)\sin\theta}}, \qquad (16)$$

which permits more direct comparison with this prior work. In particular, our use of $|t|^2$ to represent the strength of the electric field squared below the surface is inherently more accurate and versatile in application than the factor $[1-R][\sin\theta_{h\nu}/\sin\theta_{h\nu}']$ used by Henke in his prior analysis. An additional difference in the two approaches is that all quantities in the last expression are treated as real by

Henke, whereas we have shown that a more accurate expression related to this earlier formalism is a factor $[1-R][\sin\theta_{h\nu}/(Re\{n_r\sin\theta_{h\nu}'\})]$, with n_r and $\theta_{h\nu}'$ here treated as complex. In addition, the inverse x-ray attenuation length perpendicular to the surface in this prior work and appearing here as the first term in the denominator of Eq. (16) was further simplified by Henke, and finally is different from ours by a factor of $1/[\sin\theta_{h\nu}']^2$. In describing scanned-energy resonant data however, we find it essential to use the form in Eq. (15), or with some approximation, that in Eq. (16).

To gain further insight into the relationship of photoemission intensity to δ and β, we can further approximate Eq. (15) to the conditions of the measurements shown here, for which δ and β are both much less than unity (cf. Fig. 2(b)) and the reflectivity R is also small (with a maximum value for all cases considered here of 0.18 at $\theta_{h\nu} = 5°$), and this finally yields, after suppressing the obvious dependences on photon energy

$$I(h\nu) \approx \frac{d\sigma}{d\Omega}\cdot\frac{1+\delta}{\frac{4\pi\beta\sin\theta_{h\nu}}{\lambda_x}+\frac{1}{\Lambda_e\sin\theta}}. \qquad (17)$$

From this expression, it is clear that the variation of intensity with photon energy as normalized to the values on either side of a resonance should qualitatively follow δ, just as observed. The magnitude of this variation is also enhanced by the change in β, whose increase over the resonance generally acts to decrease intensity over the same region. The negative excursion of δ just before the resonance, together with the increase in β, thus produces the strong dips in intensity seen at about 639.5 eV in Figs. 2(a) and 2(d).

Although the numerical results from the microscopic model embodied in Eqs. (1)-(11) can be reduced to a continuum x-ray optical picture, provided we include higher-order effects representing multiple light scattering, it should nonetheless permit future calculations of such interatomic resonant photoemission effects from first principles, including in particular an allowance for nearest-neighbor many-body interactions that are only effectively included in the optical approach. Of course, any microscopic model is in a sense simply calculating the x-ray optical response of the system, but for nearest-neighbor effects, in free molecules, and for small clusters of atoms on the nanometer scale, it is not clear that an x-ray optical approach is particularly useful, or even appropriate. Beyond this, the excellent numerical agreement between the microscopic and macroscopic continuum dielectric descriptions presented above is expected to break down when the wavelength of the radiation is of the

order of, or smaller than, the relevant interatomic distances. Thus, if the resonating atoms do not form a compact enough lattice (as Mn does in MnO), the continuum dielectric treatment is not appropriate. Some possible examples of this are atoms situated inside the cages of fullerites or zeolites, and/or systems subjected to resonant excitation by shorter-wavelength radiation. The continuum dielectric model also is not appropriate for calculating such effects in nanometer-scale objects or systems with nanometer-scale heterogeneity or clustering in which the detailed atomic positions are to be allowed for, even if this model can be extended via methods such as Mie theory so as to apply to special cases such as small metal clusters of regular shape [34]. Neither is the continuum model appropriate for free molecules, in which core-core interatomic resonance effects appear to have recently been observed in angular distributions [12].

We also comment briefly on an intermediate theoretical approach that would involve assigning each atom a complex scattering factor based on some combination of measured and/or calculated optical constants, somehow partitioned among the different constituents so as to allow for element-specific resonance effects, with standard formulas for this appearing elsewhere [30b]. This method could in principle be applied to any arbitrary cluster of atoms, and with sufficient long-range order would lead to Bragg scattering effects at shorter wavelengths. However, this approach could not incorporate any unique nearest-neighbor effects, nor in its standard formulation would it explicity allow for the multiple scattering effects on resonance that we find to be important.

Regardless of the theoretical model that is most appropriate to use, such interatomic resonance effects (even though generally smaller and of different form than discussed previously) still represent an experimental probe that should be able for various situations to provide information on the near-neighbor identities and bonding of atoms B that surround a given emitter A, as suggested in prior work [1-4].

Finally, we note that both of the theoretical models discussed above can be extended to describe fluorescent x-ray emission. For the x-ray optical model, and for the case of a fluorescent energy that is far from any resonance and at a fluorescence exit angle θ^F that is large enough to minimize refraction and reflection at the surface, this would involve simply replacing $\Lambda_e \sin\theta$ with $\Lambda_x^F \sin\theta^F$ in Eqs. (15)-(17), with Λ_x^F equal to the fluorescent x-ray attenuation length along path length or $\lambda_x^F/[4\pi\beta^F]$ in obvious notation. With this replacement, Eqs. (15)-(17) thus represent different levels of approximation for handling what essentially reduces to the well-known self-absorption effects in x-ray

fluorescence that have been discussed previously in connection with MARPE [4,14]. In fact, viewed in this light, MARPE in x-ray emission can be viewed as having self absorption as a key ingredient, but via near-neighbor effects not the only ingredient. The microscopic model could also be similarly extended to predict fluorescence intensities, but we will not present these details here.

V. CONCLUSIONS

In summary, we have pointed out that a proper allowance for detector non-linearity is essential for accurately measuring multi-atom resonant photoemission effects, with the magnitude and form of the corrected results being significantly different from previous reports [1-4,6,7a]. A microscopic theoretical model proposed previously for describing these results [5] is found to well describe the observed effects, and confirms via agreement with experiment that they can be considered as interatomic resonance phenomenon. For the specific case of O 1s emission from MnO in the vicinity of the Mn 2p resonances treated here, this microscopic model, with the inclusion of higher-order interactions not considered previously, is also found to be reducible to a classical x-ray optical treatment using experimental optical constants. The x-ray optical model is furthermore found to well describe the observed intensity profiles as a function of both photon energy and x-ray incidence angle. It is thus of interest in future studies to explore the degree to which such effects, particularly with the expected enhancement of nearest-neighbor interactions, for more spatially dispersed resonating atoms so as to go beyond the simple x-ray optical picture, in nanometer-scale objects, and/or in free molecules, can provide an element-specific probe of near-neighbor properties and many-electron interactions. The experimental and theoretical approaches outlined here should provide a sound framework for such work, both for photoelectron and fluorescent x-ray emission. The microscopic theoretical model outlined here should also be capable of describing such core-core interatomic resonance effects in the intensities and angular distributions in photoemission from free molecules [12], as well as with straightforward generalization the valence-core interatomic resonance effects mentioned previously [8-10]. Finally, we point out that the demonstrated importance of multiple scattering of soft x-ray radiation in the vicinity of strong core-level resonances should be of relevance in the analysis of resonant elastic and inelastic x-ray scattering, other topics of high current interest [35].

ACKNOWLEDGEMENTS

We are grateful to M.G. Garnier, D. Nordlund, A. Nilsson and R. Denecke for pointing out the potential importance of detector non-linearity in our measurements, and to A. Kikas, M.P. Seah, J.B. Kortright, N. Brookes, M. Finazzi, G. Paolucci, and K. Prince for helpful comments. This work was supported by the U.S. Department of Energy, Office of Science, Office of Basic Energy Sciences, Materials Sciences Division, under Contract No. DE-AC03-76SF00098. Additional support was provided by the Basque Government and by the Fulbright Foundation (J G. de A., Grant No. 22726216-98), as well as the Miller Institute, U.C. Berkeley (E. A.).

REFERENCES

1. A. Kay, E. Arenholz, B.S. Mun, F.J. Garcia de Abajo, C.S. Fadley, R. Denecke, Z. Hussain, and M.A. Van Hove, *Science* **281**, 679(1998).

2. A.W. Kay, E. Arenholz, B.S. Mun, F.J. Garcia de Abajo, C.S. Fadley, R. Denecke, Z. Hussain, M.A. Van Hove, *J. Electron Spectrosc. Relat. Phenom.*. 103, 647 (1999).

3. (a) C.S. Fadley, E. Arenholz, A.W. Kay, J. Garcia de Abajo, B.S. Mun, S.-H. Yang, Z. Hussain, and M.A. Van Hove, in X-ray and Inner Shell Processes, AIP Conference Proceedings No. 506. R.W. Dunford et al., Eds. (AIP, New York, 2000), pp. 251-272, and (b) E. Arenholz and A.W. Kay, unpublished results.

4. E. Arenholz, A.W. Kay, C.S. Fadley, M.M. Grush, T.A. Callcott, D.L. Ederer, C. Heske, and Z. Hussain, *Phys. Rev. B* **61**, 7183 (2000).

5. F.J. Garcia de Abajo, C.S. Fadley, and M.A. Van Hove, *Phys. Rev. Lett.* **82**, 4126 (1999).

6. A. Kikas, E. Nommiste, R. Ruus, A. Saar, and I. Martinson, Sol. St. Commun. **115**, 275 (2000).

7. (a) M.G. Garnier, N. Witkowski, R. Denecke, D. Nordlund, A. Nilsson, M. Nagasono, and N. Mårtensson, and A. Föhlisch, Maxlab Annual Report for 1999 and private communication correcting this data; (b) D. Nordlund, M. G. Garnier, N. Witowsky, R. Denecke, A. Nilsson, M. Nagasono, N. Mårtensson and A. Föhlisch, to be published..

8. K.L.I. Kobayashi, N. Watanabe, H. Nakashima, M. Kubota, H. Daimon, and Y. Murata, *Phys. Rev. Lett.* **52**, 160 (1984).

9. P. Pervan, M. Milun, and D.P. Woodruff, *Phys. Rev. Lett.* **81**, 4995 (1999).

10. Y.F. Hu, G.M. Bancroft, and K.H. Tan, *Inorganic Chemistry* **39**, 1255-1264 (2000).

11. S.-H. Yang, B. S. Mun, A. W. Kay, S.-K. Kim,.J. B. Kortright, J. H. Underwood, Z. Hussain, C. S. Fadley, *Surf. Sci.* **461**, 557 (2000).

12. H. Wang, O. Hemmers, P. Focke, M. M. Sant'Anna, D. Lukic, C. Heske, R. C. C. Perera, I. Sellin, and D. Lindle, unpublished results.

13. M. Finazzi, G. Ghiringhelli, O. Tjernberg, L. Duo, A. Tagliaferri, P. Ohressser, and N.B. Brookes, to be published.

14. A. Moewes, E.Z. Kurmaev, D.L. Ederer, and T.A. Callcott, to be published.

15. (a) N. Mårtensson, P. Baltzer, P.A. Bruhwiler, J.-O. Forsell, A. Nilsson, A. Stenborg, and B. Wannberg, *J. Electron Spectrosc. Relat. Phenom.* **70**, 117 (1994); (b) C.S. Fadley et al., Prog. in Surf. Sci. 54, 341 (1997).

16. M.P. Seah, I.S. Gilmore, and S.J. Spencer, *J. Electron Spectrosc. Relat. Phenom.* **104**, 73 (1999) and earlier references therein.

17. A.W. Kay, Ph.D. dissertation (University of California-Davis, 2000), Chapters 4 and 5.

18. A. Gromko, C. Yi, A. Fedorov, and D. Dessau, private communication.

19. T. Valla and P.D. Johnson, private communication.

20. J.J. Yeh and I. Lindau, *At. Data and Nuc. Data Tables* **32**, 1 (1985).

21. C.S. Fadley et al., *Prog. in Surf. Sci.* 54, 341 (1997) and refs. therein.

22. F. J. García de Abajo, M. A. Van Hove, and C. S. Fadley, *Phys. Rev. B*, to appear, and unpublished results.

23. A. Messiah, *Quantum Mechanics* (North-Holland, New York, 1969), Vol. II, p. 849.

24. A. Tanaka and T. Jo, *J. Phys. Soc. Jpn.* **63**, 2788 (1994).

25. N.F. Mott and I.N. Sneddon, *Wave Mechanics and its Applications*, London, Oxford University Press, 1948), pp. 338-339.

26. J. P. Desclaux, in *Relativistic Effects in Atoms, Molecules, and Solids*, edited by G. L. Malli (Plenum Press, New York, 1981), pp. 115-143.

27. The Gaunt normalization is chosen such that

$< Y_{1\mu} | Y_{1\lambda} Y_{00} > = the\ integral\ over\ solid\ angle\ \Omega\ of\ Y^*_{1\mu}(\Omega) Y_{1\lambda}(\Omega) Y_{00}(\Omega) = \delta(\mu,\lambda)/\sqrt{4\pi}$.

28. Y. Nishino and G. Materlik, *Phys. Rev. B* **60**, 15074 (1999).

29. C. Cohen-Tannoudji, J. Dupont-Roc, and G. Grynberg, *Photon & Atoms. Introduction to Quantum Electrodynamics* (John Wiley & Sons, New York, 1989).

30. (a) B.L. Henke, Phys. Rev. A **6**, 94 (1972); (b) B. L. Henke, E. M. Gullikson, J. C. Davis, *Atomic Data and Nuclear Data Tables* 55, 34 (1993).

31. C. T. Chantler, *J. Phys. Chem. Ref. Data* 24, 71 (1995).

32. The sign convention for the imaginary part of the index of refraction used here is different from that used elsewhere of $n_r = 1 - \alpha - i\beta$ [25,27], but we choose it to be consistent with the use of retarded Green functions for G_0.

33. G. van der Laan and B.T. Thole, *J. Electron Spectrosc.* 46, 123 (1988).

34. S.V. Fomichev and D.F. Zaretsky, J. Phys. B: At. Mol. Opt. Phys. **32**, 5083 (1999) and references therein.

35. P. M. Platzman and E. D. Isaacs, *Phys. Rev. B* **57**, 11107 (1998); P. Kuiper, J. H. Guo, C. Sathe, J. Nordgren; J. J. M. Pothuizen, F. M. F.deGroot, G.A Sawatzky, Phys. Rev. Lett. **80**, 5204 (1998).

FIGURE CAPTIONS

FIG. 1. (a) The measured response function of our multichannel detection system (dashed curves), as plotted against the linear reference of an ideal detector (solid lines). The ordinate is measured counts per energy pixel, and the abscissa is proportional to the "true countrate" expected, which is in turn proportional to the emission current of the x-ray tube and thus incident x-ray flux. The inset shows the same kind of plot over a much broader countrate range. The solid lines for the ideal detector are chosen to asymptotically agree with the slope of the measured curve at the lowest countrates, although the final corrected results in (b)-(d) do not depend on this choice of reference. (b) O 1s spectra from MnO(001) off resonance (photon energy $h\nu = 637.6$ eV) and on resonance ($h\nu = 640.2$ eV) are shown before (dashed curves) and after (solid curves) applying the correction for detector non-linearity. The inset shows the experimental geometry, with x-ray incidence for this case at $\theta_{h\nu} = 20°$ and electron exit along the surface normal at $\theta_e = 90°$. The radiation is linear p-polarized, with the electric field vector $\bar{e}$ lying in the plane of the figure. (c) O 1s intensities derived from fitting analytical peak shapes to uncorrected (dashed curve) and corrected (solid curve) spectra such as those in (b) as a function of photon energy over the Mn $2p_{3/2}$ absorption range and still for $\theta_{h\nu} = 20°$, $\theta_e = 90°$. Also shown in the bottom of the panel is the Mn $2p_{3/2}$ absorption coefficient, as measured via the inelastic background underneath the O 1s peak. (d) As (c), but for $\theta_{h\nu} = 10°$, $\theta_e = 90°$ and extending over the full Mn $2p_{3/2,1/2}$ range. The countrates here were actually higher than in (c), but spanned a smaller portion of the detector dynamic range, and hence the corrections are smaller in magnitude. (e) As (b), but with a broader energy range which clearly shows the oscillation associated with scanned-energy photoelectron diffraction.

FIG. 2. (a) O 1s intensity from MnO(001) as a function of photon energy and for $\theta_{hv} = 10°$, $\theta_e = 90°$: experimental data (connected points) are compared to theoretical curves calculated using Eq. (8) (thin solid line, second order microscopic many-body theory = single radiation scattering), Eq. (11) (thick solid line, infinite-order microscopic theory = multiple radiation scattering), and x-ray optical dielectric theory based on Eq. (15) and the experimental constants shown in (b) (dashed curve). (b) The x-ray optical constants δ and β of MnO over the Mn 2p absorption region, as derived from microscopic many-body theory (dashed curves) and from experiment with corrected data for the absorption coefficient μ and Kramers-Kronig analysis. (c) Calculations of the O 1s intensity as a function of photon energy based on the experimental optical constants in (b) and Eq. (15) from x-ray optical theory. Curves are shown for various x-ray incidence angles. The inset shows the normalized magnitude of the negative-to-positive excursion in % as a function of x-ray incidence angle, as calculated using x-ray optical theory (solid points) and as measured in this study (large open circles).

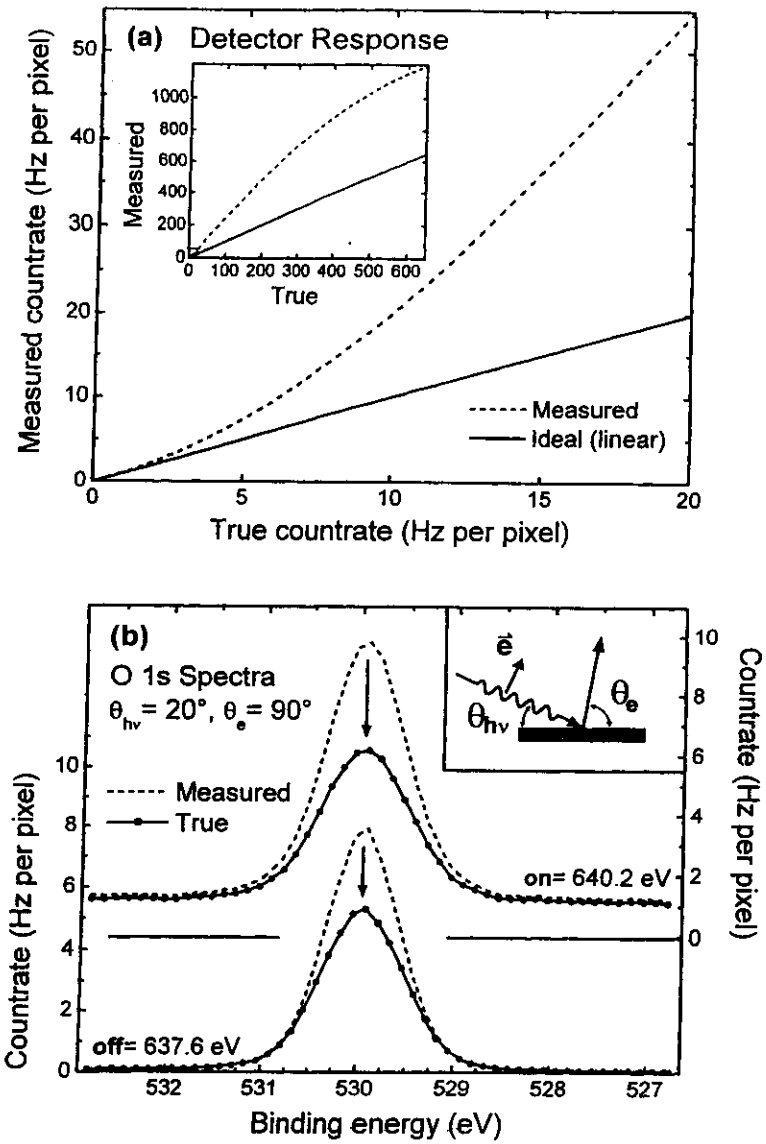

Figures 1(a), (b)

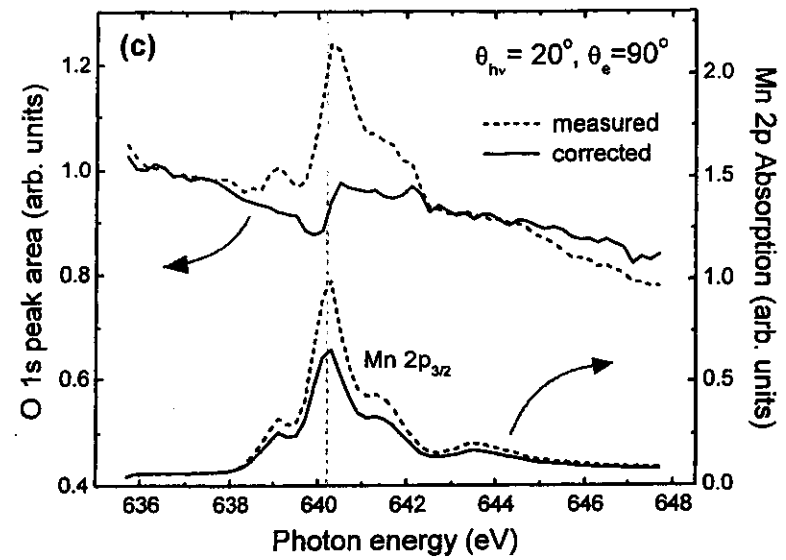

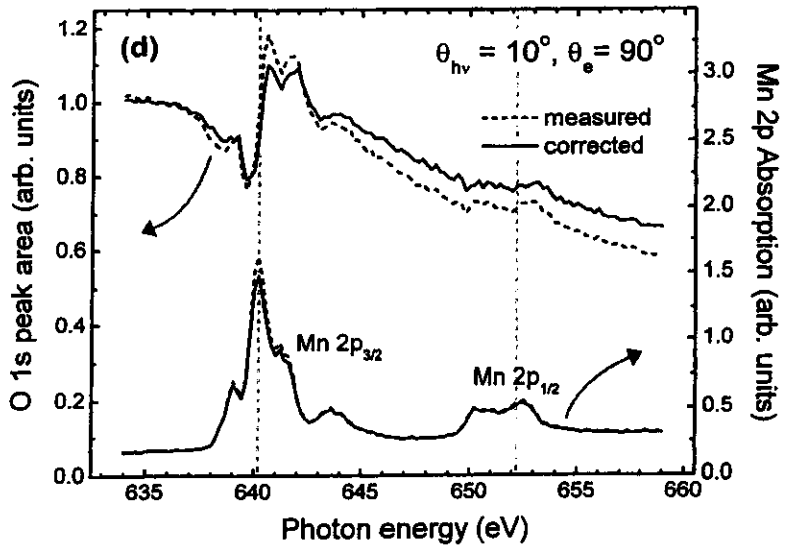

Figures 1(c), (d)

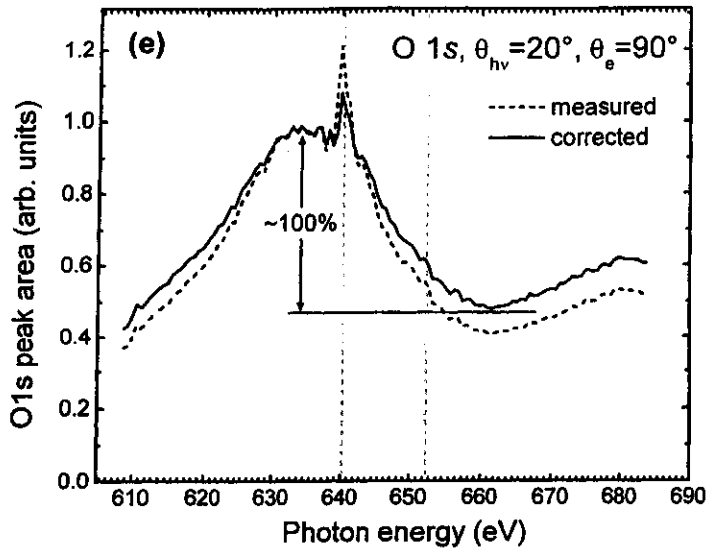

Figure 1(e)

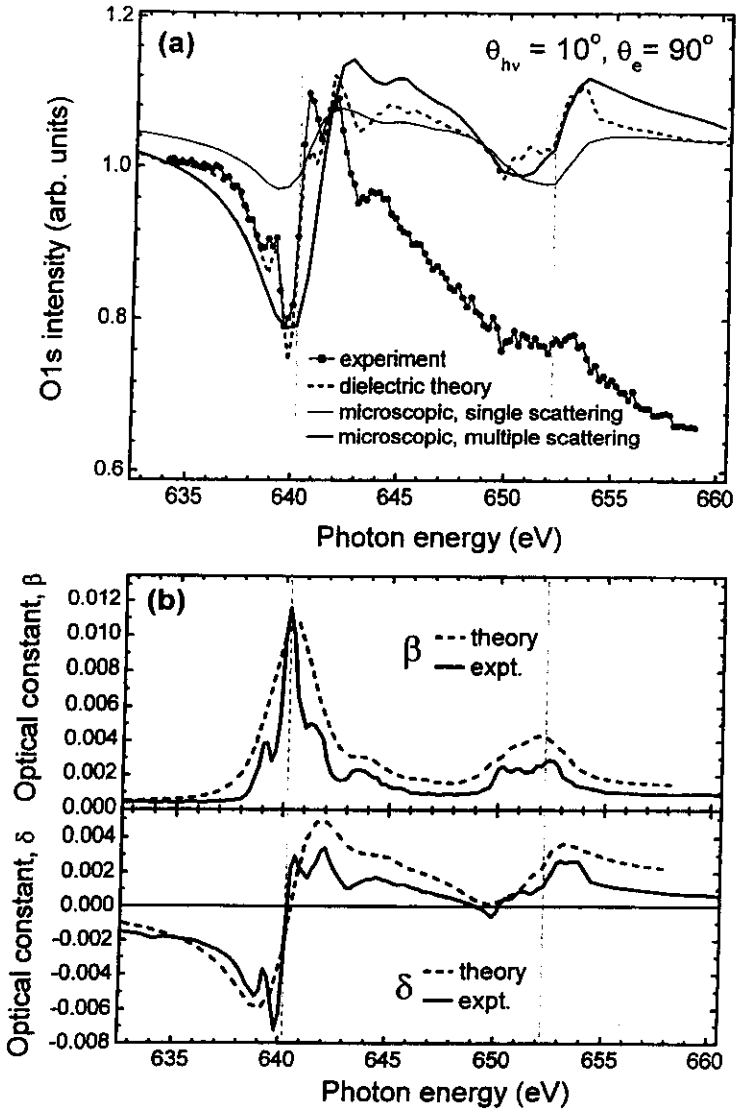

Figures 2(a), (b)

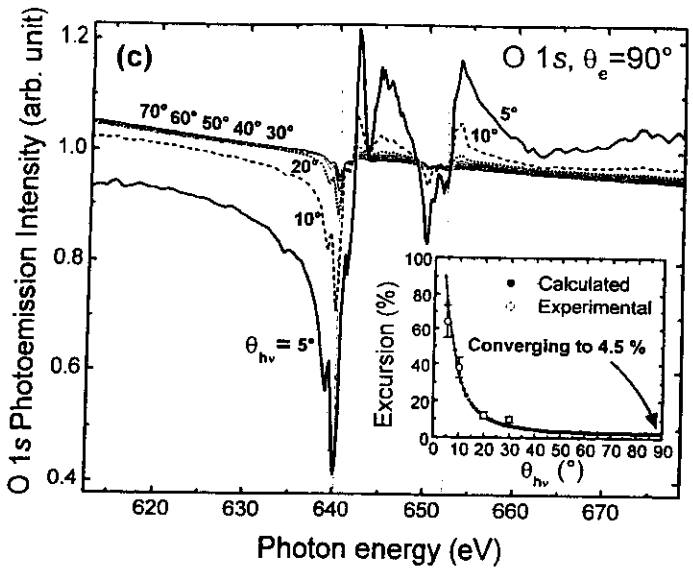

Figure 2(c)

Phys. Rev. B, to appear

Multiple scattering of electrons in solids and molecules: a novel cluster-model approach

F. J. García de Abajo,[1,2,*] M. A. Van Hove,[1,3] and C. S. Fadley[1,3]
[1] *Materials Sciences Division, Lawrence Berkeley National Laboratory, Berkeley, CA 94720, USA*
[2] *Centro Mixto CSIC-UPV/EHU, San Sebastián, Spain*
[3] *Department of Physics, University of California, Davis, CA 95616, USA*
(May 26, 2000)

A new method for the simulation of electron scattering and diffraction in solids and molecules within the cluster approach is presented with explicit applications to photoelectron diffraction, electron scattering in molecules, and LEED. No approximations are made beyond the muffin-tin model, and in particular, an exact representation of the free-electron Green function is used. All multiple scattering paths are accounted for up to an order of scattering that ensures convergence. The new method relies upon a convenient separation of the free-electron Green function in rotation matrices and translations along the z axis, which greatly reduces the computation time and storage demand. The evaluation of the multiple scattering expansion is implemented using the divergent-free recursion method, which permits performing an iterative refinement of the final-state wave function, as expressed in the basis set of spherical harmonics attached to each atom of the cluster. Examples are offered in which divergences encountered when using either direct multiple scattering or the more sophisticated simultaneous relaxation method are eliminated by using the recursion method. The computation time needed by the resulting computer program of electron diffraction in atomic clusters (EDAC) to determine the self-consistently-scattered wave function is proportional to $N^2(l_{\max}+1)^4$, where N is the number of atoms in the cluster and $l_{\max}$ is the maximum angular momentum for which the scattering phase shifts take non-negligible values. Within this method it is possible to establish that in practical cases $N > 1000$ might be needed for convergence of the cluster size, although the angular averaging inherent in many experiments may reduce this. The recursion method has also been modified to reduce the effort in computing angular distributions of photoelectrons and low-energy diffracted electrons, which now take negligible time for each angle of emission once the wave function has been determined for a given electron energy. Angle and energy distributions of core-level photoemission, elastic scattering of electrons from a free molecule, and low-energy electron diffraction in large-unit-cell surfaces are calculated.

61.14.-x, 61.14.Dc, 61.14.Qp

I. INTRODUCTION

Multiple elastic scattering (MS) plays a central role in the description of electron transport inside solids and molecules in different experimental spectroscopies like photoelectron diffraction (PD),[1–3] low-energy electron diffraction (LEED),[4,5] Auger electron diffraction (AED),[6] x-ray-absorption fine structure (XAFS),[7] and related techniques.

Various approximations are customarily employed to efficiently calculate MS effects. For relatively high electron energies like the ones considered in this work (> 50 eV above the Fermi level), electron scattering is rather insensitive to the outermost region of the atomic potentials that make up the solid or molecule. Therefore, the atomic potentials can be well approximated by spherically-symmetric muffin-tin potentials.[4] In addition, inelastic scattering is usually treated in a phenomenological way via a complex optical potential, or equivalently, inelastic mean free paths.[4]

Two different categories of computational schemes can be distinguished, depending on the use made of the symmetry of the atomic structure in the case of solids: layer-by-layer methods and cluster methods. The former have been primarily developed in the context of LEED and take advantage of the fact that the atoms of an oriented crystal are disposed in layers parallel to the surface, resulting in remarkably efficient algorithms for the transport between layers.[4,8–10] The latter do not require any sort of long-range order and can be applied to other classes of problems.[11–17]

In particular, when translational crystal symmetry is broken due to either the presence of randomly distributed adsorbates and defects or a localized character of the electron source as in the case of PD and AED, cluster models provide a natural approach for simulating MS effects that is suggested by the fact that excited electrons cannot travel large distances in real solids without suffering inelastic losses, so that the region which actually contributes to the emission of elastically scattered electrons defines a finite cluster surrounding the adsorbate, defect, or emitter.[11–17] This approach is also suitable for dealing with similar scattering phenomena in adsorbed or free molecules.

A hybrid model consisting of treating MS within a cluster formed by concentric spherical shells was proposed by Pendry[18] and implemented by Saldin *et al.*[19–21] to simulate x-ray-absorption near-edge structure (XANES),[19] LEED,[20] AED, and PD.[21] This method can in fact be advantageous in LEED calculations when large surface unit cells are considered.[20]

The more straightforward cluster approach adopted in the present work has been extensively employed in the past within a single-scattering approximation, and it has been found to reproduce qualitatively, and in several respects quantitatively, many of the experimental features in both XAFS[7,22] and PD.[2,6,23] However, higher orders of MS are needed to improve accuracy and structural analyses.[24] For example, by interpreting the terms of the MS series as paths that the electron follows connecting atoms in the cluster in all possible ways,[25] characteristic MS effects like forward focussing and defocussing along rows of atoms have been discerned in PD experiments.[24]

A basis set suited to describe the electron wave function is provided by spherical harmonics and spherical Bessel functions attached to each atom of the cluster. This incorporates curved-wave effects in a natural way. Unfortunately, the propagation of these functions between cluster atoms is computationally very demanding.[26,27,4] Since no intensive use of crystal symmetry is made in cluster models, further approximations have been introduced in the past in order to make feasible the calculation of the MS series.[28–37,2,7,6,11,13–15,21,22]

In the high-energy limit, the propagation reduces to plane-wave factors (hence the name plane-wave approximation) and each term in the MS series becomes a product of scattering amplitudes.[7] Different expansions of the propagated wave function in the finite region centered around each cluster atom lead to the so-called small-atom approximations.[33,11] Among them, the point-scattering approximation goes beyond the plane-wave approximation by multiplying the scattering amplitude by appropriate curved-wave factors.[35]

As the experimental resolution increases, more accurate theoretical analyses become necessary. These are complicated by the fact that the number of multipole terms that are needed rises rapidly with increasing electron energies. The maximum of the significant angular momentum quantum numbers scales roughly as $l_{\max} \sim kr_{\mathrm{mt}}$, where k is the electron momentum and r_{mt} is the muffin-tin radius of the scatterers. Upon inspection of actual calculations, $l_{\max}$ is of the order of $5-20$ for electron energies in the range $50-700$ eV. Since the number of different multipole components (l,m) used to describe the electron wave function around each atom is $(l_{\max}+1)^2$, the aforementioned propagation between each pair of atoms involves multiplication by propagation matrices, requiring $(l_{\max}+1)^4$ complex products.

On the other hand, the number of atoms N needed in a cluster to reach convergence is also important in the evaluation of the computational demand of the problem. This number scales as the cube of the electron inelastic mean free path (imfp), λ_i. We estimate N as the number of sites of a simple cubic lattice of lattice constant 2.5 Å that are contained in a sphere of radius $1.5\lambda_i$. The dependence of the universal imfp curve on the electron energy must be also allowed for.[38–40] The relation between $l_{\max}$ and the electron momentum discussed above has been assumed for a typical muffin-tin radius $r_{\mathrm{mt}} = 1.5$ Å. In this way, one obtains the relation between N and $l_{\max}$ shown in Fig. 1 by the solid curve.

In order to overcome the rapidly-growing computational demand with increasing $l_{\max}$, Rehr and Albers[13] (R-A) provided a clever procedure based upon a separable representation of the free-electron Green function that allows one to generalize the scattering amplitudes, substituting them by matrices that describe each scattering event for a given type of atoms in such a way that the leading element of each matrix reproduces the point-scattering approximation. Their method, which produces reliable results when keeping only a few more relevant elements in those matrices,[13] is particularly suitable to calculate the contribution of different individual electron paths, and it has been implemented for PD calculations by Kaduwela *et al.*[17] and by Chen *et al.*[41]

Rather than including all possible electron paths, Zabinsky *et al.*[36] have also shown that only a small fraction of all paths contribute significantly to the MS series in XAFS. This has permitted them to reduce substantially the total computational effort by only including in the calculation selected paths whose contributions are non-negligible already within the plane-wave approximation. Their approach is very efficient in particular if the so-called second-order R-A separable representation is used, where each scattering event within a given electron path is typically represented by a 6×6 matrix.

More recently, Chen *et al.*[41] have used a similar approach in the case of PD, incorporating an iterative evaluation of the MS expansion within the framework of the R-A separable representation.[13] In this approach, the number of complex multiplications per iteration is $36N^3$.

In the present work, the MS expansion is evaluated using an exact representation of the Green function propagator. An iterative procedure is followed that requires $\approx (10/3)N^2(l_{\max}+1)^3$ multiplications per iteration. Wu and Tong[42] have reported divergences in the exact MS expansion and claimed that these divergences can be prevented by using the simultaneous relaxation method,[43] consisting of both mixing the result of each iteration with that of the previous one and using the updated components of the wave function as they are calculated rather than waiting for a given iteration to be completed. That iteration procedure is compared in the present paper with the Haydock recursion method,[44–46] which is shown to be more robust and to prevent divergences not avoided by the former. In addition, the recursion method results in faster convergence as compared with either the direct MS expansion or the simultaneous relaxation method. These ideas have been implemented in a new fully-automated computer code for calculating electron diffraction in atomic clusters (EDAC). A similar approach has been recently employed in the description of photon scattering in nanostructures.[47] The computational performance of EDAC as compared with

Submitted to Phys. Rev. B

second-order R-A is shown in Fig. 1 (broken curve): the EDAC method is faster outside the shadowed area.

The MS theory is reviewed in Sec. II in a way suitable to be employed within the selected iterative scheme. Further computational details are given in Sec. III. In particular, several iteration methods are discussed and a modification of the recursion method is introduced to allow calculating scattered or emitted electron intensities for multiple directions simultaneously from a single MS calculation (Sec. III A). Moreover, the free electron propagators are decomposed into rotations and translations along the z axis, resulting in a significant reduction both in time and in storage demand (Sec. III B). Particular examples of application to PD, elastic electron scattering from molecules, and LEED from surface structures with large unit cells are presented in in Secs. IV, V, and VI, respectively. Finally, the main conclusions are summarized in Sec: VII.

Atomic units (a.u., i.e., $e = m = \hbar = 1$) will be used from now on, unless otherwise specified. The notation of Messiah[48] for spherical Bessel and Hankel functions, spherical harmonics, and rotation matrices will be adopted.

II. MULTIPLE SCATTERING THEORY

Let us begin by introducing the standard elements of multiple scattering theory in a Green's function approach. Consider an electron of energy E described by the wave function $\varphi^0(\mathbf{r})$ that satisfies the free-electron Schrödinger equation

$$(H_0 - E)\varphi^0 = 0, \tag{1}$$

where $H_0 = -\nabla^2/2$.

The presence of a solid or molecule introduces a strong perturbation that can be represented by the potential

$$V(\mathbf{r}) = \sum_\alpha V_\alpha(\mathbf{r}),$$

where the sum is extended over atomic positions $\mathbf{R}_\alpha$. Within the muffin-tin model adopted here, each atomic potential V_α vanishes outside a sphere of radius $r^\alpha_{\rm mt}$ (the muffin-tin radius) centered at $\mathbf{R}_\alpha$. These are non-overlapping spheres and $V(\mathbf{r})$ is set to a constant (the muffin-tin zero) in the interstitial region.

The wave function φ that satisfies the full Schrödinger equation $(H_0 + V - E)\varphi = 0$ can be written $\varphi = \varphi^0 + \phi$, where ϕ is the scattered part. Using matrix notation,[49] the latter can be expressed in terms of the atomic-cluster T matrix as

$$\phi = G_0 T \varphi^0, \tag{2}$$

where G_0 is the free-electron propagator that satisfies $(E - H_0)G_0 = 1$ and $k = \sqrt{2E}$ is the electron momentum. Defining the cluster Green function G via $(E - H_0 - V)G = 1$, the T matrix can be written $T = V + VGV$. An implicit dependence on E is understood in these expressions.

The key ingredient of MS theories is the reduction of the T matrix of the cluster to the T_α matrices of the individual muffin-tin potentials V_α. The latter are defined by the self-consistent relation

$$T_\alpha = V_\alpha + V_\alpha T_\alpha V_\alpha. \tag{3}$$

Following Beeby,[25] T can be written as a series expansion whose terms represent all possible electron scattering paths. More precisely,

$$T = \sum_\alpha \Lambda_\alpha,$$

where

$$\Lambda_\alpha = T_\alpha + \sum_{\beta\neq\alpha} T_\beta G_0 T_\alpha + \sum_{\gamma\neq\beta}\sum_{\beta\neq\alpha} T_\gamma G_0 T_\beta G_0 T_\alpha + \dots \tag{4}$$

accounts for MS paths in which the first scattering event occurs at atom α and two consecutive scattering events take place always at different atoms of the cluster. From Eq. (4), T can alternatively be defined as

$$\begin{aligned} T &= \sum_\alpha (T_\alpha + \sum_{\beta\neq\alpha} \Lambda_\beta G_0 T_\alpha), \\ &= T_{\alpha_0} + \sum_{\beta\neq\alpha_0} (\Lambda_\beta + \Lambda_\beta G_0 T_{\alpha_0}), \end{aligned} \tag{5}$$

for any atom α_0.

Inserting Eq. (5) into Eq. (2), the scattered wave reduces to

$$\phi = \sum_\alpha (\phi^0_\alpha + \sum_{\beta\neq\alpha} G_0 \Lambda_\beta \phi^0_\alpha), \tag{6}$$

where

$$\phi^0_\alpha = G_0 T_\alpha \varphi^0 \tag{7}$$

represents the first-order contribution to MS. The second term on the right hand side of Eq. (6) can be understood as the propagation of the results of scattering at atom α to every other atom of the cluster β, followed by subsequent MS starting at the latter.

Some information on the structure of the scattered wave function can be gained by considering explicit expressions for G_0. Namely,

$$\begin{aligned} G_0(\mathbf{r}-\mathbf{r}') &= \frac{-1}{2\pi}\frac{e^{ik|\mathbf{r}-\mathbf{r}'|}}{|\mathbf{r}-\mathbf{r}'|} \\ &= -2k\sum_L h^{(+)}_L(k\mathbf{r}) j_{l-m}(k\mathbf{r}')(-1)^{l+m}, \quad (r > r') \end{aligned} \tag{8}$$

where $h^{(+)}_L(k\mathbf{r}) = i^l h^{(+)}_l(kr) Y_L(\Omega_r)$ represents an outgoing spherical wave, $j_L(k\mathbf{r}') = i^l j_l(kr') Y_L(\Omega_{r'})$ is a mixture of outgoing and incoming spherical waves that exhibits no net flux into or out of a closed surface containing the origin, $h^{(+)}_l$ is a spherical Hankel function,[48] j_l is a spherical Bessel function, and $L = (l, m)$ labels spherical harmonics Y_L. Since, by virtue of Eq. (3), T_α vanishes outside the muffin-tin sphere α, one finds, using Eqs. (7) and (8),

$$\phi^0_\alpha(\mathbf{r}) = \sum_L h^{(+)}_L[k(\mathbf{r}-\mathbf{R}_\alpha)]\,\phi^0_{\alpha,L} \tag{9}$$

for $|\mathbf{r} - \mathbf{R}_\alpha| > r^\alpha_{\rm mt}$.[50] Therefore, ϕ^0_α is a superposition of outgoing spherical waves centered on $\mathbf{R}_\alpha$. Following a similar argument, the self-consistently scattered wave can be written

$$\phi(\mathbf{r}) = \sum_\alpha \sum_L h^{(+)}_L[k(\mathbf{r}-\mathbf{R}_\alpha)]\,\phi_{\alpha,L} \tag{10}$$

for $\mathbf{r}$ outside the muffin-tin spheres. Eq. (10) states that the scattered wave finds its sources in the muffin-tin spheres, from where it emerges as a combination of outgoing spherical waves.

The propagation of ϕ^0_α from atom α to atom β, which is needed in the evaluation of Eq. (6), can be performed by using Eq. (9) and the translation formula of spherical harmonics[26,27,4]

$$h^{(+)}_{L'}[k(\mathbf{r}-\mathbf{R}_\beta)] = \sum_L j_L[k(\mathbf{r}-\mathbf{R}_\alpha)] G_{\alpha\beta,LL'}, \tag{11}$$

where

$$G_{\alpha\beta,LL'} = 4\pi \sum_{L''} h^{(+)}_{L''}[k(\mathbf{R}_\alpha - \mathbf{R}_\beta)] \times \int d\Omega\, Y_L(\Omega) Y_{L''}(\Omega) Y^*_{L'}(\Omega).$$

Eq. (11) is valid provided that $|\mathbf{r} - \mathbf{R}_\alpha| < |\mathbf{R}_\alpha - \mathbf{R}_\beta|$; this condition is satisfied when $\mathbf{r}$ is contained inside the muffin-tin sphere $\beta \neq \alpha$ and non-overlapping spheres are considered. It is also convenient to represent G_0 in the basis set of spherical harmonics attached to each atom of the cluster. Using Eqs. (8) and (11), one finds[26,27,4]

$$G_0(\mathbf{r}-\mathbf{r}') = -2k \sum_{LL'} j_L[k(\mathbf{r}-\mathbf{R}_\alpha)] j_{l'-m'}[k(\mathbf{r}'-\mathbf{R}_\beta)] \times (-1)^{l'+m'} G_{\alpha\beta,LL'}, \tag{12}$$

and this expression is valid in the present context for $\alpha \neq \beta$, and $\mathbf{r}$ and $\mathbf{r}'$ lying inside different non-overlapping muffin-tin spheres.

With the help of these expressions, all spatial integrals that are implicit in Eqs. (4) and (6) (see Ref. [49]) can be collected in the so-called scattering matrix elements,

$$t_{\alpha,LL'} = -2k \int d\mathbf{r} d\mathbf{r}'\, j_{l-m}[k(\mathbf{r}-\mathbf{R}_\alpha)](-1)^{l+m} \times T_\alpha(\mathbf{r},\mathbf{r}')\, j_{L'}[k(\mathbf{r}'-\mathbf{R}_\alpha)]. \tag{13}$$

For spherically-symmetric potentials, $t_{\alpha,LL'}$ becomes diagonal and it is given in terms of the scattering phase shifts δ^α_l as[48]

$$t_{\alpha,LL'} = t_{\alpha,l}\delta_{LL'} = \sin\delta^\alpha_l e^{i\delta^\alpha_l}\delta_{LL'}. \tag{14}$$

Finally, using Eqs. (4) and (9)–(13), and identifying coefficients that multiply into the same functions $h^{(+)}_L[k(\mathbf{r}-\mathbf{R}_\alpha)]$, Eq. (6) reduces to

$$\begin{aligned} \bar{\phi}_\alpha &= \bar{\phi}^0_\alpha + \sum_{\beta\neq\alpha} t_\alpha G_{\alpha\beta}\bar{\phi}^0_\beta \\ &\quad + \sum_{\gamma\neq\beta}\sum_{\beta\neq\alpha} t_\alpha G_{\alpha\beta} t_\beta G_{\beta\gamma}\bar{\phi}^0_\gamma + \dots, \end{aligned} \tag{15}$$

where $\bar{\phi}^0_\alpha$ and $\bar{\phi}_\alpha$ denote column vectors of components $\phi^0_{\alpha,L}$ and $\phi_{\alpha,L}$, respectively, $G_{\alpha\beta}$ represents the matrix of components $G_{\alpha\beta,LL'}$, the scattering matrix t_α has components given by Eq. (14), and matrix multiplication involves summation over indices L, L', etc.

III. COMPUTATIONAL PROCEDURE

The time employed in the direct evaluation of Eq. (15) grows exponentially with the number of terms on the right hand side. However, an iterative procedure makes it feasible to evaluate the MS series until convergence is achieved, as discussed below in Sec. III A,[41,42,47] where several iteration methods are examined in connection with the solution of that equation, including a new modification of the recursion method that allows us to calculate intensities simultaneously for many angles in the far electron field from a single MS calculation.

An exact representation of the free electron Green function is used in the present work, and this is made possible in part thanks to the saving in both computation time and storage demand achieved through the method introduced in Sec. III B: decomposition of the Green function into elementary rotations and translations while keeping track of the latter, so that they are not unnecessarily re-calculated during the full MS evaluation.

A. Iterative solution of the MS series

It is easy to see that the sum of the first $n+1$ terms on the right hand side of Eq. (15), $\bar{\phi}^n_\alpha$, obeys the following recurrence relation:

$$\bar{\phi}^n_\alpha = \bar{\phi}^0_\alpha + t_\alpha \sum_{\beta\neq\alpha} G_{\alpha\beta}\bar{\phi}^{n-1}_\beta, \quad (n > 0). \tag{16}$$

That is, the difference between $\bar{\phi}^n_\alpha$ and $\bar{\phi}^{n-1}_\alpha$ is just the $n^{\rm th}$ sum on the right hand side of Eq. (15). Each term in that sum contains n products by matrices t_α, that is,

it can be interpreted as the contribution of paths along which the electron undergoes n atomic-scattering events.

Taking the $n \to \infty$ limit in Eq. (16), one finds

$$\tilde{\phi}_\alpha = \tilde{\phi}^0_\alpha + t_\alpha \sum_{\beta \neq \alpha} G_{\alpha\beta} \tilde{\phi}_\beta. \tag{17}$$

The direct inversion of Eq. (17), sometimes called giant-matrix inversion (GMI), is prohibitive in many cases, since it requires performing $\sim N^3(l_{\max}+1)^6$ complex products. However, this has been carried out by some authors for small values of N and $l_{\max}$[51,52] and is also commonly used within individual layers in a surface with small number of atoms per surface unit cell.[4,5]

Three different iterative techniques have been used and compared in the present work to evaluate Eq. (15): (a) direct Jacobi iteration, (b) simultaneous relaxation,[43] previously used in this context,[42] and (c) the Haydock recursion method.[44–46]

(a) *Direct Jacobi iteration.* This method is based upon the iterative evaluation of Eq. (16). Starting with $\tilde{\phi}^0_\alpha$, each iteration of Eq. (16) leads to the next order of scattering, and this procedure has to be carried out until convergence is achieved. Substituting $\phi^n_{\alpha,L}$ for $\phi_{\alpha,L}$ in Eq. (10), one obtains the approximate wave function calculated up to order n of MS. Since the wave function coefficients $\phi_{\alpha,L}$ span a space of dimension $(l_{\max}+1)^2 N$, Eq. (16) can also be regarded as the power series inversion formula $1/(1-X)|\phi\rangle = (1+X+X^2+\ldots)|\phi\rangle$, where X is a matrix that operates on that space, defined in terms of t_α and $G_{\alpha\beta}$, and $|\phi\rangle$ is the vector of coefficients $\phi_{\alpha,L}$. Unfortunately, when any of the eigenvalues of X has a magnitude larger than 1, this expansion series fails to converge. This problem has already been discussed in the context of LEED[4] and PD.[42] Faster convergent schemes can be found that do not require an extra computational effort, at the price of dismissing the intuitive physical picture of going to the next order of scattering with each iteration step. This is the case of the simultaneous relaxation method and the recursion method discussed next.

(b) *Simultaneous relaxation method* (SR). This consists of using the latest values of $\tilde{\phi}^n_\alpha$ as soon as they are calculated. In addition, the result obtained from its iteration is mixed with the previous result to improve convergence. Then, the iteration formula becomes

$$\tilde{\phi}''^n_\alpha = \tilde{\phi}^0_\alpha + t_\alpha \sum_{\beta \neq \alpha} G_{\alpha\beta} \tilde{\phi}'^n_\beta$$

and

$$\tilde{\phi}^n_\alpha = \eta \tilde{\phi}''^n_\alpha + (1-\eta)\tilde{\phi}^{n-1}_\alpha,$$

where $\tilde{\phi}'^n_\beta = \tilde{\phi}''^n_\beta$ for $\beta < \alpha$ and $\tilde{\phi}'^n_\beta = \tilde{\phi}^{n-1}_\beta$ otherwise, and η is a mixing parameter typically adjusted in the range $0 < \eta < 2$ in order to accelerate convergence. For $0 < \eta < 1$ one has what is termed underrelaxation.[43]

(c) *Modified recursion method.* With the notation of point (a) above, Eq. (17) can be written $|\phi\rangle = (\lambda - X)^{-1}|\phi^0\rangle$ ($\lambda = 1$). The relevant magnitude in which we are interested is the electron current at the detector, which is proportional to $|\langle f|\phi\rangle|^2$ with a suitable definition of the final detected wave function in a given direction $\langle f|$ (e.g., see Sec. IV below). Haydock's recursion method[44–46] permits obtaining this matrix element by iterative refinement. Here, λ plays the same role as the energy in calculations of solid ground state properties.[45,46] Although we are only interested in the value $\lambda = 1$ in the present case, the recursion method is advantageous because it is fully convergent for any matrix X. Actually, it produces rigorously exact values when the iteration is carried out $(l_{\max}+1)^2 N$ times, although convergence is achieved much earlier, typically in less than 20 iterations in the examples presented in the present work.

In many cases, one is interested in calculating angular distributions of emitted or scattered electrons (e.g., in Fig. 3). Unfortunately, the recursion method requires carrying out the MS iteration procedure for each direction of emission (i.e., for each $\langle f|$). Here, we have modified the recursion method so that it allows one to obtain intensities for various directions of emission with a single MS calculation, provided one stores the moments $\mu_n = \langle f|X^n|\phi^0\rangle$ for each $\langle f|$ and each iteration step n. Our modified method is based upon the double recurrence

$$|\alpha_{p+1}\rangle = [(X^\dagger - a^*_p)|\alpha_p\rangle - b^*_p|\alpha_{p-1}\rangle]/b^*_{p+1} \tag{18}$$

and

$$|\beta_{q+1}\rangle = [(X - a_q)|\beta_q\rangle - b_q|\beta_{q-1}\rangle]/b_{q+1}, \tag{19}$$

where the starting values are $|\alpha_{-1}\rangle = |\beta_{-1}\rangle = 0$, $|\alpha_0\rangle = |f\rangle/\sqrt{\mu^*_0}$, and $|\beta_0\rangle = |\phi_0\rangle/\sqrt{\mu_0}$, and a_n and b_n are complex numbers. Upon inspection, one can easily prove that

$$\langle \alpha_i|\beta_j\rangle = \delta_{ij} \tag{20}$$

if one chooses

$$a_n = \langle \alpha_n|X|\beta_n\rangle \tag{21}$$

and b_{p+1} such that $\langle \alpha_{p+1}|\beta_{p+1}\rangle = 1$. Haydock's recursion method is recovered in the special case where $X = X^\dagger$ and $|f\rangle = |\phi_0\rangle$.[44] These recurrences share in common with Haydock's method the property that the matrix of components $\langle \alpha_i|X|\beta_j\rangle$ is tridiagonal, as can be seen from Eqs. (18), (19), and (20), and this permits writing the desired matrix element as the continued fraction[44]

$$\langle f|(\lambda - X)^{-1}|\phi_0\rangle = \cfrac{\langle f|\phi 0\rangle}{\lambda - a_1 - \cfrac{b_1^2}{\lambda - a_2 - \cfrac{b_2^2}{\lambda - a_3 - \ldots}}}. \tag{22}$$

Different terminations of the iteration procedure have been proposed,[44] but in the present context, our results are quite insensitive to the particular choice.

Rather than directly evaluating these recurrences, an equivalent recurrence can instead be constructed using the quantities

$$I^n_{pq} = \langle \alpha_p|X^n|\beta_q\rangle.$$

Multiplying Eq. (19) by $\langle \alpha_p|$, one finds

$$I^n_{pq+1} = [I^{n+1}_{pq} - a_q I^n_{pq} - b_q I^n_{pq-1}]/b_{q+1}, \tag{23}$$

and similarly, from Eq. (18),

$$I^n_{p+1,q} = [I^{n+1}_{pq} - a_p I^n_{pq} - b_p I^n_{p-1,q}]/b_{p+1}. \tag{24}$$

Moreover, Eq. (21) can be recast

$$a_p = I^1_{p,p} \tag{25}$$

and the normalization factor b_{p+1} becomes

$$b_{p+1} = \sqrt{I^2_{pp} - a^2_p - b^2_p}. \tag{26}$$

Now, a_p and b_p, and therefore also Eq. (22), can be evaluated using Eqs (23), (24), (25), and (26) recursively with the starting values $I^n_{00} = \mu_n/\mu_0$ and $I^n_{p,-1} = I^n_{-1,q} = 0$. The relevance of this procedure is that it permits calculating the matrix element (22) directly from the moments μ_n, which are in turn obtained from a single MS calculation for as many $\langle f|$'s as desired.

Comparisons of rapidity of convergence using these iteration methods are offered in Figs. 2, 3, and 4 for PD, and in Fig. 7 for electron scattering. The results are discussed in more detail in Secs. IV and V.

An important point about the iteration methods just described is that the number of products of scattering matrices t_α per iteration is N in all of them, whereas the number of $G_{\alpha\beta}\tilde{\phi}_\beta$ products is $N(N-1)$. Therefore, in realistic clusters, where $N > 100$ (see Fig. 1), no substantial relative increase in computational effort is introduced if one goes beyond the commonly used spherical muffin-tin approximation, that is, if non-diagonal scattering matrices like those needed to represent non-spherical potentials[53–55] (e.g., in photoelectron diffraction in oriented molecules[56]) or spin-orbit coupling[53] are considered.

Since most of the computational effort is invested in products by $G_{\alpha\beta}$ matrices (vector addition takes a negligible time), we have devoted Sec. III B to a description of how to minimise their computational cost.

B. Optimization of products of Green functions

Following previous authors,[26,13,14] the Green function $G_{\alpha\beta}$ that propagates a free electron along an inter-atomic bond vector $\mathbf{d}_{\alpha\beta} = \mathbf{R}_\alpha - \mathbf{R}_\beta$ will be expressed in terms of the propagator along the z axis by using rotation matrices $R^{(l)}_{mm'}(\alpha\beta\gamma)$, where $(\alpha\beta\gamma)$ are the corresponding Euler angles.[48] In a first step, the bond vector $\mathbf{d}_{\alpha\beta}$ is rotated onto the z azis by applying the matrix[13,48]

$$R_{\alpha\beta,LL'} = \delta_{ll'} R^{(l)}_{mm'}(0,\theta,\pi-\varphi), \tag{27}$$

where (θ,φ) are the polar angles of $\mathbf{d}_{\alpha\beta}$. Then, the electron is propagated along the bond vector, directed now along the z axis and for which the Green function reduces to

$$G^z_{\alpha\beta,LL'} = \delta_{mm'}\sqrt{4\pi}\sum_{l''}\sqrt{2l''+1}\,\mathrm{i}^{l''} h^{(+)}_{l''}(kd_{\alpha\beta}) \times \int d\Omega\, Y_{lm}(\Omega) Y_{l''0}(\Omega) Y^*_{l'm}(\Omega). \tag{28}$$

Finally, the bond vector is rotated back to the original position, and one finds[13,41]

$$G_{\alpha\beta} = R^{-1}_{\alpha\beta} G^z_{\alpha\beta} R_{\alpha\beta}. \tag{29}$$

A recurrence relation has been reported that permits evaluating Eq. (28) efficiently.[15] The rotation matrices can be in turn decomposed into azimuthal and polar rotations as[48]

$$R^{(l)}_{mm'}(0,\theta,\pi-\varphi) = R^{(l)}_{mm'}(0,\theta,0)\,(-1)^{m'} \mathrm{e}^{\mathrm{i}\varphi m'}.$$

This decomposition of the Green function permits us to reduce both *(i)* the storage required to evaluate the MS series and *(ii)* the computational effort.

(i) A significant reduction in memory demand can be accomplished if the coefficients of each polar rotation $R^{(l)}_{mm'}(0,\theta,0)$, each azimuthal rotation $(-1)^{m'}\mathrm{e}^{\mathrm{i}\varphi m'}$, and each propagation along a bond distance $G^z_{\alpha\beta,LL'}$ are computed and stored once and for all the first time that they are encountered during the full calculation. Since actual clusters on which MS calculations are to be performed possess in general a certain degree of symmetry, the total number of different bond distances and bond polar angles is considerably reduced as compared with the total number of bond vectors. To illustrate this, let us take the example of a simple-cubic-lattice cube of side p in units of the lattice constant; this cluster contains p^3 atoms and $(2p-1)^3-1$ different bond vectors, a number that has to be compared with at most $3p^2$ bond distances, since the square of the distance between any pair of atoms has to be equal to an integral number, and the distance between opposite corners is $\sqrt{3}p$. A better estimate for this case results in $\approx 1.8p^2$ different bond distances.

(ii) For a given maximum value of the angular momentum number $l_{\max}$, the dimension of each vector $\tilde{\phi}_\alpha$ is $(l_{\max}+1)^2$, so that every matrix-vector product $G_{\alpha\beta}\tilde{\phi}_\beta$ involves $(l_{\max}+1)^4$ complex multiplications. However, all of the three matrices that appear on the right hand side of Eq. (29) are sparse, as can be seen from Eqs. (27) and (28). A detailed inspection leads to the conclusion that only $\approx (10/3)(l_{\max}+1)^3$ complex multiplications are needed to evaluate the product $G_{\alpha\beta}\tilde{\phi}_\beta$ when $G_{\alpha\beta}$ is decomposed as shown in Eq. (29). This is a factor of

$\approx 3l_{max}/10$ smaller than the direct matrix-vector product.

Further reduction in computational and storage demand can be achieved if symmetry relations for the Green function and the rotation matrices[48] are used (e.g., $G^z_{\alpha\beta,lm,l'm} = G^z_{\alpha\beta,l'-m,l-m}$).

In the examples reported below, the time needed to calculate and store the matrices defined in Eqs. (27) and (28) is negligible compared with the time spent in the iterative evaluation of Eq. (16).

C. Electron attenuation, temperature effects, and surface barrier

The effect of electron inelastic scattering is easily accounted for in a phenomenological way by multiplying the propagator $G^z_{\alpha\beta}$ of Eq. (28) by an exponentially-decaying function of the bond distance, $\exp(-d_{\alpha\beta}/2\lambda_i)$, where λ_i is the inelastic electron mean free path[36–40] and the 1/2 factor reflects the fact that this function goes inside the wave function rather than the electron probability. Also, the propagation from each atom to the detector has to be accompanied by the corresponding exponential attenuation that takes care of the part of the path contained inside the cluster (or below the surface in the case of a solid sample, of which the cluster represents just a part). Inelastic scattering, together with MS, reduces the scattering range, making LEED and PD excellent surface analysis techniques. In the case of core-level photoemission, the photoelectrons ejected from a solid or molecule thus provide information only on the vicinity of the ionized atom, and features coming from the interaction with distant atoms are attenuated by a finite inelastic mean free path.

The effect of thermal vibrations has been incorporated as is generally done in LEED analyses[4] by means of temperature dependent phase shifts that take into account an average displacement of the cluster atoms in their thermal motion.

Refraction at the surface barrier or inner potential V_0 requires correlating the direction of emission as seen from inside a solid with the actual direction of detection outside of it. The relation between these two is easily obtained by invoking conservation of electron momentum parallel to the surface and taking into account the loss of electron kinetic energy in the motion normal to the surface. A transmission factor is also needed,[37] specially for nearly grazing emission (i.e., when the normal kinetic energy is only a few eV above the vacuum threshold). Diffraction of electron components reflected back from the surface has been neglected, although we note that this can play a very important role at very low normal kinetic energies.

We now apply this general methodology to three important classes of experiment: core-level photoelectron diffraction, elastic electron scattering from molecules, and low-energy electron diffraction at surfaces.

IV. CORE-LEVEL PHOTOELECTRON DIFFRACTION

In this section, our methods are applied to the case of photoelectron diffraction. Describing the interaction with the external radiation H_{rad} to first order, the perturbed part of the time-dependent wave function, $\phi(\mathbf{r})\exp(-iEt)$, is given by

$$\phi(\mathbf{r}) = \int d\mathbf{r}'\, G(\mathbf{r},\mathbf{r}')H_{rad}(\mathbf{r}')\phi_i(\mathbf{r}'), \qquad (30)$$

where $\phi_i(\mathbf{r})$ is the initial-state core-electron wave function and $G(\mathbf{r},\mathbf{r}')$ is the cluster Green function discussed in Sec. II and evaluated at the final electron energy E. The photo-excitation of a core-level electron in a solid or molecule can be well described within the dipole approximation when the radiation wavelength is much larger than the dimensions of the initial core-electron state, in which case one can take $H_{rad} = C\hat{\epsilon}\cdot\mathbf{r}$, where $\hat{\epsilon}$ is the photon-polarization unit vector and C is a normalization constant.

In matrix notation, expressing G in terms of T as $G = G_0 + G_0TG_0$ and using Eq. (5), Eq. (30) becomes

$$\begin{aligned}\phi = {} & G_0H_{rad}\phi_i + G_0T_{\alpha_0}G_0H_{rad}\phi_i \\ & + \sum_{\beta\neq\alpha_0} G_0\Lambda_\beta G_0H_{rad}\phi_i \\ & + \sum_{\beta\neq\alpha_0} G_0\Lambda_\beta G_0T_{\alpha_0}G_0H_{rad}\phi_i,\end{aligned}$$

where α_0 is taken to be the emitter. Noticing that $G_{\alpha_0} = G_0 + G_0T_{\alpha_0}G_0$ is the Green function of atom α_0, one finds

$$\phi = G_{\alpha_0}H_{rad}\phi_i + \sum_{\beta\neq\alpha_0} G_0\Lambda_\beta G_{\alpha_0}H_{rad}\phi_i,$$

which can be compared to Eq. (6) to redefine

$$\phi^0_{\alpha}(\mathbf{r}) = \delta_{\alpha\alpha_0}C\int d\mathbf{r}'\, G_{\alpha_0}(\mathbf{r},\mathbf{r}')\,\hat{\epsilon}\cdot\mathbf{r}'\,\phi_i(\mathbf{r}'). \qquad (31)$$

We are interested in values of $\mathbf{r}$ outside the muffin-tin sphere of the emitter α_0, whereas the integral in Eq. (31) involves $\mathbf{r}'$ inside the muffin-tin sphere (i.e., the region where the core-electron wave function takes non-negligible values). Under these conditions, G_{α_0} can be written as[48]

$$\begin{aligned}& G_{\alpha_0}(\mathbf{r},\mathbf{r}') \\ & = -2k\sum_L h^{(+)}_L[k(\mathbf{r}-\mathbf{R}_{\alpha_0})]F^{\alpha_0}_L(\mathbf{r}')\exp(i\delta^{\alpha_0}_l), \qquad (32)\end{aligned}$$

where $F_L(\mathbf{r}) = i^l F_l(r)Y_L(\Omega_r)$ is a solution of $(H_0 + V_{\alpha_0} - E)F_L = 0$ and F_l is chosen such that it is finite at the origin (the regular solution). Inserting Eq. (32) into Eq. (31) and comparing the result with Eq. (9), one obtains

$$\phi^0_{\alpha,L} = -2kC\delta_{\alpha\alpha_0}e^{i\delta^{\alpha_0}_l}\langle F_L|\epsilon\cdot\mathbf{r}|\phi_i\rangle,$$

which includes the dipole matrix elements $\langle F_L|\epsilon\cdot\mathbf{r}|\phi_i\rangle$ and phase shifts $\delta^{\alpha_0}_l$ that are well known in the theory of atomic photoelectric cross sections.[48] Finally, the MS coefficients $\phi_{\alpha,L}$ are obtained from $\phi^0_{\alpha,L}$ as explained in Sec. III and $\phi(\mathbf{r})$ is given by Eq. (10) outside the muffin-tin spheres.

When $\mathbf{r}$ lies at the electron detector (i.e., for r much larger than the interatomic distances of the cluster) we are in the far-field limit and can approximate $h_L[k(\mathbf{r}-\mathbf{R}_\alpha)] \approx \exp(ikr - i\mathbf{k}_f\cdot\mathbf{R}_\alpha)Y_L(\Omega)/kr$, where $\mathbf{k}_f = k\mathbf{r}/r$ and Ω is the polar direction of $\mathbf{r}$ (i.e., the detector). Therefore, using Eq. (10), the measured electron intensity per unit of solid angle in the far field becomes

$$I(\Omega) = |\frac{C}{k}\sum_\alpha e^{-i\mathbf{k}_f\cdot\mathbf{R}_\alpha - \zeta_\alpha/2\lambda_i}\sum_L Y_L(\Omega)\phi_{\alpha,L}|^2, \qquad (33)$$

where ζ_α is the distance from atom α to the surface along the direction of emission and λ_i is the inelastic electron mean free path. In general, comparison with experiments requires performing an incoherent sum over different degenerate initial states and possibly over various emitters α_0.

For PD from atoms on or below a solid surface, and for which the entire (focussed) photon beam is intercepted by the sample, the intensity can be given in electrons per steradian per incoming photon by choosing the normalization constant as $|C|^2 = 4\pi k\sigma(\omega/c)^2/\cos\theta_i$, where ω is the photon energy, c is the speed of light, θ_i is the polar angle of incidence of the light with respect to the surface normal, and σ is the surface density of emitters equivalent to α_0 (i.e., those of a given layer parallel to the surface).

The present formalism is particularly efficient when calculating photoelectron angular distributions: once the coefficients $\phi_{\alpha,L}$ have been obtained for a given electron energy, the photoelectron intensity for each emission direction is readily calculated using Eq. (33). When using the modified recursion method outlined in Sec. III A, $\langle f|\phi\rangle$ corresponds to the expression inside the modulus in Eq. (33) and the moment n is given by $\mu_n = \langle f|\phi^n\rangle - \langle f|\phi^{n-1}\rangle$, where $\langle f|\phi^n\rangle$ is calculated from the coefficients $\phi^n_{\alpha L}$ obtained in the n^{th} iteration.

The relative performances of the various iteration methods discussed in Sec. III A for calculating PD from a simple sample consisting of two carbon atoms is analyzed in Fig. 2, where the inset illustrates the details of the geometry (the interatomic distance corresponds to nearest neighbors in graphite). This constitutes a severe test of multiple scattering, since the interatomic distance is relatively small. Within the resolution of the figure, the recursion method (solid circles) converges in just seven iterations to the result of the exact giant-matrix inversion (GMI). In single scattering (SS), that is, at iteration 1, the direct Jacobi iteration (open circles) is already much worse, and subsequent scattering orders lead to divergence. Neither are such divergences prevented by using the SR method (broken curves) over a wide range of the relaxation parameter η. The lower the value of η, the slower is the increase in intensity with iteration step, but the divergent behavior remains.

Divergences such as these are encountered in MS when the absolute value of any of the eigenvalues of the matrix X discussed in Sec. III A is larger than 1. In a basis set that makes this matrix diagonal, each eigenvalue x_i enters the direct Jacobi MS expansion of $1/(1-X)$ as $1/(1-x_i) = 1 + x_i + x_i^2 + \ldots$, and this expansion is only convergent when $|x_i| < 1$. This is a well-known problem in LEED,[4,5] where various schemes have been devised to prevent it, such as renormalized forward scattering[4,5,9] and reverse scattering perturbation.[5,19] The SR method provides a cure in many cases,[42] but it is not sufficiently general, as illustrated by Fig. 2. Instead, the recursion method has a well-established convergent behavior,[44] and therefore, it will be employed from now on unless otherwise specified.

Fig. 3(a) shows our choice of the cluster used to represent photoemission from a given atom (darker circle) within a solid surface. The cluster is formed by those atoms contained within a parabolic surface where the emitter coincides with its focus. The parameter d_{max} determines the size of the cluster (see figure). The parabolic surface comes from the condition that the maximum electron path length inside the solid, where the inelastic attenuation is effective, be at most d_{max} within SS for normal emission.

Convergence with the number of cluster atoms $N \propto d^3_{max}$ is analyzed in Fig. 3(b) for photoemission from a Cu2s level situated on the third layer of a Cu(111) surface and at a polar emission angle of $\theta = 35°$. The geometry under consideration is illustrated schematically in the lower left corner of the figure, and the atoms are again within the paraboloid of Fig. 3(a). Plotted here is the reliability factor defined as[58]

$$R_{ave} = \frac{\overline{|I^N - I^\infty|}}{\overline{I^\infty}}, \qquad (34)$$

where the average is taken over all asimuthal directions of emission (cf. inset), I^N is the intensity calculated for an N-atom cluster, and I^∞ is actually obtained for $N = 1856$. The solid curve and circles correspond to the result obtained from the recursion method, where convergence is achieved in less than 20 iterations. A smooth convergence can be seen in the $N \to \infty$ limit. For $N \approx 160$, which is suggested by Fig. 1 as a convergence criterion for the electron energy under consideration (100 eV), one has $R_{ave} = 0.16$. The inset shows azimuthal scans obtained for different cluster sizes, in order to facilitate the understanding of the actual meaning of R_{ave} in terms of curve comparisons. For $N = 944$ (dot-

ted curve in the inset), one has $R_{ave} = 0.03$ and convergence is already quite good as compared to the $N = 1856$ case, although some small discrepancies can still be distinguished in the height of the peaks around 30°, 60°, and 90°, so that over 1000 atoms are needed to obtain convergence within the resolution of the figure. We note however that most real experimental situations involve averaging over some finite solid angles, and this can lead to an effective reduction in the cluster size needed.

The open circles in Fig. 3(b) show the reliability factor obtained from the Jacobi method for various scattering orders (5, 9, 13, 17, 21, and 25), where the spread in the position of the circles makes evident a divergent behavior. The latter is more pronounced for larger clusters. In this sense, the Jacobi method has to be regarded as an asymptotic series unable to converge below a certain reliability factor in the present case.

Figs. 4(a) and 4(b) show the performance of the recursion method (solid circles, for which only odd iteration orders introduce variations by construction of the method) as compared with that of direct Jacobi iteration (open circles) as a function of iteration step for 4f photoemission from the third W layer in a W(110) surface covered with one monolayer of (1 × 1) O and with an emission angle of 46°.[59] Two different definitions of the reliability factor have been used, based upon either the relative average deviation given by Eq. (34) by substituting N by the iteration step n (R_{ave}, thick curves), or the maximum deviation over the azimuthal scan (thin curves)

$$R_{max} = \frac{\max\{|I^n - I^\infty|\}}{\overline{I^\infty}}, \tag{35}$$

respectively, where the average is performed over azimuthal scans for a polar angle of emission $\theta = 46°$. Both iteration methods show similar convergence behavior for the relatively small cluster of Fig. 4(a), consisting of $N = 65$ atoms. However, for the larger cluster of Fig. 4(b) ($N = 189$), the Jacobi method fails to converge, whereas the recursion method shows a steady convergent trend.

As pointed out above, the computational cost of EDAC scales as $(l_{max} + 1)^3$ with l_{max}. Consequently, it is desirable to have a criterion to limit the value of l_{max} used in actual MS calculations while maintaining the required degree of accuracy. This criterion is provided by the reliability factor for the atomic scattering amplitude f,

$$R_f \simeq \frac{1}{3}\sqrt{\frac{\int d\Omega\,|f^{l_{max}} - f^{l_{max}=\infty}|^2}{\int d\Omega\,|f^{l_{max}=\infty}|^2}}, \tag{36}$$

where the integrals are extended over all scattering directions Ω. Fig. 4(c) shows the dependence of R_f on l_{max} for 250-eV electrons scattered on W atoms (open circles) as compared with the reliability factor for MS under the same conditions as in Fig. 4(a) for $N = 123$ atoms (solid circles). The latter has been obtained from Eq. (34) by varying l_{max} rather than N for azimuthal scans with polar angle of emission $\theta = 46°$. Both Eq. (34) and Eq. (36) are proportional to relative variations of the atomic scattering amplitude, so that one is comparing quantities of the same order of magnitude. Actually, they exhibit a similar behavior with l_{max}, as shown in Fig. 4(c), which indicates that Eq. (36), whose computation requires a negligible time as compared with MS calculations, offers a good estimate of the error that is made when finite values of l_{max} are used, thus providing a criterion to determine the appropriate value of l_{max} before performing actual MS calculations. Similar results are obtained for other values of θ. Interestingly, all angles of scattering enter in the definition of R_f, and this is consistent with the fact that MS in a solid involves a dense set of single scattering angles. Also shown in Fig. 4(c) is the l_{max} value obtained from the simple criterion mentioned earlier ($l_{max} = kr_{mt}$), which is 11.3.

As another PD example, Fig. 5 shows the angular distribution over the upper-hemisphere for W4f photoelectrons coming from the outer W layer of a W(110) surface covered with one monolayer of (1 × 1) O and illuminated with left-circularly polarized (LCP) light under normal incidence, as shown in the insets. The quantity actually plotted is $[I(\theta,\varphi) - I_0(\theta)]/I_0(\theta)$, where I_0 is the average of the intensity over azimuthal angles. In calculating the data displayed in Fig. 5(a), the MS procedure has been carried out only once for all directions of emission, as explained in Sec. III A, thus saving considerable time. Fig. 5(a) exhibits reduced symmetry with respect to that expected for W(110) owing to the fact that LCP light is used and also because the oxygen atoms are displaced with respect to a center of symmetry of the surface (see the schematic top view). Two different domains can also exist on this surface:[59] the one depicted in the insets and another one with the oxygen lying in a mirror-image symmetry-equivalent W valley. The average over the result obtained from both domains has been performed. The maximum intensity (bright regions) near the [001] azimuthal direction is rotated clockwise, as expected from the use of LCP light and f core levels.[60,61,59] This rotation reproduces very well the available experimental data shown in Fig. 5(b) and taken from Ref. [59].

As a last example of PD, we consider photoemission from atoms near surface steps, where the lack of symmetry makes it difficult to use layer-by-layer methods in simulations, while the cluster approach is perfectly suited for that purpose. Prior x-ray PD experiments on O adsorbed on stepped Cu surfaces have, for instance, indicated high sensitivity to structure via SS calculations.[62] Here, we show calculated azimuthal scans of photoelectrons coming from Xe atoms adsorbed near a step on a Pt(111) surface (Fig. 6). The insets on the right hand side of the figure show schematically the geometry under consideration. Two different possible structures have been studied: one row of Xe atoms located either on the lower terrace (upper part of the figure) or on the upper terrace (lower part), continuing the bulk Pt structure in both cases. Experimental evidence coming from low-energy ion scattering[63] indicates that the lower terrace is the preferred geometry. The results presented in Fig. 6 permit concluding that the features exhibited by PD scans would allow one to distinguish between the two possibilities, although no actual experimental data is available for this case. Moreover, at least 100 atoms are needed to obtain the dominant features when the Xe atoms are sitting on the upper terrace. However, strong forward scattering, dominated by nearest neighbors of the emitter, occurs when the Xe atoms are sitting on the lower terrace, and therefore, a 22-atom cluster produces good qualitative results. In both cases, convergence in the fine structure requires approximately 500 atoms.

V. ELASTIC ELECTRON SCATTERING FROM MOLECULES

The scattering of an external electron beam from a molecule represented by an atomic cluster is discussed in this section. The initial electron state of Eq. (1) will be described by a plane wave $\varphi^0(\mathbf{r}) = \exp(i\mathbf{k}_i\cdot\mathbf{r})$, which can be expanded in partial waves around each of the cluster atoms, and using Eqs. (7)-(9) and (13), one finds

$$\phi^0_{\alpha,L} = 4\pi i^l Y_{l-m}(\Omega_k)(-1)^m e^{i\mathbf{k}_i\cdot\mathbf{R}_\alpha - \zeta_\alpha/2\lambda_i}, \tag{37}$$

where ζ_α has the same meaning as in Eq. (33), with the *surface* now defined as the boundary of the molecular electronic charge distribution. These are the input wavefunction coefficients from which one can obtain those of the self-consistent wave function (10), $\phi_{\alpha,L}$, after MS is performed using the methods described in Sec. III. The latter permits, upon insertion into Eq. (33), computing the diffracted electron intensity. Choosing $C = 1$, Eq. (33) represents the scattering cross section.

This has been done for C_{60} molecules and 809-eV electrons in Fig. 7(a), where experimental results taken from Ref. [64] are compared with single scattering (SS, also reported in Ref. [64]) and MS calculations represented by broken and solid curves, respectively, as a function of scattering angle. MS results in better agreement for the relative height of the prominent diffraction peaks at around 5° and 8.5°, as compared with the SS analysis.

In order to emphasize the contribution of MS, lower electron energies (100 eV) and a back-scattering geometry have been considered in Fig. 7(b) for electron scattering by C_{60} molecules. The thick solid curve represents the fully-converged result obtained by using the recursion method (convergence has been obtained after 11 iterations within the scale of the figure). The thin solid curve shows the results obtained after only 5 iterations, which are in qualitative good agreement with the exact result. By contrast, direct Jacobi iteration is far from convergence even after 25 iterations (thick broken curve). The C_{60} molecule, like the C-C cluster of Sec. IV, is a severe test of multiple scattering because the carbon atoms are reasonably strong scatterers placed relatively close together.

VI. LOW-ENERGY ELECTRON DIFFRACTION

The cluster approach followed in this work finds application in the simulation of LEED intensities for large-unit-cell surfaces, where conventional layer-by-layer schemes become quite expensive computationally. It is also directly applicable to non-periodic surfaces, including disordered overlayers, disordered alloys, point defects, steps and kinks, adsorbed clusters, quasicrystals, etc.

In a periodic surface, the scattering of electrons in any surface unit cell differs from that of the first unit cell by a phase factor, $\exp[i(\mathbf{k}_i - \mathbf{k}_f)\mathbf{R}_a]$, where $\mathbf{k}_i$ ($\mathbf{k}_f$) is the incoming (outgoing) electron momentum vector, and $\mathbf{R}_a$ is a Bravais lattice vector. Therefore, LEED intensities can be calculated within the present cluster approach by taking ϕ^0_α as in Eq. (37) for the atoms of the first unit cell and zero elsewhere. One obtains

$$I_{LEED}(\Omega) = I(\Omega)|S(\mathbf{k}_i^{||} - \mathbf{k}_f^{||})|^2, \tag{38}$$

where

$$S = \sum_a e^{i(\mathbf{k}_i - \mathbf{k}_f)\mathbf{R}_a},$$

is the surface structure factor[4] and $I(\Omega)$ is an envelope function given by Eq. (33), where the coefficients $\phi_{\alpha,L}$ are obtained from a MS calculation within a cluster containing the first unit cell and atoms around it up to a distance far enough to guarantee convergence. The cluster size is thus determined by the electron inelastic mean free path and the size of the first unit cell, with the cluster extending beyond the unit cell by roughly the electron inelastic attenuation length.

For an infinitely extended incoming beam and a perfect infinite surface, the two-dimensional structure factor S vanishes except along those directions for which the components of $\mathbf{k}_i - \mathbf{k}_f$ parallel to the surface equal a reciprocal surface lattice vector G denoted by Miller indices (hk), giving rise to a factor $\delta(\mathbf{k}_i^{||} - \mathbf{k}_f^{||} - \mathbf{G})$; this corresponds to the so-called (hk) beam at the polar direction Ω_G. Integrating over directions of emission around Ω_G, the probability that the electron is reflected along such a direction is found to be

$$P_G = \left(\frac{2\pi}{Ak}\right)^2 \frac{I(\Omega_G)}{\cos\theta_i \cos\theta_f},$$

where θ_i (θ_f) is the polar angle of incidence (reflection) with respect to the surface normal, A is the surface unit-cell area, and k is the electron momentum. With the normalization of Eq. (37) and taking $C = 1$ in Eq. (33), P_G is actually the fraction of incoming electrons that are reflected in the G beam.

In practice, the electron beam has a finite coherence width of the order of 100 Å, depending on the angular and energy spread of the electron gun. This effect can be accounted for in a phenomenological way by considering that only a fraction of the unit cells contribute coherently with respect to an arbitrarily chosen central unit cell. Assuming a Gaussian profile for this effect with half width H and furthermore that there is no substantial variation of coherence across any given unit cell, one finds

$$S = \sum_{\alpha} e^{-R^2/2H^2} e^{i(\mathbf{k}_i - \mathbf{k}_f)\mathbf{R}_\alpha}$$

$$= (2\pi)^3 \frac{H^2}{A} \sum_{\mathbf{G}} e^{-|\mathbf{k}_i^{\parallel} - \mathbf{k}_f^{\parallel} - \mathbf{G}|^2 H^2/2}, \qquad (39)$$

where the first (last) sum is extended over surface lattice sites $\mathbf{R}_\alpha$ (reciprocal surface lattice vectors G). Obviously, the sum in reciprocal space reduces to a single term at most in the $H \to \infty$ limit, and a few more terms allow achieving good convergence for typical values of $H \sim 100$ Å. Inserting Eq. (39) into Eq. (38), one finds a finite reflection probability for every direction Ω.

The present formalism has been applied to the Si(111)-(7 × 7) surface. The atomic positions have been taken from a previous LEED analysis,[65] in which intensive use was made of the symmetry of the surface. By contrast, the results presented here have been obtained directly without any symmetry considerations beyond the surface unit-cell geometry. Fig. 8 shows the final LEED pattern I_{LEED} (right figure) as well as the surface structure factor S^2 (upper left figure) and the envelope function I (lower left figure) for an incident beam of 50-eV electrons coming along the surface normal. The axis labels represent the components of the electron momentum parallel to the surface. The structure factor exhibits a dense spot pattern that reflects the symmetry of the large unit cell of the Si(111)-(7 × 7) surface. This is a purely geometrical quantity which does not contain any information about the actual positions of the atoms within the surface unit cell, but does reflect the quality of the electron beam via Eq. (39). That information is fully contained in the envelope function (lower left figure), which presents marked maxima near the positions expected for the LEED spots of the unreconstructed Si(111) surface (see the six prominent peaks in the figure). The envelope function modulates the intensity that is observed around each of the spots of the structure factor, leading to the complex LEED pattern shown in the right part of the figure.

The calculation of the envelope function $I(\Omega)$ has been performed using a cluster consisting of 1545 atoms, of which only 494 are contained within the surface unit cell. The cluster extends up to 15 Å below the surface and the electron inelastic mean free path has been taken as 5.5 Å.

This calculation has been compared with experimental observations in Fig. 9 both for 50-eV electrons and for 75-eV electrons (left and right side of the figure, respectively).[66] Note the large change in the measured distribution of the brightest spots when one goes from 50 eV to 75 eV (upper figures), which is well reproduced by the present calculation (lower figures) using an inner potential of 10 eV.

As another example of application of the present method to LEED with a large unit cell, the case of a W(110) surface covered with one monolayer of Gd is considered in Fig. 10. Various experimental LEED studies of this structure have been reported in the past.[67,68] Fig. 10(a) shows the model (A) proposed by Tober *et al.*,[68] wherein the Gd overlayer forms a rectangular coincidence lattice with (7 × 14) periodicity and with a mismatch of 0.6% area increase relative to bulk Gd(0001). The calculated LEED pattern represented in Fig. 10(b) for this model has been obtained from Eqs. (38) and (39) for an electron beam diameter of 100 Å and an energy of 102 eV. The surface has been described by five W layers below the Gd overlayer, so that 648 atoms are contained in the surface unit cell, and 2516 atoms have been used in the calculation to include the regions surrounding the surface unit cell. Some of the spots are clearly highlighted by the envelope function, and in particular the six brighter spots coming from the Gd overlayer. Six satellites around each of them are clearly highlighted forming a quasi-six-fold satellite pattern (see the white lines drawn to guide the eye), in reasonable agreement with the experimental result shown in Fig. 10(c) (taken from Ref. [68]).

Since the spot pattern imposed by S for this model is a rectangular one, leading to the emergence of spurious satellites not observed in the experiment, a different model structure (model B) with a 1.8% overall area reduction relative to Gd(0001) has been tried, as represented in Figs. 8(c)-(d). Two different domains are possible in this case. The corresponding LEED pattern averaged over both domains is shown in Fig. 8(d). This results in a somewhat poorer agreement with experimental observations[68] [Fig. 10(c)] and demonstrates the power of such simulations to assist in structural studies.

In summary, the present method allows calculating LEED patterns for complex structures using large clusters of up to several thousand atoms, which are now beyond practical reach of currently available layer-by-layer methods of LEED simulation.

VII. CONCLUSIONS

A new method for the simulation of electron diffraction in atomic clusters (EDAC) has been introduced. The computation time has been shown to behave like $N^2(l_{\max}+1)^3$, where N is the number of atoms and $l_{\max}$ is the maximum angular momentum quantum number. Actual calculations using above 1000 atoms have been presented. This is made possible via a convenient separation of the exact free-electron Green functions into rotation matrices and propagators along the z axis.

The resulting EDAC code relies on the iterative solution of the multiple scattering (MS) secular equation, for which various iteration techniques have been compared. In particular, the recursion method has been shown to prevent divergences and to result in faster convergence as compared with the direct MS approach. A modified recursion method has been introduced in order to be able to quickly obtain angular distributions of scattered or emitted electrons from a single MS calculation (see Sec. III A.

The computational effort in EDAC is not very sensitive to the detailed form of the atomic scattering $t-$matrices (e.g., diagonal vs non-diagonal), and it therefore constitutes a good platform for including the effects of non-spherical atoms in MS. Further research in this direction is in progress.[56]

Examples of application of EDAC to PD have been given for Cu(111), O/W(110), and Xe adsorbed near steps of a Pt(111) surface. The present cluster approach is particularly suitable for these cases due to the lack of translational symmetry. Also, PD from a C-C dimer has been shown to lead to divergences in the MS expansion (even at a relatively large electron energy of 850 eV), which are easily prevented by using the recursion method.

Electron elastic scattering on C_{60} molecules has also been discussed, and MS has been shown to result in improved agreement with experiment as compared to single scattering.

Finally, a formalism for studying LEED within the cluster approach has been presented and applied to LEED from large-unit-cell surfaces. In particular, the relative intensity of the different LEED spots observed experimentally for the Si(111)-(7×7) are well reproduced by this theory. Also, two different models for the surface structure of one monolayer of Gd on W(110) have been considered, and the resulting LEED patterns have been discussed in the light of the available experimental results. The formalism can also be applied to a wide variety of non-periodic surface structures, including free molecules.

ACKNOWLEDGMENTS

The authors would like to thank R. X. Ynsunza, F. J. Palomares, and E. Tober for providing the experimental data of Figs. 5, 9, and 10, respectively. This work was supported in part by the University of the Basque Country and the Spanish Ministerio de Educación y Cultura (Fulbright grant FU-98-22726216), and by the Director, Office of Science, Basic Energy Sciences, Materials Sciences Division of the U.S. Department of Energy under Contract No. DE-AC03-76SF00098.

* E-mail: ccpgaabf@photon.lbl.gov

[1] C. S. Fadley and S. Å. L. Bergström, Phys. Lett. A 35, 375 (1971).
[2] A. Liebsch, Phys. Rev. Lett. 32, 1203 (1974).
[3] S. Kono, C. S. Fadley, N. F. T. Hall, and Z. Hussain, Phys. Rev. Lett. 41, 117 (1978); D. P. Woodruff, D. Norman, B. W. Holland, N. V. Smith, H. H. Farrell, and M. M. Traum, Phys. Rev. Lett. 41, 1130 (1978); S. D. Kevan, D. H. Rosenblatt, D. Denley, B.-C. Lu, and D. A. Shirley, Phys. Rev. Lett. 41, 1565 (1978); S. Kono, S. M. Goldberg, N. F. T. Hall, and C. S. Fadley, Phys. Rev. Lett. 41, 1831 (1978).
[4] J. B. Pendry, *Low Energy Electron Diffraction* (Academic Press, London, 1974).
[5] M. A. Van Hove, W. H. Weinberg, and C.-M. Chan, *Low Energy Electron Diffraction* (Springer-Verlag, Heidelberg, 1986).
[6] S. A. Chambers, Adv. Phys. 40, 357 (1991).
[7] P. A. Lee and J. B. Pendry, Phys. Rev. B 11, 2795 (1975).
[8] J. B. Pendry, Surf. Sci. 57, 679 (1976).
[9] C. H. Li, A. R. Lubinsky, and S. Y. Tong, Phys. Rev. B 17, 3128 (1978).
[10] C. H. Li and S. Y. Tong, Phys. Rev. Lett. 42, 901 (1979).
[11] J. J. Barton and D. A. Shirley, Phys. Rev. B 32, 1906 (1985).
[12] J. J. Barton, M.-L. Xu, and M. A. Van Hove, Phys. Rev. B 37, 10475 (1988).
[13] J. J. Rehr and R. C. Albers, Phys. Rev. B 41, 8139 (1990).
[14] V. Fritzsche, J. Phys.: Condens. Matter 2, 1413 (1990).
[15] V. Fritzsche, J. Phys.: Condens. Matter 2, 9735 (1990).
[16] D. J. Friedman and C. S. Fadley, J. Electron Spectrosc. 51, 689 (1990).
[17] A. P. Kaduwela, D. J. Friedman, and C. S. Fadley, J. Electron Spectrosc. 57, 223 (1991).
[18] J. B. Pendry, in *Determination of Surface Structure by LEED*, edited by P. M. Marcus and F. Jona (Plenum Press, New York, 1984), p. 3.
[19] D. D. Vvedensky, D. K. Saldin, and J. B. Pendry, Surf. Sci. 156, 845 (1985).
[20] D. K. Saldin and J. B. Pendry, Surf. Sci. 162, 941 (1985).
[21] D. K. Saldin, G. R. Harp, and X. Chen, Phys. Rev. B 48, 8234 (1993).
[22] J. E. Müller and W. L. Schaich, Phys. Rev. B 27, 6489 (1983).
[23] C. S. Fadley, in *Synchrotron Radiation Research: Advances in Surface and Interface Science*, edited by R. Z. Bachrach (Plenum Press, New York, 1992), p. 421.
[24] C. S. Fadley *et al.*, Prog. in Surf. Sci. 54, 341 (1997).
[25] J. L. Beeby, Proc. R. Soc. A 302, 113 (1967).
[26] M. Danos and L. C. Maximon, J. Math. Phys. 6, 766 (1965).
[27] R. Nozawa, Nucl. Instrum. Methods B 100, 1 (1966).
[28] W. L. Schaich, Phys. Rev. B 8, 4028 (1973).

[29] C. A. Ashley and S. Doniach, Phys. Rev. B 11, 1279 (1975).
[30] W. L. Schaich, Phys. Rev. B 29, 6513 (1984).
[31] S. J. Gurman, N. Binsted, and I. Ross, J. Phys.: Condens. Matter 17, 143 (1984).
[32] S. J. Gurman, N. Binsted, and I. Ross, J. Phys.: Condens. Matter 19, 1845 (1986).
[33] J. J. Barton and D. A. Shirley, Phys. Rev. A 32, 1019 (1985).
[34] M. Sagurton, E. L. Bullock, R. Saiki, A. Kaduwela, C. R. Brundle, C. S. Fadley, and J. J. Rehr, Phys. Rev. B 33, 2207 (1986).
[35] J. Mustre de Leon, J. J. Rehr, C. R. Natoli, C. S. Fadley, and J. Osterwalder, Phys. Rev. B 39, 5632 (1989).
[36] S. I. Zabinsky, J. J. Rehr, A. Ankudinov, R. C. Albers, and M. J. Eller, Phys. Rev. B 39, 5632 (1989).
[37] A. Ankudinov and J. J. Rehr, Phys. Rev. B 52, 10214 (1995).
[38] G. E. Laramore, C. B. Duke, and N. O. Lipari, Phys. Rev. B 10, 2246 (1974).
[39] C. J. Tung and R. H. Ritchie, Phys. Rev. B 16, 4302 (1977).
[40] C. J. Powell and A. Jablonski, Physical and Chemical Reference Data 28, 19 (1999).
[41] Y. Chen, F. J. García de Abajo, A. Chassé, R. X. Yuxunza, A. P. Kaduwela, M. A. Van Hove, and C. S. Fadley, Phys. Rev. B 58, 13121 (1998).
[42] H. Wu and S. Y. Tong, Phys. Rev. B 59, 1657 (1999).
[43] W. H. Press, S. A. Teukolsky, W. T. Vetterling, and B. P. Flannery, *Numerical Recipes* (Cambridge University Press, New York, 1992).
[44] R. Haydock, Solid State Physics 35, 215 (1980).
[45] V. Heine, Solid State Physics 35, 1 (1980).
[46] R. Haydock, Phys. Rev. B 61, 7953 (2000).
[47] F. J. García de Abajo, Phys. Rev. Lett. 82, 2776 (1999).
[48] A. Messiah, *Quantum Mechanics* (North-Holland, New York, 1966).
[49] Matrices will be represented in upper case (e.g., T) and vectors in lower case (e.g., φ^0). Spatial coordinates are providing matrix and vector indices, so that, products like $T\varphi^0$ involve spatial integrals: $\int d\mathbf{r}' T(\mathbf{r},\mathbf{r}')\varphi^0(\mathbf{r}')$. The unit matrix stands for $\delta(\mathbf{r}-\mathbf{r}')$, and the potential V, when understood as a matrix, represents $V(\mathbf{r})\delta(\mathbf{r}-\mathbf{r}')$.
[50] The explicit form of the coefficients $\phi^0_{\alpha,L}$ is not relevant, but the important point is that $\phi^0_\alpha(\mathbf{r})$ is a superposition of outgoing spherical waves $h^{(+)}_L[k(\mathbf{r}-\mathbf{R}_\alpha)]$ for $\mathbf{r}$ outside the muffin-tin sphere α.
[51] C. R. Natoli and M. Benfatto, J. Physique Colloque 47, C8 (1986).
[52] V. L. Shneerson, W. T. Tysoe, and D. K. Saldin, Phys. Rev. B 53, 10177 (1996).
[53] P. Strange, J. Staunton, and B. L. Gyorffy, J. Phys. C 17, 3355 (1984).
[54] H. Ebert, Phys. Rev. B 38, 9390 (1988).
[55] P. Strange, H. Ebert, J. Staunton, and B. L. Gyorffy, J. Phys.: Condens. Matter 1, 2959 (1989).
[56] R. Diez Muiño, S. Rolles, F. J. García de Abajo, M. A. Van Hove, and C. S. Fadley (in preparation).
[57] M. Rösler and F. J. García de Abajo, Phys. Rev. B 54, 17158 (1996).
[58] The choice of the reliability factor R_{ave} is appropriate here, since we are comparing different theoretical calculations in which no experimental uncertainties in the zero of energy and angle scales are introduced.
[59] R. X. Yuxunza *et al.*, J. Electron Spectrosc. 106, 7 (2000).
[60] T. Nakatani, S. Imaga, S. Suga, Y. Kagoshima, and T. Miyahara, Jpn. J. Appl. Phys. 32, L1480 (1993).
[61] M. A. Van Hove, A. P. Kaduwela, H. Xiao, W. Schattke, and C. S. Fadley, J. Electron Spectrosc. 80, 137 (1996).
[62] K. A. Thompson and C. S. Fadley, Surf. Sci. 146, 281 (1984).
[63] V. Pouthier, C. Ramseyer, C. Girardet, K. Kuhnke, V. Marsico, M. Blanc, R. Schuster, and K. Kern, Phys. Rev. B 56, 4211 (1997).
[64] L. G. Gerchikov, P. V. Efimov, V. M. Mikoushkin, and A. V. Solov'yov, Phys. Rev. Lett. 81, 2707 (1998).
[65] S. Y. Tong, H. Huang, C. M. Wei, W. E. Packard, F. K. Men, G. Glanders, and M. B. Webb, J. of Vacuum Sci. and Technology A 6, 615 (1987).
[66] F. J. Palomares, unpublished.
[67] J. Kolaczkiewicz and E. Bauer, Surf. Sci. 175, 487 (1986).
[68] E. D. Tober, R. X. Yuxunza, C. Westphal, and C. S. Fadley, Phys. Rev. B 53, 5444 (1996).

FIG. 1. Minimum criteria for convergence on cluster size and angular momenta in multiple scattering calculations (solid curve) and relative speeds of the present EDAC method versus the second-order Rehr-Albers (R-A) separable representation (broken curve). Criteria are expressed in terms of the number of atoms N as a function of the maximum angular-momentum quantum number l_{max}. The value of N for which convergence is achieved (solid curve) is estimated as the number of atoms contained within a sphere of radius equal to 1.5 times the universal inelastic mean free path, λ_l, assuming an average nearest-neighbor separation of 2.5 Å. λ_l depends upon the electron momentum k, which is in turn related to l_{max} via $l_{max} = kr_{mt}$ for a typical muffin-tin radius of $r_{mt} = 1.5$Å. The number of complex multiplications needed per iteration is $(10/3)N^2(l_{max}+1)^3$ in EDAC and $36N^2$ in R-A, and therefore, EDAC requires a shorter computation time as compared with R-A when $N > 0.1(l_{max}+1)^3$ (white area above the broken curve) if all scattering paths are accounted for.

FIG. 2. C1s photoemission intensity in a cluster formed by two carbon atoms separated by 1.4 Å as a function of iteration step. The incoming light is linearly polarized with the polarization vector parallel to the interatomic axis. The emission occurs in the forward scattering direction (see inset). The electron energy is 850 eV. Results obtained from different iteration methods are compared: the recursion method of this work (solid circles), which converges rapidly to the exact result derived via giant-matrix inversion (GMI); the direct Jacobi iteration (open circles), for which the number of iteration steps equals the scattering order; and the simultaneous relaxation (SR) method[42,43] for various values of the relaxation parameter η (thin broken curves). The intensity has been normalized to that of the isolated C atom.

FIG. 3. (a): Schematic representation of the cluster used in photoelectron diffraction calculations. Only atoms whose sum of distances to the emitter (darkest atom) and to the surface is smaller than d_{max} are included in the calculation (gray atoms). This criterion leads to a parabolic surface with the focus coinciding with the emitter. (b): R−factor [Eq. (34)] variation with the number of atoms N for Cu2s photoemission from the third layer of a Cu(111) surface. Azimuthal scans have been considered with a polar angle of emission of 35°, a photoelectron energy of 100 eV, and p-polarized light under normal incidence conditions, as shown schematically in the lower left corner of the figure. The inset shows the intensity as a function of azimuthal angle for various cluster sizes, as indicated by labels, normalized to that of the direct emission without inelastic attenuation.

FIG. 4. (a): R−factor variation with scattering order for azimuthal scans of W4f photoemission from a W(110) surface covered with one monolayer of (1 × 1) O.[59] The emitter is taken to be in the third W layer, the photoelectron is emitted with an energy of 250 eV and polar angle of 46°, and the incident light is circularly polarized and coming perpendicular to the surface (see inset). The cluster consists of $N = 65$ atoms [$d_{max} = 1$ nm; see Fig. 3(a)]. Results derived from the recursion method (solid curves and circles) are compared with those obtained using direct Jacobi iteration (broken curves and open circles). Thick and thin curves show R−factor values according to the definitions of Eqs. (34) and (35), respectively (i.e., the relative value of the average deviation and the maximum deviation, respectively). (b): Same as (a) for $N = 189$ atoms [$d_{max} = 1.4$ nm; see Fig. 3(a)]. (c): R−factor variation with l_{max} under the same conditions as in (a) for $d_{max} = 1.2$ nm (solid curve and solid circles). The variation of the R factor for the atomic scattering amplitude as defined by Eq. (36) is shown by the broken curve and open circles. Also shown is the expected l_{max} value based on the simple criterion of $l_{max} = kr_{mt}$.

FIG. 5. W4f photoemission intensity as a function of the polar direction of emission for a W(110) surface covered with one monolayer of (1 × 1) O and illuminated with left-circularly-polarized light.[59] Represented is $[I(\theta,\varphi) - I_0(\theta)]/I_0(\theta)$, where $I_0(\theta)$ is the average of the intensity over azimuthal angles. The photoelectron energy is 250 eV. The emission takes place from the top-most (oxide) W layer. Dark regions correspond to high intensity. (a): EDAC calculation for a cluster consisting of $N = 393$ atoms ($d_{max} = 18$Å). The position of the oxygen is shown schematically in the inset. The average over the two symmetry-equivalent positions of the oxygen has been performed. The direction of normal emission corresponds to the center of the figure, and the polar angle θ is proportional to the distance to that point (the range actually plotted is $46° \le \theta \le 63.5°$). (b): Experimental results taken from Ref. [59].

FIG. 6. Azimuthal dependence of the photoemission intensity from s levels of a row of Xe atoms adsorbed near a step in a Pt(111) surface. Top part: the Xe atom is on the lower terrace at the step edge. Bottom part: the Xe atom is on the upper terrace. In all cases, the Xe atoms are located in Pt continuation sites. (See the schematic representations on the right hand side.) The photoelectron kinetic energy is 60 eV. The electron take-off angle is 30°. The light is unpolarized and incident perpendicular to the terraces.

FIG. 7. (a): Scattering probability of 809-eV electrons from C_{60} molecules as a function of scattering angle. Experimental results (circles) taken from Ref. [64] are compared with single-scattering (broken curve) and multiple-scattering (solid curve) calculations. An average over molecular orientations has been performed. (b): Scattering probability of 100-eV electrons from C_{60} molecules as a function of scattering angle calculated for various iteration steps (see labels) using the recursion method (solid curves) and direct Jacobi iteration (broken curves).

FIG. 8. Calculation of the LEED pattern of the Si(111)-(7 × 7) surface for 50-eV electrons coming along the surface normal. The surface structure factor S^2 (upper-left figure) has been obtained for the symmetry of the Si(111)-(7×7) surface and for a beam diameter of 100 Å. The envelope function I (lower-left figure, in logarithmic scale), which contains all the information about the atomic positions within a given surface unit cell as well as near-neighbor scattering, stands for the angular distribution of scattered electrons assuming that the first atomic scattering event occurs within the selected unit cell. The full LEED pattern (right figure, in linear scale) is obtained as the direct product of the structure factor and the envelope function [Eq. (38)]. The axis labels represent the components of the electron momentum parallel to the surface.

FIG. 9. Comparison of observed (upper figures, from Ref. [66]) and calculated (lower figures) LEED patterns for the Si(111)-(7 × 7) surface using two different electron energies: 50 eV (left) and 75 eV (right). The electron beam is coming perpendicular to the surface and it has a diameter of 100 Å. The axis labels represent the components of the electron momentum parallel to the surface. Some white lines have been drawn to guide the eye.

FIG. 10. (a)-(d): Calculated LEED patterns for a W(110) surface covered with one monolayer of Gd. The electron energy is 102 eV. The electron beam is coming along the surface normal and its diameter is 100 Å. (a): Schematic representation of model A for the structure with W (solid circles) and Gd (open circles) shown, leading to a large Moiré structure. (b): LEED intensity for model A. (c)-(d): Same as (a)-(b) for model B as shown in (c). The average over the geometry depicted in (c) and its mirror reflection with respect to the W[001] direction has been performed in (d). (f): Experimental result, taken from Ref. [68]. The axis labels represent the components of the electron momentum parallel to the surface. Some white lines have been drawn on the LEED images to guide the eye.

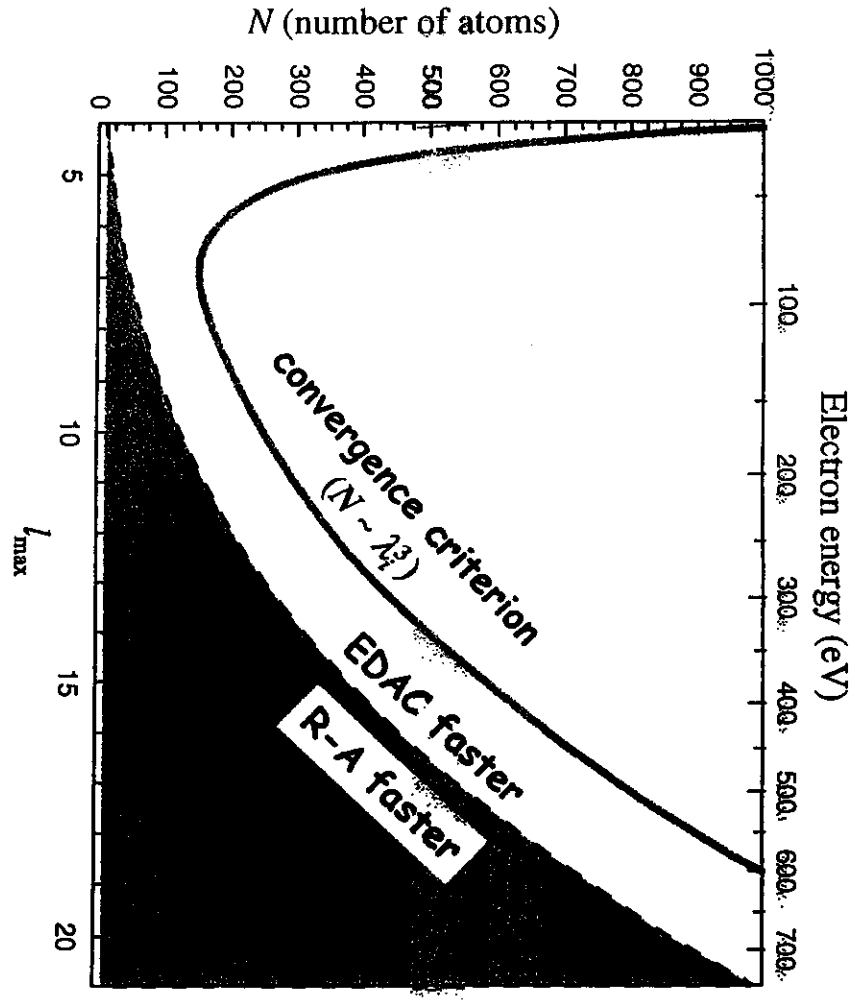

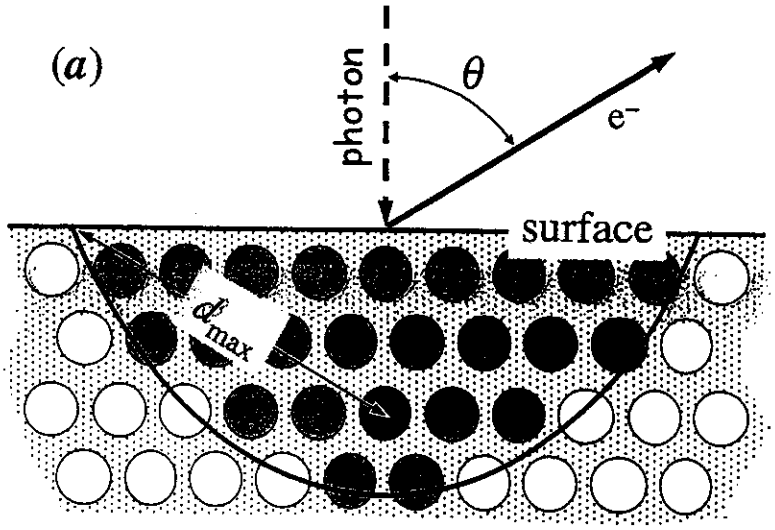
(a)
photon
θ
e⁻
surface
d_{max}

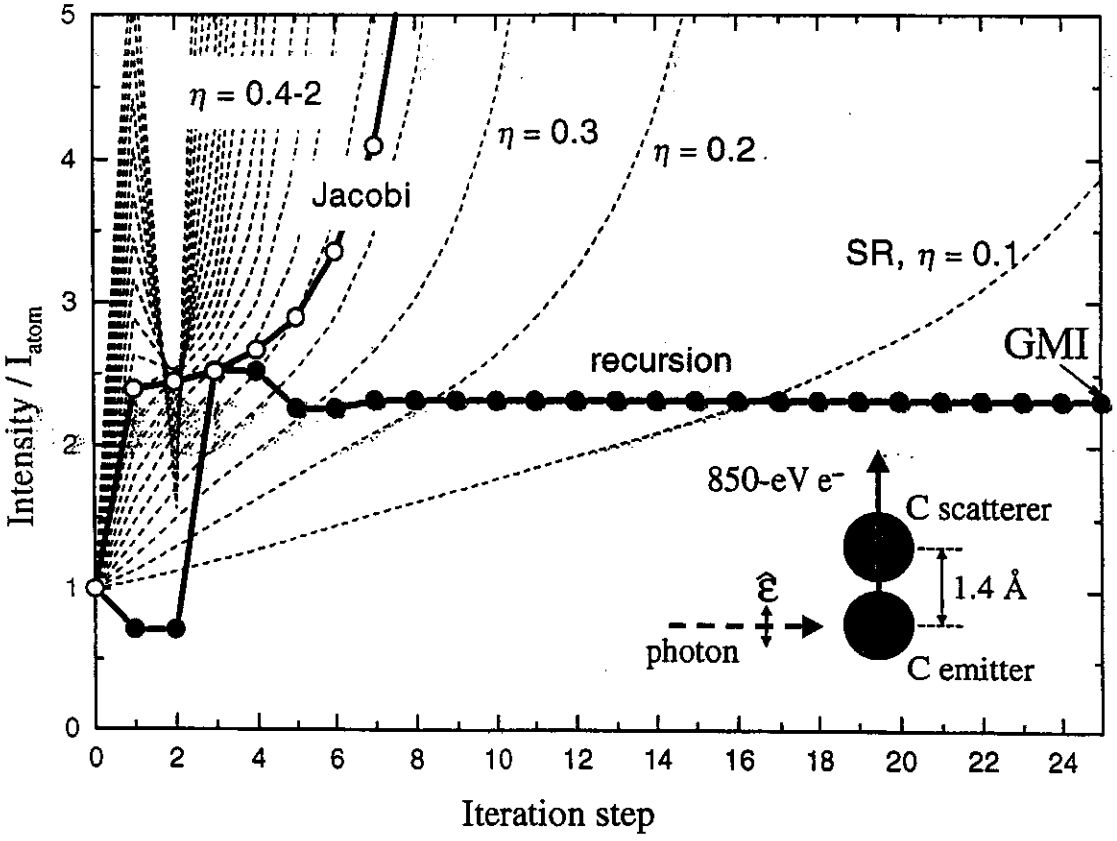
η = 0.4-2
η = 0.3
η = 0.2
Jacobi
SR, η = 0.1
recursion
GMI
850-eV e⁻
C scatterer
1.4 Å
photon
C emitter
Intensity / I_{atom}
Iteration step
0
1
2
3
4
5
0
2
4
6
8
10
12
14
16
18
20
22
24

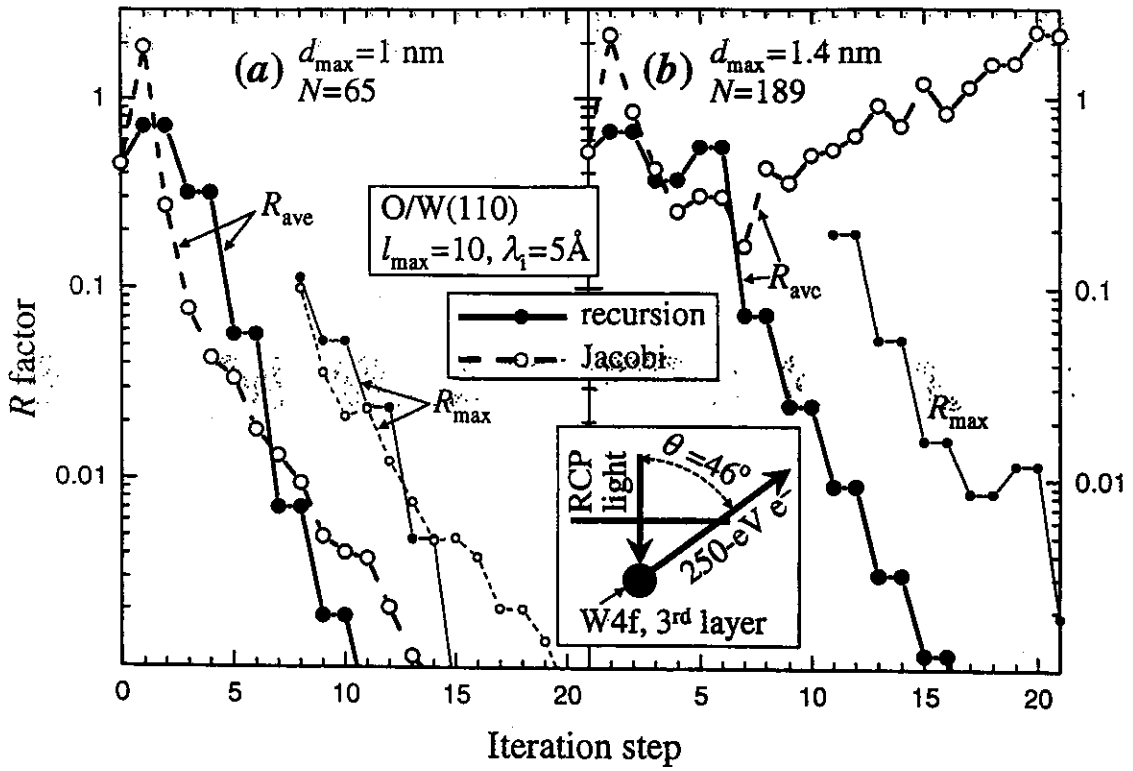
(a) d_{max}=1 nm
N=65
(b) d_{max}=1.4 nm
N=189
O/W(110)
l_{max}=10, λ_i=5Å
recursion
Jacobi
R_{ave}
R_{max}
RCP light
θ=46°
250-eV é
W4f, 3rd layer
R factor
Iteration step

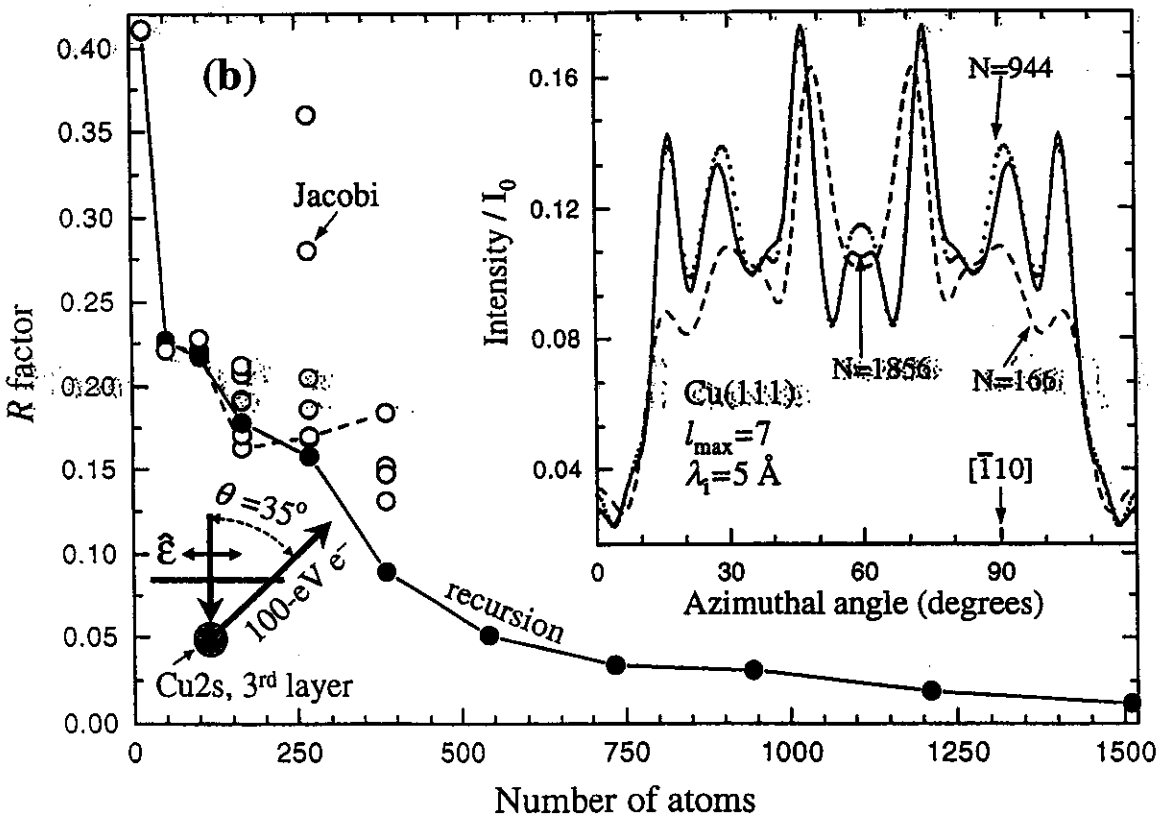
(b)
Jacobi
recursion
θ=35°
100-eV é
Cu2s, 3rd layer
R factor
Number of atoms
Intensity / I_0
N=944
N=1856
N=166
Cu(111)
l_{max}=7
λ_i=5 Å
[$\bar{1}$10]
Azimuthal angle (degrees)

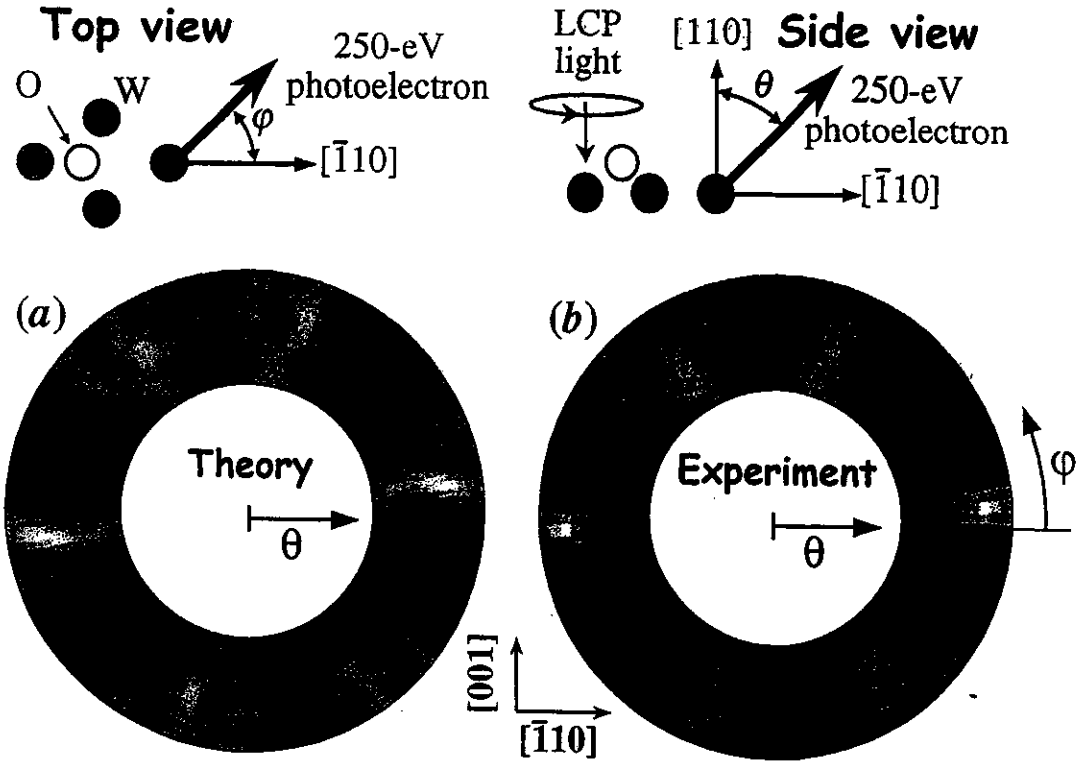
Top view
O
W
250-eV
photoelectron
φ
[1̄10]
LCP
light
[110]
Side view
θ
250-eV
photoelectron
[1̄10]
(a)
Theory
θ
(b)
Experiment
θ
φ
[001]
[1̄10]

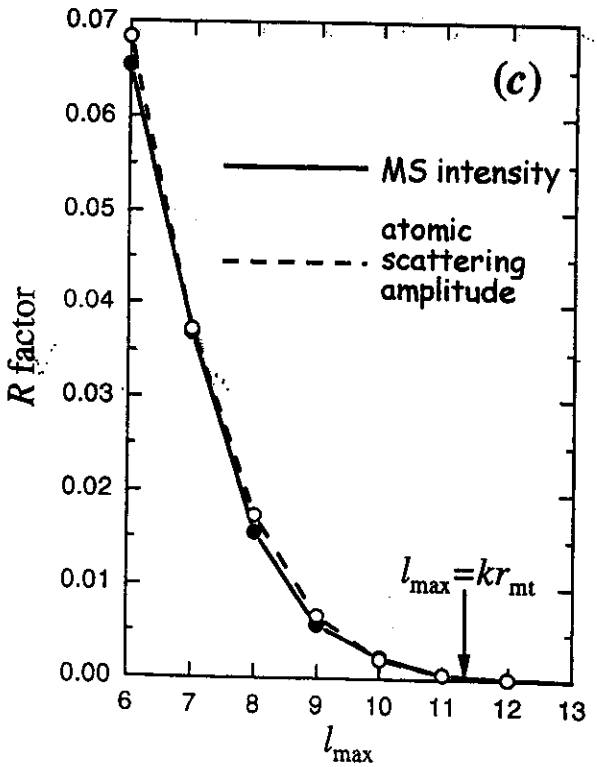
(c)
MS intensity
atomic
scattering
amplitude
R factor
$l_{max}=kr_{mt}$
0.07
0.06
0.05
0.04
0.03
0.02
0.01
0.00
6
7
8
9
10
11
12
13
l_{max}

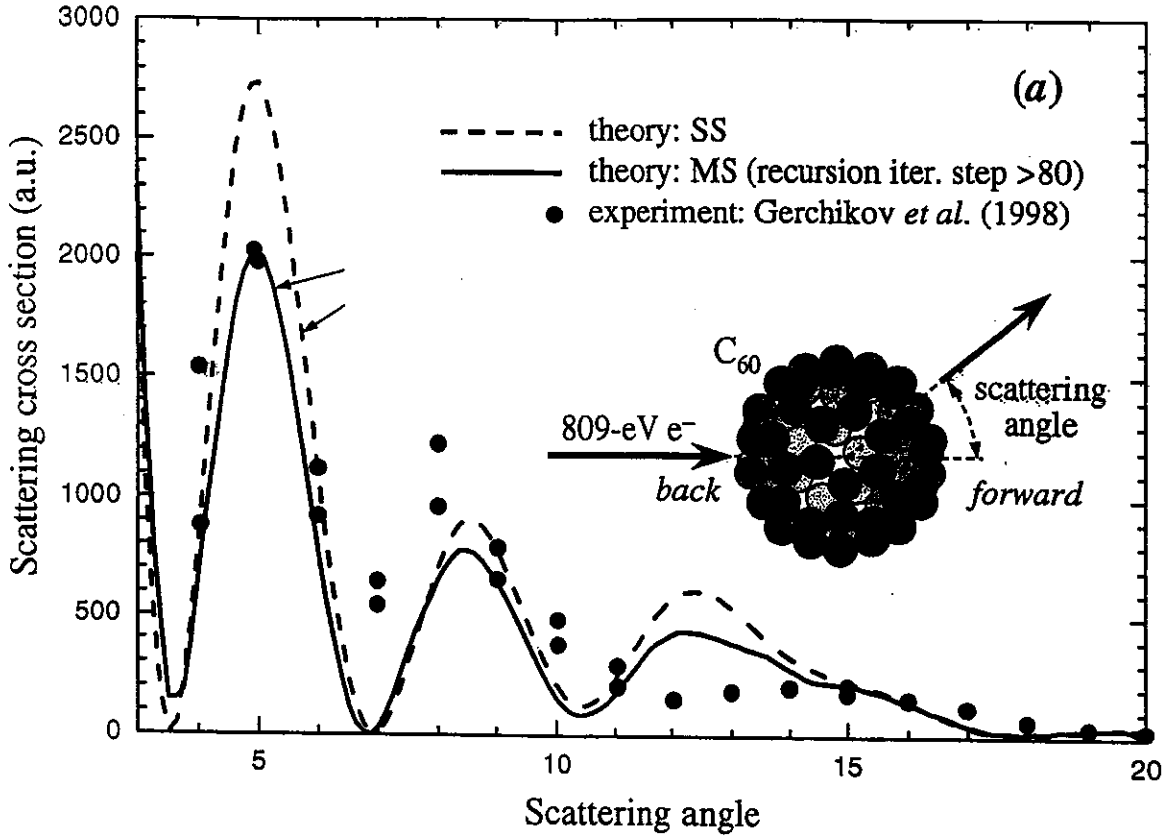
(a)
theory: SS
theory: MS (recursion iter. step >80)
experiment: Gerchikov et al. (1998)
C60
809-eV e⁻
back
forward
scattering angle
Scattering cross section (a.u.)
Scattering angle
3000
2500
2000
1500
1000
500
0
5
10
15
20

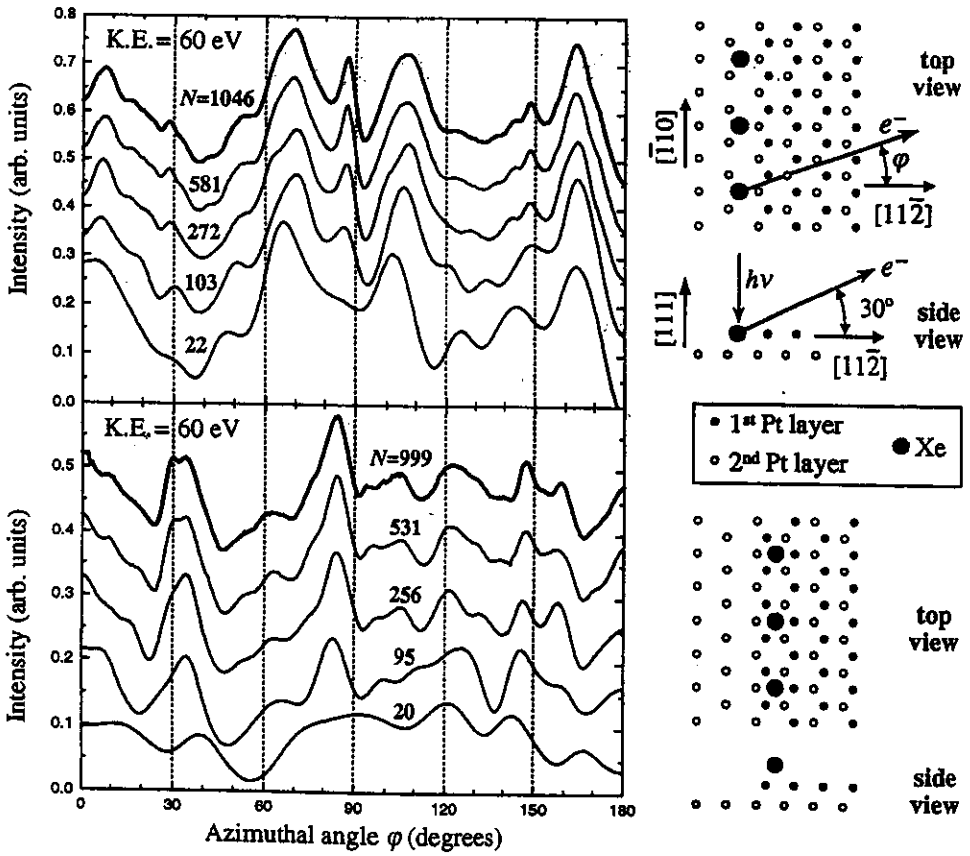
K.E.=60 eV
N=1046
581
272
103
22
K.E.=60 eV
N=999
531
256
95
20
Intensity (arb. units)
Azimuthal angle φ (degrees)
top view
side view
[1̄10]
[11̄2]
[111]
e⁻
hν
30°
φ
1st Pt layer
2nd Pt layer
Xe

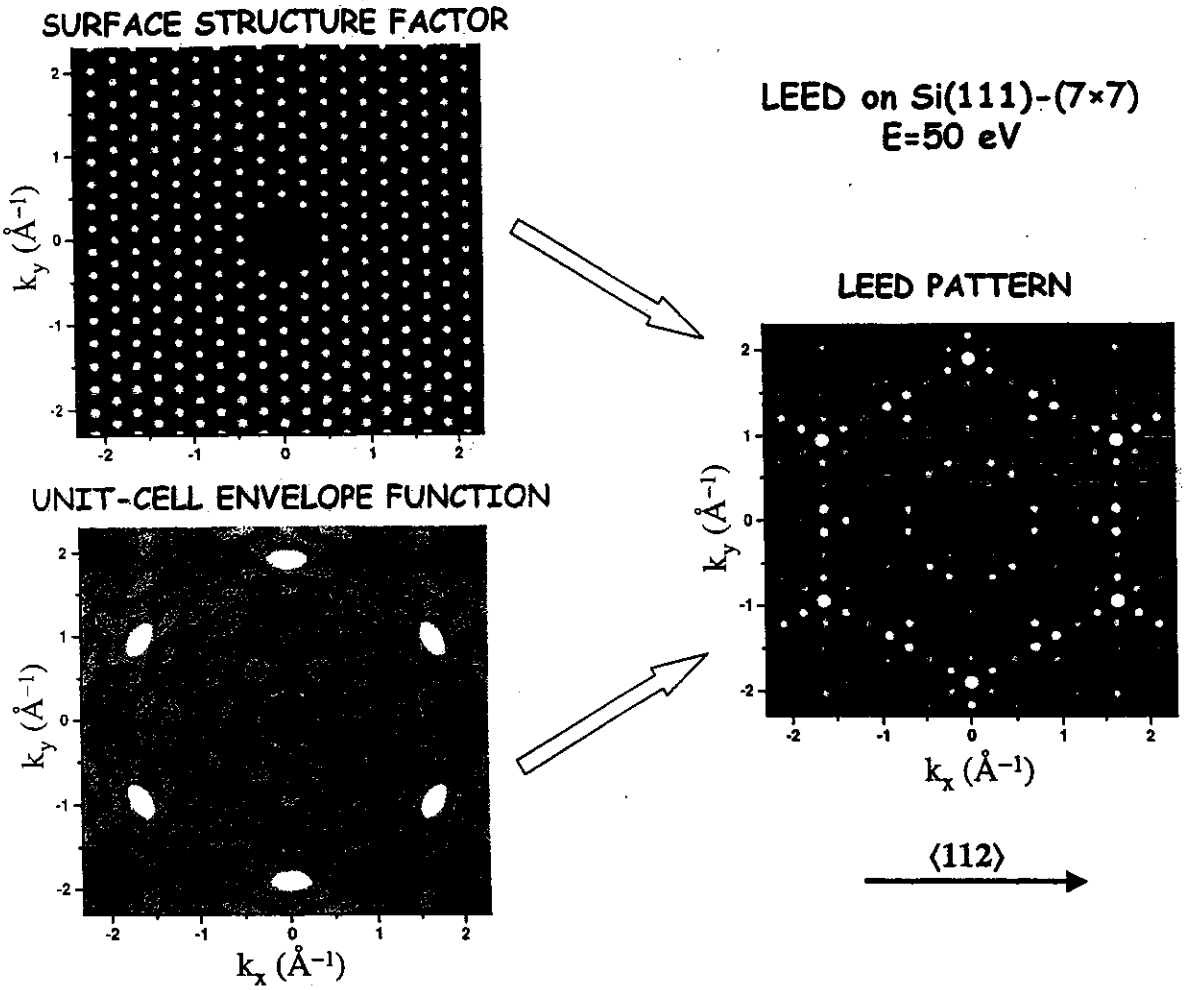
SURFACE STRUCTURE FACTOR
LEED on Si(111)-(7×7)
E=50 eV
LEED PATTERN
UNIT-CELL ENVELOPE FUNCTION
k_y (Å^{-1})
k_x (Å^{-1})
⟨112⟩

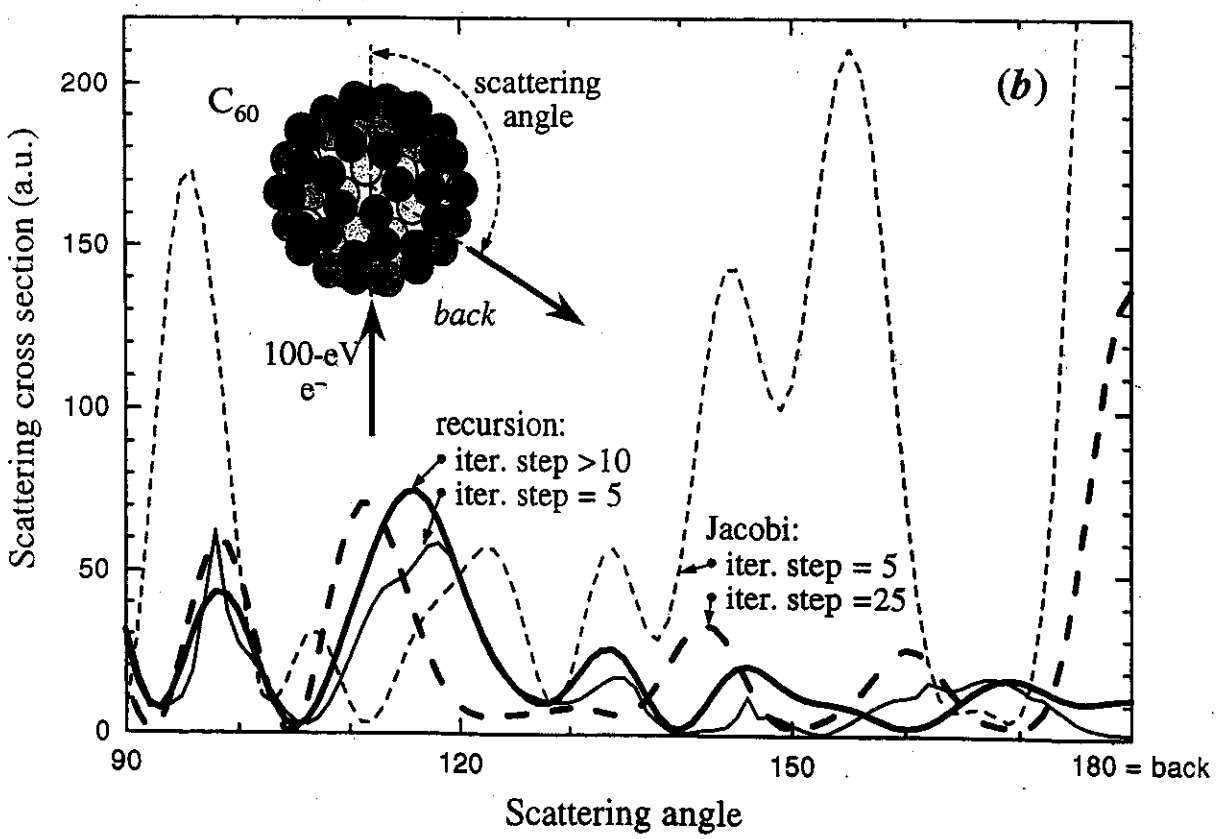
(b)
C_{60}
scattering angle
back
100-eV e⁻
recursion:
iter. step >10
iter. step = 5
Jacobi:
iter. step = 5
iter. step =25
Scattering cross section (a.u.)
Scattering angle
90
120
150
180 = back

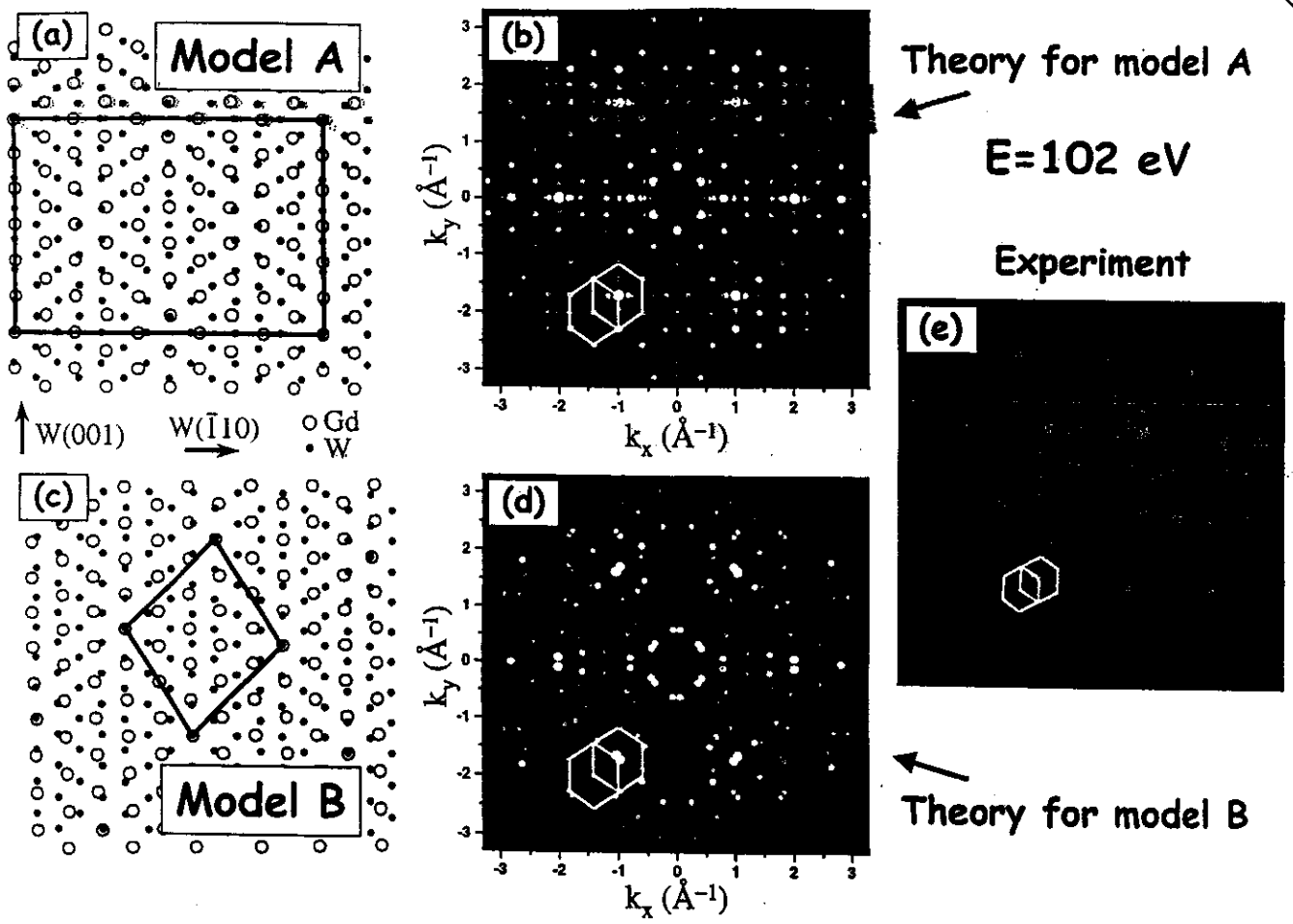
(a)
Model A
W(001)
W(1̄10)
Gd
W
(c)
Model B
(b)
(d)
k_y (Å^{-1})
k_x (Å^{-1})
Theory for model A
E=102 eV
Experiment
(e)
Theory for model B

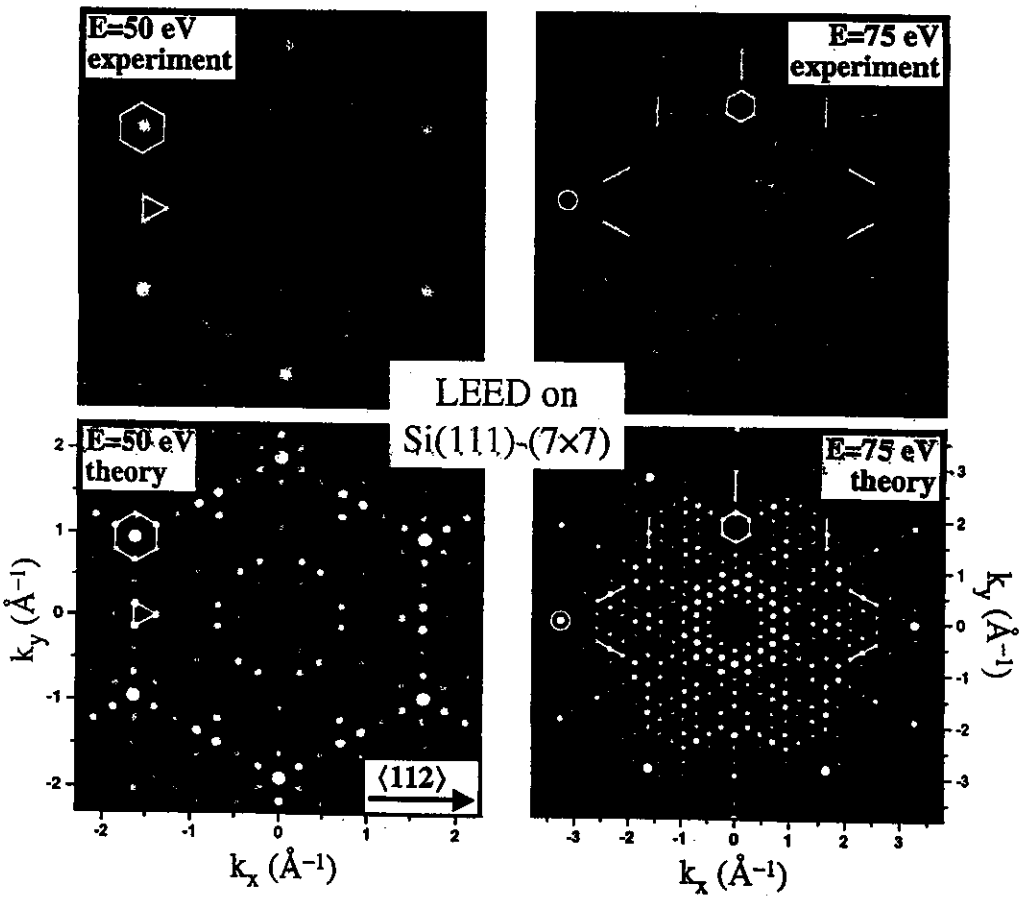
E=50 eV
experiment
E=75 eV
experiment
LEED on
Si(111)-(7×7)
E=50 eV
theory
E=75 eV
theory
⟨112⟩
k_y (Å^{-1})
k_x (Å^{-1})

Surface Review and Letters, Vol. 4, No. 2 (1997) 391–408

FERMI SURFACE MAPPING BY PHOTOEMISSION*

J. OSTERWALDER
Physik-Institut, Universität Zürich-Irchel,
Winterhurerstr. 190, CH-8057 Zürich, Switzerland

Received 13 March 1996

Angle-resolved ultraviolet photoelectron spectroscopy (ARUPS) data are usually measured spectrum by spectrum at various emission angles or photon energies in order to observe the dispersion of energy bands in solids and on their surfaces. In these lecture notes an alternative experimental procedure is described which yields a direct mapping of constant energy surfaces within the band structure, and specifically of the Fermi surface. This approach appears very promising, in particular when applied to magnetic systems and systems with narrow bands. Fermi surfaces of surface states are seen in direct relation to the underlying bulk Fermi surface.

1. Introduction

The shape and volume of the Fermi surface of a metal are intimately related to many of its physical properties.[1] It is therefore not surprising that some of the first precise measurements of the electronic structure of metals were carried out at their Fermi surfaces using the de-Haas–van-Alphen (dHvA) and related effects where the oscillatory behavior of some physical property, such as the magnetic susceptibility, is recorded as a function of the applied magnetic field. Extremal orbits on the Fermi surface within the plane perpendicular to the magnetic field direction are determined very accurately, and by combining the information on such orbits for many field orientations the whole Fermi surface can be reconstructed. Other Fermi surface probes have been developed since, using for example Compton scattering[2] or positron annihilation.[3] While these other techniques put much less stringent requirements on sample quality and temperature, they offer relatively limited resolution in k space. All these methods are volume-sensitive probes and provide no surface-related information.

In the meantime, angle-resolved ultraviolet photoelectron spectroscopy (ARUPS) has been developed into a powerful tool for studying occupied electronic bands also further away from the Fermi energy, providing both volume- and surface-sensitive information.[4] Early on, Fermi surface data from dHvA experiments were used for calibrating the absolute k locations of certain bands crossing the Fermi level. This calibration was found necessary as the photoelectron carries direct information on $k_\parallel$, the k component parallel to the surface, while its normal component $k_\perp$ is affected by the surface potential energy step, by details of the final state dispersion relation $E(k)$, and by the smearing associated with the short photoelectron escape depth.[4] On the other hand, it was soon realized that this technique provided access to the complete band structure, including the Fermi surface, of two-dimensional (2D) systems, including surface states, where $k_\parallel$ is the relevant quantum number. These latter experiments locate Fermi level crossings of energy bands in measured angle-resolved energy spectra in order to trace Fermi surface contours.[5]

*These lecture notes are based on experimental results obtained at the Université de Fribourg in collaboration with P. Aebi, R. Fasel and L. Schlapbach of the Institut de Physique, Université de Fribourg, and with T. J. Kreutz and P. Schwaller of the Physik-Institut, Universität Zürich.

Alternatively, a few groups have recently begun to map Fermi surfaces by measuring intensities of photoelectrons emitted from the Fermi edge as a function of emission angles relative to the crystal axes[6–12] and thus as a function of $k_\parallel$. In principle, the two experimental procedures for locating Fermi surface contours are equivalent: at those $k_\parallel$ positions where a band crosses the Fermi level, the photoemission intensity at the Fermi level rises sharply, contributing to the measured contour in the intensity map.

In this lecture this latter experimental technique will be introduced. The important test case of copper will be discussed, providing a simple and intuitive connection between the measured 2D contours and the well-known Fermi surface of 3D copper. Recent measurements on ferromagnetic nickel will be given and compared with Fermi surface data from dHvA experiments. Applications to 2D systems include high temperature superconductors, where the relevant conduction electrons are quasi-2D, and sp-derived surface states on Cu and Al surfaces.

2. Angle-Resolved Photoemission

The theory of angle-resolved photoemission has been excellently reviewed by Hüfner.[4] We limit our discussion here to a few simple concepts that are necessary in order to intuitively understand the Fermi surface mapping experiments. For conceptual simplicity we shall remain within the so-called three-step model, which describes the photoemission process as a sequence of (i) the photoexcitation of a band electron into an empty band, (ii) the propagation of this excited electron to the surface, and (iii) the transmission of this electron through the surface into the vacuum. We make the approximation of a free electron final state to describe the photoexcited electron within the solid, which often is a good starting point for the interpretation of ARUPS data.

In the photoexcitation process (i), energy and crystal momentum are conserved. For a given photon energy $h\nu$ and for an initial state with wave vector $\mathbf{k}_i$ and energy $E_i(\mathbf{k}_i)$, we thus have

$$E_f(\mathbf{k}_f) = E_i(\mathbf{k}_i) + h\nu\,, \qquad (1)$$

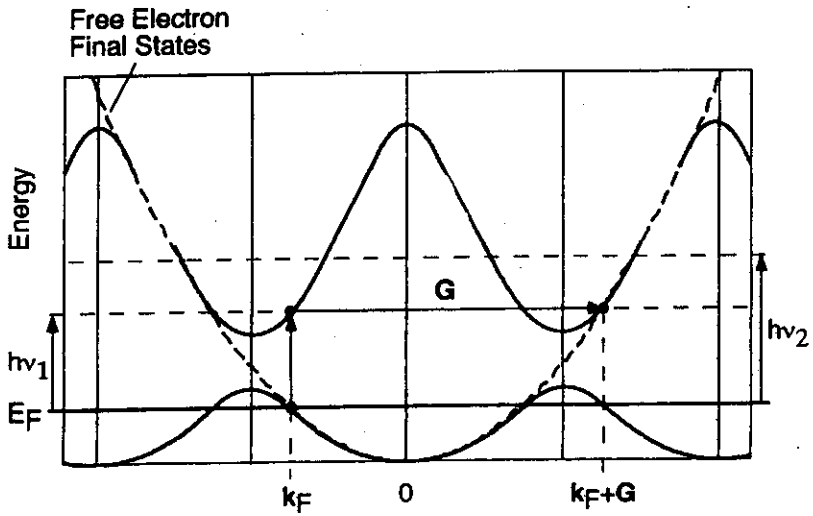

Fig. 1. Illustration of a direct transition (DT) from the Fermi surface of a solid. The band structure $E(k)$ (solid curves) is given in the repeated zone scheme while the free electron final state parabola (dashed curve) is drawn in the extended zone scheme. Along this particular direction of k there is a DT for the photon energy $h\nu_1$ and not for $h\nu_2$.

$$\mathbf{k}_f = \mathbf{k}_i + \mathbf{k}_{h\nu} + \mathbf{G}\,. \qquad (2)$$

For photon energies of the order of 20 eV the associated photon wave vector $\mathbf{k}_{h\nu}$ is not more than a percent of typical Brillouin zone dimensions and can thus be neglected in Eq. (2). The 3D reciprocal lattice vector G is needed in order to provide the momentum for the electron to escape from the crystal. These conservation laws imply that the dominant emission features appear as vertical or direct transitions (DT's) within the band structure of a solid, as is depicted in Fig. 1. If we now consider transitions from the Fermi surface only, we must find locations $\mathbf{k}_F$, where a band crosses the Fermi energy E_F, and which is separated vertically from some empty band by the photon energy used in the experiment. Figure 1 illustrates how such locations can be conveniently found by viewing the initial state band, and thus the Fermi surface, in the repeated zone scheme and the free electron final state parabola in the extended zone scheme. The figure also makes clear that these conservation laws put rather stringent conditions on k and that they can be fulfilled only along a few directions for a given photon energy. In order to provide an overview of where such transitions are to be expected in reciprocal space, Fig. 2 shows a planar section through k space parallel to the ($\bar{1}$10) plane of the face-centered cubic lattice of copper and containing the origin Γ. Brillouin zones are indicated and the Fermi surface is given in the repeated zone scheme. The large circles give the possible free electron wave vectors for the final states associated with two different photon energies, specifically He I (21.2 eV) and He II (40.8 eV) radiation. According to Fig. 1 direct transitions occur at intersections of these spheres with the Fermi surface. Since the free electron final state sphere and the Fermi surface represent intersecting hypersurfaces in 3D reciprocal space, we expect these locations to be sets of continuous lines. Figure 3 illustrates such a set of lines as one should observe for Fermi surface emission from a Cu(001) surface using He I radiation. Within the ($\bar{1}$10) plane shown in Fig. 2, there is no intersection as the final state falls into the well-known necks associated with the zone boundaries near equivalent L points. However, for emission planes other than that a Fermi level crossing should be observed, thus giving a rounded-square-like Fermi contour, and so providing a direct mapping of the Fermi surface.

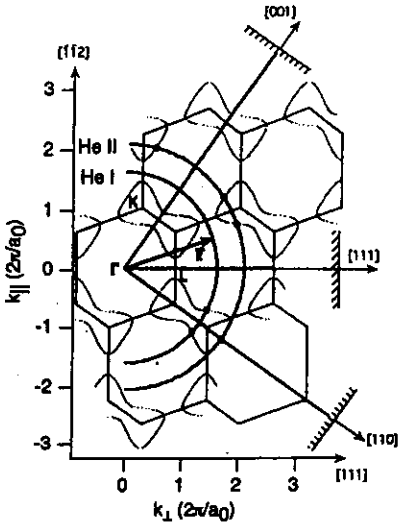

Fig. 2. High symmetry plane perpendicular to the [$\bar{1}$10] direction in the reciprocal lattice of copper. The solid polygons correspond to a section through the bulk Brillouin zones. Fermi surface sections are given by dotted curves. Large circles indicate free electron final states for He I and He II radiation (21.2 eV and 40.8 eV, respectively). The orientation of three low index surfaces is indicated.

We neglect the scattering processes that the excited electrons undergo while propagating to the surface in step (ii). They affect essentially the transition intensities and widths and not their positions. On the other hand we have to consider the refraction effects due to the surface potential energy step (iii). For a given photon energy $h\nu$, the measured kinetic energy E^m_{kin} of the electrons emitted from the Fermi level is given by

$$E^m_{kin} = h\nu - \Phi\,, \qquad (3)$$

where Φ is the work function of the sample. Inside the solid the kinetic energy of the same electrons is higher by an amount given by the inner potential V_0, i.e. the average attractive potential due to the Coulomb interaction with the ion cores and the other

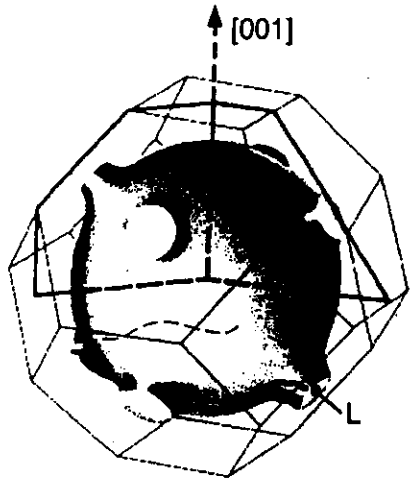

Fig. 3. 3D representation of the Fermi surface of copper, displaying the necks at equivalent L points. The solid and dashed curves near the bottom indicate the section measured at a photon energy of 21.2 eV.

valence electrons. We thus have

$$E_f(\mathbf{k}_f) = E^m_{kin} + V_0\,. \qquad (4)$$

Assuming free electron dispersion relations in both cases, i.e.

$$E_f(\mathbf{k}_f) = \frac{\hbar^2 \mathbf{k}_f{}^2}{2m}, \quad E^m_{kin} = \frac{\hbar^2 \mathbf{k}_m{}^2}{2m}, \qquad (5)$$

and considering the conservation of parallel momentum, one arrives at the equivalent of Snell's law of refraction (Fig. 4):

$$\sin\theta = \sin\theta_m \sqrt{\frac{h\nu - \Phi}{h\nu - \Phi + V_0}}\,. \qquad (6)$$

Here, θ_m is the polar angle relative to the surface normal under which the photoelectrons are detected while θ is the internal polar angle of the same electrons prior to leaving the surface. Values for V_0 and Φ can be found in the literature for many crystal surfaces. By taking E^m_{kin} according to Eq. (3) and by defining theelectron detection direction by the polar

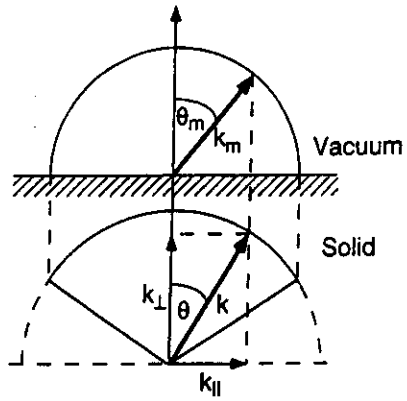

Fig. 4. Refraction at the surface potential step: photoelectrons have longer wave vectors inside the solid (larger circle) than outside. For periodic surfaces $\mathbf{k}_{\parallel}$ is strictly conserved.

angle θ_m (Fig. 4) and the azimuthal angle ϕ_m, one can thus determine, within this simplified model, absolute k positions inside the solid:

$$\mathbf{k} = \frac{1}{\hbar}\sqrt{2m(h\nu - \Phi + V_0)} \times(\sin\theta\cos\phi_m, \sin\theta\sin\phi_m, \cos\theta)\,, \qquad (7)$$

where ϕ_m is usually measured relative to some high symmetry direction of the crystal.

These concepts can be readily transposed to the case of a 2D system. In this case the initial states are defined by $\mathbf{k}_{\parallel}$ while we consider the same 3D free electron final states. Since $\mathbf{k}_{\parallel}$ is conserved rigorously and since the final state can pick up any amount of $\mathbf{k}_{\perp}$ needed from the underlying crystal — there is no quantization of $\mathbf{k}_{\perp}$ for a 2D system — the same intuitive picture arises if the Fermi surface is viewed as a prismatic hypersurface in 3D k space with the 2D Fermi surface as its base in the $\mathbf{k}_{\parallel}$ plane (Fig. 5). Obviously, one can here map the entire Fermi surface out to the refraction-corrected free electron sphere using a single photon energy, while one obtains only slices in the 3D case. However, using tunable synchrotron radiation for excitation, such slices can be measured for various sphere radii and the full Fermi

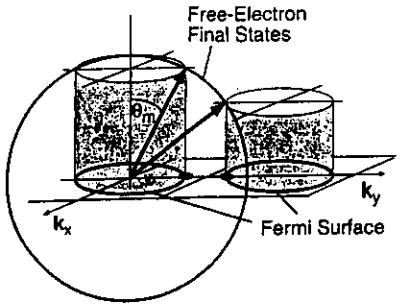

Fig. 5. Condition for the occurrence of a direct transition in k space for a 2D system: the Fermi surface is represented by a prismatic hypersurface in 3D k space. Free electron final states are indicated by the solid circle.

surface can in principle be constructed also for a 3D crystal.

3. Experimental Considerations

As outlined in the preceding section, mapping a Fermi surface consists in finding all those k vectors where direct transitions from the Fermi surface produce photoelectron intensities. In fact elastic and quasielastic electron–electron, electron–phonon and electron–defect scattering leads to non-k-conserving, so-called nondirect transitions[13] that produce intensities also away from the direct transitions, though usually much weaker. For a fixed photon energy the detected electron emission direction is swept over a large part of the hemisphere above the surface while the emission intensity at the Fermi level is monitored. Two different experimental approaches have been followed for this procedure. In the first Fermi surface mapping experiment presented by Santoni *et al.*,[8] a display type analyzer[14] was used for parallel detection of a large piece of solid angle. While this device permits a very efficient data collection with acquisition times of the order of a few minutes, it has certain limitations due to angular distortions, low signal-to-background ratios, detector inhomogeneities, and limited energy resolution by today's standards. The first three points make a set of careful calibration measurements necessary each time, which reduces somewhat the efficiency of this approach.

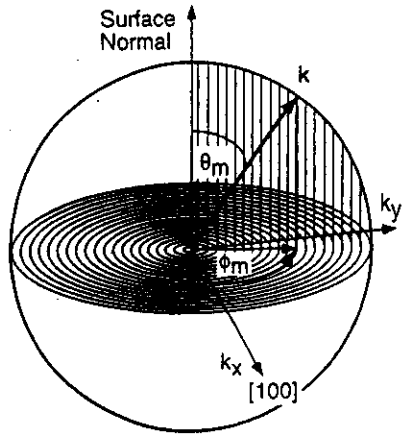

Fig. 6. Sequential angle-scanning mode for a mapping of $k_\parallel$ with a uniform sampling density by crystal rotation. Scanning starts at grazing emission angles and proceeds in an azimuthal fashion up to the surface normal, covering several thousand angular settings.

More accurate measurements have been carried out using a sequential data acquisition of one angle at a time. In this case a highly optimized angle- and energy-resolving electron detector can be used. The setup used in the University of Fribourg laboratory, from which all the data presented in these notes are taken, has a geometry in which this analyzer sits fixed in space while the sample is rotated so as to cover all emission directions relative to the crystal axes. The angle scanning is done by computer-controlled stepping motors that drive both a polar tilt axis and an azimuthal rotation of the sample about its normal. A sequence of azimuthal circles at decreasing polar angles (Fig. 6) has proven very successful, as each closing circle provides a consistency test for experimental stability and reproducibility.[15] A uniform sampling density in $k_\parallel$ is achieved by varying the polar step size with $1/\cos\theta_m$ and by increasing azimuthal steps with decreasing polar angle. Typically more than 4000 angles are sampled and mapped onto $k_\parallel$, with intensity values represented in a linear gray scale, with acquisition times being in the range of one to several hours. Even though

surface cleanliness is a concern with such measuring times, ultrahigh vacuum conditions in the low 10^{-11} mbar range have made it possible to study reactive systems such as Na layers on Al surfaces.[16] In this procedure the detection efficiency as well as the angular and energy resolution are completely uniform for the entire solid angle which is measured. Resolutions of $< 1°$ in angle and about 30 meV in energy are routinely achieved. The He discharge lamp can be maintained at stable conditions to within 5% for extended measuring times. Due to the low background intensities and the constant detection efficiency, even weak features on the Fermi surface can be observed.

One additional mode of operation could be to keep the sample fixed in space and to sweep a small angle-resolving analyzer across the emission hemisphere. In fact, this measuring mode for intensity mapping has been successfully applied to Auger electron diffraction,[17] and more recently also to Fermi surface mapping.[12] There is one principal difference between the fixed crystal (which is present also for the display type analyzer) and rotating crystal approaches: in the first case the light incidence is at a fixed angle relative to the crystal lattice, while in the second case it is at a fixed angle relative to the electron emission direction. In the latter case we expect the excitation matrix element to be constant for equivalent initial and final states, and the produced Fermi surface maps should thus present the full symmetry of the surface under study. As a matter of fact, if the light incidence is outside the plane swept by the surface normal (Fig. 7), mirror symmetries will be broken due to light polarization effects, as we shall see below. In the first case, with the light polarization residing fixed inside the crystal, very strong asymmetries are seen in the resulting images.[11] These asymmetries can provide information on the orbital character of the states on the Fermi surface, but they can also obscure its shape in unfavorable cases. Quite generally it can be said that any feature containing well-defined contours, regardless of their intensities, provides information on the location and shape of the Fermi surface. Caution is indicated if the used excitation radiation is not "clean," i.e. if weak satellites produce additional weak contours that are associated with a different photon energy.

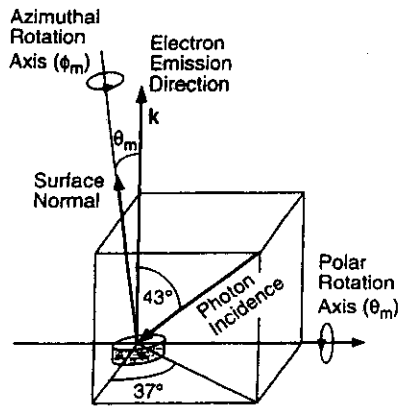

Fig. 7. Geometry of the experimental setup used for all data presented in this paper. Note that the photon incidence direction is outside the plane swept by the surface normal.

4. Three-Dimensional Systems

4.1. *Copper as a test case*

The Fermi surface of Cu is maybe the best studied of all solids and its dimensions and shape are well known from dHvA experiments[1,18] (see Fig. 3). Also, from the point of view of the photoemission experiment, Cu has the advantage of producing clean and nonreconstructed low index surfaces after standard preparation techniques, which remain stable for extended periods of time under ultrahigh vacuum conditions.

In Figs. 8(a)–8(c) we present Fermi surface maps from three differently oriented Cu surfaces, all taken at a photon energy of 21.2 eV.[8] As expected, we observe sets of well-defined, continuous lines for all three cases. Figure 9 illustrates, for one azimuthal trace of the measurement of Fig. 8(b) ($\theta_m = 66°$), how these lines of high emission intensities are actually formed by direct transitions moving through the Fermi level: the fast-dispersing sp band is occupied along the $[\bar{1}\bar{1}2]$ azimuth of the Cu(111) surface. Rotation away from this azimuth finds the

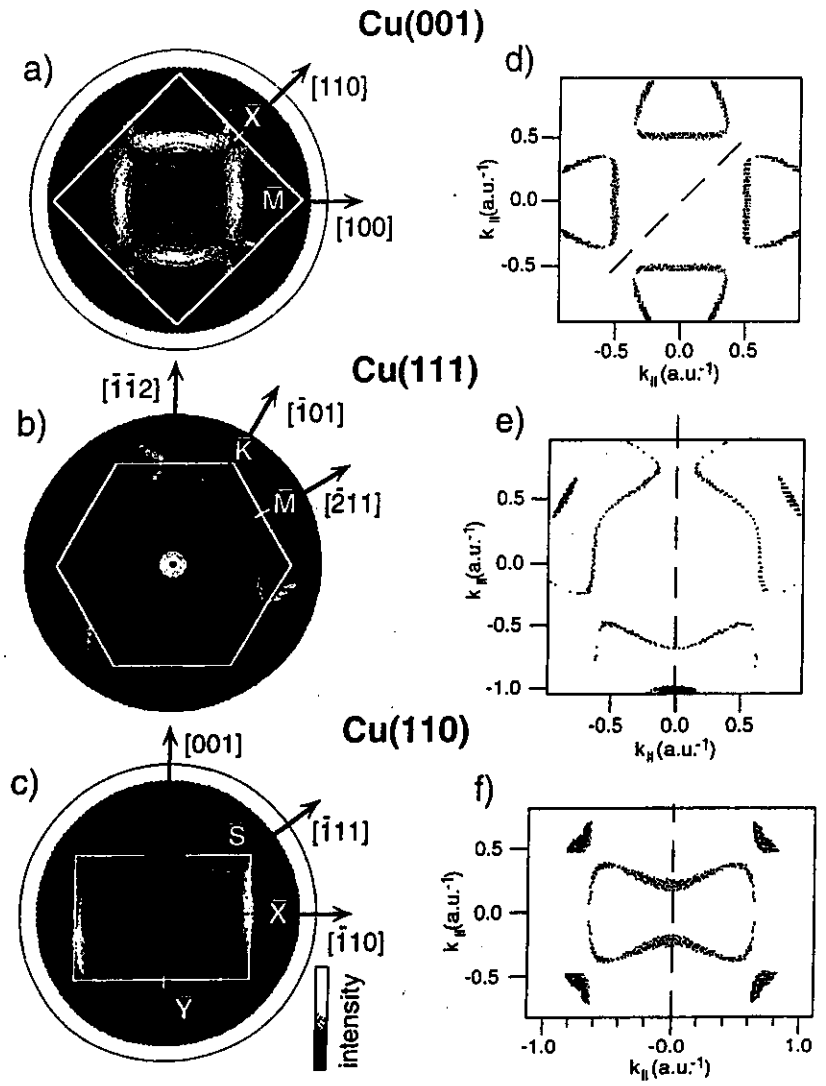

Fig. 8. Fermi surface maps from (a) Cu(001), (b) Cu(111) and (c) Cu(110). The different surface Brillouin zones (white lines) and high symmetry points and directions are indicated. Normal emission is at the center of each figure. (d)–(f) Calculated sections through the bulk Fermi surface using a free electron final state (see text). The dashed lines represent the plane shown in Fig. 2.

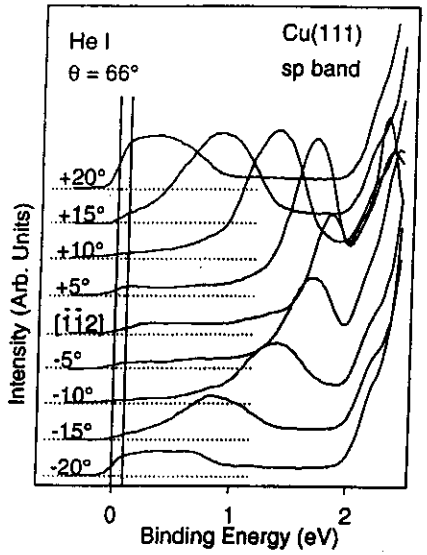

Fig. 9. He I excited energy spectra from Cu(111) at a polar angle of 66°. Azimuthal angles around the [1̄1̄2] direction are indicated. Vertical lines limit the energy window applied to the angle scans of Fig. 8.

transition moving towards E_F, where it crosses at some azimuthal angle. If the DT peak in the energy spectrum were infinitely sharp, this crossing would produce an equally sharp intensity rise at the crossing angles. As can be seen in Fig. 9, the energy peaks are by no means sharp delta functions but they are broadened, in this case by limited angle and energy resolution, or intrinsically by electron–phonon, electron–defect and electron–electron scattering.[19,20] Consequently, the Fermi level crossings will have some width as a function of the emission angle and thus in k space. It is clear that experimental energy and angular resolution are intimately interconnected by the band structure $E(\mathbf{k})$.

Now that we have seen the formation of Fermi contours, we have to establish the precision and reliability with which the real Fermi surface is represented by these contours when using free electron final states for data interpretation. For to this purpose we give in Figs. 8(d)–8(f) the results of a theoretical calculation for these contours. A Fermi surface of Cu was calculated using the layer Korringa–Kohn–Rostocker (LKKR) formalism, which is in good agreement with dHvA data. This Fermi surface was then intersected with the free electron final state sphere [the dashed lines indicate the (1̄10) plane of Fig. 2], which had previously been corrected for refraction effects (Fig. 4) in order to give a one-to-one comparison with the measured contours. In doing so, a value of 13.5 eV was taken for V_0 [21] and 4.7 eV for Φ. The agreement found in Fig. 8 for the main contours puts in evidence that this is a viable technique to obtain reliable Fermi surface information and that the free electron final state approximation is a very good starting point for accurate 3D k space mapping. It further appears that $\mathbf{k}_\perp$ is relatively well defined, otherwise the contours should be much more smeared out.

As mentioned earlier, photon polarization effects manifest themselves, for the given experimental configuration of Fig. 7, as asymmetries in contour intensities for k points that are otherwise related to each other by mirror symmetry operations. This phenomenon can be seen, for example in the data from the (111) surface [Fig. 8(b)], where the measurement touches the L-point necks at three places. Each time the intensity on the clockwise side of the neck is significantly weaker than it is on the counterclockwise side. Although the experiment has been carried out with unpolarized radiation, the oblique orientation of the photon incidence direction nevertheless means a tilt of the polarization plane with respect to the scattering plane, defined by the photoelectron emission direction and the surface normal. Clockwise rotation then moves the states near the neck further away from the polarization plane while the opposite sense moves them closer. Similar mirror-symmetry-breaking effects have been observed in core level photoelectron diffraction and Auger electron diffraction experiments.[22]

Besides the main contours seen both in experiment and in theory, the measured images show additional structure. Most prominently, there is a very bright small ring at the center of the surface Brillouin zone of the Cu(111) surface [Fig. 8(b)], which is absent in the calculations [Fig. 8(e)].

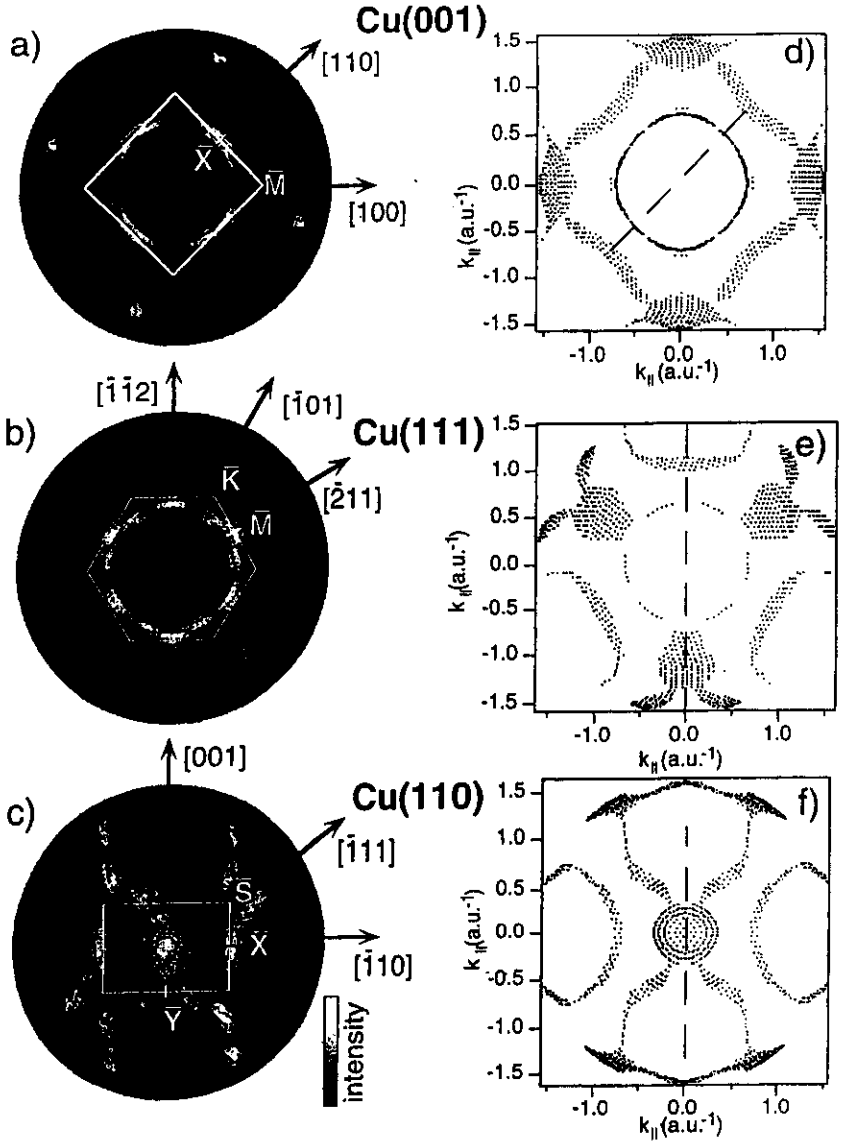

Fig. 10. Same as Fig. 8 but for excitation with He II radiation (40.8 eV).

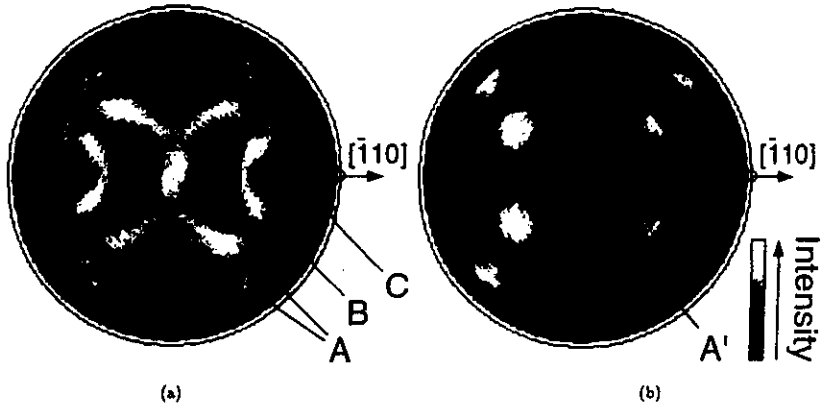

Fig. 11. (a) Room temperature Fermi surface map from Ni(110), excited with He I radiation and using an energy window of 30 meV centered at the Fermi energy. (b) Same as (a), but for a temperature of 700 K, which is above the critical temperature (631 K) of ferromagnetic nickel. Several features are marked by capital letters in order to facilitate their discussion.

This feature can be identified with the well-known Shockley type surface state.[23] It does not appear in the calculation which has been carried out considering bulk Bloch states only. Similar but much weaker surface state features are found near the $\bar{Y}$ point on the Cu(110) surface (see below). Additional structure can be found in the background region between the main contours. Some of this must be due to satellite contributions to the unmonochromatized He I radiation, others due to nondirect transitions. In fact a small step at E_F can be seen for all angles in Fig. 9, also away from the Fermi level crossings of the sp band.

In Figs. 10(a)–10(c) we give a similar presentation of measured FS contours from the same Cu surfaces, measured at a higher photon energy of 40.8 eV (He II). The corresponding final state sphere has been indicated in Fig. 2, and we give in Figs. 10(d)–10(f) again the calculated contours from intersecting it with the Fermi surface. Again, excellent agreement is found. A wider region in k space is accessible at this energy. Quite remarkably, in the Cu(110) measurement the final state sphere touches the Fermi surface in normal emission, producing an extended circular region of higher intensity, modulated by matrix element effects.

4.2. *Nickel, a magnetic case*

While the Fermi surface of Cu has been perfectly accessible with other techniques, Ni presents an interesting case where strong temperature effects are expected on the Fermi surface due to the phase transition from an itinerant ferromagnetic state below a critical temperature of $T_c = 631$ K to a paramagnetic state at higher temperatures. Clearly, dHvA or related experiments cannot be applied in this elevated temperature range as all scattering rates become prohibitively high. In such a situation, photoemission can play an important role in providing unique high resolution Fermi surface information.

A section through the room temperature Fermi surface of Ni, as viewed through the (110) surface analogous to the situation shown in Fig. 2, is given in Fig. 11(a).[24] Various pieces of Fermi surface are contained in this section. We illustrate two different procedures that can be applied to analyze such raw photoemission data when dealing with a less well-known Fermi surface, as is the case here. First we compare the experimental contours, like in the copper case, to calculated Fermi surface contours, now obtained using the spinpolarized LKKR formalism. In this case, Ni is in a ferromagnetic state and we have to consider the two spin systems

separately. The majority spin or spin-up system will have a Fermi surface composed of essentially sp-like states, because the d shell is filled for electrons with their spins aligned parallel to the sample magnetization. This part of the Fermi surface is indicated by blue contours in Fig. 12. The minority spin electrons contribute the red contours. Black regions correspond to k locations where the two Fermi surfaces overlap. Comparing now Figs. 11(a) and 12 we find an excellent agreement as to the positions of Fermi contours, thus providing us with a means for spin assignment of the measured features. Even the fine splitting of minority-and majority-related contours labled $\Sigma_1^\downarrow$ and $\Sigma_1^\uparrow$ in Fig. 12, which are of sp-like origin as a band structure calculation[25] tells us, can be clearly seen in the experimental data (feature C). This splitting becomes much more apparent in a section through these data along the [$\bar{1}$10] azimuth [Fig. 13(a)]: two intensity maxima are well separated with angular positions of 54.5° and 49.5°. The strong arc-shaped feature B is of minority d-like origin, while for feature A no clear spin assignment can be given from this comparison.

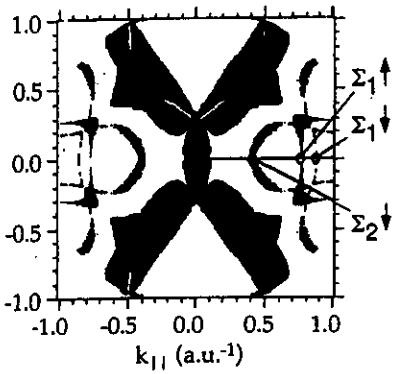

Fig. 12. Calculated section through the bulk Fermi surface of ferromagnetic nickel using the spin-polarized LKKR scheme for the initial state and a free electron final state. Majority spins are given in blue, minority spins in red. Overlapping regions appear in black.

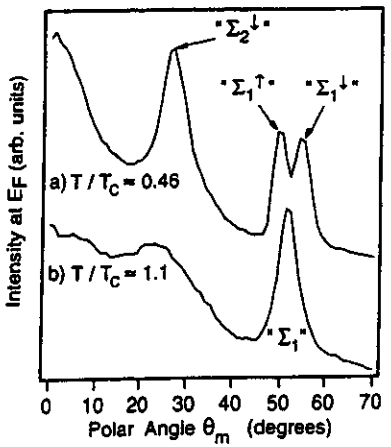

Fig. 13. (a) Polar section through the room temperature Fermi surface map of Fig. 11(a) along the [$\bar{1}$10] azimuth. (b) Same as (a) but for a temperature of 700 K.

An alternative method for analyzing this sort of data is to compare quantitatively some Fermi surface locations to existing low temperature dHvA measurements.[26] In order to do this, it is useful to project the measured Fermi surface sections, which intersect the final state sphere in the second Brillouin zone (Fig. 2), into the first zone. The procedure is as follows. Using Eqs. (6) and (7) for each intensity measurement $I(\theta_m, \phi_m)$ the corresponding k point inside the solid is calculated. The nearest reciprocal lattice vector G is then determined and subsequently subtracted from this k point, translating it into the first Brillouin zone. Figure 14 shows the image produced that way in the first zone. The measured data set now lies on a series of four spherical sectors, each sphere centered at some reciprocal lattice vector. As before, intensities are given in a linear gray scale, producing bright contours where the measurement surface intersects the Fermi surface. Figure 15 gives a section through this plot, showing one irreducible part of the Brillouin zone in the (001) plane. The measurement surface is indicated by the dashed circular line, and Fermi surface intersections by black ovals. The dHvA data[26] are given by open symbols. We find rather good, though not fully quantitative, agreement between the two techniques. Small deviations may arise due to the use of the free electron final state model, or maybe just because the two measurements were carried out at different temperatures. In any case this indicates the sort of accuracy that can be expected from these experiments given this simple level of interpretation.

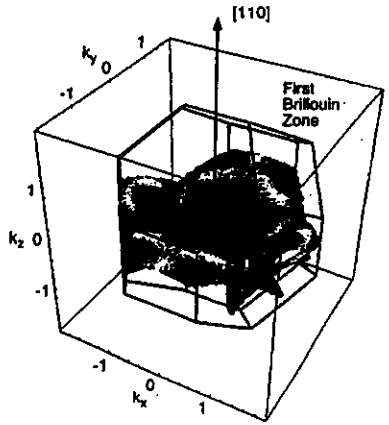

Fig. 14. 3D view of the Fermi surface map of Fig. 11(a) after projection into the first Brillouin zone. Note the reversed order in which the contours appear when moving from the zone center towards the boundaries as compared to Fig. 11(a).

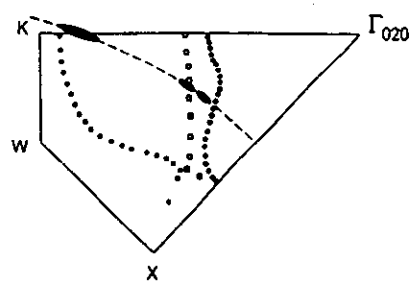

Fig. 15. Fermi surface cross sections of Ni in the (001) plane obtained from de-Haas-van-Alphen experiments (open symbols, from Ref. 26) compared to the data extracted from Fig. 14 (filled ellipses).

Apart from these possible systematic deviations due to this final state approximation, we shall discuss the question of k space resolution. The measured Fermi surface locations are given by black ovals of a size that represents the angular width of the corresponding contour in the measurement. As can be seen from Fig. 13, the two sp band transitions are significantly sharper than the minority d band transition ($\Sigma_2^\downarrow$). This difference may be attributed to the more grazing emission angles of the first two transitions. As mentioned earlier, there is some smearing-out associated with $k_\perp$ and essentially none with $k_\parallel$. Consequently, the more weight $k_\parallel$ has at a particular measuring angle, the better that particular k point is defined. This means that different sections of a Fermi surface can be measured with varying precision, depending on the crystal face of the solid one chooses for the photoemission experiment. One should also not forget that the group velocities of the initial state bands will play a role in the measaured contour width. For a flat band like the minority d band a certain energy spread in the detector window will cause a larger k smearing than for the steeper sp band.[19]

We now discuss the changes in the Fermi surface contours as the temperature is raised slightly above the critical point. Without entering much into the ongoing debate about the behavior of the exchange splitting between the two spin subbands, the intensity-versus-angle sections given in Fig. 13 show that the minority and majority contours associated with sp band emission coalesce near the critical temperature but remain otherwise as a well-defined feature in the Fermi contour plot of Fig. 11(b). The minority d band-related features A and B appear to merge, forming a rather extended region of high intensity in between them. There are two physical explanations for the occurrence of such bright regions. A first one we have encountered in the He II excited data from Cu(110) [Figs. 2, 10(c), 10(f)]: when the measuring sphere touches the Fermi surface glancingly, the direct transition condition is fulfilled for many k locations in an extended region. A similar situation can arise in cases where there is a very flat band, and thus a high density of states very near to the Fermi energy. It is not clear which of these two mechanisms is involved in the present case. Closer inspection of this region indicates, however, that some parts of the room temperature Fermi surface remain visible (feature A'), indicating at least partly the coexistence of spin-polarized and paramagnetic

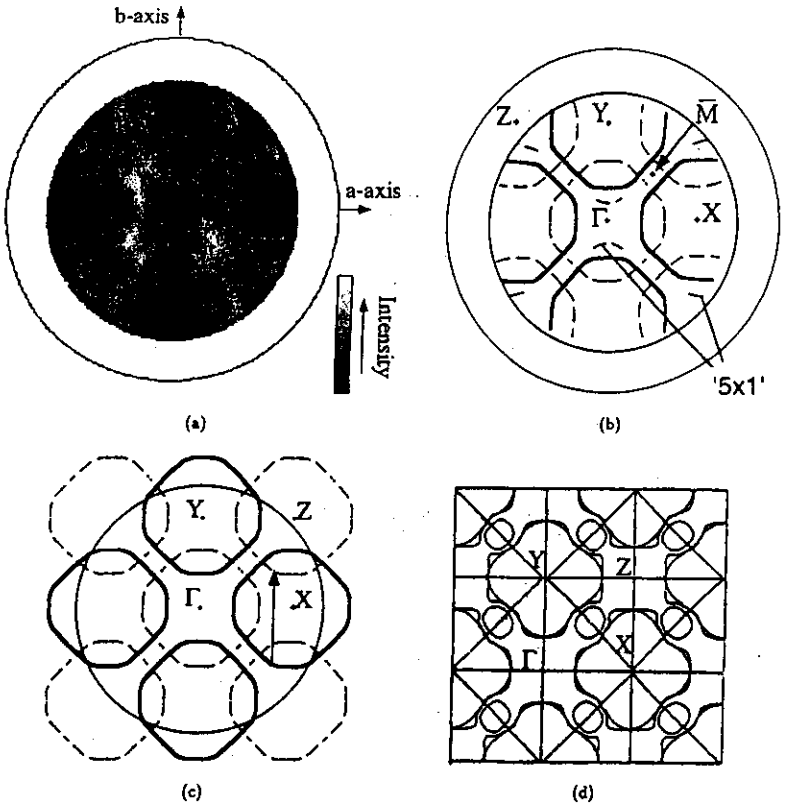

Fig. 16. (a) Fermi surface mapping of $Bi_2Sr_2CaCu_2O_{8+\delta}(001)$ using an energy window of 30 meV, centered at E_F. A logarithmic intensity scale is used for gray levels in order to enhance weaker features. (b) Outline of (a), emphasizing the fine lines observed in the measurement and distinguishing between the stronger (thick lines) and weaker (dashed lines) sets of contours. (c) This drawing shows how these lines have the symmetry of a c(2 × 2) superstructure. (d) For comparison, the calculated Fermi surface for this compound from Ref. 29.

bands in these Fermi surface contours above T_c. The significance of the kind of data presented here is that the information is on the Fermi surface directly, which should be closely linked with the driving force for the magnetic phase transition. In conjunction with theoretical models describing the temperature-dependent evolution of the band structure, these data should serve as an important benchmark, in addition to providing some intuitive idea as to the behavior of the various bands over an extended region in k space.

5. Two-Dimensional Systems

5.1. *$Bi_2Sr_2CaCu_2O_{8+\delta}$ high temperature superconductor*

Before addressing truly surface-related Fermi surface contours, we give a brief description of our

experiments on cuprate high temperature superconductors[9,27] which represent quasi-2D systems as far as the relevant electronic bands near the Fermi surface are concerned. $Bi_2Sr_2CaCu_2O_{8+\delta}$ crystals have a layered structure of alternating metal oxide planes.[28] They cleave nicely between two Van-der-Waals-bonded Bi–O planes. The bands forming the Fermi surface are constituted by states that are located on the two Cu–O planes separated by Ca atoms, and they are known to be essentially two-dimensional.[29]

Fermi surface contours have been constructed by Dessau *et al.*[30] by tracing, for various azimuthal directions ϕ_m, $k_\parallel$ locations where a dispersing peak crosses the Fermi level. This procedure relies on a detailed line shape analysis of the spectra near E_F. In these strongly correlated systems where the photoemission signal is composed of a dispersing quasiparticle peak and a large incoherent background, finding the exact crossing point is no simple task. We have therefore conducted Fermi surface mapping experiments on such samples. Complementary to the experiments by Dessau *et al.*,[30] this approach relies on the measurement of the absolute intensities at E_F, a quantity which is not exploited in their approach. Figure 16(a) shows the resulting intensity map. In order to enhance weaker features, intensities are here translated logarithmically into gray levels. Well-defined continuous lines are observed, with some minor but significant deviations from the result of Dessau *et al.* A Fermi surface calculation[29] for this same material [Fig. 16(d)] agrees very well with the most prominent subset of contours seen in the data. Specifically, the general shape of the Fermi surface is well reproduced in the calculation, and the position of the Fermi wave vector along the ΓX direction is quite accurate. On the other hand, the small circular contour halfway between Γ and Z, which the calculation attributes to hole pockets associated with the Bi–O planes, is not seen in the data. Whether it is not present in the bulk electronic structure of $Bi_2Sr_2CaCu_2O_{8+\delta}$, or whether it is solely absent in the surface layer Bi–O plane, cannot be resolved by this experiment. The first bulk like Bi–O plane is buried about 13 Å below the surface and hardly contributes to the measured photoemission intensities. Moreover, in the calculation two Cu–O bands contribute to the Fermi surface, leading to the split contours, especially around the Z point. Experimentally we find that the measured contours have a full width at half maximum in $k_\parallel$ of the order of 0.1 $Å^{-1}$, which is just about the maximum separation of the two bands at the Fermi level and which can thus hardly be resolved. We are here not limited by the angular or energy resolution of the experiment but by the intrinsic width of the features.

In addition to these strong Fermi surface contours, we observed additional features, some of which are due to a c(2 × 2) superstructure on the Fermi surface[9] [dashed lines in Fig. 16(c)] and others due to the quasi-(5 × 1) incommensurate lattice modulation[27] which is a structural peculiarity of these Bi cuprates. The observation of such superstructures may be important in understanding the normal state electronic structure of these materials and will not be discussed at this place. We emphasize, however, that these features had not been seen experimentally before, and that the visualization of photoemission intensities in this 2D fashion greatly enhances the sensitivity to weak extra features.

5.2. *sp surface states on Cu(111) and Cu(110)*

In the discussion of the Cu bulk Fermi surface mapping we have already pointed out that a surface state appears at the center of the surface Brillouin zone on the (111) surface [Fig. 8(b)]. In Fig. 17(a) we give a higher resolution map of this surface state, displaying clearly the free-electron-like circular shape. A polar section through these data shows the high signal-to-background ratio and the width of the surface Fermi surface contour, which is less than 3° full width at half maximum. The existence of this surface state is closely related to the gap in the surface-projected band structure associated with the necks around the L points. Similar gaps in $k_\parallel$ exist on the (110) surface, and a surface state has also been observed here.[31] Figure 17(c) gives a nice view of how this surface state, also rather circular in shape, is situated relative to the bulk Fermi surface contours. If one considers the projected band structure more closely, one finds that this state has already moved out of the projected band gap by the time it reaches the Fermi energy,[31] at least along the $\bar{\Gamma}\bar{Y}$ direction. Strictly speaking, the circular Fermi contours are thus associated with a surface resonance rather than with a true surface state. Translational symmetry within

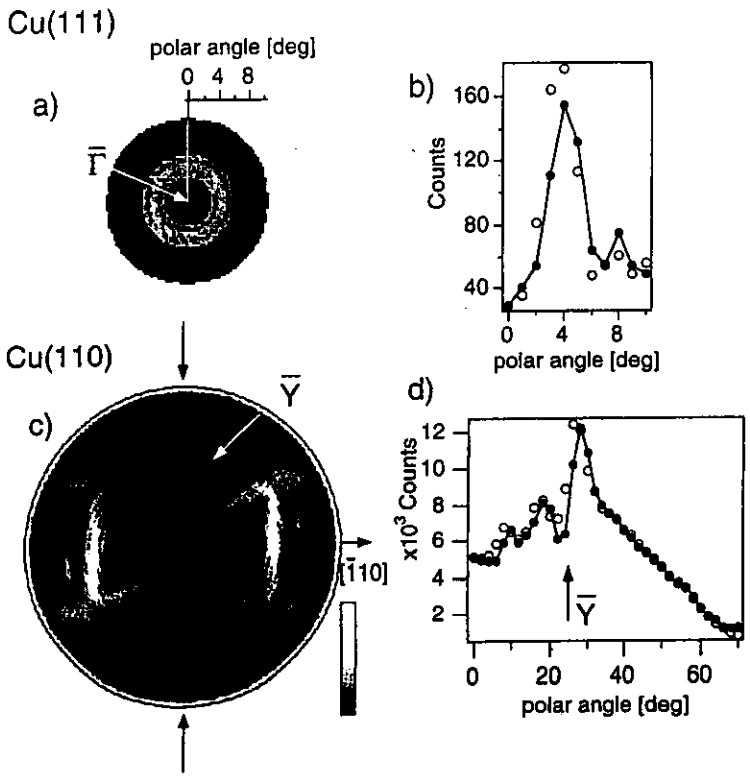

Fig. 17. (a) High resolution map (more than 2000 angular settings) of Fermi level intensities near the center of the surface Brillouin zone of Cu(111), showing the Shockley surface state. (b) Two polar sections through these data (open and closed circles) spaced by 180° in azimuth. (c) Fermi surface map from Cu(110) indicating the surface state centered at the $\bar{Y}$ point. (d) Sections through the data of (c) along the azimuths indicated by black arrows.

the (110) surface demands that this circle be centered precisely on the zone boundary. From this condition we can verify independently the accuracy of our k space mapping procedure. We know the exact location of the $\bar{Y}$ point relative to the $\bar{\Gamma}$ point, the distance being $\bar{\Gamma}\bar{Y} = \pi/a_0 = 0.87$ Å^{-1} ($a_0 = 3.61$ Å). From Eqs. (3) and (5) we obtain the relation

$$k_\parallel = \frac{1}{\hbar}\sqrt{2m(h\nu - \Phi)}\,\sin\theta_m = \bar{\Gamma}\bar{Y}\,. \qquad (8)$$

Taking the well-established work function value of 4.48 eV for Cu(110) obtained from photoemission cutoff measurements,[32] we arrive at a polar angle of $\theta_m = 24.5°$ for $\bar{Y}$. Figure 17(d) providing a polar section along the $\bar{\Gamma}\bar{Y}$ direction, indicates that we ovserve the center of the surface state at a slightly smaller polar angle of 22±1°.

5.3. *sp surface state on Al(001)*

A similar sp-derived surface state has been observed on Al(001).[33] In this case the maximum binding energy is 2.75 eV, while it was only 0.4 eV in the case of the Cu sp surface states. Its Fermi surface

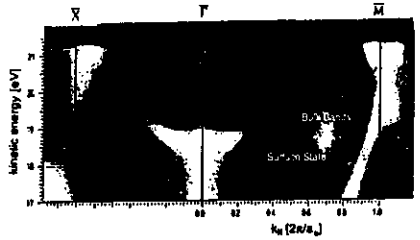

Fig. 18. Series of energy spectra from clean Al(001), representing polar scans along the [100] azimuth ($\bar{\Gamma}\bar{M}$) and the [110] azimuth ($\bar{\Gamma}\bar{X}$). The presentation is in a linear gray scale with low intensities in black and high intensities in white. Surface and bulk transitions are indicated.

will therefore cover a much larger area in $k_\parallel$, and it should be interesting to see how it interacts with various bulk bands. Figure 18 shows the highly parabolic dispersion of this state, which can be well fitted with an effective mass of $m^* = 1.18m_e$, in excellent agreement with earlier data.[33,34] This plot represents a series of spectra measured on a dense grid of polar angles along the $\bar{\Gamma}\bar{X}$ and $\bar{\Gamma}\bar{M}$ directions which have been mapped onto $k_\parallel$ according to

$$k_\parallel = \frac{1}{\hbar}\sqrt{2m(h\nu - E_B - \Phi)}\,\sin\theta_m\,, \qquad (9)$$

where E_B is the measured binding energy within the spectra. Intensities are given in a linear gray scale much like it is done in the Fermi surface maps, providing a very direct representation of the dispersion.[35] Even though emission from the surface state becomes rather weak away from the $\bar{\Gamma}$ point, this sort of plot permits a clear tracing of the dispersion and of the Fermi level crossing which occurs at 0.60 in units of $2\pi/a_0$.

A Fermi surface map is given in Fig. 19, measured with He I radiation. while the Fermi contours are here much more complex than in Cu, an intuitive understanding of all features is still possible within the simple framework discussed earlier. Figure 20 gives a schematic view of the situation in k space, along the $\bar{\Gamma}\bar{M}$ direction, i.e. within the (100) plane. A simplified free electron Fermi surface for Al is plotted centered about four reciprocal lattice points which are relevant to this geometry. We neglect here the

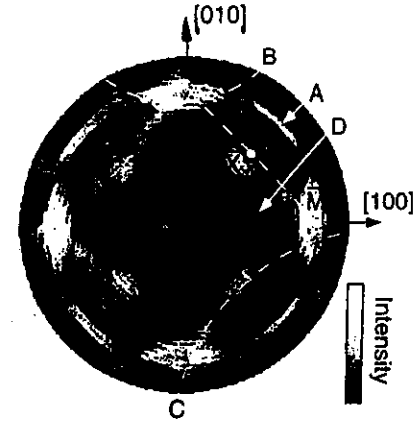

Fig. 19. Fermi surface map from clean Al(001). Several features are emphasized by dashed curves in one of the four symmetry-equivalent places and marked by capital letters. The boundary of the surface Brillouin zone is given at one place by the straight dashed line.

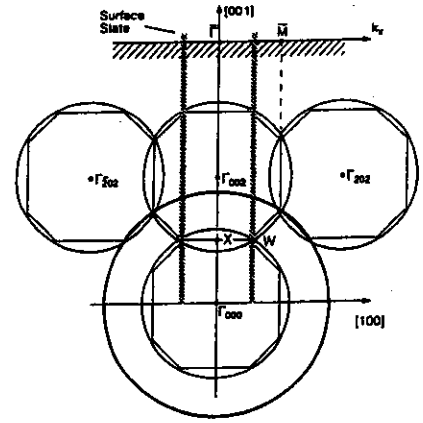

Fig. 20. Section through the reciprocal lattice of Al parallel to the (010) plane, analogous to Fig. 2. The bulk Brillouin zones are given by the polygons, and the idealized free electron Fermi surface of Al is draw around four reciprocal lattice points. The large circle represents the final states for He I excitation. The location of the surface surface state is indicated by the hatched bars.

effects of the lattice potential on the Fermi surface, since we just want to be able to give an assignment to the various measured contours. Like in Fig. 2, a free electron final state for excitation with He I radiation is also given, which here reaches further out due to the smaller Brillouin zone dimensions in Al as compared to Cu. We can now immediately understand the large circular contour A in the data as being due to the intersection with the Γ_{002}-centered Fermi sphere. The Γ_{202} spheres give rise to the arc-shaped contours B, while the Γ_{111} spheres (not shown in Fig. 20) produce the four symmetry-related arcs C. Most of the observed contours are readily accounted for in this simple picture. The surface state appears as a weak circular contour D touching the bulk bands in the $\overline{\Gamma X}$ directions. The corresponding regions of $k_{\parallel}$ are indicated in Fig. 20. This figure suggests that the state might actually be associated with a small gap at the W points and thus be a true surface state even at the Fermi energy. In other directions, especially along $\overline{\Gamma X}$, the $k_{\parallel}$ values would pass near the U points of the bulk Brillouin zone where there is no gap at E_F. This contour D comprises thus both true surface states and surface resonances.

6. Conclusions and Outlook

The examples presented in these notes demonstrate that this new approach to the photoemission experiment provides a very powerful tool for mapping Fermi surfaces directly. It can be applied to any material that can be prepared in single crystalline form of a few mm^2 surface area and thickness down to atomic monolayers. 3D and 2D systems can be measured. Given the wide open parameter space accessible by photoemission experiments (temperature, concentrations, film thickness, dimension (2D $\rightarrow$ 3D), etc.) this technique should be particularly useful for studying phase transitions and their interrelation with the Fermi surface.[36]

While the positions of the Fermi surface contours are well explained within the simple free electron final state model, there is now also a growing understanding of the intensity variations along the contours. A more sophisticated final state wave function is needed here, which takes into account the angular momentum character of the photoelectron wave and the elastic scattering within the surface region.[7,37,38] Finally, the analysis of the widths of such contours might be of considerable interest in studying low energy excitations in correlated systems. The analysis of line widths in energy spectra has attracted a great deal of attention in this context.[19] Very recently we have shown that in momentum space such line widths can be extracted more precisely due to a simpler line shape and a better-defined background.[39,40] It should be mentioned that other constant energy surfaces below the Fermi surface can be measured equally well, such that all the studies discussed here can be extended to higher binding energies.[27,41]

References

1. N. W. Ashcroft and N. D. Mermin, *Solid State Physics* (Holt, Rinehart and Winston, New York, 1976).
2. R. Ribberfors, *Phys. Rev.* **B12**, 3136 (1975).
3. S. Berko, in *Momentum Densities*, eds. R. N. Silver and P. E. Sokol (Plenum, 1989).
4. S. Hüfner, *Photoelectron Spectroscopy* (Springer, Berlin, 1995).
5. R. H. Gaylord, K. Jeong and S. D. Kevan, *Phys. Rev. Lett.* **62**, 203 (1989).
6. A. Santoni, L. J. Terminello, F. J. Himpsel and T. Takahashi, *Appl. Phys.* **A52**, 229 (1991).
7. J. Osterwalder, A. Stuck, T. Greber, P. Aebi, L. Schlapbach and S. Hüfner, in *Proc. 10th Vacuum Ultraviolet Radiation Physics*, eds. F. J. Wuilleumier, Y. Petroff and I. Nenner (World Scientific, Singapore, 1993), p. 475.
8. P. Aebi, J. Osterwalder, R. Fasel, D. Naumovic and L. Schlapbach, *Surf. Sci.* **307–309**, 917 (1994).
9. P. Aebi, J. Osterwalder, P. Schwaller, L. Schlapbach, M. Shimoda, T. Mochiku and K. Kadowaki, *Phys. Rev. Lett.* **72**, 2757 (1994).
10. R. Leckey and J. Riley, *Aust. J. Phys.* **48**, 217 (1995).
11. Zhe Qu, A. Goonewardene, K. Subramanian, J. Karunamuni, N. Mainkar, L. Ye, R. L. Stockbauer and R. L. Kurtz, *Surf. Sci.* **324**, 133 (1995).
12. J. Avila, C. Casado, M. C. Asensio, J. L. Perez, M. C. Munoz and F. Soria, *J. Vac. Sci. Technol.* **A13**, 1501 (1995).
13. S. Doniach, *Phys. Rev.* **B2**, 3898 (1970); N. J. Shevchik, *Phys. Rev.* **B16**, 3428 (1977).
14. D. E. Eastman, J. J. Donelon, C. Hien and F. J. Himpsel, *Nucl. Instrum. Methods* **172**, 327 (1980).
15. J. Osterwalder, T. Greber, A. Stuck and L. Schlapbach, *Phys. Rev.* **B44**, 13764 (1991).
16. R. Fasel and J. Osterwalder, *Surf. Rev. Lett.* **2**, 359 (1995).
17. D. G. Frank, N. Battina, R. Golden, F. Lu and A. T. Hubbard, *Science* **247**, 182 (1990).

18. D. Shoenberg and D. J. Roaf, *Phil. Trans. Roy. Soc.* **225**, 85 (1962).
19. N. V. Smith, P. Thiry and Y. Petroff, *Phys. Rev.* **B47**, 15476 (1993).
20. B. A. McDougall, T. Balasubramaian and E. Jensen, *Phys. Rev.* **B51**, 13891 (1995).
21. J. B. Pendry, *Low Energy Electron Diffraction* (Academic London, 1974), p. 23.
22. T. Greber, J. Osterwalder, S. Hüfner and L. Schlapbach, *Phys. Rev.* **B45**, 4540 (1992).
23. P. O. Gartland and B. J. Slagsvold, *Phys. Rev.* **B12**, 4047 (1975).
24. P. Aebi, T. J. Kreutz, J. Osterwalder, R. Fasel, P. Schwaller and L. Schlapbach, *Phys. Rev. Lett.* **76**, 1150 (1996).
25. H. Eckardt and L. Fritsche, *J. Phys.* **F17**, 925 (1987).
26. Unpublished results of Stark; see C. S. Wang and J. Callaway, *Phys. Rev.* **B9**, 4897 (1974).
27. J. Osterwalder, P. Aebi, P. Schwaller, L. Schlapbach, M. Shimoda, T. Mochiku and K. Kadowaki, *Appl. Phys.* **A60**, 247 (1995).
28. A. Yamamoto, M. Onoda, E. Takayama-Muromachi, F. Izumi, T. Ishigaki and H. Asano, *Phys. Rev.* **B42**, 4228 (1990).
29. S. Massidda, Jaejun Yu and A. J. Freeman, *Physica (Amsterdam)* **C158** 251 (1988).
30. D. S. Dessau, Z.-X. Shen, D. M. King, D. S. Marshall, L. W. Lombardo, P. H. Dickinson, A. G. Loeser, J. DiCarlo, C.-H. Park, A. Kapitulnik and W. E. Spicer, *Phys. Rev. Lett.* **71**, 2781 (1993).
31. P. Heimann, J. Hermanson, H. Miosga and H. Neddermeyer, *Surf. Sci.* **85**, 263 (1979).
32. *CRC Handbook of Chemistry and Physics*, eds. R. C. Weast and M. J. Astle (CRC, Boca Raton, 1980), p. E-82.
33. P. O. Gartland and B. J. Slagsvold, *Solid State Commun.* **25**, 489 (1978); G. V. Hansson and S. A. Flodstrom, *Phys. Rev.* **B18**, 1562 (1978).
34. H. J. Levinson, F. Greuter and E. W. Plummer, *Phys. Rev.* **B27**, 727 (1983).
35. R. Fasel, P. Aebi, R. G. Agostino, J. Osterwalder and L. Schlapbach, *Phys. Rev.* **B54**, 5893 (1996).
36. S. D. Kevan, *Surf. Sci.* **307–309**, 832 (1994).
37. E. L. Shirley, L. J. Terminello, A. Santoni and F. J. Himpsel, *Phys. Rev.* **B51**, 13614 (1995).
38. H. Daimon, S. Imada, H. Nishimoto and S. Suga, *J. Electron Spectrosc. Relat. Phenom.* **76**, 487 (1996).
39. T. J. Kreutz, P. Aebi and J. Osterwalder, *Solid. State Commun.* **96**, 339 (1995).
40. P. Schwaller, P. Aebi, H. Berger, C. Beeli, J. Osterwalder and L. Schlapbach, *J. Electron Spectrosc. Relat. Phenom.* **76**, 127 (1996).
41. T. J. Kreutz, J. Osterwalder and L. Schlapbach, *J. Electron Spectrosc. Relat. Phenom.* **76**, 601 (1996).